University of Southampton

Faculty of Natural and Environmental Sciences

School of Ocean and Earth Sciences

National Oceanography Centre

DETERMINING THE PROVENANCE, RECURRENCE, MAGNITUDES AND FAILURE MECHANISMS OF SUBMARINE LANDSLIDES FROM THE MOROCCAN MARGIN AND CANARY ISLANDS USING DISTAL TURBIDITE RECORDS

by

James Edward Hunt

Thesis submitted for the degree of Doctor of Philosophy

May 2012

Graduate School of the
National Oceanography Centre, Southampton

This Ph.D. dissertation by

James Edward Hunt

Has been produced under the supervision of the following persons:

Supervisors

Russell B. Wynn

Douglas Connelly

Damon A.H. Teagle

Chair of Advisory Panel

Rex Taylor

ABSTRACT

UNIVERSITY OF SOUTHAMPTON
FACULTY OF NATURAL AND ENVIRONMENTAL SCIENCES
SCHOOL OF OCEAN AND EARTH SCIENCES

Doctor of Philosophy

DETERMINING THE PROVENANCE, RECURRENCE, MAGNITUDES AND FAILURE MECHANISMS OF SUBMARINE LANDSLIDES FROM THE MOROCCAN MARGIN AND CANARY ISLANDS USING DISTAL TURBIDITE RECORDS

by **James Edward Hunt**

The Moroccan continental margin and Canary Islands have been subjected to repeat submarine mass wasting. This thesis aims to investigate the sediment gravity flow deposits associated with these submarine landslides. The Agadir Basin represents a deepwater depocentre and conduit for turbidity currents sourced from the Agadir Canyon and Western Canary Islands. A previous basin stratigraphy is re-analysed and extended to cover the last 600 ka. This stratigraphy is validated by using down-core geophysics and chemostratigraphy. ITRAX mudcap geochemistry has been used to assess turbidite provenance. Siliciclastic turbidites in this record have been shown to occur predominantly at transitions from glacial to interglacial periods.

The latest landslides identified from the Western Canary Islands, the El Golfo and Icod landslides, have been proposed to be multistage. This is based on the presence of multiple fining-upwards sequences, known as subunits, within the associated sediment gravity flow deposits. Grain-size data, core petrophysics, bulk geochemistry and volcanic glass geochemistry has shown that the subunits within the Icod deposit originate from a multistage collapse. The Late Quaternary volcaniclastic turbidites in the Madeira Abyssal Plain in the last 1.5 Ma are also investigated, and found to potentially represent the El Golfo, Icod, Cumbre Nueva, Orotava, El Julán, Güímar, Tinor and Rogues de García landslides from the Western Canary Islands. These deposits also represent multistage landslides, which show that this failure mechanism is more common and has major implications for tsunamigenesis. Furthermore, analysis of ODP volcaniclastic turbidites (0-17 Ma) shows that deposits are coincidental in age and provenance with periods of voluminous and explosive volcanism on specific islands.

FOR MY MOTHER

IN LOVING MEMORY OF MY GRANDAD
TOM JENKINS (1926-2012)

Contents

Declaration of Authorship

I, James Edward Hunt, declare that this thesis, 'Determining the Provenance, Recurrence, Magnitudes and Failure Mechanisms of Submarine Landslides from the Moroccan Margin and Canary Islands using Distal Turbidite Records', and the work presented in it are my own and have been generated by me as the result of my own original research.

I confirm that:

1. This work was done wholly while in candidature for a research degree at this University;
2. Where any part of this thesis has previously been submitted for a degree or any other qualification at this University or any other institution, this has been clearly stated;
3. Where I have consulted the published work of others, this is always clearly attributed;
4. Where I have quoted from the work of others, the source is always given. With the exception of such quotations, this thesis is entirely my own work;
5. I have acknowledged all main sources of help;
6. Where the thesis is based on work done by myself jointly with others, I have made clear exactly what has been done by others and what I have contributed myself;
7. Parts of this work have been published as:

   Hunt, J.E., R.B. Wynn, D.G. Masson, P.J. Talling, and D.A.H. Teagle (2011), Sedimentological and geochemical evidence for multistage failure of volcanic island landslides: A case study from Icod landslide on north Tenerife, Canary Islands, *Geochem. Geophys. Geosyst.*, 12, 12, Q12007, doi:10.1029/2011GC003740

8. Work during preparation of this thesis has also been contributed to:

   Masson, D.G., R.G. Arzola, R.B. Wynn, **J.E. Hunt**, and P.P.E. Weaver (2011), Seismic triggering of landslides and turbidity currents offshore Portugal, *Geochem. Geophys. Geosyst.*, 12, 12, Q12011, doi:10.1029/2011GC003839.

   C.J. Stevenson, P.J. Talling, R.B. Wynn, D.G. Masson, **J.E. Hunt**, M. Frenz, A. Akhmetzhanov, and B.T. Cronin (in press), The flows that left no trace: very large-volume turbidity currents that bypassed sediment through submarine channels without eroding the seafloor, *Petrol. Mar. Geol.*, doi:10.1016/j.marpetgeo.2012.008.

9. Work directly and indirectly related to this thesis has been presented at numerous conferences:

   British Sedimentological Research Group AGM 2009

   Hunt, J.E., R.B. Wynn, P.J. Talling, M. Frenz, and D.G. Masson (2009), Emplacement of the El Golfo and Icod Turbidites in the Moroccan Turbidite System: Implications for Landslide Mechanisms and Turbidity Current Processes, *BSRG AGM*, Bangor Wales, 21-22 December 2009.

   Hunt, J.E., R.B. Wynn, A. Georgiopoulou, V. Catteral, and D.G. Masson (2009), An Investigation of Volcaniclastic Turbidite Emplacement in the Canary Basin: Implications for Volcanic Landslide Events, *BSRG AGM*, Bangor Wales, 21-22 December 2009.

   European Geoscience Union AGM 2010

   Hunt, J.E., R.B. Wynn, D.G. Masson, and I.W. Croudace (2010), Geochemical evidence of multistage retrogressive failure during the 160 ka Icod landslide from turbidite facies analysis: multidisciplinary investigative approaches using destructive and non-destructive methodologies, *EGU 2010*, Vienna Austria, 3-7 May 2010.

   Hunt, J.E., and R.B. Wynn (2010), Complexities within distal sheet turbidite deposits: case study 160 ka Icod Turbidite, Moroccan Turbidite System, *EGU 2010*, Vienna Austria, 3-7 May 2010.

Hunt, J.E., R.B. Wynn, and P.J. Talling (2010), The Moroccan Turbidite System: a modern example of a multi-basin mixed siliciclastic-volcaniclastic deep-water sedimentary system, *EGU 2010*, Vienna Austria, 3-7 May 2010.

18th International Sediment Congress 2010

Hunt, J.E., R.B. Wynn, D.G. Masson, and P.J. Talling (2010), Can distal turbidites record the associated landslide mechanism at source and tsunamigenic potential? *ISC 2011*, Mendoza Argentina, 27 September – 2 October 2010.

Hunt, J.E., R.B. Wynn, A. Georgiopoulou, and D.G. Masson (2010), Volcaniclastic turbidity current depositional facies and architectures indicate potential mode of emplacement and provide insights into flow behaviour *ISC 2011*, Mendoza Argentina, 27 September – 2 October 2010.

European Geoscience Union AGM 2011

Hunt, J.E., R.B. Wynn, D.G. Masson, and P.J. Talling (2011), Resolving the landslide mechanism and tsunamigenic potential of catastrophic volcanic island flank collapses: Canary and Madeira Archipelagos, *EGU 2011*, Vienna Austria, 3-8 April 2011.

British Sedimentological Research Group AGM 2011

Hunt, J.E., R.B. Wynn, P.J. Talling, and C.J. Stevenson (2011), Insights into provenance, transport history and diagenesis, *BSRG 2011*, Imperial College, 12-13 December, 2011.

10. Additional components of this thesis have been written with the intention of submission to scientific journals. Where this applies to a piece of work, it will be acknowledged in the chapter introduction.

Signed: James E. Hunt

Date: 24/05/2012

Acknowledgements

I would firstly like to acknowledge my girlfriend Claire. Claire has supported me through my every endeavour, and without her love and support I definitely would not be in the position I am today. Whether it be my obsession over trilobites, the long hours spent with sediment cores, or my knack for injuring myself at every opportunity, Claire has been there for me. Words cannot truly explain the love and appreciation I have for her, and I would not have been able to complete this thesis without her. I would also like to acknowledge my mother Susan. Whether work, sport or simply getting up to mischief, she has always been enthusiastic about whatever I do. Her unrivalled enthusiasm has provided motivation for me when I needed to conquer those sometimes bleak days of PhD life, and because of her, I always see the bright side of life, although with a bit of satirical humour.

My family has always supported me down whatever path I have taken, but my late Grandad Tom greatly influenced me to pursue a road into academia. Grandad taught me the importance of pushing myself. He managed to escape the mines of South Wales and attend the University of London during times of tremendous adversity. Grandad served his country during our truly darkest hours by applying the knowledge he fought so hard to achieve. I can only hope that my research benefits our community a fraction of what his did. I dedicate this thesis to my Grandad Tom, who passed away in February of this year; he was my Grandad, my friend and my hero.

I owe a great deal to my supervisor Russell Wynn. Russell gave me the opportunity to study at NOCS and I cannot thank him enough for taking on such a green researcher. Russell has helped me immensely during my studies, being patient as I developed my writing style and fighting day-in-day-out to keep me from venturing off on my many tangents. I think my catch phrase of 'I was just wondering...' followed by my latest ponderings will give him nightmares for some time to come. I thank Doug Masson and Peter Talling for becoming honorary supervisors during my studies. They have always been keen to listen to my theories and been on hand to give me advice on my work. I would also like to thank my supervisors Doug Connelly and Damon Teagle, and my panel chair Rex Taylor. I also thank the Marine Geoscience Group for providing my PhD funding and my funding extension to allow me to prepare my chapters as papers.

Even before starting my PhD I had the great fortune to have a close group of friends that I could always turn to. James Connolly, Martina Hannaford and Verity

Weatherhead unwisely chose to live with me at university, and have been stuck with me ever since. James has been one of my closest friends since we met one fateful day as freshmen. Our times conquering the battlefields of Europe between essay writing will also remain amongst my fondest memories of Beech Tree Avenue.

I would like to thank my office-mates Hector Moreno, Chris Stevenson and Giuseppe Malgesini. They have had to put up with the 'organised chaos' that is my work space and my many ramblings about sediments. I will definitely miss the white-board sessions and our Pictionary-based discussions about turbidites. I have been lucky enough to be part of a very active and friendly postgraduate community. Joseph Stewart, Claudia Alt and James 'Dawg' French have offered me great friendship and many many good meals. Joe has also been my partner in crime while opening the batting for the NOCS and Post grad cricket teams. Regardless of the results, we have always been able to talk a good game. I would like to thank those of the inner sanctum, Mike Cassidy, Ed Smith, Chris Atkinson, Jeff Hawkes and Casey Nixon. As well as being part of an all-conquering 5-a-side team, they were good enough to share many-a-beverage with me. Memories of the 'great escape' from relegation in 2010 and the epic victory over Oxford University will remain with me long after I hang up my boots. I would like thank all the members of the NOCS football and cricket teams, you all gave me a welcome distraction from laboratory protocols and manuscript preparation.

I would like to thank Suzie MacLachlan and Guy Rothwell of BOSCORF for enabling me to use the facilities, and helping out when the instruments decided to fail. I certainly learnt the power of 'turn it off, turn it back on again' as a means of troubleshooting. I would also like to thank Darryl Green and Belinda Alker for their help in teaching me my laboratory protocols.

I would like to thank all those at the British Sedimentological Research Group. Chris Jackson, Gary Hampston, Ian Kane, Dave Hodgson and Jeff Peakall have all left a lasting impression on me, and I look forward to joining the ranks as a clastic sedimentologist.

Lastly, I would like to thank my examiners Ian Jarvis and Sebastian Watt for their thorough and incredibly helpful review of my work. Their insight was very much appreciated.

List of Figures

List of Tables

List of Referenced Appendices

Chapter 3

Appendix 3.1 Sediment isopachs for turbidites in the Madeira Abyssal Plain.

Appendix 3.2 Sediment isopachs for turbidites in Agadir Basin.

Appendix 3.3 Coccolithophore biostratigraphy samples for CD166/12.

Appendix 3.4 ICP-OES Geochemical Results of Turbidite Mudcap Samples from CD166/12 used to calibrate the ITRAX μXRF data from CD166/12.

Appendix 3.5 ITRAX μXRF Calibration Curves.

Chapter 4

Appendix 4.1 Bulk geochemical compositions of samples of turbidite mud and hemipelagite sediment from core CD166/12, analysed using ICP-OES.

Appendix 4.2 Bulk geochemical compositions of SRMs analysed by ICP-OES.

Appendix 4.3 Calibration curves for major element analyses by ITRAX μXRF.

Appendix 4.4 Coccolith counts for coccolith biostratigraphy in JC27/13.

Chapter 5

Appendix 5.1 Detailed methodologies applied during the present study.

Appendix 5.2 Isopach maps for each subunit and the mudcap of the Icod Event Bed in Agadir Basin, a) SBU1 Isopach, b) SBU2 Isopach, c) SBU3 Isopach, d) SBU4 Isopach, e) SBU5 Isopach, f) SBU6 Isopach, g) SBU7 Isopach, and h) Mudcap Isopach.

Appendix 5.3 Isopach maps for the sand/silt and mudcap fractions for the Icod Event Bed in the Madeira Abyssal Plain, a) Sand Fraction Isopach, and b) Mudcap Isopach.

Appendix 5.4 Alteration Box Plot of CCPI vs AI for altered volcanic glasses from SBU1 in the Icod Event Bed in JC27/02. Bright grains equate to mafic glasses of high density, dark grains equate to phonolitic glasses of reduced density and altered glasses are those with visible alteration.

Appendix 5.5 Elemental Alteration Box Plots for altered volcanic glasses from SBU1 in the Icod Event Bed, a) CCPI vs SiO_2, b) AI vs SiO_2, c) Na_2O vs AI, and d) K_2O vs AI.

Appendix 5.6 Standard Reference Materials Analysed by ICP-OES.

Appendix 5.7 Bulk ICP-OES results from basal subunit samples of the Icod Event Bed at core sites in Agadir Basin.

Appendix 5.8 Standard Reference Materials Analysed by SEM EDS.

Appendix 5.9 Volcanic Glass SEM-EDS results from samples taken from subunits of the Icod Event Bed in JC27/02.

Chapter 6

Appendix 6.1 SEM EDS Results from Volcanic Glasses extracted from the basal subunits of the volcaniclastic turbidites recovered from the Madeira Abyssal Plain.

Appendix 6.1 Detailed methodology for calculating the decompacted volume of turbidites recovered in the ODP core from the Madeira Abyssal Plain.

Appendix 6.3 Depth-porosity values from ODP sites 950, 951 and 952 (black line) and the depth-porosity models used for decompaction calculations; the Baldwin and Butler (1985) model (blue line), Arth (1930) model (green line), and present study (red line).

Appendix 6.4 Porosity-Depth data taken from the three ODP holes in Madeira Abyssal Plain (950, 951 and 952) (black line). Overlain are the porosity-depth models of Baldwin and Butler (1985) (blue line), Arth (1930) (green line), present study (red line).

Chapter 8

Appendix 8.1 Standard Reference Materials Analysed by ICP-OES.

Appendix 8.2 Bulk ICP-OES results from volcaniclastic sands sample from volcaniclastic turbidites from the submarine aprons of the Western Canary Islands and Madeira.

List of Additional Appendices

Core Panels

Agadir Basin CD166/13, CD166/14, CD166/19, CD166/22, CD166/23, CD166/24, CD166/25, CD166/26, CD166/27, CD166/28, CD166/29, CD166/30, CD166/31, CD166/33, CD166/34, CD166/42, CD166/46, CD166/48, CD166/49, CD166/50, CD166/51, CD166/54, CD166/55, CD166/56, CD166/57, CD166/58, CD166/59, CD166/60, CD166/61, CD126/01, CD126/02, D13071

Madeira Slope 90PCM01, 90PCM03, 90PCM05, 90PCM06, 90PCM07, 90PCM08, 90PCM09, 90PCM11, 90PCM12, 90PCM13, 90PCM14, 90PCM15, 90PCM16, 90PCM17, 90PCM18, 90PCM19, 90PCM20, 90PCM21, 90PCM22, 90PCM23, 90PCM24, 90PCM25, 90PCM26, 90PCM27, 90PCM28, 90PCM29, 90PCM31, 90PCM32

Selvagen Islands JC27/01, JC27/02, JC27/03, VM29/171, VM23/096

La Palma CD126/03, CD126/04, CD56/24, CD56/25, CD56/26, CD56/27, CD56/28,

El Hierro D126/16, D126/17, D126/18, D126/19, D126/20, D126/22, D126/23, D126/24, D126/25, VM32/032, CD126/05, CD126/06, CD126/08, CD126/09, CD126/10, CD126/11, CD126/12, CD126/13, CD126/14, CD126/16, VM30/068

Madeira Abyssal Plain D10688, D10698, D10699, D10982, D11809, D11810, D11811, D11812, D11813, D11814, D11818, D11821, D11822, D11823,

Core Petrophysical Data

Agadir Basin CD166/12, CD166/13, CD166/14, CD166/15, CD166/16, CD166/17, CD166/18, CD166/19, CD166/20, CD166/21, CD166/22, CD166/23, CD166/24, CD166/25, CD166/26, CD166/27, CD166/28, CD166/29, CD166/30, CD166/31, CD166/33, CD166/34, CD166/48, CD166/49, CD166/50, CD166/51, CD166/52, CD166/53, CD166/55, CD166/56, CD166/57, CD166/58

Core Spectrophotometry (and Magnetic Susceptibility) Data

Agadir Basin CD166/12, CD166/19, CD166/22, CD166/23, CD166/24, CD166/25, CD166/26, CD166/27, CD166/28, CD166/29, CD166/30, CD166/31, CD166/33, CD166/34, CD166/48, CD166/49, CD166/50, CD166/51, CD166/54, CD166/55,

CD166/56, CD166/57, CD166/58, CD166/59, CD166/60, CD166/61, CD126/01, D13071, D13073, JC27/13

Madeira Abyssal Plain D11813, D11818, D11821

ITRAX µXRF Data

Agadir Basin CD166/12, CD166/19, CD166/31, CD166/48, CD166/57, D13073, JC27/13

Icod Deposit CD166/27

Mineralogy

Icod Deposit

Grain Size Data

Icod Deposit

Published Articles

- Hunt, J.E., R.B. Wynn, D.G. Masson, P.J. Talling, and D.A.H. Teagle (2011), Sedimentological and geochemical evidence for multistage failure of volcanic island landslides: A case study from Icod landslide on north Tenerife, Canary Islands, *Geochem. Geophys. Geosyst.*, 12, 12, Q12007, doi: 10.1029/2011GC003740
- Masson, D.G., R.G. Arzola, R.B. Wynn, J.E. Hunt, and P.P.E. Weaver (2011), Seismic triggering of landslides and turbidity currents offshore Portugal, *Geochem. Geophys. Geosyst.*, 12, 12, Q12011, doi:10.1029/2011GC003839.
- C.J. Stevenson, P.J. Talling, R.B. Wynn, D.G. Masson, J.E. Hunt, M. Frenz, A. Akhmetzhanov, and B.T. Cronin (in press), The flows that left no trace: very large-volume turbidity currents that bypassed sediment through submarine channels without eroding the seafloor, *Petrol. Mar. Geol.*, doi: 10.1016/j.marpetgeo.2012.008.

Chapter 1
Introduction

1.1 Rationale

Submarine landslides and their associated sediment gravity flows are capable of displacing large volumes of sediment beyond the continental slope (Hampton *et al.*, 1996; Masson *et al.*, 2002, and references therein; Hühnerbach *et al.*, 2004; Maslin *et al.*, 2004, and references therein; Chaytor *et al.*, 2009). Indeed, these can have volumes far in excess of 100 km^3, where examples from the Hawaiian archipelago and Norwegian continental slope exceed 3,000 km^3 (Moore *et al.*, 1989, 1994; Haflidason, 2004, 2005). These mass movements are capable of destabilising and destroying seafloor infrastructure such as offshore drilling platforms, pipelines and telecommunication cables (Piper *et al.*, 1985, 1999; Allan, 1998; Nisbet and Piper, 1998; Venturi and Bughi, 2001; Porter *et al.*, 2004; Parker *et al.*, 2008; Zakeri *et al.*, 2008; Hsu *et al.*, 2008; Yuan *et al.*, 2012). However, submarine landslides also present significant geohazards as they potentially produce catastrophic tsunamis (Driscoll *et al.*, 2000; Ward and Day, 2001; Tappin *et al.*, 2001; Synolakis *et al.*, 2002; Masson *et al.*, 2006; Løvholt *et al.*, 2006). Owing to the hazard that submarine landslides pose to a given seaboard, there is a necessity to resolve their provenance, recurrence intervals, magnitudes, and failure mechanisms.

The modern deepwater sedimentary systems of the Northwest African passive margin are amongst the most intensely studied in the world. The complexity of this geographic region in regards to the oceanography, bathymetry and sedimentary processes, has greatly extended our knowledge of deep-water sedimentary processes. The deepwater Northwest African passive margin is dominated by the Moroccan Turbidite System (MTS) (Wynn *et al.*, 2000a). The MTS comprises three interconnected depocentres: Agadir Basin, Seine Abyssal Plain and Madeira Abyssal Plain (Wynn *et al.*, 2000a, 2002a). Previous work on the more distal Madeira Abyssal Plain, to the west, has highlighted the potential for single turbidity currents to deposit tens-to-hundreds of cubic kilometres of sediment (Rothwell *et al.*, 1992; Weaver *et al.*, 1992). Following these extensive works on the Madeira Abyssal Plain (Weaver and Kuijpers, 1983; Kuijpers *et al.*, 1984; de Lange *et al.*, 1987; Weaver and Rothwell, 1987; McCave and Jones, 1988; Jones *et al.*, 1992; Rothwell *et al.*, 1992; Weaver *et al.*, 1992; Weaver and Thomson, 1993), investigations were carried out in the more

proximal Agadir Basin (Wynn *et al.,* 2002a; Frenz *et al.,* 2009) and Seine Abyssal Plain (Davies *et al.,* 1997; Wynn *et al.,* 2002a). These studies have suggested that the large-volume turbidites are sourced from submarine landslides from the Moroccan continental slope and Western Canary Islands (Weaver *et al.,* 1992; Pearce and Jarvis, 1992, 1995; Masson *et al*., 2002; Wynn *et al.,* 2002a; Frenz *et al.,* 2009).

In addition to the purely scientific questions surrounding the occurrence of submarine landslides and their associated sediment gravity flows, there are several economic aspects that necessitate the need for this study. As aforementioned, the Northwest African margin and Canary Islands are susceptible to large-volume submarine landslides. This study area is in proximity to the densely populated Western European Atlantic margin and U.S. Atlantic Exclusive Economic Zone. This thesis will provide a landslide history that can inform geohazard mitigation and re-insurance of marine and coastal infrastructure in the North and Central Atlantic. In addition, ancient sand-rich turbidites pose significant hydrocarbon reservoirs; understanding the influences on turbidite occurrence and magnitude from this study will also serve to inform hydrocarbon exploration.

1.2. Project Aims and Thesis Structure

This PhD thesis aims at resolving the timing, magnitude, provenance and failure mechanisms of submarine landslides on the Northwest African passive margin. This will be completed by studying the associated sediment gravity flow deposits in the Moroccan Turbidite System. Over 300 archived piston cores within the Moroccan Turbidite System will provide records of turbidites sourced from continental slope and volcanic island submarine landslides in the last 600 ka. Furthermore, three ODP sites from leg 157 (sites 950, 951 and 952) in the Madeira Abyssal Plain will provide insight into the older 22 Ma record of landslide-derived turbidite deposition on the margin. The project aims are summarised as follows:

1. Construct a complete Late Quaternary (600 ka to recent) turbidite stratigraphy for Agadir Basin and derive the provenance of these deposits from the geochemical composition.
2. Investigate the potential preconditioning and trigger factors of these events.
3. Determine whether turbidite depositional characteristics can provide information on the failure mechanism of the original landslide.

4. Integrate the long-time ODP record of turbidite deposition within the Madeira Abyssal Plain. This will enable investigation into the influences on turbidite occurrence, magnitude and provenance over the last 22 Ma.

This first Chapter offers an introduction to the themes of the thesis, and the topics discussed in the subsequent Chapters. This includes a brief review of the processes responsible for sediment redistribution in deepwater environments, and a classification of these processes. The principal preconditioning and trigger factors for submarine landslides will be discussed, and how associated turbidity currents are initiated. The last component of the first Chapter will be an introduction to the study area and a brief summary of previous work conducted there.

The second Chapter provides an overview of the data utilised in this project and the methodologies employed to gather and process that data. These analytical techniques span a number of disciplines including sedimentology, geochemistry and geophysics.

The third Chapter concerns construction of a 600 ka to recent turbidite history in the Agadir Basin region of the Moroccan Turbidite System. This involved reanalysing a previously published 165 ka to recent stratigraphy, and then extending this to 600 ka. With a robust turbidite stratigraphy in place, the factors controlling both turbidite occurrence and magnitude were assessed. The stratigraphy and event history of Agadir Basin introduced in this Chapter will be focused on in subsequent Chapters.

The fourth Chapter investigates the provenance of the turbidites from the Agadir Basin stratigraphy, previously identified in Chapter 3. This is done by using major element compositions of the turbidite mudcaps analysed using ITRAX μXRF. This Chapter demonstrates an ability to not only discriminate the volcaniclastic, siliciclastic and calcareous turbidites, but also discriminate the different sources of the volcaniclastics (Tenerife, El Hierro and Madeira). Furthermore, subtle down-basin changes in bulk mudcap geochemistry of the siliciclastic turbidites can also be used to signify turbidity current erosion.

Chapters 3 and 4 have introduced and examined the Agadir Basin stratigraphy and identified the provenance of the turbidites therein. Chapter 5 investigates the landslide mechanisms responsible for the turbidites, and in particular a notion of multistage retrogressive failure. The Icod landslide will be used initially as a case study, whereby the multiple upwards-fining turbidite sands and muds (subunits) that comprise the bed are proposed to signify an originally multistage landslide failure.

With the Icod landslide and turbidite examined in Chapter 5, the remainder of the volcaniclastic turbidite record is investigated in Chapter 6. The Agadir Basin records only two large-volume volcaniclastic beds in the last 165 ka, representing the Icod landslide (bed A14) and younger El Golfo landslide (bed A2). The modern Madeira Abyssal Plain records eight such large-volume events over a longer time frame (1.5 Ma). Thus Chapter 6 firstly aims to delineate the Late Quaternary volcaniclastic event history in the Madeira Abyssal Plain from a suite of piston cores. This includes identifying precise provenances of those beds and ultimately correlating each bed to a specific landslide. The ODP records from the Madeira Abyssal Plain are utilised to provide an older 17 Ma history of landslides from the Canary Islands.

Chapter 6 resolves the Late Quaternary (0-1.5 Ma) volcanic island landslide history determined from the volcaniclastic turbidite record in the Madeira Abyssal Plain. Chapter 7 investigates whether the subunits present in these beds originate from multistage failures. Demonstration that multistage failures are ubiquitous across numerous events is of first order importance in understanding landslide emplacement dynamics, which effects tsunami modelling.

Chapter 8 represents a summary chapter of preliminary results from a number of studies that are ongoing. The work presented here supplements the work presented in the previous Chapters (Chapters 3-7). However, these studies do not form the main body of the thesis, but their inclusion will allow for more comprehensive discussions. These studies include an appraisal of the volcaniclastic turbidites records from the proximal submarine aprons of Madeira and the Western Canary Islands. This also includes an examination of the composition of volcanic glasses from the Icod and Orotava deposits from Tenerife. This particular study may provide insight into the relationship between explosive phonolitic eruptions and large-volume flank failures. Another short piece of ongoing research investigates records of landslides associated with the inception, emergence and growth of the Western Canary Islands. The pale grey non-volcanic turbidites, from the ODP records, are proposed to represent failures of submarine sediment caused by doming of the sea floor in response to magma ascension and dyke intrusion. Lastly, there are preliminary results from an investigation into the records of siliciclastic turbidites at the ODP sites in the Madeira Abyssal Plain (sites 950, 951 and 952). This 17 Ma turbidite record enables an evaluation of the occurrence, magnitude, preconditioning factors, and failure mechanisms of continental margin submarine landslides.

The results and interpretations from the previous Chapters (Chapters 3-8) are discussed within Chapter 9. Lastly, Chapter 10 serves to conclude the thesis and present proposals for future work. The Appendices contain copies of published works from this thesis, conference abstracts, supplementary chapters, data tables, and core data panels. These are provided on a series of data storage CDs.

1.3 Classification of Processes Governing Deepwater Mass Movements

This section is dedicated to outlining the sedimentary processes that occur in the deep ocean and their associated deposits. The deep marine environment is defined as the area below the level of the continental shelf; this includes the shelf break, the continental slope, submarine canyon systems, and distal abyssal plain. It is paramount to define the processes that operate here, since the occurrence or absence of these processes can have implications on the geological evolution of a region. For the purposes of this work the classification schemes of Mulder and Cochonat (1996) and Mulder and Alexander (2001) have been utilised in part, since the schemes are process based. However significant modifications have been made to fully incorporate the full spectrum of possible processes (Figure 1.1). Although occurring as discrete processes, these mass movements can evolve from one another, such that slides and slumps can disaggregate and form granular debris flows and turbidity currents (Figure 1.2).

1.3.1. Coherent Mass Transport

Coherent mass transport refers to transport mechanisms that move blocks of previously deposited materials. This material is moved where the original bedding is still coherent, and where the sediment failed is not disaggregated and is often lithified.

Creep

Creep is a process that involves slow strain rate deformation of a body in a down-slope vector. This results primarily from the weight of the sediment and its potential energy (Stow *et al.,* 1996). Mulder and Cochonat (1996) further extended this definition by supporting a notion of low deformation rates involving an elastic strain, which commonly exploit sediment with a high content of clay, due to its elasticity and cohesiveness. The key notion here is that there is no shear fracturing, and that the sediment involved does not become detached. Once the plastic deformation limit (or yield strength as defined by the Coulomb fracture criterion) is reached, a creep may

develop into a slide or a plastic flow, thus areas characterised by creep may be later prone to further gravity-driven failure (Mulder and Cochonat, 1996).

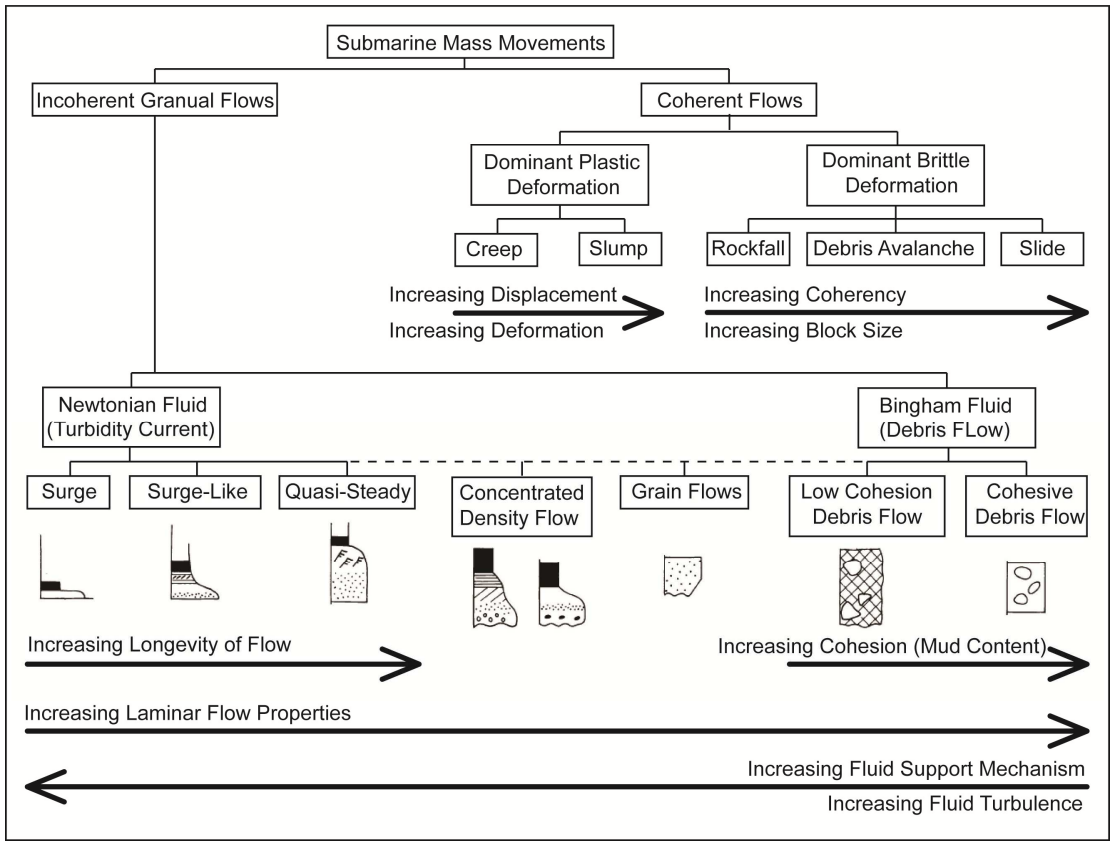

Figure 1.1 Classification Scheme for Submarine Mass Movements, based on the classifications of Mulder and Cochonant (1996) and Mulder and Alexander (2001).

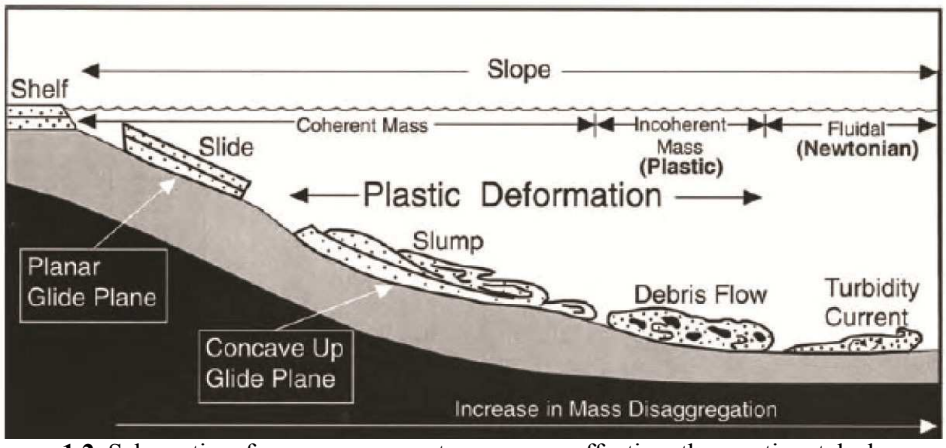

Figure 1.2 Schematic of mass movement processes affecting the continental slopes and volcanic island flanks (Shanmugam *et al.* 2004). Schematic demonstrates the ability of flow processes to evolve from slides to debris flows to turbidity currents through sediment disaggregation and water entrainment.

Submarine Slide

Slides and slumps have been previously separated by definition (Stow *et al.,* 1996; Shanmugam, 2006). However, Mulder and Cochonat (1996) stated that slumps are simply a type of slide, invoking that the transport process is the same but that subtle variations can enable subdivision of an overall slide process. Masson *et al.* (2006) gave a concise definition of a slide as a "*movement of a coherent mass of sediment bound by a distinct failure plane*". Eckel (1958), Schuster and Krizek (1978), Stow *et al.* (1996), Hampton *et al.* (1996), and Shanmugam (2006) agreed on a basal glide plane or rupture surface as being the primary zone of shear. The nature of this glide plane offers subdivisions of the slide terminology, Mulder and Cochonat (1996) proposed delineation depending on a Skempton ratio (height/length): (1) translational slides (Skempton ratio <0.15) and (2) rotational slides (Skempton ratio >0.33). Mulder and Cochonat (1996) and Hampton *et al.* (1996) also attributed the rotational slides as being slumps, a misconstrued attribution, and based on morphological features rather than on a transportation process.

Stow *et al.* (1996) and Shanmugam (2006) state that slides move with little internal deformation and involve lithified or partially lithified sediment, compared to slumps that occur on relatively low gradients involving volumes of fine-grained sediment that are unconsolidated, and can involve intense internal deformation. This thesis defines slides and slumps on the grounds of the deformation and consolidation of the sediment, since the two factors are inter-related. Slides are a coherent mass of lithified or partially lithified sediment, where movement occurs along a basal glide plane involving extensive basal shearing and variable internal brittle deformation. Slides can occur along a continuum of glide planes from slope-parallel (translational) or listric (rotational). This is supported by Stow *et al.* (1996) and Shanmugam (2006), and in keeping with the classification of Mulder and Cochonat (1996). However the terminology of 'slump' is void regarding slide nomenclature. The occurrence of brittle internal deformation in slides is in reference to up-slope extensional faulting, internal extensional and compressional faults and down-slope compressional thrusts (Crans *et al.,* 1980; Martinsen, 1989).

The sediment is cited here as being lithified or partially lithified sediment. Lithified sediment has greater rigidity, thus for a given applied force brittle deformation, rather than plastic deformation, is likely to ensue. Typical glide planes include mud/salt

rheological decollement surface, overpressured mud, or clathrate deposits, all of which invoke bedding being parallel-to-slope to enable slope-parallel displacement.

Mulder and Cochonat (1996) motioned that slides can be located in two categories based on whether there was a single event or a series of multiple events: (1) Simple (Atlantic-type), or (2) Mixed/Complex (Ranger-type). Simple slides are those where the main slide body does not generate any other significant failure(s), namely retrogressive slide failures. Complex slides are those where the initial slide causes instability in the surrounding area, and causes subsequent slides to be generated. Mulder and Cochonat (1996) recognised a number of different complex slide regimes: (1) successive overlapped slides (simple retrogradational or complex laterally retrogradational and channelized progradational), (2) successive adjacent flows (rotational retrograding or with translational failure surfaces), (3) fitted-together slides, and (4) successive (domino-like).

Submarine Slump

As stated in the previous 'slide' definition, the use of slide and slump terminology has not been consistent. In a similar fashion to slides, the slumping processes involves a coherent mass of sediment bound by a lower zone of concentrated shear along which movement occurs (Shanmugam, 2006). It is also the case that numerous authors agree that the glide plane at the base of the slump forms a concave-up feature (Mulder and Cochonat, 1996; Shanmugam, 2006). The transport process, rather than a morphological feature, should be the defining criteria for a slump or slide. Mulder and Cochonat (1996) and Stow *et al.* (1996) stated that slides occur on a range of glide plane surfaces from purely slope-parallel to listric.

However, documented slumps are characteristically different from those of pure slides, where the internal fabric of the slide is maintained; slumps often involve intense deformation. The deformation involved is primarily plastic causing intense bed contortion with high-shear sheath folds. Stow *et al.* (1996) noted the predominance of plastic deformation and the notion of the sediment being relatively unconsolidated within slumps, thus these elements are incorporated as the defining characteristics of this process. Thus slumps involve a coherent mass of unconsolidated to partially consolidated and predominantly fine-grained sediment. Movement occurs along a basal glide plane involving extensive basal shearing and intense internal plastic deformation. The predominance of fine-grained sediment with higher yield strengths and sediment

that has not been lithified enables plastic deformation to occur with an applied stress rather than brittle deformation.

Submarine Rockfall

Submarine rockfalls have been added as a variant from debris avalanches (see below), on the grounds of the volume of rock, distance of transport, lack of fluid involvement, and lack of interaction of clasts in transport (Mulder and Cochonat, 1996). These are localised deposits proximal to steep gradients and structural highs. Stow *et al.* (1996) defined rockfall events as being short lived and where lithified material simply falls or rolls down a slope by traction under the force of gravity. Clasts move from a location of high gravitational potential to one of low gravitational potential, being deposited where they are gravitationally stable. Importantly, Stow *et al.* (1996) stated that during transport falling clasts have minimal interaction and interference with each other, a defining attribute when compared to debris avalanches.

Debris Avalanches

Debris avalanches are rapid flows of cohesionless rock fragments down slope, involving the dissipation of flow energy through clast collisions and shear resistance of the substrate (Masson *et al.,* 2006). Debris avalanches have been separated from rock fall processes due to the scale of mass failure, the distance of transport, and the interaction of the clasts during transport (Mulder and Cochonat, 1996). Stow *et al.* (1996) linked debris avalanches specifically to oceanic volcanic islands edifices and active continental margins, associated with large-scale slope failures. Masson *et al.,* (2002) attributed debris avalanches to be one of the most common mass failure mechanisms at volcanic islands, but only affect the 'superficial' parts of the volcanic edifice. Debris avalanche aprons are prevalent around the submarine flanks of the Canary and Hawaiian archipelagos (Moore *et al.,* 1989, 1994; Urgeles *et al.,* 1997, 1999; Masson *et al.,* 2002). They may cover areas >2,500 km^2 of the sea floor with volumes >100 km^3 (Moore *et al.,* 1989; Masson *et al.,* 2002).

1.3.2 Incoherent Mass Transport

Incoherent mass transport is where the failed sediment is fully disaggregated. Therefore the transport mechanisms affect singular grains within a granular flow.

Grain Flow

Lowe (1976) presents a definition of grain flows as: '*cohesionless solids maintained in a dispersed state against the force of gravity by an intergranular dispersive pressure arising from grain interactions within shearing sediment*'. Although this definition is correct, it does not remove enough ambiguity from a debris flow definition. Importantly, Lowe (1976) stated that the fluid within the flow offers the grain-support mechanism, and that this fluid is the same as the ambient fluid.

There is a potential continuum that exists between grain flow and debris flow mechanisms (Shanmugam, 1997, 2006; Stow *et al*., 1996). "Cohesive" debris flows would rely on the grain matrix providing the grain support mechanism. While grain flows represent a contrasting "cohesionless" debris flow end member, which rely on a purely interstitial fluid grain-support mechanism. However, grain flows are different from debris flows.

Dasgupta (2003) drew a distinct boundary between grain flows and debris flows based on a misconception that grain flows involve laminar flow. Laminar flow invokes a stream-lined prevalence where mixing of adjacent flow layers is only on a molecular level, and where interlaminar mass transfer and sediment differentiation cannot occur, as stated by Reynolds (1885) (Dasgupta, 2003). In grain flows dispersive pressure has an increased dominance, causing mass transfer at high angles to the flow, thus grain flows are not laminar. Since debris flows are defined by laminar flow, grain flows cannot be associated with them, unlike the classifications of Lowe (1979), Postma (1986), Stow *et al*. (1996) and Shanmugam (1997, 2006) (Dasgupta, 2003).

This places concern over Shanmugam (1997, 2006) and Stow *et al*. (1997) attributing grain flows (cohesionless) and mud flows (cohesive) as two end-members of a continuum of 'debris flows', with sandy debris flows forming an intermediate. Mulder and Cochonat (1996) did not associate grain flows with debris flows, instead identifying grain flows as a member of 'fluidised flows'. Although the interstitial fluid acts as the grain-support mechanism, fluidised and liquefied flows are different from grain flows. The interstitial fluid in grain flows is the same as the ambient fluid, while for fluidised flows at least, the interstitial fluid represents an external flux (Dasgupta, 2003). For this thesis grainflows are placed within a broad continuum with debris flows and turbidity currents, similar to the classification of Mulder and Alexander (2001), but define a separate and distinct type of flow mechanism.

Debris Flow

Debris flows have been ascribed as being flows of granular materials within non-Newtonian (Bingham) fluids and invoking a laminar flow behaviour, akin to the inertia flows of Bagnold (1954) (Figure 1.3) (Johnson, 1970; Middleton and Hampton, 1973; Rodine and Johnson, 1976; Mulder and Cochonat, 1996; Leeder, 1999; Dasgupta, 2003). The definition and classification of a spectrum of debris flows casts ambiguity. Shanmugam (1997, 2006) and Stow *et al*. (1996) describe two types of debris flow: cohesive and non-cohesive. Cohesive debris flows are described as being sustained by the cohesive strength of the water-sediment matrix, which forms the dominant clast-support mechanism, and supplemented by a buoyancy effect within the flow (Johnson, 1970; Hampton, 1975, 1979; Nemec and Steel, 1984; Pickering *et al.,* 1986; Stow *et al.,* 1996; Shanmugam, 2006).

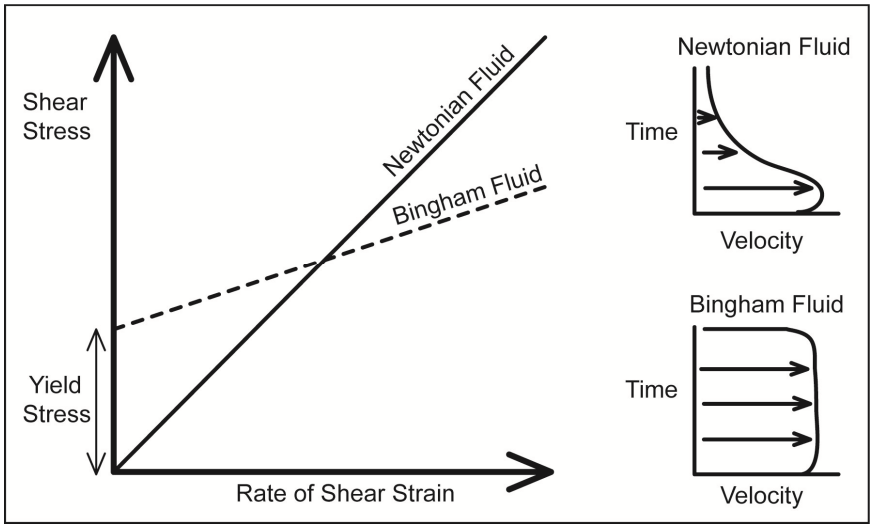

Figure 1.3 Shear stress to rate of shear strain relationships for Newtonian (turbulent) and Bingham (laminar) fluids. Newtonian fluids will begin to deform the moment that shear stress is applied, while Bingham fluids require a yield stress (strength) to be overcome. Also featured are velocity profiles through the two fluids, showing the gradual decay in velocity synonymous with Newtonian (turbulent) flows and the rapid decay synonymous with Bingham (laminar) flows.

However, Stow *et al.* (1996) also described non-cohesive debris flows as being grain flows, whereby intergranular collisions generate a dispersive pressure that enables mobility when under shear. The problem with the previous statement is that for dispersive pressure to occur the laminar flow regime breaks down due to mixing with the ambient fluid and substrate (Dasgupta, 2003). This precludes grain flows being classed as debris flows. However, Dasgupta (2003) still utilised the cohesive and non-cohesive nomenclature while classifying debris flows. Cohesive flows are attributed to cohesive debris flows, and frictional flows attributed to non-cohesive debris flows

(Dasgupta, 2003). Contrary to this, Mulder and Alexander (2001) stated that frictional flows involve discrete particles that can develop high intergranular spacing during flow. There was no specific mention of laminar flow as a prerequisite, and as such the frictional flow (non-cohesive debris flows of Dasgupta (2003)) describes a grain flow and not a debris flow.

The definition of Masson *et al.* (2006) described debris flows effectively as only cohesive flows. As such, in this thesis 'cohesive debris flows' and 'debris flows' are synonymous. Thus the non-cohesive debris flow terminology is redundant and should be replaced by a separate grain flow process. Debris flows can thus be defined as flows of cohesive sediment with high pore pressures, within a laminar Bingham fluid regime, and above a basal shear zone of negligible erosive power.

Hampton (1975) stated that in 'real' debris flows the grain-support is often supplemented by addition forces of dispersive pressure and turbulence. This places debris flows within a broad continuum with turbidity currents and grain flows. The cohesion found in debris flows is present due to the concentration of mud within the matrix. Mud-rich sediments will develop higher levels of cohesion, whereas sand-rich sediments have reduced clay contents and will have lower levels of cohesion. These sand-rich debris flows will involve direct grain collisions, which will develop a dispersive pressure. Caution should be exercised, since a high dispersive pressure will cause a break-down in laminar flow. In the case of the sand-rich debris flow the dispersive pressure is not a driving mechanism, but acts as a supplement to the matrix strength grain-support mechanism (Bagnold, 1954; Shanmugam, 1997). As a result two-members are provided: mud-rich (high cohesion) and sand-rich (low cohesion) debris flows.

Turbidity Currents

The foundation of the 'turbidite paradigm' was established by Kuenen and Migliorini (1950), stating that normal graded bedding developed from turbidity currents. Bagnold (1956) described gravity flows as having two layers: lower inertia region and upper viscous turbulent flow. However, these two processes form flows distinct from one another. Kuenen (1957) first designated deposits from turbulent flow as turbidites. A turbidity current is defined as: a flow involving granular materials held in suspension primarily by fluid turbulence as a Newtonian fluid (Figure 1.3).

There have been numerous attempts to classify different turbidite textures (Figure 1.4). Firstly, there is a classification of Pickering *et al.* (1986) based on the grain size. Here the high-density turbidites of Lowe (1982) are named coarse-grained turbidites, the typical Bouma sequence (Bouma, 1962) of turbidites represents deposits form medium-grain turbidites, and finally the Stow series (Stow and Shanmugam, 1980) define fine-grained turbidites.

The Pickering *et al.* (1986) classification is based solely on the dominant clast size, whereby this effects the concentration and density of the flow characteristics. Concentration of the flow has been utilised for defining two end-members of low-density and high-density turbidite flows in additional classifications (Middleton and Hampton, 1973, 1976; Lowe, 1982; Mulder and Cochonat, 1996; Dasgupta, 2003).

Mulder and Alexander (2001) discussed the difficulty is applying density and concentration terminology, since concentration purely defines the proportion of the flow that is composed of grains, while the density of the flow relates to the combined density of the grains and the ambient fluids. Mulder and Alexander (2001) proposed a classification based on cohesivity of the particles, flow duration, sediment concentration and particle-support mechanism. Mulder and Alexander (2001) suggested three different types of turbulent flow: (1) surge, (2) surge-like flow, and (3) quasi-steady turbulent flow, here the processes are detailed as varying according to the duration of the flow.

By definition, turbidity currents are Newtonian fluids, where an application of shear will cause instantaneous and proportional onset of a strain rate. These flows are maintained primarily by the action of fluid turbulence within a feedback loop known as autosuspension (Kuenen, 1951; Bagnold, 1962). Autosuspension is generated from excess density in the suspension, which originates from the load in suspension. To maintain turbulent flow the energy lost through friction and gravitational settling must be balanced as the flow moves down slope. Pantin (1979) stated that the autosuspension feedback will only occur if the density of the suspended load exceeds a critical point.

Middleton (1993) divided turbidity current architecture into horizontal elements along its flow path, namely the head, body and tail, which possess different dynamics. Secondly, Middleton (1993) divided the vertical profile of the whole flow into lower and upper boundary layers. An issue with the lower layer of the flow is that sediment grains held in suspension may begin to settle out during the flow. A question here is whether this settled sediment is re-entrained back into the flow or not (Middleton, 1993). There is a further question as to whether sediment is fully re-entrained into

suspension or whether it is moved by traction. In regards to the upper layer of the flow, an issue arises from attempting to calculate flow depth and average flow velocity from an upslope discharge. This is due to downslope drag and entrainment of ambient fluid within the flow. A mixing process can occur at the boundary between the upper flow and the ambient fluid, this can be characterised by use of the Richardson number (Middleton, 1993).

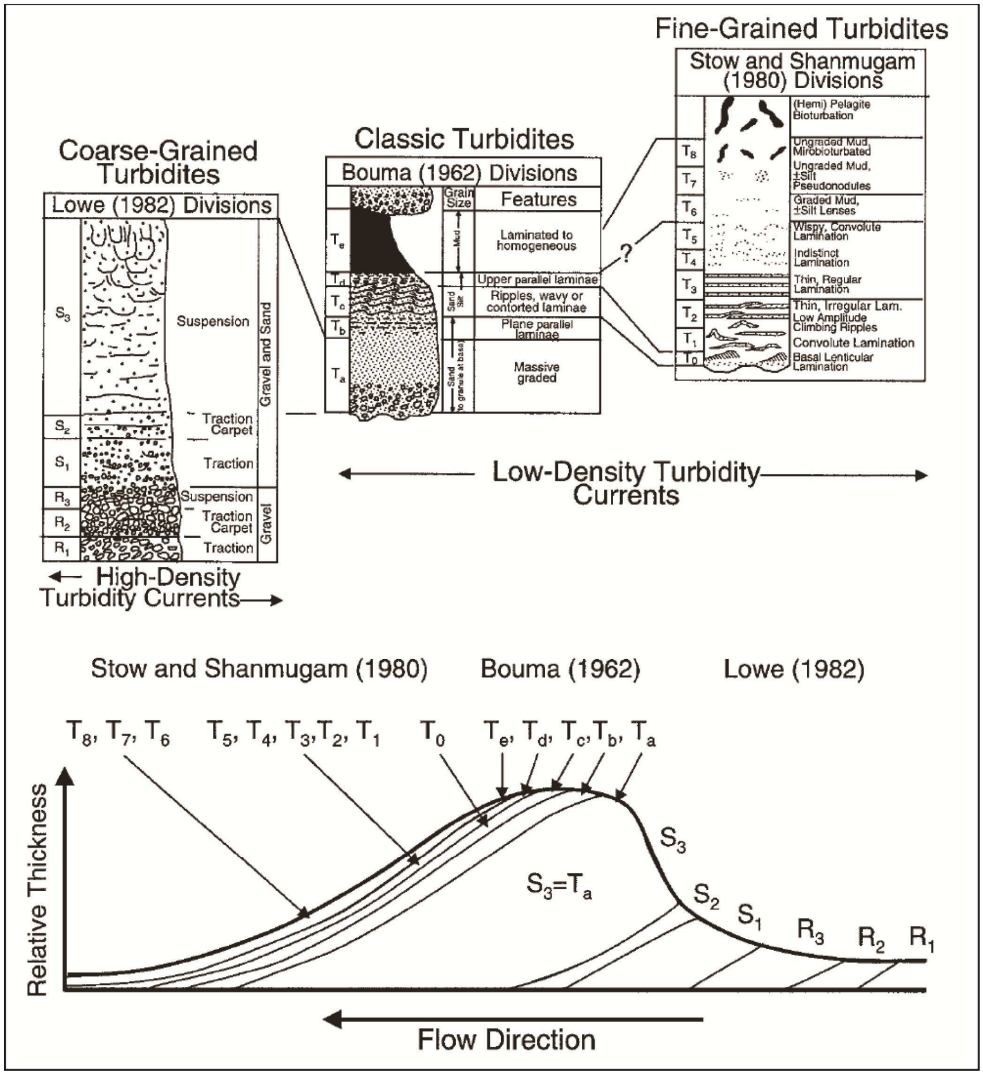

Figure 1.4 Combined coarse-grained, medium-grained (classic) and fine-grained turbidite classifications of Lowe (1982), Bouma (1962) and Stow and Shanmugam (1980) (after Pickering *et al.* (1986) and Shanmugam (2000, 2006)). These turbidite divisions are included on the lower diagram to show their theoretical thickness in a down-slope direction (after Lowe (1982) and Shanmugam (2000, 2006)).

For this thesis high-density and low-density turbidity currents have been regarded as end-member processes. High-density turbidity currents cannot have concentrations >9%, known as the Bagnold limit (Bagnold, 1962). Beyond this Bagnold limit fluid turbulence is no longer the primary grain support mechanism, and laminar flow

processes become increasingly important (Bagnold, 1962). In low-density turbulent flows two dominant processes other than the generation of turbulence are present: (1) slow fallout where fallout occurs from a dilute suspension accompanied by traction, which develops flow ripples and amalgamates clay-silt laminations, and (2) concentration where a dilute suspension will decelerate as turbulence is dampened (Stow *et al.,* 1996).

In high-density turbidity currents there are four key processes: (1) collapse fallout, (2) flow transformation due to hyperconcentration, (3) continuous aggradation, and (4) continuous traction (Stow *et al.,* 1996). Collapse fallout occurs as a turbidity current loses momentum and deposits sediment out of suspension. However, this sediment may enter a near-bed layer of hindered settling where modified grain flow, fluidised flow and liquefied flow act on the sediment to maintain a sediment suspension. Flow modification or transformation from a turbidity current into a debris flow occurs where the concentration, and thus density, of the flow exceeds a critical point whereby the traction carpet is swamped and autosuspension fails (Haughton *et al.,* 2003, 2009; Talling *et al*., 2004, 2007).

1.3.3 Other Deepwater Deposits and Processes

Liquefaction

This process involves a loss of shear resistance of sediment, due to the increasing pore-fluid pressures (Allen, 1977). This usually takes place in sediments with low cohesive strength. During liquefaction enhanced pore-fluid pressure causes total collapse of the sediment structure, with the sediment completely dispersed within the fluid medium (Dasgupta, 2003). Whether there is lateral transport is debatable, however this process at least results in resuspension of the granular material. For liquefaction a distinction is made that there is neither an influx of fluid nor a change in volume (Dasgupta, 2003). The increasing pore-fluid pressures responsible for liquefaction are generated from cyclic loading, e.g. by earthquakes (Martin *et al.*, 1975).

Fluidisation

As with liquefaction, this process involves a loss of the shear resistance within the sediment. Rising pore fluids increase local pore-fluid pressures, unlike liquefaction where there is no influx of pore fluids (Dasgupta, 2003). This increase in pore-fluid pressures supply sufficient energy to suppress van der Waals forces, liquid bridges and

sintering (Seville *et al.,* 2000). During fluidisation the upward component of fluid pressure is only required until the weight of the immersed granular material is balanced by the fluid drag (Dasgupta, 2003). Although complete resuspension occurs here, whether significant remobilisation occurs is debatable.

Contourites

Contourites are sediments deposited from thermohaline-driven bottom currents following bathymetric contours (Heezen *et al.,* 1966; Faugères *et al.,* 1984; Hollister, 1993; Faugères and Stow, 1993). Faugères and Stow (1993) advocated a constraint on contourite nomenclature to those deposits from or significantly reworked by stable geostrophic currents in relatively deep water (>500 m). A general facies model for both muddy and sandy contourites was proposed by Stow *et al.* (1998, 2002), based on earlier summary models of modern depositional patterns in the Gulf of Cadiz (Gonthier *et al.,* 1994). This demonstrated a basal negatively (inversely) graded unit, which is followed by a positively (normally) graded unit, and where bioturbation is ubiquitous throughout (Stow *et al.,* 1998).

However, Shanmugam (2006) presented some issues with contourite facies models. Firstly, that the term sandy applies to sediments where sand-sized grains that only comprise 5% of the sediment, thus the nomenclature is misleading (Shanmugam, 2006). Secondly, although contourites represent evidence of contour-parallel currents, the facies themselves do not demonstrate any evidence of deposition from or reworking by currents (Shanmugam, 2006). Lastly, bioturbation is designated as a key identifier for contourites, although bioturbation is often extensive within turbidites and hemipelagites (Shanmugam, 2006).

Hemipelagic/Pelagic Processes

Pelagites represent deposits of principally biogenic materials that form by suspension settling from the water column. Hemipelagites comprise both vertical suspension settling and a component of slow lateral advection (Stow and Tabrez, 1998; Evans *et al.,* 1998). Stow and Piper (1984) originally defined hemipelagite facies as sediments with >10% biogenic and >10% terrigenous material, whereby >40% of the terrigenous material is silt sized (4-63 μm). The sediment can be regarded as being poorly sorted due to this bi-modality between the finer clay fraction (<4 μm) and this >10-20% coarse fraction.

These deposits are generally devoid of primary sedimentary structures and are intensely bioturbated. Although a general facies model was proposed by Stow and Tabrez (1998), the authors acknowledged that recovery of such deposits from a wide geographic area and wide range of bathymetric depths precludes a narrow definition of expected facies. Therefore Stow and Tabrez (1998) broadly defined a hemipelagite as: "*fine-grained sediment typically occurring in marginally deep-water settings. They comprise an admixture of biogenic pelagic materials (generally >10%) and terrigenous or volcanogenic material (>10%), in which a significant proportion (>40%) of terrigenous (or volcanogenic) fraction is of silt-size or greater (>4 μm), and the overall grain-size distribution is poorly sorted. They are deposited by a combination of vertical settling and slow lateral advection.*"

1.4 Processes Initiating Submarine Landslides and Turbidity Currents

This section serves to summarise the processes that precondition and trigger landslides, and the processes that initiate turbidity currents. Concepts from this summary section are elaborated in later Chapters.

1.4.1 Submarine Landslide Preconditioning Factors and Triggers

Preconditioning factors are those that increase the probability of a failure occurring, whereas the trigger represents the mechanism responsible for initiating a failure. This summary will serve to make distinctions between the preconditioning and trigger factors present on continental margins and volcanic islands. On continental margins preconditioning and trigger factors include: tectonics, loading and under-consolidation (overpressure), slope parallel weak layers, gas hydrate dissolution, and sea level change. Coleman and Prior (1988) and Masson *et al.* (2006) present summaries of many of these factors in relation to continental margins. Trigger factors primarily involve earthquakes, and to a minor degree cyclic loading by hurricanes and storms.

Volcanic islands present environments that facilitate submarine landslides with numerous preconditioning and trigger factors, including: volcanic activity (trigger and loading), over-steepening, dyke intrusion, magmatic inflation, seismicity, climate, and development of weak layers (McGuire, 1996, and references therein).

Tectonics, Earthquakes and Volcanism

Although slope angle has been shown to pose minor-to-no influence on the occurrence of submarine landslides (Hühnerbach *et al.,* 2004), rapid increases in slope angle through tectonic processes of faulting or vertical salt movement could theoretically instigate failure. Tectonic forces are commonly manifested in earthquakes. Earthquakes have been attributed to trigger several submarine mass movements, including the 1929 Grand Banks landslide (Fine *et al.,* 2005), 1946 Aleutian island landslide (Fryer *et al.,* 2003), and the 1998 Papua New Guinea slump (Tappin *et al.,* 2001). In addition, numerous turbidite sequences, of presumed landslide origin, have been linked to earthquakes (Goldfinger *et al.,* 2003; García-Orellana *et al.,* 2010; Masson *et al.,* 2011; Goldfinger *et al.,* 2011, and references therein). In volcanic islands, seismicity is synonymous with eruptions, for example seismicity on the flanks of Mount Etna has been linked to slope instabilities (Montalto *et al.*, 1996). Volcanism alone has also been linked to lateral flank collapses, whereby vertical caldera-collapses associated with explosive eruptions have been proposed to weaken edifice flanks and precondition failure (Marti *et al.,* 1997; Hürlimann *et al.,* 1999a, 2000a). Smaller-scale eruptions have also been found to generate landslides, such as those of Vesuvius and Stromboli (Milia *et al.,* 2003; Maramai *et al.,* 2005).

Rapid Sedimentation

Rapid sedimentation rates on the continental shelf or slope can precondition failures. Rapid sedimentation rates act to firstly load the slope. Secondly rapid sedimentation prevents effective dewatering, thus can lead to excess hydrostatic pressures (overpressure) (Coleman and Prior, 1988). An example would be sediment instabilities caused by rapid sedimentation on the Mississippi delta front (Prior and Coleman, 1982). In the volcanic island setting, eruptions of lavas and pyroclastics coupled with intrusions can often gradually load the submarine and subaerial flanks, leading to generation of slope instabilities (Swanson *et al.,* 1976; McGuire *et al.,* 1990, 1991; Begét and Kienle, 1992; McGuire, 1996; Murray and Voight, 1996).

Gas Hydrate Dissociation

Biochemical reactions producing free methane in organic-rich sediments and gas hydrate dissociation have been linked to instabilities facilitating the occurrence of landslides (Whelan *et al.,* 1977; Maslin *et al.*, 1998; Berndt *et al.,* 2005; Mienert *et al.,*

2005). Examples of this potentially include those from the Amazon Fan (Maslin *et al.,* 1998), the Storegga Slide on the Norwegian continental margin (Berndt *et al.,* 2005; Mienert *et al.,* 2005), and those on the Ebro margin (Lastras *et al.,* 2004). Hydrate dissociation provides overpressure through expulsion of gas and generation of a weak layer that can act as the failure plain. The bubble phase of gas creates an expansion pressure, which reduces the effective yield stress of sediment, increasing the susceptibility of sediment to fail (Prior *et al*., 1982; Kayen and Lee, 1991; Mienert *et al.,* 1998; Dillon *et al.,* 1998; Sultan *et al.,* 2004).

Climate

Climate has been linked to landslide occurrence. Firstly, cyclic loading by hurricanes has been tentatively proposed as triggering delta front collapses on the Mississippi delta (Prior and Coleman, 1982). Broader time-scale climatic changes such as transitions between glacial and interglacial conditions have been linked to the occurrence of large-volume submarine landslides on the Northwest African continental margin (Weaver and Kuijpers, 1983). Whether this is the action of sea level oscillation or changes in sediment accumulation rates linked to deglaciations or ocean productivity is debatable. Climate influences have also been proposed for the occurrence of volcanic island landslides from the Hawaiian archipelago (McMurtry *et al.,* 2004). Warmer and wetter conditions associated with glacial to interglacial transitions have been correlated to the occurrence of large-volume volcanic island landslides (McMurtry *et al.,* 2004).

Formation of Weak Layers

The concept of 'weak layers' parallel to sedimentary bedding controlling the location of continental margin landslides is not novel, as Masson *et al*. (2006) discuss while citing O'Leary (1991). Indeed, the presence of weak layers has been attributed to many continental margin landslides, including the Storegga slide (Bryn *et al.,* 2005; Kvalstad *et al.*, 2005). These weak layers may develop due to overpressuses as the result of under-consoldiation (Bryn *et al.,* 2003; Strout and Tjelta, 2005), differential shear stresses due to compositional variations, sapropels and contourites (Sultan *et al.,* 2004), and liquefaction in sand-rich horizons (Wilson *et al.,* 2003; Sultan *et al.,* 2004). Weak layers can also form in volcanic island environments; indeed residual soils have been implied to be one of the main preconditioning factors for landslides from northern Tenerife (Hürlimann *et al.,* 1999b, 2000b 2001).

1.4.2 Submarine Failures and Morphology

Numerous factors act to precondition a slope to fail, without which even the presence of an earthquake may not result in the triggering of a submarine landslide (Masson *et al.*, 2006). The initiation of a submarine landslide occurs when the shear stress orientated down-slope exceeds the shear strength of the sediment (Hampton *et al.,* 1996). This is defined within the Mohr-Coulomb failure criterion:

$$\tau_f = c + (\sigma - u)\tan\phi \quad [1]$$

Where τ_f is the shear strength, c is the effective cohesion, ϕ is the friction angle, σ is the shear stress normal to the failure plain, and u is the pore water pressure. The shear stresses exerted on the strata can be purely gravitational, seismically-induced or storm wave-induced (Hampton *et al*., 1996).

As aforementioned submarine landslides can be classified as simple (Atlantic-style) or complex (Ranger-style), depending on the resultant morphology of the landslide deposit. Simple Atlantic-style failures are synonymous with single-slab failures, while complex Ranger-style failures are synonymous with multistage failures. Two modes of failure are proposed in this more complex multistage example: (1) retrogressive spreading and (2) extensional slab (Micallef *et al.,* 2007). Principally, retrogressive sliding involves unloading of the headwall at the base of slope, which develops shear planes that define an inverted triangle which accelerates down-slope (Micallef *et al.,* 2007). Removal of this material causes further unloading and destabilisation of the flank, leading to subsequent failures. Slab extension involves an initial slab failure, which experiences tension stresses. The tensional stresses cause extensional rupture into coherent blocks with a ridge and trough morphology (Micallef *et al.,* 2007).

1.4.3 Tsunami Generation

Numerous studies have highlighted the potential for submarine-landslides to generate catastrophic tsunamis (Latter, 1981; Kulikov *et al.,* 1994; Tinti *et al.,* 1999, 2000; Assier-Rzadkieaicz *et al.,* 2000; Tappin *et al.,* 2001; Synolakis *et al.,* 2002; Ward and Day, 2001, 2003; Gelfenbaum and Jaffe, 2003; Fryer *et al.*, 2003; Fine *et al.,* 2005; Fritz *et al.,* 2009; Paris *et al.*, 2011; Giachetti *et al.,* 2011). Determining the characteristics of tsunamis generated from submarine landslides is of great importance for informing hazard assessments of particular regions. Tsunami wave formation and propagation is divided into four parts: landslide dynamics, energy transfer from landslide motion to wave motion, wave propagation in open wave, and wave run-up on

opposing shorelines (Harbtiz *et al.,* 2006). However, the characteristics of the tsunami primarily depend upon the volume, landslide dynamics (initial acceleration and maximum velocity), and the water depth (Ward, 2001; Tinti *et al.,* 2000; Murty *et al.,* 2003; Løvholt *et al.,* 2005; Haugen *et al.,* 2005; Grilli and Watts, 2005; Harbitz *et al.,* 2006; Masson *et al.,* 2006; Tappin *et al*., 2010).

Ward and Day (2001) modelled a landslide-generated tsunami from the forecasted Cumbre Vieja landslide from the western flank of La Palma, Western Canary Islands. This model predicted a 10-25 m-high tsunami would inundate the Eastern United States Atlantic seaboard. This and similar models have utilised single sliding-block models (Heinrich *et al.,* 1999; Tinti *et al.,* 1999, 2000; Ward and Day, 2001, 2003; Mader *et al.,* 2001; Gisler *et al.,* 2006). However, studies of the turbidites associated with past volcanic island landslides have highlighted that these landslides could be multistage (Garcia, 1996; Wynn and Masson, 2003; Di Roberto *et al.,* 2010). Landslide volume is a key parameter in generating tsunamis, thus occurrence of a multistage failure would result in staggered introduction of smaller landslide masses into the ocean, resulting in smaller amplitude waves (Wynn and Masson, 2003; Harbtiz *et al.,* 2006; Masson *et al.,* 2006; Giachetti *et al.,* 2011). Furthermore, time lags on the order of minutes would also result in the development of discrete waves from a multistage landslide, with an absence of positive interference (Harbitz *et al.,* 2006; Masson *et al.,* 2006). This is further evident in tsunami modelling of case studies from Fogo, Cape Verde Islands, and Tenerife, Canary Islands (Paris *et al.,* 2011; Giachetti *et al.,* 2011), which show the reduction in tsunami wave amplitude by applying multistage landslide mechanisms with time lags.

1.4.4 Processes Initiating Turbidite Currents

Turbidity currents are the principal process by which clastic sediment is transported to deepwater regions beyond the continental shelf. Although much work has been completed to understand the depositional morphology and controlling processes of turbidity currents, there is a gulf in our understanding of how they are originally initiated and how the process of initiation influence the subsequent transport and depositional processes (Piper and Normark, 2009). Normark and Piper (1991) suggest three primary methods of turbidite initiation: transformation from slumps, hyperpycnal flows from rivers, and storm-generated flows near the shelf edge. These processes of initiation are later revisited and reviewed by Piper and Normark (2009).

Slump/slide-generated turbidity currents are frequently associated with an earthquake trigger. The magnitude of the trigger does not reflect the size of the flow, rather the availability of sediment to fail is the primary control on flow size (Piper and Normark, 2009). Turbidity currents are initiated from the disaggregation of originally coherent sediment into incoherent granular masses. The entrainment of water acts to dilute this disaggregated granular flow and enable fluid turbulence to suspend the grains (Lick, 1982; Shanmugam, 1997; Mulder *et al.,* 1997; Pirmez, 2003). Sediment-laden flows from rivers directly onto narrow shelves or into submarine canyons can initiate turbidity currents as hyperpyncal flows (Mulder *et al.,* 1995; Mulder *et al.,* 2003; Plink-Björklund *et al*., 2004; Dadson *et al.,* 2005; Lamb *et al.,* 2009). Lastly, storm-initiated turbidity currents form where there is offshore advection of material, which is suspended due to agitation of unconsolidated marine sediment by storm activity on the shelf (Mulder *et al.,* 2001).

1.5 Regional Setting of Study Area

This section serves to describe the geological detail of the study area. The turbidites within the Moroccan Turbidite System have provenances from the Moroccan and Western Saharan continental margins, Western Canary Islands and Madeira (de Lange *et al.,* 1987; Pearce and Jarvis, 1995; Frenz *et al.,* 2009). As a result, it would be prudent to report on the geology of these regions.

1.5.1 Onshore Geology

Northwest Africa

The physiographic provinces of Northwest Africa are defined after Summerhayes *et al.* (1976) (Figure 1.5). The most northern region represents the Rif Mountains, to the south of which is the stable Meseta peneplain. Farther south are the High Atlas and Anti-Atlas mountain chains, which are separated by the Sous Trough. The Sous Trough represents the drainage basin for the Sous River that debauches onto the west Moroccan shelf. Further south of these mountain chains are the broader Aaiun and Tindouf basins.

The Palaeozoic basins of Northwest Africa were gently folded and thrusted during the late Devonian and Westphalian, with gentle folding of the Anti-Atlas (Pique and Michard, 1989). Early opening of the Atlantic produced Triassic-Jurassic extensional basins containing continental fluvial clastics, shallow marine evaporites and carbonates, and later thick Cretaceous sequences (Figure 1.6) (Dillon, 1974; Beauchamp, 1999).

These Cretaceous deposits represent deep water shales and turbidites following a major marine regression (Le Roy *et al.,* 1998; Steiner *et al.,* 1998).

Extension within the Bay of Biscay commenced in the Triassic, with major rotation of the Iberian plate occurring in the Late Cretaceous (Ries, 1978). The Atlas Mountains, forming the northern boundary to the Sous Trough, comprise an intracontinental fold belt (Figure 1.6). This mountain chain developed in response to inversion of a previous Mesozoic Rift (Giese and Jacobshagen, 1992; Beauchamp, 1999). Early Tertiary inversion forming the High Atlas is the product of collisional tectonism associated with increasing Iberian-North African convergence (Beauchamp, 1999; Morabet *et al.,* 1998). Iberian-North African convergence is driven by rotation of the Iberian plate as the result of seafloor spreading within the Bay of Biscay (Williams, 1975; Ries, 1978; Gong *et al.,* 2008). A series of inversion basins developed, including Rharb and Pre-Rif Basins, Doukkala Basin, Essaouira-Hana Basin, and Tarfaya-Aaiun Basin (Davison, 2005).

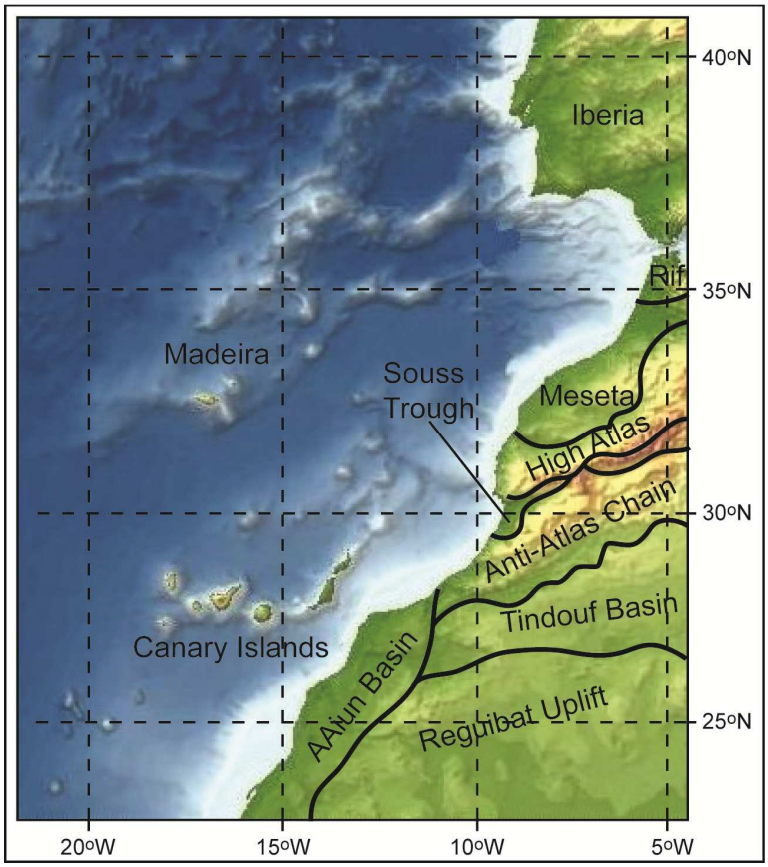

Figure 1.5 Physiographic provenances of Northwest Africa (after Summerhayes *et al.* 1976).

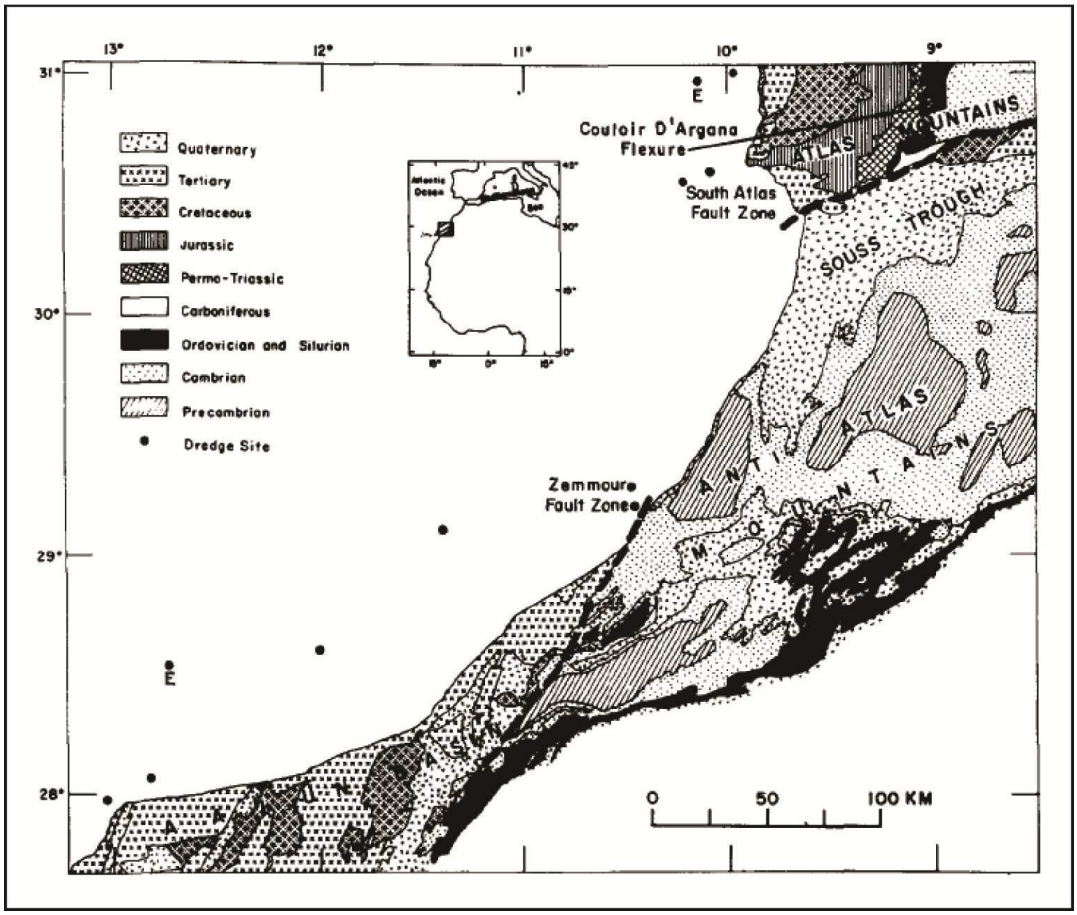

Figure 1.6 Geological map of the continent adjacent to the Moroccan continental shelf (Dillon, 1974).

Canary Islands

The Canary archipelago represents an east-to-west chain of volcanic islands extending over ~500 km of the Northwest African passive margin (Figures 1.5 and 1.7). The Canary Islands form an archipelago associated with movement of Jurassic-age (156-176 Ma) Atlantic oceanic crust over a mantle plume (Klitgort and Schouten, 1986; Hoernle and Schmincke 1993; Hoernle *et al.,* 1995; Carracedo *et al.,* 1998; Schmincke *et al.,* 1998). The islands developed in a general east-to-west age progression (Figure 1.7) (Schmincke, 1982; Carracedo *et al.,* 1998; Carracedo, 1999).

The origin of this archipelago has been much debated, and competing theories exist: propagating fracture model (Anguita and Hernán, 1975; Robertson and Stillman, 1979), uplift of tectonic blocks (Araña and Ortiz, 1986), Canary rift model (Fúster, 1975; Oyarzun *et al.,* 1997), classic plume model (Morgan, 1971; Burke and Wilson, 1972; Schmincke, 1973; Vogt, 1974; Khan, 1974; Morgan, 1983; Carracedo, *et al.*, 1998), blob model (Hoernle and Schmincke, 1993) and upwelling sheet model (Anderson *et al.,* 1992; Hoernle *et al.*, 1995).

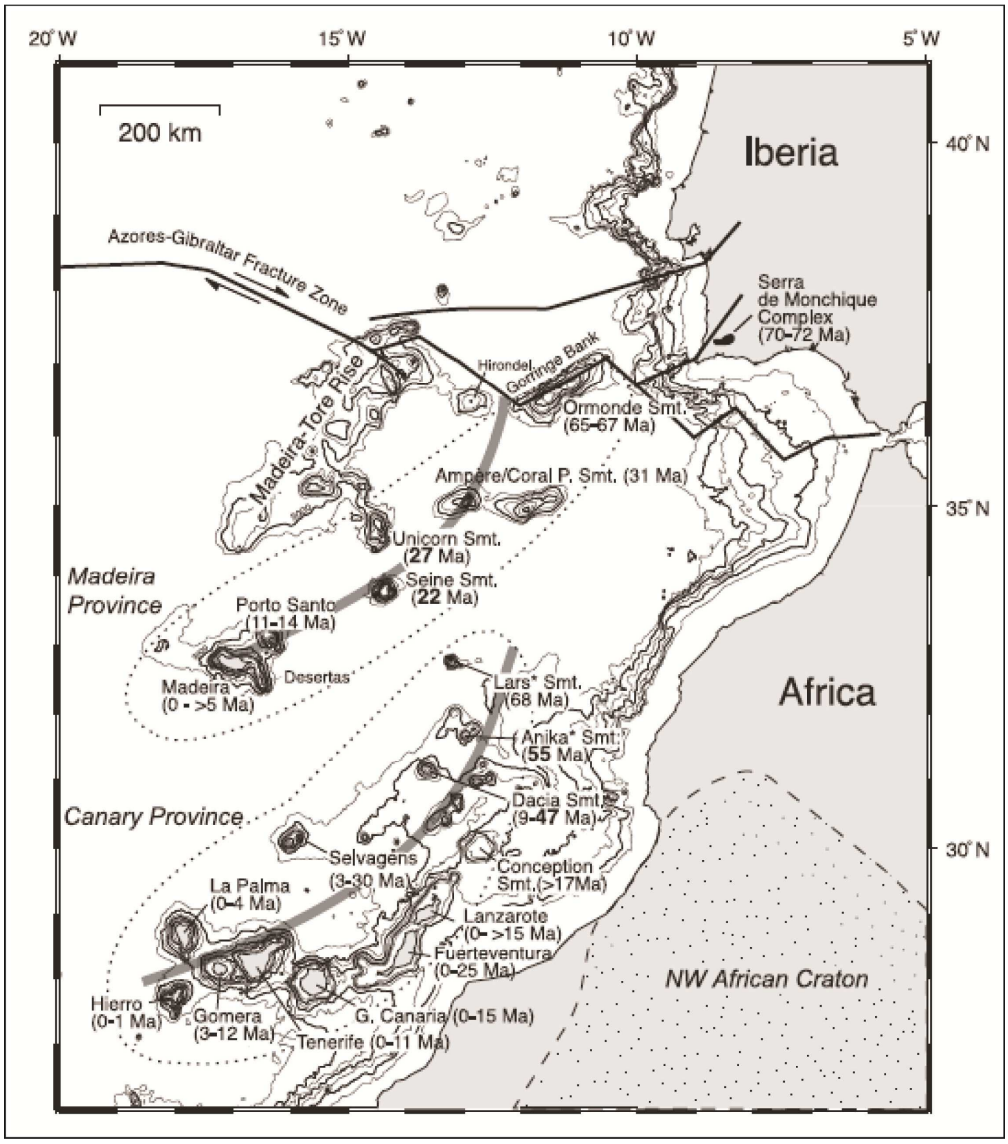

Figure 1.7 Map showing the age progression of the volcanic islands and seamounts that comprise the Canary and Madeira archipelagos (Geldmacher *et al.,* 2005). The Madeira archipelago follows a gradual east-west age progression, whereas the Canary archipelago has a general east-west age progression but with much temporal and spatial divergence.

The propagating fracture model of Anguita and Hernán (1975) and Robertson and Stillman, (1979) suggests that there is a tectonic connection between the Canary Islands and the Atlas Mountains. Tensional tectonic phases result in volcanism through decompression melting, while compressive tectonic phases result in volcanic quiescence (Anguita and Hernán, 1975). However, this model does not account for uplift of insular blocks, absence of Cenozoic faults between the islands and termination of the South Atlas fault at Agadir (Anguita and Hernán, 2000).

The model proposing uplift of tectonic blocks involves compressive tectonics causing seafloor shortening and thickening, forming the current Canary Islands (Araña

and Ortiz, 1986). Although explaining the height of the current landforms, this model fails to explain magma genesis (Anguita and Hernán, 2000).

The Canary rift model is based on faulting within the basal complexes of the islands, which is proposed to be the result of a regional extensional structure (Fúster, 1975; Oyarzun *et al.,* 1997). However, the age of the oceanic crust, orientation of dyke swarms on the islands, and deep troughs between the islands pose significant problems for this model (Anguita and Hernán, 2000).

The classic Canary plume model is based on the Hawaiian plume model (Wilson, 1963). This represents a vertical plume of upwelling mantle that rises and erupts on the seafloor (Morgan, 1971; Burke and Wilson, 1972; Schmincke, 1973; Vogt, 1974; Khan, 1974; Morgan, 1983; Carracedo, *et al*., 1998). However, there are problems with this model: long quiescent periods between island emergence, irregular time sequence of westward progression of subaerial volcanism, separation in the volcanic line resulting in La Palma and El Hierro, long-lasting islands (at least 30 Ma), and low melt productivity (Anguita and Hernán, 1975; Hoernle and Schmincke, 1993).

In response to issues with the classic Canary plume model, Hoernle and Schmincke (1993) developed the blob model. This model advocates a dipping magmatic conduit, which underlies the whole archipelago and dips to the west due to viscous drag caused by the African plate (Hoernle and Schmincke, 1993). However, issues arise from the geometry of the proposed plume and the expected topographic swell and geoid high (Anguita and Hernán, 2000). The upwelling sheet model is another model expanding on the classic plume model. It is based on a broad thermal anomaly with a sheet-like geometry below the continental margin. However, there are problems with this model regarding the melt geochemistry and tectonics (Anguita and Hernán, 2000).

Anguita and Hernán (2000) generate a further unifying theory on the origin of the Canary Islands, combining the key notions of the aforementioned models. Carracedo *et al.* (1999, 2001) state that evidence thus far at least supports growth of the islands on a slow moving plate above a mantle plume. A viable unifying theory needs to explain the 40 Ma long volcanic history at single volcanic centres, long hiatuses in volcanic activity, and the apparent irregular distribution of islands and seamounts along the proposed plume track (Figure 1.7) (Geldmacher *et al.,* 2005). Geldmacher *et al.* (2005) suggest that interaction of the Canary mantle plume with 'small-scale mantle processes' such as edge-driven convection could also generate the observed inconsistencies with the classical hotspot model.

Madeira

Madeira formed at ~5 Ma and is the western most volcanic formation in a curved line of seamounts and islands, including the Ormonde (67 Ma), Ampère (31 Ma), Coral Patch, Unicorn and Seine seamounts, and Desertas (3.2 Ma) and Porto Santo (14 Ma) islands (Geldmacher and Hoernle, 2000; Geldmacher *et al.,* 2005). The age progression of this archipelago is thought to represent the northeast to southwest passage of the oceanic crust over a >70 Ma old mantle plume, finally residing at its current location beneath Madeira under 140 Ma Atlantic oceanic crust (Geldmacher and Hoernle, 2000; Geldmacher *et al.,* 2005). Indeed, the age progression is more akin to the classical hotspot model (Figure 1.7), albeit for the protracted periods of volcanism at each site (Geldmacher *et al,* 2005). The islands and seamounts of the Madeira archipelago also form a geomorphological boundary for the northern margin of Agadir Basin and Seine Abyssal Plain within the study area.

1.5.2 Offshore Geology

Moroccan Continental Shelf and Deepwater Basins

The Moroccan shelf has developed through prograding sedimentation through the Mesozoic and Tertiary (Summerhayes, 1971). Indeed, the continental shelf comprises seawards dipping Cretaceous and Tertiary sediments (Summerhayes *et al.,* 1976). Bathymetric details show that the shelf opposing the Moroccan margin is between 35-60 km wide (Wynn *et al*., 2000a), which increases to >100 km south of the Canary Islands opposing the Western Saharan margin. The continental slopes along this margin range from 1^{o}-6^{o}, with the continental rise having gradients of $<1^{o}$ (Masson *et al.,* 1992).

Major sediment sources to the shelf are the Sous river (terrigenous sediment) and from upwelling cells (marine productivity) (Weaver *et al*., 2000; Wynn *et al.,* 2002a; Weaver, 2003). However, there is only minor fluvial input to the margin owing to the arid climate (Weaver *et al.,* 2000).

The Agadir Canyon forms the most prominent feature on the continental margin. The Agadir Canyon represents a 460 km-long conduit for sediment sourced from the shelf and slope (Figure 1.8) (Wynn *et al.,* 2000a). The mouth of the Agadir Canyon issues unconfined turbidity currents onto the basin floor of Agadir Basin, which forms part of the Moroccan Turbidite System (Ercilla *et al.,* 1998; Wynn *et al*., 2000a, 2002a). Beyond the mouth of the Agadir Canyon are numerous kilometre-scale megascours and

amalgamated scours, which are testament to the erosive capabilities of flows exiting the canyon (MacDonald *et al.*, 2011).

The Moroccan Turbidite System comprises the Agadir Basin proximal to the Agadir Canyon in water depths of 4,000-4,400 m, the Seine Abyssal Plain in 4,000-4,300 m water depths to the north, and the Madeira Abyssal Plain in 5,000-5,300 m water depths to the west (Figure 1.8) (Wynn *et al.*, 2002a). The Seine Abyssal Plain is connected to the Agadir Basin via a 10-40 m-high topographic feature known as the Casablanca Ridge (Davies *et al.*, 1997; Wynn *et al.*, 2002a). Agadir Basin forms a conduit for sediment travelling to the Madeira Abyssal Plain. The Madeira Distributary Channel System connects Agadir Basin to this distal depocentre (Masson, 1994; Weaver *et al.*, 2000; Wynn *et al.*, 2002a; Stephenson *et al.*, 2012).

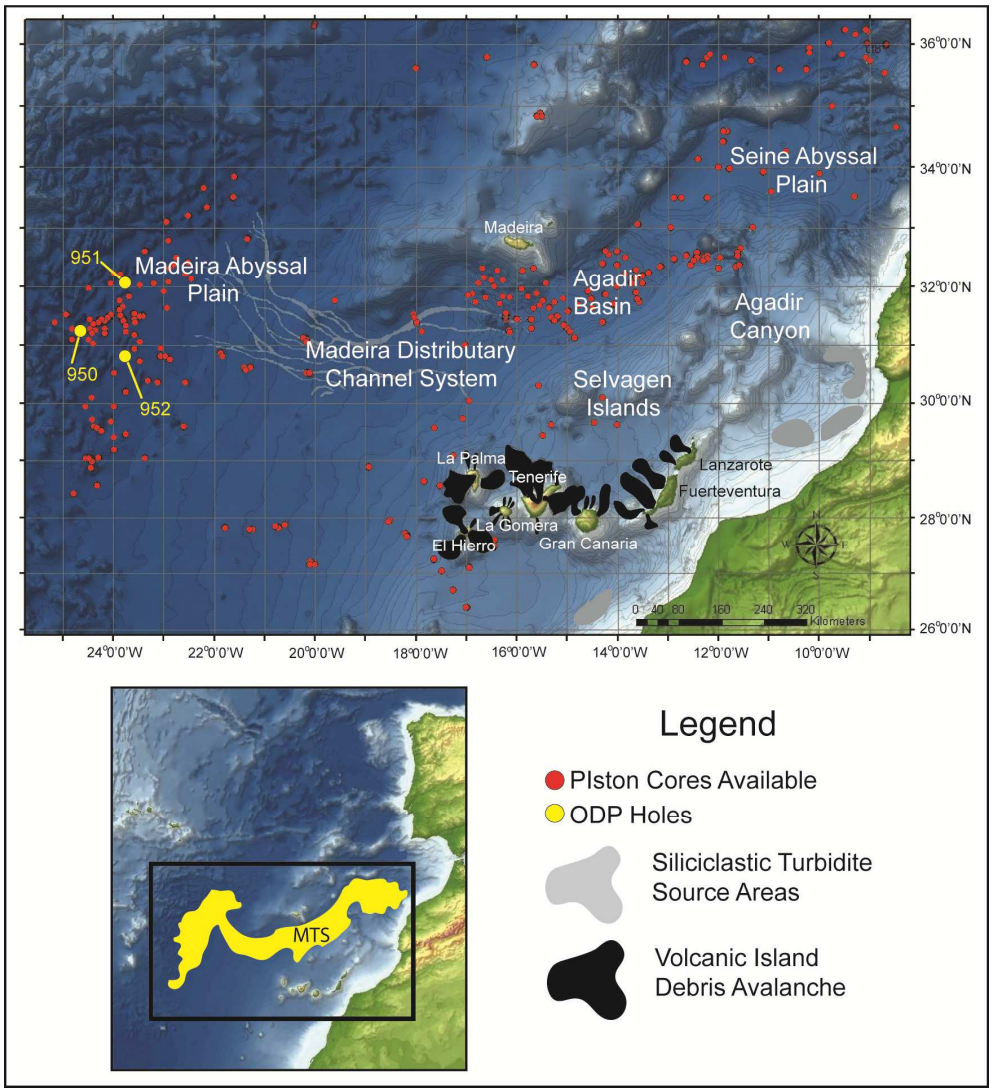

Figure 1.8 Map of the Moroccan Turbidite System study area. Map firstly shows the main physiogeographic regions, including Agadir Basin, Madeira Abyssal Plain and Seine Abyssal Plain. The Map also shows the available piston core coverage and the ODP holes in the Madeira Abyssal Plain.

Canary Island Debris Aprons

Numerous geophysical studies have been completed to investigate the architecture and composition of the submarine flanks of the Canary Islands (Holcomb and Searle, 1992; Watts and Masson, 1995, 2001; Urgeles *et al*., 1997, 1999, 2001; Wynn *et al.,* 2000b; Kastrel *et al*., 2001; Masson *et al.,* 2002; Acosta *et al.*, 2003). The Western Canary Islands of Tenerife, La Palma and El Hierro have been subjected to recent (last 500 ka) submarine landslide activity (Masson *et al.*, 2002, and references therein; Acosta *et al.,* 2003, and references therein), which has resulted in the development of extensive 750-2,200 km^2 debris avalanche lobes.

These debris avalanche lobes represent the failure of 50-500 km^3 of island flank (Masson *et al.,* 2002, and references therein). The morphology of these debris avalanches appears to fall within two end members. One end member is represented by the lobate shape of the El Golfo debris avalanche, which lacks flow structures and where the blocks are scattered randomly (Masson *et al.,* 2006). The alternate end member is represent by the elongate shape of the Icod debris avalanche, where blocks are orientated to the margins and comprise flow structures such as shear zones and pressure ridges (Masson *et al.,* 2006).

1.5.3 Oceanography and Climate

Northwest Africa (17°N to 28°N) represents an arid climate with annual precipitations <100 mm (Sarnthein *et al*., 1982). The highest rainfall in the region is restricted to the northern region of the study area, in the Rif Mountains, High Atlas Mountains and northern Meseta (Summerhayes *et al.,* 1976).

The primary wind systems within the study area are the Saharan Air Layer and the Northern Trade Winds. The Saharan Air Layer comprises two jets: a northward jet that disperses aeolian sediments over the Northeast Atlantic, and a westward jet that disperses sediments far offshore (Prospero and Carlson, 1972).

In regards to ocean circulation, the dominant deepwater currents within the study area of the Northwest African passive margin are North Atlantic Deep Water (NADW) and the Antarctic Bottom Water (AABW). The North Atlantic Deep Water flows southward at water depths of 2,000-3,800 m water depths (Dickinson and Brown, 1994), while the Antarctic Bottom Water travels northwards below 3,800 m water depth (Lonsdale, 1982; Orsi *et al*., 1999).

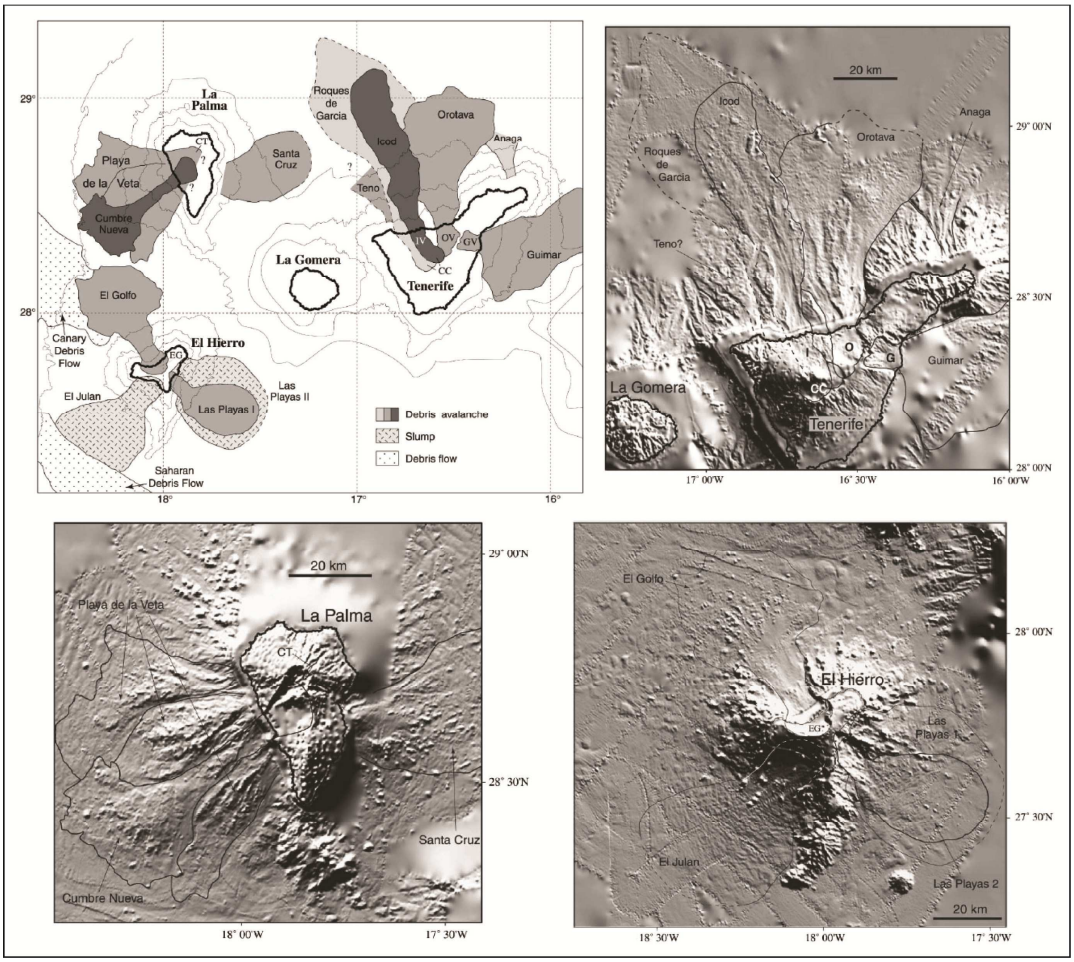

Figure 1.9 Map of the Western Canary Islands (Masson *et al.,* 2002), which have undergone relatively recent mass wasting. In addition are shaded relief images of Tenerife, El Hierro and La Palma (Masson *et al.,* 2002), showing the offshore debris avalanche lobe generated from large-volume submarine flank collapses.

These bottom-water currents are currently travelling at velocities of <5 cm/s (Lonsdale, 1982). In contrast to these bottom-water currents is the main surface-water current, named the Canary Current, which is driven by the Northeast Trade Winds. The Canary Current, in combination with the Northeast Trade Winds, contributes to the North Atlantic gyre, which flows southward along the Northwest African continental shelf and generates an upwelling cell (Sarnthein *et al.,* 1982; Ternois *et al.,* 2000; Freudenthal *et al.,* 2002; Henderiks *et al.*, 2002; Knoll *et al.,* 2002).

Chapter 2
Methodologies and Data

The data collected during this study involved a dataset of >300 piston cores from the Moroccan Turbidite System. These were collected over three decades of research expeditions to the basins of the Northeast Atlantic, including the most recent CD166 cruise to Agadir Basin in 2006. Subsequent Chapters utilise specific components of the multi-disciplinary methodologies outlined below.

2.1 Sedimentology

2.1.1 Sediment Core Logging

Visual logs and photographic cataloguing of the >300 sediment cores formed the initial framework for this thesis. This involved the identification of colour, facies, and visual grain size assessed using a grain-size comparator. Particular attention was made to the turbidites and the lithologies of the hemipelagite sediment.

2.1.2 Sediment Sieving

Sediment sieving was performed to separate grain size fractions for mineral and geochemical analysis, rather than conduct grain-size analyses. The 63 μm sieve was used to wet-sieve sediment and separate out the clay and fine silt, providing the coarse fraction for later mineralogy analyses. The sieve residues were dried in an oven at 60^{o}C and then placed in inert plastic pots.

2.1.3 Laser Diffraction Grain-size Analysis

Targeted turbidites were sampled at 1 cm intervals, from which 1 cm^3 samples were taken. These samples were then added to 30 mL RO water with a 0.05% sodium hexametaphosphate dispersant. The dispersed sediment solutions were analysed using the *Malvern Mastersizer 2000* particle size analyser. Typically three aliquots were measured to assess precision. Standard materials of mean average 32 μm and 125 μm were used to monitor accuracy, while repeat samples were used to further monitor precision (reported at <0.5% standard deviation).

2.1.4 Sediment Core X-radiography

X-radiographs were produced to study the bedforms within the turbidites and analyse turbidite muds for the presence of post-depositional deformation and bioturbation. Split core sections were passed through the ITRAX μXRF core scanner. With x-radiography conditions were 60 kV and 45 mA, with a dwell time of 800 ms, and at a resolution of 200 μm.

2.2 Geochemistry

2.2.1 ICP-OES

Bulk samples were taken from turbidite mudcaps in Agadir Basin and from the bases of volcaniclastic turbidites. Mudcap samples were analysed as bulk samples including the carbonate content, since the aim was to provide elemental concentrations to calibrate the ITRAX results. In regards to the volcaniclastic sand samples only the coarse fraction was required, thus samples were wet sieved to remove the <63 μm fraction. Samples were dried and weighed before the carbonate content was leached by addition of 5 ml 10% acetic acid.

Then 100 μg aliquots of each sample were powdered for acid digestion. The first stage of acid digestion used 5 ml aqua regia (3:1 $HCl:HNO_3$). The solution was dried-down before a second stage of digestion, which involved 3 ml HF and 2.25 ml $HClO_4$. This was dried-down again before a further 2 ml perchloric acid was added and a subsequent evaporation stage completed. The silica-free residue was finally dissolved in 10 ml of 6 M HCl to produce a stock mother solution, from which 0.6 M HCl daughter solutions were produced for analysis.

Calibration method of data was achieved using five standards, which were artificially created as 0.6 M stock solutions. The concentrations of these standards were derived to encompass the likely range of concentrations from the samples analysed. Each element solution was gravimetrically added to enable exact compositions to be back-calculated.

A number of terrigenous (MAG-1, SCo-1 and SRG-1) and volcanic (BHVO-2, BIR-1, JB-1a, JB-2, JB-3, JGb-1 and MRG-1) standard reference materials (SRMs) were used to assess precision, with sample and SRM duplicates used to assess the accuracy of the methodology. The standard reference materials demonstrated that major element analyses produced average precisions of 2.1% and average accuracies to the standard reference materials to within 2.3% (Table 2.1 and Appendix 5.6). With regards to trace elements, precision is between 2.0% and 20.8% (averaging 7.8%) with accuracies

ranging to within 2.8% to 39.9% (averaging 16.4%) (Table 2.1 and Appendix 5.6). Those trace elements with accuracies beyond 15% were discounted from use. A blank and artificial standard (drift monitor) were analysed between every 10 samples.

Table 2.1 Summary table of the average precision upon repeat and accuracies to certificate data for SRMs analysed by ICP-OES

	Av St Dev Precision (%)	Av St Dev Accuracy (%)
TiO_2	1.7%	2.3%
Al_2O_3	2.1%	1.8%
Fe_2O_3	2.1%	2.7%
MnO	2.4%	4.8%
MgO	1.8%	1.3%
CaO	2.1%	3.6%
Na_2O	1.9%	1.1%
K_2O	2.5%	4.5%
P_2O_5	9.1%	16.4%
Li	3.5%	2.9%
Sc	20.8%	30.0%
V	2.0%	5.5%
Cr	11.0%	19.4%
Co	2.6%	3.2%
Ni	10.6%	12.1%
Cu	2.3%	6.7%
Zn	6.2%	26.2%
Sr	11.1%	6.6%
Nb	5.2%	19.7%
Y	2.5%	14.2%
Zr	5.4%	38.0%
Ba	10.5%	4.5%
La	8.9%	17.4%
Ce	14.1%	39.9%

2.2.2 ITRAX µXRF

The methodology involves split core sections being moved progressively past a 3 kW Mo-tube X-ray source and XRF Si-drift chamber detector (Croudace et al., 2006). The instrument operated at 60 kV and 45 mA, with a dwell time of 800 ms and a resolution of 500 µm. The K-shell peak areas are automatically measured and converted to intensity (counts) for a designated element. The validity of the data was maintained by

monitoring the element integral profiles, Compton scatter integral and detector-sediment distance. The element intensities are normalised to incoherence values, and then calibrated. Appropriate calibration curves were generated using 1 cm-wide samples taken from the studied cores analysed using ICP-OES or WD-XRF. ITRAX intensities measured over the 1 cm sample locations were averaged for calibration. The calibration coefficients for the ITRAX methodology produced R^2 values of 0.74-0.96 (Appendix 3.2).

Attempts thus far to convert XRF core scanner outputs to elemental concentrations have only been moderately successful (Weltje and Tjallingii, 2008, and references therein). Intensity-concentration cross-plots show scatter and potential biasing as a result of sample inhomogeneity, variable water content and a lack of sample geometry (Weltje and Tjallingii, 2008, and references therein). Averaging intensities over the 1 cm sampled for ICP-OES analysis will aid reduction in the effects of small scale inhomogenetities on the calibration. Issues with sample geometry and signal-to-noise can be negated due to the ability of the ITRAX detector to adjust position relative to the split core surface (Croudace et al., 2006). Water content may be variable, however the cores chosen for study are of the same vintage and have been kept sealed in cold storage, so differential water loss by drying should be minimal. Utilising the mudcaps for comparisons of the turbidite compositions maintains analysis of materials with similar porosity-permeability characteristics, thus further reducing the effects of variable water content.

Sediments within the cores studied vary in grain-size, with hemipelagite averaging 10-30 μm, turbidite muds averaging 4-8 μm, and turbidite sands averaging 90-180 μm (d90 350 μm). The 500 μm ITRAX resolution is far greater than the size of the largest grains recovered; therefore issues regarding sample geometry will be further reduced. For provenance comparisons of the turbidites, the compositions of the mudcaps will be compared. This will maintain comparison of compositions of similar grain-size distributions (2-12 μm), again reducing effects of sample geometry. Furthermore, these finer homogenous sediments mirror the homogenous fine powders used in conventional XRF analysis (Haug *et al.,* 2001, 2003; Weltje and Tjallingii, 2008, and references therein).

Although attempts have been made here to calibrate the ITRAX intensities to element concentrations, ultimately element ratios will be used. This is because elemental ratios reduce the effects of some of the issues outlined above, but most

importantly will reduce the effects caused by unit-sum constraint and dilution (Weltje and Tjallingii, 2008, and references therein). Numerous studies have advocated using ratios and here selected ratios are used according to Croudace *et al.* (2006) and Rothwell *et al.* (2006). Specifically, the Ca/Fe and Sr/Ca ratios are used to monitor the carbonate composition, while K/Rb and Zr/Ti are used to monitor the detrital clay and heavy mineral compositions (Croudace *et al.,* 2006). Weltje and Tjallingii (2008) further advocated using log-ratios to both calibrate the raw data and for comparing data. Compositional cross-plots of the present study only utilise elemental ratios, since log-ratios appear to show the same relationships, albeit reducing the scatter.

2.2.3 SEM-EDS (LEO 1450 and TM1000)

This methodology was used to analyse the composition of volcanic glasses and lithics extracted from volcaniclastic turbidites within Agadir Basin and the Madeira Abyssal Plain. Samples were sieved at 63 µm and leached with 10% acetic acid to remove carbonate and wash grain surfaces. Grains of 63-125 µm grain-sizes were analysed. For the LEO 1450 method samples were made into polished 30 µm carbon-coated thin sections. The LEO 1450 variable pressure SEM and PGT microanalysis EDS was then used to produce both images and analyse the geochemical compositions of the volcanic glass assemblages. Operating conditions were 50 µm aperture size, beam current 80 µA, and EHT target 20 kV. Samples were analysed quantitatively using internal standards and international reference materials. The backscatter application gave an appreciation of grain internal density and contrasts between grains during sample mapping. In addition to two pre-prepared glass standards (BIR-1g and BRR-1g), a series of additional glasses (JGB-1, UMAT-1, JB-3, JB-1a and JB-2) were produced to encompass the desired range in K_2O. This was done using 20 µg of powdered standard melted, homogenised and solidified on an iridium strip, in an argon filled chamber, and utilising a thermocouple.

Precision varies according to concentration whereby low concentrations (<0.1 wt%) at or below the detection limits of the instrument have reproducibilities >20%. Whereas for concentrations >0.1 wt% the precision averaged at 2.9% (Table 2.2 and Appendix 5.8). The accuracy of the data comparing SRMs to certificate data varied, but averaged at 4.0% (Table 2.2 and Appendix 5.8).

Table 2.2 Summary table of the average precision upon repeat and accuracies to certificate data for SRMs analysed by SEM-EDS using LEO1450

	Av St Dev Precision (%)	Av St Dev Accuracy (%)
SiO_2	0.4%	0.8%
TiO_2	6.7%	4.4%
Al_2O_3	1.1%	4.7%
Fe_2O_3	1.6%	4.1%
MnO	37.6%*	16.4%*
MgO	3.1%	13.6%
CaO	1.5%	6.3%
Na_2O	3.6%	12.3%
K_2O	6.0%*	15.5%*
P_2O_5	5.8%*	95.4%*

* elevated error due to low concentrations of particular oxides at or below detection limits (<0.05 wt%).

The *Hitachi* TM1000 SEM poses a more novel methodology, whereby the instrument does not require significant sample preparation. Again samples from volcaniclastic turbidites were sieved for the >63 μm fraction and subjected to acetic acid (10%) leaching to remove carbonate content and wash grain surfaces. The volcanic grains were then mounted on a semi-conductor pad and placed within the vacuum chamber of the Hitachi TM1000 SEM. Volcanic glasses and lithics of 90-125 μm size were analysed at 15 kV with a dwell time of 120 s.

Results were reported as elemental wt% normalised to 100%. Standard suites of major elements were analysed, and converted to oxide wt% for consistency with igneous rock analyses. Output results were calibrated against a series of 18 powdered standard reference materials. These powdered standards best represent the materials being examined in regards to sample geometries. Calibration curves were produced with R^2 of 0.80 to 0.99 (excluding MnO and P_2O_5) (Figure 2.1). Calibrated results were verified for accuracy and precision using a series of glass standards produced from international standard reference materials. Concentrations between 1-2 wt% have precisions of 4-6% of the value, 2-10 wt% values have precisions to within 2-5%, while those values >10 wt% have precisions of 0.5-4% (Figure 2.2). Accuracies were generally within 1-5% of the certified value for the suite of standard reference materials, where accuracies were higher with increasing concentration (Table 2.2). Poor average

errors on precision and accuracy as a result of addition of results from analyses of small concentrations at or below detection limits (Figure 2.2).

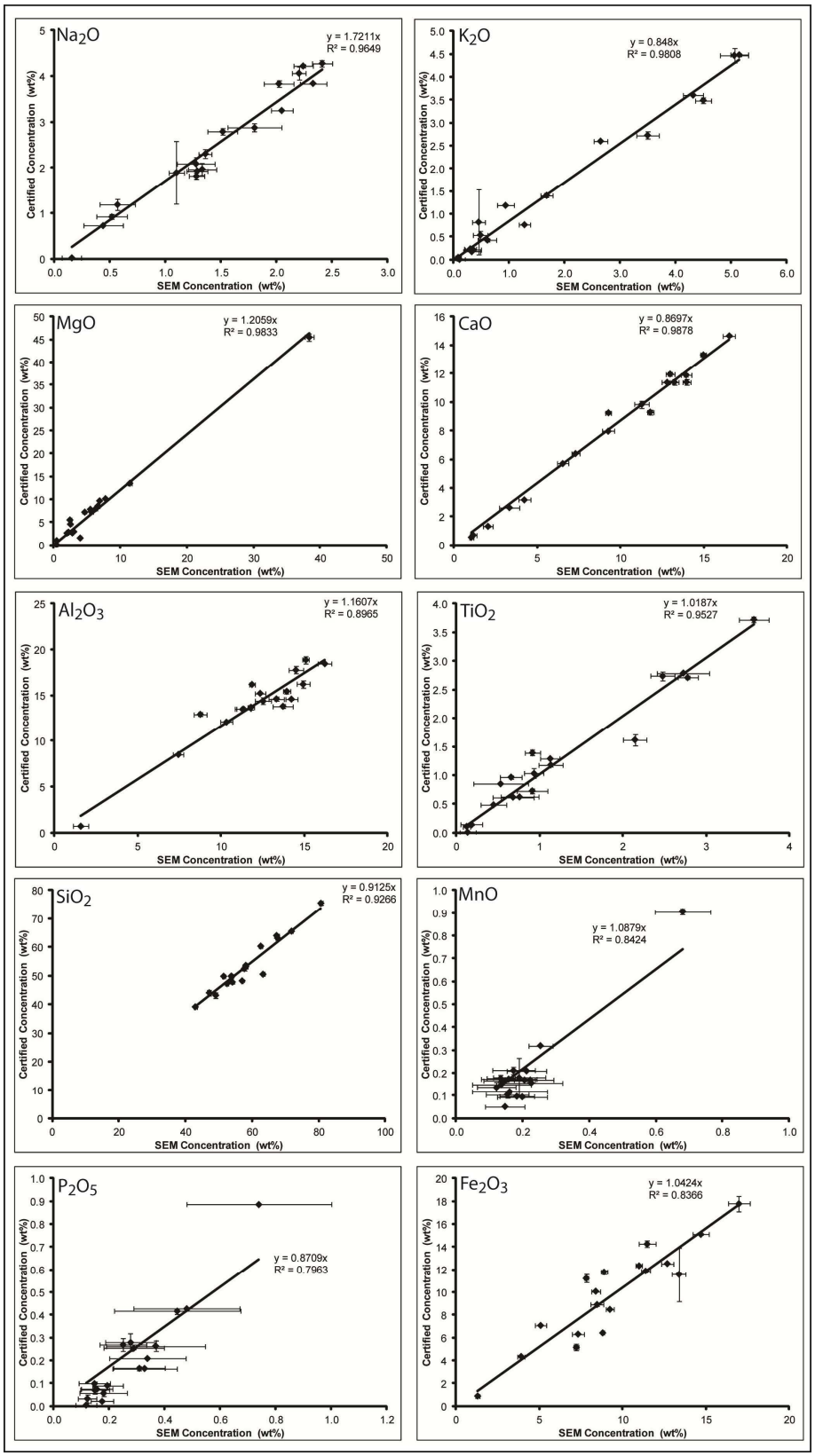

Figure 2.1 Calibration curves for major-elements analysed by *Hitachi* TM1000 SEM EDS system.

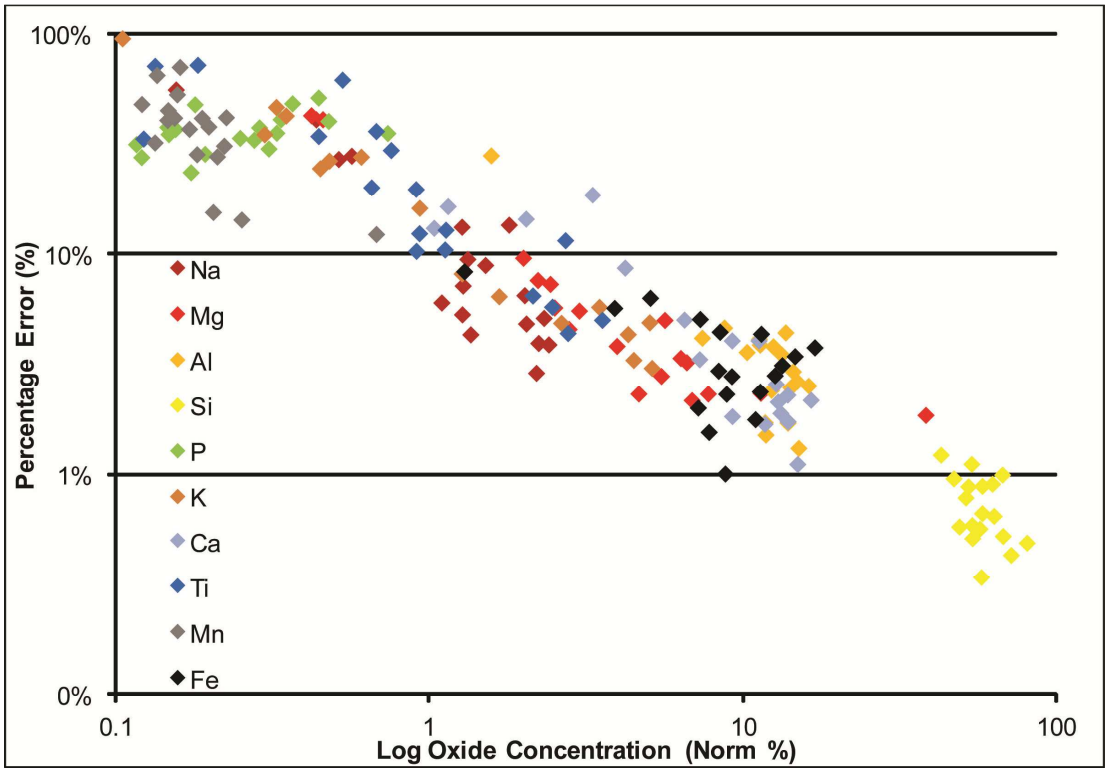

Figure 2.2 Log-Log Plot of standard deviation as percentage of value against the concentration.

Table 2.2 Summary table of the average precision upon repeat and accuracies to certificate data for SRMs analysed by SEM-EDS using *Hitachi* TM100

	Av St Dev Precision (%)*	Av St Dev (Accuracy (%)*
SiO_2	0.77%	2.52%
TiO_2	11.49%	11.13%
Al_2O_3	1.52%	3.00%
Fe_2O_3	2.98%	7.76%
MnO	41.30%	69.60%
MgO	2.49%	2.71%
CaO	2.39%	4.07%
Na_2O	10.30%	4.05%
K_2O	16.53%	8.10%
P_2O_5	48.95%	136.65%

* larger than expected errors on precision and accuracy due to larger errors at small concentrations at or below detection limits (see Figure 2.2), which skew data.

2.2.4 CO_2 Coulometry

Inorganic carbon (carbonate) measurements were taken through the hemipelagite in core CD166/12 at 1 cm intervals (Chapter 3) and from the subunits in the Icod deposit

(Chapter 5). Samples of 25 µg were oven dried (at 60°C with a final 20 min evaporation at 105°C) and ground, and then subjected to a potentiometric back-titration using a coulometer. The carbonate content is calculated from the CO_2 volume liberated from the sample mass by a phosphoric acid-decomposition. Reproducibility was within 0.5%, while accuracy to 100% and 87% $CaCO_3$ standards were to within 1%.

2.3 Geophysics

2.3.1 P-wave Velocity Core Analysis

Down-core p-wave velocity profiles aided identification of turbidite sands, and often provided insight into the properties of the turbidite deposits. P-wave velocity provides a proxy for grain size, whereby turbidite sands record greater values of p-wave velocity. Madeira Abyssal Plain cores had p-wave velocity profiles previously collected using a p-wave velocity profiler. New p-wave velocity profiles were gathered for Agadir Basin cores using the *GeoTek* MSCL (multi-sensor core logger). The MSCL used ultrasonic transducers known as Acoustic Rolling Contact (ARC) transducers. The centre frequency used here is 230 kHz, this lower frequency provides a higher signal/noise ratio.

Firstly, the down-core core thickness is measured. This utilises displacement transducers calibrated against a calibration block of known thickness:

$$X = RCT - W + CTD / 10 \quad [1]$$

Where RCT is reference core thickness, W is wall liner thickness and CTD is core thickness deviation. The p-wave velocity is the product of:

$$Vp = (1000) \times X / TT \quad [2]$$

Where X is sediment thickness and TT is travel time. Travel time is a product of:

$$TT = TOT - PTO \quad [3]$$

Where TOT is recorded time and PTO is p-wave travel time offset, which accounts for the passage through the liner and transducers, where PTO is:

$$PTO = TOT - (D - W) \times Vf \quad [4]$$

Where D is distance between transducers and Vf is the p-wave velocity through distilled water. The final p-wave velocity result requires a last correction:

$$Vp_{corr} = Vp \times Vp_{fac} \quad [5]$$

Where Vp_{fac} represent the ratio of the p-wave velocity in distilled water at the room temperature during calibration and while the measurement was taken. The Vp_{corr} represent the final value reported.

2.3.2 Gamma-ray Density Core Analysis

The density of the core materials further aided identification of turbidite sands, turbidite sands, and hemipelagite sediments. Density is often highest in the turbidite sands, compared to turbidite muds or hemipelagite. Gamma-ray density profiles were obtained using the *GeoTek* MSCL, which utilises gamma-ray attenuation porosity evaluator (GRAPE) to ascertain sediment density. A caesium-137 source is used to emit a narrow beam of gamma rays with energies of 0.662 MeV. Attenuation is the product of scattering upon interaction with electrons within the sediment. Unattenuated gamma rays (transmitted gamma photons of similar energy to source) thus provide a means of calculating the density of the same measured:

$$\rho = 1 / \mu d \times \ln(I_o/I) \quad [6]$$

Where μ is the Crompton scatter coefficient, d is the thickness, I_o is the gamma source intensity and I is the gamma intensity transmitted through the sample. The initial source intensity is empirically measured by using a calibration block.

2.3.3 Magnetic Susceptibility Analysis

Magnetic susceptibility is useful for aiding identification of volcaniclastic sediments, but can also be used to record glacial-interglacial transitions in hemipelagite sediments. Magnetic susceptibility records positive excursions in the presence of magnetic grains, thus highlights the presence of volcaniclastic turbidites. Down-core magnetic susceptibility profiles were collected using both *GeoTek* MSCL and XYZ core loggers. Both systems use the same method. The split core section is passed under a *Barrington* point sensor (MS2E), which is pre-calibrated by *GeoTek*, thus results are absolute. Principally the sensor will detect the degree of magnetisation in response to an applied magnetic field, whereby the magnetic field is strengthened by the presence of a magnetic material. Generally reproducibility is between 1-3% standard deviation.

2.3.4 Spectrophotometry Core Analysis

Spectrophotometry provides a quantitative assessment of the colour of the sediment. Colour is a viable correlative tool in lithostratigraphy of turbidites, especially with turbidites from different provenances and the change in hemipelagite lithology (colour and texture) during interglacial and glacial conditions. The data here was typically gathered using a *Konica Minolta* colour spectrophotometer attached to the *GeoTek* XYZ core logger. The instrument is calibrated against a white tile and in free-air in a dark

environment. The data are exported as CIE L*a*b* results and as intensity within 10 nm bins between 360-740 nm.

2.4 Petrology

2.4.1 Binocular Microscopy

Sand fraction samples were taken from the base of turbidites. These were wet-sieved to remove the <63 μm fraction. The carbonate material was removed by leaching with 10% acetic acid. Samples were then scattered in a graduated tray with counting cells. Cells were selected at random and the minerals present were point counted (total of 300 minimum).

2.4.2 Polarising Thin-section Microscopy

Thin sections (30 μm and polished) were produced from selected samples, to enable a more traditional assessment of the mineralogy present. Polarising thin-section microscopy allowed properties such as relief, extinction angles, cleavage and birefringence to be assessed.

2.4.3 SEM

Mineral identification was also taken further by using the *Hitachi TM1000 SEM*. This enabled high resolution (1,000-10,000x) images of grains to be taken. Importantly, this also enabled use of the EDS system to identify grain chemistry, and thus mineralogy. XRD methodologies were not required in this study.

2.5 Biostratigraphy

2.5.1 Coccolithophore Biostratigraphy

To provide accurate and robust datum horizons coccolithophore biostratigraphy is used. Smear slides of toothpick hemipelagite samples were made from which species abundance counts are made. The sample is smeared on a microscope slide using RO water and then dried on a hotplate. A coverslip is adhered using UV activated glue. A microscope with greater than 1,000x magnification that enables observation in cross-polarised light is required. The species present in each sample are counted for abundance, with >300 counts made.

Weaver and Kuijpers (1983) and Weaver (1994) demonstrated that relative abundances of *Pseudoemiliania lacunose*, *Gephyrocapsa caribbeanica*, *Gephyrocapsa*

aperta, *Gephyrocapsa mullerae* and *Emiliania huxleyi* could be calibrated to oxygen isotope stage (OIS) boundaries. Indeed, changes in these relative abundances include defined acme zones: disappearance of *P. lacunosa* at 443 ka, dominance in *G. caribbeanica* below OIS 7 with a marked decrease from the OIS8-OIS7 boundary (250 ka), onset in dominance of *G. aperta* during OIS7 and OIS6, onset in dominance of *G. mullerae* at ~115 ka within OIS5, and onset in the dominance of *E. huxleyi* from OIS5 onwards (71 ka) (Weaver and Kuijpers, 1983).

In addition there are also a number of biozones based on the first occurrence (FO) and last occurrence (LO) of particular species. The NN19 Pseudoemiliania lacunosa Zone of Gartner (1969) is defined by a period commencing with the LO of *Discoaster brouweri* (2 Ma) and the LO of *P. lacunosa* (0.443 Ma) (Hine, 1990; Wei and Peleo-Alampay, 1993). The NN20 Gephyrocapsa oceanica Zone is defined by the LO of *P. lacunosa* (0.443 Ma in NE Atlantic) and the FO of *E. huxleyi* (0.268 Ma) (Boudreaux and Hay, 1967; Hine, 1990). The NN21 Emiliania huxleyi Zone commences from the FO of *E. huxleyi* and extents to recent.

There are also a series of additional species that create biozones. The LO of *Calcidiscus macintyrei* at 1.54 Ma (Wei and Peleo-Alampay, 1993). The FO of *Helicosphaera sellii* occurs at 1.37 Ma (Backman and Shackleton, 1983). The FO of *Reticulofenestra asanoi* occurs at 1.06 Ma (Takayama and Sato, 1987; Sata and Takayama, 1992), while the LO is at 0.8 Ma (Takayama and Sato, 1987; Hine, 1990; Sata and Takayama, 1992). The LO of *Helicosphaera inversa* is at 140 ka (Hine, 1990), and the LO of *Gephyrocapsa ericsonii* is at 15 ka (Biekart, 1989).

Chapter 3

Stratigraphy of the Modern Agadir Basin

3.1 Introduction and Aims

Agadir Basin forms a proximal depocentre in the Moroccan Turbidite System, offshore Northwest African passive margin. It also acts as a conduit for large-volume turbidity currents flowing to the more distal Madeira Abyssal Plain to the west and Seine Abyssal Plain to the north. Previous studies have aimed to resolve the stratigraphy of Agadir Basin (Wynn *et al.,* 2002a; Frenz *et al.,* 2009). Although Wynn *et al.* (2002a) provided coccolithophore biostratigraphy to validate a proposed stratigraphy, there were only five cores existing in the basin at that time. After the CD166 cruise in 2004 there was a new dataset of 50 cores, in addition to 40 cores recovered from the Geological Survey of the Netherlands. Frenz *et al.* (2009) offer a summary of the 0-165 ka stratigraphy of the Agadir Basin based on the CD166 core dataset. However, no validation of this stratigraphy is offered, other than sediment colour and turbidite position within the vertical sequence. This core dataset offers an unprecedented opportunity to study correlated turbidites along their entire flow pathway, investigate the recurrence of turbidites of both large- and small-volumes, and identify potential controlling factors on the recurrence and volume of these events. Therefore a number of aims are presented:

1. Validate the previous 0-165 ka Agadir Basin stratigraphy, and extend to 600 ka. This will cover the full available modern stratigraphy, incorporating events of both large- and small-volume.
2. Define the recurrence intervals of siliciclastic turbidites (Moroccan continental slope provenance), volcaniclastic turbidites (from Tenerife, El Hierro and Madeira) and calcareous turbidites (from local seamounts).
3. Determine the primary controlling factors of turbidite occurrence and magnitude, with special reference to the siliciclastic turbidites sourced from the Moroccan continental slope.

This Chapter will be submitted, in its current format, to *Marine and Petroleum Geology* (September 2012). All analyses and interpretations were completed by me, with editorial help provided by the co-authors.

Temporal Occurrence of Turbidites within the mixed siliciclastic volcaniclastic Agadir Basin, Moroccan Turbidite System

James E. Hunt[1], Russell B. Wynn[1], D.G. Masson[1], P.J. Talling[1]

[1]National Oceanography Centre, European Way, Southampton, Hampshire, SO14 3ZH

Abstract

Sequence stratigraphic models suggest that submarine landslide and turbidite activity is greatest during sea-level lowstands. However, growing evidence indicates that many turbidite systems are also active during sea-level highstands. The Moroccan Turbidite System is a mixed siliciclastic-volcaniclastic deepwater province offshore Northwest Africa. It comprises three depocentres, of which Agadir Basin is closest to the Moroccan shelf and Canary archipelago. The excellent core coverage and dating control afforded to Agadir Basin deposits has provided an unparalleled opportunity to derive accurate records of turbidite (and associated landslide) frequency and volume for the last 600 ka. Previous studies in the more distal Madeira Abyssal Plain depocentre of the Moroccan Turbidite System have indicated that large volume (>50 km^3) turbidites occurred at oxygen isotope stage (OIS) boundaries. This study of Agadir Basin confirms that major turbidites (>50 km^3) occurred at high sea-levels either immediately prior to or after each OIS boundary. Patterns in siliciclastic turbidite frequency indicate increases in the number and magnitude of events during the transgression from glacial lowstand to interglacial highstand. However, numerous large-volume and smaller-volume events also occur during mid-OIS interglacial highstands. In addition to climate change and associated rising sea-level, the present study indicates that sediment flux, including ocean productivity, continental erosion (siliciclastic) and effusive volcanism (volcaniclastic) are potentially significant preconditioning factors for submarine landsliding and turbidite generation.

Introduction

Submarine landslides and associated tsunamis can present significant geohazards to local and far-field populations and infrastructure (Lee *et al.,* 2003; Watts, 2003; Masson *et al.,* 2006). Understanding recurrence intervals of such events, through dating of the landslide deposits is critical for appropriate geohazard assessment. However, dating of proximal landslide deposits is often hindered by erosion of hemipelagic sediments, and associated amalgamation of multiple landslide deposits (Watts and Masson, 1995).

Disintegrative submarine landslides can generate long run-out sediment gravity flows, e.g. turbidity currents, the distal deposits of which can contribute to more accurate assessments of recurrence intervals and landslide initial volumes than studies of the proximal landslide deposit (Weaver, 2003; Gracia *et al.,* 2010; Hunt *et al*., 2011; Masson *et al.*, 2011). Landslide-generated sediment gravity flows are capable of spreading over extensive abyssal plains and submarine fans (Piper and Normark, 1982; Weaver *et al.,* 1992; Wynn *et al.,* 2002a; Skene and Piper, 2003, 2006; Talling *et al.,* 2007; Wynn *et al.,* 2010; Hunt *et al.*, 2011), which are often low-energy and non-erosive environments (Weaver and Thomson, 1993; Weaver, 1994). Consequently, hemipelagic/pelagic sediment is usually deposited and preserved between flow events, facilitating relatively accurate dating of the turbidite record (Weaver and Kuijpers, 1983; Weaver *et al.,* 1992).

Traditional sequence stratigraphic models, often based on study of outcrop or subsurface systems, suggest that submarine landslides and development of turbidite fans occur predominantly during lowstands and rapid regressions of sea-level, with only minor activity expected during highstands (Vail *et al.,* 1977; Mitchum *et al.,* 1977a, b; Vail and Todd, 1981; Mitchum, 1985; Vail, 1987; Shanmugam and Moiola, 1982; Kolla and Macurda, 1988; Posamentier and Vail, 1988; Posamentier *et al.,* 1988; Kolla, 1993; Kolla and Perlmutter, 1993). In addition, investigations of Late Quaternary submarine landslide occurrence in the Atlantic Ocean has reported that landslide activity is 1.7 to 3.5 times more prevalent during sea-level lowstands associated with glacial periods (Piper *et al.,* 2003; Hutton and Syvitski, 2004; Lee, 2009). However, there is growing evidence to suggest that there is also significant submarine landslide and turbidity current activity during sea-level transgressions and highstands associated with interglacial periods, e.g. on the Bengal, Indus, Amazon, Mississippi, Nile, and La Jolla fans (Flood *et al.,* 1991; Kolla and Perlmutter, 1993; Weber *et al.,* 1997; Prins and Postma, 2000; Carvajal and Steel, 2006; Covault *et al.,* 2007; Ducassou *et al.,* 2009;

Covault and Graham, 2010). A thorough study of submarine landslide and turbidity current activity in a given area enables better assessment of recurrence intervals, the factors controlling affecting recurrence, and enable improvement of sequence stratigraphic models used in hydrocarbon exploration.

The present study focuses on the modern deepwater mixed siliciclastic-volcaniclastic Agadir Basin of the Moroccan Turbidite System (MTS), on the Northwest African passive continental margin (Figure 3.1) (Wynn *et al.,* 2000a, 2002). The influence of climate change (and consequent change in eustatic sea-level) on landslide occurrence in the Moroccan Turbidite System has been previously interpreted through study of large-volume (10-150 km^3) turbidites in the distal Madeira Abyssal Plain (Weaver and Kuijpers, 1983). Turbidites from the last 730 ka recorded in the Madeira Abyssal Plain were correlated and dated using hemipelagite coccolith biostratigraphy and mudcap coccolith compositions (Weaver and Kuijpers, 1983; Weaver *et al.,* 1992). Turbidites were predominantly emplaced at oxygen isotope stage (OIS) boundaries, associated with major phases of climate change and sea-level rise or fall (Weaver and Kuijpers, 1983; Weaver *et al.,* 1992). This concept contradicts sequence stratigraphic conventions, where landslides and associated turbidity current activity is expected during sea-level lowstands and regressions.

The 'background' hemipelagic sedimentation rate in the Madeira Abyssal Plain is low (~0.5 cm/1000 years), which hinders accurate dating of turbidites (Weaver and Kuijpers, 1983). In addition, this distal depocentre only records the largest flows, capable of running out for almost 2,000 km (Weaver *et al.,* 1992; Wynn *et al.,* 2002a; Talling *et al.,* 2007). Farther east, Agadir Basin is the depocentre most proximal to Agadir Canyon (Figure 3.1), which is interpreted to be the source for siliciclastic flows in the Moroccan Turbidite System. Agadir Basin comprises two subtle sub-basins: upper to the east and lower to the west (Wynn *et al.,* 2002a; Talling *et al.,* 2007; Wynn *et al.,* 2010, 2012). Agadir Basin is also supplied with volcaniclastic and calcareous-rich flows derived from adjacent seamounts and volcanic islands (Wynn *et al.,* 2002a; Frenz *et al.,* 2009). The more proximal location of Agadir Basin, relative to the Moroccan shelf, means that the basin deposits include additional siliciclastic turbidites of lower magnitude than those recorded in the Madeira Abyssal Plain. Also, the background sedimentation rate in Agadir Basin is higher than on the Madeira Abyssal Plain, at 1.2-1.8 cm/1000 years (this paper). This provides greater temporal resolution when dating individual turbidites.

The principal aims of this study are to validate the Frenz *et al.* (2009) turbidite stratigraphy of Agadir Basin, examine the temporal distribution of siliciclastic turbidites during the last 600 ka, and discuss potential controls on their recurrence and magnitude. Another supporting aim is to examine the spatial and temporal variations in the hemipelagic record. This is undertaken because the correlation and dating of turbidites is based on the position of the bed within the near-continuously deposited hemipelagite. A thorough understanding of the variability in hemipelagic sedimentation rates and composition are pivotal for determining the hemipelagite geochronology, which ultimately enables dating and correlation of turbidites. In addition, study of the variable composition of the hemipelagite may provide insight into the factors influencing turbidite occurrence, by highlighting periods of increased ocean productivity and terrigenous sediment flux.

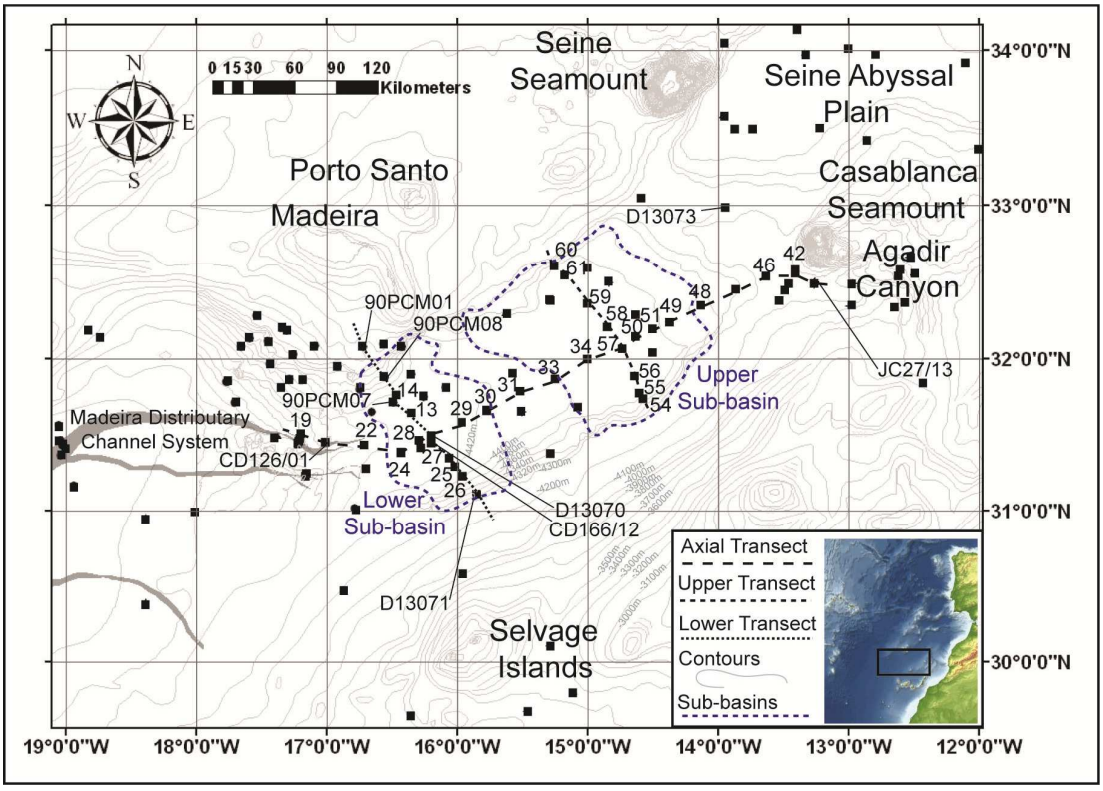

Figure 3.1 Contour map of Agadir Basin located outbound of Agadir Canyon on the Northwest African passive margin. The map demonstrates the core coverage available and the location of correlation panel transects. Contours generated from GEBCO bathymetry at 100 m intervals to 4,300 m and then at 20 m intervals at >4,300 m. Black squares denote piston cores in the study area, where the numbered cores represent cores shown in this study. Axial transect shown in Figure 3.7, upper transect shown in Figure 3.8 and lower transect shown in Figure 3.9.

Methodology and Data

The dataset utilised in this study primarily comprises shallow piston cores collected during the *RRS Charles Darwin* expedition CD166 in 2004. Additional piston cores from the JC027, D225, CD126 and 90PCM expeditions have also been incorporated into this dataset (Figure 3.1). In total over 100 piston cores from Agadir Basin and adjacent slopes were available for this study.

Although the complete core dataset were logged, only selected cores were used for detailed stratigraphic analysis. Core CD166/12 is the 'type locality' in Agadir Basin (location Figure 3.1), as it contains the full stratigraphy to bed A14 (Icod turbidite) at ~165 ka (Wynn *et al*., 2002a; Frenz *et al*., 2009; Hunt *et al*., 2011). A number of additional core sites were also chosen, including CD166/19 from the Madeira Distributary Channel System (Stevenson *et al*., 2011), CD166/31 from the lower (western) sub-basin, CD166/57 and CD166/48 from the upper (eastern) sub-basin, and D13073 from the Casablanca Ridge north of Agadir Canyon (locations on Figure 3.1).

Cores recovered from the floor of Agadir Basin contain a well-developed hemipelagic stratigraphy, and therefore provide an opportunity to examine whether turbidites can be correlated by where they occur within this hemipelagic record. However, because of the thickness of the basin floor sequence, cores from the basin floor typically only penetrate down to sediments of maximum age 165-250 ka. In contrast, core site D13073 contains a sequence of siliciclastic turbidites sourced from the Agadir Canyon that extends back to 600 ka (Wynn *et al.,* 2002a).

Coccolith biostratigraphy provides datum horizons used to create age models to date the turbidites. However, the resolution depends on both the sampling strategy (commonly every 5 cm) and the hemipelagite sedimentation rate (0.5-2 cm/1000 years). Species specific foraminiferal $\delta^{18}O$ and bulk hemipelagite carbonate profiles can be used to identify glacial-interglacial cycles, but resolutions are still generally coarse at 1-10 cm, and ultimately require independent datum horizons. Although coccolith biostratigraphy exists for Agadir Basin (Wynn *et al.,* 2002a), the ITRAX CaO proxy carbonate record potentially offers a higher resolution and more refined age-model for these deposits.

Visual Logging, Mineralogy and Volumetrics

Visual sedimentological logging (including facies descriptions) was initially undertaken on all cores. Positions of turbidite deposits in relation to depth in core and position within the hemipelagic sequence were recorded, and turbidite grain-size profiles were collected. In addition, 1.0 cm^3 samples were taken from the turbidite bases for mineral assemblage identification, of which the >63 μm grain fraction was analysed by binocular microscope. Visual identification of glacial/interglacial hemipelagite sequences aided visual correlation and subsequent dating of the turbidite record. These visual descriptions and initial correlations are supported by the subsequent methodologies. The correlations allow single beds to be mapped out through the Agadir Basin. In conjunction with previous turbidite correlations in the Madeira Abyssal Plain sediment isopachs of individual beds can be generated (Appendix 3.1 and 3.2), from which volumetric calculations are made.

Petrophysical Logging

P-wave velocity (accurate to within 0.2%), gamma-ray density (accurate to within 1%) and magnetic susceptibility (accurate to within 2%) were gathered using the *GeoTek* MSCL line core logger. Measurements were taken every 0.5 cm down-core. These data are used to constrain turbidite identification and bed correlations, e.g. p-wave velocity and gamma-ray density can be used as proxies for grain size with positive excursions in turbidite sands. Magnetic susceptibility can be used to aid identification of volcaniclastic turbidite sands, whereby the presence of volcanic materials results in a positive excursion in the magnetic susceptibility. Volcaniclastic turbidites A2 and A14 (containing multiple fining-upwards sequences), in addition to the basaltic A8 turbidite sand, can be used as effective marker beds for constraining turbidite correlations within Agadir Basin and in the eastern Madeira Channels (Frenz *et al.*, 2009).

Coccolith Biostratigraphy

Coccolith biostratigraphy was previously completed on core D13070 (Wynn *et al.*, 2002a), which is at the same location as CD166/12 used in this study (Figure 3.1). Coccolith biostratigraphy from core CD166/12 provides accurate and robust datum horizons for validation of later hemipelagite oxygen isotope and ITRAX CaO down-core profiles. Coccolith biostratigraphy was also completed on cores CD166/31, CD166/57 and CD166/48 within Agadir Basin (locations Figure 3.1), to constrain

dating of hemipelagite sediment and aid turbidite correlation. High resolution sampling (<3 cm) was also completed on core D13073 (location Figure 3.1) to provide the necessary dating control on the >600 ka record.

Biozones can be created based on the first occurrence (FO) and last occurrence (LO) of particular species. The FO of *Helicosphaera inversa* is at 510 ka and LO at 140 ka (Hine, 1990; Hine and Weaver, 1998; Sato *et al.,* 1999). The LO of *Pseudoemiliania lacunosa* is at 443-451 ka (Hine, 1990; Sato *et al.,* 1999). The FO of *Emiliania huxleyi* is at 290 ka (Hine, 1990; Hine and Weaver, 1998), and finally the FO and LO of *Gephyrocapsa ericsonii* are 380 ka and 15 ka respectively (Biekart, 1989; Hine and Weaver, 1998).

Weaver and Kuijpers (1983) and Weaver (1994) also demonstrated that relative abundances of *Pseudoemiliania lacunosa*, *Gephyrocapsa caribbeanica*, *Gephyrocapsa aperta*, *Gephyrocapsa mullerae* and *Emiliania huxleyi* could define a series of acme zones and calibrated these zones relative to oxygen isotope stage (OIS) boundaries. These acme zones provide another sequence of potential datum horizons. Noteworthy changes in relative species abundances include: dominance of *G. aperta* below ~575 ka within the lower stages of OIS15, and dominance in *G. caribbeanica* from the upper stages of OIS15 to the lower stages of OIS8 (~290 ka), onset in dominance of *G. aperta* from OIS 8 to lower stages OIS5, onset in dominance of *G. mullerae* at ~120 ka during OIS5, and finally onset in the dominance of *E. huxleyi* from the end of OIS5 onwards (71 ka) (Weaver and Kuijpers, 1983; Hine and Weaver, 1998).

Samples were taken every 3-5 cm through the hemipelagite intervals, and above and below every turbidite. In this study, pinhead-sized samples were smeared onto SEM semi-conductor pads and gently dispersed using acetone. The *Hitachi TM1000* SEM at BOSCORF was then used to perform species identification at x1000 magnifications. Each sample had >300 specimen counts to assess species abundances, and these were completed from a combination of at least three fields of view (Appendix 3.3). Some glacial clays lacked sufficient numbers and/or specimens, demonstrating the effects of dissolution. Precision upon repeat was found to be within a 3% standard deviation.

Oxygen Isotopes

Oxygen isotope records have long been used to provide records of relative sea-level change (Chappell and Shackleton, 1986; Shackleton, 1987; Martinson *et al.,* 1987; Shackleton, 2006, and references therein). Samples were taken at 5-10 cm intervals

from hemipelagic intervals separating turbidites in core CD166/12 (location Figure 3.1), in order to construct a down-core hemipelagic $\delta^{18}O$ record (Dallmeier-Tiessen, 2005). This record can be used to assess temporal climate and sea-level variations, and can be directly compared to global benthic $\delta^{18}O$ curves to infer down-core age profiles. Between 10 and 15 individuals of >90 µm *Globigerinoides ruber* foraminifera were extracted from each sample. These sampled foraminifera were analysed for their stable oxygen isotope composition using a mass accelerator spectrometer at Bremen University (Dallmeier-Tiessen, 2005). The $\delta^{18}O$ results were then correlated to available stable oxygen isotope curves of cores from neighbouring regions from Matthewson *et al.* (1995) (site CD53-30 on the continental rise ~1,500 km south of Agadir Basin) and Moreno *et al.* (2002) (site GeoB5559-2 <100km to the east on Dacia Seamount above Agadir Canyon).

CO_2 Coulometry

Inorganic carbon (carbonate) measurements were taken through the hemipelagite in core CD166/12 at 1 cm intervals. This was done to determine the carbonate content of the glacial-interglacial cycles in the hemipelagite. Sample aliquots of 25 µg were oven dried (60°C) and ground, and then subjected to a potentiometric back-titration using a coulometer. The carbonate content is calculated from the CO_2 volume liberated from the sample by a phosphoric acid-decomposition. Reproducibility was within 0.5%, while accuracy to a standard was to within 1%.

ITRAX µXRF Geochemistry

ITRAX µXRF is a non-destructive analytical technique used to collected high resolution (500-2,500 µm) major element geochemical records from the split core (Croudace *et al.*, 2006). Core CD166/12 (location Figure 3.1) was analysed and results calibrated to 10 down-core bulk samples analysed by ICP-OES (Appendix 3.4 and 3.5). Agadir Basin is relatively isolated from the continental shelf (Figure 3.1), so the composition of the hemipelagite sediments primarily reflects ocean conditions (glacial/interglacial) and geochemistry, rather than recording lithogenic flux from the hinterland. Hemipelagic material is generally >70% carbonate (de Lange *et al.*, 1987; Weaver and Rothwell, 1987; Matthewson *et al.*, 1995; Moreno *et al.*, 2002), thus the calibrated ITRAX CaO wt% profile through the hemipelagic record should mirror carbonate composition.

In the Moroccan Turbidite System the composition of the hemipelagic sediment is affected by the chemistry of bottom water currents which affect the position of the carbonate compensation depth (CCD) (Berger, 1970; Crowley, 1983; Jarvis and Higgs, 1987; Weaver and Rothwell, 1987). During interglacial highstands, North Atlantic Deep Water (NADW) production increases and white carbonate-rich hemipelagic sediment is preserved (Crowley, 1983). This is because the carbonate-ion concentration exerts a control on the position of the CCD (Broecker and Takahashi, 1978; Thunell, 1982), and is in turn governed by relative mixing between the NADW and Antarctic Bottom Water (AABW). Greater NADW production and mixing during interglacials facilitates carbonate preservation due to the resultant bottom water being less corrosive. Therefore the CaO proxy carbonate record reflects the oxygen isotope curve and climate record. The calibrated ITRAX Fe_2O_3 wt% record in the hemipelagic intervals should also be a proxy for carbonate dissolution, and thus anti-correlate with the carbonate content, providing an addition proxy record for climate and relative sea-level. Hemipelagite ITRAX CaO profiles from CD166/12, CD166/19, CD166/31, CD166/57 and CD166/48 provide a higher resolution time series to both correlate and date the turbidites, than biostratigraphy, hemipelagite carbonate composition or $\delta^{18}O$ profiles. The hemipelagite ITRAX CaO profile in D13073 also serves to provide a higher resolution time series for the >600 ka turbidite record.

Additional Proxies derived from ITRAX µXRF Geochemistry

Additional information can be gathered from geochemical studies of the hemipelagic record, offering potential insight into external factors influencing landslide and turbidity current occurrence, such as sedimentation flux and climate. For this the >600 ka record from D13073 is used, not just for the longer time-frame recovered, but its proximal location. Barium has been used as a proxy for ocean productivity (Dymond *et al.,* 1992). However, Klump *et al.* (2002) stated that barium is not a reliable proxy for paleoproductivity in sediments of predominantly terrigenous source. This is because biogenic barium calculations rely on a terrigenous Ba/Al ratio to be calculated and used to normalise the barium data (Klump *et al.,* 2002). However, in the distal deepwater setting of Agadir Basin this effect is likely to be negligible. Indeed, Croudace *et al.* (2006) suggest that either Ba counts or Ba/Ti from ITRAX µXRF analyses can be used as productivity indicators.

Croudace *et al.* (2006) also suggest that K/Rb can indicate the enhanced deposition of detrital clays and Zr/Rb can indicate enhanced heavy mineral deposition. The Si hemipelagic record can also be used as a terrigenous sediment indicator (Croudace *et al.,* 2006). Furthermore, concentrations of Br and S are linked to concentrations in organic carbon. However, Br/Cl and S/Cl ratios cited by Croudace *et al.* (2006) may not represent organic carbon fluxes due to potential influence of NaCl in saline pore fluids.

In addition, Ca/Sr and Si/Sr can be used to monitor composition of detrital carbonate and silicates (Croudace *et al.,* 2006; Hoddell *et al.,* 2008). The relationship between the peaks in these two ratio profiles can determine the relative importance of Heinrich events verses events of silicate concentration due to biogenic carbonate dissolution. Determining the presence of deglaciation events is important for investigating the relative impact of these events on preconditioning slope failures.

Sediment Facies

For the present study, turbidites are defined as deposits from sediment gravity flows where the principal grain-support mechanism is inferred to be fluid turbulence (Middleton, 1993). Turbidites are identified in cored deposits by a sharp basal boundary representing a sudden influx of sediment, typically overlain by a normally graded sequence representing deposition through layer-on-layer aggradation beneath a turbidity current. Turbidites typically possess a diffuse upper boundary, where turbidite mud becomes intermixed with overlying hemipelagic sediments through bioturbation.

Pelagic sedimentation involves purely vertical transfer of biogenic-rich sediment as ‘marine snow’ from the water column to the seafloor. Hemipelagic sedimentation involves near-vertical transfer of sediment from the water column with a variable component of lateral advection and suspension cascading (Stow and Tabrez, 1998). Hemipelagic sediment has a higher component of terrigenous or volcanic detritus than pure pelagic sediment, largely due to lateral advection of detrital sediment from the basin margins. Hemipelagic sediments have two primary facies types in Agadir Basin: pale cream/brown carbonate-rich interglacial marl/ooze and homogenous red-brown glacial clay, both are typically heavily bioturbated.

Hemipelagic sediment can be distinguished from turbidite mud because the latter is homogenous and very fine-grained (<10 μm). Conversely, hemipelagic sediment often contains randomly dispersed foraminifera, lacks primary sedimentary structures, and is often mottled due to bioturbation. In this study the turbidite-hemipelagite boundary at

the top of the turbidite is determined to occur at the depth where the turbidite mud ceases to be the dominant matrix component. In cases where excessive bioturbation has obscured the turbidite-hemipelagite boundary a mid-point is taken. In most cases the error on this boundary is in the region of 10-20 mm.

Results

Deriving the Hemipelagic Climate Record

The first task is to validate the concept of using hemipelagite ITRAX CaO as a proxy for climate and relative sea-level in the Moroccan Turbidite System. Core CD166/12 in the centre of the western lower sub-basin of Agadir Basin was chosen for detailed analysis (Figures 3.2-3.3). Firstly, a series of datum horizons were derived for CD166/12 using coccolithophore biostratigraphy in conjunction with oxygen isotopes (Figure 3.2). The base of the core is shown to be mid-OIS6 with the presence of turbidite A14 from Tenerife (165 ka from Hunt *et al.,* 2011). Although *G. aperta* are present during OIS6, *G. mullerae* are found to be more abundant during this glacial period due to their resistance to corrosion. *G. aperta* dominance re-establishes above the OIS6-OIS5 boundary at 180 cm (Figure 3.2). *G. mullerae* later become dominant shortly before turbidite A11 at ~120 ka at 164 cm (Figure 3.2), with a sharp and constant decline in *G. aperta*. *E. huxleyi* become dominant from the OIS5-OIS4 boundary (71 ka) at 98 cm onwards, although there are two perturbations within the glacial red clays of OIS4 and OIS2, where *G. mullerae* re-establish dominance (Figure 3.2). These perturbations in *G. mullerae* abundance during the glacial OIS6, OIS4 and OIS2 are due to preferential preservation of *G. mullerae* and relative dissolution of the delicate *G. aperta* and *E. huxleyi* coccolith shields (Figure 3.2). Two further biozone dates are resolved from last occurrence of rare *H. inversa* at ~140 ka prior to OIS5 at 183 cm and small *G. ericsonii* prior to OIS1 at 15 ka at 24 cm.

A high-resolution (1 cm) carbonate profile through the hemipelagite in CD166/12 can be compared to the dated oxygen isotope curve from Dallmeier-Tiessen (2005). Carbonate compositions <60 wt% occur within red/brown clays during glacial OIS2 and OIS4, where the most positive $\delta^{18}O$ value in OIS4 (~2‰) corresponds to the lowest carbonate values of 30 wt% (Figure 3.2). Conversely carbonate compositions >65 wt% correspond to pale foraminifera oozes associated with interglacial periods with more negative $\delta^{18}O$ values (<1‰), e.g. OIS1, OIS3 and OIS5. This carbonate profile is found

to broadly correlate to the ITRAX CaO wt% profile and anticorrelate to the ITRAX Fe_2O_3 wt% profile. These ITRAX profiles are critiqued below.

The high resolution ITRAX CaO wt% depth profile in CD166/12 shows significantly reduced CaO values (<20 wt%) between 85-100 cm and around 200 cm (Figure 3.2). Biomarkers from coccolith biostratigraphy (Figure 3.2) indicate that the down-core reduction in CaO values at 85 cm corresponds to the OIS 3-4 boundary (coincident with emplacement of turbidite A5), while low CaO values at 195 cm correspond to the middle of OIS 6 (coincident with emplacement of turbidite A14) (Figure 3.2). The upper 80 cm of the core has a more subdued signal, but low CaO values (<25 wt%) between 25-40 cm can be linked to OIS 2 based on comparison with the coupled regional oxygen isotope record, $CaCO_3$ profiles and coccolith biostratigraphy (Figures 3.2-3.3). Turbidite A2 at 25 cm hemipelagite depth has previously been linked to the OIS 1-2 boundary (Wynn *et al.,* 2002a), supporting this interpretation.

The lowest values of CaO in core CD166/12 generally correspond to dark brown clays of OIS2, 4 and 6, while elevated CaO values correspond to paler cream or brown marls deposited during OIS1, 3 and 5 (Figure 3.2-3.3). However, there are some anomalies. Low CaO values (<25 wt%) between 120-125 cm are related to a distinctive grey muddy hemipelagite above volcaniclastic turbidite A8 (Figures 3.2-3.3). This grey hemipelagite is probably due to elevated levels of volcaniclastic terrigenous material admixed within hemipelagic sediments overlying this turbidite.

The reduced CaO and carbonate content (<25 wt% and <75 wt% respectively) in the upper few cm of core CD166/12 does not fit with global stacked-oxygen isotope records (Figures 3.2-3.3). This trend is also detected in carbonate profiles from other regional cores (Figure 3.3), and has previously been reported from Madeira Abyssal Plain cores (Jarvis and Higgs, 1987). This is potentially the result of recent oxidation and penetration of the present-day oxidation front through the uppermost hemipelagic sediment. This may be represented by precipitation of immobile Fe^{2+} as brown iron oxyhydroxide haloes under oxic conditions (Jarvis and Higg, 1987, and references therein). Alternatively, the variability in the top 23 cm in both $CaCO_3$ and ITRAX CaO records may actually reflect local variability in climate associated with the Bølling-Allerød and Younger Dryas deglaciation events (Filipsson *et al.,* 2011).

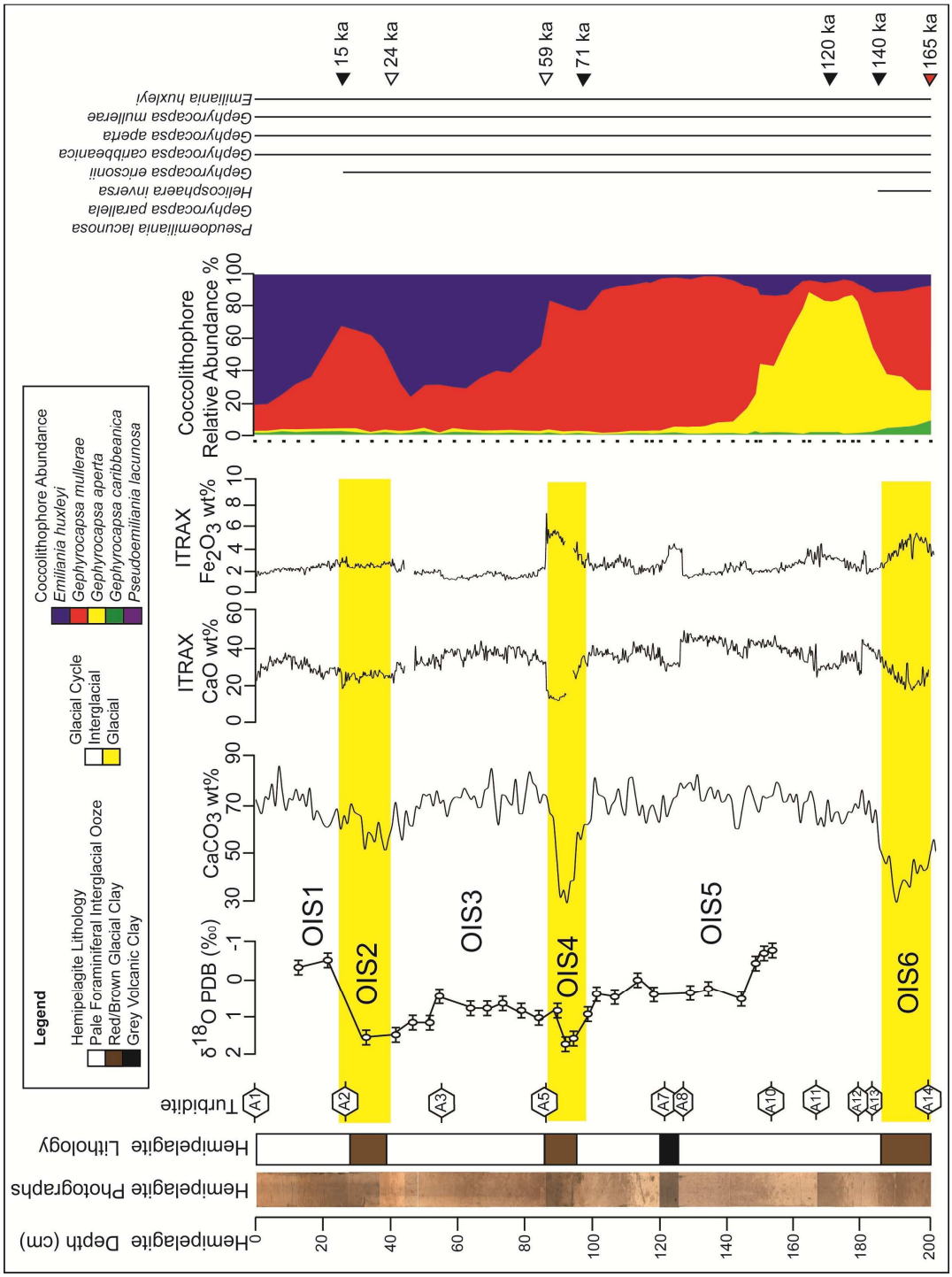

Figure 3.2 Hemipelagite composition in core CD166/12 showing variation in sediment colour, hemipelagite lithology, ITRAX CaO and Fe_2O_3 composition, bulk sediment, oxygen isotope composition, carbonate content and coccolithophore biostratigraphy. The position of turbidites within the hemipelagite record are signified by the hexagons with A# nomenclature. The small black squares denote the position of samples for biostratigraphy. Relative abundances are produced after Weaver and Kuijpers (1983). Biozones for the relevant coccolithophores are presented. Down-core ages are shown with distinct biomarkers as black triangles and biomarkers signifying effects of glacial dissolution as open triangles.

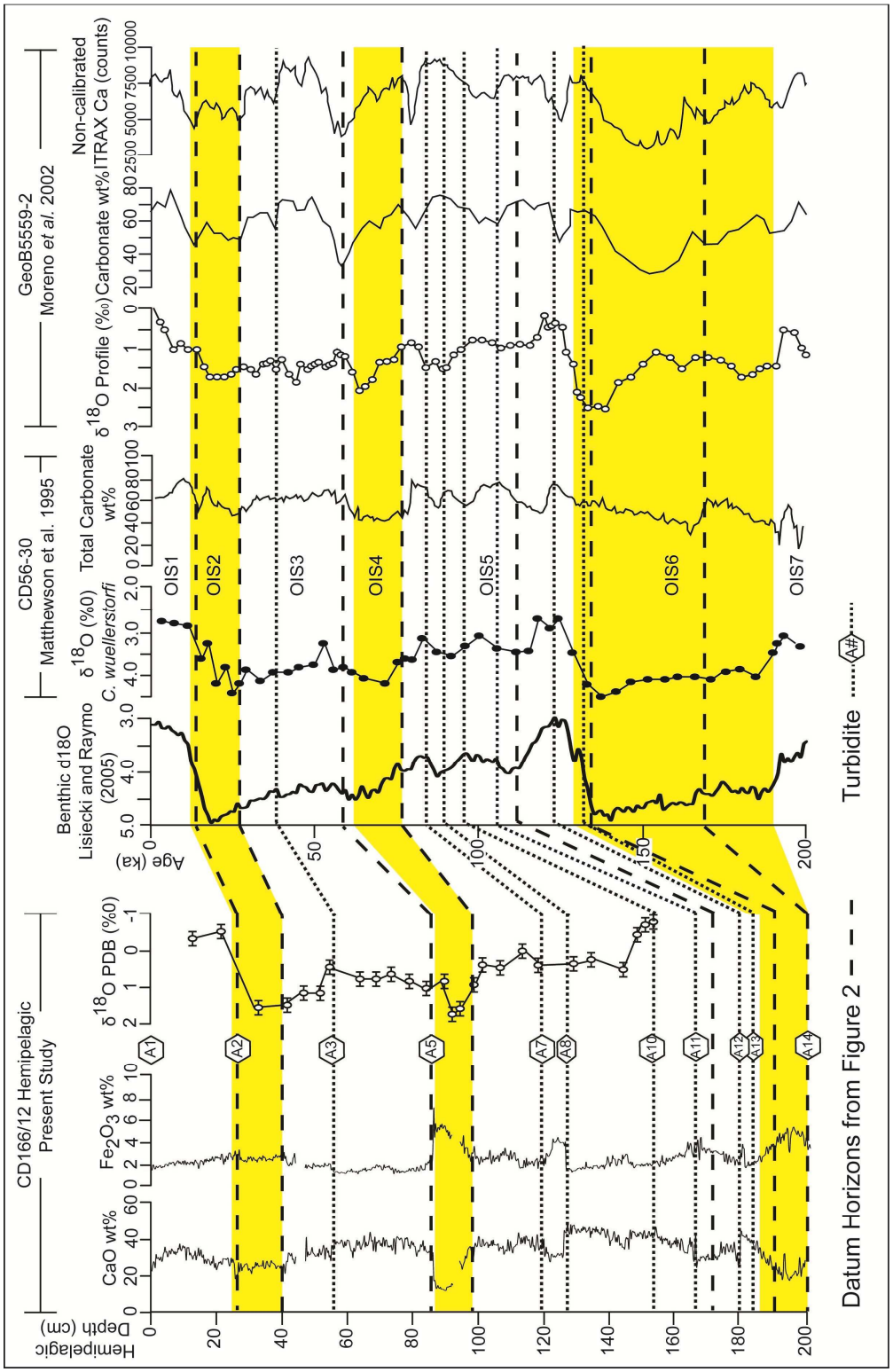

Figure 3.3 Hemipelagic records of ITRAX CaO and Fe_2O_3 at CD166/12 (location Figure 3.1) compared to the oxygen isotope record through the hemipelagite at CD166/12, and alternate hemipelagic records at sites on the Northwest African passive margin, including: benthic foraminifera oxygen isotopes (Lisiecki and Raymo 2005), *C. wuellerstorfi* oxygen isotopes and bulk sediment carbonate (Matthewson *et al.,* 1995), and a bulk oxygen isotope profile, carbonate and non-calibrated Ca counts (Moreno *et al.,* 2002). Turbidite positions (A1 to A14) projected to the right are interpretations. Biostratigraphic markers are taken from the coccolithophore biostratigraphy of CD166/12 (Figure 3.2). Positions of oxygen isotope stages (OISs) are projected over data, with lowstands of sea level shaded yellow.

Core Correlations and Turbidite Stratigraphy

The hemipelagic sequence in other cores within Agadir Basin reveals a similar pattern of down-core ITRAX CaO fluctuations (Figure 3.4). For example, all cores show markedly reduced ITRAX CaO values (<20-25 wt%) below turbidites A2 and A5, and surrounding turbidite A14, associated with glacial red clays of OIS2, 4 and 6. The signal becomes less clear towards the eastern basin margin, proximal to the source of siliciclastic flows, e.g. core CD166/48 (Figure 3.4). The increased sedimentation rate in the upper 50 cm of hemipelagite in core CD166/48 shows evidence of oxidation effects or increased sediment accumulation capturing variations associated with the Bølling-Allerød and Younger Dryas deglaciation events (Filipsson *et al.,* 2011).

Previous studies have correlated the turbidite sequence across Agadir Basin to a depth coincident with turbidite A14, dated at ~165 ka (Wynn *et al*., 2002a; Frenz *et al*., 2009; Hunt *et al.*, 2011). The hemipelagic CaO wt% record derived from this study (Figure 3.4), can be used to support core correlations and date turbidites intersecting the record (Figure 3.4). However, this high resolution record is most powerful when used in combination with coccolith biostratigraphy, down-core petrophysical data and mineralogical analysis of turbidite sandy bases (Figures 3.5-3.6 and Table 3.1).

For example bed A2 occurs consistently above a marked excursion in *G. mullerae* abundance in coincidence with OIS2 (Figure 3.5). Bed A5 occurs consistently above a marked excursion in *G. mullerae* abundance in coincidence with OIS4 (Figure 3.5). Bed A11 occurs at a point where *G. aperta* begins in a sharp decrease in abundance and *G. mullerae* increases in abundance (Figure 3.5). Finally, beds A12 and A13 occur above an excursion in *G. mullerae* abundance in coincidence with OIS6, in which bed A14 occurs.

In regards to core petrophysics, elevations in p-wave velocity and gamma-ray density regularly indicate the presence of sandy turbidite bases (Figure 3.6). In addition, magnetic susceptibility profiles can be used to identify sandy bases of volcaniclastic marker beds A2, A8 and A14 (Figure 3.6).

Core correlation panels orientated along the Agadir Basin axis and across the upper and lower sub-basins indicate the progressive pinch-out of siliciclastic turbidites to the west and of volcaniclastic turbidites towards the east (Figures 3.7-3.9). They also show the ratio of siliciclastic to volcaniclastic turbidites progressively decreasing to the west (Figures 3.7-3.9), due to the relative proximity to their respective source areas. Core penetration below bed A14 is variable between cores, and is generally restricted to sites

in the western Agadir Basin (distal to the siliciclastic source) or on basin margins where many turbidites are poorly developed or absent (Figures 3.7-3.9).

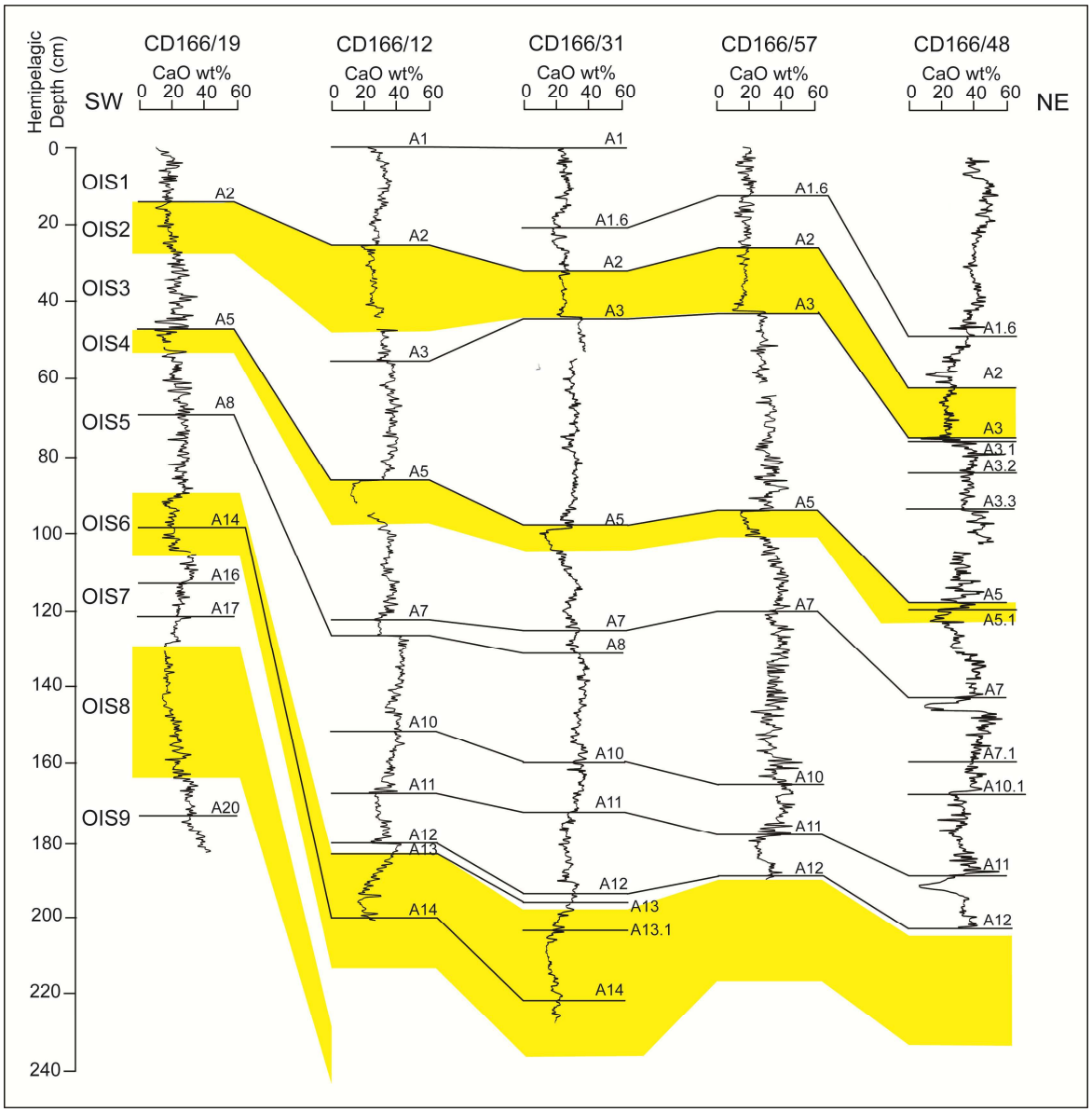

Figure 3.4 Hemipelagic records of ITRAX CaO at CD166/12 and alternate cores within Agadir Basin (locations Figure 3.1). Black lines denote the location of the specific turbidite in the hemipelagite section, which are then correlated between sites. Positions of oxygen isotope stages (OISs) are projected over data, with lowstands of sea level shaded yellow.

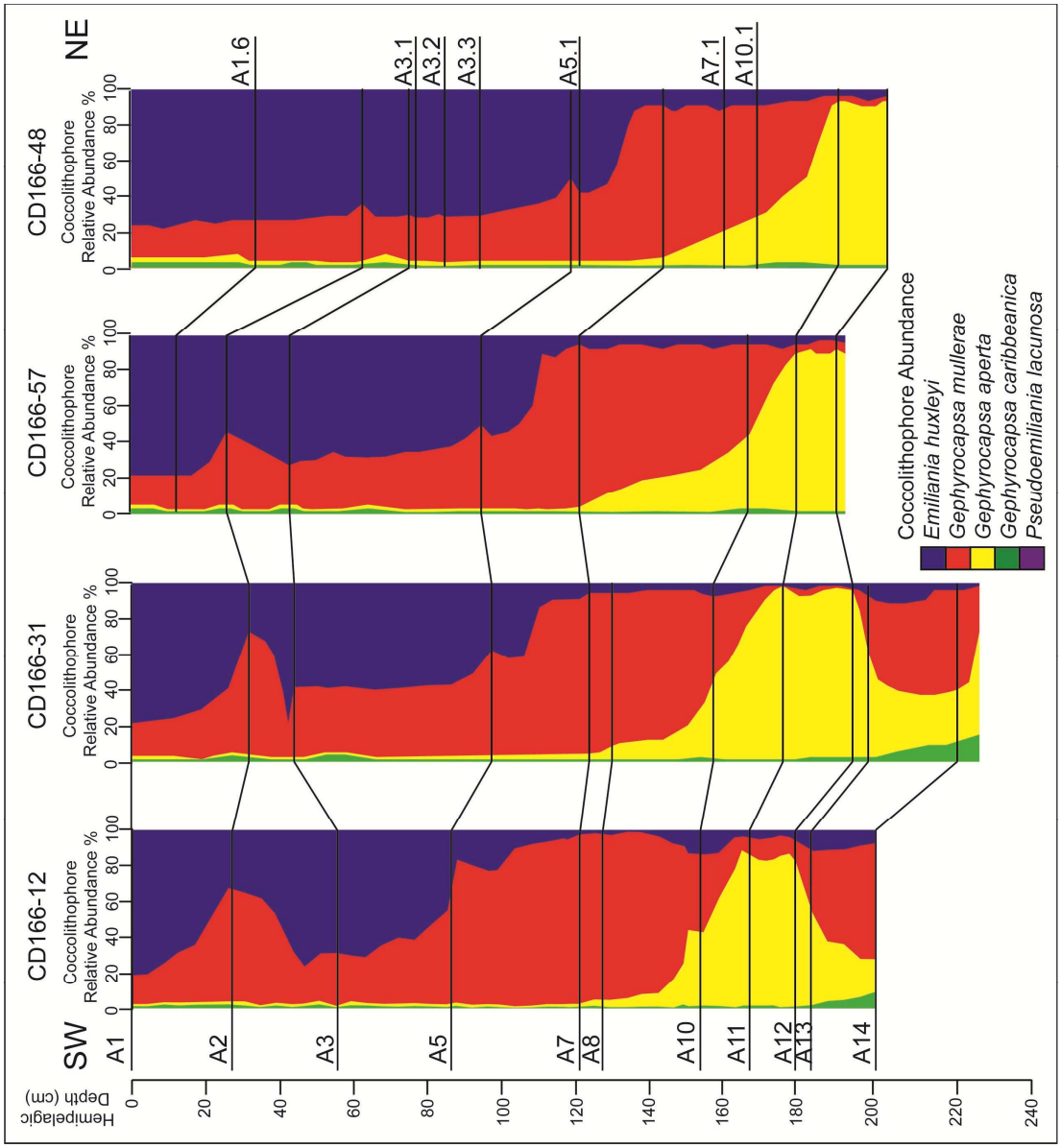

Figure 3.5 Coccolith relative abundances for Agadir Basin cores CD166/12, CD166/31, CD166/57 and CD166/48. This shows the consistent occurrence of bed A2 at an excursion in G. mullerae abundance associated with OIS2, bed A5 at an excursion in G. mullerae abundance associated with OIS4, bed A11 at the decrease in G. aperta and increase in G. mullerae abundance, and beds A12 and A13 above an excursion in G. mullerae abundance associated with OIS6.

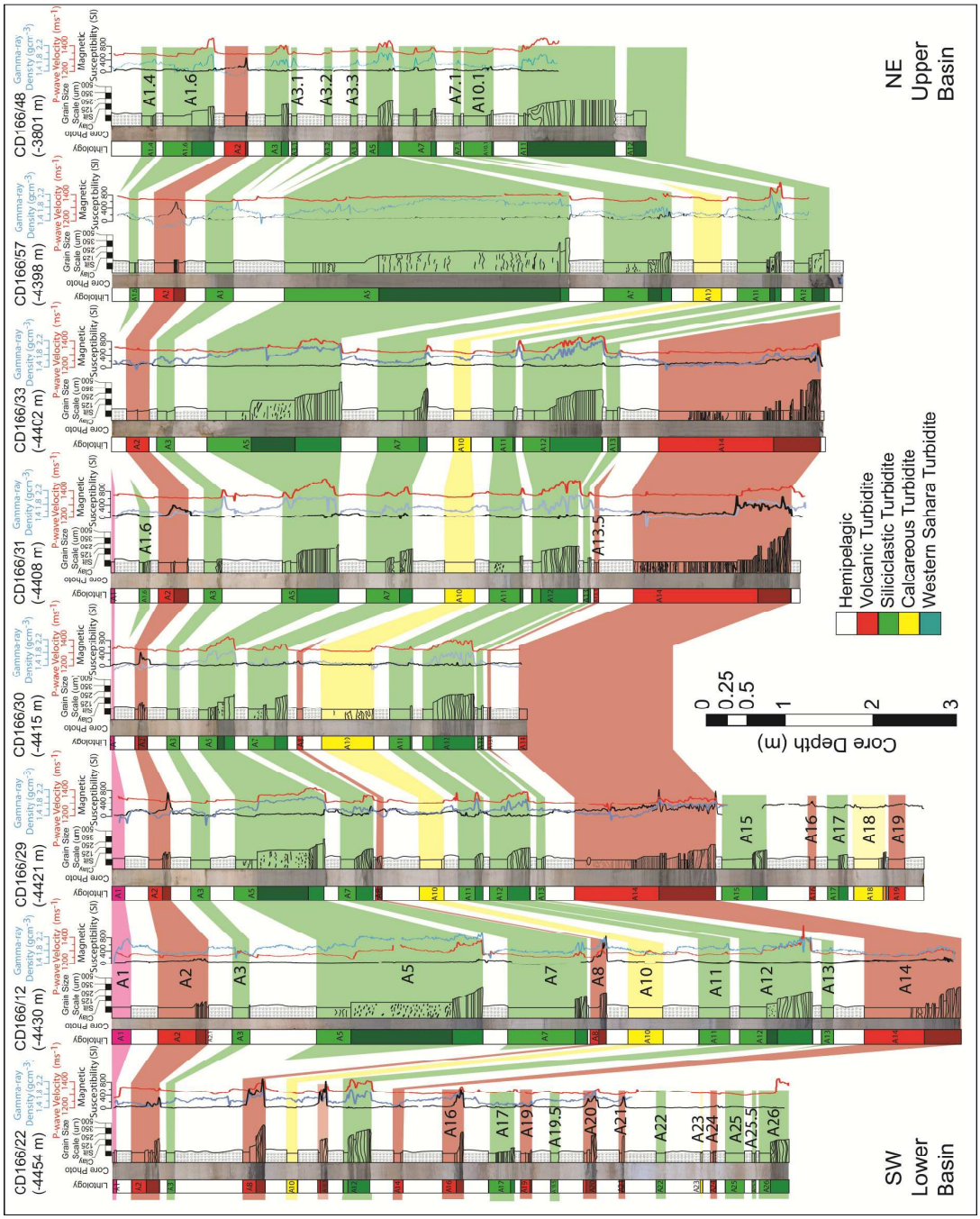

Figure 3.6 Axial core transect showing the down-core petrophysical data profiles (p-wave velocity, gamma-ray density and magnetic susceptibility) used to support the turbidite stratigraphy of Agadir Basin. Graphic logs shows support of identification and correlation of turbidites. Elevated p-wave velocity and gamma-ray density provide support for identification of turbidite sands, while elevated magnetic susceptibility provides support for identification of volcaniclastic turbidites.

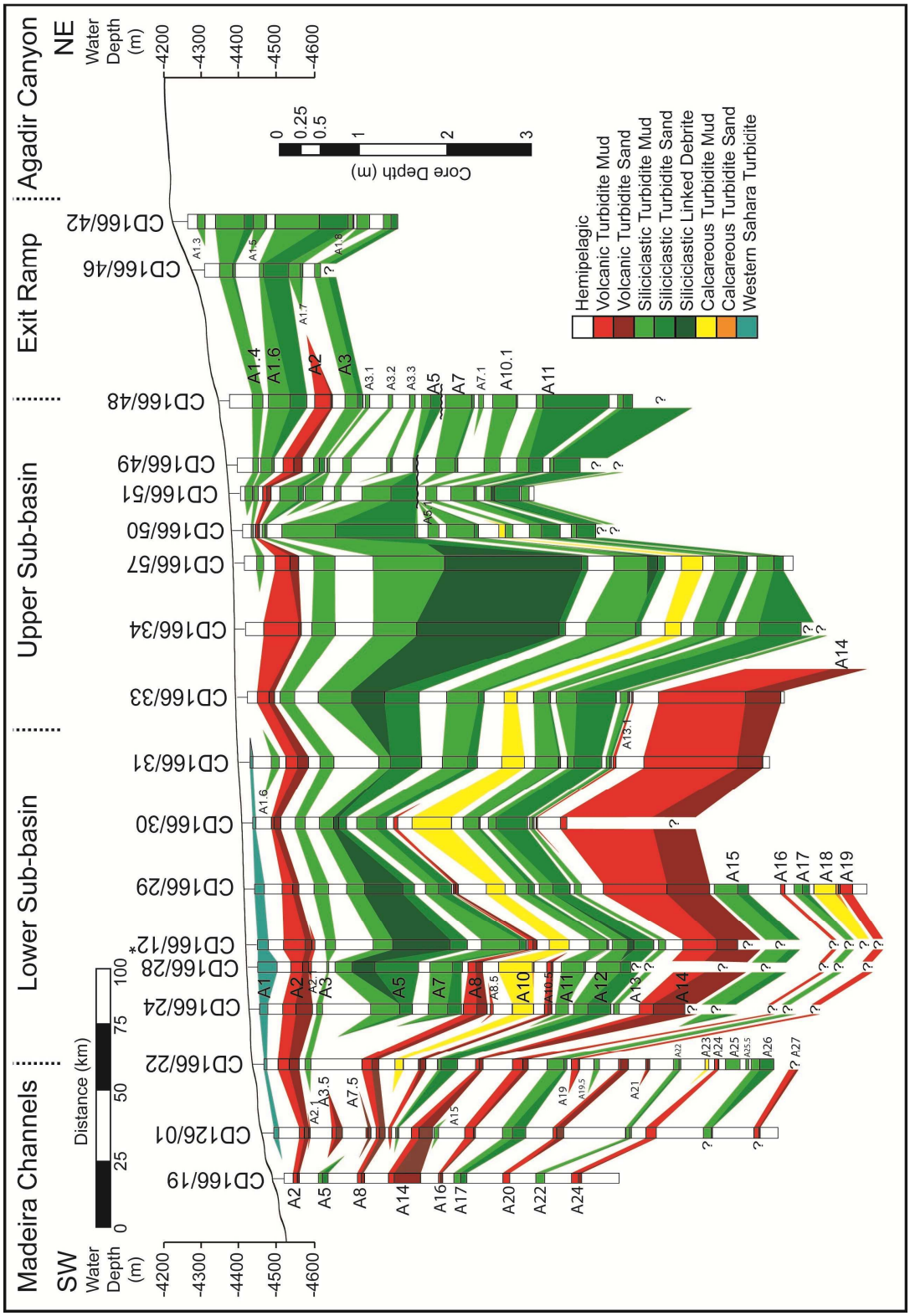

Figure 3.7 Core correlation panel through the centre of Agadir Basin from Agadir Canyon to the Madeira Distributary Channels, hung off the sea-floor bathymetry (location Figure 3.1). Stratigraphy to turbidite A14 is based on the Frenz *et al.* (2009) stratigraphy. Core sticks represent the position of turbidite and hemipelagite sequences, where CD166/12 (denoted by *) has been condensed by x0.5 to fit on diagram. This panel shows the ponding of turbidite mudcaps into the centres of the sub-basins.

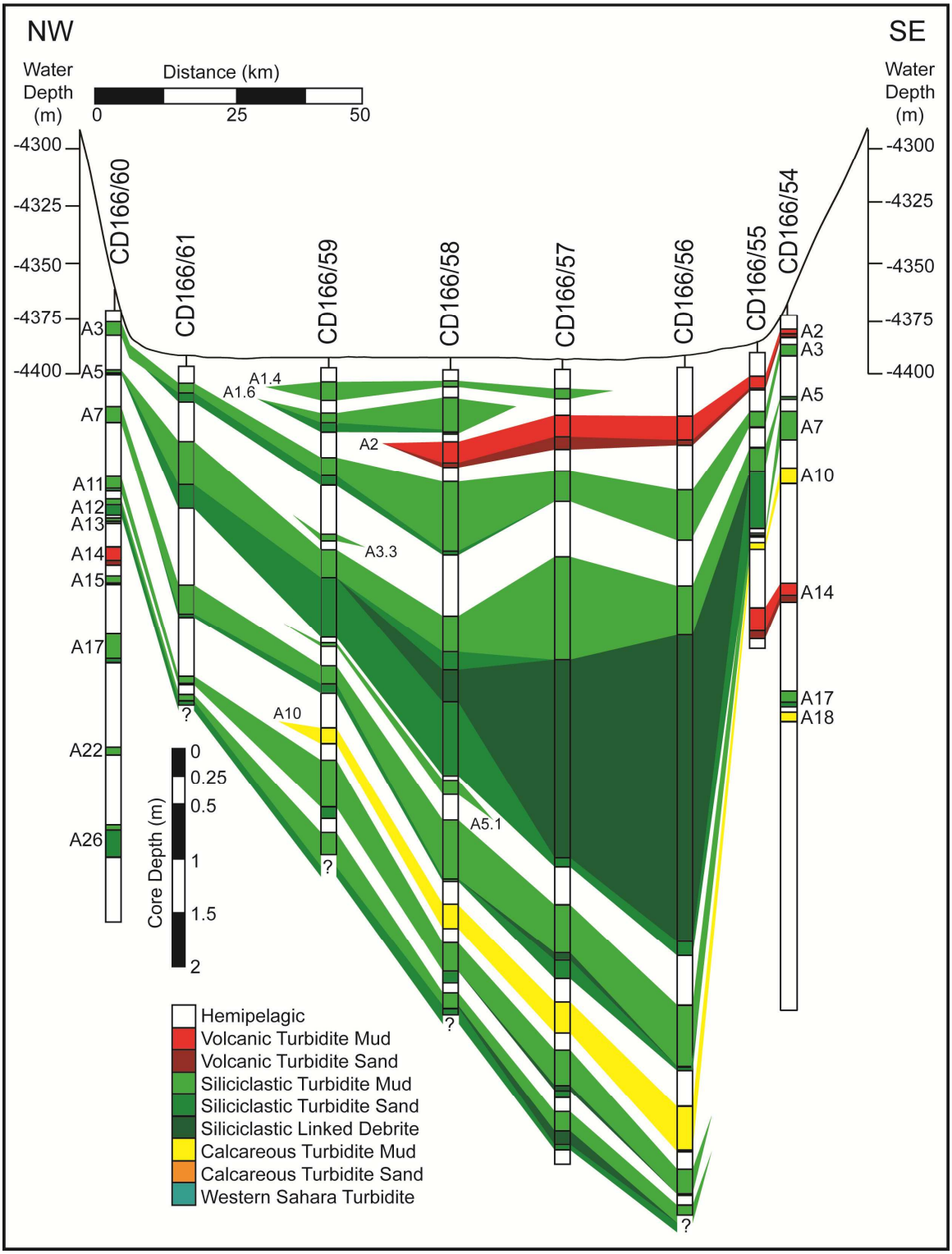

Figure 3.8 Core correlation panel across the upper sub-basin of Agadir Basin hung off sea-floor bathymetry (location Figure 3.1). There are only two volcaniclastic turbidites represented here, these are the large-volume A2 and A14 events. This panel also exemplifies the ponding of the fine-grained mudcaps into the centre of the basin.

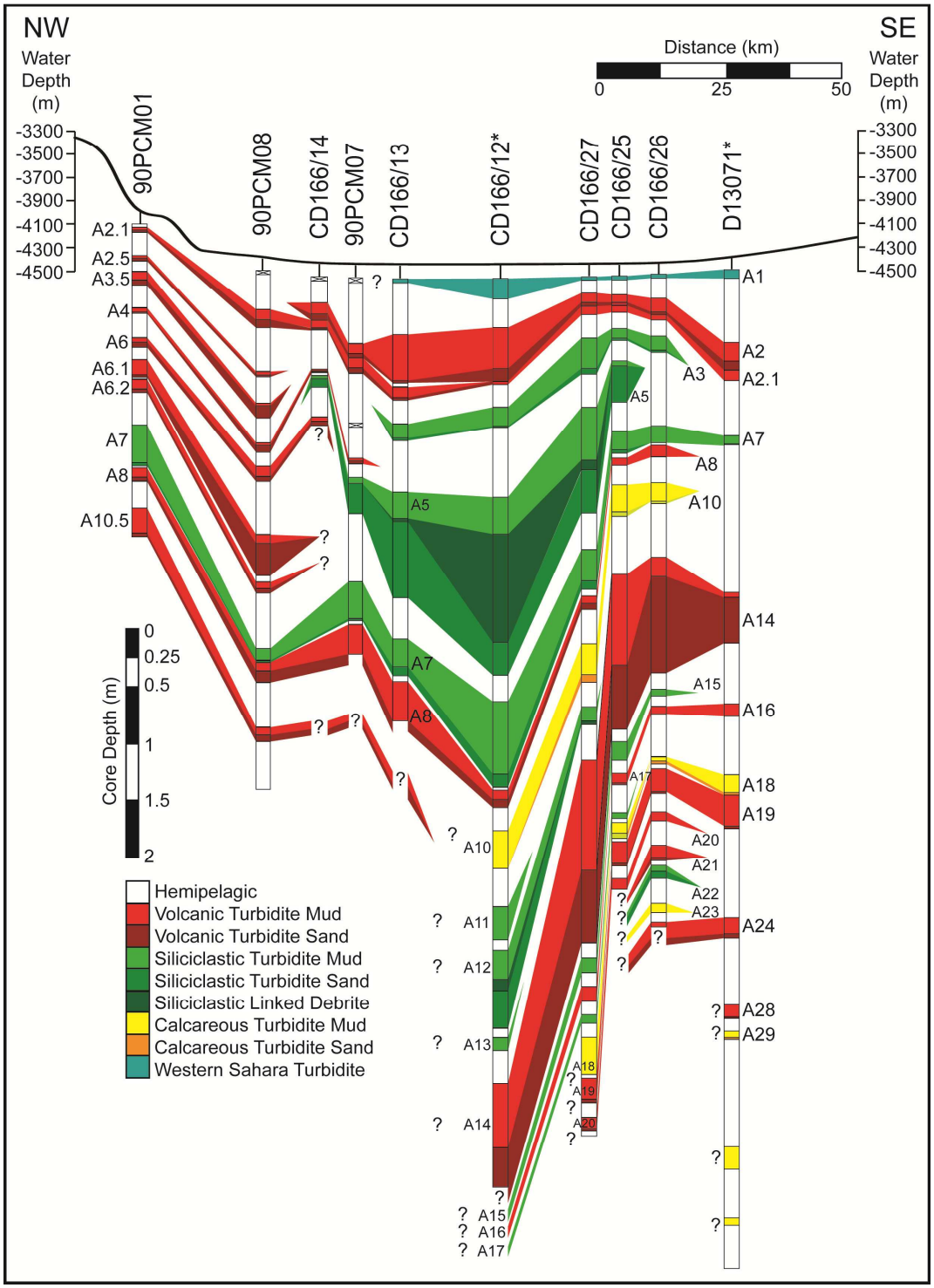

Figure 3.9 Core correlation panel across the lower sub-basin of Agadir Basin hung off sea-floor bathymetry (location Figure 3.1). This transect shows the increased number of volcaniclastic turbidites associated with Madeira and calcareous turbidites associated with the Selvage Islands.

In contrast, core D13073, located on the Casablanca Ridge ~60 km northwest of Agadir Canyon mouth (location Figure 3.1), contains an extensive sequence of siliciclastic turbidites to a depth greater than 10 m (Wynn *et al*., 2002a; Figures 3.10-3.11). This core site is elevated at a height of 40 m above the basin floor, and is therefore unaffected by erosion beneath high-energy flows. Mineralogical and MSCL data have allowed a sequence of at least 40 turbidites to be identified, including the A14 volcaniclastic turbidite dated at ~165 ka (Figure 3.10).

Previous coccolith biostratigraphy from this core has provided four dates down-core (Wynn et al., 2002a; Figure 3.10), indicating that the sequence extends back beyond 480 ka. New high-resolution biostratigraphy provides an additional set of datum horizons (Figure 3.10). They include dates attributed to both coccolith first (FO) and last occurrences (LO) and acme zones (Figure 3.10), verifying dates from Wynn *et al.* (2002a). These include LO of *G. ericsonii* at 4 cm hemipelagite depth and FO at 245 cm, FO of *E. huxleyi* at 167 cm, LO of *H. inversa* at 60 cm and FO at 310 cm, LO of *P. lacunosa* at 468 cm, and LO of *G. parallela* at 279 cm (Figure 3.10). Furthermore, a series of acme zones are defined as commencement of *E. huxleyi* abundance at 27 cm (QAZ1 zone, Hine (1990)), increase in *G. mullerae* abundance at 45 cm (QAZ2 zone), increase in *G. aperta* abundance at 170 cm, and dominance of *G. caribbeanica* above 369 cm (Figure 3.10).

Our comparison of the ITRAX CaO record with the global-stacked benthic oxygen isotope record of Lisiecki and Raymo (2005) reveals that the base of the core actually corresponds to at least OIS 17 (>600 ka) (Figure 3.11), verified with coccolith biostratigraphy (Figure 3.10). As with cores from within Agadir Basin, the ITRAX CaO record in the hemipelagic sequence of D13073 shows a good correspondence with this oxygen isotope record (Figure 3.11). Hemipelagic sediments with ≤ 20 wt% CaO almost exclusively correspond to $\delta^{18}O$ values >4.4-4.5, which relate to relatively cold periods and sea-level lowstands (Figure 3.11). Sediments with ≥ 30 wt% CaO almost exclusively correspond to $\delta^{18}O$ values >3.5-3.6, which relate to relatively warm periods and sea-level highstands (Figure 3.11).

Peaks and troughs in the CaO record clearly correlate to those present in the Lisiecki and Raymo (2005) benthic $\delta^{18}O$ curve (Figure 3.11). However, the interpreted glacial lowstand regions of the ITRAX CaO record are condensed in core compared to the representation of the lowstands in the temporal benthic $\delta^{18}O$ record (Figure 3.11). Conversely, interglacial highstand regions of the ITRAX CaO record are expanded

compared to the temporal benthic $\delta^{18}O$ record (Figure 3.11). This is principally due to the decreased primary carbonate productivity and increased carbonate dissolution during glacial periods.

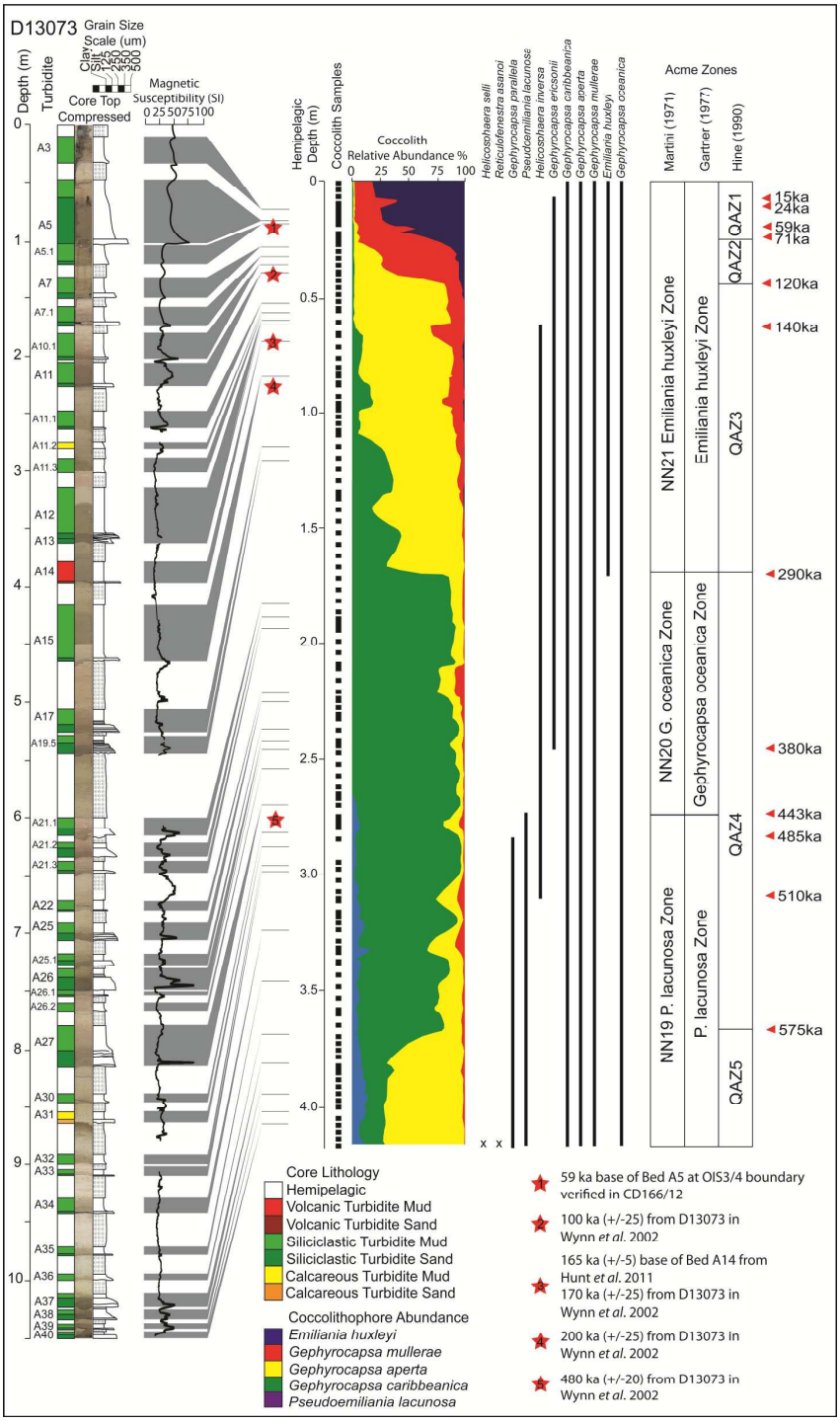

Figure 3.10 Core panel for D13073 (location Figure 3.1) and the 0-550 ka record of turbidites exiting the Agadir Canyon. Magnetic susceptibility profile highlights the location of most turbidites as a proxy for grain-size. Turbidites are removed from the hemipelagic CaO profile, with the locations marked by a black line. Turbidite positions are then projected onto the stacked Lisiecki and Raymo. (2005) benthic $\delta^{18}O$ record tied to the CaO profile using datum horizons taken from coccolith biostratigraphy.

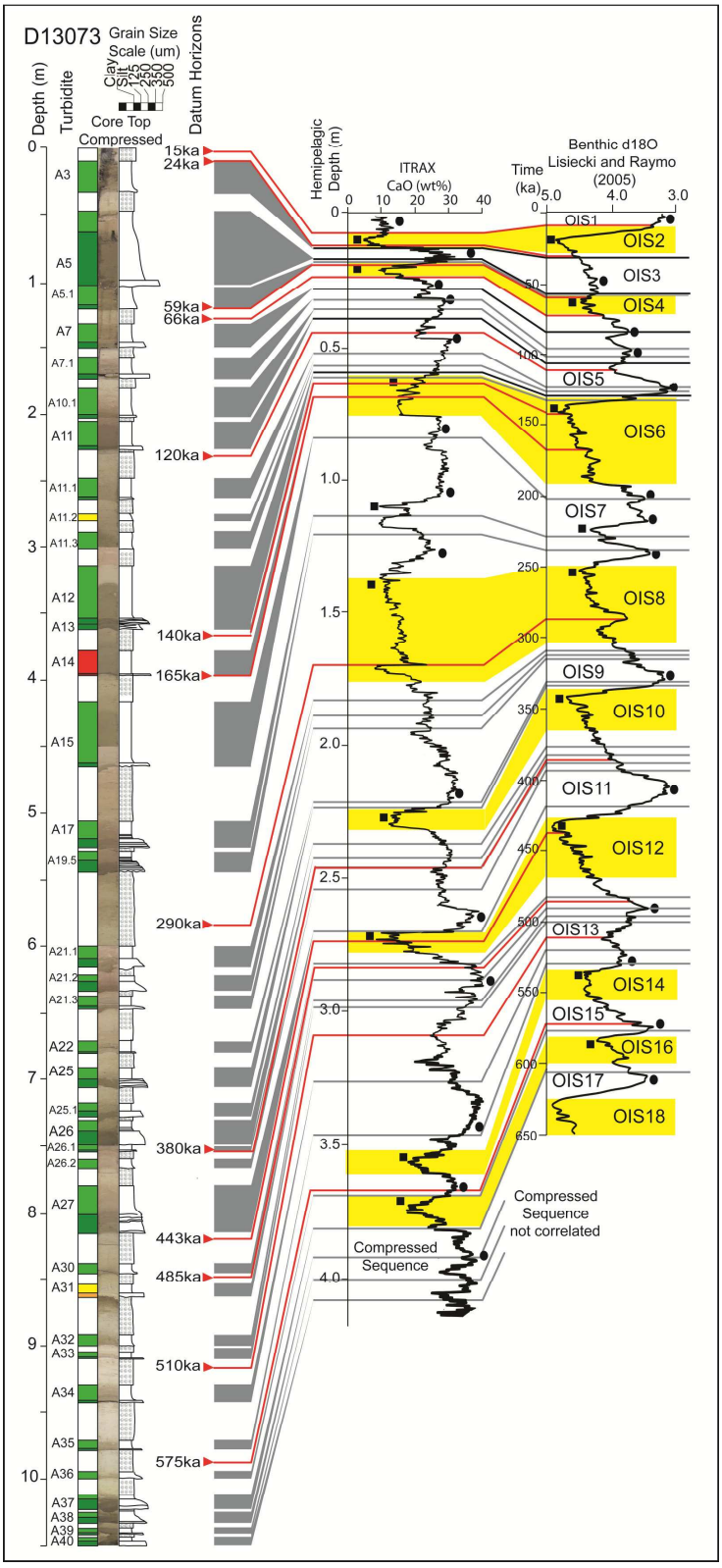

Figure 3.11 Core panel for D13073 showing hemipelagite ITRAX CaO profile with datum horizons from Figure 3.10 that correlate the profile to the global benthic foraminifera $\delta^{18}O$ record of Liseicki and Raymo (2005). Grey lines denote position of turbidites in hemipelagite record and interpreted position in Lisiecki and Raymo (2005) $\delta^{18}O$ record. Black lines denote large-volume turbidites. Red lines denote datum horizons from Figure 3.10. Black circles represent correlated interglacial peaks and black squares represent correlated glacial troughs.

In regards to these peaks and troughs in composition, the absolute concentrations of these peaks and troughs match those in the global benthic $\delta^{18}O$ curve (Figure 3.11). For example, the lowest concentrations in CaO during the interpreted OIS2 and OIS12, match with the highest values of benthic $\delta^{18}O$ found at OIS2 and OIS12 (Figure 3.11). Furthermore, from the interpreted OIS8, OIS10 to OIS12 in the CaO record there are increases in the minimum concentration of CaO, a pattern matched in increases in the maximum benthic $\delta^{18}O$ curve composition from OIS8, OIS10 to OIS12 (Figure 3.11).

Turbidites deposited within the hemipelagic sediment sequence in this core can be placed within a chronostratigraphic (and sequence stratigraphic) framework based upon the oxygen isotope record. Chronological errors vary, with greater accuracy at defined points in changing oceanic conditions at OIS boundaries, while decreased accuracy is inherent in deriving dates between these key markers. A combination of the high resolution (3-5 cm) coccolith biostratigraphy and hemipelagite ITRAX CaO profile provides potential errors conservatively at ±5 ka.

Temporal Occurrence of Siliciclastic Turbidites

In addition to the cores within Agadir Basin, core site D13073 located on the Casablanca Ridge provides an extensive 0-600 ka record of large-volume siliciclastic flows exiting Agadir Canyon (Figures 3.10-3.11). The long-temporal turbidite chronology from D13073 is extracted by coccolith biostratigraphic dating and correlation of the hemipelagic ITRAX CaO record to the Lisiecki and Raymo (2005) benthic $\delta^{18}O$ curve. This is further supported by identification of the A14 volcaniclastic turbidite and coarse large-volume A5 and A12 siliciclastic turbidites, which are previously dated marker beds (Figures 3.2 and 3.10).

Turbidites have been recorded in Agadir Basin throughout the last 600 ka (Figure 3.12). Between 150-600 ka twenty-four siliciclastic turbidites were recorded at a ~18 ka recurrence and average volume <5 km^3 (Figure 3.12 and Appendix 3.1-3.2). Weaver *et al*. (1992) report only sparse siliciclastic turbidites on the Madeira Abyssal Plain during this period, all with a proposed provenance south of the Canary Islands. Thus, although the volumes for the 150-600 ka period turbidites in the Agadir Basin cannot be resolved accurately, they can be presumed to be relatively small (0.2-5.0 km^3), since they are not large enough to be represented on the Madeira Abyssal Plain. Twenty turbidites are recorded after 150 ka at an average 7.5 ka recurrence (Figure 3.12). Although many of

these deposits are <5 km^3 in volume, this period includes large-volume turbidites A5, A7 and A12, with total volumes >100 km^3 (Table 3.1).

A siliciclastic turbidite is recorded at, or at least within five thousand years of, every OIS boundary within the Moroccan Turbidite System (MTS) (Figure 3.12), as previously reported by Weaver and Kuijpers (1983). The present study also confirms that the largest siliciclastic turbidites in the 0-600 ka record in Agadir Basin, namely beds A5 and A12, occur at glacial-to-interglacial OIS boundaries 3/4 and 5/6. Furthermore, large-volume beds A7 and A11 also occur at transitions between climatic cold (lowstand) and warm (highstand) intervals 5b to 5a and 5d to 5c respectively, within interglacial OIS5. Although large-volume volcaniclastic bed A2 occurs at the OIS1/2 boundary, volcaniclastic bed A14 occurred during the OIS 6 glacial (Figure 3.10). Thus, the largest volcaniclastic bed A14 (>110 km^3) does not occur at an OIS boundary as previously reported by Weaver and Kuijpers (1983) and Weaver *et al.* (1992).

Although the dating controls for the older 600 to 150 ka sequence are subject to greater error, there is a pattern in the temporal occurrence of siliciclastic turbidites in this 600 ka record. There is visible clustering of siliciclastic turbidite occurrence, showing preferential (>90% of beds) deposition during interglacial periods (representing 60% of time) (Figure 3.12). Overall, only four of forty four beds occur within glacial periods, with a further two occurring at OIS boundaries (Figure 3.12). However, no beds are found within the peak glacial periods typified by the most positive $\delta^{18}O$ values and lowest sea-level.

Even if the ages of these turbidites are increased or decreased within an error of ±10 ka, glacials and especially the point of lowest sea-level stand remain under-represented by turbidites, while sea-level transgressions and interglacial highstands remain over-represented. Unfortunately this study only involved forty four beds, which precludes valid use of the Hurst exponent to evaluate temporal clustering (Chen and Hiscott, 1999), requiring N>100. However, tentative application of the Hurst exponent provides a K value of 0.51, implying that even with clustering identified, the occurrence of a turbidity current is independent of the previous event.

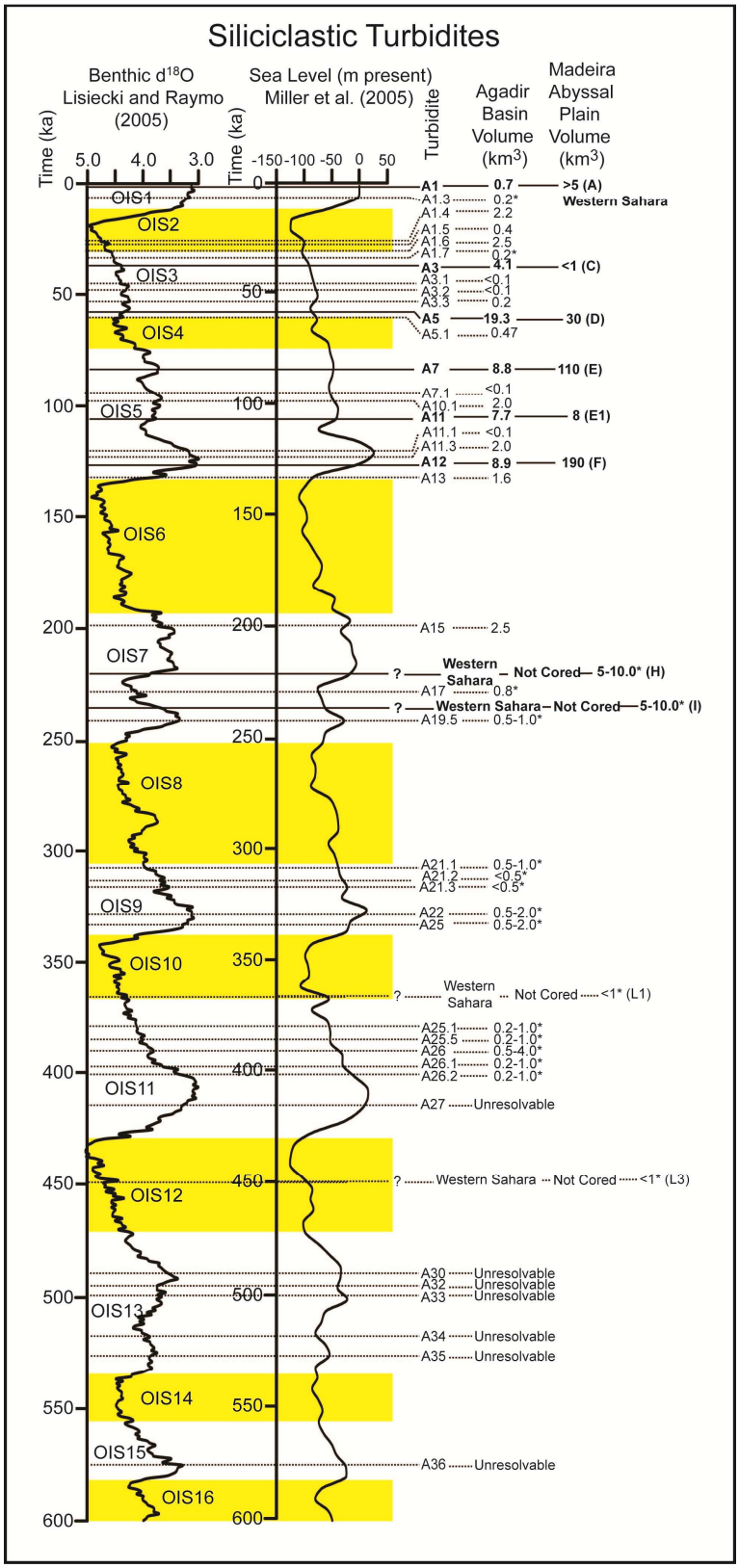

Figure 3.12 Temporal records of siliciclastic, volcaniclastic, and calcareous turbidites of the Agadir Basin plotted against the Lisiecki and Raymo (2005) global benthic foraminifera $\delta^{18}O$ record and Miller *et al.* (2005) sea level record. Turbidites highlighted in bold signify turbidites present on the Madeira Abyssal Plain. Additional interpretative sequence stratigraphic systems tracts placed on the sea level record.

Turbidite Provenance and Stratigraphy

Previous studies have described the turbidite stratigraphy in Agadir Basin back to ~165 ka (Wynn *et al.,* 2002a; Frenz *et al.,* 2009; Figures 3.7-3.9 and Table 3.1). These studies propose three compositional classes of turbidite related to provenance: siliciclastic, volcaniclastic and calcareous turbidites. A similar classification was previously proposed for the turbidite sequence in the Madeira Abyssal Plain (Weaver and Kuijpers, 1983; Weaver *et al.,* 1992; Pearce and Jarvis, 1992, 1995; Rothwell *et al.,* 1992).

The present study, based on a more extensive core dataset within and adjacent to Agadir Basin, supports this classification. Siliciclastic turbidites from Moroccan Shelf (Siliciclastic Subgroup 1) and Western Sahara Shelf (Siliciclastic Subgroup 2) are both quartz-rich (Table 3.1). Volcaniclastic turbidites from Tenerife (Volcaniclastic Subgroup 1) are distinguished from El Hierro (Volcaniclastic Subgroup 2) and Madeira (Volcaniclastic Subgroup 3) by presence of phonolitic glasses and phonolite/trachyte lithics, compared to the basalt-rich El Hierro and Madeira deposits (Table 3.1). Furthermore, basaltic sands from El Hierro (Volcaniclastic Subgroup 2) have a noticeable presence of basaltic volcanic glass. In contrast, the volcanic sands from Madeira (Volcaniclastic Subgroup 3) are dominated by basaltic lithics only. The calcareous turbidites sourced from seamount failures are distinguished by being foraminifera-rich with low-to-rare amounts of volcanic lithics and pyrite (Table 3.1).

Spatial and Temporal Variations in Hemipelagic Sedimentation

Development of a chronostratigraphic record also allows more detailed analysis of spatial and temporal variations in hemipelagic sedimentation within Agadir Basin; this analysis reveals subtle, but consistent, differences between core locations. Sedimentation rates are generally lower during glacial stages than interglacial stages (Figures 3.2 and 3.11). For example, sedimentation rates are generally lower during glacial stages OIS2 and OIS 4 than alternate interglacial stages (Figure 3.13). However, inflections in sedimentation rate also appear coeval with the occurrence of large-volume siliciclastic turbidites, i.e. A5, A7 and A12 (Figure 3.13), which could highlight effects of intermixing of the uppermost turbidite mudcap and hemipelagite sediments.

Table 3.1 Sediment provenance of Agadir Basin turbidites, with examples, compositions and volumes.

Type	Subgroup	Provenance	Composition	Volume	Examples	Notes
Siliciclastic	1	Moroccan Shelf	Quartz rich with minor glauconite, pyrite, biotite and aeolian dust. Bioclasts as forams and sponge spicules.	Unresolved	A29, A30, A32-40	
				<1 km^3	A1.3, A1.5, A1.7, A1.8, A3.1-3, A5.1, A7.1, A9, A9.1, A11.1, A13.2-6, A19.5, A25.1, A25.5, A26.1-2	Predominantly restricted to the Agadir Canyon mouth.
				1-5 km^3	A1.4, A1.6, A10.1, A13, A15, A17, A22, A25 and A26	Restricted to the upper Agadir sub-basin.
				10-15 km^3	A3 and A11	Restricted to Agadir Basin with a small volume restricted to the NE Madeira Abyssal Plain.
				>100 km^3	A5, A7 A12	Found in Agadir Basin with a large volume in the Madeira Abyssal Plain.
	2	Western Sahara Shelf	Quartz rich with minor pyrite. Bioclasts as foraminifera and bivalve shell fragments.		A1	Coarsest south of the Canary Islands. Fines and pinches out up-dip through the Agadir Basin.
Volcaniclastic	1	Tenerife	Phonolite glass rich with abundant phonolite lithics and minor pyroxenes and feldspars.	1-3 km^3	A16	Distribution indicates Western Canary source, composition of Tenerife.
				>100 km^3	A14	Both found to fine and pinch out from SW to NW through Agadir Basin, also a large volume within Madeira Abyssal Plain.
	2	El Hierro	Basalt lithic rich with abundant basaltic glasses.	>100 km^3	A2	
	1	Madeira	Basalt lithic rich only.	<1 km^3	A2.1, A3.5, A4, A6, A6.1, A6.2. A8.5, A10.5. A13.1	Restricted to South Madeira Slope.
				1-5 km^3	A8, A19, A20, A21, A24, A27	Restricted to lower Agadir sub-basin.
Calcareous			Foram rich with minor volcanic lithics and pyrite.	0.5-2.5 km^3	A10, A18, A28, A31	Found throughout the Agadir Basin.

Spatial variability has been examined for the hemipelagic sequence back to bed A12 (~125 ka), as most piston cores penetrate to this interval. Depth-averaged hemipelagic sedimentation rates are all in the range of 0.4-1.8 cm/1000 yrs (Figures 3.14), although within the flatter regions of Agadir Basin, i.e. the upper and lower sub-basins, they are restricted to 1.3-1.8 cm/1000 yrs (Figures 3.14). Conversely, sedimentation rates on the gently-sloping margins of Agadir Basin are lower (0.6-1.1 cm/1000 years) than on the adjacent basin floor (1.6-1.8 cm/1000 years) (Figure 3.14).The lowest depth-averaged hemipelagic sedimentation rates of <0.5 cm/1000 year occur at sites affected by localised erosion or bypass beneath flows, e.g. on the outer bend of lower Agadir Canyon and within some parts of the Madeira Channels (Figure 3.14) (Stevenson *et al.,* 2012).

Although variations in sedimentation rate may be partly due to errors in assignment of the hemipelagite-turbidite boundary (at the top of turbidite mud caps), the high level of consistency shown in the temporal hemipelagic sedimentation rates along particular transects indicates that these boundaries were interpreted consistently (Figure 3.13).

Temporal Variability in Hemipelagic Composition

The CaO and Fe_2O_3 geochemical properties can be linked to the sea level and climatic conditions governing the deposition and preservation of carbonate materials in the deep sea. Other than these, there are additional properties that can be gleaned. These can potentially provide insight into influences on turbidite occurrence, such as enhanced sediment (terrigenous and organic) flux to the shelf. The Ba and Ba/Ca from foraminifera have been previously used productivity indicators (Dymond *et al.,* 1992). Figure 3.13 demonstrates the temporal variability in organic barium, organic carbon and lithogenic flux of Matthewson *et al.* (1995) and Moreno *et al.* (2002). Figure 3.14 then shows the correspondence of these properties to sea level and the occurrence and volume of the 0-200 ka Agadir Basin siliciclastic turbidites. In addition, ITRAX down-core profiles also show further interesting results (Figure 3.15).

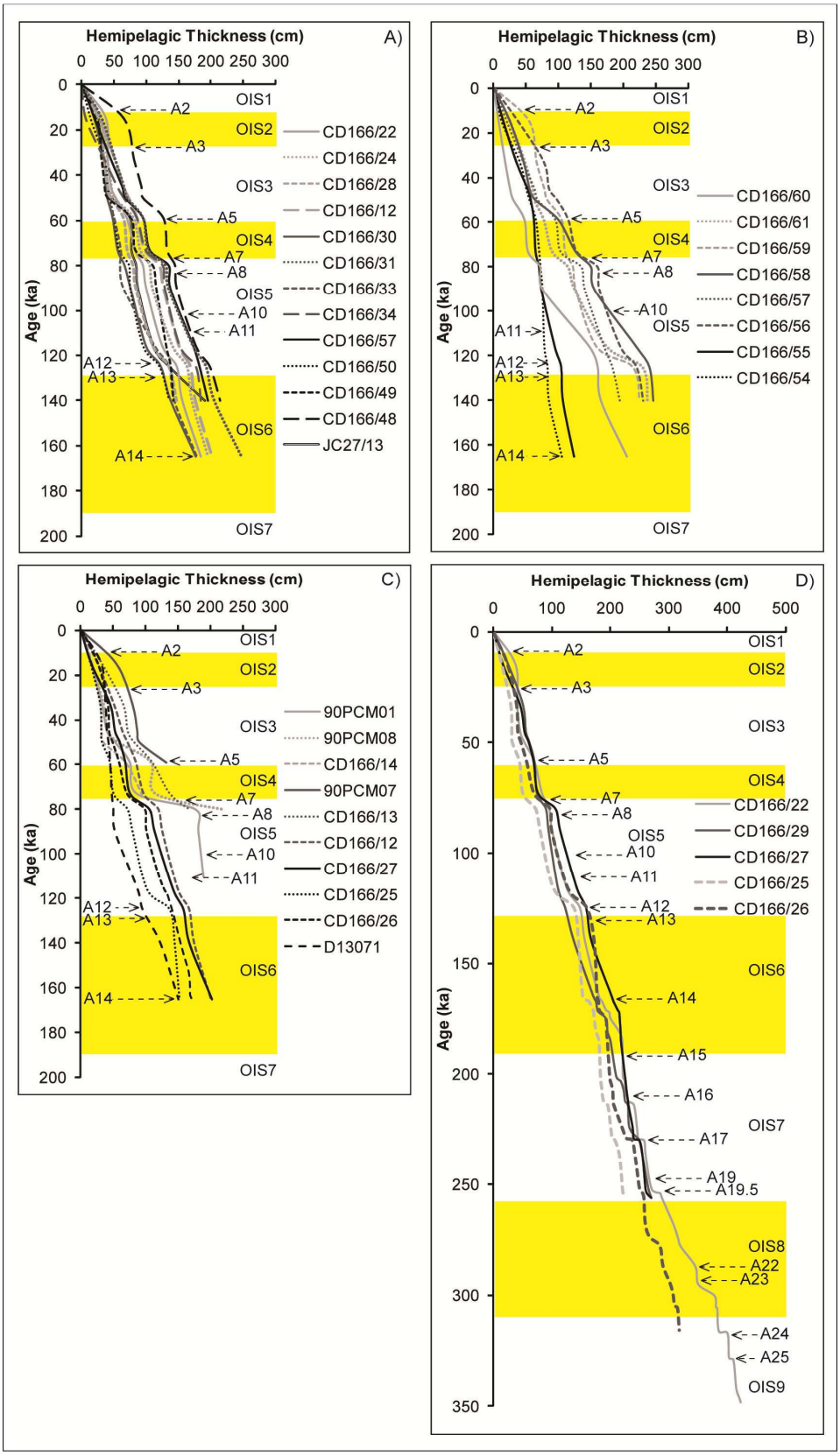

Figure 3.13 Hemipelagic sedimentation rates down-core. A) Axial transect core hemipelagic sedimentation rates to turbidite A14 at 160 ka. B) Upper transect core hemipelagic sedimentation rates to turbidite A14 at 160 ka. C) Lower transect core hemipelagic sedimentation rates to turbidite A14 at 160 ka. D) Extended core hemipelagic sedimentation rates to a maximum of 350 ka. Positions of the turbidites are highlighted with labelled arrows. Core positions and correlation panels on Figure 3.1.

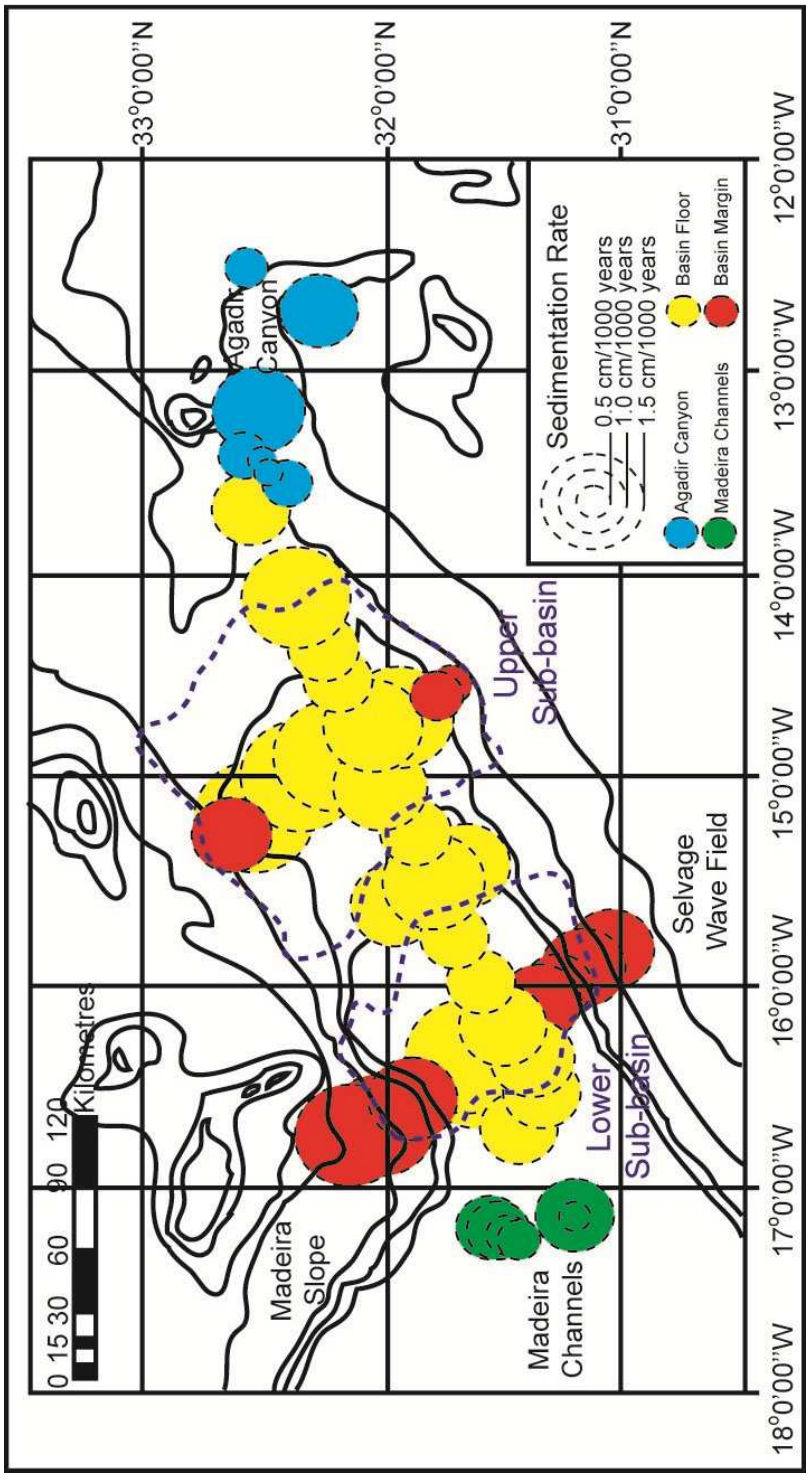

Figure 3.14 Spatial variability in hemipelagic sedimentation rates at the core sites in Agadir Basin. Sedimentation rates calculated to ~125 ka at turbidite A12. Hemipelagic sedimentation rates are highest within the sub-basin centres compared to basin margins.

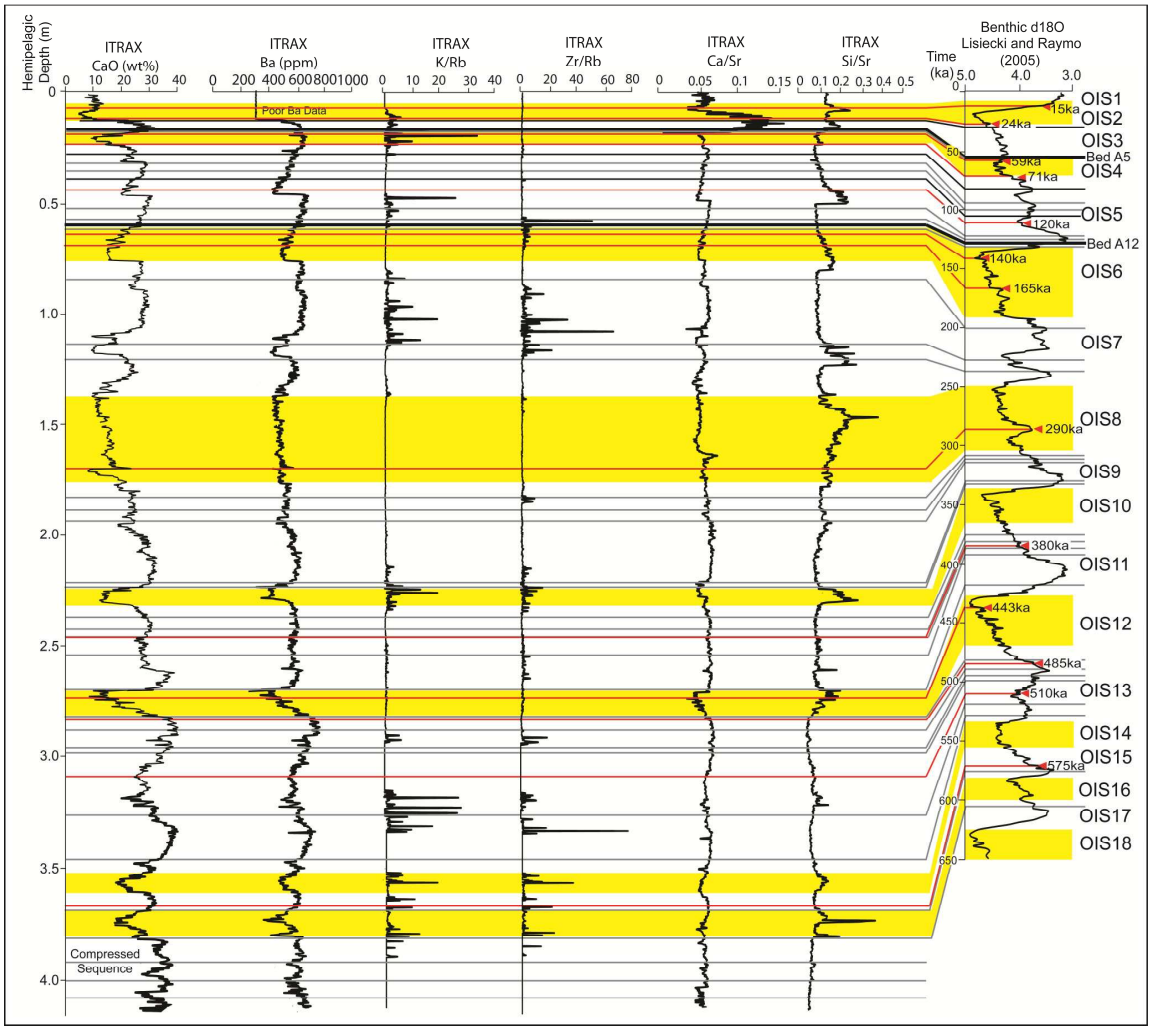

Figure 3.15 D13073 ITRAX hemipelagic record of productivity (Ba and Ba/Ti), in addition to terrigenous lithogenic flux (K/Rb), and detrital carbonate (Ca/Sr and Si/Sr).

Discussion

Climate Records from Hemipelagic ITRAX XRF

Validation of the Wynn *et al.* (2002a) and Frenz *et al.* (2009) stratigraphy (Figures 3.7-3.9) is shown here by the derivation of a dateable hemipelagic climate record that supports correlations and dating of turbidites within this record (Figures 2-5). The calibrated ITRAX CaO wt% profile corresponds to carbonate content of the hemipelagite, and correlates to the $\delta^{18}O$ within core and benthic $\delta^{18}O$ sea-level records (Figure 3.3). These variations in calcium carbonate and iron-rich clay contents are due to the variable influence of NADW, which in turn is controlled by climate and relative sea-level (Crowley, 1983; Weaver and Rothwell, 1987). During sea-level lowstands bottom water is more corrosive resulting in dissolution of carbonate (Crowley, 1983; Weaver and Rothwell, 1987). This also results in the deposition of red iron-rich clays

and overall condensed thickness of the lowstand sequences (Figures 3.2, 3.3, 3.10 and 3.11). These ITRAX CaO records are effective in constraining the dates of the turbidites within the basin (Figures 3.3 and 3.11), as well as supporting correlations of turbidite lithostratigraphy (Figure 3.4).

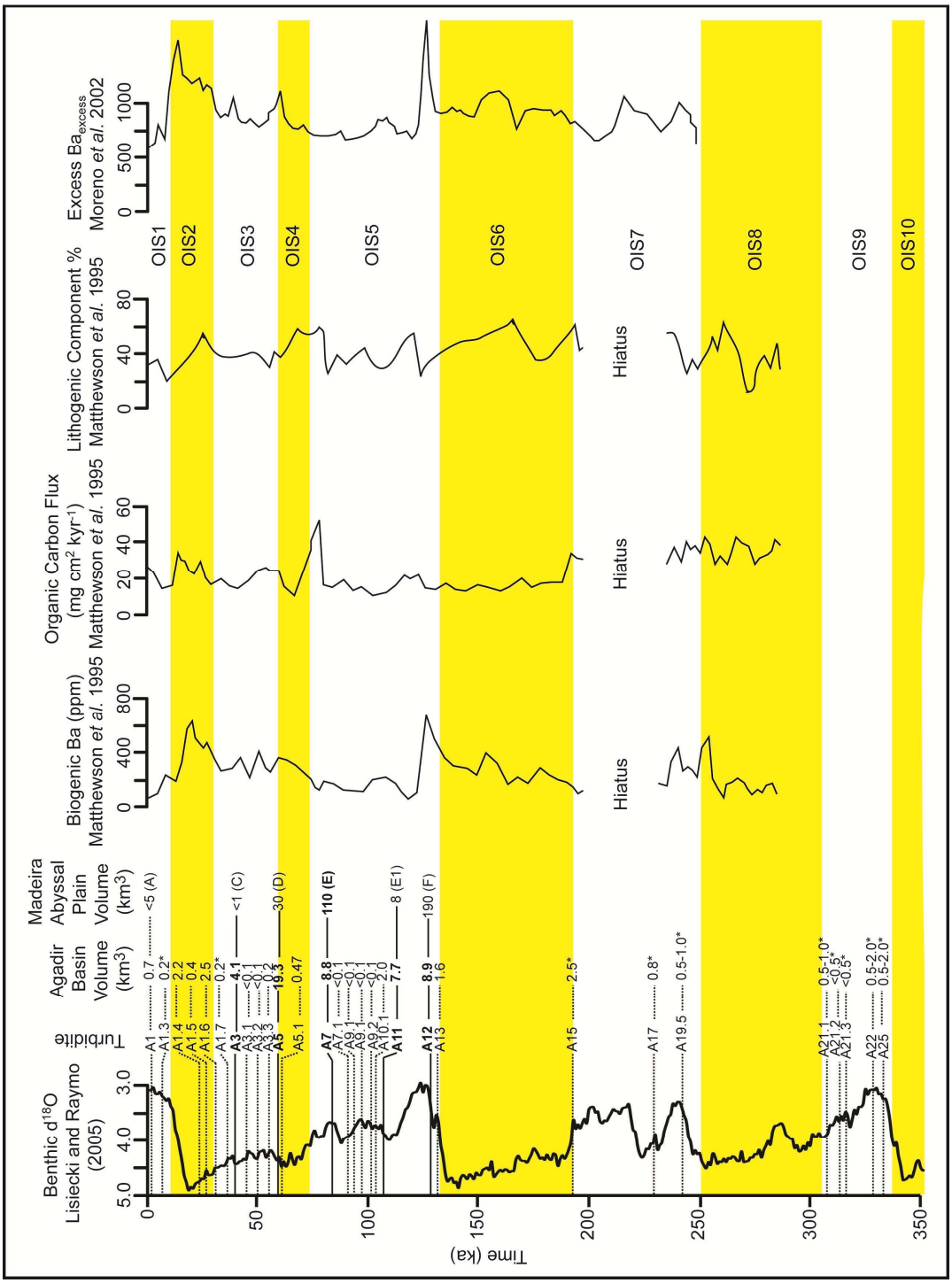

Figure 3.16 Siliciclastic turbidite record plotted against the temporal records of terrigenous and organic carbon flux to the continental shelf of Matthewson *et al.* (1995) and Moreno *et al.* (2002).

These ITRAX records of carbonate content do have limitations, in that the records still ultimately require datum horizons. Furthermore, there are concerns about the effects of modern oxidation fronts in the top 10-20 cm of the cores and effects of defining upper turbidite boundaries. Raw counts provide semi-quantitative results, while calibration is needed to produce quantitative results. However, the ITRAX methodology is capable of gathering high resolution (500-2,500 μm) records, which provide an equivalent 100 year measurement resolution. This high resolution record is invaluable in locations with low 0.5-2.0 cm/1000 year sedimentation rates. Although caution must be made where intense bioturbation is identified. However, the methodology is also non-destructive, enabling preservation of the core.

Temporal and Spatial Variations in Hemipelagic Sedimentation Rates

Correlation and dating of turbidites within the Moroccan Turbidite System is based on the temporal variation in hemipelagite and where the turbidites intersect this record. Indeed, previous works on the Madeira Abyssal Plain have advocated utilising hemipelagite lithology and coccolith biostratigraphy to correlate and date turbidites (Weaver and Kuijpers, 1983; Weaver *et al.,* 1987; Weaver *et al.,* 1992; Wynn *et al.,* 2002a). It is important to have an understanding of both the temporal and spatial variability of the hemipelagic sedimentation rates. There are minor and consistent decreases in hemipelagic sedimentation rate associated with glacials. Inflections in the record are found to coincide with the largest-volume turbidites A5, A7 and A12 turbidites. These inflections in sedimentation rate are potentially due to the influence of deposition of the fine-grained suspension fallout from these large-volume events over protracted periods of time, which result in a diffuse upper boundary with 'pure' hemipelagite.

It might be inferred that background pelagic/hemipelagite sediment rates would be relatively uniform in deepwater settings. Agadir Basin shows degrees of spatial variability with hemipelagite sedimentation rates, with depth averaged hemipelagic sedimentation rates within the whole system varying from 0.5 to 1.8 cm/1000 years (Figures 3.13-3.14). The lower sedimentation rates in Agadir Canyon and Madeira Channels are expected due to erosion, bypass and gravity flow influence (Figure 3.14) (Stevenson *et al.,* 2012). Indeed, the less erosive inner bend of the Agadir Canyon shows higher sedimentation rates than the more erosive outer bend. Higher sedimentation rates on the southern Madeira slope in the lower western sub-basin are

expected due to the advection of volcanic materials (Figure 3.14). However, basin margin sedimentation rates are lower than those of the basin centre (Figures 3.13-3.14).

The Selvage Sediment Wave Field forms the southern margin of Agadir Basin on the slope rising to the Selvage Islands (Wynn *et al.,* 2000b). Sediment wave migration has been found to be dependent on turbidity current and hemipelagic advective processes (Wynn *et al.,* 2000b). The lateral advection processes of hemipelagic material within the sediment wave field may be the principal reason for the spatial variability in the hemipelagic sedimentation rates within Agadir Basin.

Agadir Basin Turbidite Record and Landslide Activity on the Northwest African Margin

This study highlights the turbidite record in the Agadir Basin of the Moroccan Turbidite System. Combining this with the Madeira Abyssal Plain record presents a more complete history of sediment gravity flows on the Northwest African passive margin (Figure 3.12). The overall recurrence period of siliciclastic turbidites in the Moroccan Turbidite System is 7.5-15 ka. Prior to 150 ka there is no evidence in the more distal Madeira Abyssal Plain of siliciclastic flows originating from the Moroccan Shelf (Weaver *et al.,* 1992; Rothwell *et al.,* 1992). Indeed, Rothwell *et al.* (1992) attribute Madeira Abyssal Plain siliciclastic turbidite provenance prior to 200 ka as originating from a source south of the Canary Islands. However, in Agadir Basin the present study shows that from 600 to 150 ka there was still siliciclastic turbidite activity originating from the Moroccan shelf via Agadir Canyon. However, during this period there are no turbidites of volume or runout great enough to enter the Madeira Abyssal Plain (Figure 3.12).

The siliciclastic turbidites sourced from the Moroccan shelf demonstrate a potential pattern of clustering in their recurrence. The siliciclastic turbidites are found predominantly during transgressions and interglacials (90% of events in 60% of the time) (Figure 3.12). The Dakar Canyon, and associated turbidite system to the south of the Moroccan Turbidite System, is an analogous system with minor fluvial and eolian sediment supply (Pierau *et al.,* 2010, 2011, and references therein). Turbidites in the Dakar Canyon were emplaced at the end of glacial lowstands, during marine transgressions, and during the subsequent peak interglacial highstand (Pierau *et al.,* 2010, 2011). There are issues with the location of the cores used in the Dakar Canyon studies, with respect to the turbidity current channels, and with the general lack of core

coverage over the turbidite system. However, the trends in turbidite occurrence in the Dakar Canyon are consistent with patterns in turbidite occurrence in the Moroccan Turbidite System.

Studies of shelf and slope sediment flux may provide insight into the preconditioning factors that facilitate the frequency and volume of siliciclastic submarine landslides, and associated turbidity currents. During the glacial lowstands (OIS8, 6, 4 and 2) biogenic barium flux increases from initial regression towards the later transgression and onset of interglacial period (Figures 3.15-3.16; Matthewson *et al.,* 1995; Moreno *et al.,* 2002). This indicates that oceanic productivity increases through the glacial and peaks during the marine transgression immediately prior to the interglacial stage (Figure 3.16, e.g. ~250 ka, ~125 ka, ~60 ka and ~15 ka respectively) (Matthewson *et al.,* 1995; Moreno *et al.,* 2002). This is supported by the ITRAX Ba record from D13073 that also increases at the onset of OIS5 interglacial and OIS3 interglacial (Figure 3.15). Thus the ITRAX BA record coincides with the barium productivity records from the Matthewson *et al.* (1995) and Moreno *et al.* (2002) (Figures 3.15-3.16).

These elevations in or trends in increasing biogenic barium and thus oceanic productivity coincide with a number of significant turbidites (>100 km^3) including A12 (~125 ka) and A5 (~59 ka). However, the 0-600 ka record at D13073 shows that turbidites do not necessarily coincide with elevations in Ba. Thus patterns in productivity may not influence submarine and turbidity current occurrence, although higher pelagic sedimentation rates may precondition the volume of sediment available to fail (Figures 3.15-3.16). Records of elevated terrigenous sediment flux show varying coincidence with turbidite occurrence, which negates terrigenous sediment flux as being a major preconditioning factor for sediment failure.

Weaver (2003) presents a study of the 0-17 Ma turbidite record at ODP sites in the Madeira Abyssal Plain, in which the frequency and volume of siliciclastic turbidites is implied to reflect rate of sediment accumulation on the Northwest African slope, associated with variations in upwelling and resultant oceanic productivity. However, the present contribution indicates that rapid sediment flux to the shelf cannot be conclusively attributed as being a primary preconditioning factor for submarine landslide occurrence. However, biogenic sediment flux does tentatively appear to influence the volume of the failures.

Although from a different climate zone, Pierau *et al.* (2010) attribute turbidite activity at glacial terminations as reflecting remobilisation of sediment previously

deposited on the exposed shelf during prior arid glacial periods. The occurrence of turbidites in the present study potentially supports this timing of sediment remobilisation as a preconditioning factor.

Turbidite clustering within interglacial periods has been highlighted. Initial evaluation of turbidite recurrence intervals from this study provides a Hurst exponential of K=0.51 from N=44, which would imply that turbidite occurrence is independent of previous events. This random distribution of turbidite recurrence demonstrates that a Poisson-like process triggers initial instigation of turbidites. Given the geographic proximity to the Atlas Mountains and Eurasian-African plate boundary, earthquakes are likely important in triggering submarine landslides that generate these turbidites. Given the sample size as being N<100, use of the Hurst exponent should be done with caution.

The data presented in this contribution highlights that there is a coincidence of the siliciclastic, and indeed the major volcaniclastic, turbidites with periods of rising and high sea-level. This pattern in siliciclastic turbidite recurrence is not in accordance with sequence stratigraphic models, which previously identify sea-level lowstands as periods of greatest turbidite activity. Indeed, as highlighted by previous work, (Weber *et al.*, 1997; Prins and Postma, 2000; Caravajal and Steel, 2006; Covault and Graham, 2010), turbidite activity can remain high during rising and highstands of sea-level.

The present contribution presents results that enable a discussion on preconditioning factors influencing submarine landslide occurrence. Increased sediment flux to the continental slope associated with climate variations appears coincidental with occurrence of large-volume beds A5 and A12. However, other than potentially influencing the volume of particular events the data presented here shows no definitive link between sediment flux and turbidite occurrence. Although clustering can be visually recognised, the occurrence of turbidites is statistically random. A Poisson-like process, such as earthquakes, is implicated as being the trigger mechanism for these turbidites. However, an importance assertion is that for an earthquake to generate a submarine landslide or sediment gravity flow there must be sediment available to fail. Therefore, sediment delivery to shelf may have an influence on the failure volume, as discussed for beds A5 and A12.

Conclusions

Common misconceptions are that turbidite and landslide activity is restricted to periods of lowstands and falling sea-level. The turbidite record of Agadir Basin demonstrates

that this is not the case. The turbidite record shows a prevalence of siliciclastic turbidites during interglacial highstands. Climate change and sediment accumulation during deglaciations are potential preconditioning factors for continental slope landsliding. However, the triggering of such submarine landslides is random process, suggested here as being driven by earthquakes. Although sediment flux does not influence turbidite occurrence, it may influence the volume of sediment available to fail.

The hemipelagic sediment deposited in Agadir Basin records an accurate history of climate and sea-level change. Sedimentation rates are broadly constant through time, although minor decreases in sedimentation rate during glacials and increases are associated with emplacement of some larger turbidites. Furthermore, although the hemipelagic sedimentation rates within Agadir Basin are always in the range of 1.2-1.8 cm/1000 years, there is spatial variability across basin. Indeed, highest sedimentation rates are found in the centres of the upper and lower Agadir sub-basins, compared to lower sedimentation rates on the basin margins.

The findings of the present study demonstrate an ability to correlate turbidite beds across hundreds of kilometres of sea floor. Accurate correlation and dating of these beds and the excellent core coverage has enabled detailed records of landslide frequency and volume for the Moroccan continental margin.

Acknowledgements

JEH would like to acknowledge the PhD funding from NOCS and the Marine Geoscience Group at NOCS, which has contributed to the completion of this study. The authors would like to acknowledge the help of S. MacLachlan and R.G. Rothwell in the curatorial services in maintaining the cores and instruments at BOSCORF. The authors would also like to acknowledge the help of D. Green at NOCS in preparation of the ICP-OES for analysis of the bulk samples used to calibrate the ITRAX.

3.3 Summary

Firstly, this Chapter has served to validate and extend the existing Agadir Basin turbidite stratigraphy. In addition to an axial down-basin correlation panel, two transverse correlations panels are presented through the upper and lower sub-basins. The geochemistry (CaO) of the hemipelagite between the turbidites has been shown to support turbidite correlations. Furthermore, the CaO hemipelagite profiles also provide potential dates for these events, when correlated to the Lisiecki and Raymo (2005) global benthic foraminifera $\delta^{18}O$ curve. Geophysical data (p-wave velocity, gamma-ray density and magnetic susceptibility) has also been presented here to further support the turbidite correlations and basin stratigraphy.

Secondly, the largest-volume events (beds A5 and A12) were found to occur at transitions between glacial and interglacial climate conditions. These were also coincidental with increased sediment flux to the shelf. A general observation is that most of the siliciclastic turbidites also occur at glacial-interglacial transitions. This implies that periods of deglaciation and increased sediment flux may represent the preconditioning factors for Late Quaternary submarine landslide activity from the Moroccan continental margin.

In the context of this thesis, this Chapter serves to introduce the stratigraphy of the Agadir Basin, which will be utilised in subsequent Chapters 4, 5, and 7.

Chapter 4

Provenance of Agadir Basin Turbidites

4.1 Introduction and Aims

The previous Chapter 3 presents a series of turbidite correlation panels that can be used to construct a turbidite stratigraphy for Agadir Basin. Mudcap geochemistry has been previously used in the Madeira Abyssal Plain to provide a chemostratigraphy and investigate the provenance of the turbidites recovered (de Lange *et al.,* 1987; Pearce and Jarvis, 1995). However, these studies have utilised a limited number of samples from each mudcap analysed using destructive methodologies. This Chapter demonstrates the application of non-destructive, high-resolution ITRAX μXRF in deriving the bulk geochemical composition of turbidite mudcaps from numerous core sites within Agadir Basin. These mudcap compositions can be used to support turbidite correlations constructed in the previous Chapter 3, and to better investigate the provenances of those turbidites. A number of aims are presented below:

1. Use ITRAX chemostratigraphy within the turbidite and hemipelagite records to support the existing turbidite correlatations.
2. Demonstrate the geochemical variations between siliciclastic, volcaniclastic and calcareous turbidite provenances.
3. Determine whether erosion by siliciclastic turbidity currents upon exiting the Agadir Canyon can be detected in variations in mudcap geochemistry, using the ITRAX μXRF methodology.

This Chapter will be submitted, in its current format, to *Marine Geology* (July 2012). All data analyses and interpretations are my own, with additional editorial support from my co-authors.

High resolution geochemical assessment of deepwater sediments in the Agadir Basin, Northwest African passive margin

James E. Hunt[1,2]*, R.B. Wynn[1], I.W. Croudace[1], P.J. Talling[1], D.G. Masson[1]

[1]National Oceanography Centre, University of Southampton Waterfront Campus, European Way, Southampton SO143ZH, UK

[2]School of Ocean and Earth Science, National Oceanography Centre Southampton, University of Southampton, European Way, Southampton SO143ZH, UK

* Corresponding author: jeh2g08@soton.ac.uk

Abstract

The use of ITRAX μXRF in the study of sediment cores in Agadir Basin has enabled a detailed appraisal of the turbidite stratigraphy and provenance. Evaluation of the mudcap geochemistry of basin turbidites has supported the original distinction of siliciclastic, volcaniclastic and calcareous turbidite types. Indeed, this detailed ITRAX μXRF study has also highlighted three separate provenances for the three volcaniclastic turbidites as theorised in previous studies. These include determination of the phonolitic Tenerife source for A14, and individual basaltic sources for A2 (El Hierro) and A8 (Madeira). Further study of siliciclastic mudcap geochemisties has shown that, although a similar regional source (Moroccan shelf/slope) is theorised, there are subtle variations in composition indicating different local sources or thickness of sediment column failed. Previous and ongoing research has indicated that siliciclastic turbidity currents exiting the Agadir Canyon are erosive. Thus basinal turbidite compositions could be the result of differential erosion at the canyon mouth. Indeed, on comparison of the composition of the same large-volume turbidites from the Agadir Canyon and Agadir Basin sites, the canyon composition is offset from that of the basin. Small-volume turbidites are found to have similar compositions in the canyon and in the basin, thus unlike the larger-volume flows, these small-volume events are principally non-erosive. Analysis of the complete series of turbidites in the Agadir Canyon displays subtly different geochemical compositions, supporting early notions of different local sources within the same geographic area.

Introduction

The Moroccan Turbidite System (MTS) is a multi-basin deepwater province located on the Northwest African passive margin (Figure 4.1). The MTS comprises three interconnected depocentres: Agadir Basin, Madeira Abyssal Plain and Seine Abyssal Plain (Wynn *et al.*, 2000, 2002). Agadir Basin presents an unconfined conduit for siliciclastic organic-rich turbidity currents sourced from the Moroccan continental slope via the Agadir Canyon (Figure 4.1). It also represents a depocentre to volcaniclastic turbidites derived from the Western Canary Islands and Madeira (Wynn *et al.*, 2002; Frenz *et al.*, 2009). The study of turbidity current depositional processes within this system is reliant on the robust correlation of individual beds and determination of their flow pathway. The present detailed geochemical study of the turbidites from Agadir Basin will allow both a critique of the basin stratigraphy and the provenance of the deposits.

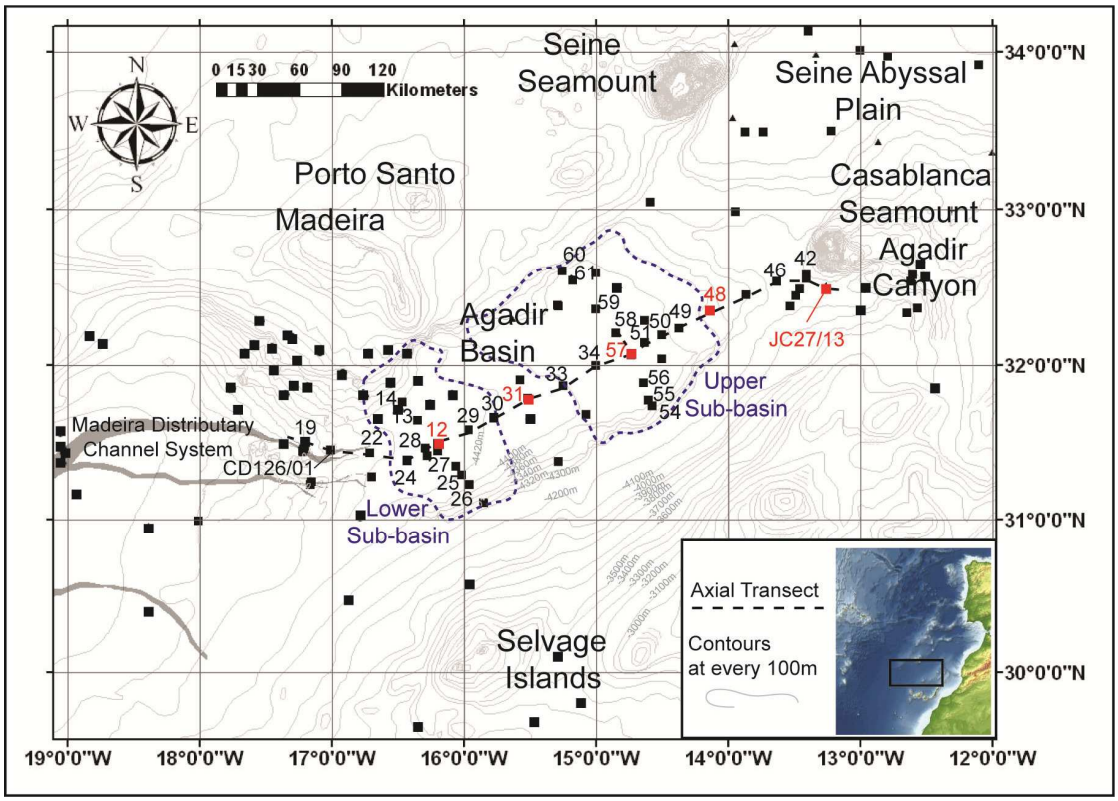

Figure 4.1 Contour map of the Agadir Basin demonstrating the core coverage and the location of the cores selected for the present study (in red).

Previous studies of the Madeira Abyssal Plain have used the geochemical composition of turbidite mudcaps, in addition to coccolith biostratigraphy, to aid the correlation of turbidites and identify their provenance (Weaver and Kuijpers, 1983; de

Lange *et al.,* 1987; Weaver and Rothwell, 1987; Pearce and Jarvis, 1992, 1995; Weaver *et al.,* 1992; Rothwell *et al.,* 1992). These bulk geochemical studies identified organic-rich siliciclastic, volcaniclastic and calcareous turbidite sources (de Lange *et al.,* 1987; Pearce and Jarvis, 1992, 1995; Jarvis *et al.,* 1998). Indeed, subtleties in the major element compositions have enabled identification of evolved and basic igneous Canary Island sources for the volcaniclastic turbidites (de Lange *et al.,* 1987; Pearce and Jarvis, 1992, 1995). Furthermore, moderate and high potassium organic-rich siliciclastic turbidites were identified by Pearce and Jarvis (1995) and Jarvis *et al.* (1998) from the older turbidite sequences in the Madeira Abyssal Plain. These were theorised to reflect a northern Moroccan shelf source with high K/Al and a source south of the Canary Islands with moderate-low K/Al (Jarvis *et al.,* 1998).

These previous studies utilised a number of bulk samples taken from each turbidite mudcap analysed using ICP-AES (de Lange *et al.,* 1987; Pearce and Jarvis, 1995; Jarvis *et al.,* 1998). The use of traditional bulk sample analyses is time-consuming and expensive (Croudace *et al.,* 2006). Non-destructive geochemical core scanners such as the ITRAX µXRF core scanner at BOSCORF (British Ocean Sediment Core Research Facility) provides an ability to measure the geochemical composition of the cored sediment at resolutions of <500 µm (Croudace *et al.,* 2006).

The XRF data from these scanners has been previously used for turbidite correlation and provenance studies (Rothwell *et al.,* 2006; Marsh *et al.,* 2007; Giresse *et al.,* 2009), sediment diagenesis studies (Rothwell *et al.,* 2006; Thomson *et al.,* 2006; Cronan *et al.,* 2010; Löwemark *et al.,* 2011), palaeoenvironmental studies (Corella *et al.,* 2010; Burnett *et al.,* 2011; Löwemark *et al.,* 2011; Moy *et al.,* 2011; Scholz *et al.,* 2011; Marshall *et al.,* in press) and pollutant dispersal studies (Lepland *et al.,* 2010). ITRAX µXRF data has also been previously used in the study of the turbidites from Agadir Basin to aid identification of volcaniclastic and siliciclastic turbidites (Frenz *et al.,* 2009). However, the Frenz *et al.* (2009) study directly compared the geochemical signatures from both the sand and mud components of the turbidites at a single core site (CD166/12). Since geochemical compositions can be dependent on the grain-size distribution of the sample, this initial study requires revision.

The present study utilises ITRAX µXRF data from six piston cores from Agadir Basin (Figure 4.1 for location). The aim is to firstly show the ability of using ITRAX µXRF core scanner data to correlate turbidites and assess their provenance. This will aid correlation of turbidites between sites >50 km apart and assess the flow pathway based

on the provenance. Variations in the turbidite mudcap geochemical compositions were utilised to more accurately assess provenance. Geochemical records have a dependency on grain-size, thus like-for-like mudcaps will be compared for greater validity. The high resolution measurement interval and use of multiple cores will also enable a more detailed evaluation of the provenance of these turbidites compared to previous studies.

A final aim will be to compare the composition of the correlated siliciclastic turbidites from the Agadir Canyon to those in the basin. This will assess whether significant differential erosion at the mouth of the Agadir Canyon is responsible for any heterogeneities in siliciclastic turbidite composition. Site JC27/13 is located before turbidity current erosion upon exiting the canyon. The generation of hydrid beds or linked debrites in the Agadir Basin, e.g. bed A5, has been associated with erosive addition of cohesive sediments upon exiting the canyon, resulting in turbulence suppression (Talling *et al.,* 2007). Resolving the erosive nature of these flows is thus important for understanding its impact on flow dynamics. Furthermore, the compositional variations recorded at this site, prior to erosion, will demonstrate whether all siliciclastic turbidites are sourced from the same location on the continental slope.

Geological Setting

The Moroccan Turbidite System (MTS) forms a series of interconnected depocentres on the deepwater passive margin of Northwest Africa (Figure 4.1). The Madeira Abyssal Plain forms the most distal region of the MTS to the west, in water depths of up to 5,440 m. The Madeira Abyssal Plain is connected to Agadir Basin via a series of shallow (10-20 m-deep) submarine channels known as the Madeira Distributary Channel System (Masson, 1994; Weaver *et al.,* 2000; Stevenson *et al.,* 2012).

Agadir Basin represents a depocentre proximal to the Moroccan shelf and fed directly by Agadir Canyon (Figure 1) (Wynn *et al.,* 2002). Its geometry comprises two sub-basins: upper to east and lower to the west, which are separated by a subtle gradient change (Talling *et al.,* 2007; Wynn *et al.,* 2011). Agadir Basin acts as both a sediment depocentre and a conduit for siliciclastic turbidity currents travelling to the more distal Madeira Abyssal Plain from the Agadir Canyon. Furthermore, Agadir Basin is also connected to the Seine Abyssal Plain to the north via the 10-40 m high Casablanca Ridge (Figure 4.1) (Davies *et al.,* 1997). Wynn *et al.* (2002) demonstrated that the turbidite stratigraphy of Agadir Basin, Madeira Abyssal Plain and Seine Abyssal Plain

can be correlated, with individual events spanning the >200,000 km^2 area across all the basins.

The turbidites within Agadir Basin represent a sequence of organic-rich siliciclastic, volcaniclastic and calcareous deposits that range in volume from 1 to 250 km^3 (Frenz *et al.,* 2009; Chapter 3). These have been shown to not only possess graded patterns of deposition synonymous with turbidity currents, but also coeval debris flow deposits 'sandwiched' within the turbidites, known as linked debrites or hybrid beds (Talling *et al.,* 2007; Frenz *et al.,* 2009; Wynn *et al.,* 2010). The large-volume volcaniclastic turbidites are found to develop as vertically stacked fining-upwards sequences (known as subunits), which are the result of multistage failures at source (Wynn and Masson, 2003; Hunt *et al.,* 2011). These include beds A2 (~15 ka El Golfo landslide) and A14 (~165 ka Icod landslide).

Methodology and Data

Visual and Sedimentological Logging

A dataset of >60 cores from Agadir Basin were subjected to visual logging of the sediment sequence recovered. Sedimentological features of colour, grain-size, sedimentary structures and mineralogy were all documented.

ITRAX μXRF

This instrument has enabled non-destructive geochemical analysis of the cored deposits at sites CD166/12, CD166/31, CD166/57, and CD166/48 within Agadir Basin (Figure 4.1 for locations). These cores were chosen to provide examples from the entry slope to the basin (CD166/48), the upper sub-basin (CD166/57), gradient change between upper and lower sub-basins (CD166/31), and the lower sub-basin (CD166/12). Further cores from the Agadir Canyon (JC27/13) and the Casablanca Ridge (D13073) were also utilised for provenance studies.

This methodology involves split core sections progressively moved past a 3 kW Mo-tube X-ray source and XRF Si-drift chamber detector (Croudace *et al.,* 2006). The instrument operated at 60 kV and 45 mA, with a dwell time of 800 ms, and a resolution of 500 μm. Utilising the K-shell peak areas, a value of counts (intensity) is derived for each of the chosen elements detected. Monitoring the element integral profiles, Compton scatter integral and detector-sediment distance aided evaluation of the validity of the results. The incoherence normalised element intensities were then calibrated

against a suite of 1 cm-wide samples taken from the studied cores analysed using ICP-OES. The ICP-OES analyses required traditional destructive acid digestions (Appendix 4.1 and 4.2). Measurements of these ICP-OES samples were taken in order to provide quantified results for the deposits, and for calibrating the raw ITRAX elemental counts using calibration coefficients (Appendix 4.3). ITRAX intensities over the 1 cm sampled were averaged for calibration. The calibration coefficients for the ITRAX methodology produced R^2 values of 0.74-0.96 (Appendix 4.3).

However, attempts thus far to convert XRF core scanner outputs to elemental concentrations have only been moderately successful (Weltje and Tjallingii, 2008, and references therein). Intensity-concentration cross-plots show scatter and potential biasing as a result of sample inhomogeneity, variable water content, and a lack of sample geometry (Weltje and Tjallingii, 2008, and references therein). Averaging intensities over the 1 cm sampled for ICP-OES analysis will aid reduction in the effects of small scale inhomogenetities on the calibration. Issues with sample geometry and signal-to-noise can be negated due to the ability of the ITRAX detector to adjust position relative to the split core surface (Croudace *et al.,* 2006). Water content may be variable, however the cores studied are of the same vintage and have been kept sealed in cold storage (4-6^{o}C), so water loss by drying should be minimal. Comparing compositions of turbidite mudcaps with similar grain-size distributions also maintains analysis of materials with similar porosity-permeability characteristics, thus further reducing the effects of variable water content.

Sediment within the cores studied vary in grain-size, with hemipelagites averaging 10-30 µm, turbidite muds averaging 4-10 µm, and turbidite sands averaging 90-180 µm (d90 fraction at 350 µm). The 500 µm ITRAX resolution is far greater than the size of the largest grains recovered; therefore issues regarding sample geometry will be further reduced. For provenance studies of the turbidites, the compositions of the mudcaps will be compared. This will maintain comparison of compositions of similar grain-size distributions, again reducing effects of sample geometry. Furthermore these finer homogeneous sediments mirror the homogeneous fine powders used in conventional XRF analysis (Haug *et al.*, 2001, 2003; Weltje and Tjallingii, 2008, and references therein).

Although attempts have been made here to calibrate the ITRAX intensities to element concentrations, ultimately element ratios will be used in this study. This is because elemental ratios reduce the effects of some of the issues outlined above, but

most importantly will reduce the effects caused by unit-sum constraint and dilution (Weltje and Tjallingii, 2008, and references therein). Numerous studies have advocated using ratios, and here selected ratios are used according to Croudace *et al.* (2006) and Rothwell *et al.* (2006). Specifically, the Ca/Fe and Sr/Ca ratios are used to monitor the carbonate composition, while K/Rb and Zr/Ti are used to monitor the detrital clay and heavy mineral compositions (Croudace *et al.,* 2006). In the absence of Al, due to its low atomic weight and subsequent attenuation of K-shell x-rays, immobile Ti was used to normalise the data. Due to the better calibration afforded to Ti, it is used over Rb which would otherwise have better reflected Al composition. Weltje and Tjallingii (2008) further advocate using log-ratios to both calibrate the raw data and for comparing datasets. Compositional cross-plots of the present study only utilise elemental ratios, since log-ratios here appear to show the same relationships, albeit reducing the scatter.

ICP-OES

Bulk sediment geochemistry by conventional destructive methodologies was completed to enable calibration of the ITRAX µXRF element intensities. Although XRF WD would represent a similar analytical method to ITRAX µXRF, the ICP-OES methodology was in-line with on-going provenance studies. Bulk samples were taken from the turbidite mudcaps from the selected cores from Agadir Basin analysed by ITRAX (Appendix 4.1). The samples were dried and powdered by agate pestle and mortar for acid digestion. The first acid digest stage was 5 mL aqua rega (3:1 $HCl:HNO_3$), and then secondly with 3 mL HF and 2.25 mL perchloric acid. The final silica-free residue was dissolved in 6 M HCl, from which 0.6 M HCl daughter solutions were made for analysis. A number of terrigenous (MAG-1 and ScO-1) and volcanic (BHVO-2, BIR-1, Jb-1a, JB-2, JB-3 and JGB-1) standard reference materials (SRMs) were used to assess accuracy, with sample and SRM duplicates used to also assess precision of the methodology (Appendix 4.2). The ranges of concentrations used in the production of artificial standards were defined by elemental concentrations from previous studies of Madeira Abyssal Plain turbidites (de Lange *et al.,* 1987; Pearce and Jarvis, 1995). Analysis of standard reference materials demonstrated that major-element analyses (Na, Mg, Al, K, Ca, Ti, and Fe) had average precisions of 2.1-3.1% and average accuracies to the standard reference materials of 1.5-3.3% (Appendix 4.2). With regards to trace-elements, precision varied with Li, V, Co, Cr, Cu, Sr, Zr, Ba and La

between 3.6% and 9.7%, and with accuracies ranging to within 2.2% to 8.9% (averaging 16.4%) (Appendix 4.2). Trace elements Sc, Zn, Y, Ce, and to a lesser extent Zr experienced precisions of >10% and accuracies to standard reference materials to within >10%.

Coccolith Biostratigraphy

Coccolith biostratigraphy was previously used to both correlate and date turbidites in Agadir Basin, but also demonstrate the validity of using ITRAX hemipelagite Cao records (Wynn *et al.,* 2002; Chapter 3). Coccolith biostratigraphy was completed on JC27/13 to provide accurate and robust datum horizons for the ITRAX CaO down-core profile used to correlate beds from the Agadir Basin back to the Agadir Canyon. The last occurrence of *Helicosphaera inversa* is at 140 ka (Hine, 1990), while the last occurrence of *Gephyrocapsa ericsonii* is at 15 ka (Biekart, 1989). The relative abundances of *Pseudoemiliania lacunosa*, *Gephyrocapsa caribbeanica*, *Gephyrocapsa aperta*, *Gephyrocapsa mullerae* and *Emiliania huxleyi* can be used to construct acme zones that correlate to oxygen-isotope stage (OIS) boundaries (Weaver and Kuijpers, 1983; Weaver, 1994). Indeed, noteworthy changes in these relative abundances include: dominance in *G. caribbeanica* below OIS 7 with a marked decrease from the OIS8-OIS7 boundary (290 ka), onset in dominance of *G. aperta* during OIS7 and OIS6, onset in dominance of *G. mullerae* at ~120 ka within OIS5, and onset in the dominance of *E. huxleyi* from OIS5 onwards (71 ka) (Weaver and Kuijpers, 1983).

Samples were taken every 5 cm through the hemipelagite in JC27/13, at 1-3 cm intervals at hemipelagite lithological boundaries, and above and below every turbidite. These were diluted and smeared onto SEM semi-conductor stubs using acetone. Using the *Hitachi TM1000* bench-top SEM, each sample had >300 specimens counted to assess species abundances (Appendix 4.4), although some glacial clays lacked sufficient numbers and/or specimens demonstrating the effects of dissolution. Precision was found to be within a 2-4% standard deviation upon repeat sampling.

Five samples were also taken through the turbidite mudcap intervals used for ITRAX mudcap provenance analyses from CD166/12, CD166/31, CD166/57 and CD166/48 within Agadir Basin and JC27/13 within Agadir Canyon. The coccolith ratios of the mudcaps are used as an additional monitor of seafloor erosion, since erosion of seafloor by a flow with potentially alter the original coccolith composition.

Results

Turbidite Correlations

The down-core ITRAX μXRF data demonstrate that the organic-rich siliciclastic, volcaniclastic and calcareous turbidites can be correlated according to preferential concentrations of selected major elements (Figures 4.3). This supports previous correlations of turbidites within Agadir Basin (Wynn *et al.*, 2002; Frenz *et al.,* 2009; Chapter 3). Calibrated results are shown for CD166/12 (Figure 4.2), and elemental ratios are used to support correlations of turbidites between cores (Figure 4.3). The elemental ratios used are according to Croudace *et al.* (2006) and Rothwell *et al.* (2006). These include Ca/Fe and Sr/Ca to evaluate carbonate component, such that high Ca/Fe report high carbonate content, and high Sr/Ca will report higher components of aragonite. Si/Ti, Fe/Ti and K/Rb report on detrital mineral and clay contents, whereby high Si/Ti denote high silica content, Fe/Ti define heavy mineral components, and high K/Rb will determinate high detrital clay contents of illite over kaolinite.

Volcaniclastic Turbidites (A2, A8 and A14)

Turbidite A2 has been previously linked with the El Golfo landslide from El Hierro (Masson *et al.,* 2002; Frenz *et al.,* 2009). Pearce and Jarvis (1992, 1995) stated that the low SiO_2 and K_2O contents of both the turbidite mud and sand component indicated a primitive basaltic composition. Frenz *et al.* (2009) directly compared the composition of A2 with that of A8 and A14 (Icod turbidite). Turbidite A8 is represented by a 10-30 cm-thick coarse basaltic sand, which is incorrectly directly compared to the finer deposits of A2 and A14. Turbidite A8 has elevated TiO_2 compared to A2 and A14 (Figure 4.2). However, this is primarily a function of grain-size, as seen in the grain-size data of Frenz *et al.* (2009, authors' Appendix 3) and Figure 2. However, the generally elevated TiO_2, Zr and Fe_2O_3 in the volcaniclastic turbidites enable clear discrimination of these events from siliciclastic and calcareous turbidites (Figure 4.2). In regards to elemental ratio profiles through the whole deposit, the volcaniclastic turbidites have high Sr/Ca but low Si/Ti and Zr/Ti (Figure 4.3).

Organic-rich Siliciclastic Turbidites (A1, A3, A5, A7, A11, A12 and A13)

SiO_2 is naturally highest in the coarse fraction of the siliciclastic turbidites (Figures 4.2 and 4.3). However, due to the evolved phonolitic composition of the A14 Icod turbidite (Hunt *et al.,* 2011), the SiO_2 content cannot be reliably used to correlate these events

(Figures 2, 3 and 5). As an indicator of detrital clays, K_2O is highest in the siliciclastic turbidites (Figures 2, 3 and 5). However, again the high K_2O content of the phonolitic A14 Icod turbidite precludes exclusive use of K_2O to correlate siliciclastic turbidites. The siliciclastic turbidites have elevated CaO compared to the volcaniclastic turbidites, although the calcareous turbidites (e.g. A10) also naturally have elevated CaO. Therefore a combination of SiO_2, K_2O, Fe_2O_3 and Sr (instead of CaO) can be used to successfully identify the siliciclastic turbidites. In regards to elemental ratio profiles through the whole deposit, the siliciclastic turbidites have low Sr/Ca but high Si/Ti and Zr/Ti (Figure 3).

Calcareous Turbidites (A10)

The A10 turbidite has a composition with elevated CaO and Sr above that of the siliciclastic and volcaniclastic turbidites. In addition, low compositions of Fe_2O_3 and K_2O can also be used to correlate the calcareous turbidites.

Hemipelagite Correlations

Chapter 3 demonstrate that the ITRAX CaO record could reliably record the variations in carbonate preservation during glacial-interglacial cycles within Agadir Basin hemipelagic sediment. Values of CaO regularly below 20 wt% are associated with glacial oxygen-isotope stages or recognised minor glaciations during interglacial oxygen-isotope stages (Figure 4.4). While interglacial stages are associated with CaO value above 35-40 wt% (Figure 4). Summarily the carbonate content record is elevated during interglacial highstands and declines through glacial lowstands (Crawley, 1983; Weaver and Rothwell, 1987; Chapter 3). Thus, the position of each turbidite within the hemipelagite profiles could be used to support the chemostratigraphy used to initially correlate the beds (Figure 4.4).

The CaO record effectively represents a proxy for the oxygen-isotope stages, and can thus be used to not only correlate, but also to date the turbidites. Figure 4.4 demonstrates this correlation of turbidites through Agadir Basin based on the CaO and Fe_2O_3 (anticorrelation) hemipelagic records (Figure 4.4).

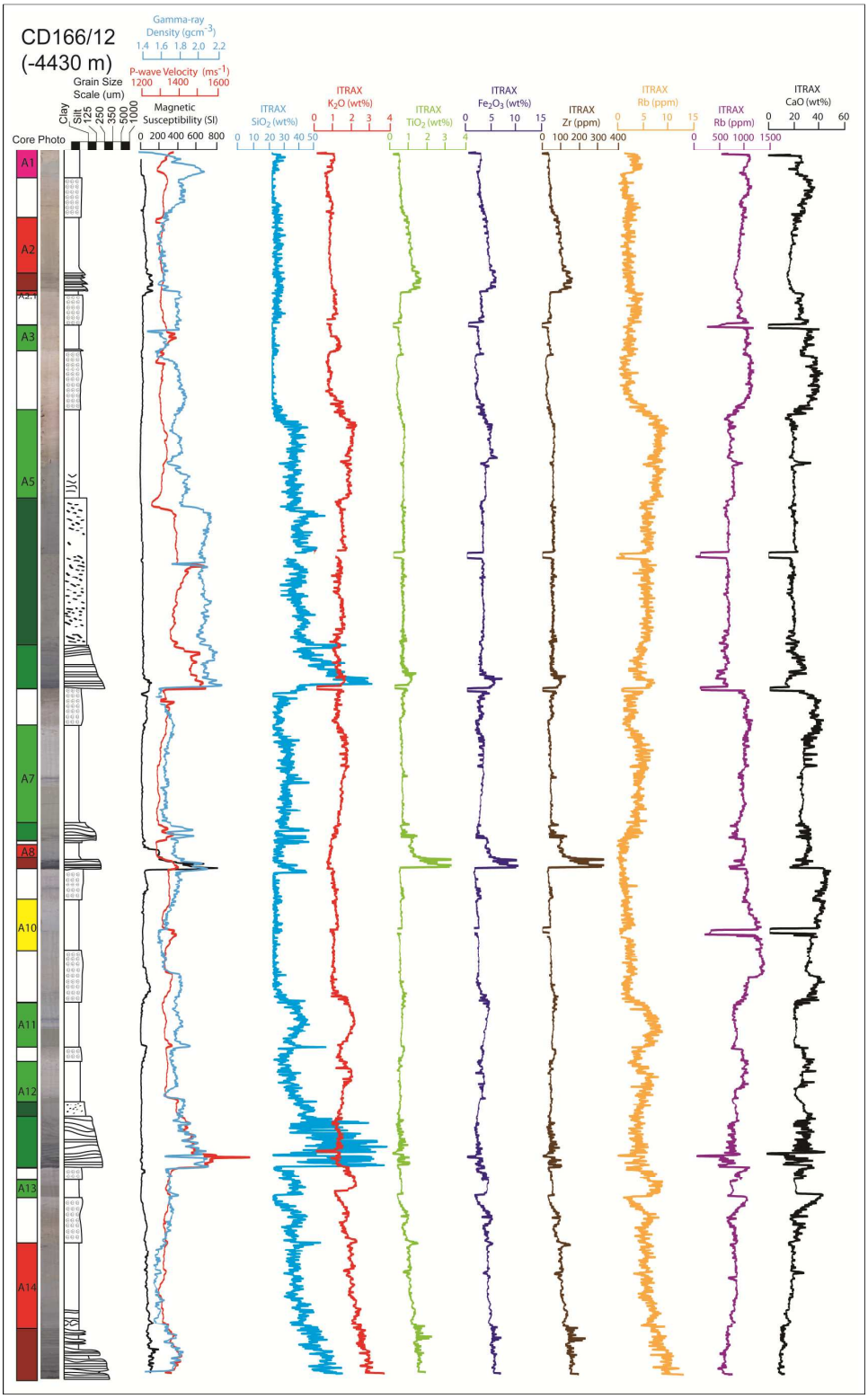

Figure 4.2 Core panel for CD166/12 showing geophysical profiles (p-wave, gamma-ray density and magnetic susceptibility) and calibrated ITRAX geochemical profiles, against the lithological and sedimentological logs.

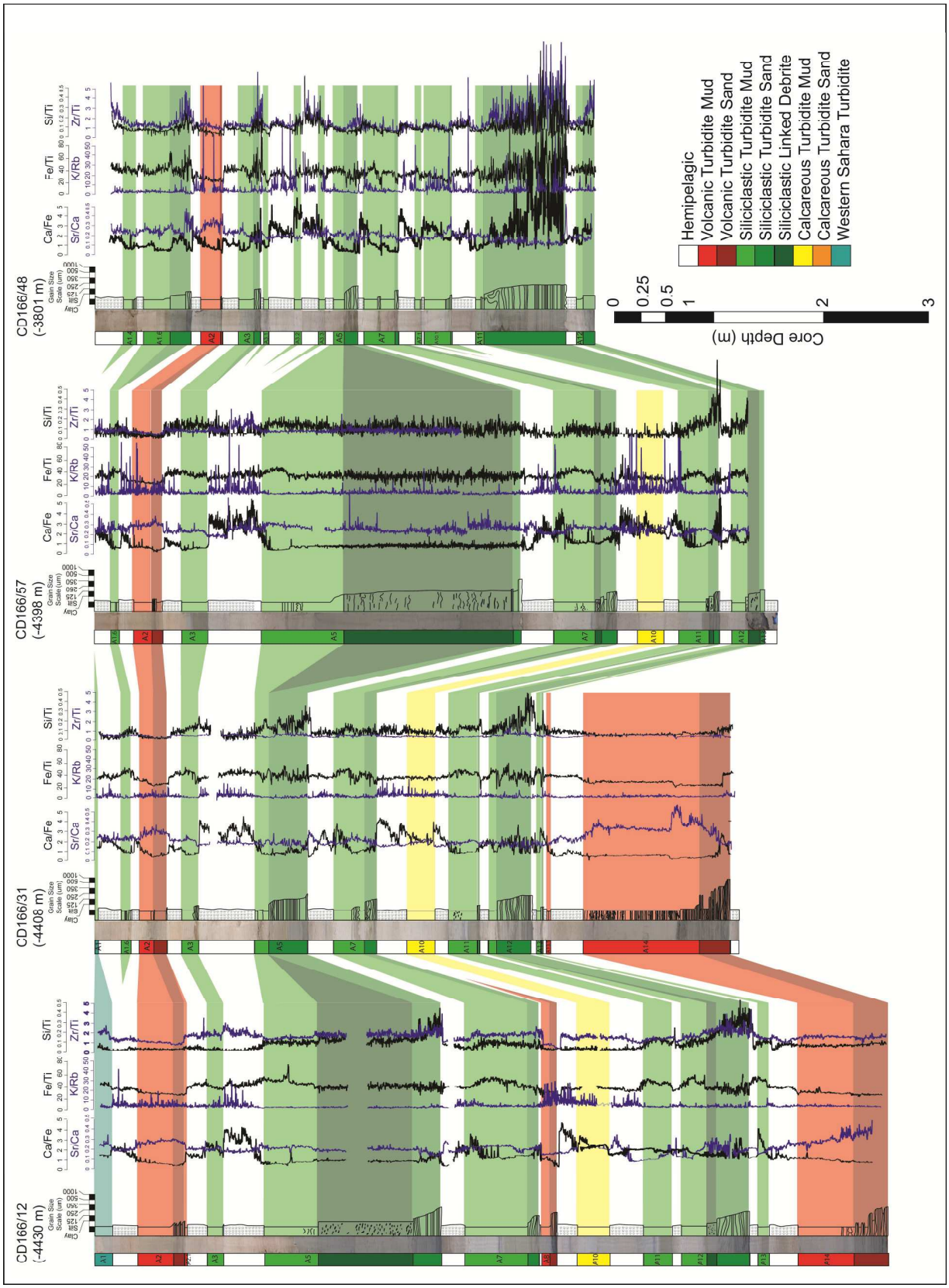

Figure 4.3 Correlation panel through the axis of the Agadir Basin showing the correlation of turbidites from the Agadir Canyon (JC27/13) to the Madeira Distributary Channel System (CD166/19). The correlation here utilises Ca/Fe and Sr/Ca (measure carbonate composition and sediment grading), Fe/Ti and K/Rb (measure of the clay component composition through the deposits), and Si/Ti and Zr/Ti (measure of the silicate and heavy mineral compositions).

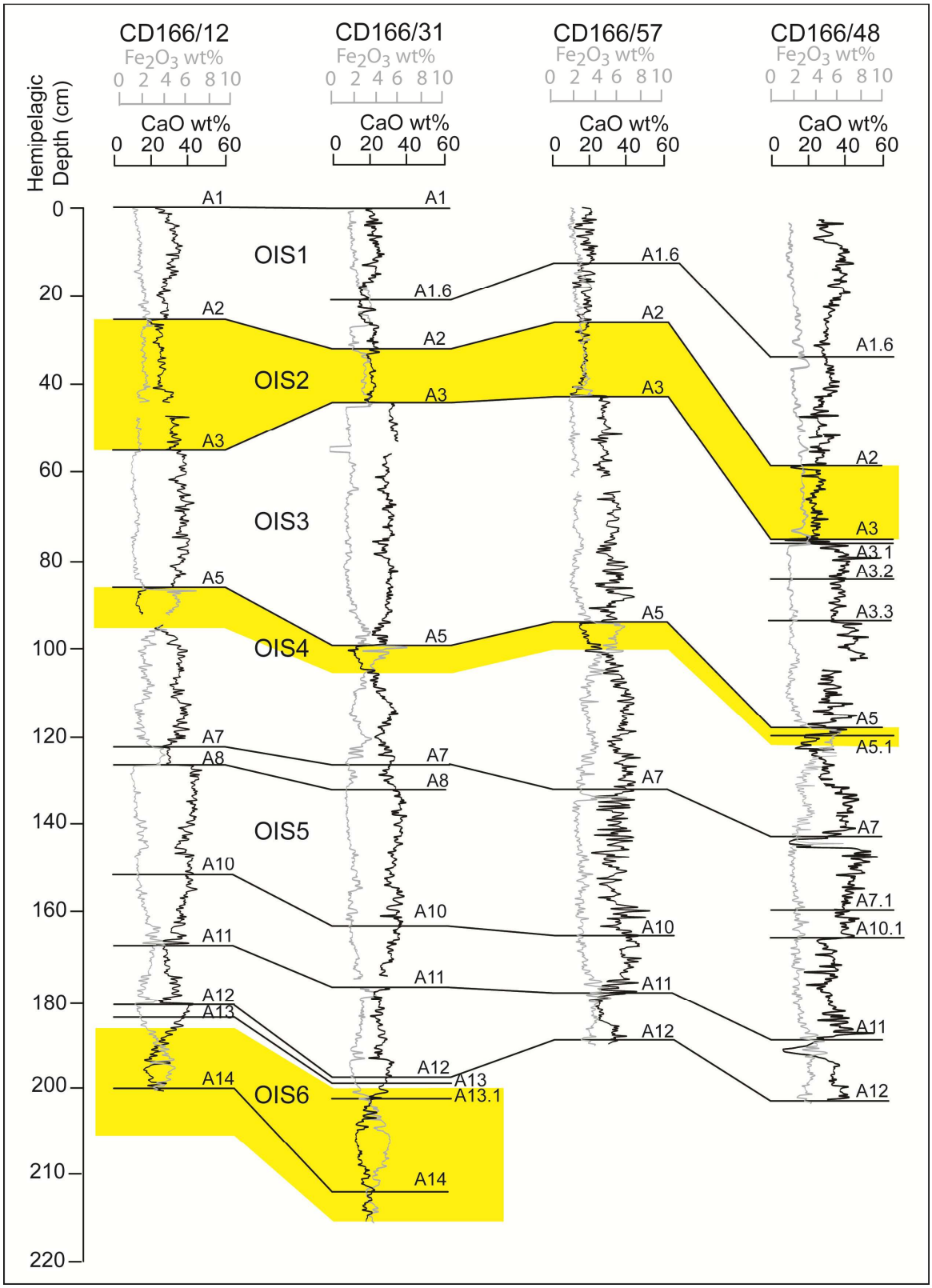

Figure 4.4 Hemipelagite CaO and Fe_2O_3 calibrated ITRAX profiles from the cores in Agadir Basin. Black lines indidate the positions of the turbidites within the hemipelagite record at each site. Yellow overlays indicate glacial oxygen isotope stage (OIS) lowstands, while white indicates interglacial OIS highstands.

Individual Agadir Basin Turbidite Mudcap Geochemistry

The calibrated ITRAX data provides major-elemental concentrations in wt% and trace-elements in ppm. The turbidite muds were initially studied in core CD166/12 due to the detailed studies previously undertaken at this core site. With calibrations showing that meaningful data could be acquired and studied utilising this method on CD166/12, further core analyses were undertaken. Correlations (Figures 4) and comparisons of unoxidised mudcap geochemistries (Figures 5-7) between core sites were undertaken. This quantified data can also enable comparison to data collected by previous bulk geochemistry studies. In addition elemental ratios were also employed to study the compositions of the individual turbidite mudaps.

Organic-rich Siliciclastic Turbidites

There are essentially two primary provenances for the siliciclastic turbidites: Moroccan and Western Saharan continental slopes, as deduced from previous studies (Pearce and Jarvis, 1992, 1995; Weaver *et al.,* 1992; Rothwell *et al.,* 1992; Wynn *et al.,* 2002; Frenz *et al.,* 2009). Frenz *et al.* (2009) showed that the most recent 1 ka A1 turbidite represents a siliciclastic turbidite originating from a reactivation of the Saharan Slide headwall on the Western Saharan slope, south of the Canary Islands. Study of the chemical composition of the A1 turbidite has highlighted variations in composition relative to the other siliciclastic turbidites. The A1 turbidite has lower concentrations of TiO_2 and K_2O of 0.28-0.35 wt% and 0.74-1.00 wt% respectively (Figure 4.5). There are also low Fe_2O_3 values of 2.26-2.70 wt% and low SiO_2 values 23.5-35.5 wt%. The A1 turbidite also has a high composition of Sr with values ranging from 880 to 990 ppm.

The other siliciclastic turbidites (A3, A5, A7, A11, A12 and A13) within Agadir Basin originate from the Moroccan shelf sourced via the Agadir canyon. This is deduced from the depositional and fining patterns displayed by Frenz *et al.* (2009). However, study of the geochemistry of the turbidite muds utilising ITRAX has demonstrated compositional variability between these organic-rich siliciclastic turbidites. Geochemical variation plots of the major elements have demonstrated that a number of compositional fields can delineate the different siliciclastic turbidites in Agadir Basin along discrete compositional arrays (Figures 4.5-4.7).

In regards to Fe_2O_3 and TiO_2, turbidite A3 has a composition with a similar range in TiO_2 to A1, but has a reduced composition of Fe_2O_3 at 1.8-2.6 wt% compared to A1 at 2.3-2.8 wt%. The Fe_2O_3 and TiO_2 composition demonstrates additional trends (Figure

4.5). Such that A5 has a wide range of composition (0.3-0.6 wt% TiO_2 and 2.7-5.2 wt% Fe_2O_3) compared to the other turbidites. The A7 turbidite has a more restricted composition 0.35-0.5 wt% TiO_2 and lower 2.4-3.0 wt% Fe_2O_5. The A11 and A12 turbidites also have restricted compositions of Fe_2O_3 with 2.85-3.7 wt%, although A11 has a higher composition of TiO_2 at 0.4-0.5 wt% compared to A12 at 0.33-0.45 wt% (Figure 4.5). Lastly, turbidite A13 has a TiO_2 and Fe_2O_3 composition of 0.45-0.52 wt% and 4.1-4.5 wt% respectively, which is a composition higher than A1, A3, A7, A11 and A12 (Figure 4.5).

Similar features can be seen when comparing other major-elements for the turbidite muds. Indeed, in regards to K_2O there are similar trends as seen in Fe_2O_3 composition, whereby A3 has the lowest composition (0.67-0.98 wt%) (Figure 5). This is followed by A1 with a K_2O composition of 0.75-1.06 wt%. A7 has a composition of 1.2-1.55 wt% K_2O, with greater amounts of K_2O found in A11 and A12 (1.59-2.06 wt%), and further in A13 (1.76-2.27 wt%); while A5 has a broad composition 1.23-2.41 wt% K_2O (Figure 5). Additional trends are present in the CaO and Sr compositions that enable the delineation of discrete compositional fields that define each of the organic-rich siliciclastic turbidites (Figure 6). The elevated Sr compositions of A1 and A3 may reflect increased composition of aragonite, indicating shallower slope failures (Figure 6). Following this, large-volume beds A5, A7 and A12 have higher Sr compositions than beds A11 and A13, possibly implying a failure from shallower on the slope (Figure 6).

Elemental ratios also enable discrimination of the different siliciclastic turbidite muds. A1 can be signified by high Zr/Ti and Sr/Ca, low K/Rb, K/Ti, and moderate Ca/Fe and Fe/Ti (Figure 7). Turbidite A3 has a moderate K/Ti, high Ca/Fe but low Fe/Ti, compared to A5 with higher K/Ti, Zr/Ti, but low Sr/Ca and Ca/Fe (Figure 7). Turbidite A7 has a similar K/Rb, Fe/Ti, Zr/Ti and Ca/Fe, but lower K/Ti and higher Sr/Ca (Figure 7). Turbidite A11 has similar Sr/Ca, Ca/Fe, K/Rb and Zr/Ti composition to A5, while A13 has higher Fe/Ti and Sr/Ca, but lower Ca/Fe and Zr/Ti. Finally is A12 has highest K/Ti and Fe/Ti, with high Zr/Ti comparable to A3 and A7, moderate Ca/Fe, and low Sr/Ca.

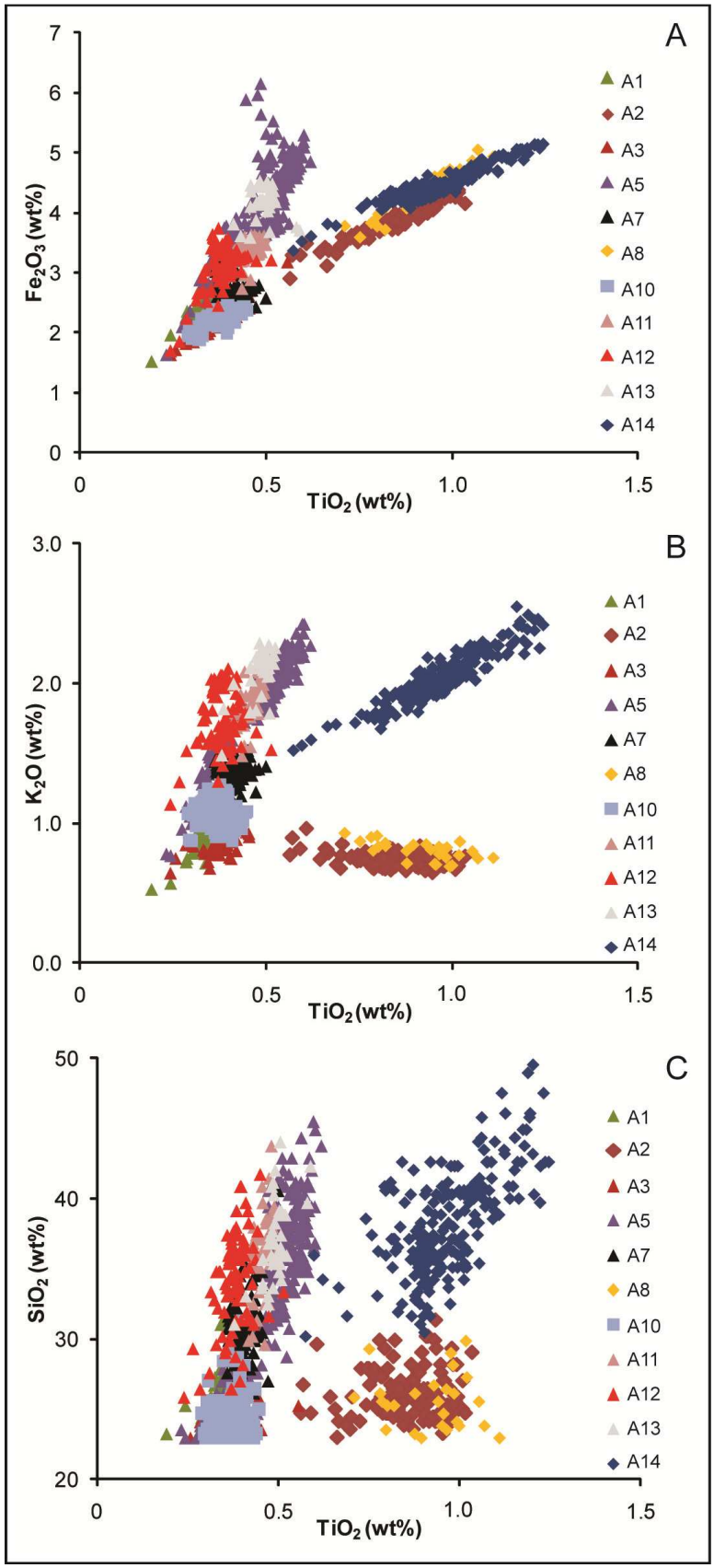

Figure 4.5 Calibrated ITRAX XRF compositions of the unoxidised mudcaps in Agadir Basin turbidites at site CD166/12. A) Fe_2O_3 vs TiO_2, B) K_2O vs TiO_2, and C) SiO_2 vs TiO_2. Variation plots show the delineation of discrete compositional fields and arrays for turbidites beyond assignment to siliciclastic (triangles), volcaniclastic (diamonds) or calcareous type (squares).

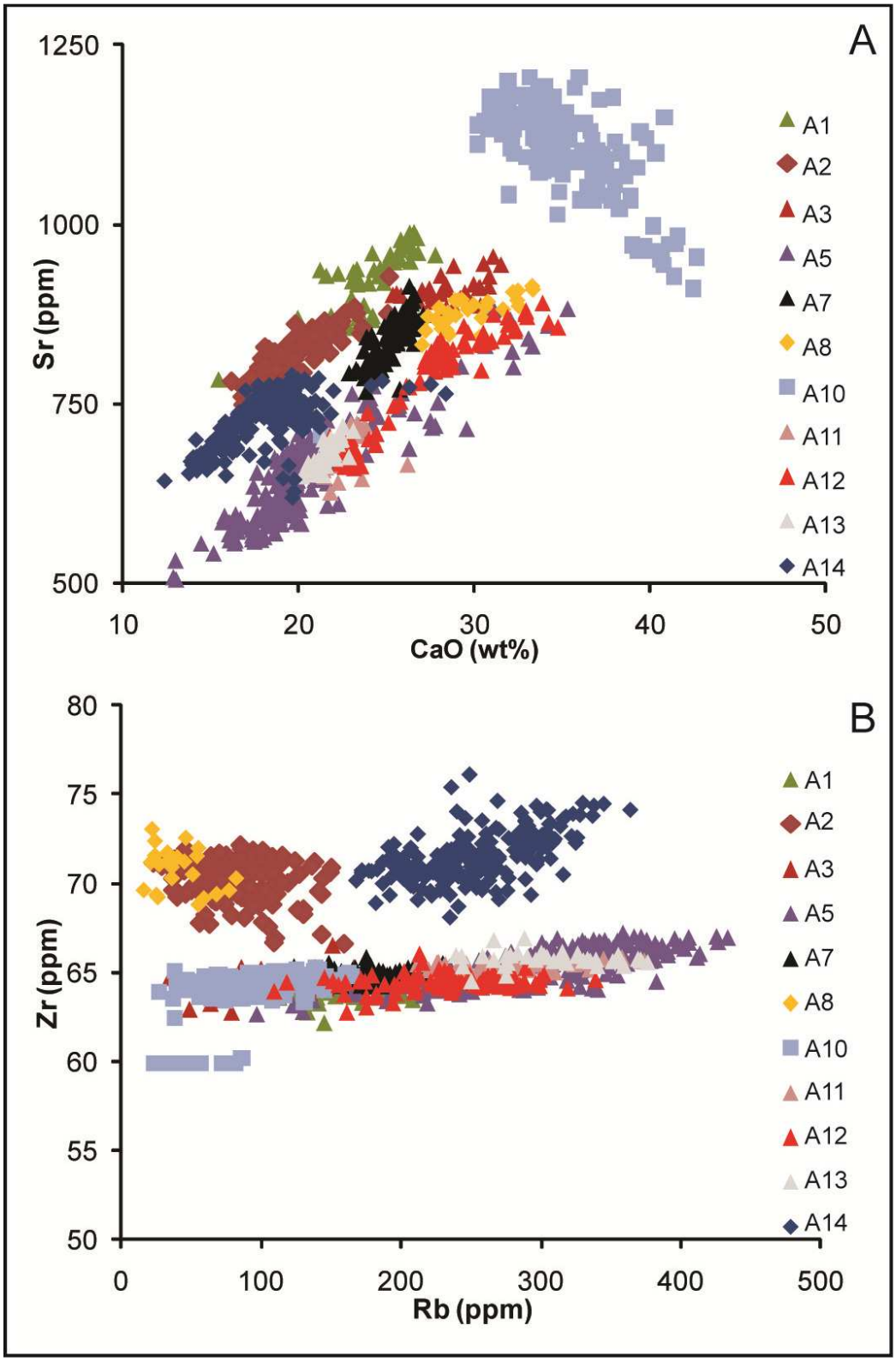

Figure 4.6 Calibrated ITRAX XRF compositions of the unoxidised mudcaps in Agadir Basin as site CD166/12. A) Sr vs CaO, and B) Zr vs Rb. The variations plots investigate the carbonate composition (Sr/CaO) and heavy mineral to clay composition (Zr/Rb) as provenance indicators.

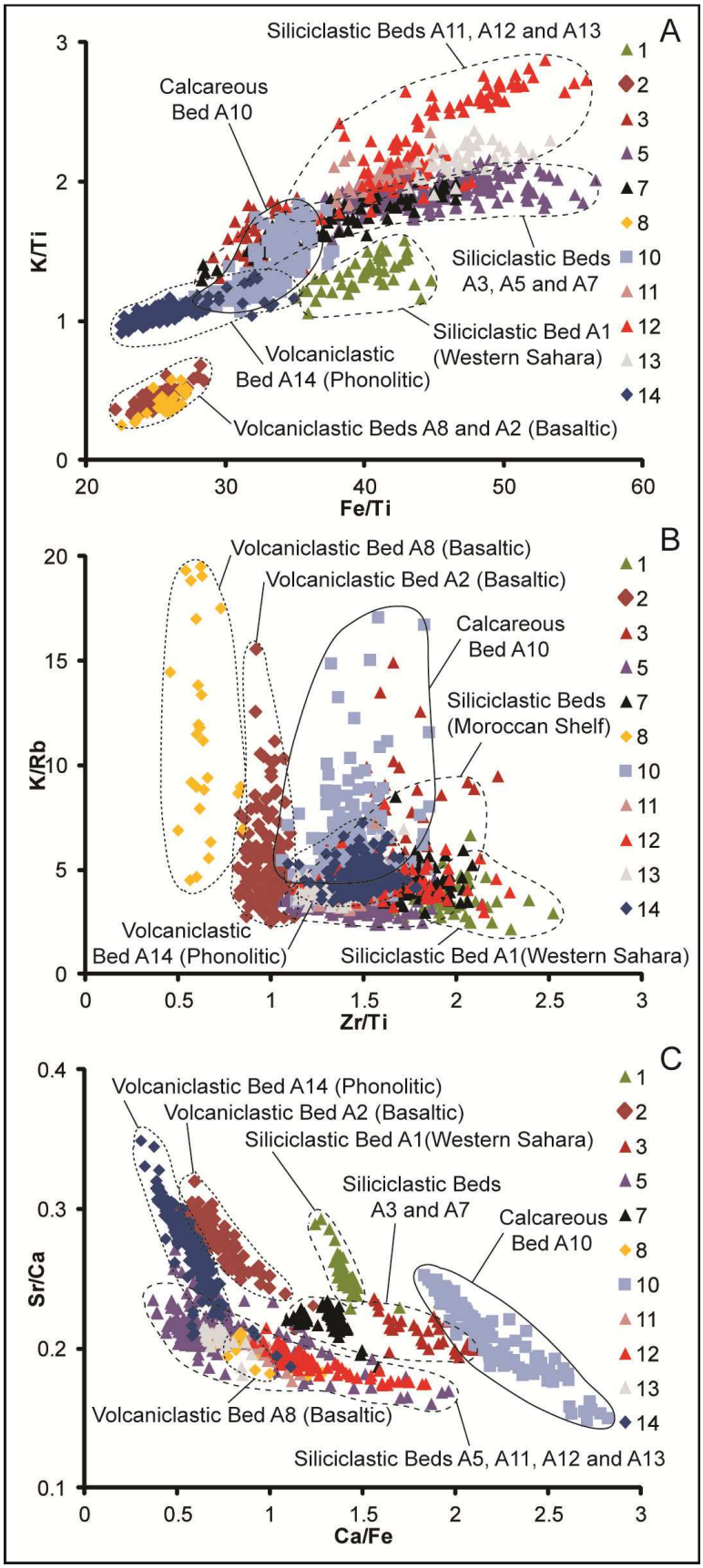

Figure 4.7 Variation cross-plots of ITRAX µXRF turbidite mudcap compositions from CD166/12. A) K/Ti vs Fe/Ti, B) K/Rb vs Zr/Ti, and C) Sr/Ca vs Ca/Fe.

Volcaniclastic Turbidites

There are three volcaniclastic turbidites recorded in Agadir Basin >5 km^3, these are the aforementioned A2, A8 and A14 turbidites. Study of the turbidite mud geochemistry has enabled determination of the provenance of these volcaniclastic turbidites, supporting previous work. Geochemical variation plots for these turbidite mudcaps demonstrate that compositional fields can be constructed to delineate each of beds A2, A8 and A14 (Figures 4.5 and 4.6). Fe_2O_3 against TiO_2 plot demonstrates that the Icod turbidite (A14) has a higher range in TiO_2 concentration (0.75-1.23 wt%) and a high Fe_2O_3 concentration (4.0-5.1 wt%) (Figure 4.5). The El Golfo turbidite (A2) and A8 turbidite have subtly different compositional arrays (Figure 4.5). Turbidite A2 has a Fe_2O_3 and TiO_2 composition of 3.1-4.5 wt% and 0.55-1.0 wt% respectively, whereas A8 has a composition of Fe_2O_3 3.6-5.0 and TiO_2 0.75-1.1 wt% (Figure 4.5).

Further differences are highlighted in the study of the K_2O composition (Figure 4.5). The Icod turbidite (A14) has a higher composition of K_2O at 1.5-2.5 wt%, whereas the El Golfo turbidite (A2) and A8 turbidite has lower K_2O concentrations 0.65-0.95 wt% (Figure 5). The A8 turbidite can be distinguished from the El Golfo turbidite (A2) by slightly elevated K_2O composition. The SiO_2 composition can also discriminate between these volcaniclastic turbidites, where the Icod turbidite (A14) has a higher SiO_2 31-49 wt% compared to the El Golfo turbidite (A2) with 23.5-31.5 wt% and the A8 turbidite with 23.2-27.2 wt% (Figure 5). The A8 turbidite can be best discriminated from the Icod (A14) and El Golfo (A2) turbidites by comparison of the CaO concentrations in the mudcap. The A8 turbidite has a CaO concentration of 27.0-33.3 wt% compared to 16.8-26.3 wt% and 14.0-26.4 wt% for the El Golfo for Icod turbidites respectively (Figure 4.6).

Elemental ratios allow discrimination of these volcaniclastic events (Figure 4.7). Turbidite A14 has relatively high K/Ti and Zr/Ti, with low CaO. Turbidite A2 has lower K/Ti and Zr/Ti, but higher Ca/Fe when compared to A14. However, turbidite A8 has similar Fe/Ti to A2, but slightly lower K/Ti. Furthermore A8 has lower Zr/Ti and Sr/Ca compared to A14 and A2 (Figure 4.7).

Relation of Basin Turbidite Mud Geochemistry to Hemipelagite Composition Below

The organic-rich siliciclastic turbidites from the Moroccan shelf involve sediment issued onto the shelf from terrigenous provenance, calcareous sediment from biogenic influx and material eroded from the floor of the Agadir Canyon and basin. Thus plots

comparing the composition of respective turbidite mud with the hemipelagite below has potential to show whether hemipelagite material is incorporated into the turbidity current by erosion in the basin (Figure 4.8). The hemipelagite layers are named HP#-# denoting the number of the turbidites the hemipelagite is located between.

The A5 turbidite demonstrates a disparity between the composition of the turbidite mud and the oxygen-isotope stage (OIS) four interglacial hemipelagite component immediately below the turbidite (Figure 8A). However, there is overlap between the A5 mudcap composition and the OIS5 interglacial hemipelagite further below (Figure 8A). The siliciclastic turbidites A3, A7, A11, A12 and A13 display significant compositional disparities with the hemipelagite intervals below (Figure 4.8).

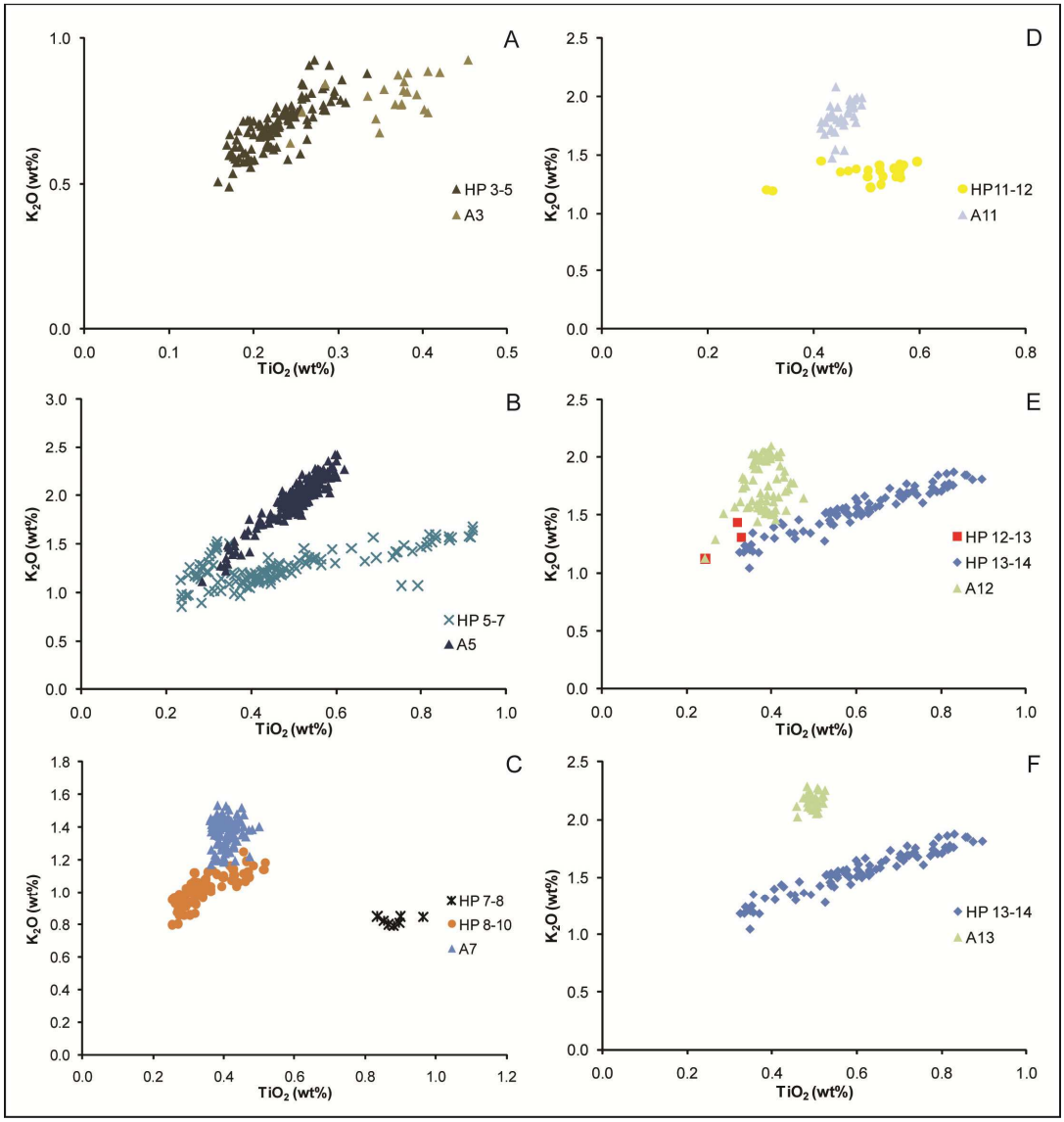

Figure 4.8 Comparison of unoxidised turbidite mudcaps in Agadir Basin (CD166/12) to the hemipelagic sediment interval immediately below. A) Turbidite *A3*, B) Turbidite *A5*, C) Turbidite *A7*, D) Turbidite *A11*, E) Turbidite *A12*, and F) Turbidite *A13*. Hemipelagite nomenclature HP #-# indicates the hemipelagite between two stated turbidites.

Comparison of Basin Turbidite Geochemical Compositions with Correlated Equivalent Deposits from the Agadir Canyon

Compositional variations between the siliciclastic turbidite mudcaps within the Agadir Basin (highlighted at CD166/12) maybe due to variations in the composition of the source landslide materials. Conversely the composition of turbidites may be due to erosion of the gravity flows upon exiting the canyon. This is tested by comparing the composition of correlated turbidites between the Agadir Canyon (core JC27/13) and Agadir Basin. Variations in composition of the same turbidite found in both canyon and basin plain, would suggest the composition has changed between the two sites. This could invoke erosion by the turbidity current upon exiting the canyon, altering the composition by dilution of carbonate-rich hemipelagite, and possible previous turbidites. Whereas, if the compositions remain the same at the canyon and basin sites, then the variations in the basin turbidite compositions are due to variations in the composition of the landslide materials.

Firstly, the event bed correlation from the basin plain to the Agadir Canyon site JC27/13 is supported by the position of the beds in relation to the hemipelagite CaO record and temporal coccolith biostratigraphy (Figure 4.9). The last occurrence of *H. inversa* at 140 ka at 110 cm hemipelagite depth, last occurrence of *G. ericsonii* at 15 ka at 7 cm hemipelagite depth, and first occurrence of *E. huxleyi* at 291 ka at 178 cm hemipelagite depth provide datum horizons (Figure 4.9). Temporal variability in the abundance of a series of coccoliths can provide a further series of datum horizons (Figure 4.9). Acme zones defined by decrease in abundance of *G. caribbeanica* at 177 cm depth dated at 290 ka, decrease in abundance of *G. aperta* at 64 cm dated at 120 ka, and the decrease in *G. mullerae* and increase in *E. huxleyi* abundances dated at 71 ka provide datums (Figure 4.9). A further set of datums at 48 cm and 18 cm hemipelagite depths concern excursions in *G. mullerae* abundances due to dissolution in association with glacial OIS2 and OIS4 respectively (Figure 4.9).

A coarse gravel lag containing abundant pyrite is found above a red glacial clay, and is bed A5, dated at 59 ka using coccolith biostratigraphy (Figure 4.9). This is supported by both the hemipelagite CaO profile and an application of a 1.44 cm/1000 year hemipelagite sedimentation rate to date it. Peaks (generally >35-40 wt%) and troughs (generally <20-30 wt% CaO) within the CaO record can be correlated to respective peaks and troughs in the Lisiecki and Raymo (2005) global benthic $\delta^{18}O$ record.

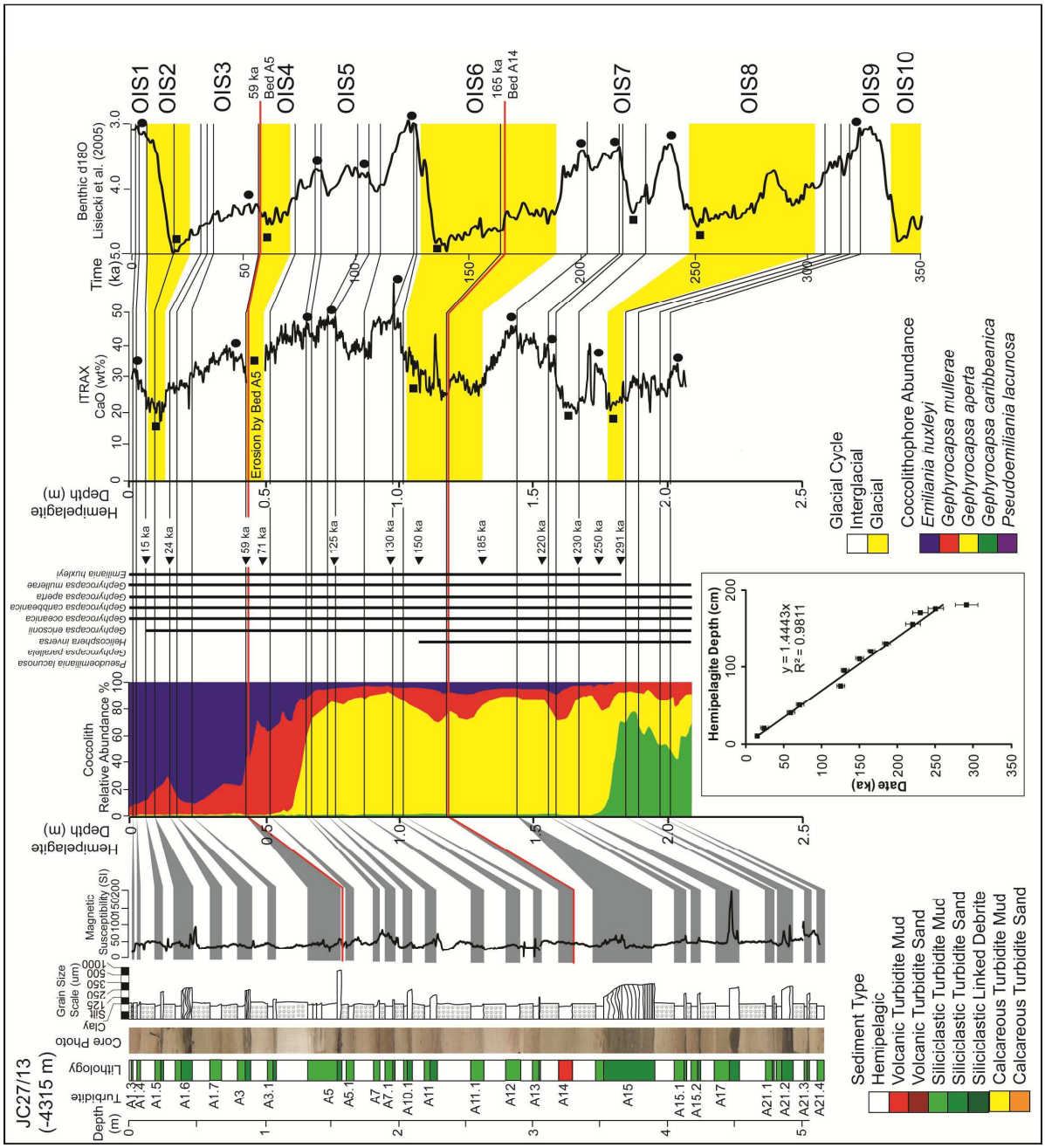

Figure 4.9 Core panel for JC27/13 (location figure 4.1) and the 0-325 ka record of turbidites exiting the Agadir Canyon. Magnetic susceptibility profile highlights the location of most turbidites as a proxy for grain-size. Turbidites are removed from the hemipelagic CaO profile, with the locations marked by a black line. Turbidite positions are then projected onto the stacked Lisiecki *et al.* (2005) benthic $\delta^{18}O$ record tied to the CaO profile using datum horizons gained from the coccolith biostratigraphy.. Dating ties are red lines, while black circles (peaks) and black squares (troughs) are correlated from the hemipelagite CaO profile to the Lisiecki *et al.* (2005) benthic $\delta^{18}O$ record.

The next coarsest turbidite resides above a white glacial clay. Here the hemipelagite CaO profile and application of a 1.44 cm/1000 year hemipelagite sedimentation rate dates the event to ~200 ka (Figure 4.9). This turbidite is designated to be the siliciclastic A15 turbidite, the red glacial above is the OIS6 clay and the white hemipelagite below is the OIS7 calcareous hemipelagite (Figure 4.9). There is a fine pale-grey turbidite mud

within the hemipelagite above the designated A15 turbidite, which represents the A14 Icod turbidite (~165 ka) (Figure 4.9). Coccolith biostratigraphy and these tie-points support the correlation of the JC27/13 hemipelagite CaO record to the Lisiecki and Raymo (2005) global benthic $\delta^{18}O$ record (Figure 4.9). The dating of the turbidites at JC27/13 using combined hemipelagite geochemistry and coccolith biostratigraphy are accurate to within ±5 ka. With the turbidites correlated between canyon and basin, comparison of the turbidite composition between this Agadir Canyon site and those in Agadir Basin can be made.

A first observation is that all respective turbidites measured at different basin plain core sites (CD166/12, CD166/31, CD166/57 and CD166/48) have similar mudcap geochemical compositions (Figure 4.10). Although, the turbidite A5 mudcap geochemical composition becomes more refined down basin, comprising a broader compositional range in the upper sub-basin (Figure 4.10B). An important result is that for the major turbidites (A5, A7, A11 and A12) the mudcap geochemical compositions on the basin plain vary from the mudcap compositions for same the turbidites in the Agadir Canyon (site JC27/13) (Figure 4.10).

Of the highlighted turbidites in Figure 10, bed A3 is seen to vary the least between the canyon and basin plain compositions (Figure 4.10A). Turbidite A5 is seen to vary significantly in geochemical composition between the Agadir Canyon site (JC27/13) and those sites in the basin (Figure 10B). Turbidite A7 is seen to also vary significantly, with a major shift and offset in the array from the canyon composition (Figure 4.10C). Turbidite A11 is seen to also vary considerably with a substantial change in the composition and array for the canyon deposit compared to the turbidite located in the basin (Figure 4.10D). The largest turbidite, bed A12, also demonstrates variability between the canyon and basin mudcap compositions (Figure 4.10E). Turbidite A13 is considered to be a smaller-volume flow pinching out within Agadir Basin. This smaller-volume A13 turbidite shows a similar mudcap geochemical composition in the canyon compared to the basin (Figure 4.10F).

The compositions of the smaller events found only in the proximal region of the upper sub-basin (CD166-48) are also compared to equivalent deposits in the Agadir Canyon (JC27/13). Beds A1.4, A1.6, A3.1, A3.2, A3.3, A7.1 and A10.1 were analysed (Figure 4.11). It was found that the unoxidised mudcaps of these small-volume turbidites both in Agadir Basin and Agadir Canyon bore similarities with little divergence (Figure 4.11).

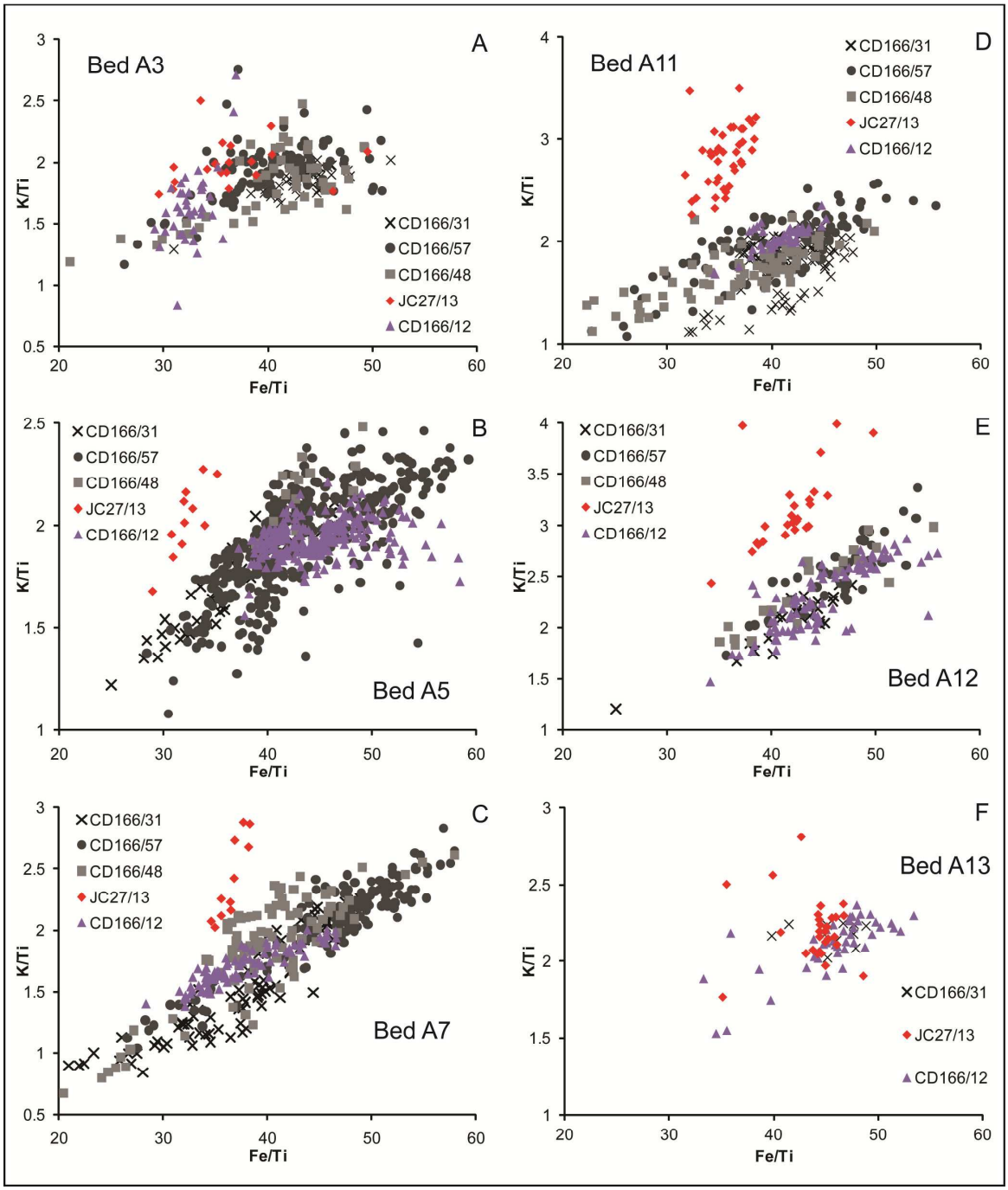

Figure 4.10 Comparison of the geochemical composition (K/Ti vs Fe/Ti) for unoxidised large-volume turbidite mudcaps in Agadir Basin (CD166/12, CD166/31, CD166/57 and CD166/48) and the Agadir Canyon (JC27/13). A) Bed A3, B) Bed A5, C) Bed A7, D) Bed A11, E) Bed A12, and F) Bed A13.

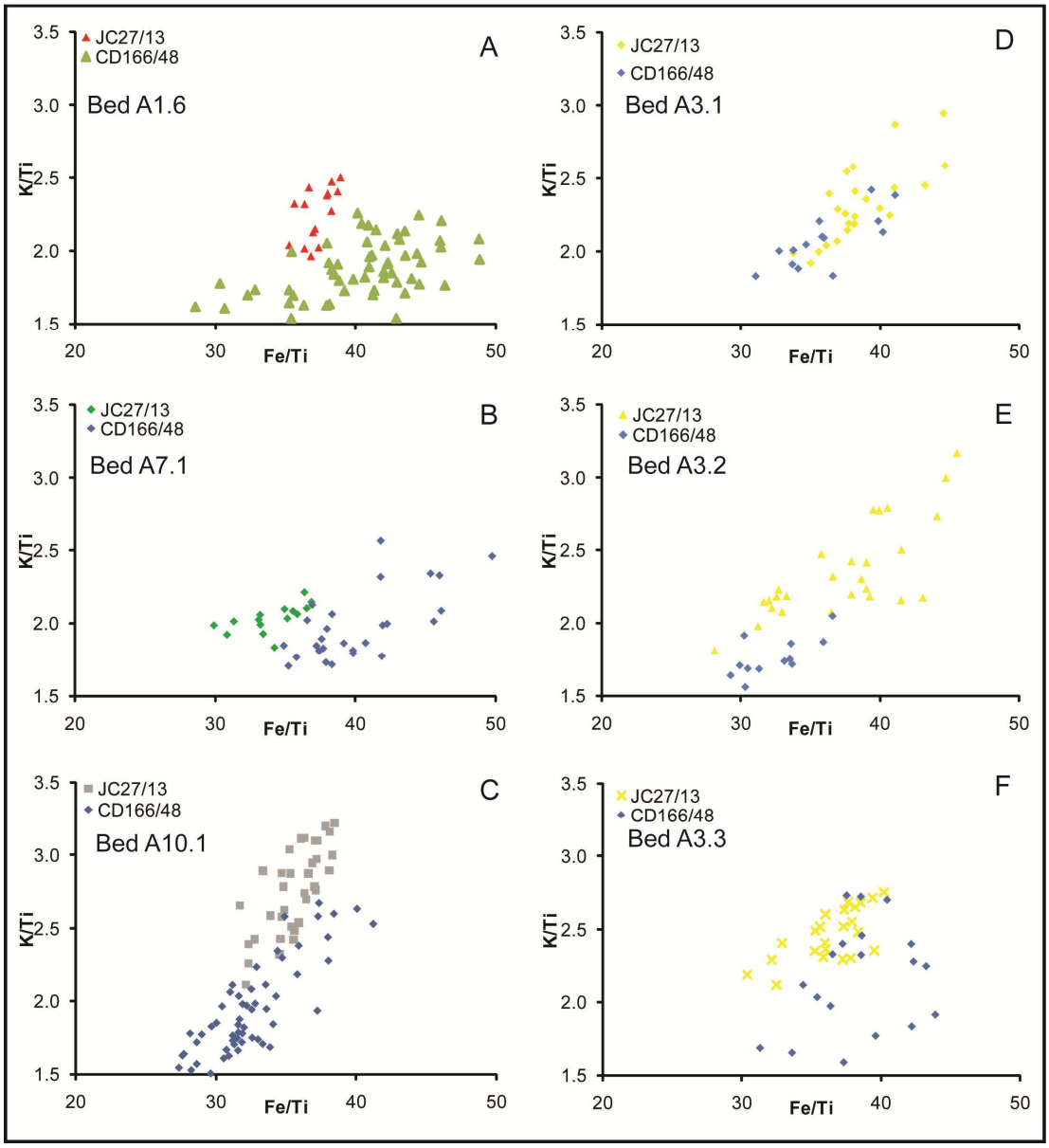

Figure 4.11 Comparison of the geochemical composition (K/Ti vs Fe/Ti) for unoxidised small-volume turbidite mudcaps in the Agadir Basin (CD166/48) and the Agadir Canyon (JC27/13). A) Bed A1.6, B) Bed A7.1, C) Bed A10.1, D) Bed A3.1, E) Bed A3.2, and F) Bed A3.3.

Turbidite Mudcap Coccolith Compositions and Turbidity Current Erosion

Coccolith assemblages of the mudcaps of the turbidites within the canyon and basin setting are analysed to investigate whether the flows have been erosive. These results are used in coincidence with the mudcap geochemistry. Firstly, at CD166/12 bed A3 has a coccolith assemblage abundant in both *E. huxleyi* and *G. mullerae*, with *G. aperta* being marginally more abundant (~40%), and a minor component of *G. carribeanica*. This coccolith assemblage for bed A3 remains consistent throughout Agadir Basin, and indeed remains similar to the composition of bed A3 in the Agadir Canyon (Figure 12).

Alternatively, bed A5 has a mudcap coccolith assemblage at CD166/12 of abundant *E. huxleyi*, *G. mullerae* and *G. caribbeanica* (15-20%), with *G. aperta* being the most abundant (40%) (Figure 4.12). At CD166/31, *G. aperta* remains the most abundant (40%), and *E. huxleyi*, *G. mullerae* and *G. caribbeanica* are abundant (10-15%), while *P. lacunosa* also registers abundance (15%) (Figure 4.12). At CD166/57 in the upper sub-basin, the bed A5 assemblage has abundant *G. mullerae* and *G. aperta* (~30%), and *E. huxleyi* and *G. carribeanica* (~20%) (Figure 4.12). At the most proximal Agadir Basin site, CD166/48, the assemblage of bed A5 has further differences, whereby *E. huxleyi and G. mullerae* are the most abundant (Figure 4.12). As demonstrated the basin mudcap coccolith assemblages of bed A5 are variable, but the Agadir Canyon composition shows further variation, where *E. huxleyi*, *G. mullerae*, *G. aperta* and *P. lacunosa* are moderately abundant (15-20%), with *G. caribbeanica* being the most abundant (>30%) (Figure 4.12).

Bed A7 has a consistent mudcap coccolith assemblage with moderately abundant *G. mullerae* and *G. caribbeanica* (~15% and ~30% respectively), but *G. aperta* is the most abundant (45-50%) (Figure 4.12). The bed A7 assemblage in Agadir Canyon is similar, but has relatively lower *G. mullerae* and *G. aperta* abundances, and higher *G. caribbeanica* and *P. lacunosa* abundance (Figure 4.12). Bed A11 has moderately abundant *G. mullerae* (10-20%) and *G. carribeanica* (20-25%), with *G. aperta* being the most abundant (45-50%), and *P. lacunosa* also registering a low abundance (~10%) (Figure 4.12). This assemblage is consistent at all sites within Agadir Basin, however the composition of the turbidite mudcap in Agadir Canyon is different. Within Agadir Canyon, bed A11 has a mudcap coccolith assemblage with lower relative abundances of *G. mullerae* and *G. caribbeanica*, while *G. aperta* and *P. lacunosa* are more abundance (Figure 4.12). Bed A12 also has a broadly consistent mudcap coccolith assemblage in Agadir Basin of low abundances of *G. mullerae* and *P. lacunosa* (<10%), moderate abundance of *G. aperta* (20-30%), and high abundance of *G. caribbeanica* (40-50%) (Figure 4.12). However, like beds A5, A7 and A11, the mudcap coccolith assemblage is different for bed A12 in the Agadir Canyon, with *G. aperta* and *G. caribbeanica* being the most abundant at ~40% (Figure 4.12).

Lastly, bed A13 has a similar mudcap coccolith assemblage amongst basin sites and between the basin and the Agadir Canyon. This assemblage comprises abundant *G. aperta* (60-70%) and moderately abundant *G. caribbeanica* (20-25%) (Figure 4.12).

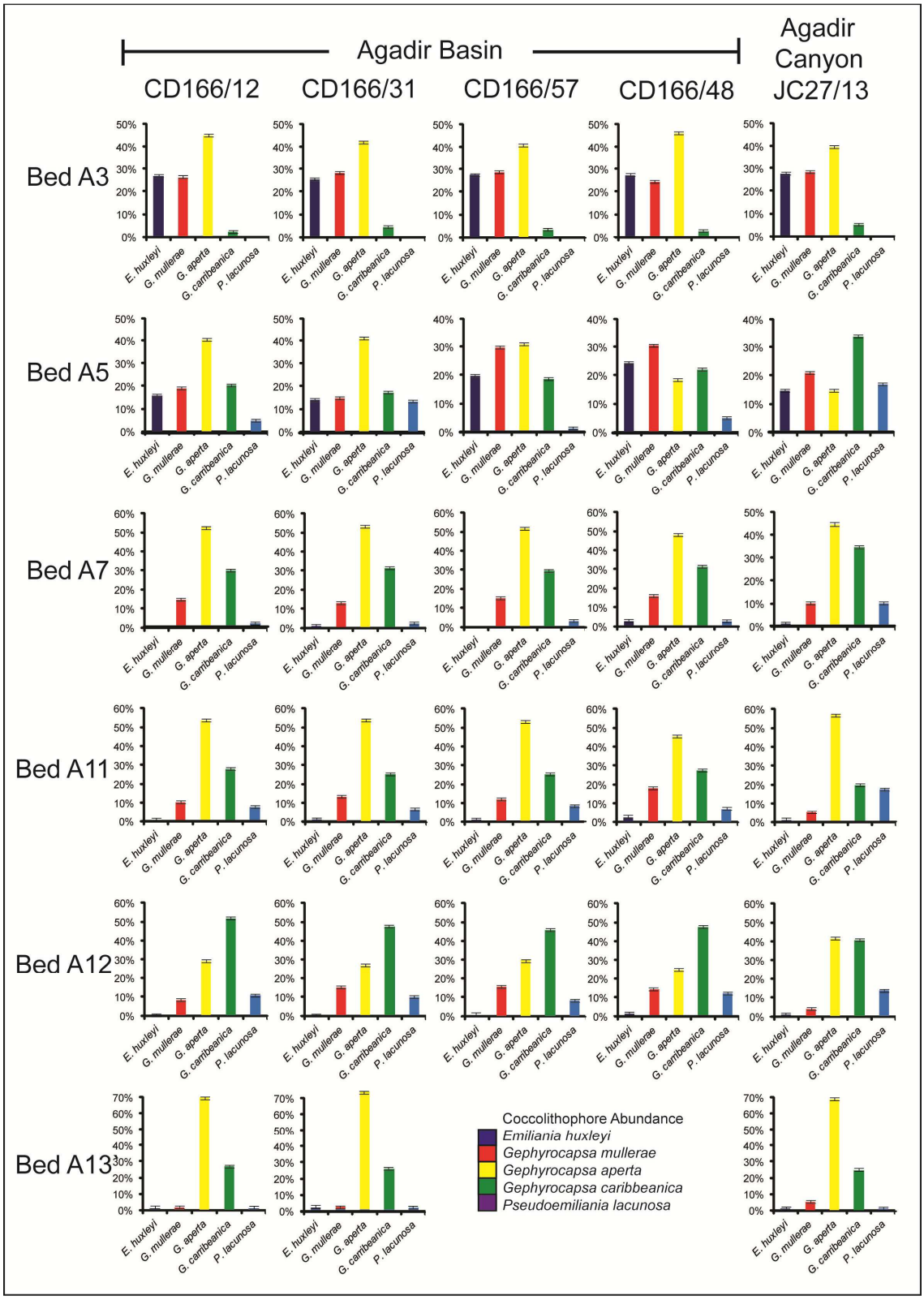

Figure 4.12 Coccolith assemblages in the turbidite mudcaps within turbidites from Agadir Basin sites (CD166/48, CD166/57, CD166/31 and CD166/12) and Agadir Canyon (JC27/13).

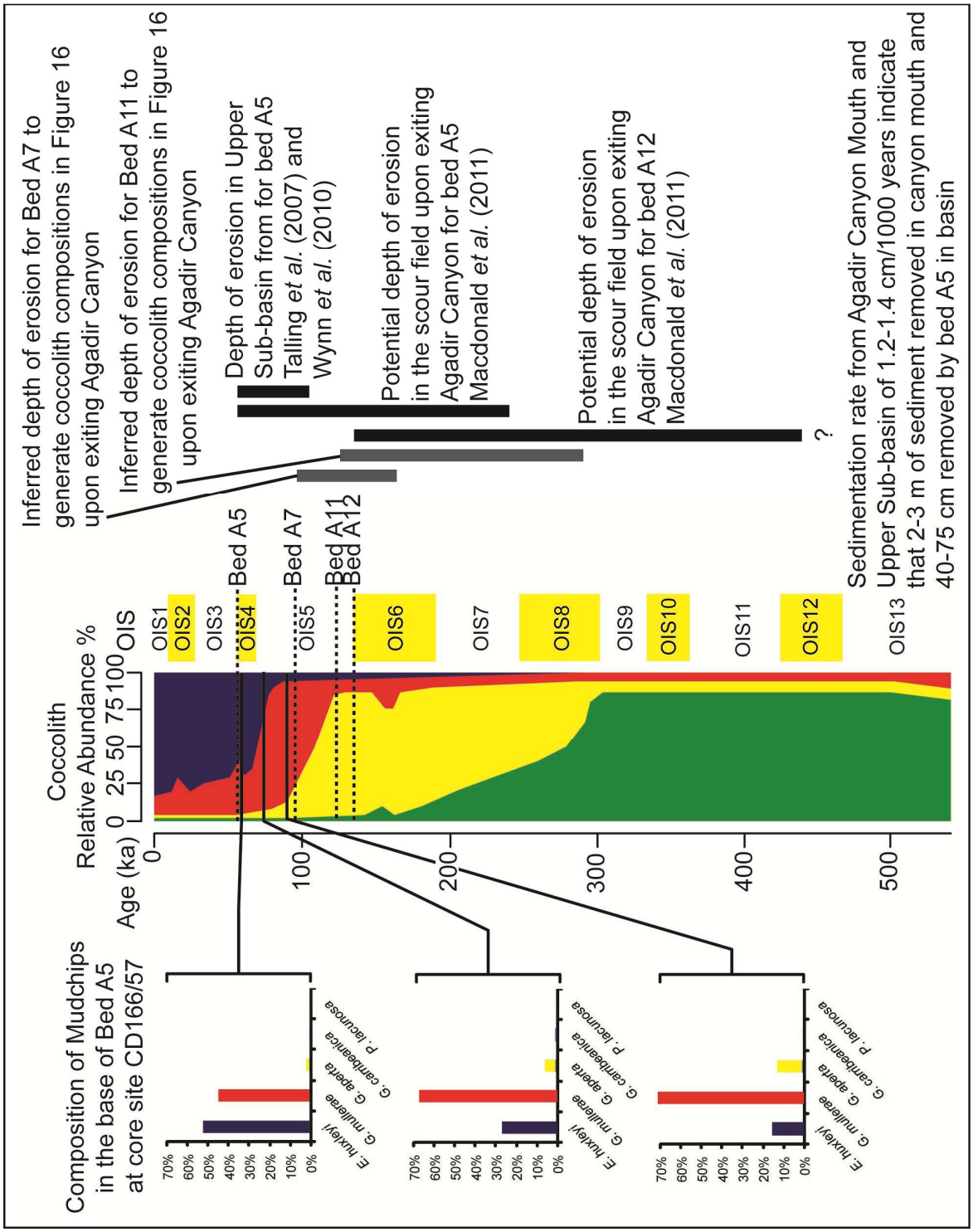

Figure 4.13 Coccolith assemblages of mud-chips of hemipelagite sediment in the base of bed A5. These are compared against an idealised temporal record of hemipelagite coccolith compositions plotted against oxygen-isotope record. Composition of mud-chips extrapolated onto idealised temporal record. Ages of turbidites are shown, along with the interpreted depths of erosion from coccolith assemblages in this figure ad from Figure 4.12.

In addition, samples were taken from mud-chips of hemipelagite sediment within the base of bed A5 at site CD166/57. These mud-chips represent the hemipelagite sediment eroded by the flow upon entry into the upper sub-basin. The lithology of these mudchips include brown glacial clay hemipelagite, pale brown glacial clay hemipelagite, and a white interglacial ooze. The coccolith assemblages of these mud-chips resemble hemipelagite sediment of OIS4 and upper OIS5 (Figure 4.13).

Geochemical Variability in Siliciclastic Turbidites within the Agadir Canyon

The geochemistry of the turbidite mudcaps within the basin have been compared earlier (Figures 4.10 and 4.11). The JC27/13 site is located before significant erosion by flows exiting the Agadir Canyon. Thus this offers an opportunity to study the siliciclastic turbidite compositions prior to major erosion. The mudcap compositions form fields that are either discrete from one another or lie on subtly different arrays (Figure 14). The K/Ti-Fe/Ti cross-plot (Figure 4.14) highlights differences between the turbidites.

The turbidites recovered from the Agadir Canyon (JC27/13) have been shown to correlate to those in the basin plain (Figure 4.14). However, as with those at CD166/12, the major siliciclastic turbidites at JC27/13 (A3, A5, A7, A11, A12 and A13) demonstrate trends in their composition (Figure 4.14A). Turbidites A11, A12 and A13 have the highest K/Ti ratios, where A12 has the highest Fe/Ti ratio. The next lowest K/Ti and Fe/Ti is turbidite A7, followed by A5 and then A3 (Figure 14A). These trends at JC27/13 are similar to those at CD166/12, where A11, A12 and A13 had the highest K_2O and Fe_2O_3 values and K/Ti and Fe/Ti ratios, followed by A7, A5 and A3 (Figures 4.3 and 4.5). However, the compositions of the major turbidites A5, A7, A11 and A12 are offset in JC27/13 when compared to sites in the basin. A significant difference is that bed A5 has a lower and more restricted range of composition compared to within the basin.

There are a number of smaller turbidites recorded at JC27/13, which do not flow out far onto the basin floor (to CD166/48). The compositions of these are compared to those of the larger volume events. Turbidites A1.4, A1.5 and A1.6 have low K/Ti and Fe/Ti, which are in keeping with the low K/Ti and Fe/Ti of the earlier bed A3 (Figure 4.14). However, the older turbidites A3.1, A3.2 and A3.3 compositions demonstrate higher K/Ti and Fe/Ti, although forming a different compositional array to bed A3 (Figure 4.14). The 5.1 turbidite has a similar composition to bed A5 at JC27/13, with a lower and restricted K/Ti and Fe/Ti composition. The highest K/Ti and Fe/Ti values are

reserved for the A9 and A10.1 turbidites, which compare with the bed A11, A12 and A13 compositions (Figure 4.14). Lastly, the older small-volume events A15.1, A15.2, A21.1, A21.2 and A21.3 have low K/Ti and Fe/Ti ratios, similar to the low values attributed to the A15 turbidite (Figure 4.14).

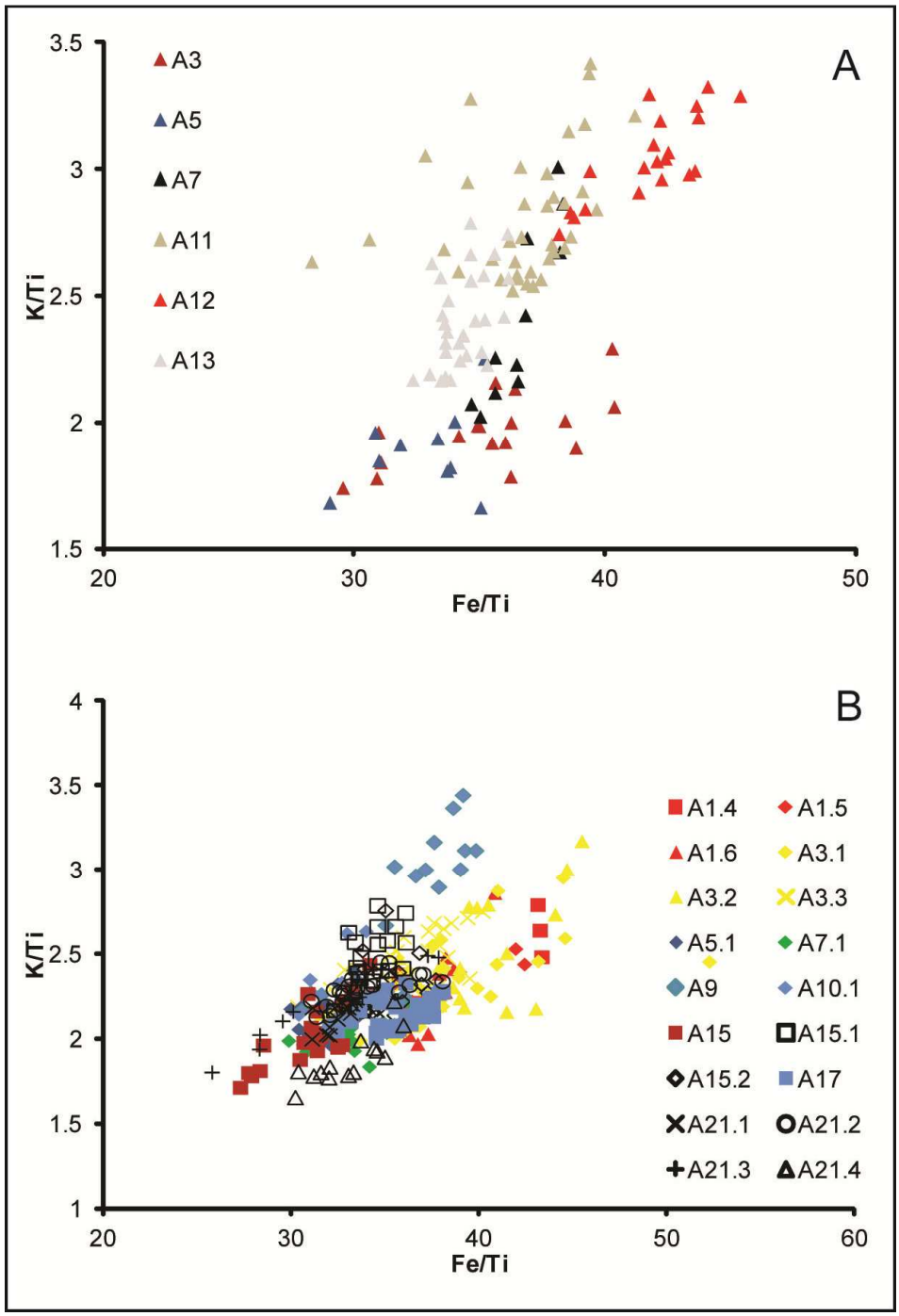

Figure 4.14 Composition of unoxidised turbidite mudcaps in the Agadir Canyon (JC27/13), sourced from the Moroccan Shelf. A) Large-volume turbidites recorded throughout the Agadir Basin, and B) Small-volume turbidites either recorded exclusively within the Agadir Canyon or with limited extent into the most proximal eastern region of the Agadir Basin.

Discussion

Turbidite Correlations

The use of the ITRAX μXRF core analysis has supported the correlation of turbidites according to their geochemical composition. The high resolution measurements (500 μm) have enabled generation of detailed down-core profiles that can aid correlation of turbidites between sites >50 km apart (Figure 4.3). Previous studies utilising turbidite geochemistry to correlate turbidites have relied on taking a limited number of samples from the turbidite mudcap. These have then been processed by acid digestion and finally prepared for analysis by ICP-AES (de Lange *et al.,* 1987; Pearce and Jarvis, 1995). These bulk sediment analyses have high levels of precision, accuracy and reproducibility. However, the ITRAX μXRF core scanner enables direct and non-destructive measurement of the chemistry of sediment *in-situ*, and has also been shown to produce measurements with high levels of precision and accuracy (Croudace *et al.,* 2006). In addition, the ITRAX methodology offers a rapid, high resolution and reliable methodology for analysing sediment cores.

The present contribution has focused on the geochemical composition of the turbidite mudcaps in Agadir Basin. The results of this study have shown that siliciclastic turbidites have moderate SiO_2 compositions, with values of 23-45 wt%. However, it is the lower values of TiO_2 (0.2-0.6 wt%) that discriminate organic-rich siliciclastic turbidites from volcaniclastic turbidites (Figure 4.2). The present study advocates higher TiO_2 and Zr concentrations as the predominant discriminating factors for volcaniclastic turbidite mudcaps (Figure 4.2), supported by previous studies in the distal Madeira Abyssal Plain (Pearce and Jarvis, 1995; Jarvis *et al.,* 1998). However, unlike the previous studies Fe_2O_3 is not indicated as a reliable discriminating factor when comparing the mudcaps.

However, when incorporating the coarser fraction at the base it is noticed that Fe_2O_3 becomes an excellent discriminator for the volcaniclastic turbidites (with sand bases) (Figure 4.2). The Fe_2O_3 also discriminates the two largest siliciclastic flows, with minor spikes in Fe_2O_3 due to increased lithics and iron-stained quartz (aeolian dust) in the basal sands (Figure 4.2). The incorporation of the coarse fraction also highlights the importance of Zr in discriminating the volcanic turbidites (Figure 2). Sr also enables discrimination of the siliciclastic turbidites when incorporating the coarse fraction.

Finally, SiO_2 definitely discriminates the coarser fraction of the siliciclastic turbidites with values of 45-80 wt%, which are more in-line with the values reported by Pearce

and Jarvis (1995) (Figures 4.2 and 4.5-4.7). However, caution must be taken when using SiO_2 as a correlative tool, since the A14 volcaniclastic turbidite has an evolved igneous source from Tenerife. The phonolitic glasses that comprise the A14 turbidite have SiO_2 of 57-64 wt% (Hunt *et al.,* 2011), and thus result in bulk sediment compositions of 42-62 wt%. In addition to the turbidite chemostratigraphy, the correlation of the hemipelagite sequences (using CaO and Fe_2O_3) supports the turbidite correlations within Agadir Basin (Figure 4.4).

The raw activity counts generated by the ITRAX can be calibrated to the results of bulk analysis of core samples (Appendix 4.3). The accuracy and precision of the ITRAX scanner has been documented in previous studies (Croudace *et al.,* 2006; Thomson *et al.*, 2006; Rothwell *et al.,* 2006). However, as shown in the calibration curves of the present study (Appendix 4.3), there is scatter in the intensity-concentration cross-plots. Furthermore, Fe and Si fail to plot through the origin. These features indicate that potential external factors could influence the ITRAX results (Weltje and Tjallingii, 2008). Unfortunately, this contribution has not been able to resolve these issues, which has resulted in much of the present work focusing on elemental ratios.

Turbidite Provenance

The results of comparing the turbidite mud compositions of each turbidite utilising data from ITRAX has enabled discrete compositional fields for each turbidite to be produced (Figures 4.5, 4.6, 4.7 and 4.14). The mudcaps were chosen in order to isolate comparisons of similar (if not identical) grain-size distributions. The mudcap represents sedimentation from suspension fallout. Thus, variations detected in the mudcaps are primarily a reflection of different chemical compositions, rather than effects of different grain-size distributions and depositional processes.

The volcaniclastic turbidites can be clearly discriminated from those of the siliciclastic or calcareous turbidites (Figures 4.5-4.7). Furthermore, the individual volcaniclastic turbidites can be discriminated from one another based on the characteristics of their provenance (Figures 4.5-4.7). The A14 turbidite (Madeira Abyssal Plain bed *g*) has been previously linked to the ~165 ka Icod landslide from Tenerife (Hunt *et al.,* 2011, and references therein). As a result the A14 turbidite has an evolved phonolitic composition, which is represented by the elevated SiO_2, Fe_2O_3, K_2O, TiO_2 and Zr, and lower values of CaO and Sr (Figures 4.5 and 4.6). The basic igneous composition of turbidites A2 and A8 are highlighted by the lower compositions of SiO_2,

TiO_2, K_2O and Zr, while having elevated concentrations of Sr and CaO (Figures 4.5 and 4.6).

The A2 turbidite has been linked to the El Golfo landslide from El Hierro (Masson *et al.,* 2002; Frenz *et al.,* 2009; Hunt *et al.,* 2011, and references therein). The El Hierro source is synonymous with a basic basaltic composition. The distribution of the A8 turbidite indicates a Madeira provenance (Frenz *et al.,* 2009), which would also infer basaltic composition. The difference between the two basaltic El Hierro and Madeira sources can be seen in the major-element mudcap comparisons. A2 turbidite (El Hierro source) has lower Fe_2O_3, K_2O and CaO and elevated SiO_2 compared to turbidite A8 (Madeira source) (Figures 4.5 and 4.6). Elemental ratios Zr/Ti and Sr/Ca also discriminate the bed A8 Madeira source from that of El Hierro or Tenerife (Figure 4.7).

The analysis of the siliciclastic turbidites also demonstrate that individual continental slope provenances can be assigned. Although all the siliciclastic turbidites (except A1 from Western Sahara slope) have a broadly similar composition, the composition of each turbidite mudcap lies on a subtly different array (Figures 4.5 and 4.6). However, these differences demonstrated at basin sites (e.g. CD166/12) could be generated by addition of material by differential erosion of seafloor sediment in the mouth of Agadir Canyon or within the proximal regions of the basin. This is because of evidence of turbidity current erosion at the mouth of the Agadir Canyon (Ercilla *et al.,* 1998; Weaver *et al.,* 2000; Wynn *et al.,* 2002; Talling *et al.,* 2007; Wynn *et al.,* 2010; MacDonald *et al.*, 2011). However, the disparities in turbidite composition could also be the product of the provenance and composition of the originally failed material (Figures 4.5 and 4.6).

The compositions of the turbidites prior to sites of erosion need to be examined to investigate whether differential provenance (thickness and/or spatial extent of failed slab) or turbidity current erosion generate the differences in turbidite mudcap geochemistry. Core JC27/13 was taken within the Agadir Canyon in a setting prior to intense erosion in the canyon mouth (Wynn *et al.,* 2002; MacDonald *et al.,* 2010). The complete sequence of turbidites, including those found in the basin, are recorded at this site (Figure 4.9). Comparison of the siliciclastic mudcap geochemistry of these turbidites show variations in geochemical compositions (Figure 4.12). Indeed, there are similar trends in composition found in the basin sites (e.g. CD166/12, Figure 4.7). As seen in the variation plots (Figure 14), turbidites A11, A12 and A13 have the highest K/Ti and Fe/Ti, a similar trend to the same beds in CD166/12 (Figures 4.7 and 4.14).

Indeed, turbidite A7 has an intermediate composition, and turbidites A3 and A5 have lower values. Apart from turbidite A5 having a broader mudcap composition, the general trends described hold true in both canyon and basin settings (Figures 4.7 and 4.14). Although the relative trends in turbidite composition from both canyon and basin settings are similar, it is important to note that the exact compositions of the large-volume turbidites (beds A5, A7, A11 and A12) within the canyon are offset from the compositions at the multiple basin sites (Figure 4.10).

Thus, in conclusion several outcomes can be summarised for the siliciclastic turbidite provenance. Firstly, geochemical composition is very similar indicating a single broad geographic source, namely the Moroccan shelf/slope. Secondly, basin plain cores demonstrate subtle variations in geochemical composition. This could potentially indicate subtle differences in the location and composition of the original failure; however the effects of differential erosion may/may not contribute. Thirdly, the Agadir Canyon core site, located prior to canyon mouth erosion, records the same turbidite sequence (although with additional minor events) as in Agadir Basin. Turbidite compositions show consistent trends in temporal variation in composition to those in the basin, however the compositions of single correlated turbidites from both canyon and basin settings are not identical. Variation in the compositions of single turbidites between the canyon and basin sites is potentially a function of erosion upon exiting that canyon. However, the variation in compositions between different turbidites is primarily a product of different failed sediment and subtly different provenance on the shelf and/or slope. Consequently, it can be suggested that turbidites A11, A12 and A13 originated from a different sector of the continental slope compared to A3, A5 and A7.

To compliment the results of the mudcap geochemistry the mudcap coccolith assemblages are investigated. The compositions of mudcap coccolith assemblages at the Agadir Canyon site show variations. Bed A3 and A5 have a similar assemblage, although bed A5 has an older component of elevated *G. caribbeanica* (Figure 4.12). Bed A7 has a similar assemblage to bed A5 with elevated *G. aperta* and *G. caribbeanica*, but lacks elevated *E. huxleyi* or *G. mullerae* (Figure 4.12). Beds A11, A12 and A13 have similar mudcap coccolith assemblages, with high abundances of *G. aperta*, although A12 has a relatively higher abundance of *G. caribbeanica* compared to A11 and A12.

Identification of Turbidity Current Erosion in the Agadir Canyon Mouth and on the Agadir Basin Plain

Firstly, the compositions of the same turbidites at the multiple basin sites (CD166/12, CD166/31, CD166/57 and CD166/48) are broadly consistent, except for turbidite A5 which has a broader composition in the proximal locations (Figure 4.10). This indicates that there is minimal to no basal erosion beneath the respective turbidity currents within the basin, which would otherwise cause fluctuations in composition. This is also supported by the comparisons of turbidite compositions to the hemipelagite directly below it (Figure 4.8). Here the basinal turbidites have disparate compositions compared to the hemipelagite below (Figure 4.8), with the exception of bed A5. This further indicates that there is no erosion beneath the respective turbidity currents in the basin, thus resulting in no mixing between final mudcap composition and the composition of the hemipelagite below. This is also supported by the consistent coccolith assemblages in the mudcaps of beds A3, A7, A11, A12 and A13 within the basin (Figure 4.12).

Turbidite A5 is an exception, whereby the mudcap composition is different from the oxygen isotope stage (OIS) four immediately below the bed, but overlaps with the composition of the OIS5 interglacial clay further below it (Figure 4.8). The affinity with the older OIS5 interglacial clay may be the result of regular erosion to this depth in the proximal area of the basin. The broader mudcap composition in the proximal sites could also be due to basal erosion. This is supported by both the change in mudcap coccolith assemblages at CD166/48 and CD166/57 and the coccolith assemblages recovered from hemipelagite mud-chips recovered from the base of bed A5 at CD166/57. The mudcap coccolith assemblages at CD166/48 and CD166/57 show increase in relative abundance of *E. huxleyi* and *G. mullerae*, which is consistent with erosion of OIS4 and OIS5 hemipelagites at those sites (Figure 4.13). Indeed, the coccolith assemblages from the mud-chips in the base of bed A5 in CD166/57 are consistent with the compositions of hemipelagites representing OIS4 and upper OIS5 immediately below bed A5. These observations support previously documented evidence that the turbidity current A5 was erosive within the proximal regions of the basin (Talling *et al.,* 2007; Wynn *et al.,* 2010).

As stated previously, the mudcap geochemical compositions between correlated turbidites in the Agadir Basin (CD166/12, CD166/31, CD166/57 and CD166/48) and the Agadir Canyon (JC27/13) do not exactly match (Figure 4.10). Indeed, when comparing specific basin-wide large-volume turbidites (e.g. A5, A7, A11 and A12)

between canyon and basin sites there is a significant offset in the compositions (Figure 4.10). Often the compositions form different arrays altogether. Thus the differences in the turbidite mudcap composition between the Agadir Canyon site (JC27/13) and those in the basin reflect a change in the composition during the flow path. This is primarily by erosive addition of sea floor sediment into the respective turbidity current, which is mixed and later deposited.

This is further supported by comparison of the mudcap coccolith assemblages of turbidites at the basin and canyon sites. Beds A5, A7, A11 and A12 show significant variations between the compositions in the canyon and compositions subsequently in the basin (Figure 4.12). Given the composition at JC27/13 and then at within the basin, estimations of the depth of erosion, in coccolith composition reflecting time, can be calculated (Figure 4.13). Bed A5 requires addition of sediment enriched in *G. aperta* to produce the assemblages at CD166/12 and CD166/31 (Figure 4.14). This equates to eroding sediment reflecting an age of 60-250 ka, with high abundances of *G. aperta*, this is supported by hiatuses of 130 ka recorded below a potential bed A5 in the Agadir Canyon mouth scour field (Macdonald *et al.*, 2011). Given the hemipelagite sedimentation rates (1.2-1.4 cm/1000 years) at these sites, this equates to erosion of 2.0-2.5 m of sediment in the canyon mouth, which is supported by Macdonald *et al.* (2011).

Furthermore, to produce the coccolith assemblage in bed A7 in the basin compared from that in the canyon, erosion of hemipelagite with high abundances of *G. aperta*, but not in *G. caribbeanica*, in required. This restricts the depth of erosion to sediment reflecting OIS5 and upper OIS6, with 0.75-1.0 m of sediment eroded. To produce the bed A11 mudcap coccolith assemblage in the basin addition of hemipelagite enriched in *G. aperta* and *G. caribbeanica*, although *G. caribbeanica* cannot be the most abundant within the eroded sediment. This equates to sediment eroded of OIS6, OIS7 and OIS8 compositions, which results in a depth of 2.2-2.5 m of sediment eroded in the canyon mouth. Finally, to produce the basin mudcap coccolith assemblage in bed A12, sediment enriched in *G. aperta* and *G. carribeanica* has to be added, where *G. caribbeanica* is the most abundant. This equates to sediment of OIS5-12 being eroded, any older than OIS12 sediment (~450 ka) would cause the *G. caribbeanica* abundance to be too high and *G. aperta* too low. This is supported by recognition of a major hiatus to OIS13 in cores from the Agadir Canyon mouth, below turbidites of 130 ka age (equivalent to beds A11 and A12) (Macdonald *et al.*, 2011). This equates to erosive removal of >3 m of sediment.

Further analysis of the turbidites that are present throughout Agadir Basin shows that turbidites A3 and A13 appear to have similar geochemical compositions between canyon and basin sites (Figure 4.10). Beds A3 and A13 also have similar mudcap coccolith assemblages between the canyon and basin sites (Figure 4.13). Thus these smaller-volume flows have not erosively adding sediment to the original flow, resulting in a basin composition similar to the canyon composition. Furthermore, geochemical compositions of the smaller events (e.g. A1.6, A3.1, A3.2, A3.3, 7.1 and A10.1) only found in the upper western sub-basin (CD166/48) show great similarity and form part of the same array compared to the composition within the canyon (Figure 4.9). Therefore, the small-volume flows (A1.6, A3.1, A3.2, A3.3, 7.1 and A10.1) in addition to small-volume turbidites A3 and A13 are not erosive on exiting the Agadir Canyon. While the alternate large-volume turbidites (A5, A7, A11 and A12) show varying degrees of erosion. The primary reason for this is that larger flows are travelling at greater velocities and carrying coarser bedload capable of greater degrees of basal erosion.

This has considerable affects on the flow dynamics of these large-volume deposits. The addition of cohesive sediment upon exiting the canyon and again on entering the upper sub-basin presents a contributing factor for the development of the linked debrite in bed A5 (Talling *et al.*, 2007).

Conclusions

The ITRAX μXRF methodology for investigating the geochemistry of deep sea sediment cores provides high resolution and accurate geochemical results. The initial elemental counts calculated on the peak area of the K-shell x-rays can be reliably calibrated to provide quantitative results in oxide wt% or ppm. The ITRAX μXRF methodology has provide support for the correlation of the turbidites in Agadir Basin based on chemostratigraphy, both of the turbidites and the isolated hemipelagic record in which the turbidites are deposited. In similar results to previous studies of turbidites in the Madeira Abyssal Plain, the chemostratigraphy employed in Agadir Basin has demonstrated the correlation of siliciclastic, volcaniclastic and calcareous turbidites.

Comparison of the geochemical composition of the mudcaps provides a means of assessing the provenance of each turbidite. The mudcap geochemistries have shown that individual provenance signatures can be identified for the Tenerife, El Hierro and Madeira sources. Furthermore, although the siliciclastic turbidites have a similar broad composition, individual events form discrete compositional fields with different arrays.

These variations found amongst the large-volume siliciclastic turbidites in the basin could be the result of subtle variations in the material involved in the initial landslide, although differential erosion could be responsible here. Further analysis showed that basinal compositions of the respective turbidites were consistent within the basin indicating that the turbidity currents were non-erosive in the basin. Only turbidite A5 shows degrees of compositional variation between basin sites, and this is in line with its erosive behaviour in the western upper sub-basin. Combination of ITRAX geochemistry and coccolith assemblages enable determination of the age and amount of hemipelagite sediment eroded by bed A5 in the upper sub-basin.

Differences in the mudcap geochemical compositions and coccolith assemblages between the same turbidite in the basin and the Agadir Canyon site are found in the large-volume events. This is a result of erosive addition of material upon exiting the Agadir Canyon, and is on the order of metre of sediment. Indeed, by determining the coccolith assemblages of the mudcaps at these sites, the age and amount of sediment erosively added can be calculated. Comparison of smaller-volume flows found in the Agadir Canyon and western upper sub-basin show no variation in composition, presumably because these are not erosive flows.

The composition of siliciclastic turbidites within the Agadir Canyon (JC27/13) show that compositions are similar, but still show variability. This supports a notion that they are sourced from the same geographic location (Agadir Canyon head and/or Moroccan shelf/slope) but different sections are being failed. Geochemical composition may indicate the relative water depths of these failures on the slope.

The present study reiterates the importance of conducting high resolution geochemical studies on turbidites. The ITRAX μXRF methodology has demonstrated that reliable and accurate high resolution profiles can be taken through sediment cores. This provides vital information in regards to age, provenance and erosive behaviour of the original flow. However, it is combining geochemical and biostratigraphic methodologies that provide the most robust studies on turbidite occurrence and sedimentary processes.

Acknowledgements

The authors would like to acknowledge the crews and officers of the CD166 and JC27 research cruises on which the cores studied were taken. JEH would also like to acknowledge the PhD funding utilised for this study provided by a NOCS studentship

within the Marine Geoscience Group there. The curators at BOSCORF are also thanked for their diligent care in both archiving the cores and maintaining the analytical instruments.

4.3 Summary

Geochemical variations in mudcap compositions between siliciclastic, volcaniclastic and calcareous turbidites allow development of a chemostratigraphy. The chemostratigraphy presented here, between selected core sites in Agadir Basin, supports the turbidite correlations of the previous Chapter 3 and existing Agadir Basin stratigraphy.

The geochemical compositions of the volcaniclastic turbidites have been shown to form discrete compositional fields. This highlights an evolved phonolitic source of bed A14, namely Tenerife, and given the age presented in the last Chapter, can be linked to the Icod landslide. Bed A2 has a proposed provenance from El Hierro, and from the El Golfo landslide in particular (Masson, 1996; Wynn and Masson, 2003; Frenz *et al.,* 2009). The mudcap geochemistry of this Chapter indicates a different basaltic provenance of bed A2 to the basaltic provenance of bed A8, which has been inferred to be Madeira from the sediment distribution (Frenz *et al.,* 2009).

This Chapter also demonstrates that there are subtle geochemical heterogeneities between the siliciclastic turbidites. Subtle variations in the mudcap geochemistry between the canyon and basin sites of deposition for the large-volume turbidites have been shown to be due to erosive addition of material. In contrast, small-volume turbidites have been shown to be non-erosive. However, geochemical differences between turbidites A11, A12 and A13 and turbidites A3, A5 and A7 are the product of different locations of failure.

The details taken from this Chapter inform the provenance of the turbidites that comprise the stratigraphy presented in the previous Chapter 3. Bed A14 has been identified as a volcaniclastic turbidite dated at 165 ka in the previous Chapter and shown in this Chapter to have an evolved (high Si and K) composition, supporting a previously proposed provenance from Tenerife. This A14 turbidite (Icod event bed) is the focus of the next Chapter (Chapter 5).

Chapter 5
Evidence of Multistage Landslide Mechanism from the Icod Event

5.1 Introduction and Aims

The sediment gravity flow deposits generated from the El Golfo (15 ka from El Hierro) and Icod landslides (165 ka from Tenerife) have been shown to possess a series of fining-upwards turbidite sequences, called subunits (Wynn and Masson, 2003). The origin of these subunits has been proposed to be the result of multistage landslides (Wynn and Masson, 2003). The implication is that the landslide volume introduced to the ocean at any one time will be smaller, compared to one single failure, thus reducing tsunamigenic potential.

This Chapter serves to firstly investigate the distribution of these subunits within the Icod event bed. Basal grain-size data will be used to trace the dispersal of these subunit events to identify their origin. Geochemical compositions of these subunits will be investigated to determine whether a multistage and retrogressive failure mechanism can be established. The Icod event has been chosen as the focus of this study because Tenerife, the source of the landslide, has a heterogeneous onshore geology (represented by basaltic to phonolitic volcanism). This onshore heterogeneity may be reflected in the composition of the subunits within the event bed. The following aims for this Chapter are outlined below:

1. Determine the subunit distributed within the Icod event bed in the Agadir Basin opposing the northern flank of Tenerife and Seine Abyssal Plain to the northeast.
2. Determine the mode of emplacement of the subunits using grain-size data.
3. Using bulk and volcanic glass geochemistry, determine the origin of subunits.

The analysis and interpretation of results is my own, with editorial help provided by my co-authors. This Chapter was accepted in its current format as a paper with *Geochemistry Geophysics Geosystems* (December 2011):

Hunt, J.E., R.B. Wynn, D.G. Masson, P.J. Talling, and D.A.H. Teagle (2011), Sedimentological and geochemical evidence for multistage failure of volcanic island landslides: a case study from Icod landslide on north Tenerife, *Geochem. Geophys. Geosyst.*, 12, Q12007, doi:10.1029/2011GC003740.

Sedimentological and geochemical evidence for multistage failure of volcanic island landslides: a case study from Icod landslide on north Tenerife, Canary Islands

James E. Hunt[1,2]*, Russell B. Wynn[1], Douglas G. Masson[1], Peter J. Talling[1] and Damon A.H. Teagle[2]

[1]National Oceanography Centre, University of Southampton Waterfront Campus, European Way, Southampton SO143ZH, UK

[2]School of Ocean and Earth Science, National Oceanography Centre Southampton, University of Southampton, European Way, Southampton SO143ZH, UK

* Corresponding author: jeh2g08@soton.ac.uk

Abstract

Volcanic island landslides can pose a significant geohazard through landslide-generated tsunamis. However, a lack of direct observations means that factors influencing the tsunamigenic potential of landslides remain poorly constrained. The study of distal turbidites generated from past landslides can provide useful insights into key aspects of the landslide dynamics and emplacement process, such as total event volume and whether landslides occurred as single or multiple events. The northern flank of Tenerife has undergone multiple landslide events, the most recent being the Icod landslide dated at ~165 ka. The Icod landslide generated a turbidite with a deposit volume of ~210 km3, covering 355,000 km^2 of seafloor off northwest Africa. The Icod turbidite architecture displays a stacked sequence of seven normally graded sand and mud intervals (named subunits SBU1-7). Evidence from subunit bulk geochemistry, volume, basal grain size, volcanic glass composition and sand mineralogy, combined with petrophysical and geophysical data, suggests that the subunit facies represents multistage retrogressive failure of the Icod landslide. The basal subunits (SBU1-3) indicate that the first three stages of the landslide had a submarine component, whereas the upper subunits (SBU4-7) originated above sea level. The presence of thin, non-bioturbated, mud intervals between subunit sands suggests a likely time interval of at least several days between each stage of failure. These results have important implications for tsunamigenesis from such landslides, as multistage retrogressive failures, separated by hours to several days and with both a submarine and subaerial component, will have markedly lower tsunamigenic potential than a single-block failure.

Introduction

Landslides are a critical process in the evolution of volcanic islands, with examples documented from the Canary, Cape Verde, Réunion and Hawaiian archipelagos (Moore *et al*., 1989, 1994; Labazuy, 1996; Watts and Masson, 1995, 2001; Masson *et al*., 2002, 2008; Oehler *et al*., 2004, 2008; Le Bas *et al.,* 2007). Volcanic island landslides occur most frequently during the early shield-building and subsequent erosional stages of island development (Moore, 1989, 1994; Carracedo, 1994, 1999). Furthermore, volcanic island landslides have the potential to generate catastrophic tsunamis (Latter, 1981; Keating and McGuire, 2000; Ward and Day, 2001, 2003; Tappin *et al.,* 2001; Synolakis *et al*., 2002; Whelan and Kelletat, 2003; McGuire, 2006; Gisler *et al.,* 2010). Several major volcanic island landslides have occurred in the geologically recent past. For example in the last 2 Ma there have been 14 flank collapses in the Western Canary Islands alone (Masson *et al.,* 2002, 2006), while the majority of the 68 large mass movements reported from the Hawaiian archipelago also occurred in this period (Moore *et al.,* 1989). Volcanic island landsides are therefore a potential geohazard at the present day, necessitating characterisation of the mechanics of these failures and their tsunamigenic potential.

Despite their geohazard potential, the processes driving initiation and evolution of volcanic island landslides and associated tsunamis are not well understood (Tinti *et al.,* 2000). Initial tsunami characteristics are highly sensitive to key landslide parameters, which are mostly poorly constrained through lack of direct observations. These include: landslide water depth, volume, initial acceleration, maximum velocity, initial position of sliding block relative to sea level, and whether the failure is multistage and/or retrogressive (Harbitz *et al.,* 1992, 1993, 2006; Fine *et al.,* 2001, 2003; Ward, 2001; Trifunac and Todorovska, 2002; Murty, 2003; Haugen *et al*., 2005; Løvholt *et al*., 2005, 2008). In the absence of measured data on key landslide parameters, many studies have assumed that a single rapidly moving landslide is most appropriate for tsunami models. Examples of these models include simulations of the hypothetical landslide-generated tsunamis from La Palma (Ward and Day, 2001; Mader, 2001; Gisler *et al.,* 2006), of the 1888 Ritter Island lateral collapse (Ward and Day, 2003), of the 1988 landslide-induced tsunami on Vulcano Island (Tinti *et al.,* 1999), and the Langrangian-view model of a theorised collapse from Stromboli (Tinti *et al.,* 2000).

It has been suggested that recent instabilities on the southwest Cumbre Vieja flank of La Palma could yield a future lateral collapse with a volume of 150-500 km^3 (Ward and

Day, 2001). Modelling this collapse as a 500 km^3 volume and 1,400 m-thick single sliding-block landslide produces a tsunami with a ~900 m initial wave height. Furthermore, this 'worst-case scenario' model suggests that the landslide-induced tsunami could propagate across the North Atlantic, resulting in 25 m waves that inundate the east coast of North America (Ward and Day, 2001). Subsequent discussion of this tsunami model has focussed on the various input parameters used and the scale of the resulting tsunami (Mader, 2001; Pararas-Carayannis, 2002; Wynn and Masson, 2003; Gisler *et al.*, 2006; Løvholt *et al.*, 2008). Although there is no consensus on far-field impacts, most authors agree that near-field impacts from any future La Palma landslide-tsunamis will be severe. This is supported by modelling of a much smaller 1 km^3 landslide from the western flank of Stromboli, which has been found to be capable of producing proximal waves with 10 to 40 m heights (Tinti *et al.*, 2000).

It has been argued that a single fast-moving landslide is not always applicable for major volcanic island flank collapses, as failure could occur in multiple stages (Garcia and Hull, 1994; Wynn and Masson, 2003; Di Roberto *et al.*, 2010). A multistage landslide involving retrogressive failure (Kvalstad *et al.*, 2005; Haugen *et al.*, 2005; Micallef *et al.*, 2007) will inevitably produce smaller tsunamis compared with a single block failure (Paris *et al.*, 2011; Giachetti *et al.*, 2011). Giachetti *et al.* (2011) modelled the 830 ka Güímar landslide from Tenerife and found that results from a retrogressive failure produced tsunami wave characteristics supported by onshore deposits in the Agaete Valley on Gran Canaria.

Determining the time intervals between each stage of failure is important: short time intervals will enable subsequent failures to generate tsunami waves with constructive interference (Haugen *et al.*, 2005, and references therein), longer time intervals will lead to lower amplitudes but a longer overall wavelength of the wave train (Masson *et al.*, 2006; Harbitz *et al.*, 2006), while even longer time intervals will generate discrete tsunami waves. This is exemplified by a two-dimensional retrogressive slide model of Storegga Slide, which demonstrated that time intervals of <1 minute were enough to reduce surface elevations of the tsunami wave train by half (Haugen *et al.*, 2005; Masson *et al.*, 2006). Furthermore, numerical modelling of a tsunami produced from the 86-123 ka Monte Amarelo flank collapse from Fogo Island in the Cape Verde archipelago demonstrates a probable multistage retrogressive failure (Paris *et al.*, 2011). Paris *et al.* (2011) demonstrate that when the debris is released over 300 s rather than all

in one go, the tsunami wave is reduced by 75%, and reduced by 89% when the time interval is increased to 600 s.

The Icod landslide represents the most recent (~165 ka) catastrophic flank collapse from north Tenerife (Figure 5.1) and was responsible for forming the Icod valley onshore and Icod landslide immediately offshore. The landslide disaggregated during its passage downslope and spawned a highly mobile turbidity current, which deposited the extensive Icod turbidite across the Moroccan Turbidite System (Figures 5.1 and 5.2). Preliminary sedimentological studies of Icod turbidite, and the younger El Golfo turbidite (~15 ka; derived from El Golfo landslide on El Hierro), have provided indications for multistage failure of the source landslides (Wynn and Masson, 2003; Masson *et al*., 2006). This followed a study by Garcia (1996), who also suggested that structures in distal turbidites from offshore Hawaii (sampled in ODP core) might represent multistage failure of volcanic landslides.

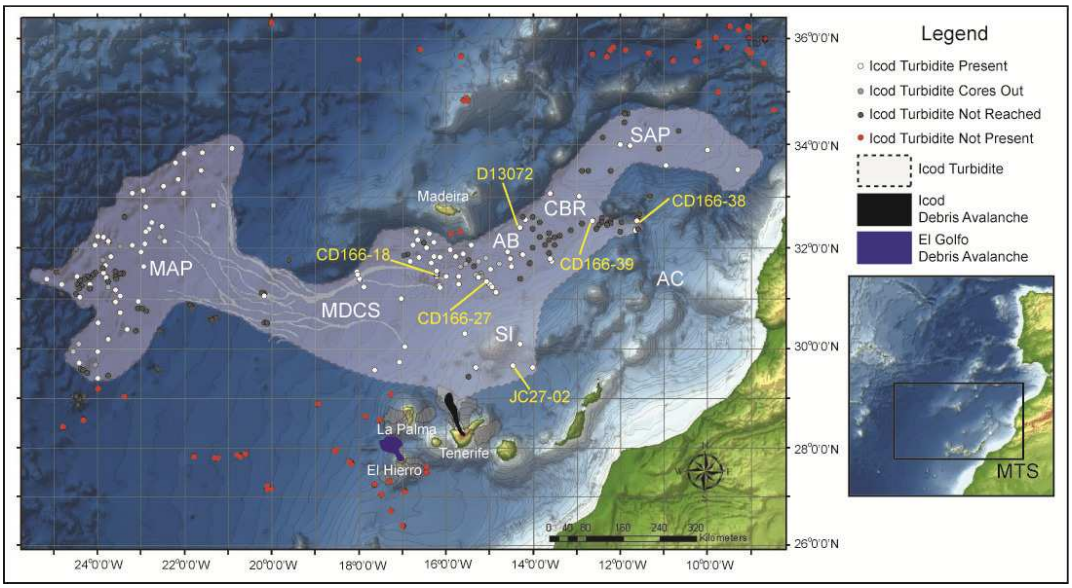

Figure 5.1 GEBCO bathymetry map of the Moroccan Turbidite System (MTS) showing core coverage and the spatial distribution of Icod landslide and turbidite. Map abbreviations as follows: AB = Agadir Basin, SAP = Seine Abyssal Plain, MAP = Madeira Abyssal Plain, MDCS = Madeira Distributary Channel System, AC = Agadir Canyon, SI = Selvage Islands, and CBR = Casablanca Ridge. Note the spatial extent of the Icod event bed, covering an area >355,000 km^2 with a runout of >860 km to the SAP and >800 km to the MAP. Inset map (bottom right) shows general location of the MTS off northwest Africa.

This contribution utilises an unusually extensive shallow core dataset, combined with geochemical and sedimentological analyses, in order to test the hypothesis that distal turbidites derived from volcanic island landslides can be used to provide information on landslide process and tsunamigenic potential. The Icod landslide and turbidite is the focus of this study, due to the excellent core control throughout the Moroccan Turbidite

System that comprise Agadir Basin (42 cores), Madeira Abyssal Plain (38 cores) and Seine Abyssal Plain (6 cores) (Figure 5.1). This detailed core coverage allows appropriate interrogation of the spatial extent, grain-size distribution and geochemical signatures of the individual subunits within Icod turbidite (e.g. Figure 5.2).

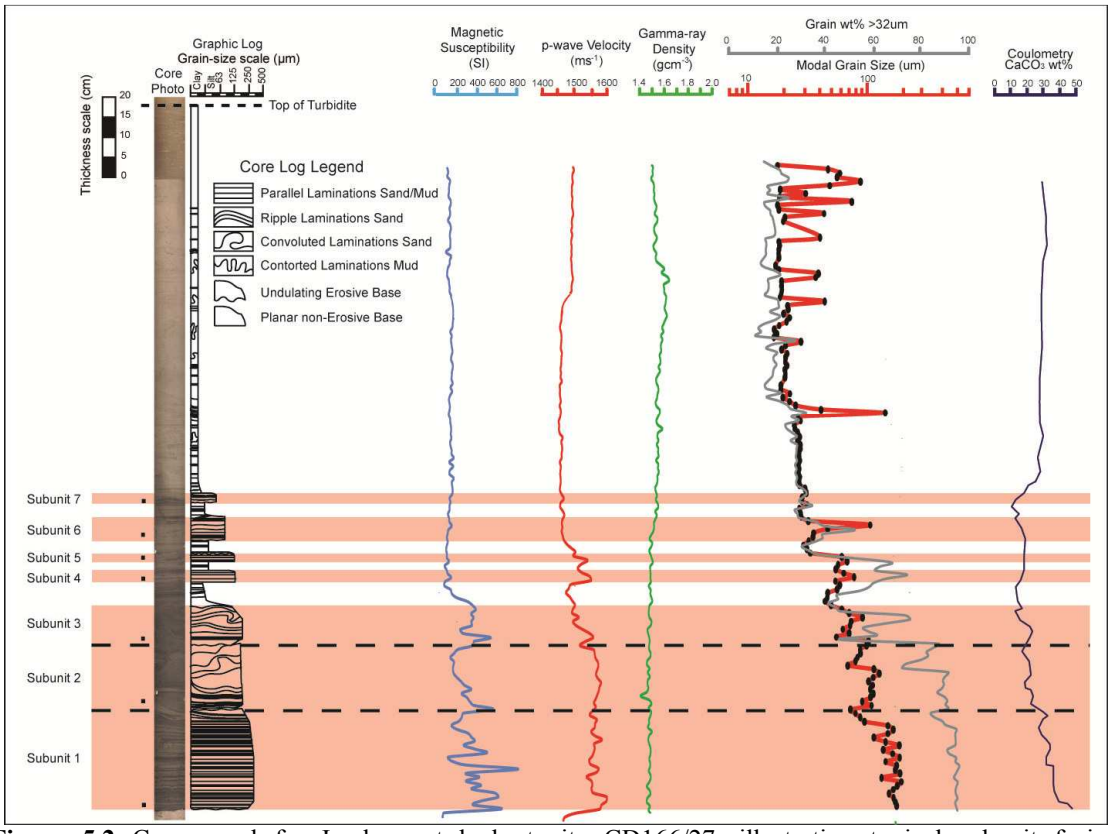

Figure 5.2 Core panel for Icod event bed at site CD166/27, illustrating typical subunit facies, sedimentary structures, petrophysical properties, vertical grain size profile and carbonate content. See figure 5.1 for core location.

Previous work on Tenerife landslides and their Deposits

The Eruptive History of Tenerife

The Icod valley has been inferred to be the onshore landslide scar for the Icod landslide (Watts and Masson, 1995; Cantagrel *et al.,* 1999; Ablay and Hürlimann, 2000). Thus the landslide and turbidite will likely reflect the composition of the material failed on the northern flank of Tenerife. A brief description of the volcanic history of Tenerife is therefore appropriate to this study.

Tenerife originally developed from three massifs: Roque del Conde (Ancochea *et al.* 1990; Guillou *et al.,* 2004), Teno (Ancochea *et al.* 1990; Thirwall *et al.,* 2000) and Anaga (Ancochea *et al.* 1990; Thirwall *et al.,* 2000). These massifs are dated at 11.9-6.4

Ma, 6.7-5.0 Ma, and 6.5-4.5 Ma respectively (Ancochea *et al.* 1990; Thirwall *et al.*, 2000; Guillou *et al.*, 2004), and comprise thick sequences of basalt to phonolite lavas and volcaniclastic debris. The development of these massifs is thought to represent the shield-building phase of the island (Carracedo, 1999).

Since 3.5 Ma there have been four phases of central composite edifice eruptions on Tenerife: Cañadas I, II, and III, and the currently active Teide-Pico Viejo complex (Cañadas IV). Prior to the recent volcanism, the Cañadas III edifice was built from three cycles of extrusive trachy-basaltic lava flows and phonolitic pyroclastics from 1.1-0.16 Ma (Ancochea *et al.*, 1990). The Las Américas ignimbrites represent cycle one (terminating at ~0.88 Ma), with the Bandas del Sur ignimbrites representing cycles two (terminating at ~0.57 Ma with the Granadilla member) and three (terminating at ~0.168 Ma with the El Abrigo member) (Bryan *et al.*, 2002; Huertas *et al.*, 2002; Brown *et al.*, 2003).

The Diego Hernandez Formation represents the pyroclastic deposits from the third and final cycle of Bandas del Sur phonolitic volcanism of the Cañadas III edifice. Importantly, the Diego Hernandez Formation also represents the eruptive events immediately preceding the Icod landslide, culminating in the caldera-forming pyroclastic events of the El Abrigo member (Edgar *et al.*, 2007). The overall volcaniclastic record prior to the Icod landslide demonstrates a succession of intervening phreatomagmatic, fall, surge and flow deposits with a highly evolved phonolitic composition with K_2O and Zr, in addition to basaltic rift volcanism (Bryan *et al.*, 2002; Edgar *et al.*, 2007).

Landslide History of the Northern Flank of Tenerife

The northern flank of Tenerife has experienced several major flank collapses. These have occurred primarily at the termination of major volcanic eruptive phases and cycles (Hűrlimann *et al.*, 1999; Huertas *et al.*, 2002). These include the Tigaiga (~2.4 Ma), Roques de Garcia (0.6-1.4 Ma), Orotava (540-690 ka) and Icod (150-170 ka) landslides (Ablay and Hürlimann, 2000; Masson *et al.*, 2002). Large caldera-forming eruptive events also occur at the termination of volcanic phases and cycles. Caldera-forming eruptions are capable of destabilising island flanks and could potentially trigger subsequent lateral flank failures (Marti *et al.*, 1997; Hürlimann *et al.*, 1999). The relative contributions of lateral flank and vertical caldera collapses in producing the current geomorphology of Tenerife remain uncertain. Indeed, the origin of the current

Cañadas Caldera is debated strongly between either lateral (Ancochea *et al.,* 1990, 1998, 1999; Carracedo, 1994; Watts and Masson, 1995, 1998, 2001; Cantagrel *et al.,* 1999; Arnaud *et al.,* 2001; Masson *et al.,* 2002) or vertical collapse (Ridley, 1971; Marti *et al.,* 1994, 1997; Bryan *et al.,* 1998b; Marti and Gudmundsson, 2000; Coppo *et al.,* 2008, 2009; Marti *et al.*, 2010); although it is likely that these two processes are interlinked.

The Icod Landslide

The northern flank of Tenerife, and the offshore Icod landslide deposit in particular, has been subjected to intensive study with seismic reflection profiles, TOBI sidescan sonar and multibeam (swath) bathymetry (Watts and Masson, 1995, 2001; Ablay and Hürlimann, 2000; Masson *et al.,* 2002). The Icod proximal landslide covers an area of 1700 km^2, with an estimated deposit volume of 110±40 km^3 and a runout distance of 105 km (Masson *et al.,* 2002).

The morphology of Icod landslide suggests that it began as a debris avalanche but evolved, at least in part, into a debris flow (Figure 5.3; Watts and Masson, 2001; Masson et al, 2002). The Icod debris avalanche/flow deposit has 45 m-high lateral ridges and a halo of coarser material (individual blocks up to 1.5 km diameter) around the periphery (Watts and Masson, 2001; Masson *et al.,* 2002). Most of the deposit surface is covered with scattered blocks that are tens to a hundred metres across, as well as linear shear structures, scours, sediment waves and pressure ridges. This suggests that coherency of the initial landslide block was low, enabling rapid disaggregation into finer material that could be transported as debris flow (Masson *et al*., 2002).

The Icod Turbidite

The Icod turbidite is a volcaniclastic turbidite generated by Icod landslide and is deposited throughout the Moroccan Turbidite System (Figure 5.1). This mixed siliciclastic-volcaniclastic turbidite system is located in water depths of >4,000 m on the northwest African passive continental margin. Volcanic islands and seamounts separate a number of interconnected depocentres, including Agadir Basin and the Madeira and Seine Abyssal Plains (Weaver and Rothwell, 1987; Rothwell *et al.,* 1992; Weaver *et al.,* 1992, Wynn *et al.,* 2002a; Frenz *et al.,* 2009). Studies in Madeira Abyssal Plain identified only two major volcaniclastic turbidites in the last 300 ka: these are the

authors' beds *b* (~15 ka) and *g* (originally dated at ~190 ka below an erosive base) (Weaver *et al.*, 1992).

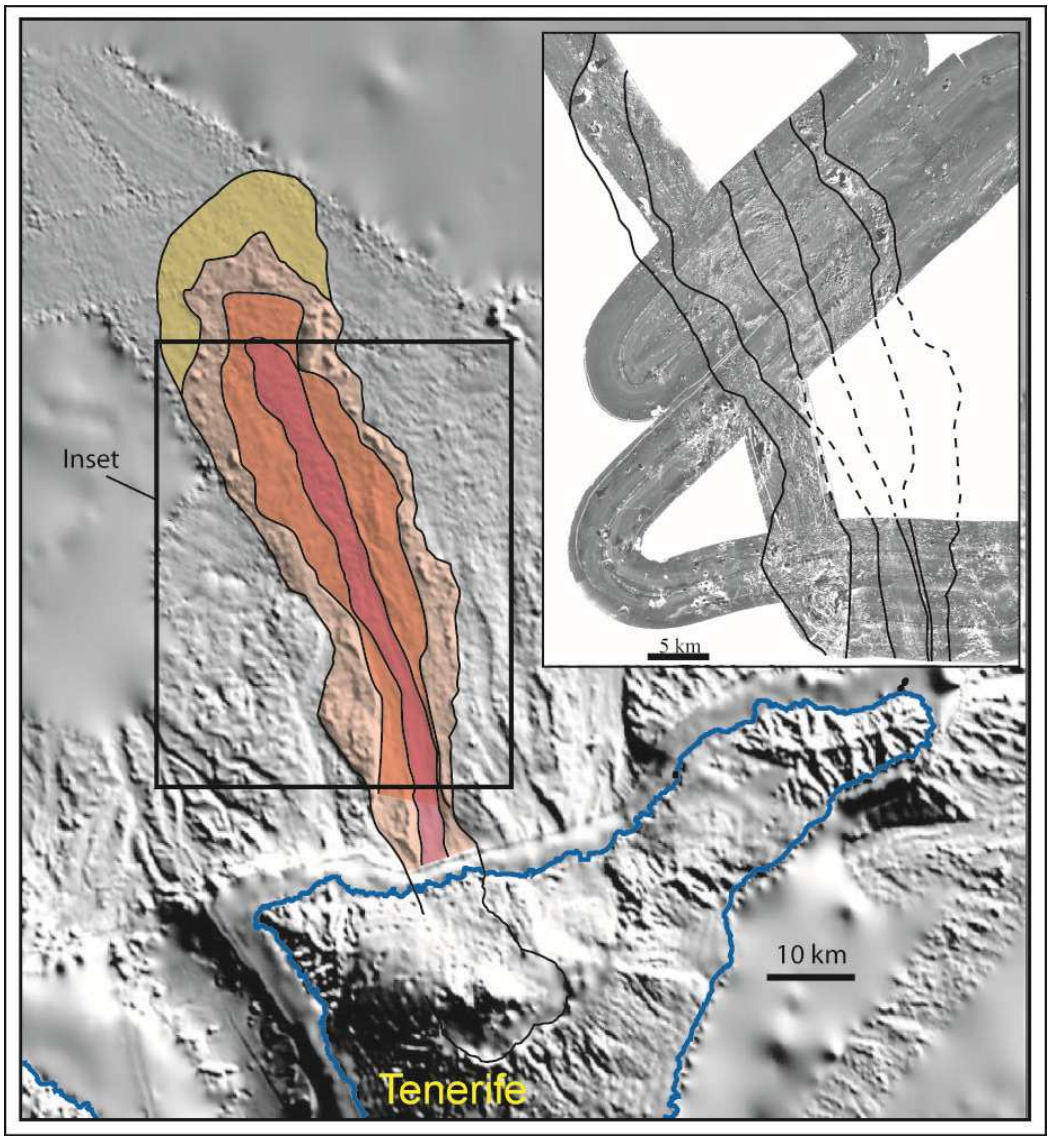

Figure 5.3 Shaded relief image of the north slope of Tenerife, derived from multibeam bathymetry and topographic data, with interpretation of the Icod landslide superimposed. The morphological subdivision of the landslide is based on 30 kHz sidescan sonar data (inset, top right), with boundaries extrapolated using bathymetric data for areas outside sidescan sonar coverage. A series of well-defined lobes can be recognised.

The provenance of these beds was investigated utilising bulk geochemistry of turbidite muds and sand fraction petrography (de Lange *et al.*, 1987; Pearce and Jarvis, 1992, 1995). Bed *g* (representing the Icod turbidite) in Madeira Abyssal Plain was found to contain phonolitic glasses and had a fractionated volcanic geochemical signature (Pearce and Jarvis, 1992). Tenerife was identified as the probable source due to the extensive phonolitic onshore deposits that could have contributed to the original

landslide (de Lange *et al.*, 1987; Pearce and Jarvis, 1992; Rothwell *et al.*, 1992). Bed *g* of the Madeira Abyssal Plain studies has been correlated by coccolithophore biostratigraphy to bed AB14 in the Agadir Basin (Wynn *et al.*, 2002a; Frenz *et al.*, 2009) and bed *m* in the Seine Abyssal Plain (Davies *et al.*, 1997; Wynn *et al.*, 2002a). In the present study, this bed is simply referred to as Icod turbidite throughout the study area.

Dating constraints linking Icod landslide and turbidite can be gained from 1) the proximal Icod valley-infilling igneous successions, 2) the proximal debris avalanche and 3) the distal turbidite deposit (Table 5.1). The valley-infilling successions and debris avalanche date the Icod landslide at 170-180 ka (Mitjavila, 1990; Mitjavila and Villa, 1993; Bryan *et al.*, 2002; Brown *et al.*, 2003; Watts and Masson, 1995). The position of Icod turbidite in the centre of the interglacial clay of Oxygen Isotope Stage (OIS) 6 dates the deposit at 165±15 ka, which is supported by coccolithophore biostratigraphy in Agadir Basin (Table 5.1; Wynn *et al.*, 2002a; Frenz *et al.*, 2009).

The Icod turbidite is compositionally separable from continental margin derived turbidites and other volcaniclastic turbidites due to its bulk geochemical composition (de Lange *et al.*, 1987). Indeed, the Icod turbidite can be characterised by high zirconium concentrations (>350 ppm), Al_2O_3 at 17 wt%, relatively high K_2O (>2.6 wt%), and low TiO_2 (<0.65 wt%) (Pearce and Jarvis, 1992, 1995). Weaver and Rothwell (1987) and Pearce and Jarvis (1992) describe a high proportion of phonolitic volcanic glass, basaltic and trachyte lithic clasts, sanidine feldspars, titanaugite and Fe-Ti oxides within Icod turbidite, which they attribute to a trachyte-phonolite source. The bulk geochemistry is supplemented by clay mineral analysis utilising XRD, whereby the Icod turbidite is typified by calcite composition of ~40-60% and kaolinite/chlorite ratio of 1.0-1.4 (Pearce and Jarvis, 1992). A high smectite content of 41-45%, relative to a kaolinite content of 13-18%, is also observed. The excess smectite is thought to reflect greater alteration of volcanic materials compared to other volcaniclastic and siliciclastic turbidites (Pearce and Jarvis, 1992). Altered volcanic lithic clasts and glasses further support the action of chemical alteration within the deposit (Pearce and Jarvis, 1992).

Table 5.1 Dating constraints on the Icod Landslide and Turbidite

	Date	Dating Details
Onshore	175 ka	The youngest pre-landslide rocks on Tenerife have been dated at 173-176 ka (Kr-Ar method, Mitjavila, 1990), and 179-183 ka ($^{40}Ar/^{39}Ar$ method, Mitjavila and Villa, 1993).
Related Volcanism	168 ka	168±1 ka age for the El Abrigo pyroclastic unit, which represents the final plinian-style eruption of the Cañadas III volcanic centre prior to the landslide (Bryan *et al.,* 2002; Brown *et al.,* 2003).
Debris Avalanche	170 ka	Icod landslide has been dated at ~170 ka from shallow seismic (Watts and Masson, 1995). This is based on a ~10 m drape of hemipelagic sediment over the debris avalanche interpreted from shallow seismic and a sediment accumulation rate of 6 cm/ka from core.
Madeira Abyssal Plain Turbidite	190 ka	For the distal turbidite in the Madeira Abyssal Plain, $\delta^{18}O$ measurements from pelagic intervals imply a date below the turbidite of ~190 ka at site D10688, although this was in an erosive setting in the northern sub-basin (Weaver and Rothwell, 1987).
Agadir Basin Turbidite	165 ka	The Icod turbidite was found deposited at a mid-point in an Oxygen Isotope Stage 6 glacial clay in non-erosive environments: a levee of the Madeira Distributary Channel System in the Agadir Basin (site CD166/18), 220 m up on the inner bend of the Agadir Canyon (site CD166/36), and 335 m up on the outer bend of the Agadir Canyon (CD166/38). This provides an age of ~160 ka (Frenz *et al*., 2009). This is supported by coccolithophore biostratigraphic ages of 155±20 ka and 175±25 ka in the Agadir basin at sites D13071 and D13072 respectively (Wynn, 2002a).

Subunit Architecture of Icod Turbidite

The above studies identified the source of Icod turbidite as the Icod landslide on the northern flank of Tenerife, based on timing, turbidite mineralogy and turbidite geochemistry. An 'ideal' turbidite deposit has a sharp, commonly erosional base, a graded, often bioturbated top, and a vertical facies association comprising one or more of massive sand (Ta), parallel laminated sand (Tb), cross- and ripple- laminated sand (Tc), laminated silt and mud (Td) and graded mud (Te) arranged in a single fining-upwards sequence (e.g. Bouma, 1962). However, initial studies on Madeira Abyssal Plain described a number of turbidites (including Icod turbidite) that contain multiple

sequences of fining-upwards turbidite sands and non-bioturbated muds, without intervening hemipelagic intervals (Rothwell *et al.,* 1992). For the purposes of this study the individual, sharp-based, fining-upwards sand/mud layers in these deposits are called subunits, while the combined sequence of stacked subunits within a single bed (either amalgamated or separated by intervening turbidite muds) is called subunit facies.

However, since each of these subunits potentially represents deposition from a discrete turbidity current, naming the overall deposit containing the subunit facies a turbidite (singular) e.g. Icod turbidite is incorrect. Therefore the cumulative deposit of subunit facies should be referred to as an Event Bed e.g. Icod Event Bed (Figure 5.2). Individual Event Beds displaying subunit facies are bounded above and below by hemipelagic sediments, which are identified by the lack of sedimentary structures and the presence of randomly dispersed foraminifera (representing slow suspension settling) (Figure 5.2). This implies that the subunit turbidity currents are deposited in association with each other, over a short time period during a genetically linked landslide event.

The subunit facies within the Madeira Abyssal Plain was initially attributed to three potential mechanisms (Rothwell *et al.,* 1992): 1) retrogressive landslides generating a series of individual surge-type turbidity currents (Pickering, 1979; Lowe, 1982), 2) earthquake triggering of landslides at multiple locations, which generated flows that merged when deposited within the basin (Einsele and Kelts, 1982), and 3) flow reflection, in this case, from seamounts and seafloor escarpments (Hiscott and Pickering, 1984; Kneller and McCaffrey, 1999). A sidescan sonar survey over the region connecting Agadir Basin and Madeira Abyssal Plain subsequently revealed a complex series of channels, named the Madeira Distributary Channel System (Masson, 1994). Turbidity currents passing through these channels could potentially emerge on Madeira Abyssal Plain at different times, generating the observed subunit facies (Masson, 1994).

The presence of the Madeira Distributary Channel System and numerous seamounts means that the origin of the subunit facies in the Icod Event Bed cannot be resolved unambiguously on Madeira Abyssal Plain. Therefore, a subsequent study, based on a small number of piston cores, focussed on Agadir Basin (Wynn and Masson, 2003; Masson *et al.*, 2006); this depocentre is closer to Tenerife and is fed directly by unconfined flows due to an absence of channels (Figure 5.1). Subunits and subunit facies in the Icod Event Bed were identified in three core sites in central Agadir Basin, and were tentatively linked to a retrogressive multistage landslide failure mechanism

(Wynn and Masson, 2003; Masson *et al.*, 2006). However, this initial study only involved two basin margin cores and a site in the basin centre where the Icod Event Bed was not fully penetrated. The extended core coverage and analytical techniques applied during the present study demonstrates a significant advance on the previous investigations.

Additional Examples of Potential Multistage Volcanic Island Landslides

It is important to highlight that the subunit facies described above is common to many turbidites associated with volcanic island landslides, and is not solely characteristic of the Icod event. However, restricted core coverage has hindered detailed analysis of these turbidites.

Within Agadir Basin, five subunits are recognised in a turbidite associated with El Golfo landslide from El Hierro (bed *AB2* of Wynn *et al.* (2002a), Wynn and Masson (2003) and Frenz *et al.* (2009)). Unlike the Icod Event Bed, the El Golfo Event Bed shows progressive pinch-out of subunits distally in central Agadir Basin, owing to the larger distance from source (Frenz *et al.*, 2009). Interestingly, the proximal Icod and El Golfo landslide deposits have very different characters: the El Golfo landslide is a typical debris avalanche deposit comprising randomly scattered blocks, whereas Icod landslide represents a transition from debris avalanche to debris flow with blocks sorted to the deposit periphery (Masson *et al.*, 2002). Subunit facies are present in distal turbidites derived from both landslides, implying that subunit facies reflects the initial landslide mechanism rather than the flow processes that affected the landslide mass during its emplacement.

A 12-cm thick turbidite (Layer 2) from ODP Hole 842A, offshore Hawaii, is reported to be composed of a series of stacked volcaniclastic sands (Garcia and Hull, 1994; Garcia, 1996). In this example a multistage event is deduced from volcanic glass compositions and radiolarian assemblages. This deposit is an analogue to the Icod event in that it is 1) composed primarily of volcanic glass, 2) the turbidity current has travelled hundreds of kilometres from source (325 km west from Alika landslide scar), and 3) the flow surmounted a major topographic feature (~500 m high Hawaiian Arch). However, this turbidite has only been sampled at a single core site.

Turbidites composed of vertical stacked sands were produced by several volcanic landslides and at least two flank collapses (Neostromboli collapse at ~5 ka and a Recent Stromboli period at ~1 ka) on Stromboli island (Di Roberto *et al.*, 2010) The stacked

sand architecture is related to retrogressive landslide failure through variations in volcanic glasses and sand components, which show a progression from Neostromboli compositions to those of recent Stromboli activity (Di Roberto *et al.,* 2010). However, this study also only involved two core sites.

Methodology and Data

The cores used in this study were largely obtained during research cruises to the Moroccan Turbidite System in 2004 (RRS Charles Darwin cruise 166) and 2007 (RRS James Cook cruise 027). Some cores, in particular those from Madeira Abyssal Plain, were also obtained on earlier cruises on RRS Discovery (see Rothwell *et al*. (1992) and Weaver *et al*. (1992) for details). All cores are housed in a refrigerated store at the British Ocean Sediment Core Facility (BOSCORF), based at the National Oceanography Centre, Southampton, UK. This section represents summaries of the methodologies and data, with full methodology descriptions detailed in Appendix 5.1.

Visual core logs, petrophysical data and grain size analysis

Visual sedimentary logs and core photographs were used initially to identify turbidite facies, architecture and grain size (Figure 5.2). In addition, logging of hemipelagic sediments above and below the Icod Event Bed enabled supportive dating of the event and calculation of the relative amount of basal erosion. The GeoTek^{TM} MSCL-S (Multi-Sensor Core Logger) was used to collect p-wave velocity, gamma-ray density and magnetic susceptibility physical property measurements (Figure 5.2) (full details in Appendix 5.1).

Grain-size analysis was undertaken on every example of the Icod Event Bed recovered. The complete bed was sampled every 1 cm with basal grain-sizes focussed upon in the present study to show flow pathways. Grain-size analysis was undertaken using laser-diffraction (full details in Appendix 5.1).

Calculation of Subunit Volumes

Isopach maps for each subunit and the mud cap were generated to calculate bulk volumes of the Icod Event Bed and individual subunits (see Appendices 5.2 and 5.3). A ratio, based on individual subunit sand volumes, was used to attribute a mud volume to each subunit from the total mud cap. The error on the volume calculations is 10% based

on numerous iterations of isopach maps with degrees of uncertainty incorporated (full details in Appendix 5.1).

Sand Fraction Petrography

Bulk samples were taken from all the Icod Event Bed subunit sand intervals within Agadir Basin and Seine Abyssal Plain. The carbonate-free bulk sample at grain-size fractions of 63-90 μm, 90-125 μm and 125-250 μm were point counted to >300 grains for mineralogy (full details in Appendix 5.1).

ICP-OES Bulk Geochemistry

Bulk samples were taken from each subunit sand interval from each available core in Agadir Basin and Seine Abyssal Plain. The >32μm fraction was separated by wet sieving, dried and weighed before the carbonate content was leached by addition of 5 ml 10% acetic acid. Sub-samples of 100 μg carbonate-free sample were powdered for acid digestion, using firstly aqua regia (3:1 HCl:HNO_3), and then HF and perchloric acids. The final silica-free residue was dissolved in 6 M HCl, from which 0.6 M HCl daughter solutions were made for analysis (full details in Appendix 5.1). A number of terrigenous and volcanic standard reference materials (SRMs) were used to assess precision, with sample and SRM duplicates used to assess accuracy of the methodology (Appendix 5.6). Bulk geochemical results are tabulated in Appendix 5.7.

LEO1450 SEM and EDS

Samples of, carbonate-free, 90-125 μm grain size material from subunit sand intervals at site JC27/02 (see Figure 5.1 for location) were made into carbon-coated thin sections. Site JC27/02 is the most proximal core site to Tenerife, and here the Icod Event Bed contains the coarsest grains available for analysis. The LEO 1450 variable pressure SEM and PGT microanalysis EDS was then used to produce both images and geochemical compositions of volcanic glass assemblages (full details in Appendix 5.1). Analysis of SRMs and subunits volcanic glass samples are tabulated in Appendices 5.8 and 5.9.

TM1000 SEM

The TM1000 tabletop SEM was used to take high resolution images of grains from each sand interval in core CD166/27 (Agadir Basin, Figure 5.1) and JC27/02 (Selvage

Seamount, Figure 5.1). The advantage of this SEM is that minimal preparation is required to take images of 3D grains.

CO_2 Coulometry

Inorganic carbon (carbonate) measurements were taken through a type core (CD166/27) at 1 cm intervals. To determine the carbonate content of both the subunits and turbidite mud (full details in appendix 5.1).

Results

Identification of the Icod Event Bed Subunit Facies within Agadir Basin

The Icod Event Bed in Agadir Basin (Figure 5.1) can be divided into seven regular subunits, named SBU1-7 (Figure 5.2). The seven laterally continuous subunits are identified in 42 cores in Agadir Basin (Figures 5.4 to 5.8). Relative stratigraphic position, grain-size data, magnetic susceptibility, gamma-ray density and p-wave velocity logs, supported by geochemical data, enable spatial correlation of subunits within the deposit (Figures 5.4 to 5.6).

In the southwest Agadir Basin, proximal to source, the Icod Event Bed consists of an amalgamated basal unit with an erosive base that cuts down through the dark brown OIS6 interglacial clay to a pale hemipelagic interval (Figures 5.2, 5.4 and 5.7). The basal amalgamated sand of the proximal the Icod Event Bed is 10-50 cm thick, depending on distance from source (Figures 5.2, 5.4 and 5.7). This sand represents an amalgamation of three subunits (SBU1-3), each composed of a fining-upwards sequence of parallel laminations, ripple cross-laminations and convoluted laminations above an erosional surface (Figures 5.2, 5.4 and 5.5). The SBU1-3 amalgamated interval is capped by a sand-to-mud grain-size break, with a laminated silty mud between it and the next subunit sand interval (SBU4). The subsequent SBU4-7 subunits are characterised by an erosive base, above which 2-10 cm-thick parallel laminated and cross-laminated fine sands are deposited. Each upper subunit (SBU4-7) is then capped by a sand-to-mud grain-size break above which a laminated or ungraded silty mud interval occurs (5-20 cm-thick) (Figures 5.2, 5.4 and 5.5).

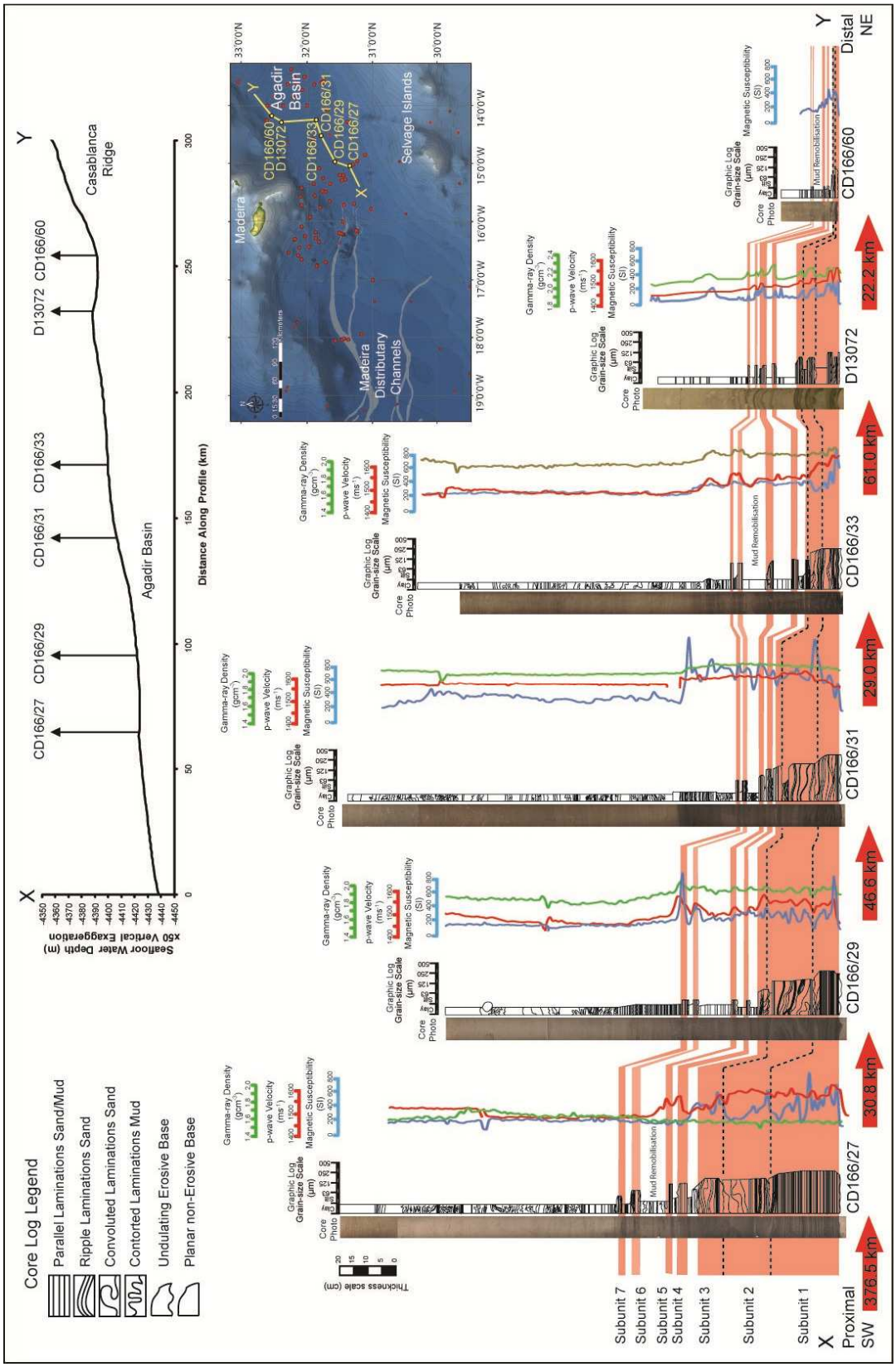

Figure 5.4 Correlation panel of the Icod event bed along the axis of Agadir Basin, showing interpreted core logs and petrophysical properties used for correlation. Inset bathymetric map shows that the panel (yellow line) runs parallel to flow direction, from southwest (proximal to Icod source) to northeast (distal). Core locations indicated by yellow circles. Cross-sectional profile shows seafloor gradient along the panel line. Red arrows indicate distance between core sites. Note the seven spatially extensive subunits that progressively thin and fine away from source.

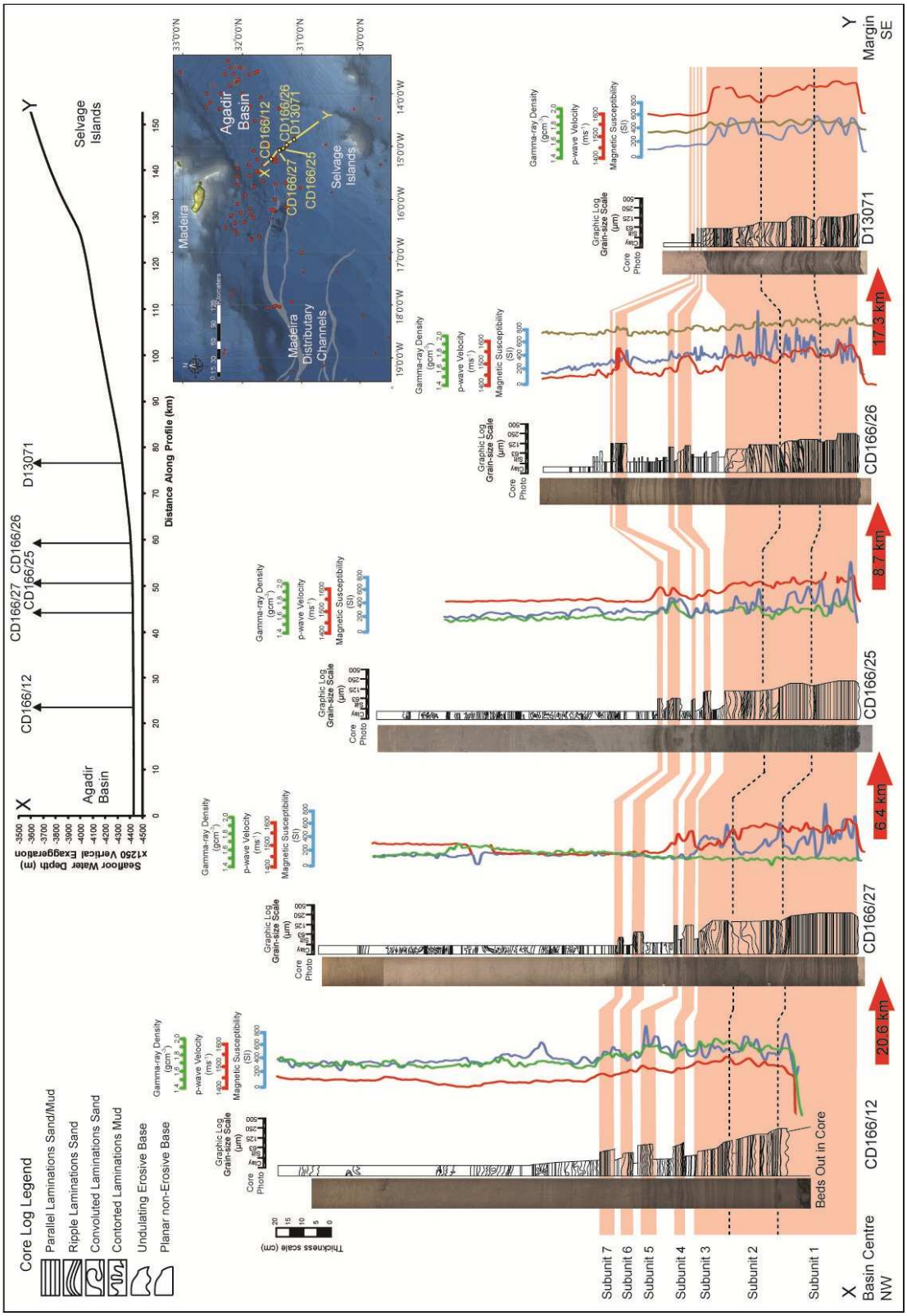

Figure 5.5 Correlation panel of the Icod event bed across Agadir Basin from basin floor to southern margin, showing interpreted core logs and petrophysical properties used for correlation. Inset bathymetric map shows that the panel (yellow line) runs perpendicular to flow direction, from northwest (basin floor) to southeast (southern basin margin). Core locations indicated by yellow circles. Cross-sectional profile shows seafloor gradient along the panel line. Red arrows indicate distance between core sites. Note the progressive thinning and fining of all seven subunits towards the basin margin.

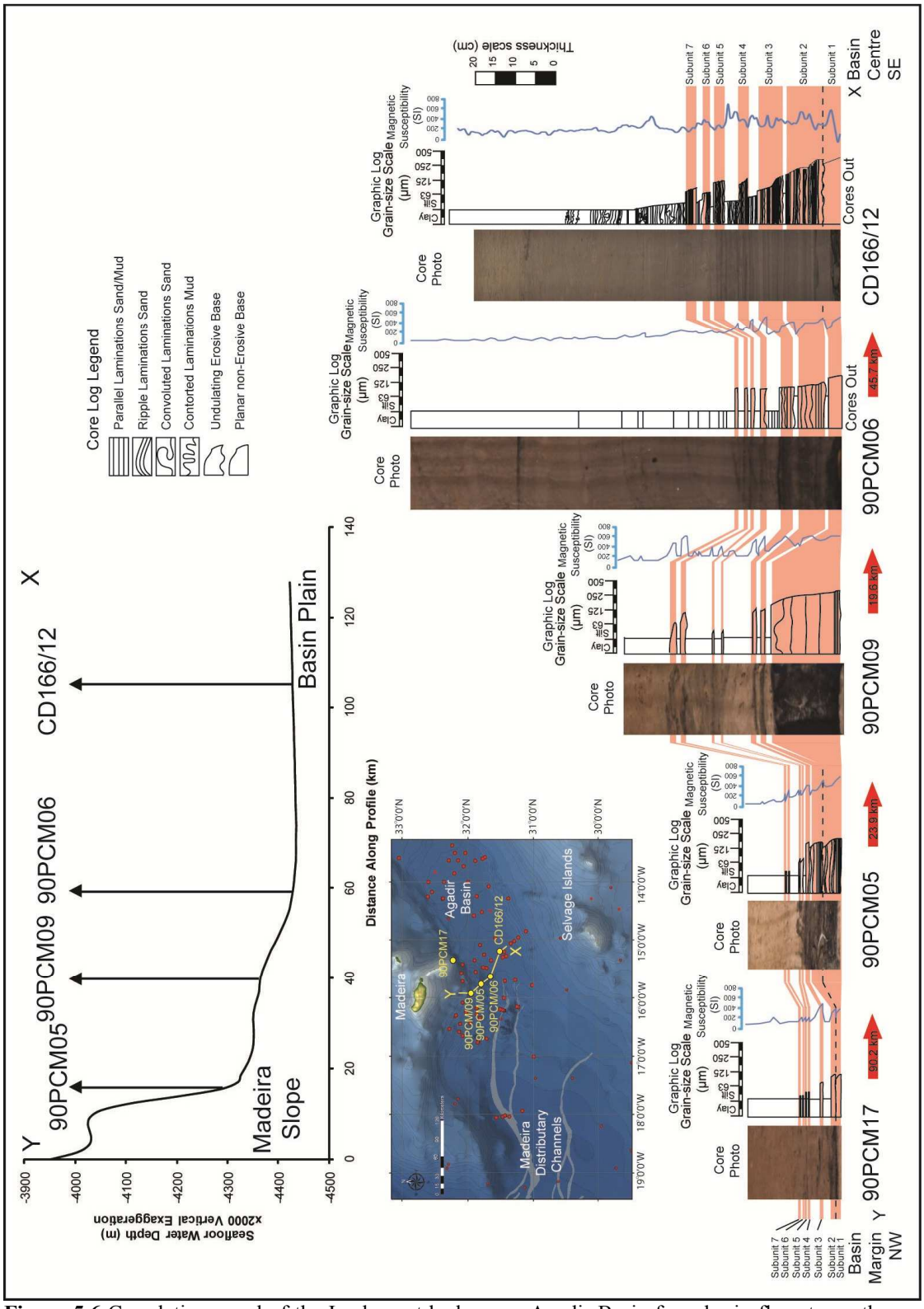

Figure 5.6 Correlation panel of the Icod event bed across Agadir Basin from basin floor to northern margin, showing interpreted core logs and petrophysical properties used for correlation. Inset bathymetric map shows that the panel (yellow line) runs perpendicular to flow direction, from southeast (basin floor) to northwest (northern basin margin). Core locations indicated by yellow circles. Cross-sectional profile shows seafloor gradient along the panel line. Red arrows indicate distance between core sites. Note the progressive thinning and fining of all seven subunits towards the basin margin.

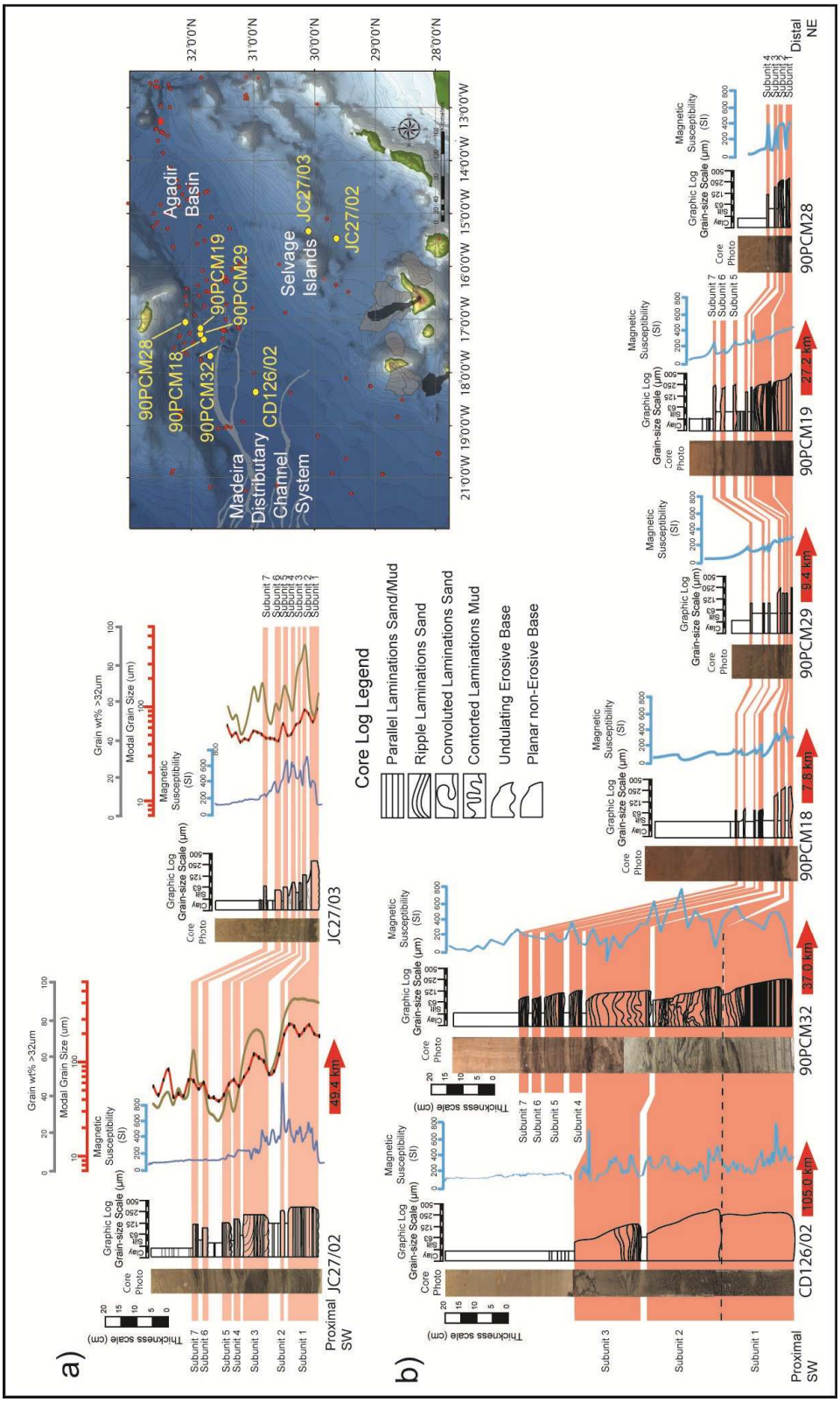

Figure 5.7 Correlation panels of the Icod event bed showing contrasting subunit facies. a) Correlation panel through cores JC27/02 and JC27/03, relatively proximal to source but located laterally to the Icod landslide and displaying a full sequence of subunits. b) Correlation panel through CD126/02 to 90PCM38 on the southern slopes of Madeira, immediately downflow of Icod landslide. Inset bathymetric map shows core locations (yellow circles). Red arrows indicate distance between core sites. Note the progressive thinning and fining of all seven subunits towards the basin margin.

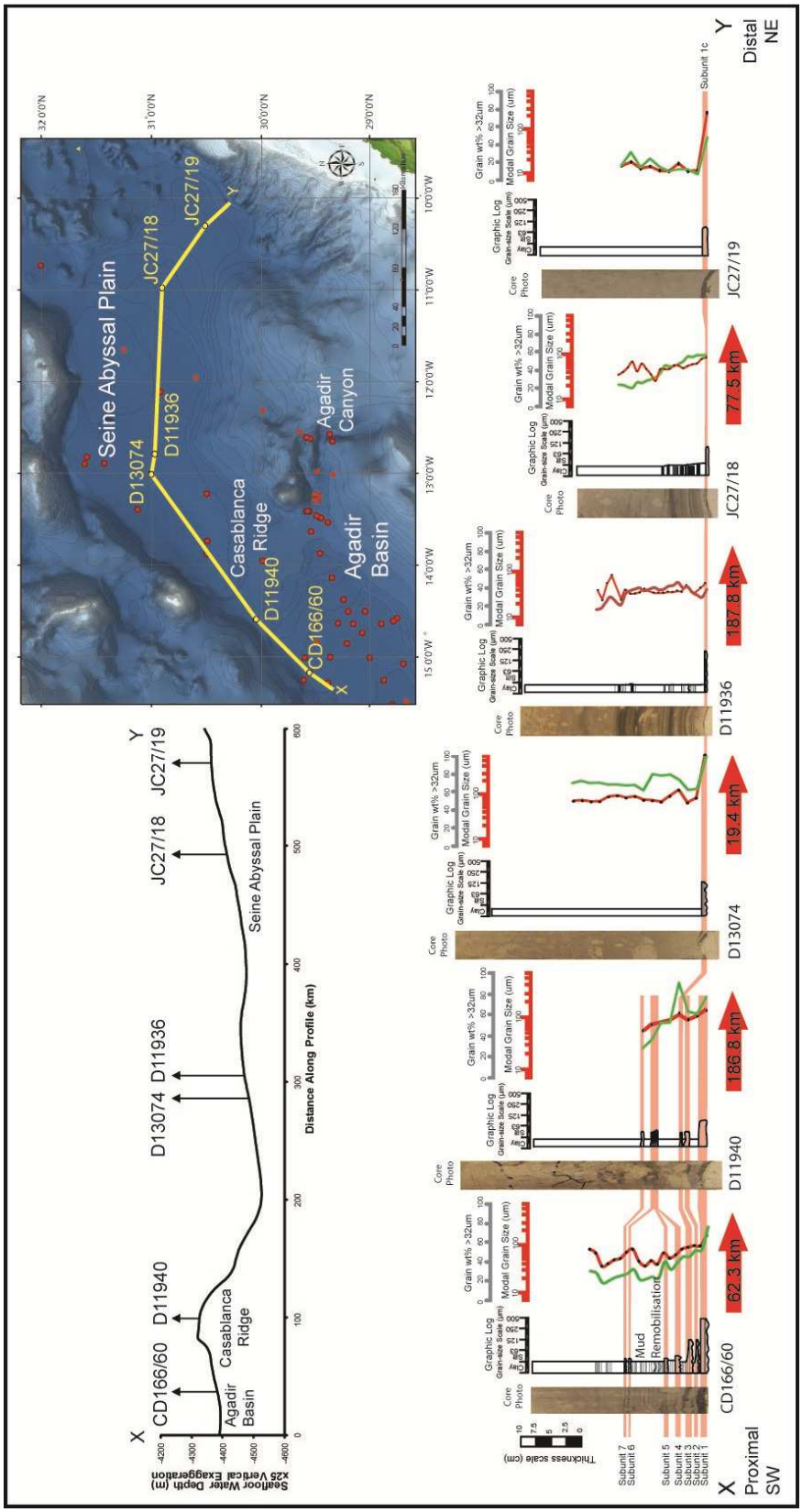

Figure 5.8 Correlation panel of the Icod event bed across eastern Agadir Basin and Seine Abyssal Plain, showing interpreted core logs and grain-size data. Inset bathymetric map shows that the panel (yellow line) runs parallel to flow direction, from west to east. Core locations indicated by yellow circles. Cross-sectional profile shows seafloor gradient along the panel line. Red arrows indicate distance between core sites. Note the loss of subunits across Casablanca Ridge, and the extensive runout across the almost flat Seine Abyssal Plain.

Cores within Agadir Basin that are more distal to source all show seven subunits in the Icod Event Bed, separated by intervening muds that represent suspension fallout. For example, cores from the basin margin (Figure 5.7) and northeast basin floor (core D13072 in Figures 5.4 and 5.8) contain sandy subunit bases separated by laminated silty muds, with no evidence for post-depositional remobilisation. Distally, the base of each subunit is generally planar, suggesting no basal erosion, although minor scouring or loading was noticed in core D13072 between SBU2 and SBU3. There is no evidence for bioturbation within these intervening muds, indicating that insufficient time has passed between subunit events to allow for recolonisation by benthic organisms. Stacked subunits in the Icod Event Bed are overlain by a turbidite mud cap (0.5-1.5 m thick), which was deposited after SBU7 (Figures 5.2 and 5.4 to 5.8).

Spatial extent of the Icod Event Bed and Volumes of Subunits

The Icod Event Bed was logged in 86 cores covering an area >355,000 km^2 within the Moroccan Turbidite System (Figure 5.1). The proximal flow pathway extends for 320 km from the northern flank of Tenerife to the floor of Agadir Basin and the upper Madeira Distributary Channel System. The flow that deposited the Icod Event Bed then spread laterally northeast through Agadir Basin and Seine Abyssal Plain, passing over essentially flat seafloor (average slope 0.02^o) for up to 860 km (Figures 5.4 and 5.8). However, no subunits are recognised in the Icod Event Bed in Seine Abyssal Plain, instead there is a single volcanic glass-rich sand overlain by 10 to 20 cm of laminated to structureless mud (Figure 5.8). The turbidity currents of the Icod Event Bed also flowed 1100-1300 km westwards onto the southwest Madeira Abyssal Plain. The flow entered the Madeira Abyssal Plain from the northeast via the Madeira Distributary Channel System, depositing the coarsest material in the northeast and fining towards the southwest. A ponded mud cap is found in the basin centre that thins towards the southwest. There is no evidence for the Icod Event Bed on the low-gradient slopes west and south of La Palma (Georgiopoulou, 2006).

The Icod Event Bed has a total volume of 210±20 km^3, which, in addition to the volume of 110±40 km^3 confined to the proximal landslide deposit (Masson *et al.*, 2002), produces a total deposit volume of 320±45 km^3. This maximum volume represents the volume of the original landslide plus sediment eroded from the seafloor by the turbidity current. The degree of seafloor erosion by the source landslide cannot be calculated accurately; however, an attempt was made to quantify the amount of erosion by the

turbidity current. This is calculated by comparing the thickness of hemipelagic intervals below the Icod Event Bed in a typical erosive (CD166/27) and non-erosive (CD166/18) setting. The maximum depth of erosion is 11.5 cm. If it is assumed that the average erosion depth is 50% of this value (i.e. 5.8 cm), and that this occurs over a proximal erosive area of ~105,000 km^2 (as defined by evidence of basal erosion from core), then it can be estimated that 6-7 km^3 of carbonate-rich hemipelagic sediment (70-80 wt% $CaCO_3$) was added to the flow due to seafloor erosion by the turbidity current. This addition of calcareous material is an order of magnitude less than the error of the total volume calculation. If the above assumptions are broadly correct and basin floor erosion contributes <10 km^3 to the turbidite deposit, then the remaining carbonate content (average 35%) of the Icod Event Bed is derived from material from the original landslide mass and slope erosion by the landslide. Based on an initial landslide volume of 310±60 km^3, the carbonate component of the turbidite can be estimated at 40-80 km^3 (average 65 km^3 at 35% carbonate content).

A perspective on the relative volumes of Icod Event Bed subunits can be gained from volumetric analysis of correlated subunits in Agadir Basin and Seine Abyssal Plain. The volumes of SBU1-3 are 33 km^3, 35 km^3 and 36 km^3 respectively, while intervals SBU4-7 have volumes of 8 km^3, 8 km^3, 9 km^3 and 8 km^3 respectively, with an error of ±2 km^3. By extrapolation of volume ratios from Agadir Basin to Madeira Abyssal Plain, the total volumes of each subunit (SBU1 to SBU7) are: 80 km^3, 85 km^3, 88 km^3, 19 km^3, 19 km^3, 22 km^3 and 19 km^3 respectively, with an error of ±6 km^3. This shows that the SBU1-3 intervals are the most volumetrically significant, being four times larger than SBU4-7.

Grain size data

Grain size data from multiple cores demonstrates important trends in subunit development. Along the axis of Agadir Basin each subunit becomes progressively finer-grained and thinner away from source (Figures 5.4 and 5.9a). In addition, individual subunits thin and fine from the centre of the basin towards both margins (Figures 5.5, 5.6 and 5.9b). The average basal grain size data also show a trend in the progressive vertical fining of subunit sands from SBU1 to SBU7 at any given site (Figure 5.9). The additional sand units in core CD166/26 (Figure 5.5) are an isolated occurrence, and as yet cannot be explained.

Petrophysical property variations within subunits

Petrophysical properties (p-wave velocity, gamma-ray density and magnetic susceptibility) and grain size data were used to aid identification of subunits and correlate them across Agadir Basin (Figures 5.4 and 5.5). Physical properties also differ between subunits, since they are strongly influenced by grain-size distribution (as shown by the example of CD166/27, which represents a typical Icod Event Bed deposit; Figure 5.2).

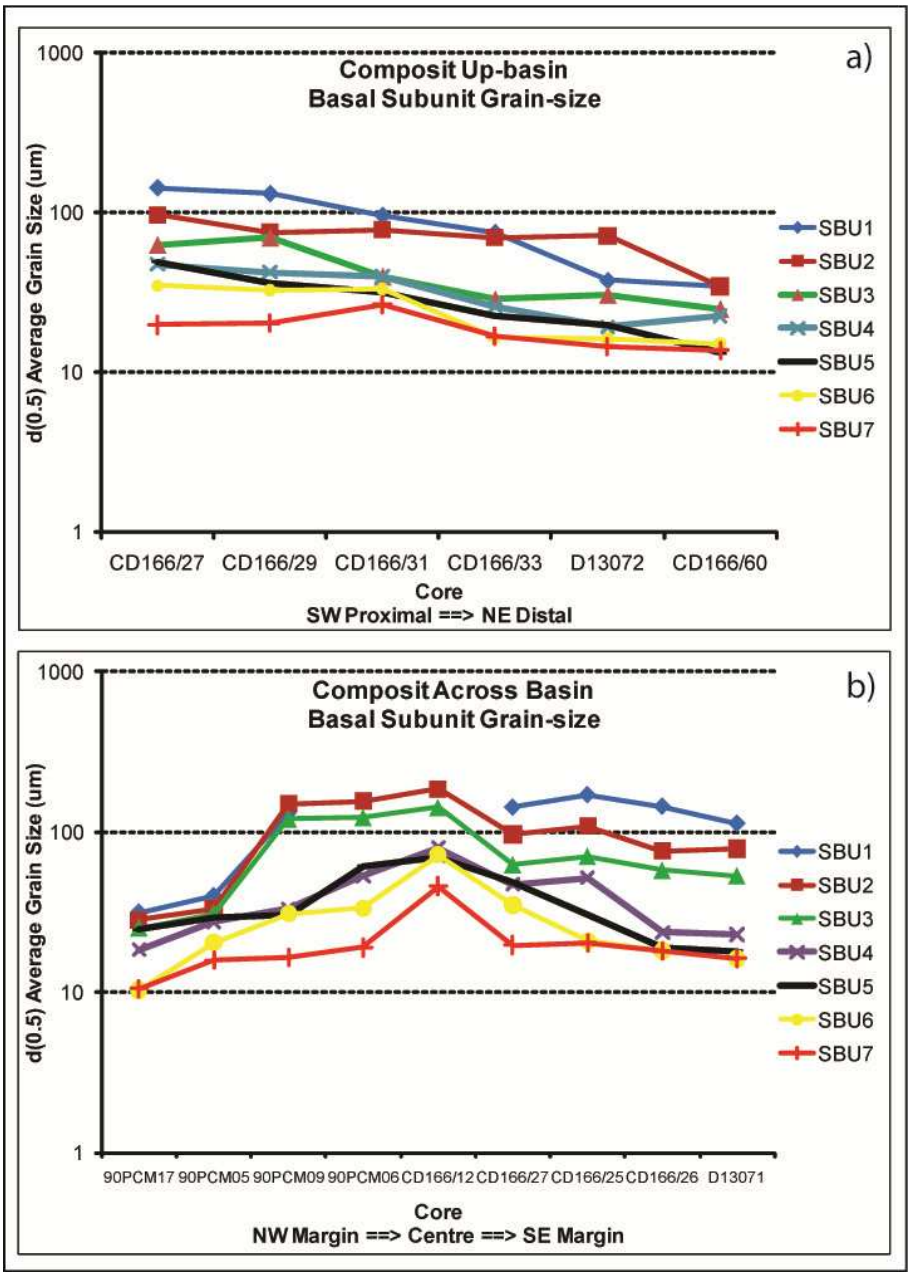

Figure 5.9 Subunit interval basal grain size analysis for the Icod event bed in Agadir Basin, along an axial (a) and across-basin (b) transect. Subunits are found to decrease in d0.5 average grain size away from source (a) and towards both basin margins (a). In both transects the subunits are seen to become progressively finer vertically from SBU1 to SBU7. Core locations are shown in figure 5.1 and core logs shown in figures 5.4 to 5.6.

Sand Fraction Petrography

The carbonate-free >63 μm fraction of the Icod Event Bed is composed primarily of volcanic glass and mafic volcanic lithic clasts, with minor loose grains of pyroxene, amphibole and alkali feldspars, and rarer phonolite-trachyte phenocryst-rich clasts (Figure 5.10). The proportion of volcanic glass increases from SBU1 to SBU7 (40-60 to 85-95 wt% respectively), while the proportion of mafic volcanic lithic clasts decreases from SBU1 to SBU7 (8-35 to 1-9 wt% respectively) (Figures 5.10).

Phonolite-trachyte phenocryst-rich lithic clasts are present in subunit SBU1 and reoccur in SBU7. Furthermore, except in proximal core JC27/02, clinopyroxenes and amphiboles occur only in SBU1-3 (Figure 5.10). Altered grains are lithics, volcanic glasses and minerals that have been subjected to chemical alteration and/or overgrowth of authigenic mineral phases. These grains have been previously identified in turbidites of the Madeira Abyssal Plain (Pearce and Jarvis, 1992). The restriction of altered grains to basal subunits SBU1-3 is an important observation (Figures 5.10 and 5.11), and delineates highlights two compositional groups: SBU1-3 (with altered glass/altered mafic lithics) and SBU4-7 (without altered glass/altered mafic lithics). Altered volcanic glass comprises 5-18 wt% of SBU1, decreasing in SBU2 and SBU3 to 4-12 wt% and 3-8 wt% respectively. This decreasing trend in altered grains is also a feature of the mafic volcanic clasts (Figure 5.10).

The presence of altered grains in the basal subunits (SBU1-3) and not in the upper intervals (SBU4-7) indicates that alteration is not a function of a diagenetic process acting on the turbidite deposit, but rather a function of a chemical process that acted on the material prior to initial failure and incorporation into the turbidity current. Two main alteration textures can be distinguished petrographically within the volcanic glasses: 1) a colour change from colourless to yellow-brown, and 2) generation of authigenic opaque minerals and clays.

The first texture is supported by SEM backscatter images showing variable densities across altered glass shards (Figure 5.11e). The second volcanic glass alteration texture is supported by SEM images from the TM1000 and LEO1450 VP SEM instruments. Grain surface images from the TM1000 show authigenic grains growing out of the volcanic glasses (Figure 5.11b and c). Furthermore, backscatter images and EDS analysis show cross-section images of volcanic glasses with high density Fe-Ti oxide grains present (Figure 5.11e and f). Grain boundaries of altered glasses are undulating with evidence for chemical disintegration and alteration rims, and often the altered glass contains clay-

filled cracks (Figure 5.11b and c). Alteration of mafic volcanic lithic clasts is shown by reddened Fe-oxide coatings.

The SEM backscatter contrast observations were also used for the identification and description of altered textures of volcanic glasses. As aforementioned these displayed 1) mottled density contrasts across the grain developed from mobilisation of elements, 2) undulating grain boundaries from chemical disintegration and 3) growth of high density authigenic Fe-Ti and Fe-Mn oxides. Altered glasses were only identified in SBU1-3 and were analysed to investigate elemental mobilisation. Unaltered phonolitic, altered and basaltic glasses identified in SBU1 in core JC27/02 were analysed separately to identify trends in altered glass derivatives by contrasting glass densities. However, this alteration has not resulted in a high degree of element mobilisation, with the altered glass compositions still following magmatic trends (Appendix 5.4 and 5.5).

In order to demonstrate that the exclusive presence of altered volcanic glass and lithics in basal subunits (SBU1-3) is not simply a result of density sorting, different grain size fractions were taken and analysed for their grain composition. The ratio of altered to unaltered glass in SBU1-3 was found to be nearly constant through a series of grain size ranges (63-90 µm, 90-125 µm and 125-250 µm) (Figure 5.10e-g). This implies that, although subsequent subunits have finer grain sizes, the altered glass would still be present if it had been part of the original composition. Therefore, altered glass is present in SBU1-3 but not in SBU4-7, and this distribution is not a function of density sorting.

Bulk ICP-OES Variations between Subunits

Bulk geochemical compositions for the Icod Event Bed were measured in all subunits from every core in Agadir Basin containing material >63µm. MgO values are highest in SBU1 and SBU2. Up-core decreasing trends in average MgO content are seen through SBU1-3 and from SBU4-7 (Figure 5.12 and Table 5.2). In addition, decreasing up-core trends are seen in the bulk major element concentrations of P_2O_5, CaO, TiO_2 and Fe_2O_3. Conversely, trends in Na_2O, SiO_2, K_2O increase from basal subunits (SBU1-3) to upper subunits (SBU4-7) (Figure 5.12 and Table 5.2).

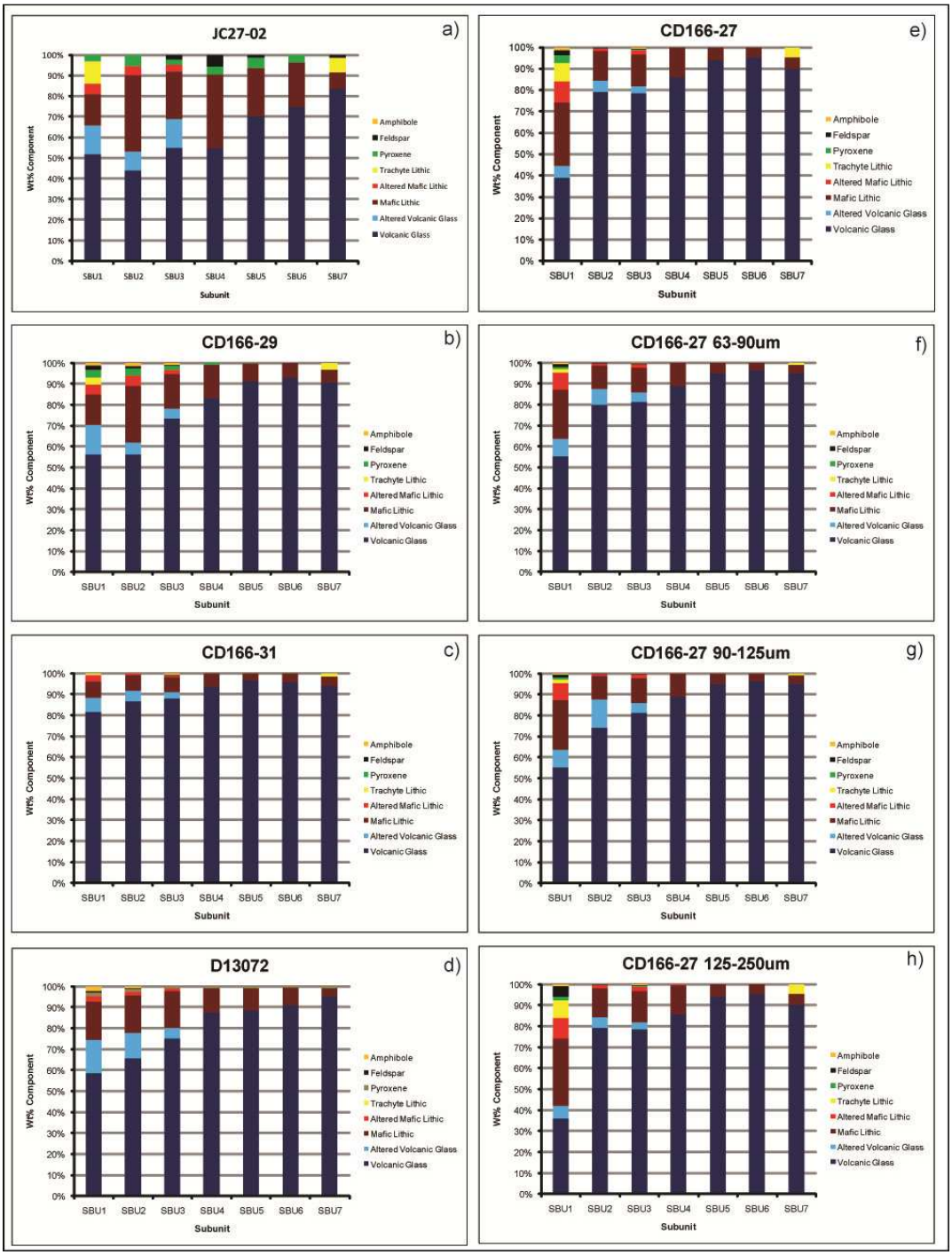

Figure 5.10 Petrographic charts of the Icod event bed showing mineralogical composition of subunit sand intervals at various core sites. Altered volcanic glass and altered mafic lithics are exclusively found in SBU1 to SBU3, while SBU4 to SBU7 are composed predominantly of unaltered glass.

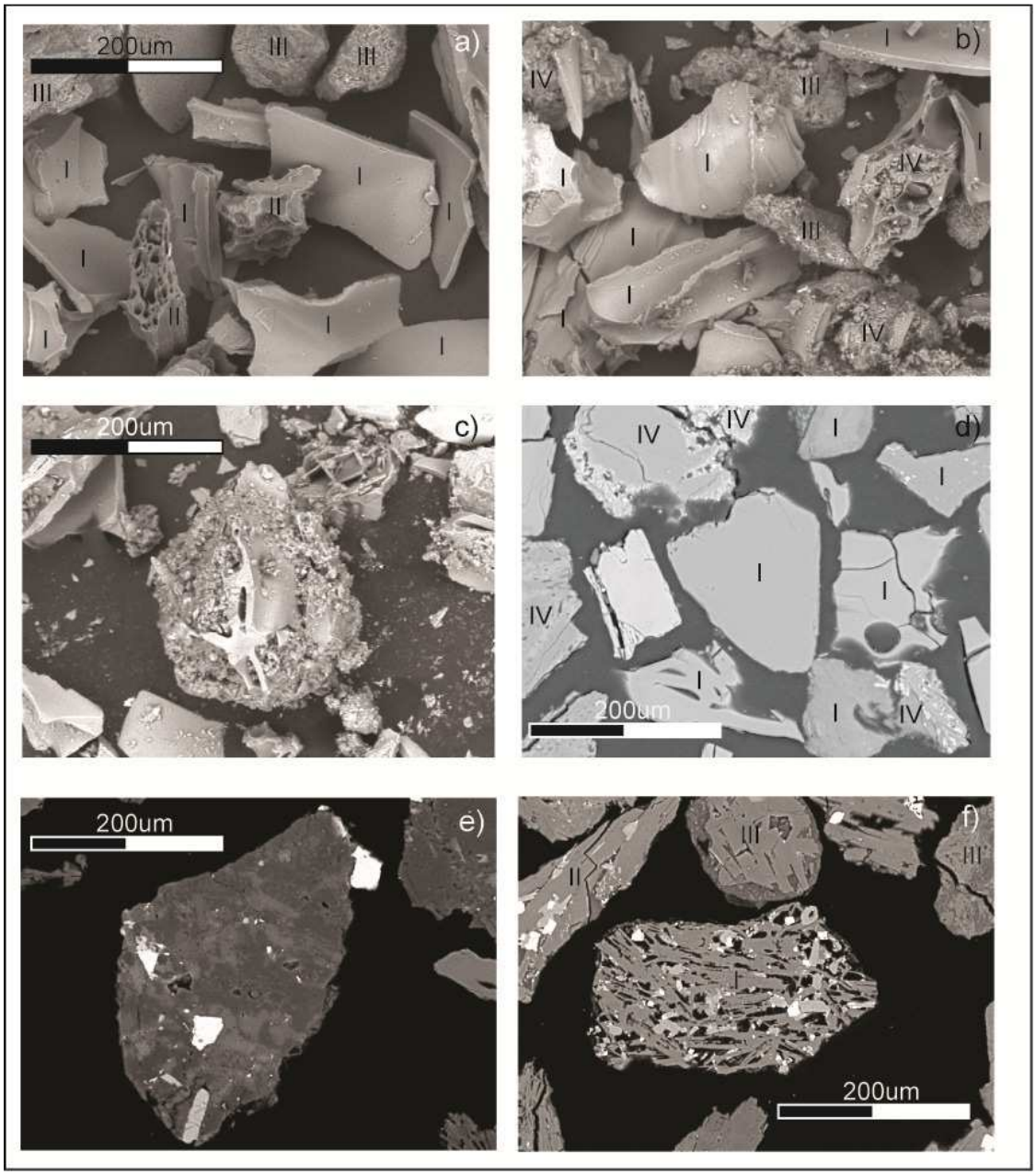

Figure 5.11 Grain images of volcanic glasses from the Icod event bed including: a) TM1000 SEM image of unaltered volcanic glass (I), pumaceous glass (II) and mafic lithics (III) from SBU4 of CD166/27, b) TM1000 SEM image of unaltered volcanic glass (I), mafic lithics (III) and altered glasses (IV) from SBU2 of JC27/02, c) TM1000 SEM image of altered volcanic glass in SBU1 of CD166/27, d) LEO1450 SEM image of unaltered volcanic glasses (I) and altered volcanic glass with alteration rims (IV) from SBU2 of JC27/02, e) LEO1450 SEM image of altered glass from SBU1 from JC27/02, f) LEO1450 SEM image of altered glasses from SBU1 from JC27/02 showing mottled density backscatter (III), filled fractures (II and III), undulating edges (II) and authigenic mineral growths (II) with a large lithic grain centre image (I).

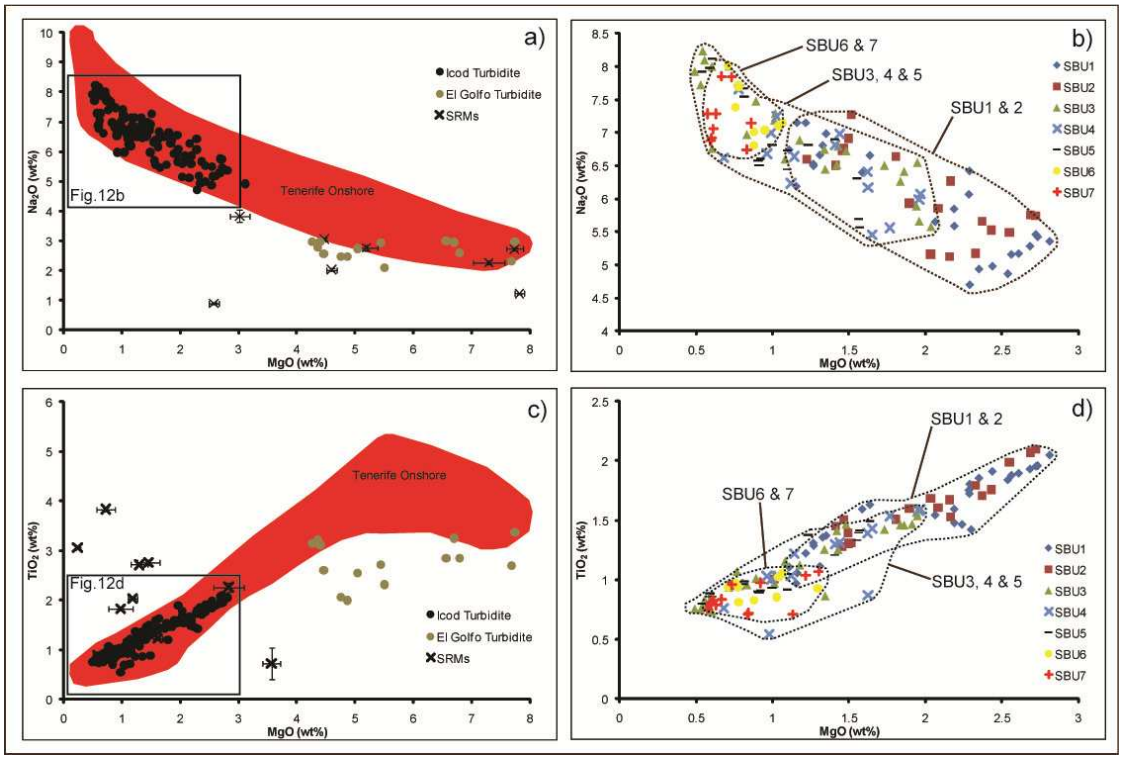

Figure 5.12 ICP-OES data from the Icod event bed demonstrating segregation of compositional fields for the subunits with MgO discriminator: a) MgO against Na_2O showing raw data from subunits, with onshore collated data for Tenerife and points associated with standard reference materials (SRMs) with percentage error bars; b) MgO against Na_2O showing raw data from subunits, showing delineation into three broad compositional groups; c) MgO against TiO_2 showing relation to onshore data and SRMs; d) MgO against TiO_2 showing subunit samples and delineation of three compositional groups. In regards to accuracy and precision the MgO measurements of SRMs produce standards deviations of 0.3-2.6%, while the results vary from the reference values by an order of 0.03-3.5%. Geochemical comparison can be made with the basaltic El Hierro source of the El Golfo turbidite. Tenerife onshore data from GEOROCS database.

Compositional fields in variation diagrams show relationships between subunits, dividing the subunits into three groups. Firstly, Na_2O, P_2O_5, CaO, TiO_2 and Fe_2O_3 indicate that SBU1 and SBU2 have broadly similar ranges. SBU3, SBU4 and SBU5 have more restricted ranges covering similar fields of concentration. Finally, SBU6 and SBU7 have similar compositional fields displaying further restricted ranges (Figures 5.12 and 5.13). Trace element concentrations also highlight variations between subunits. Successive subunits generally show decreasing Sc, V, Cr, Co, Cu and Sr (Figure 5.13), whereas concentrations increase in Zr and Ce from SBU1 to SBU7.

These results indicate that volcanic material in the Icod Event Bed has an overall phonolitic-trachyte composition that is consistent with a Tenerife source. Furthermore, the composition of each successive subunit has a progressively more evolved phonolitic signature. However, there appears to be a moderate correlation between increasing grain size and sediment immaturity, as shown by the increasing component of mafic volcanic

lithics in the coarsest sediment fractions (Figure 5.14). Since the bulk ICP-OES compositions are related to mineral composition, grain size could exert a partial control on mineral composition and chemistry (Figure 5.14). Thus, density sorting of different grain types could generate the observed disparities between subunit compositional fields. This demonstrates a requirement to look at compositional variation within a single grain type, namely the volcanic glasses as conducted by Garcia and Hull (1994) and Di Roberto *et al.* (2010).

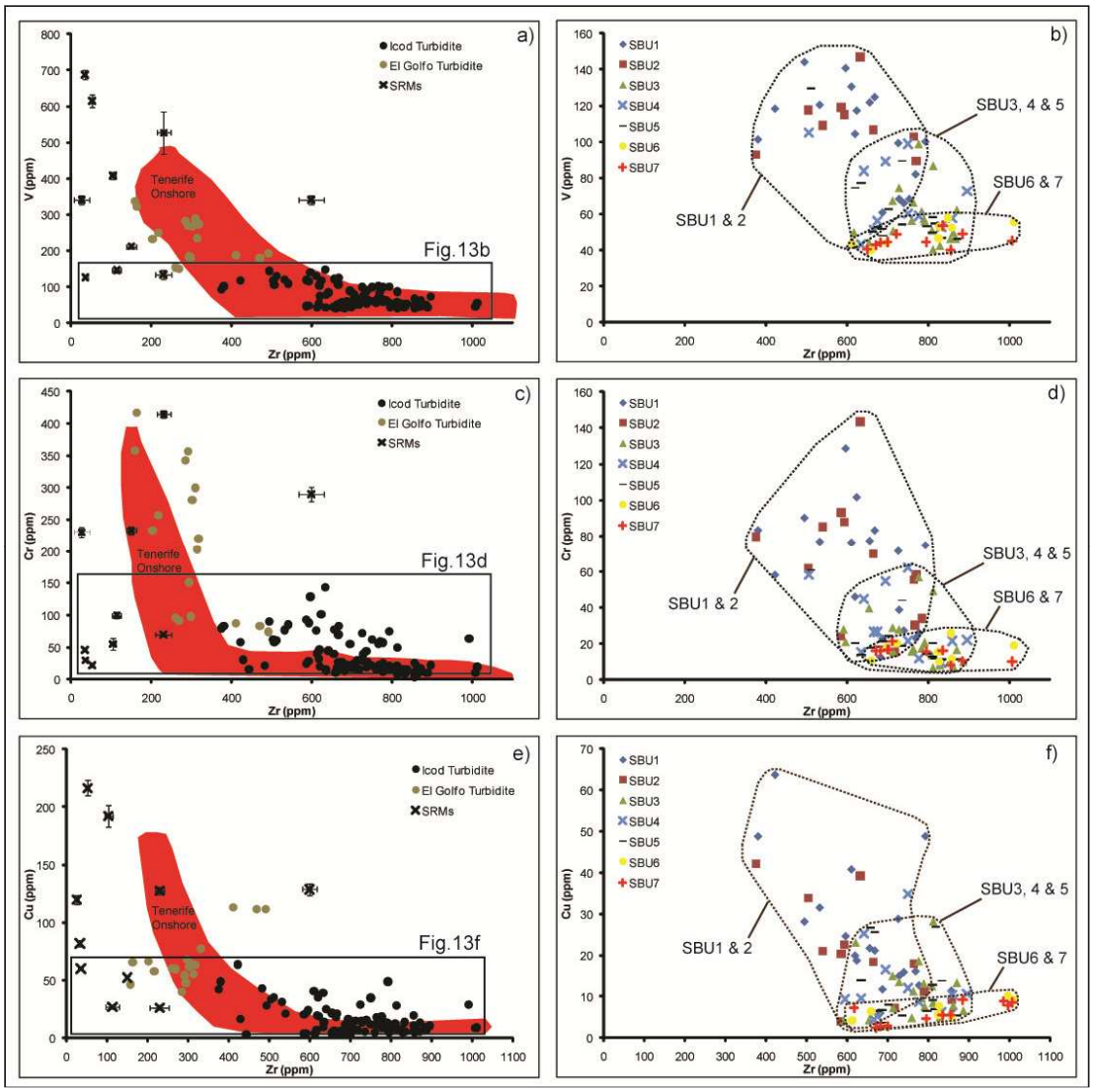

Figure 5.13 ICP-OES data from The Icod event bed demonstrating segregation of compositional fields for the subunits with Zr (ppm) discriminator: a) V (ppm) against Zr showing samples against onshore Tenerife, SRMs and El Golfo composition for comparison; b) V (ppm) against Zr showing three compositional groups for The Icod event bed; c) Cr (ppm) against Zr with onshore Tenerife, SRMs and El Golfo composition, d) Cr (ppm) against Zr showing two compositional groups for The Icod event bed; e) Cu (ppm) against Zr showing samples against Tenerife onshore, SRMs and El Golfo composition for comparison, f) Cu (ppm) against Zr showing three compositional groups in The Icod event bed. Note the contrast in the fractionated phonolitic-trachyte composition of The Icod event bed with the basic El Golfo turbidite composition from El Hierro.

Table 5.2 Summary table of bulk ICP-OES data for the major and trace elements in SBU1-7.

	SBU1		SBU2		SBU3		SBU4		SBU5		SBU6		SBU7		General Trends
	n=32		n=22		n=27		n=16		n=19		n=9		n=14		
	Min	Max	Min	Max	Min	Max	Min	Max	Min	Max	Min	Max	Min	Max	
TiO_2	0.69	2.07	0.75	2.09	0.21	1.78	0.54	1.60	0.80	1.41	0.66	1.06	0.71	1.07	Decreasing concentration
Al_2O_3	9.44	18.96	12.21	19.29	7.89	20.00	8.55	19.04	9.59	19.06	10.52	18.96	7.87	18.73	Decreasing concentration
Fe_2O_3	3.17	0.96	2.78	7.16	2.70	8.06	2.78	7.67	2.90	7.64	0.86	5.72	2.24	7.69	Decreasing concentration
MnO	0.13	0.29	0.14	0.21	0.03	0.31	0.10	0.22	0.13	0.37	0.14	0.25	0.08	0.24	No trend
MgO	1.04	3.12	1.22	2.72	0.49	2.04	0.68	1.97	0.54	1.62	0.71	1.49	0.58	1.33	Decreasing concentration
CaO	1.02	5.89	1.07	5.05	0.95	8.38	1.53	7.78	1.03	4.14	1.46	3.07	1.04	2.47	Decreasing concentration
Na_2O	6.80	7.14	5.13	7.21	1.51	8.65	3.98	7.66	5.57	8.11	4.94	8.01	3.15	7.85	Increasing concentration
K_2O	2.74	4.36	2.70	4.94	3.05	5.05	2.30	4.47	2.89	7.34	3.19	4.80	2.20	4.93	Increasing concentration
P_2O_5	0.09	0.77	0.02	0.76	0.05	0.54	0.12	0.72	0.13	0.61	0.13	0.34	0.11	0.26	Decreasing concentration
Li	11.39	25.23	14.93	24.80	10.26	26.26	12.33	28.10	16.73	43.02	15.69	24.45	16.00	28.70	No trend
Sc	1.25	19.92	1.56	15.94	0.98	6.99	1.95	6.60	1.43	7.92	1.52	3.89	1.29	13.27	Decreasing concentration
V	39.90	143.87	46.50	148.84	28.60	121.97	30.96	107.67	46.37	129.62	39.99	68.08	39.91	79.54	Decreasing concentration
Cr	3.65	128.49	8.33	143.48	6.87	61.61	9.44	62.03	11.43	63.61	10.14	40.38	7.92	31.72	Decreasing concentration
Co	3.17	27.96	3.16	22.12	1.30	14.09	1.50	11.48	2.56	14.53	1.83	12.61	1.70	12.91	Decreasing concentration
Ni	1.34	111.94	4.44	106.05	1.75	164.42	4.89	111.60	6.27	110.84	2.94	109.18	5.07	108.15	No trend
Cu	5.90	63.72	4.00	88.02	4.30	65.15	3.10	34.82	3.57	35.42	2.63	19.96	2.43	16.74	Decreasing concentration
Zn	91.91	160.50	53.28	155.40	42.69	140.38	58.41	137.86	96.04	212.25	71.22	128.98	25.06	133.70	No trend
Sr	112.67	750.95	141.71	693.51	87.40	425.67	112.87	718.31	88.76	911.96	82.65	280.87	55.71	405.61	Decreasing concentration
Nb			135.32	220.08					162.81	285.51	111.07	214.90	138.64	229.50	No trend
Y	23.02	37.82	21.01	36.89	6.30	42.58	20.56	35.22	25.05	67.16	24.20	37.21	17.58	37.41	Decreasing concentration
Zr	379.90	745.34	375.14	858.34	482.46	887.83	443.39	896.29	512.05	991.22	612.36	1011.95	428.32	1590.28	Increasing concentration
Ba	254.54	993.25	284.04	757.56	208.86	573.80	285.22	890.27	256.66	1043.12	247.56	513.44	205.26	720.47	No trend
La	61.49	119.28	58.89	118.97	83.27	143.88	64.38	114.58	71.02	263.09	79.29	120.48	64.55	119.30	No trend
Ce	3.46	156.31	5.33	166.23	2.68	245.94	8.23	197.49	4.54	237.64	6.15	200.41	5.59	166.03	Increasing concentration

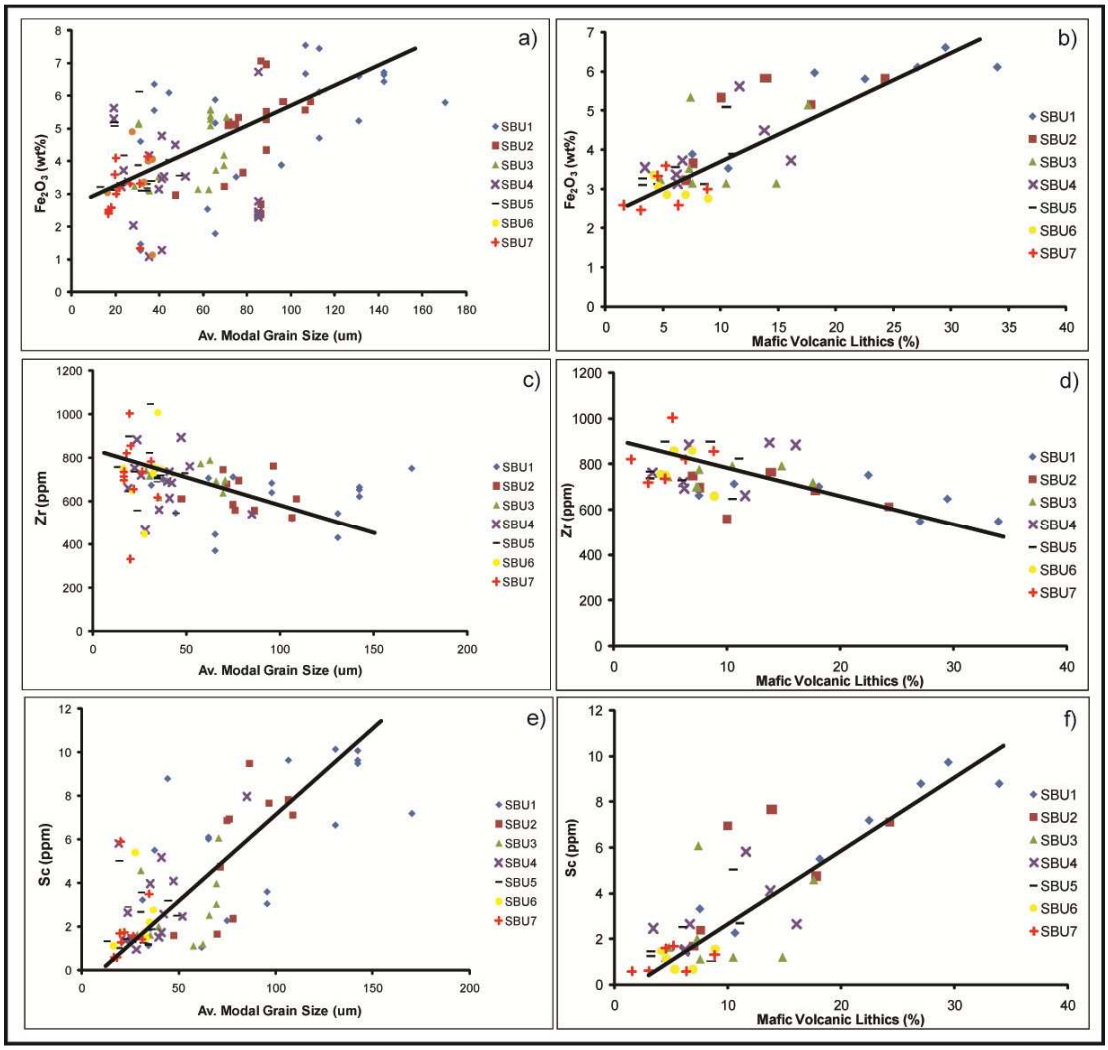

Figure 5.14 Geochemical plots for The Icod event bed showing partial control of density sorting on bulk geochemical signatures. These include: a) Fe_2O_3T wt% against modal grain size, b) Fe_2O_3T wt% against mafic volcanic lithics, c) Zr (ppm) against modal grain size, d) Zr (ppm) against mafic volcanic lithics, e) Sc (ppm) against modal grain size, and f) Sc (ppm) against mafic volcanic lithics. Plots show that grain size and percentage of mafic volcanic lithics have a weak control on the bulk geochemical composition for elements associated with basic compositions (Fe and Sc), while elements such as Zr are not affected.

SEM EDS Chemical Composition of Volcanic Glasses

The LEO1450 SEM EDS was used to assess samples from the Icod Event Bed subunits in core JC27/02, a proximal site but lateral to the main pathway of Icod landslide and turbidity current (Figures 5.1 and 5.8). The data shown in a total alkali-silica (TAS) diagram (Le Bas *et al.,* 1986) indicate that there are variations in the 90-125 µm unaltered volcanic glass populations within each subunit (Figure 5.15 and Table 5.3). Compositional classes defined here are: 1) phonolitic-alkali trachyte, 2) trachyandesite and 3) alkali basalt-basanite (Figure 5.15 and Table 5.3). All the glasses analysed fall into a compositional field for the Bandas del Sur Formation of the Cañadas III edifice (Bryan *et al.,* 2002).

SBU1 contains volcanic glasses with picro-basalt, trachy-basalt, trachy andesite and low-alkali high silica alkali trachyte compositions (Figure 5.15). SBU2 has volcanic glasses of picro-basalt composition, but these have higher alkalis (Na_2O+K_2O wt%) concentrations compared to those from SBU1 (Figure 5.15 and Table 5.3). SBU2 also has basalt-trachy-andesite and trachy-andesite glasses. SBU1 does not possess volcanic glasses of basalt-trachy-andesite composition as found in SBU2 (Figure 5.15 and Table 5.3). The trachy-andesite glasses of SBU2 are also generally higher in alkalis than SBU1. Neither SBU1 nor SBU2 have volcanic glasses of trachyte or phonolite composition (Figure 5.15 and Table 5.3).

SBU3 does not contain volcanic glasses of basic compositions. Indeed, the SBU3 volcanic glasses are amongst the most evolved analysed, between 61-66 wt% SiO_2 and generally >11 wt% alkalis (Figure 5.15 and Table 5.3). Although there is a minor trachy-andesite component, the SBU4 volcanic glasses are of predominantly phonolitic composition, with alkalis >10.5 wt% and silica 56-62 wt%. Furthermore SBU4 glasses possess the highest alkali contents 12.5-14.0 wt% (Figure 5.15 and Table 5.3). The SBU4 compositional range can certainly be differentiated from those of SBU3 and SBU5, with minor overlap with the compositions of SBU6 and SBU7. The volcanic glasses of SBU5 have a restricted composition similar to SBU3, with silica >60.5 wt% and alkalis >10.5 wt% (Figure 5.15).

SBU6 possess a number of basanite volcanic glasses, but predominantly comprises glasses of trachyte composition, with narrow ranges (60-63 wt%) of silica composition and total alkali compositions of 10-13 wt% (Figure 5.15). The volcanic glasses of SBU7 comprise a broad phonolite to trachyte range of composition, without glasses of basic composition. However, the SBU7 glasses are predominantly 9-12.5 wt% alkali and 56-62 wt% silica, and basic glasses are absent (Figure 5.15). The SBU7 glasses are found to have two compositional groups, with one more fractionated and with higher silica similar to SBU3 and the other with lower silica and lower alkalis similar to the El Abrigo ignimbrite (Figure 5.15b). Thus the volcanic glasses from core JC27/02 show disparities between the populations sampled in each subunit: geochemical variations that cannot be attributed to density or hydrodynamic sorting of the grains.

One further important result is that the composition of volcanic glass in the solitary sand interval in core JC27/19 from Seine Abyssal Plain is similar to the glass compositions of SBU3 in Agadir Basin (Figure 5.15). Seine Abyssal Plain glasses also

have an altered component, further supporting correlation with the Agadir Basin SBU3 interval.

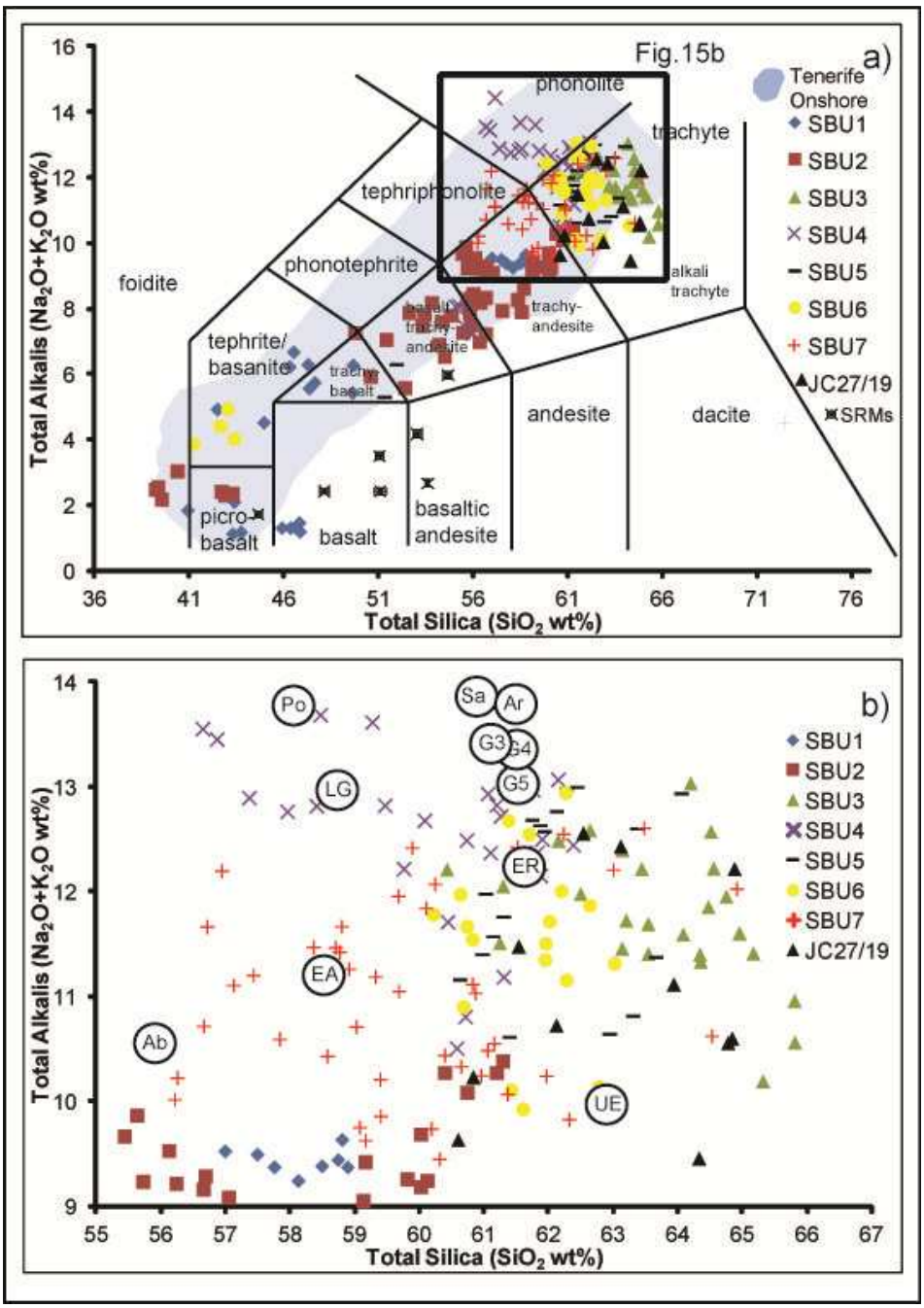

Figure 5.15 LEO1450 SEM EDS major element data for The Icod event bed from all seven JC27/02 subunits and the single unit in JC27/19: a) TAS diagram of volcanic glasses showing separate glass populations for each subunit; b) Phonolite-trachyte glasses from Figure 15a expanded to better illustrate the segregation of glass compositions. Onshore Bandas del Sur unit average composition: EA = El Abrigo, Po = Poris, LG = Lower Grey, G3-5 = Granadilla 3-5, Ab = Ablades, ER = El Rio, Ar = Arico, UE = Unit E, and Sa = Saltadero (Bryan et al., 2002). For these analyses the two standard reference materials (BIR-1g and BRR-1g) showed standard deviation on repetition of 0.11 wt% for NaO_2+K_2O and 0.20 wt% for SiO_2.

Biogenic Carbonate Content of Subunits

The basal subunit (SBU1) has the highest content of biogenic carbonate (22-54 wt%) of all the Icod subunits (Figure 5.2). This results from the high content of foraminifera and pelagic calcareous muds within this interval. Biogenic carbonate is present in the SBU2 and SBU3 intervals but in lower concentrations (19-36 wt% and 16-34 wt% respectively). The upper subunits (SBU4-7) show further reductions in biogenic carbonate (11-19 wt%). The uppermost mud cap displays a higher concentration of biogenic carbonate (30-34 wt%) due to the high coccolithophore content of the fine-grained sediment, deposited from suspension after emplacement of the coarser subunit sands.

Discussion

Origin of the Subunit Facies in the Icod Event Bed

There are several mechanisms through which the observed subunit facies can be developed: 1) multistage failure, 2) flow reflection, 3) simultaneous turbidity currents from multiple sources, 4) 'near-simultaneous' turbidity currents from a single source travelling long distances at different velocities, 5) multiple feeder channels, 6) eddying/pulsing flow and/or internal waves. By targeting cores in Agadir Basin the multiple feeder channel mechanism can be discounted, as there is no evidence for channels between the northern flank of Tenerife and Agadir Basin (Figure 5.1). Eddying/pulsing flow and internal waves are discounted due to the length scale of the spatial distribution of individual subunits (Figures 5.4 to 5.6) and lack of significant basin floor and margin topography (Wynn *et al.,* 2002a), although they may be important at a local level. For example, an interesting anomaly is observed at site CD166/26, whereby additional 15 fine silt intervals are found in the Icod Event Bed. This appears to be a localised phenomenon as it is not observed in adjacent cores. A speculative explanation for the additional intervals at this site is internal wave generation, possibly due to interaction with the break in slope or the sediment wave field upslope of this location.

Table 5.3 Summary table of SEM EDS Volcanic Glass Analysis

	Phonolitic-Alkali Trachyte	Trachyandesite	Alkali Basalt-Basanite
SBU1 (N=25)	None present.	Restricted composition 57-59 wt% silica and 9.3-9.9 wt% alkalis. Also have glasses of trachy-basalt composition.	Picro-basalt composition with low silica (41-46 wt%) and low alkalis (1.1-1.3 wt%). Also have tephrite/basanite composition.
SBU2 (N=51)	None present.	Similar to SBU1 with 55.5-57wt% silica and 9.1-9.8 wt% alkalis. Also have glasses of trachy-basalt composition, but more evolved than SBU1.	Picro-basalt composition with low silica (41-43 wt%) and low alkalis (1.1-1.3 wt%), more evolved than SBU2.
SBU3 (N=26)	Fractionated composition with 61-66 wt% silica and 11.2-12.8 wt% alkalis.	None present.	None present.
SBU4 (N=32)	Broad phonolite-trachyte composition with 10.5-14wt% silica but reduced alkalis compared to SBU3 (58-63wt%).	Restricted trachy-andesite composition to 55.2-55.9wt% silica and 7.2-8.0wt% alkalis.	None present.
SBU5 (N=38)	Composition between SBU3 and SBU4 with 60.5-63.5wt% silica but restricted alkalis (11-13wt%).	Trachy-basalt/andesite composition with 50-52 wt% SiO_2 and 5.5-6.2 wt% alkalis.	None present.
SBU6 (N=25)	Restricted composition similar to SBU3 and SBU5, with silica >60 wt% and alkali 10 wt%.	None present.	Tephrite/basanite composition with 41-43.5wt% silica and 3.8-4.9wt% alkalis.
SBU7 (N=46)	Comprises two groups of more evolved composition similar to SBU3 and a group with similar composition to the El Abrigo ignimbrite with 10-12wt% alkalis and 59-60wt% silica.	None present.	None present.
JC27/19 (N=12)	Similar composition to SBU3.	None present.	None present.

Bulk and volcanic glass geochemistry highlight Tenerife as the single source, ruling out earthquake-triggered multiple source failures (Figures 5.12, 5.13 and 5.15). For example, a comparison of the Tenerife trend (from the Icod Event Bed) and that of El Hierro (from the ~15 ka El Golfo turbidite) demonstrate clear differences in these two sources (Figures 5.12 and 5.13). Furthermore, there have not been any significant failures (>10 km^3) mapped around the other Canary Islands in the 0-200 ka period (Masson *et al.,* 2002). The remaining possibilities of flow reflection, multiple flows of different velocities, and multistage failure are assessed below on the basis of geochemistry, petrography and basal grain size distributions.

The subunit facies of the Icod Event Bed in Agadir Basin consists of a series of seven vertically stacked, fining-upwards volcaniclastic sands separated by erosive surfaces and/or mud intervals (Figure 5.2, 5.4, 5.5 and 5.6). Correlation panels and basal grain size data show laterally continuous subunits that progressively thin and fine away from source and towards the basin margins (Figure 5.9). If subunit sands were the product of flow reflection then basal grain size would show a reversed trend in these transects crossing the basin margin, resulting from outward flow travelling up the margin away from source and reflected flow returning back to the basin towards source.

It is possible that a single Icod landslide triggered a series of 'near-simultaneous' turbidity currents, and that each successive flow simply travelled across distances of 300-500 km more slowly than its predecessor. This could produce the observed grain-size distribution in the Icod Event Bed subunits, which consistently show vertical fining of each progressive subunit at each site. However, successive subunits also show compositional heterogeneities in petrology, bulk geochemistry and volcanic glass geochemistry (Figures 5.12, 5.13 and 5.15). If a single source landslide was responsible for generating essentially synchronous turbidity currents flowing at different velocities, then subunit composition would be expected to show greater uniformity.

A multistage failure can therefore be inferred because it has been demonstrated that the seven subunits, although all indicating a Tenerife source, are petrographically and geochemically distinct. The trends observed could be attributed to: 1) progressive failing of the phonolitic complex of the Cañadas III volcano with spatial control on material composition, or 2) differing mixtures of mafic volcanic lithics, trachyte lithics and phonolitic glasses reflecting changes in geochemical composition resulting from density sorting during turbidity current transport. The former can only be demonstrated if the latter can be eliminated. With regards to mineralogy, altered volcanic glasses

occur in the SBU1-3 intervals but are absent in SBU4-7, showing two distinct compositions and at least two phases of failure as a result. This is not a function of density sorting because glass particles of similar sizes were analysed for all subunits (Figure 5.10).

Furthermore, discrete bulk chemical compositional fields can be produced for each subunit, allowing three bulk geochemical compositional groups to be delineated: i) SBU1-2, ii) SBU3-5, and iii) SBU6-7 (Figures 5.12 and 5.13). However, relationships between bulk density, magnetic susceptibility and geochemistry show a partial control of density on mineralogy and geochemical compositions (Figure 5.14). For this reason, further study of geochemical differences between subunits focused on grains of similar hydrodynamic properties, namely the unaltered volcanic glass in one proximal core lateral to Icod landslide (JC27/02). The unaltered 90-125 μm phonolitic-trachyte volcanic glasses from each subunit in this core show a progressive increase in silica and alkali content (Figure 5.15). Generally the populations of glasses analysed delineate three groups similar to the bulk ICP-OES geochemical data: i) SBU1-2, ii) SBU3-6 and iii) SBU7. This suggests a failure that progressively evacuated material from the northern flank of the Cañadas III complex.

Volumetrically, there is a progressive decrease in the volumes of the initial failures (80-88 km^3 each in SBU1-3) compared to the later failures (19-22 km^3 each in SBU4-7). At all core sites in Agadir Basin the basal grain size in each successive subunit decreases, indicating that the energy and velocity maintaining coarse material in suspension has reduced for each subsequent turbidity current. This would support a retrogressive failure mechanism where each subsequent failure is of smaller magnitude.

Subaerial and/or Submarine Origin for Landslide Material

It is important to deduce the position of the initial landslide relative to sea level, since this will strongly influence tsunamigenesis (Fine *et al.,* 2003; Belotti *et al.,* 2006; van Nieuwkoop, 2007). The Fe-Ti and Fe-Mn oxides and clays generated during palagonitisation of the volcanic glasses in SBU1-3 suggest alteration in an oxic shallow marine environment prior to the Icod landslide event (Velde, 1995); this is supported by excess smectite in the Icod Event Bed mud cap (Pearce and Jarvis, 1992, 1995).

SBU1-3 have higher carbonate contents compared to SBU4-7. This is represented by abundant laminae containing reworked foraminifera. The co-occurrence of altered (palagonitised) glass, altered lithics, and biogenic carbonate with unaltered volcanic

glass and mafic lithics in SBU1-3 indicates that the landslide that formed these subunits had both a subaerial and submarine component. Two landslide mechanisms therefore appear possible for the initial failure: 1) an initial subaerial failure that eroded surficial marine sediments from the island flank (e.g. Ablay and Hürlimann (2000)), or 2) an initial failure that included both subaerial and submarine components of the island flank. The former seems unlikely because, to account for the ~65 km^3 total volume of marine carbonate material in the Icod Event Bed, the landslide and turbidity current would have had to be exceptionally erosive. The turbidity current has been estimated to contribute only 6-7 km^3 of carbonate material from basal erosion in the basin, which is over an order of magnitude less than the total deposit carbonate volume. Alternatively, for the landslide alone to contribute the carbonate component by erosion would require an average of 38 m of erosion beneath the debris avalanche deposit.

A submarine component to the initial failure is further supported by volumetric information. Coppo *et al*. (2009) calculated a minimum volume of the Icod landslide onshore as 100 km^3; the volume of 320±60 km^3 from this study is significantly in excess of this. However, Coppo *et al*. (2009) calculated a maximum of 500 km^3 when speculatively including an offshore component with a glide plane of constant 12° dip. It is suggested in the present study that the incorporation of a submarine component is a requirement for mass balance of the overall Icod landslide and the high carbonate content of the Icod Event Bed.

It is proposed that the high carbonate content of SBU1 (22-54 wt%) in the Icod Event Bed relative to SBU2 and SBU3 (16-36 wt%) results both from initial failure of submarine flank hemipelagic cover and the flow passing over an easily eroded unconsolidated seafloor. Erosive removal of the least consolidated sediment and the possible deposition of a coarse volcaniclastic lag by the SBU1 turbidity current may have limited seafloor erosion by SBU2 and SBU3. The increasing proportion of fresh volcanic glass of subaerial origin from SBU1 to SBU3 indicates a landward retrogressive migration of the landslide source area (Figure 5.10), a trend that continues through SBU4-7. In addition, the absence of altered volcanics, low biogenic carbonate and high amounts of volcanic glass from the upper subunits SBU4-7 indicate that these deposits were derived entirely from subaerial landslides of predominantly pyroclastic material.

Based on the above information, we propose a multi-stage retrogressive failure model for Icod landslide (Figure 5.16). Phases 1-3 involve large-scale failure of the

submarine and subaerial flank of north Tenerife (Figure 5.16a), primarily involving phonolitic lavas, basalt and trachyte lithics and glass in addition to carbonate materials. Furthermore, the landslide and turbidity current eroded the seafloor on the island slopes. The landslide headwall gradually migrated landwards during the much smaller failures of phases 4 and 5 (Figure 5.16b), with a larger proportion of onshore pyroclastic debris incorporated. Phases 6 and 7 acted to further stabilise the headwall, removing only subaerial pyroclastic cover (Figure 5.16c). The occurrence of a retrogressive failure is supported by a model from Acosta *et al.* (2003), modified from Jacobs (1995) and De Paolo *et al.* (2001). Here the individual failures are partitioned by horizontal layers, such as volcanic intrusions, massive basaltic flows or transition zones between basaltic and glassy flows (Acosta *et al.,* 2003).

There is ongoing debate as to whether the Las Cañadas caldera wall represents the Icod landslide headwall or a vertical collapse caldera (Marti *et al.,* 1994, 1997; Watts and Masson, 1995; Anconchea *et al.,* 1999; Marti and Gudmunsson, 2000; Bryan *et al.,* 2002). The coincidence of the caldera-forming El Abrigo eruptions with volumes >20 km^3 (Bryan *et al.,* 2002; Edgar *et al.,* 2007) and the Icod landslide event cannot be dismissed. In addition, glasses of El Abrigo composition (Bryan *et al.,* 2002) have been found in SBU7 but not in basal subunits SBU1-3 and upper subunits SBU4-6 (Figure 5.15). The El Abrigo eruption deposited material over a broad area (Edgar *et al.,* 2007), so material from this eruption should be incorporated into all stages of the flank collapse event should the eruption pre-date the landslide. The lack of El Abrigo material in the initial SBU1-3 and later SBU4-6 events suggest that these subunits, and thus the bulk of the Icod landslide, predate the El Abrigo eruption and that the landslide could therefore have been the trigger for the El Abrigo eruption itself. El Abrigo material is present in SBU7. The occurrence of the SBU7 event after this eruption could be the result of renewed flank destabilisation following vertical caldera collapse (Hürlimann *et al.,* 1999).

Relationship between Distal Turbidite and Proximal Landslide Deposits

The recognition that the seven Icod Event Bed subunits represent seven discrete failures of the source landslide supports the conclusions of earlier studies implying a multistage event (Watts and Masson, 1995, 2001; Ablay and Hürlimann, 2000; Wynn and Masson, 2003). The proximal landslide deposits have been recognised to contain at least three recognisable lobes that could be the result of a multistage event (Figure 5.3; Watts and

Masson, 1995, 2001; Ablay and Hürlimann, 2000). Ablay and Hürlimann (2000) identified three depositional lobes in the landslide deposit (Ic^{1a}, Ic^{1b} and Ic^{2}) fed by a primary channel (Ic) and two subsidiary channel (Ic^{s1} and Ic^{s2}), These erosive and depositional features could correspond to the three basal and most substantial subunits (SBU1-3). Watts and Masson (2001) recognised at least two stages of failure in sidescan sonar data from Icod landslide, and subsequent work appears to confirm the presence of three depositional lobes (Figure 5.3) (Ablay and Hürlimann, 2000). The multiple lobes and number of erosive channels support the hypothesis of a multistage landslide, rather than a single failure. However, these morphological data provide no evidence of the time period over which these multiple failures might have occurred. In addition, Watts and Masson (2001) and Wynn *et al.* (2002b) documented sediment waves overlying the landslide from sidescan sonar, indicating that later turbidity currents had flowed over this area. The present study suggests that these sediment waves could result from the later smaller and more dilute events corresponding to the SBU4-7 subunits.

The exact mechanism for turbidity current generation from each stage of Icod landslide is unknown. It is possible that seafloor loading by successive landslides led to subsequent failure and generation of multiple turbidity currents. However, the latter mechanism would result in material from the submarine volcaniclastic apron being incorporated into each flow, much of which is probably carbonate-rich hemipelagic material. To incorporate the observed high volumes of volcaniclastic material, disaggregation of an originally volcaniclastic-rich mass is required. In addition, volcanic glass geochemistry indicates that materials of predominantly Diego Hernandez formation were incorporated into each subunit of the Icod Event Bed, rather than random assortments of material from the submarine volcaniclastic apron. It therefore seems more likely that direct disaggregation of successive landslides, and mixing with ambient seawater, is the mechanism by which dilute turbidity currents were generated.

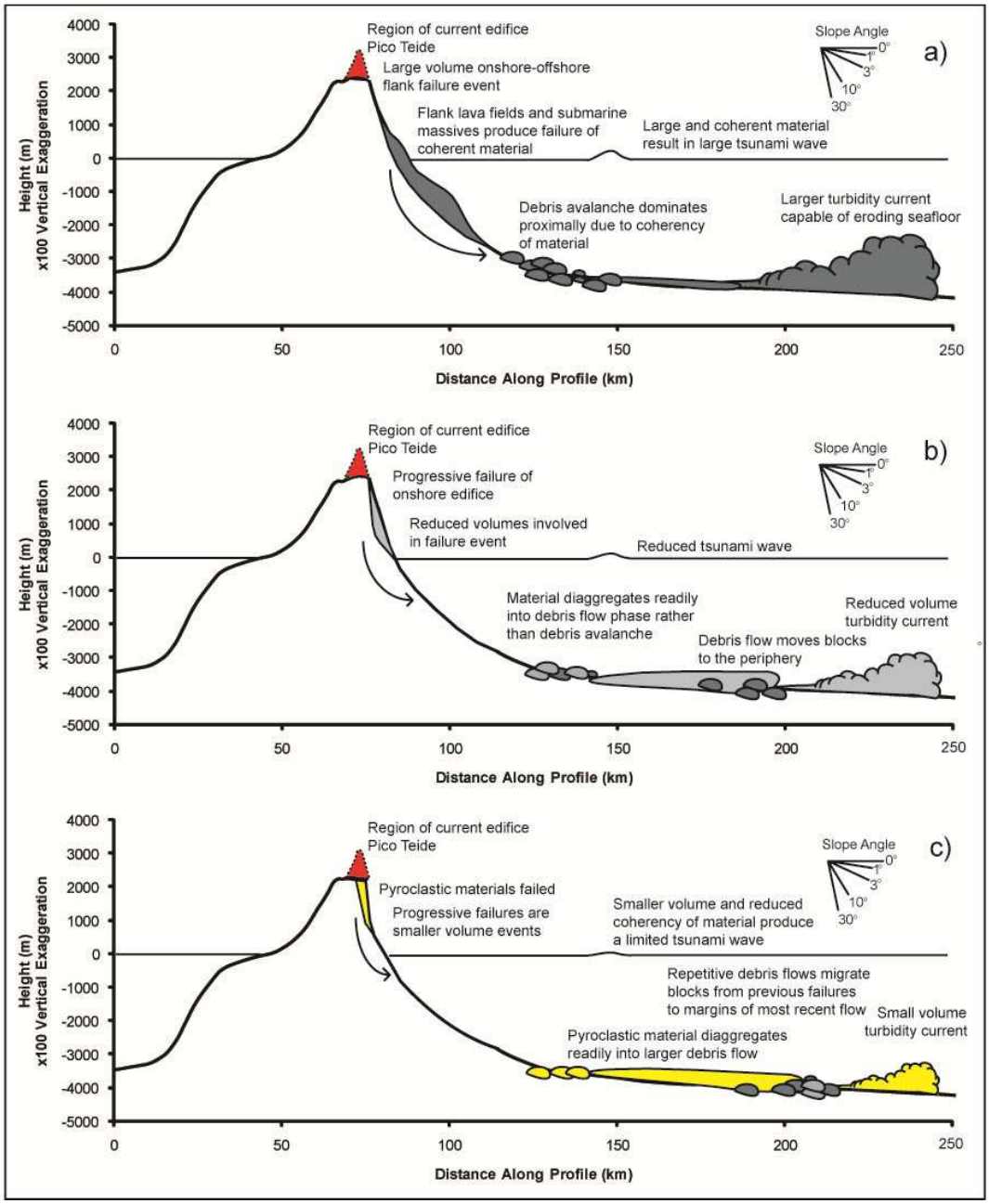

Figure 5.16 Retrogressive failure model for the Icod landslide event: a) initial subaerial-submarine failures representing SBU1-3 events, b) migration to subaerial failures representing SBU4-5 events, and c) migration to failure of edifice and pyroclastic deposits representing events SBU6-7. Model produced using GEBCO bathymetry to generate a 2D profile of the current northern flank of Tenerife.

Implications for volcanic island landslide tsunamigenic potential and modelling

The elongate morphology of Icod landslide and distribution of blocky and finer material suggest that the landslide was rapidly disaggregated and transported under debris flow conditions, implying that coherency of the initial landslide block was low (Masson *et al.*, 2002). This has implications for tsunamigenic potential, whereby failure of poorly cohesive Icod material composed of layered pyroclastics and phonolitic lavas would lower tsunami magnitude, relative to that produced by a single coherent block (Murty,

2003). Invoking a multistage retrogressive failure for Icod landslide, based on study of the associated turbidite, also has major implications for tsunami generation. Compared to a single large landslide, retrogressive failure of the Icod landslide would contribute reduced volumes (basal subunits SBU1-3 each ~25% and upper subunits SBU4-7 each ~6%) of material to each individual landslide. This would produce several tsunamis of reduced magnitude relative to a single large slide generating a mega-tsunami. This is because landslide volume is a key control on tsunami magnitude (Harbitz *et al.,* 1993, 2006; Murty, 2003).

Previous models of Canary Islands landslide tsunamis have used initial slide volumes of up to 500 km^3 to simulate the landslide and associated tsunami (e.g. Ward and Day, 2001). This large volume is crucial in constraining the size of a theorised pan-Atlantic catastrophic mega-tsunami sourced from La Palma. Icod landslide has a total volume of 320±60 km^3, which is 180 km^3 less than the 500 km^3 used for the proposed future Cumbre Vieja collapse. However, the findings of the present study demonstrate that this large volume is distributed over several smaller events with SBU1-3 each containing ~25% of the volume (80-88 km^3) and SBU4-7 each containing ~6% (19-22 km^3). Thus, the maximum subunit volume of ~90 km^3 is <20% of the maximum volume used in the aforementioned tsunami model. Previous work has indicated that the most recent landslide on the Canary Islands (El Golfo at ~15 ka) also failed in multiple stages (Wynn and Masson, 2003; Masson *et al*., 2006). It may be reasonable to assume that future landslides in the archipelago will exhibit similar behaviour.

Geochemical analysis of the Icod Event Bed indicates that the initial subunits (SBU1-3) had both a submarine and subaerial component, while SBU4-7 were probably subaerial failures. The nature of the tsunami wave can be strongly influenced by the initial position of the landslide body (Fine *et al*., 2003). Subaerial landslides generate higher amplitude tsunamis due to the displacement of water on entering the ocean and greater length scale of slide deformation (Fine *et al.,* 2003). This is because a subaerial failure will produce a frontal wave of greater magnitude compared to a submarine failure, due to the longer path in shallow water and greater displacement of water at high velocity (Fine *et al.,* 2001, 2003; Belotti *et al.,* 2006; van Nieuwkoop, 2007). A submarine failure produces a negative depression behind the landslide mass as sea water acts to fill the void evacuated, further reducing the tsunamigenesis of the sliding block. The large volume SBU1-3 events have a submarine component, thus the starting depth is below sea level. As a result the SBU1-3 events will be less effective at generating

high amplitude tsunamis than an initial subaerial failure (Fine *et al.,* 2003; LeBlond and Jones, 1995). Although SBU4-7 have been identified as being subaerial, the volume of these events is five times lower than SBU1-3.

Finally, Haugen *et al.* (2005) found that the time interval between events is important in defining the interactions of tsunami waves generated by retrogressive landslides. The mud intervals in the Icod Event Bed represent time intervals between deposition of subsequent subunits, as time is required for the mud (silt and clay) components to settle out. However, estimating this time is not simple. Initially, at low concentrations, grains will settle by Stoke's free settling (Mehta, 1991; Winterwerp and Kesteren, 2004; McAnally *et al.,* 2007). Stow and Bowen (1980) estimated the time needed to deposit a mud layer utilising only free settling of silt. However, as suspension concentration increases through time, cohesive properties of clay and fine silt (<32μm) results in flocculation. These larger flocs have a higher settling velocity, so the particulate can accumulate faster (Mehta, 1991; Winterwerp and Kesteren, 2004; McAnally *et al.,* 2007). With further increases in suspension concentration, hindered settling processes commence (Mehta, 1991; Winterwerp and Kesteren, 2004; McAnally *et al.,* 2007), which serve to decrease settling velocities and therefore increase the time for accumulation. In addition, the water-laden deposits from these suspension fallout processes would then require time to consolidate and dewater into a layer capable of resisting erosion by subsequent flows.

Accurate calculation of these time intervals is now the subject of ongoing work. However, qualitatively, the time intervals between subunits appear to be significant, whereby simple Stoke's law settling generates times of 10s to 100s of hours to deposit decimetre-thick intervening subunit muds (Stow and Bowen, 1980). Indeed, two months after the 12 January 2010 Haiti earthquake a 600 m-thick sediment plume from an associated 0.05 km^3 turbidity current is still present in the water column (McHugh *et al.,* 2011). Another consideration is that enough time must have elapsed such that the mud had consolidated sufficiently, so that it was not eroded by later flow events responsible for later subunits. However, the time intervals between subunits were not long enough for hemipelagic mud deposition (with typical accumulation rates of ~2 cm/ka) or bioturbation.

Conclusions

Distal turbidites associated with volcanic island landslides can preserve a record of source landslide mechanics. In particular, the subunit facies observed here in the Icod Event Bed, and in turbidites linked to other volcanic island landslides, can be interpreted as the result of a multistage retrogressive failure. However, the present study demonstrates the need for good spatial core coverage and a multi-disciplinary approach combining geochemistry, sedimentology, geophysics and physical properties. This approach allows alternative mechanisms for subunit facies generation, such as flow reflection and multiple source areas, to be confidently ruled out. It is also shown that analysis of single grain types (such as volcanic glasses) from individual subunits is important in resolving subtle differences in island sector provenance.

The subunit facies of the Icod Event Bed is interpreted to be the product of seven successive landslides on the northern flank of Tenerife. Volumetric analysis indicates that the first three subunits (SBU1-3) were significantly larger than the later subunits (SBU4-7). Mineralogical and sedimentological data indicate that the initial stages (SBU1-3) of the landslide were partly subaerial and partly submarine in origin, while the later stages (SBU4-7) were exclusively subaerial. Geochemical data show that the subunits can be grouped differently according to their bulk and volcanic glass compositions, with an initial group (SBU1-2), an intermediate group (SBU3-5) and a later group (SBU6-7). This is interpreted to represent retrogressive failure cutting back into the island flank.

The initial Icod landslide had an estimated volume of ~310 km^3, well in excess of the predicted minimum onshore landslide volume estimate of 100 km^3 (Coppo *et al*., 2009). This highlights the need to take into account submarine landslide deposits, some of which can be transported >1000 km from source by long runout turbidity currents.

The geohazard implications of volcanic island flank collapses require understanding of landslide mechanisms, since these have fundamental impacts on tsunami generation. In a multistage landslide, on a protracted time-scale, individual landslides will be reduced in magnitude compared to a single event and will generate separate lower magnitude tsunamis that will not have constructive interference. Furthermore, the recognition that other Canary Island landslides, such as El Golfo landslide, are also multistage events is important since it demonstrates this mechanism is not isolated to the Icod event.

Acknowledgements

The authors would like to thank the crews of the *RRS Discovery*, *RSS Charles Darwin* and *RSS James Cook* for their efforts during data collection. Thanks are also given to BOSCORF and the curators G. Rothwell and S. MacLachan for their services in maintaining the cores and aiding some of the analytical techniques. JEH would like to thank D. Green, A. Milton and M. Cooper from the Geochemistry Group at the NOC and R. Pearce, for their aid in demonstrating laboratory methodologies and data processing. JEH also acknowledges PhD funding from the Marine Geoscience group at the NOC, which has enabled this study to be completed. The authors would also like to thank the constructive and positive comments of the reviewer A. Di Roberto in completion of this manuscript.

5.3 Summary

Dating of the event coupled with the bulk and volcanic glasses geochemistry support a provenance from Tenerife, and further support attribution of this event bed to the Icod landslide from the northern flank at ~165 ka. There are seven subunits that can be regularly correlated within this event bed within Agadir Basin. Grain-size data from these subunits indicates that these both fine away from source and towards the basin margins, thus negating an origin from flow reflections from the basin margins. Volcanic glass geochemistry indicates variations in the compositions of glasses comprising each subunit. The geochemistry, mineralogy and carbonate content of the subunits not only support a multistage collapse but indicate a retrogressive style of failure, commencing with a significant submarine component.

This has implications for tsunamigenesis, since that the estimated 320 km^3 volume of the failure is divided amongst seven smaller events, potentially with significant time lag between them. This Chapter indicates potential issues with the initial landslide parameters used in modelling a forecasted Cumbre Vieja landslide from western La Palma (Ward and Day, 2001). However, this chapter represents a single case study, thus the multistage failure mechanism described here may not be ubiquitous amongst volcanic flanks collapses. The next Chapter (Chapter 6) serves to identify the provenance of eight large-volume volcaniclastic turbidites recovered from an extended 1.5 Ma to recent turbidite history from the Madeira Abyssal Plain. While the subsequent chapter 7 investigates whether, similar to Icod event featured in this Chapter, the last eight major volcaniclastic landslides from the Canary Islands have also been multistage.

Chapter 6
Turbidite Records of Large-Volume Canary Island Landslides

6.1 Introduction and Aims

The previous Chapter 5 highlights the Icod landslide from Tenerife as being a multistage regressive landslide, based on the presence of subunits within the sediment gravity flow deposit. The Late Quaternary turbidite history in the Madeira Abyssal Plain has been extended from 0.7 to 1.5 Ma in the present Chapter. The provenance and timing of these events will be linked to previous records of volcanic island landslides from the Western Canary Islands. The origin of the subunits present within these beds will be examined in the next Chapter (Chapter 7). The aims of this Chapter are outlined below:

1. Date the volcaniclastic turbidites present in the Northern Madeira Abyssal Plain piston cores.
2. Determine the provenance of those volcaniclastic turbidites.
3. Determine whether those volcaniclastic turbidites relate to those known large-volume volcanic island landslides in the Western Canaries in the last 1.5 Ma.
4. Identify the record of volcaniclastic turbidite deposition from 17 Ma to present, utilising the ODP core in the Madeira Abyssal Plain.
5. Use previously published mudcap geochemistry details combined with the dates and volumetrics of these turbidites, to interrogate the history of submarine landslide activity in the Canary Islands from 17 Ma to present.

This Chapter, after further editing to the discussions section, will be submitted to *Geochemistry Geophysics Geosystems* (September 2012) under the theme of interest: "Geodynamics of ocean islands in slow moving plates", now that the theme of interest solicitation has been accepted. All data, analyses and interpretations are my own, with editorial help from my co-authors.

Large-Volume Volcaniclastic Turbidite Deposition in the Madeira Abyssal Plain: as a Record of Volcanic Island Landslides in the Canary Islands

J. E. Hunt[1,2*], R.B. Wynn[1], D.G. Masson[1], P.J. Talling[1]

[1]National Oceanography Centre, University of Southampton Waterfront Campus, European Way, Southampton SO143ZH, UK

[2]School of Ocean and Earth Science, National Oceanography Centre Southampton, University of Southampton, European Way, Southampton SO143ZH, UK

* Corresponding author: jeh2g08@soton.ac.uk

Abstract

Volcaniclastic turbidites in the Madeira Abyssal Plain provide a long-term record of potentially very hazardous volcanic island landslides from the Canary Islands. These volcaniclastic turbidites are recovered in piston cores that span the last 1.5 Ma and ODP cores that extent back to 17 Ma. The timing, provenance and volumes of these turbidites potentially provide key information about the age, frequency and emplacement dynamics of submarine landslides from the Canary Islands, especially the western islands of Tenerife, La Palma and El Hierro. These records indicate that landslides coincided with protracted periods of volcanic edifice growth. This indicates that loading of the volcanic edifices is a key preconditioning factor for landslide occurrence. Evidence from the last large-volume failures from Tenerife suggests possible correlations with explosive eruptions at the end of eruptive cycles. In addition, the majority of large-volume landslides occur during warmer and wetter climates associated with sea level rise and subsequent highstand.

Introduction

Since the catastrophic flank collapse that instigated the Mount St. Helens eruption (May 1980), much attention has been given to characterising volcanic island flanks and investigating the contributing factors that result in their inherent instability. These studies have focused on the Hawaiian (Moore *et al.*, 1989, 1994; McMurtry *et al.*, 2004), Canarian (Holcomb and Searle, 1991; Watts and Masson, 1995, 2001; Masson *et al.*, 2002; Acosta *et al.*, 2003), Mascarene (Duffield *et al.*, 1982; Labazuy, 1996; Oehler *et al.*, 2004, 2008), Cape Verdean (Le Bas *et al.*, 2007; Masson *et al.*, 2008), Lesser Antilles (Deplus *et al.*, 2001; Le Bas *et al.*, 2011; Watt *et al.*, 2012), and French Polynesian archipelagos (Clouard *et al.*, 2001; Clouard and Bonneville, 2005; Hildenbrand *et al.*, 2006; Boulesteix *et al.*, 2008). The importance in conducting such studies is highlighted by their large scale (commonly up to 200 km^3) and their potential to generate catastrophic tsunamis (Latter, 1981; Kulikov *et al.*, 1994; Tinti *et al.*, 1999, 2001; Assier-Rzadkieaicz *et al.*, 2000; Tappin *et al.*, 2001; Synolakis *et al.*, 2002; Ward and Day, 2003; Gelfenbaum and Jaffe, 2003; Fryer *et al.*, 2004; Fine *et al.*, 2005; Fritz *et al.*, 2009).

Volcanic islands commonly comprise relatively rapidly constructed and steep flanks composed of interbedded pyroclastics, lavas and intrusive dykes (McGuire, 1996). The presence of potential weak layers and injection of magmatic intrusions are key preconditioning factors affecting volcanic island stability (Iverson, 1995; McGuire, 1996; Elsworth and Voigt, 1995, 1996; Elsworth and Day, 1999; Mitchell *et al.*, 2002 and references therein; Hürlimann *et al.*, 1999a, 2000; Masson *et al.*, 2006 and references therein; Andrade and van Wyk de Vries, 2010). Other preconditioning factors that may be present include: (1) high sedimentation rates; (2) water saturation; (3) elevated pore water pressures; (4) high rainfall; (5) hydrothermal alteration; (6) deep narrow canyons reducing lateral strength; (7) faulting; (8) dike intrusion; (9) seismic activity; (10) volcanic spreading; and (11) residual soils (Siebert 1984; Siebert *et al.*, 1987; McGuire *et al.*, 1990; Voight and Elsworth, 1997; Lo Giudice and Rasa, 1992; Borgia, 1994; Elsworth and Voight, 1995, 1996, 2001; Murray and Voight, 1996; Day, 1996; McGuire, 1996; Montalto *et al.*, 1996; Firth *et al.*, 1996; Hürlimann *et al.*, 1999a, 2000, 2004; Masson *et al.*, 2006). Recent studies have also highlighted the potential of warmer and wetter climate conditions associated with onset of interglacials as a major preconditioning factor (McMurtry *et al.*, 2004; Keating and McGuire, 2004; Deeming *et al.*, 2010; McGuire, 2010; Tappin *et al.*, 2010).

Onshore studies of volcanic island landslides are reliant on dating of the unconformities left by the respective mass movement. These dates often have significant uncertainties, since volcanics representing the headwall scarp and volcanics representing the infilling of the scarp may not have been laid down synchronously with the landslide. Furthermore the onshore record of volcanism is often discontinuous and characterised by lengthy hiatuses.

Volcanic island landslides have been shown to generate large debris avalanche deposits offshore on the proximal submarine aprons (Lipman *et al.,* 1988; Moore *et al.,* 1989, 1994; Holcomb and Searle, 1991; Watts and Masson, 1995, 1998; Ablay and Hürlimann, 2000; Keating, 2000; 2001; Deplus *et al.,* 2001; Gee *et al.,* 2001; Urgeles *et al.,* 1999, 2001; Masson *et al.,* 2002, 2008; Milia *et al.,* 2003; Oehler *et al.,* 2004; Chiocci *et al.,* 2006; Le Bas *et al.,* 2007). In turn, these debris avalanches disaggregate and generate turbidity currents that are deposited distally on the abyssal plain (Garcia and Hull, 1994; Garcia, 1996; Watts and Masson, 1995; Masson, 1996; Wynn and Masson, 2003; Hunt *et al.,* 2011). Pelagic sediment represents near-continual deposition of primarily calcareous phytoplankton from the water column. The biostratigraphy, stable-isotope composition and lithology of the hemipelagite in which a turbidite resides provide a dateable record, thus enabling direct dating of the respective landslide.

The Quaternary and Late Cenozoic volcaniclastic turbidites of the Madeira Abyssal Plain have been previously inferred to have a Canary Island provenance (Pearce and Jarvis, 1992, 1995; Jarvis *et al.,* 1998). The present study firstly investigates the 0-1.5 Ma history of volcanic island-sourced turbidites within the Madeira Abyssal Plain, based on a series of long-record piston cores (locations on Figure 6.1). Where these turbidites occur within the continuous hemipelagic sediment record will provide resolution on their age, while volcanic glasses from the turbidite sands will provide a geochemical provenance. This 0-1.5 Ma record can then be directly related to the extensive history of Late Quaternary debris avalanches existing offshore of the Western Canary Islands (Masson *et al.,* 2002).

ODP Holes 950, 951 and 952 provide a 0-17 Ma history of volcaniclastic turbidite deposition within the Madeira Abyssal Plain (locations on Figure 6.1). Therefore, a second aim is to extend the record of volcaniclastic turbidite deposition to 17 Ma (with a focus on the 7.5 Ma to recent record) and potentially relate these older turbidites to previously identified large-volume flank collapses in the Canary Islands. This will combine details on the age, volume and mudcap geochemistry of these turbidites, and

attempt to correlate them to previously identified large-volume flank collapses in the Canary Islands. Thus for the first time, volcanic island landslide histories can be constructed based on the turbidite record, which can be correlated to the known onshore and submarine landslide records. This volcaniclastic turbidite record can be used to understand volcanic island landslide magnitude, frequency and temporal clustering. Through comparison of these records to climate and island volcanism, preconditioning and trigger factors of volcanic island landslide may be better understood.

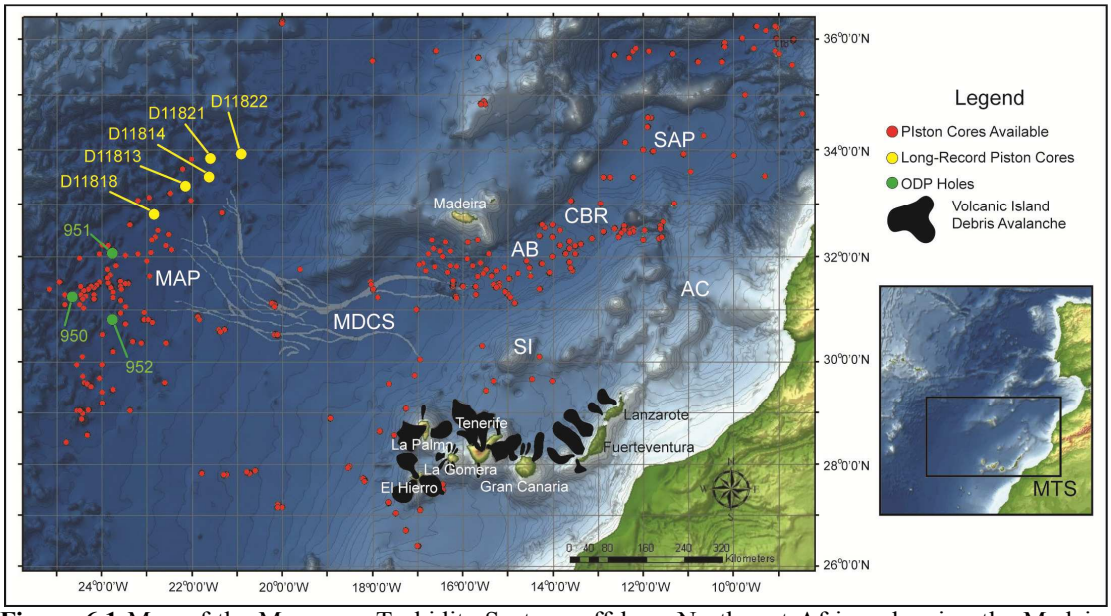

Figure 6.1 Map of the Moroccan Turbidite System, offshore Northwest Africa, showing the Madeira Abyssal Plain study area (MAP), Madeira Distributary Channel System (MDCS), Agadir Basin (AB), Seine Abyssal Plain (SAP), Selvagen Islands (SI), Agadir Canyon (AC) and Casa Blanca Ridge (CBR). Map illustrates the piston core coverage available to study, the piston cores utilised in the present study and ODP holes.

Geological Setting

The Canary Islands represent an archipelago comprising seven volcanic islands over a region of ~500 km on the Northwest African passive margin. They have developed in response to slow-movement of Jurassic-age (156-176 Ma) oceanic crust over a mantle plume (Klitgort and Schouten, 1986; Anguita and Hernán, 1990; Hoernle and Schmincke 1993; Hoernle *et al.,* 1995; Schmincke *et al.,* 1995; Carracedo *et al.,* 1998). This results in a general east-to-west age progression of the islands (Carracedo *et al.,* 1998; Carracedo, 1994, 1999). Landslide activity is most evident in the Western Canary Islands of Tenerife, La Palma and El Hierro. Here there is substantial evidence of Late Quaternary landslide activity, which form spatially extensive submarine debris

avalanche deposits (Masson *et al.,* 2002, and references therein; Acosta *et al.,* 2003, and references therein).

The focus of this study is the volcaniclastic turbidite history recorded in a selection of shallow piston cores and ODP core from the Madeira Abyssal Plain (locations in Figure 6.1). The Madeira Abyssal Plain, at water depths of 5,000-5,500 m, represents the most distal and deepest depocentre in the Moroccan Turbidite System, and is located 300 km west of the Canary Islands (Figure 6.1) (Weaver and Kuijpers, 1983; Weaver *et al.,* 1992; Wynn *et al.,* 2000, 2002). It is connected to the more proximal Agadir Basin via a 300 km-long submarine channel network known as the Madeira Distributary Channel System (Masson, 1994; Stevenson *et al.,* 2012).

History of Landslides within the Canary Islands

Numerous studies and texts have documented the volcanic and geomorphologic evolution of the Canary Islands. This review section aims to summarise the landslide history of the Canarian archipelago. This review is later synthesised with the turbidite record of the present study to offer a comprehensive evaluation of the landslide records and the influences on ocean island flank collapses.

Fuerteventura and Lanzarote

Stillman (1999) documented the destructive phases of Fuerteventura. Numerous landslides have been dated at 22 to 16.5 Ma based on the fractured nature of the basement complexes and offshore turbidites in ODP Hole 397 (Table 6.1). Acosta *et al.* (2003) proposed old collapses from the Central and Southern Volcanic Complexes (>17.5 Ma), which formed the Puerto Rosario debris avalanche and Banquete and Amanay Banks respectively (Table 6.1).

There is little literature documenting flank collapses from Lanzarote (Table 6.1). Large denuded and scalloped coastlines northwest of the Famara volcanic complex and southeast of the Los Ajaches volcanic complex could indicate large-scale flank collapses. However, neither Lanzarote nor Fuerteventura has evidence of major landslide activity that postdates 15 Ma.

Table 6.1 Summary of Volcanic Flank Collapses from Fuerteventura, Lanzarote, Gran Canaria and La Gomera in the Canary Islands.

Event	Type	Age	Volume (km^3)	Area (km^2)	Comments
Fuerteventura					
Central Volcanic Complex I Collapse	Slide	~22 Ma[1,2]	?	?	Deduced from an unconformity between Central Volcanic Complex (CVC) lavas II and I. Fractured nature of CVC I and steeper dip infers landslide event.[2]
Central Volcanic Complex II Collapse (Puerto Rosario)	Slide and DA	20-16.5 Ma[2]	?	3,500[4]	Unconformity below Melindraga and Tamacite formations.[2] Offshore evidence of buried event.[4]
Southern Volcanic Complex Collapse (Southern Puerto Rosario)	Slide and DA	>17.5 Ma[2]	?	1,200[4]	Offshore evidence of buried debris avalanche cut by gullies on opposing slope of scalloped southern shoreline.[4]
Unknown	DF	17.6 Ma[3]	?	?	Volcaniclastic debris flow v4 from ODP hole 397.[3]
Unknown	DF	17.2 Ma[3]	?	?	Volcaniclastic debris flow v3 from ODP hole 397.[3]
Unknown	DF	17.0 Ma[3]	?	?	Volcaniclastic debris flow v2 from ODP hole 397.[3]
Unknown	DF	16.5 Ma[3]	?	?	Volcaniclastic debris flow v1 from ODP hole 397.[3]
Jandía	DA	~2 Ma[10]	25[9]	250[9]	Identified in sidescan sonar.[9] Also mapped in swath bathymetry.[4]
Eastern Canary Ridge	DF	<100 ka[9]	>20[9]	>2,000[9]	Mapped using swath bathymetry, sidescan sonar and shallow 3.5kHz seismic reflections.[9]
Lanzarote					
Unknown	Slide	18-16 Ma[4]	?`	>800[4]	Buried event poorly constrained[4], possibly collapses of Los Ajaches and Famara complexes.
Gran Canaria					
Agaete (Caldera de Tejeda)	Slump and DA	~14 Ma[4,5]	>50[9]	200-500[4,9]	Erosional collapse of early basaltic shield.[5] Scalloped northwest shoreline and offshore bathymetry.[4] Two potential debris avalanches in apron ODP hole 953.[6] Also identified in seismic reflection.[8]
Horgazales Basin	DA	14-15 Ma[9]	>80[9]	>1,000[9]	Identified in seismic reflection profiles and from ODP leg 157.[6,8]
Pre-Galdar	DA	12-15 Ma[9]	>60[9]	>700[9]	Identified in seismic reflection profiles and ODP leg 157.[6,8]
Fataga Collapses	DFs	9-11.5 Ma[13]	?	?	Series of trachyphonolite-rich debris flow units encountered in ODP hole 953, related to collapses of the Fataga volcano.[13]
Las Palmas	DA	9 Ma[4]	?	1,100[4]	Older event on the northeast flank of Gran Canaria.[4]
Roque Nublo	DA	3.9-3.5[4]	~34[9]	150-330[4,9]	Forms over the area of the Las Palmas debris avalanche lobe.[4] However, debris avalanche on southwest flank identified as Roque Nublo event.[8,9,10,11,12]
Galdar	DA	3.9-3.5[4]	?	300[4]	Forms a lobe on the northern flank of Gran Canaria.[4]
La Gomera					
Unknown	DFs	~12 Ma[13]	?	?	Four basalt-rich debris flow deposits at ODP hole 956, linked to shield development on La Gomera.[13]
Tazo	DA	9.4-8.6[7]	?	?	Northwest-directed 150 m-thick breccia onshore.[7]
San Marcos	DA	9.4-8.6[7]	?	?	Onshore breccias below Tazo deposit.[7]
I (North)	DF	~4.0 Ma[4]	?	80[4]	Mapped using swath bathymetry.[4]
II (North)	DF	~4.0 Ma[4]	?	80[4]	Mapped using swath bathymetry.[4]
III (North)	DF	~4.0 Ma[4]	?	340[4]	Mapped using swath bathymetry.[4]
IV (East)	DF	~4.0 Ma[4]	?	160[4]	Mapped using swath bathymetry.[4]
V (South)	DF	~4.0 Ma[4]	?	300[4]	Mapped using swath bathymetry.[4]
VI (South)	DF	~4.0 Ma[4]	?	40[4]	Mapped using swath bathymetry.[4]
VII (West)	DF	~4.0 Ma[4]	?	50[4]	Mapped using swath bathymetry.[4]
VIII (West)	DF	~4.0 Ma[4]	?	300[4]	Mapped using swath bathymetry.[4]

[1]Ancochea *et al.,* (1996), [2]Stillman (1999), [3]Schmincke and von Rad (1979), [4]Acosta *et al.,* (2003), [5]van den Bogaard and Schmincke (1998), [6]Schmincke and Segschneider (1998), [7]Ancochea *et al.,* (2006), [8]Funck and Schmincke (1998), [9]Krastel *et al*., (2001), [10]García and Cacho (1994), [11]Schmincke *et al.,* (1995), [12]Mehl and Schmincke (1999), [13]Schmincke and Sumita (1998).

Gran Canaria

The first major phase of erosion occurred at 14.0 to 13.9 Ma with the collapse and formation of the Caldera de Tejeda (van den Bogaard and Schmicke, 1998). A related debris avalanche at ~14 Ma is identified on the northern submarine flank of Gran Canaria, and named as the Agaete debris avalanche (Table 6.1) (Acosta *et al.,* 2003). ODP core from the northern and southern aprons of Gran Canaria (Sites 953 to 956) show an extensive history of minor volcaniclastic turbidites (Schmincke and Segscheider, 1998; Carey *et al.,* 1998; Sneider *et al.*, 1998; Goldstrand, 1998).

Turbidite activity recorded in these proximal ODP cores appears to have ceased from 8.8 to 4.0 Ma, in coincidence with an onshore hiatus in volcanism (Goldstrand, 1998). Commencement of Roque Nublo volcanism occurred between 4.5 and 3.5 Ma, and coincides with recommencement of turbidite activity on the northern submarine flank (Goldstrand, 1998). The Roque Nublo caldera has been reported to represent a catastrophic caldera-forming eruption (Anguita *et al.*, 1991). Debris avalanche facies are documented onshore on the southwest flank, dated at this time (Table 6.1) (García Cacho *et al.*, 1994; Mehl and Schmincke, 1999; Acosta *et al.,* 2003). No major island flank landslides have been identified after 3.5 Ma (Table 6.1) (Acosta *et al.,* 2003).

La Gomera

Acosta *et al.* (2003) identified eight debris avalanche lobes from swath bathymetry of the submarine flanks (Table 6.1). Three lobes are identified on the northern flank, one to the east, two on the southern flank and two to the west. Llanes *et al.* (2009) further interpreted a series of scalloped embayments on the northern insular margin and numerous flat-bottomed canyons on the southern margin. In addition, there is the 150 m-thick Tazo breccia (9.4-8.6 Ma) directed towards the northwest, which resides above both the Basement Complex and Lower Old Basalts (Table 6.1) (Ancochea *et al.*, 2006). This can be linked to collapse and formation of the Garajonay embayment, within which a subsequent Vallehermoso edifice grew, and later failed at 5.4 to 5.0 Ma (Paris *et al.,* 2005).

Tenerife

The Masca (Los Gigantes) and Carrizales unconformities represent the oldest angular unconformities in the Teno Massif above the Masca Formation (6.3 to 6.0 Ma) (Table 6.2) (Walter and Schmincke 2002; Leonhardt and Soffel, 2006; Longpré *et al.*, 2009). A

debris avalanche has been recorded on the northwest submarine flank of Tenerife with a proposed date of ~6.0 Ma (Table 6.2) (Masson *et al.,* 2002; Acosta *et al.*, 2003). It is unclear whether this represents either of the aforementioned erosional events or an amalgamation of the two.

The Anaga Massif has also suffered a documented collapse (Table 6.2) (Masson *et al.,* 2002; Acosta *et al.,* 2003; Llanes *et al.,* 2003), dated at 4.7 to 4.1 Ma by Walter *et al.* (2005). The Tigaiga debris avalanche is another failure from the northern flank of Tenerife (Table 6.2), forming an onshore terrain and a buried offshore debris avalanche. This has been tentatively dated at >2.3 Ma (Cantagrel *et al.,* 1999; Krastel *et al.,* 2001; Acosta *et al.,* 2003).

On the southern flank of Tenerife a ~2 Ma, 25 km^3, failure has been reported, named the Bandas del Sur debris avalanche (Krastel *et al.,* 2001). Harris *et al.* (2011) suggest that this southern island failure is represented by the 733 ka Abona debris avalanche onshore. While the eastern flank of Tenerife is the site of the Güímar landslide, dated at 0.84 to 0.78 Ma (Table 6.2) (Ancochea *et al.,* 1990; Cantagrel *et al.,* 1999; Krastel *et al.,* 2001; Masson *et al.,* 2002). A number of <2 Ma failures have been reported on the northern flank of Tenerife, including the Roques de García, Orotava and Icod landslides (Table 2). The Roques de García debris avalanche has been mapped offshore northern Tenerife (Watts and Masson, 1995, 2001; Ablay and Hürlimann, 2000; Acosta *et al.,* 2003). This older event has a poorly constrained age, between 1.7 and 0.6 Ma (Cantagrel *et al.,* 1999). The next youngest event is the Orotava landslide dated at 0.69 to 0.54 Ma (Cantagrel *et al.,* 1999; Marti, 1998; Watts and Masson, 1995). The youngest landslide to affect Tenerife is the Icod landslide, which has been dated to ~165 Ka from a turbidite bed in the Agadir Basin and Madeira Abyssal Plain turbidite sequences (Hunt *et al.,* 2011).

La Palma

The Cumbre Nueva structure represents a collapse dated at 558 ka (Acosta *et al.* 2003) or 530-566 ka (Carracedo *et al.*, 2001; Paris and Carracedo, 2001). The origin for the Cumbre Nueva landslide is from the Cumbre Nueva Ridge during volcanism associated with the Taburiente volcano (Table 6.2) (Carracedo *et al.,* 2001; Paris and Carracedo, 2001; Acosta *et al.,* 2003). It overlies the Playa de la Veta deposit in the offshore realm, and is highlighted by a higher backscatter sonar response compared to the older Playa de la Veta debris avalanche (Urgeles *et al.*, 1999; Masson *et al.,* 2002). This enables the

Cumbre Nueva deposit to be justified as being younger. Dating of the Playa de la Veta deposit is poorly constrained, but is thought to be 1.0 to 0.8 Ma (Urgeles *et al.,* 1999; Krastel *et al.,* 2001; Masson *et al.,* 2002). Sidescan sonar has provided evidence that this older Playa de la Veta deposit may comprise three individual lobes, which may complicate age attribution.

Masson *et al.* (2002) identified an additional flank collapse named the Santa Cruz landslide from the eastern flank of La Palma. Landslide activity has also been identified on the northern flank, but these have not been dated or quantified (Acosta *et al.,* 2003).

El Hierro

The Tiñor volcano represented the first subaerial volcanism on El Hierro between 1.12 Ma and 0.88 Ma (Table 6.2) (Guillou *et al.,* 1996; Carracedo *et al.,* 1999). In mining galerías within the El Golfo embayment, Tiñor lavas below an unconformity with El Golfo lavas have been dated at 1.04 Ma (Carracedo *et al.,* 1999).

The El Julán landslide affected the southwest flank of El Hierro, and is responsible for the large scallop-shaped embayment at the head of the El Julán apron. Masson (1996) speculatively provided a date of 320-500 ka. The Las Playas I and II debris avalanche complex was defined by Gee *et al.* (2001) and Masson *et al.* (2002) on the southeast flank. Here, the younger Las Playas II event generated a debris avalanche that is superimposed on an older Las Playas I debris avalanche. Masson *et al.* (2002, and references therein) offered ages of 176-545 ka for Las Playas I and 145-176 ka for Las Playas II (Table 6.2).

The El Golfo landslide represents the youngest volcanic flank collapse in the Canary archipelago (Weaver *et al.*, 1992; Wynn *et al.,* 2002; Wynn and Masson, 2003; Frenz *et al.,* 2009). A viable date based on a mid-point in onshore ages and from study of the turbidite deposit is ~15 ka (Table 6.2) (Masson, 1996). However, erosional unconformities in onshore galerías date a major landslide as being older than 15±2 ka, with a minimum age of 39±13 ka (Longpré *et al.,* 2011). However, sampling potassium-poor post-collapse lavas may give erroneous ages constraining the lower age limit of the El Golfo collapse (Longpré *et al.,* 2011).

Table 6.2 Summary of Volcanic Flank Collapses from Tenerife, La Palma and El Hierro in the Canary Islands

Event	Type	Age	Volume (km^3)	Area (km^2)	Comments
Tenerife					
Masca (Los Gigantes)	DA	5.89-6.65 Ma[3,4,5,6]	?	?	First major collapse recorded onshore in the Teno massif[3], with dates lying around ~6.4 Ma.[3,4,5,6]
Carrizales	DA	5.89-6.27 Ma[3,4,5,6]	?	?	The Carrizales marks a second major unconformity in the onshore Teno Massif[3], with an accepted date of ~6.1 Ma.[6]
Teno	DA	~6.0 Ma[1,2,5,7]	?	400[1]	Offshore debris avalanche mapped using swath bathymetry and sidescan sonar.[1,7] Could represent either Masca and/or Carrizales events.
Anaga	DA	4.1-4.7 Ma[9]	36[10]	>400[7]	Mapped using swath bathymetry and sidescan sonar.[1,2,7]
Tigaiga	Slide and DA	2.3-2.6 Ma[1,2,5,7]	?	200[1]	Onshore deposit in addition to a buried deposit on the northern flank of Tenerife.[2,16,7]
Bandes del Sur	DA	<2 Ma[2]	25[2]	500[2]	Mapped off the southern flank of Tenerife using sidescan sonar.[2]
Roques de García	DA	0.6-1.3 Ma[1,2,7]	~500[7]	2,200-4,500[1,7]	Mapped using sidescan sonar, shallow 3.5 kHz seismic reflection, and swath bathymetry.[1,7,8,11] Dating of turbidite linked to event is 1185±20 ka.[12]
Güímar	DA	830-850 ka[13]	44-120[7,13]	1,600[7]	Mapped using swath bathymetry.[1] Deposit also found in ODP holes 953 and 954.[12]
Orotava	Slide and DA	505-530 ka[13]	500[7]	2,100[7]	Debris avalanche deposit mapped using sidescan sonar and swath bathymetry.[1,8,11,14,15] Onshore dating range has been limited to 540-690 ka.[5,7,11,16] However, associated turbidite has been dated at 530±25 ka.[12]
Icod	Slide and DA/DF	165 ka[17]	320[17]	1,700[7]	Debris avalanche deposits mapped using sidescan sonar and swath bathymetry.[1,8,11,14,15] Onshore dating of the event is between 150-170 ka.[5,7]. Dating of the debris avalanche from the sediment drape is ~170 ka.[11] The turbidite in Agadir Basin has been dated at 160-165.[17,18,19]
La Palma					
East Puerto del Mudo	DA	>1.0 Ma ?	?	400	Mapped in swath bathymetry.[1]
West Puerto del Mudo	DA	>1.0 Ma ?	?	>300	Mapped in swath bathymetry.[1]
Playa de la Veta	DA	1.185 Ma[1,7,12]	520-650 [1,2,7]	1,200-2,000[1,2,7]	Mapped using sidescan sonar, shallow seismic reflection and swath bathymetry.[1,7,20,21]
Santa Cruz	DA	0.9-1.2 Ma[1,7,22]	?	1,600[1]	Mapped using swath bathymetry.[1]
Cumbre Nueva	DA	~520 ka[7]	80-95[1,7]	700-780[1,7]	Mapped using sidescan sonar, shallow seismic reflection and swath bathymetry.[1,7,20,21] Correlated turbidite in the Madeira Abyssal Plain dated at 485±20 ka[12]
El Hierro					
Tiñor	DA (buried)	0.54-1.12 Ma[22,23]	?	?	Theorised collapse from an unconformity in mining gallerias.[23] Correlated turbidite from Madeira Abyssal Plain dated at 1,050±25 ka.[12]
San Andréas	Aborted Slump	176-545 ka	?	?	Studied from onshore faults.[24] Could be related to early phases of failure during Las Playas I or II.[7]
Las Playas I	DA	176-545 ka	?	1,700[7]	Broader debris avalanche with smoother sediment cover, mapped with sidescan sonar.[7]
El Julan	DA	320-500 ka[1,25]	60-130[1,2,7]	1,600-1,800[1,2,7]	Mapped using sidescan sonar, seismic reflection profiles and swath bathymetry, but little onshore record.[1,7] Correlated turbidite from Madeira Abyssal Plain dated at 540±20 ka.[12]
Las Playas II	Slump with DA/DF	145-176[7]	~50[7]	950[7]	Confined elongate debris flow/avalanche.[7] Possible associated turbidite dated at ~152 ka.[19]
El Golfo	DA	15[1,18,17,18,19,21,25]	150-180[1,18]	1,500-1,700[1,18]	Mapped using sidescan sonar, swath bathymetry and shallow seismic reflection.[1,18,25] Correlation to a large-volume volcaniclastic turbidite.[18,19,26]

[1]Acosta *et al.,* (2003), [2]Krastel *et al*., (2001), [3]Longpré *et al.,* (2009), [4]Leonhardt and Soffel (2006), [5]Cantagrel *et al.,* (1999), [6]Walter and Schmincke (2002), [7]Masson *et al.,* (2002), [8]Watts and Masson (1998), [9]Walter *et al.,* (2005), [10]Llanes *et al.,* (2003), [11]Watts and Masson (1995), [12]Hunt *et al.*, (present study), [13]Giachetti *et al.,* (2011), [14]Ablay and Hürlimann (2000) , [15]Hürlimann *et al.,* (2004), [16]Marti *et al.,* (1998), [17]Wynn *et al.,* (2002), [18]Frenz *et al.*, (2009), [19]Hunt *et al.,* (2011), [20]Urgeles *et al.,* (1999), [21]Urgeles *et al.,* (2001), [22]Carracedo *et al.,* (1997), [23]Carracedo *et al.,* (1999), [24]Day *et al.,* (1997), [25]Masson (1996), [26]Weaver *et al.,* (1992).

Previous work on the Madeira Abyssal Plain Turbidites

The stratigraphy and provenance of the Late Quaternary (0-730 ka) Madeira Abyssal Plain turbidite record is well established (Weaver *et al.,* 1989; Weaver *et al.,* 1992; Wynn *et al.,* 2002). This record includes volcaniclastic beds Mb (15 ka) and Mg (160-190 ka), representing the El Golfo and Icod landslides from the Western Canary landslides respectively (Wynn *et al.,* 2002a; Wynn and Masson, 2003), in addition to older volcaniclastic beds Mn, Mo and Mp (480-520 ka) (Weaver *et al.,* 1992). The lettered nomenclature first used in Weaver and Kuijpers (1983) is continued here, but with the 'M' prefix introduced by Wynn *et al.* (2002) to denote Madeira Abyssal Plain. ODP core from the Madeira Abyssal Plain displays a regular sequence of turbidites from 7.5 Ma to recent, which are correlateable across the entire basin (Weaver *et al.,* 1998). Beyond this, the record at each of the three ODP Holes (950, 951 and 952) show locally restricted turbidites owing to the presence of intrabasinal highs that were later infilled (Weaver, 2003).

Site 950 was found to have the longest turbidite record, extending back to the Upper Eocene (at 22 Ma) (Howe and Sblendorio-Levy, 1998). The Upper Eocene and Oligocene are represented by red clays and minor organic turbidites (Lebreiro *et al.,* 1998). The 16.5 Ma-old calcareous Cruiser Turbidite represents the first event capable of covering the entire Madeira Abyssal Plain. The following 16.5 to 7.5 Ma turbidite record is dominated by thin-bedded siliciclastic turbidites, with minor dark-grey volcaniclastic beds. There is a marked reduction in turbidite sedimentation between 10 to 7.5 Ma (Lebriero *et al.,* 1998; Weaver, 2003).

Correlateable turbidites regularly cover the complete basin floor after ~7.5 Ma, where volcaniclastic turbidites become prominent and >0.5 m-thick (Lebreiro *et al.,* 1998; Weaver, 2003). Jarvis *et al.* (1998) were able to discriminate basic (high Ti) and evolved (low Ti) sub-groups within the volcaniclastic turbidites. This built on previous studies identifying both basic and evolved volcanic provenances within the Late Quaternary turbidite record (Pearce and Jarvis, 1992, 1995).

Methodology and Data

This study utilises targeted cores from a dataset of >100 piston cores from the Madeira Abyssal Plain. These specific cores include D11813, D11814, D11818, D11821 and D11822, which are located in the northern region of the Madeira Abyssal Plain, and contain the most extensive temporal record of volcaniclastic turbidites. These turbidites

are the coarsest (silt and sand) sediment fraction, where the mud has bypassed. In addition, core from ODP sites 950, 951 and 952 will be utilised. The first objective is to resolve the 1.5 Ma to recent volcanic island landslide history from the piston core record, before investigating the 17 Ma to recent volcanic island landslide history in the ODP record. These landslide records are ultimately compared to the known onshore Canary Island landslide histories.

Visual and Geotechnical Logging

Visual sedimentological logging was completed to first assess the vertical sequence and depositional features of the cored turbidites. Magnetic susceptibility profiles were obtained at a 0.5 cm resolution using the *GeoTek* XYZ core scanner to aid correlation of turbidites. Magnetic susceptibility importantly supports identification of volcaniclastic turbidites, reporting high magnetic susceptibility in volcanic sands (50-800 SI). P-wave velocity data was collected using an acoustic profiler, where high p-wave values signify turbidite sands.

Coccolith Biostratigraphy

The turbidites present in the Late Quaternary Madeira Abyssal Plain, western Moroccan Turbidite System, have been dated and correlated according to coccolith biostratigraphy of the hemipelagite sediment, coccolith compositions of turbidite mudcaps and turbidite chemostratigraphy (Weaver and Kuijpers, 1983; de Lange *et al.*, 1987; Weaver and Rothwell, 1987; Weaver *et al.,* 1992; Pearce and Jarvis, 1992, 1995). Indeed, coccolith biostratigraphy has been used to correlate the large-volume turbidites throughout the Moroccan Turbidite System (Wynn *et al.*, 2002).

Standard zonation schemes for the last two million years are well established (Martini, 1971; Gartner, 1977), as summarised in Table 6.3. The relative abundances of *Pseudoemiliania lacunosa*, *Gephyrocapsa caribbeanica*, *Gephyrocapsa aperta, Gephyrocapsa mullerae* and *Emiliania huxleyi* develop a number of dateable acme zones (Weaver and Kuijpers, 1983; Hine, 1990; Hine and Weaver, 1998). These acme zones extend were extended to OIS (oxygen isotope stage) 41 by Hine (1990), as summarised in Table 6.4.

There are also a series of additional species that create biozones based on first (FO) and last (LO) occurrences. The FO of *Reticulofenestra asanoi* occurs at 1.16 Ma (Takayama and Sato, 1987; Sato and Takayama, 1992), while the LO is at 0.8 Ma

(Takayama and Sato, 1987; Hine, 1990; Sata and Takayama, 1992). The FO of *Gephyrocapsa parallela* is at 0.95 Ma, with a potential LO at 0.48 Ma (Hine and Weaver, 1998). The FO of Helicosphaera inversa is at 0.48 Ma, with the LO at 0.14 ka (Hine, 1990). Lastly, the FO of *Gephyrocapsa ericsonii* is at ~0.38 Ma, with the LO at 0.015 Ma (Biekart, 1989). The coccolith biostratigraphy used to date the older ODP record is published and documented by Howe and Sblendorio-Levy (1998).

Table 6.3 Summary of Late Quaternary Coccolith Biozones

Zone	Zone Details	Sub-zone
NN19	***Pseudoemiliania lacunosa* Zone** Defined between the LO of *Discoaster brouweri* (2 Ma) and LO of *Pseduoemiliania lacunosa* (0.443 Ma) (Gartner, 1969; Hine, 1990; Wei and Peleo-Alampay, 1993). This zone comprises a number of subzones (Gartner, 1977).	***Calcidiscus macintyrei* Subzone** Defined between LO of *Discoaster brouweri* (2 Ma) and LO of *Calcidiscus macintyrei* (1.54 Ma) (Gartner, 1977; Wei and Peleo-Alampay, 1993).
		***Helicosphaera sellii* Subzone** Defined between the LO of *Calcidiscus macintyrei* (1.54 Ma) and the LO of *Helicosphaera sellii* (1.37 Ma) (Gartner, 1977; Backman and Shackleton, 1983; Wei and Peleo-Alampay, 1993).
		Small *Gephyrocapsa* Subzone Defined between the LO of *Helicosphaera sellii* (1.37 Ma) and the last dominant occurrence of *Pseudoemiliani lacunosa* (Gartner, 1977).
		***Pseudoemiliani lacunosa* Subzone** Defined as the LO of dominant small *Gephyrocapsa* and the LO of *Pseudoemiliani lacunosa* at 0.443 Ma (Gartner, 1977; Hine, 1990; Wei and Peleo-Alampay, 1993).
NN20	***Gephyrocapsa oceanica* Zone** Defined between the LO of *Pseudoemiliania lacunosa* (0.443 Ma) and FO of *Emiliania huxleyi* (0.298 Ma) (Boudreaux and Hay, 1967; Hine, 1990).	
NN21	***Emiliania huxleyi* Zone** Defined as above the FO of *Emiliania huxleyi* (0.298 Ma) (Boudreaux and Hay, 1967; Hine, 1990).	

Table 6.4 Summary of Late Quaternary Coccolith Biostratigraphy Acme Zones (Weaver and Kuijpers, 1983; Hine and Weaver, 1998)

Zone Code	**Zone**	**Details**
QAZ7	Small *Gephyrocapsa* Acme Zone	Interval dominated by small *Gephyrocapsa* species, which extends below OIS 41 to the lower stage OIS 28 (925 ka). The top of the acme zone is defined by a reversal in dominance from small *Gephyrocapsa* species to *Gephyrocapsa caribbeanica*.
QAZ6	*Gephyrocapsa caribbeanica* Acme Zone	Defined by the dominance in *Gephyrocapsa caribbeanica*, which occurs between the lower stages of OIS 28 (925 ka) and OIS 25 (850 ka). The top of the acme zone is defined by a reversal in dominance to small *Gephyrocapsa* species.
QAZ5	Small *Gephyrocapsa* Acme Zone	Defined by a dominance of small *Gephyrocapsa* species, which are predominantly *Gephyrocapsa aperta* and small specimens of *Gephyrocapsa caribbeanica*. This zone extends from upper OIS 25 (850 ka) to the lower part of OIS 15 (290 ka). The top of the acme zone is defined by a reversal in dominance to *Gephyrocapsa caribbeanica*.
QAZ4	*Gephyrocapsa caribbeanica* Acme Zone	Defined by a dominance of *Gephyrocapsa caribbeanica*, and extends from the lower part of OIS 15 (575 ka) to the lower part of OIS 8 (290 ka). This acme zone can be distinguished from QAZ6 by the absence of *Reticulofenestra asanoi*. The top of the acme zone is defined by a reversal in dominance to *Gephyrocapsa aperta*.
QAZ3	*Gephyrocapsa aperta* Acme Zone	Interval has a dominance of *Gephyrocapsa aperta*, which extends from the lower part of OIS 8 (290 ka) to the lower part of OIS 5 (120 ka). It is distinguished from QAZ5 by the absence of *Pseudoemililani lacunosa* and presence of *Emiliania huxleyi*. The top of the acme zone is marked by a dominance in *Gephyrocapsa mullerae* during the OIS 6 glacial due to selective dissolution.
QAZ2	Transitional Zone (*Gephyrocapsa mullerae*) Acme Zone	Defined by a dominance of *Gephyrocapsa mullerae* in higher latitudes (from 120 ka), while lower latitudes are dominated by *Gephyrocapsa oceanica* and *Gephyrocapsa margerelii*. The top of the acme zone occurs during the lower part of OIS 4 and marks a decrease in abundance of *Gephyrocapsa mullerae* (and/or equivalent) and an increase in abundance of *Emiliania huxleyi* (71 ka).
QAZ1	*Emiliania huxleyi* Acme Zone	Defines a marked increase in abundance of *Emiliania huxleyi* from the lower part of OIS 4 onwards (71 ka).

Spectrophotometry

Spectrophotometric data was collected for the hemipelagite sequences interbedded with turbidites. Quantitative records of changing hemipelagite composition (principally carbonate) firstly provide support for the turbidite correlations, and secondly provide a means to potentially date the events relative to points of sea level change. Spectrophotometry was conducted primarily using a *Konica Minolta CM-2600d* fitted

to a *GeoTek* XYZ logger, and calibrated against a white tile standard and in free-air. Where cores were either degraded or inappropriate for the XYZ logger, a handheld *Minolta CM-1200* was used. This reflectance data were converted to CIE L*a*b* values. Measurements were taken every 0.5 cm down core. The L* values (0 = black and 100 = white) have been interpreted as a proxy for the carbonate content of hemipelagic sediments, and potentially reflect relative sea level (Balsam *et al.,* 1999; Helmke *et al.,* 2002; Nederbragt *et al.,* 2006; Rogerson *et al.,* 2006).

Previous studies have found that the hemipelagic sediment composition in the Moroccan Turbidite System is periodically affected by variations in bottom waters that influence the position of the CCD (Berger, 1970; Crowley, 1983; Weaver *et al.,* 1992). During interglacial highstands North Atlantic Deep-Water current (NADW) production and mixing increases, and thus white carbonate-rich hemipelagic sediment is preserved (Crowley, 1983). As well as supporting correlations between cores, spectrophotometric profiles from the hemipelagic sediment also serve as a potential record of relative sea level change, enabling relative dating of the turbidites that intersect that record. These dates (±10 ka) can be compared to existing ages of the turbidites to demonstrate both accuracy and precision.

SEM Volcanic Glass Analysis

The volcaniclastic turbidites commonly comprise multiple fining-upwards sequences, known as subunits (Hunt *et al.*, 2011). Samples (~3 cm^3) were taken from the bases of subunits within each of the volcaniclastic turbidites within the Madeira Abyssal Plain. These were sieved to remove the <63 μm fraction. The remaining sand fraction was then subjected to acetic acid (0.1 M) leeching to remove carbonate and wash grain surfaces. The volcanic grains were then mounted on a semi-conductor pad and placed within the vacuum chamber of a *Hitachi TM1000* SEM. Flat surfaces of unaltered volcanic glasses (n=30-50) of 90-125 μm size were analysed from each subunit, with operating conditions of 15 kV and a dwell time of 120 s. A series of glass standards produced from international standard reference materials allowed verification of accuracy and precision. Concentrations between 1-2 wt% have precisions of 4-6% of the value, 2-10 wt% values have precisions to within 2-5%, while those values >10 wt% have precisions of 0.5-4% (Appendix 6.1). Accuracies were generally within 1-5% of the certified value for the suite of standard reference materials, where accuracies were higher with increasing concentration. SEM EDS volcanic glass data is reported in

Appendix 6.1, SRM data in Appendix 6.2, and calibration curves presented in Appendix 6.3.

ODP Stratigraphy

The 0-17 Ma stratigraphy of the Madeira Abyssal Plain is constructed from three sites (950, 951 and 952) from ODP leg 157 (location in Figure 6.1). Turbidites can be correlated between the three sites using the position in the vertical sequence, colour, magnetic susceptibility and published biostratigraphy of Howe and Sblendorio-Levy (1998). Turbidite chronology is independently derived for each ODP site (950, 951 and 952) based on hemipelagic depositional rates. These hemipelagite depositional rates were generated from the biostratigraphy and magnetostratigraphy presented by Howe and Sblendorio-Levy (1998).

ODP Turbidite Geochemistry

Bulk geochemical analyses were undertaken and presented by Jarvis *et al.* (1998), utilising 10 mL samples taken from the mudcaps of turbidites >20 cm-thick in Hole 950. The preparation and methodology is described in Jarvis *et al.* (1998).

Turbidite Volumes based on ODP Studies

Turbidite volumes are calculated according to the method of Weaver (2003). Turbidite volumes are reported as the decompacted volume upon deposition, which allows better comparisons of magnitude between younger and older events. Here the turbidite volumes were generated based on the ratio of turbidite decompacted thickness to the decompacted thickness of the seismic unit in which it resides. This was then compared against the calculated decompacted volume of that respective seismic unit (Alibés *et al.,* 1996, 1999). The methodology is described in more detail in Appendix 6.4 and 6.5.

Results

Late Quaternary Volcaniclastic Turbidite Stratigraphy and Mudcap Geochemistry

The existing stratigraphy of the Madeira Abyssal Plain (Weaver *et al.,* 1992) was reanalysed and extended to cover the full available piston core record to ~1.5 Ma. Figure 6.2 shows a correlation panel of the northern sub-basin of the Madeira Abyssal Plain, where the northern branches of the Madeira Distributary Channels terminate. This correlation panel emphasises the main, widespread, large-volume volcaniclastic

turbidites Mb, Mg, Mn, Mo and Mp within the last 550 ka. Cores D11814 and D11821 penetrate beyond 550 ka and record three additional 0.2-0.7 m-thick, silt to fine sand-grained, volcaniclastic turbidites named Mz, Mab and Maf (Figure 6.2). There are also a number of less widespread subsidiary deposits represented as thin, grey, volcaniclastic turbidite muds (previously identified as Md1, Ml1 and Ml3, Ms2, Mv1, Mx and Mx1). These are not discussed further due to their low-volume and difficulty in ascertaining provenance.

The turbidite stratigraphy established in the Madeira Abyssal Plain piston core record can be extrapolated to the ODP holes (Figure 6.3). Indeed, the upper 55 m corresponds to the sequences recovered from piston cores in the northern sub-basin (Figures 6.2 and 6.3). The mud geochemistry of the turbidites sampled in ODP Hole 950 is recalculated on a carbonate-free basis. Volcaniclastic turbidite mud geochemistry demonstrates two clear compositional fields using the ternary diagrams of de Lange *et al.* (1987). These turbidites can be grouped into a basic igneous group (Group 1) defined by low Zr and K_2O, and high TiO_2, MgO and Fe_2O_3, and an evolved igneous group (Group 2) with higher Zr and K_2O, but lower TiO_2, MgO and Fe_2O_3 (de Lange *et al.,* 1987; Pearce and Jarvis, 1992, 1995) (Figure 6.4). Group 1 includes beds Mb, Mp and Mab and Group 2 includes beds Mg, Mo and Mz, as delineated by the Fe_2O_3-Al_2O_3-MgO, K_2O-TiO_2-Al_2O_3 and K_2O-TiO_2-Zr ternary diagrams (Figure 6.4). However, beds Mn and Maf have a more convoluted provenance, displaying geochemical affinities for both Groups 1 and 2.

In regards to Zr, beds Mn and Maf have an affinity to the lower Zr composition of Group 1 (Figure 6.4C). However, both Mn and Maf can be assigned to Group 2 within the Fe_2O_3-Al_2O_3-MgO and K_2O-TiO_2-Al_2O_3 ternary diagrams (Figures 6.4A and 6.4B). Furthermore, the K_2O-TiO_2-Zr ternary plot shows that Mn and Maf may form a disparate compositional group, where Mn has a closer affinity to Group 1 than Maf (Figure 4C). Conversely, the K_2O-TiO_2-Al_2O_3 ternary diagram shows that Maf has a closer affinity to Group 2 than Mn (Figure 6.4B).

Caution must be made when attempting to assign provenance based on such few geochemical measures, although some conclusions are clear. Beds Mp and Mab of Group 1 are compositionally associated with Mb, thus can be potentially attributed to an El Hierro provenance; since Mb has been shown to have originated from the El Golfo landslide from El Hierro (Masson *et al.,* 2002, and references therein; Frenz *et al.,* 2009). Furthermore, beds Mo and Mz of Group 2 have similar compositions to Mg, and

thus are associated with Tenerife; since bed Mg originated from the Icod landslide from Tenerife (Masson *et al.,* 2002, and references therein; Frenz *et al.,* 2009; Hunt *et al.,* 2011). The composition of Mn shows both affinities to Group 1 and 2, whereas Maf shows greater affinity to Group 2 than Group 1. There are no alternative submarine landslides recorded from El Hierro or Tenerife at ~500 ka, while La Palma records the Cumbre Nueva landslide, thus La Palma is speculated to be the provenance of bed Mn. Based on the mudcap geochemistry, the provenance of Maf could be either Tenerife or La Palma, although the older date of this bed implies a Tenerife source.

High resolution coccolith biostratigraphy was completed on core D11814 and the aforementioned piston cores from the Madeira Abyssal Plain. This biostratigraphy resolves datum horizons within the hemipelagite sediment deposited between the turbidites. This utilised first and last species occurrences and boundaries between acme zones (Figure 6.5). These datum horizons are described in Tables 6.3 and 6.4 and shown in Figure 6.5. The position of the bed in relation to specific datum horizons, e.g. in D11814 (Figure 6.5), can be used to date the beds. However, hemipelagite sedimentation rates can also be generated from these datum horizons and used to also broadly date the beds (Figure 6.6a). Hemipelagite sedimentation rates appear to decrease at ~500 ka, probably due to compaction, which causes issues with application of either broad linear or polynomial trends to these data. Linear sedimentation rates appear to underestimate and inconsistently date turbidites at 150-550 ka (beds Mg, Mn, Mo and Mp), while a polynomial sedimentation rate better dates the younger beds but underestimates and inconsistently date turbidites >800 ka (beds Mz, Mab and Maf) (Table 6.5).

Down-core variations in the L* (reflectance) profiles through the hemipelagite sediment in D11814 potentially correspond to glacial-interglacial cycles (Figure 5). Coccolith biostratigraphic datums can calibrate the L* profiles in the piston cores (Figures 6.5 and 6.7). Thus hemipelagite coccolith biostratigraphy in combination with the down-core L* profiles demonstrate that the 1.5 Ma to recent stratigraphy can be reliably correlated and dated (Figure 6.7).

Patterns in peaks and troughs in the L* and coupled b* (anticorrelation) records between the turbidites can be correlated to peaks and troughs in the Lisiecki and Raymo (2005) global benthic foraminifera $\delta^{18}O$ record. Glacial oxygen isotope stages are commonly characterised by red-brown glacial clays with <50 values on the L* greyscale. Higher L* values (generally >55) correspond to white interglacial oozes and

marls. However, these results do ultimately rely on coccolith biostratigraphy to provide robust datum horizons.

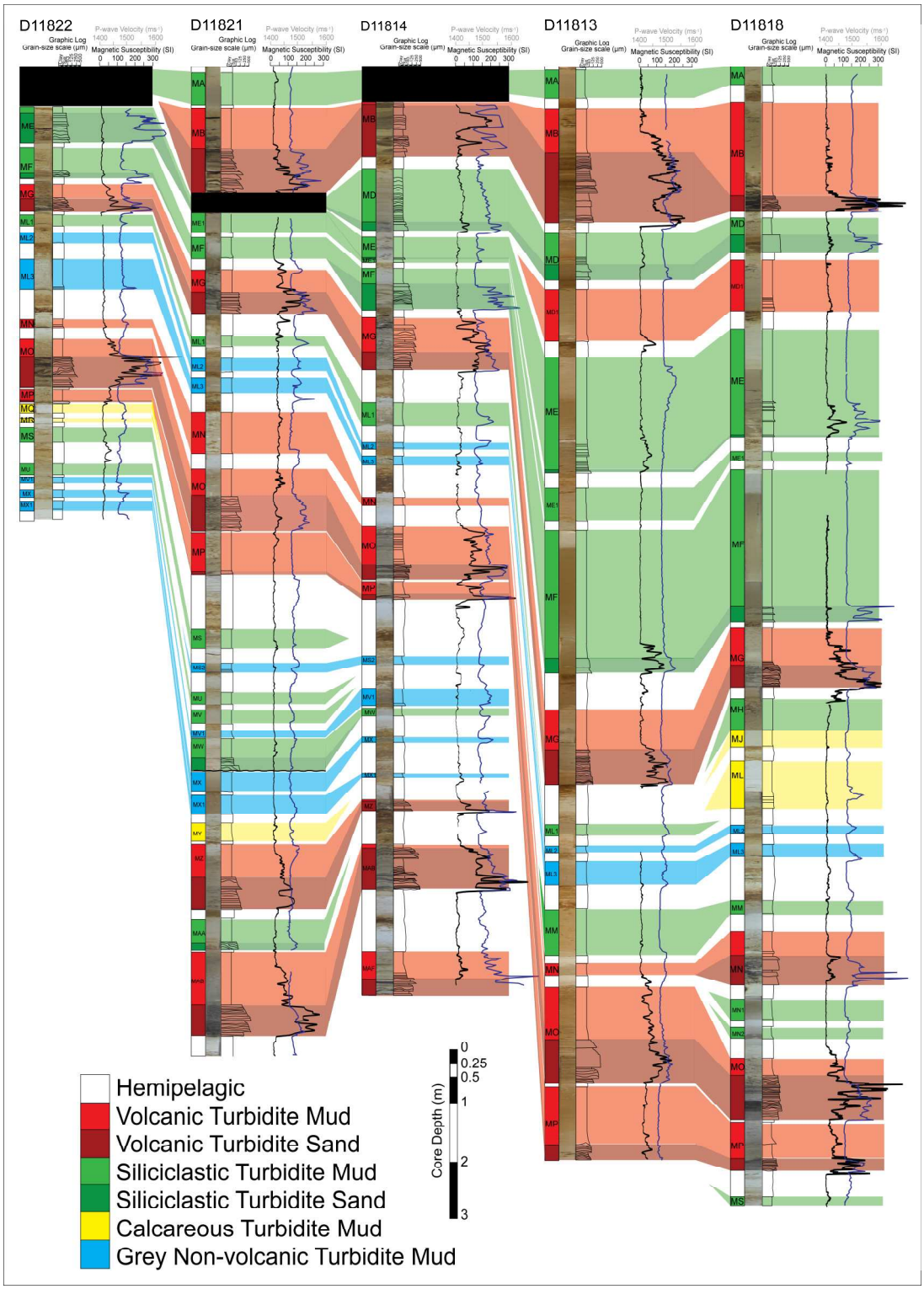

Figure 6.2 Core correlation panel of the piston cores in the Northern Madeira Abyssal Plain with the key volcanic events in red. Black areas signify missing core. P-wave velocity profiles demonstrate turbidite sands and magnetic susceptibility demonstrates presence of volcaniclastic turbidites.

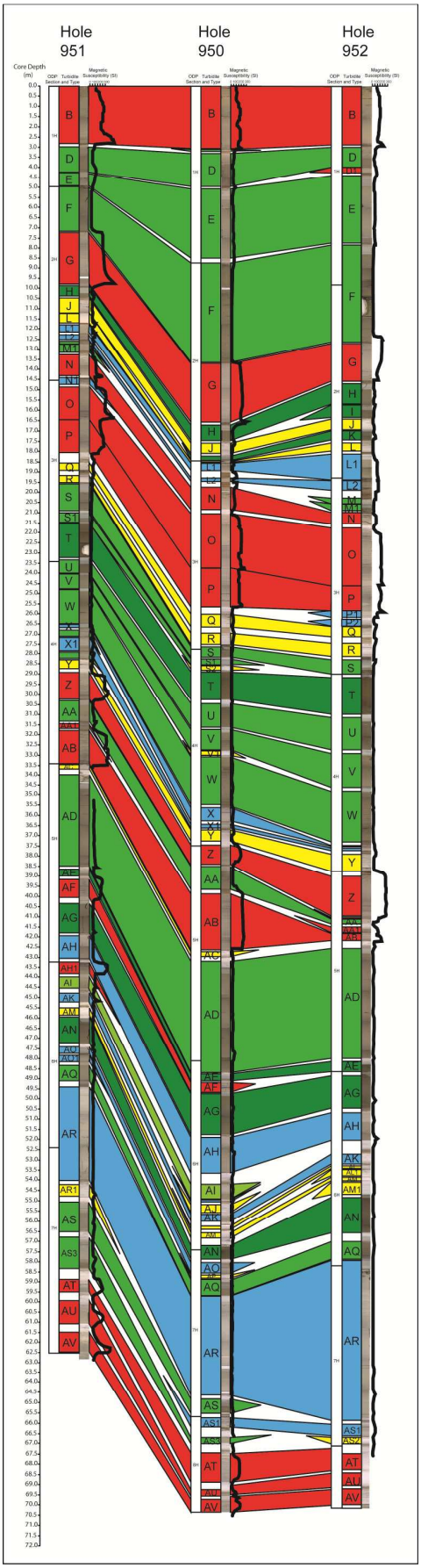

Figure 6.3 Correlation panel of ODP holes 950, 951 and 952 showing Pleistocene-age turbidites in the Madeira Abyssal Plain. Turbidite legend from figure 6.3.

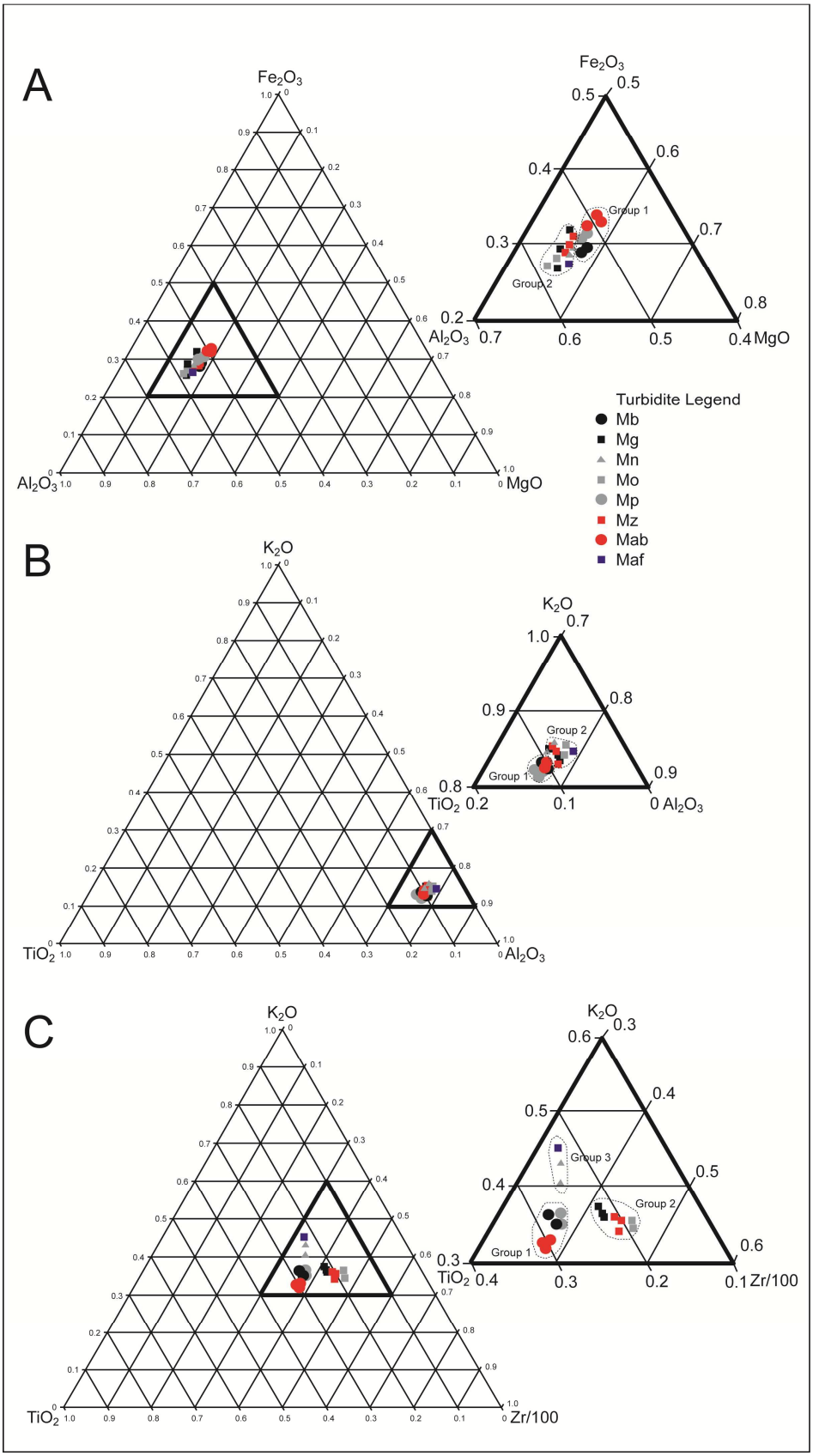

Figure 6.4 Mudcap geochemistry of 0-1.5 Ma turbidites from the piston core record. Results taken from ODP dataset of Jarvis *et al.* (1998) and plotted on ternary diagrams of de Lange *et al.* (1987).

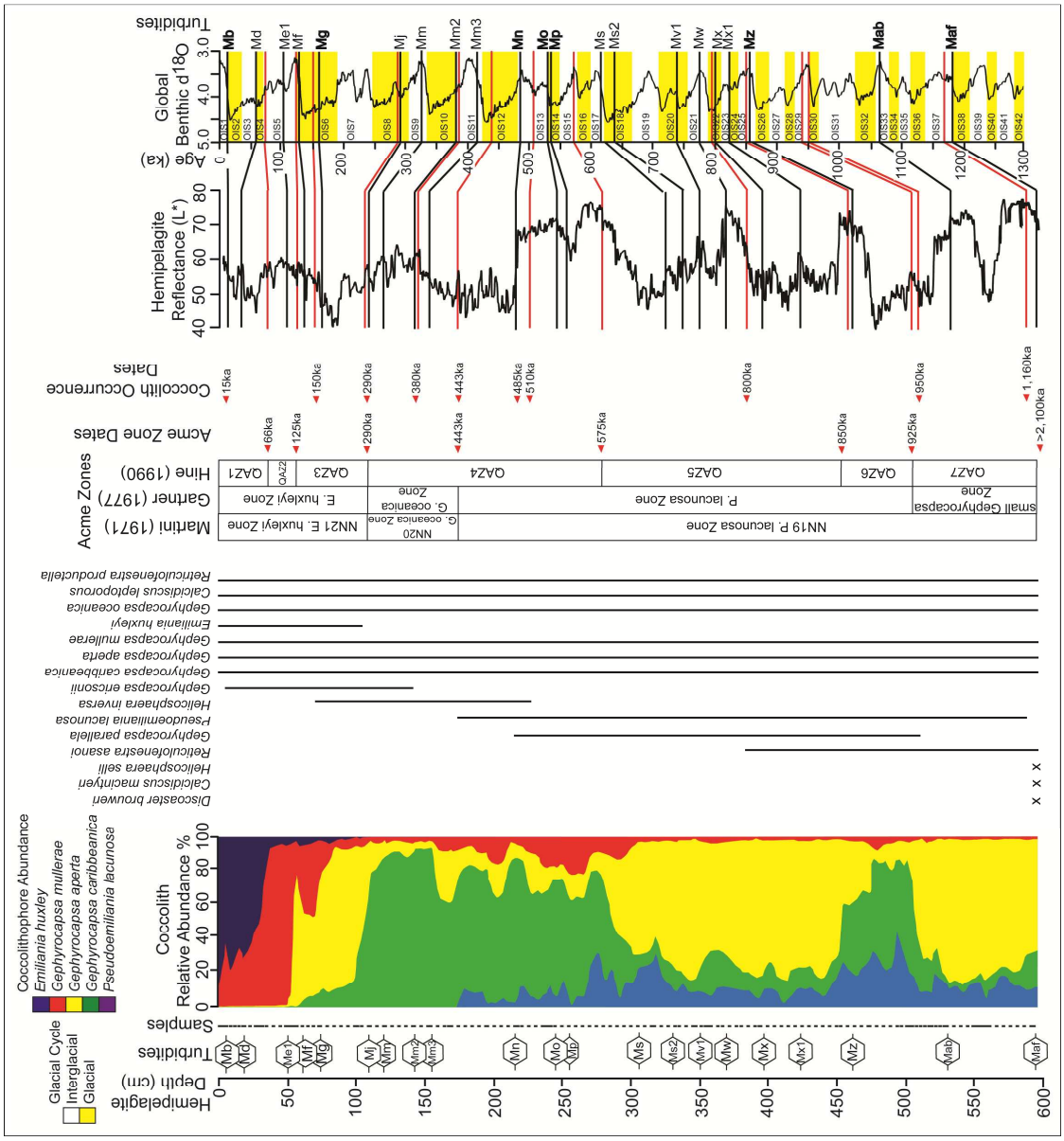

Figure 6.5 Hemipelagite coccolith biostratigraphy for core D11814 in the northern Madeira Abyssal Plain. Displays details on coccolith acme zones based on relative abundances and biozones based on species first and last occurrences. The liostratigraphic dates are used to calibrate the hemipelagite reflectance curve (L*). The biostratigraphy and L* profile is then linked to the Lisieki and Raymo (2005) benthic δ18O curve.

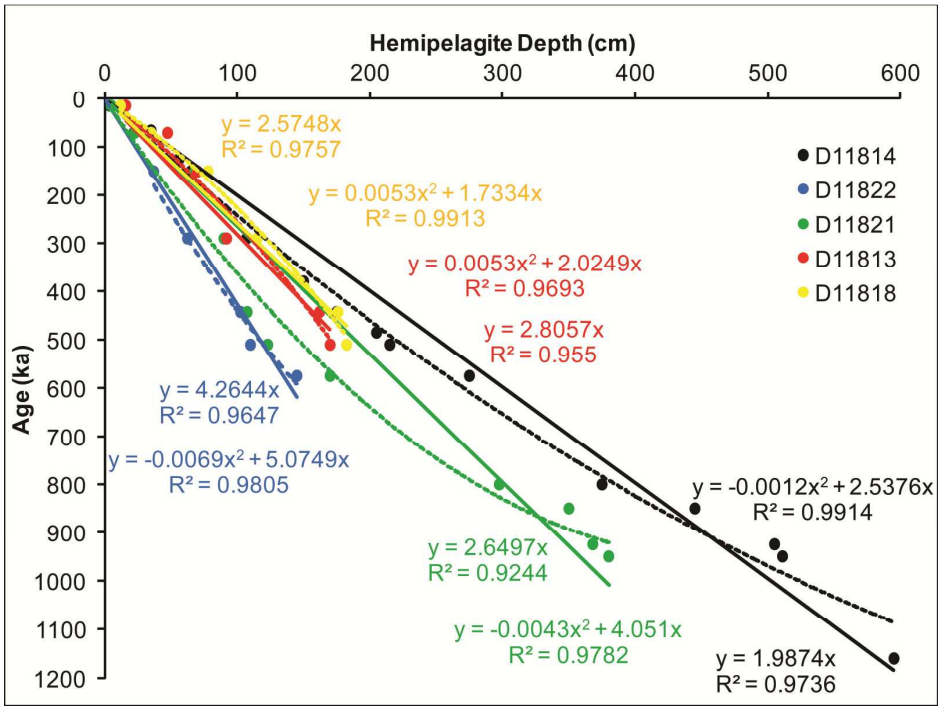

Figure 6.6 Hemipelagite sedimentation rates for the piston cores in Figure 2, based on coccolith biostratigraphy. Bold lines represent a linear trend fitted through the dates of each core, while the dashed lines represents a polynomial function.

The L* profiles demonstrate that significant negative/positive excursions relate to changes in climate/sea level, in accordance with Weaver and Kuijpers (1983). Correlating the dated L* profiles to the Lisiecki and Raymo (2005) global benthic foraminifera $\delta^{18}O$ record allows an additional method of dating the major volcaniclastic turbidites: Mb at ~15 ka, Mg at ~170 ka, Mn at ~485 ka, Mo at ~535 ka, Mp at ~540 ka, Mz at ~850 ka, Mab at ~1040 ka and Maf at ~1175 ka (Figure 6.6). Age constraints from the L* record are conservatively ±10 ka depending on depth in core. The use of high resolution biostratigraphy, often on 1cm resolutions around important datum horizons, in combination with the 0.5 cm resolution L* profiles provide these high levels of confidence in the dating of turbidites. The error is reduced where oxygen isotope stage boundaries can be clearly attributed within the L* record (±5 ka). Applying a single, broad hemipelagite sedimentation rate to date beds potentially provide ages with greater error. Rather a combination of the aforementioned high resolution methods enables dating with greater certainty. The dates obtained for these turbidites compare favourably to dates previously published by Weaver *et al.* (1992) (Table 6.5).

To further aid verification of the ages derived from biostratigraphy and L* profiles for the deposits recovered in the piston cores, previous biostratigraphic dates from ODP

studies are utilised. A biostratigraphic marker is based on a *R. asanoi* event at 36.51-37.52 m depth at ODP site 950 (5 cm above bed Mz), and is dated at 830 ka (Howe and Sblendorio-Levy, 1998). The top of the Jaramillo event (980 ka) occurs at 39.7 m core depth above bed Mab and below Mz at ODP site 950. While the bottom of the Jaramillo event (1.05 Ma) is at 42.7 m core depth immediately below bed Mab (Shipboard Scientific Party, 1995a). These ODP biostratigraphic and magnetostratigraphic ages support the dates attributed to the volcaniclastic turbidites from the piston core study and support correlation of events between the two core datasets (Table 6.5).

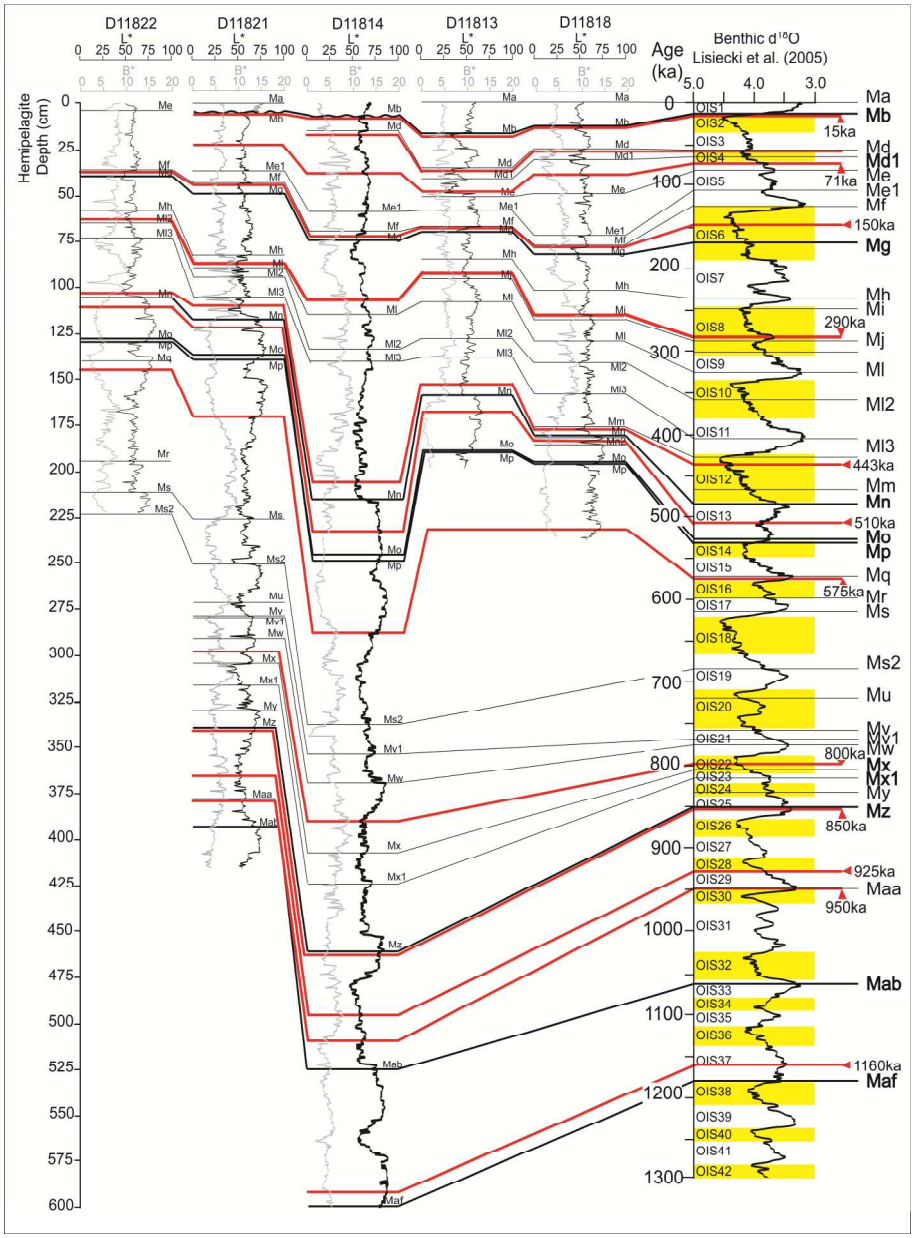

Figure 6.7 L* and b* photospectometry profiles of the hemipelagites in piston cores D11822, D11821, D11814, D11813 and D11818 in the Northern Madeira Abyssal Plain. Turbidites intervening the record are represented and correlated at black lines. Hemipelagite records and turbidites are linked to the global benthic foraminifera δ18O curve of Lisiecki and Raymo (2005).

Table 6.5 Summary of 0-1.5 Ma volcaniclastic turbidites from the Madeira Abyssal Plain

Event Name	Biostratigraphic Age (ka)	Sedimentation Rate Age (ka)*1	Photo-spectrometry Age (ka)*2	ODP Age (ka)	Turbidite Volume (km^3)*3	Mudcap Geochemistry	Volcanic Glass Geochemistry	Island Provenance	Landslide Association
Mb	15	21±1	15	?	105±15	Basic	Basalt-Trachyte	El Hierro	El Golfo
Md1	60-70	70	70	80	10	Basic	?	El Hierro	?
Mg	160-190	170±2	165	170	130±25	Evolved	Basanite-Phonolite	Tenerife	Icod
Mn	480	346±5	490	485	50±15	Evolved	Picrobasalt-Tephriphonolite	La Palma	Cumbre Nueva
Mo	500	378±5	530	505	135±30	Evolved	Basanite-Phonolite	Tenerife	Orotava
Mp	500-510	404±5	540	510	90±25	Basic	Picrobasalt-Phonolite	El Hierro	El Julan
Mz	?	870±20	850	830	90±40	Evolved	Basanite-Phonolite	Tenerife	Güimar
Mz1	?	?	?	970	10	?	?	?	?
Maa1	?	?	?	1040	22±2	?	?	?	?
Mab	?	1025±30	1060	1050	130±25	Basic	Picrobasalt-Tephriphonolite	El Hierro	Tiñor
Maf	?	1160±30	1180	1200	50±30	Evolved/Basic	Basanite-Phonolite	Tenerife	Roques de García
Mah1	?	?	?	1270	40	?	?	?	?

*1 1.91-2.31 cm/1000 year sedimentation rates from D11813, D11814, D11818 and D11821.
*2 errors of ±20 ka due to requirement for photospectrometry to be anchored by biostratigraphy.
*3 turbidite volumes are decompacted volumes calculated from ODP core using method of Weaver (2003).

Late Quaternary Volcanic Turbidite Glass Geochemistry

Bed Mb contains glasses of ultra-mafic picro-basalt to evolved trachyte-phonolite compositions. The glasses principally fall within the onshore compositional range for El Hierro on the total alkali-silica (TAS) diagram (Le Bas *et al.,* 1986). Although

composed of basalts and basanite glasses, Bed Mb also contains glasses of phonolite, trachyte and phonotephrite compositions (Figure 6.8A). The presence of evolved glasses, from the predominantly basaltic El Hierro source, is supported by original turbidite provenance work by Pearce and Jarvis (1992). Indeed, the evolved trachyte glasses analysed here have similar compositions to those measured by Pearce and Jarvis (1992). Furthermore, the onshore composition field is constrained using limited documented samples.

Bed Mg in the Madeira Abyssal Plain is a consequence of the Icod landslide on Tenerife (Hunt *et al.,* 2011, and references therein). Previously, focus has been on comparing the volcanic glasses from the subunit divisions of the Icod event bed (Hunt *et al.,* 2011). The glasses from the combined subunits from bed Mg comprise predominantly evolved phonolites, in addition to trachytes, trachy-basalts, trachy-andesites, tephriphonolites, and basalt trachy-andesites (Figure 6.8B). Together with the evolved composition of the mudcap, the glass compositions support a Tenerife provenance.

Bed Mn represents the next significant volcaniclastic turbidite, dated at ~485 ka. The volcanic glasses recovered from bed Mn lie within the onshore compositional field for La Palma (shown) and El Hierro (Figure 6.8C). The glasses lack any evolved glasses >53 wt% SiO_2. Indeed, these are principally basic in composition ranging from picrobasalts to low-alkali tephriphonolites, with <54 wt% silica and <11 wt% alkalis (Figure 6.8C). This supports an attribution of a basaltic source. With the mudcap geochemistry also showing disparity from the El Hierro source, the implication is that La Palma is the provenance for this basaltic bed.

The overall glass composition for the ~535 ka bed Mo is generally evolved, corresponding to the onshore compositional field for Tenerife (Figure 6.8D). Although a minor proportion of glasses are basalt and basanite in composition, the glasses recovered are predominantly tephriphonolitic to phonolitic (Figure 6.8D). These evolved glasses are >56 wt% SiO_2 and >8 wt% alkalis, similar to those from bed Mg.

The overall composition of the ~540 ka bed Mp spans picrobasalts to phonolites, akin to the compositional distribution of bed Mb from El Hierro (Figure 6.8E). There are a minor component of glasses with evolved tephri-phonolites and phonolites. However, the predominant glass composition is basanite.

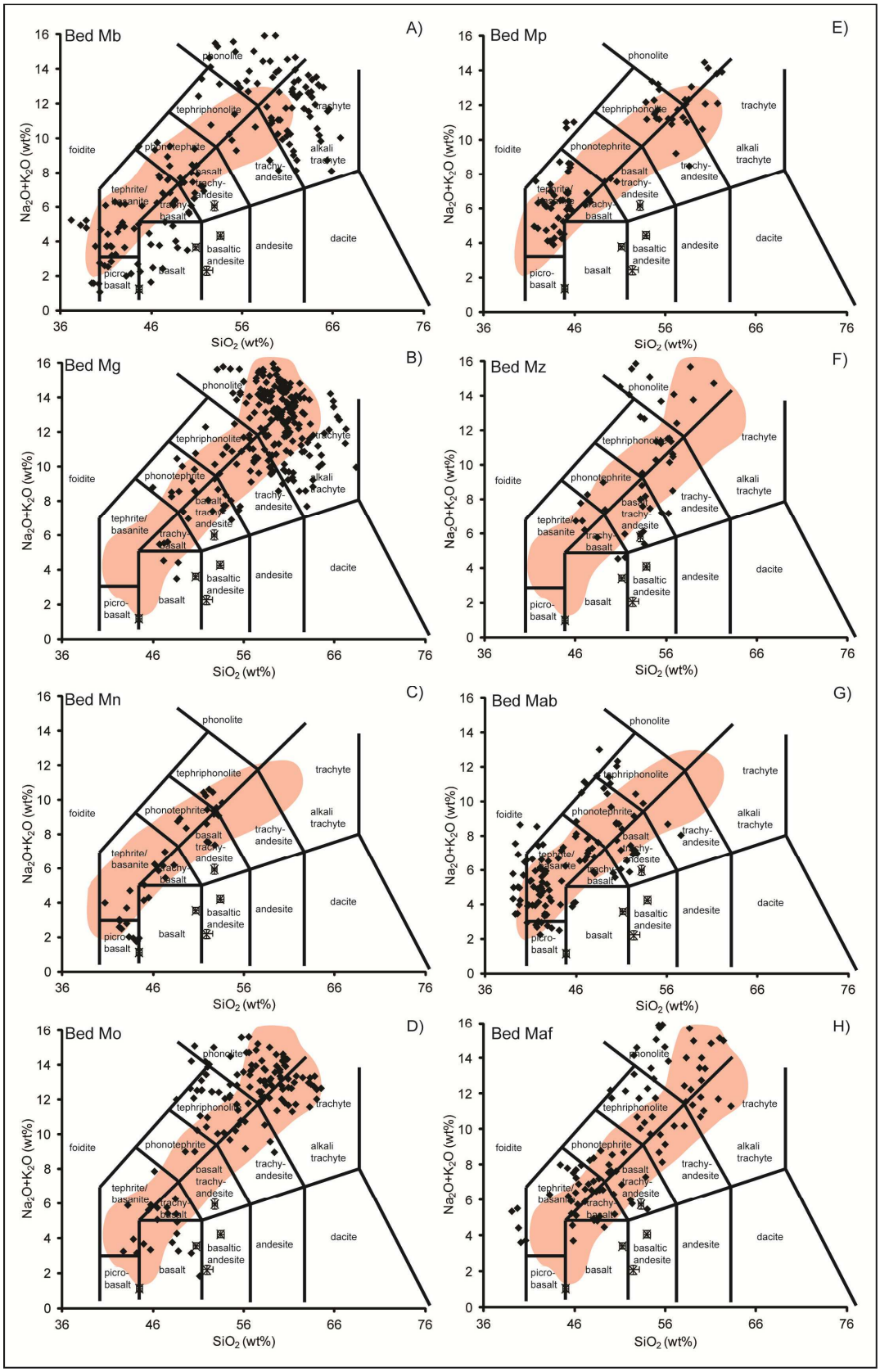

Figure 6.8 Composition of volcanic glasses recovered from the turbidite sands of the volcaniclastic turbidites Mb (A), Mg (B), Mn (C), Mo (D), Mp (E), Mz (F), Mab (G), and Maf (H). Data shown displayed on total alkali-silica diagrams. Red underlay is onshore composition of the respective island provenance. Onshore island data compiled from GeoRoc website (georoc.mpch-mainz.gwdg.de/georoc).

Bed Mz has been dated at ~850 ka, with an evolved mudcap composition. Indeed, Bed Mz lacks glasses of basic composition <46 wt% SiO_2 and <4 wt% alkalis, and is composed predominantly of evolved volcanic glasses (Figure 6.8F). This predominantly evolved composition, akin to beds Mg and Mo, supports a Tenerife provenance.

The bed Mab deposit (~1.05 Ma) has glasses that cover a compositional range from basic picrobasalts to tephriphonolites (Figure 6.8G). The dominant composition is that of basanite, with <44 wt% SiO_2 and <7 wt% alkalis (Figure 6.8G). This composition supports a basic source. The range of compositions is similar to bed Mb, and along with the mudcap composition, supports an attribution to an El Hierro provenance.

Bed Maf, which has been dated at ~1.2 Ma, has a mudcap geochemistry that indicates an affinity for the evolved Tenerife composition. This is confirmed in the volcanic glass composition. Although there are basanite glasses, there are not basalt or picrobasalt glasses. Indeed, overall the glasses comprise predominantly evolved compositions >46 wt% SiO_2, which lie within the compositional range associated with Tenerife (Figure 6.8H).

Although studies of volcanic glasses by SEM EDS are not ideal, the accuracy and precision afforded by the present study are adequate for a relatively quantitative assessment of provenance. The major-element compositions of the Canary Island volcanics are very similar and overlap. However, relative proportions of basic and evolved igneous glasses within the turbidite sand fraction, as discussed, coupled with the mudcap geochemistry can provide insight into provenance.

Summary of Turbidite Occurrence and Composition based on ODP Boreholes

The ODP volcaniclastic turbidite record forms two parts: a pre-7.5 Ma and post-7.5 Ma history. Apart from several minor 10-50 cm-thick turbidites, the post-7.5 Ma turbidite history at 0 to 230 mbsf is predominantly consistent and correlateable between the three ODP sites (Figures 6.3, 6.9, 6.10 and 6.11). This is characterised in a series of correlation panels depicting the Pleistocene (Figures 6.2 and 6.3), Late Pliocene (Figure 9), Early Pliocene (Figure 6.10) and Latest Miocene (Figure 6.11). The turbidites are organic-rich siliciclastic, volcaniclastic and calcareous in types, and commonly 0.5-11.0 m-thick, whereby the volcaniclastic turbidites range from 0.5-4.0 m-thick. These beds are dated using a sequence of hemipelagite datum horizons derived by Howe and Sblendorio-Levy (1998) at each ODP Site (Figure 6.12).

The post-7.5 Ma volcaniclastic turbidites have decompacted volumes of 5-380 km^3, which far exceed the volumes present in the pre-7.5 Ma history (Figure 13). Although there are turbidites with similar geochemical compositions to those of the pre-7.5 Ma record, there is a distinct shift in the composition in the post-7.5 Ma volcaniclastic turbidites (Figures 6.14). These post-7.5 Ma volcaniclastic turbidites have relatively increased Ti, Zr, K and Mg compositions (Figure 6.14 and 6.15).

The Zr/Al-Ti/Al cross-plot shows delineation of three compositional groups of increasing Zr/Al and Ti/Al (Figure 6.15A). There are three groups derived from K/Al-Cr/Al showing increasing K/Al with generally decreasing Cr/Al (Figure 6.15B), and three groups from Si/Al-Mg/Al showing increasing Si/Al with decreasing Mg/Al (Figure 6.15C). There are consistencies between these groups, such that a group of pre-7.5 Ma turbidites (older than FT) have low Ti and Zr, in addition to low K, low Mg and high Cr (Figures 6.14 and 6.15). A second group of lower Zr and Ti comprising younger events is also consistent with low K and low Mg (Figure 6.15). There is a group of volcaniclastic turbidites with moderate Zr and Ti, including B (Mb), P (Mp) and AB (Mab) from El Hierro and N (Mn) from La Palma, which also have moderate-to-low K and high Mg (Figure 6.15). There is final group of volcaniclastic turbidites with high Zr and Ti, including G (Mg), O (Mo) and Z (Mz) from Tenerife, which have moderate Si, moderate-to-high Mg, and high K (Figure 6.15).

The pre-7.5 Ma volcaniclastic record is characterised by 0.2-1.0 m-thick grey and dark-grey volcaniclastic turbidites, which cannot be correlated between holes 950, 951 and 952 with any certainty. The volumes of these pre-7.5 Ma volcaniclastic turbidites are minor, with most being <10 km^3 (Figure 6.13). The turbidites are also characterised by relatively low Ti, Zr, K and Mg, with relatively higher Si and Cr (Figures 6.14 and 6.15).

Specific Provenance and Timing of Volcaniclastic Turbidites from ODP History

Mid-Late Miocene 7.5-6.0 Ma Record

The first metre-thick volcaniclastic turbidites occur after 7.5 Ma, with an initial sequence from 7.5 to 6.0 Ma comprising beds FT to FD, FT, FK and FD. These represent the thickest and most voluminous turbidites of this period, indeed bed FK is the largest volcaniclastic event recorded in the Madeira Abyssal Plain (4 m-thick and 380 km^3-volume). Bed FT has moderate Zr, Ti and Mg, high K and low Si, signifying a basic, but not depleted composition (Figure 6.15). Beds FS and FR have low Zr, Ti and

Si, moderate Cr and high K, indicating more basic compositions, but are relatively low in volume. While beds FP, FO, FM, FL and FD have high-to-moderate Ti, high Zr and K, and low-to-moderate Mg and Si, which signify evolved compositions similar to those of turbidites G, O and Z from Tenerife (Figure 6.15). The aforementioned FK turbidite from the 7.0 to 6.0 Ma period has a basic and depleted composition. During this period there is volcanic activity on both La Gomera and early phase shield building on Tenerife (Thirlwall *et al.,* 2000; Paris *et al.,* 2005; Ancochea *et al.,* 2006).

Early Pliocene 5.3-4.0 Ma Record

The thickest and most volumetric turbidites are beds EK and DK, representing 1.5-2.0 m-thick and 50-60 km^3 deposits in the Madeira Abyssal Plain. These have evolved compositions, with bed DK at 4.21 Ma having a similar composition to turbidites of Tenerife provenance (Figure 6.15). The other turbidites (EI, EH, DZ, DY, DU, DL and DF) are basic to trace-element depleted in composition, but with increased potassium (Figure 6.15). During this period there is volcanic activity persisting on Tenerife and La Gomera (Thirlwall *et al.,* 2000; Paris *et al.,* 2005; Ancochea *et al.,* 2006), with activity also recommencing on Gran Canary (van den Bogaard and Schmincke, 1998).

Late-Early Pliocene to Early-Late Pliocene 3.7-3.0 Ma Record

This time frame commences with a 1.75 m-thick turbidite at 3.75 Ma (bed DB). Turbidite DB has low Zr and Ti, but high K and Mg (Figure 6.15), thus having properties similar to turbidites from the pre-7.5 Ma record associated with a trace element-depleted origin and a basic composition (Jarvis *et al.,* 1998). The following turbidites (beds CV1, CT4 and CT4) are thin-bedded and low-volume events with basic compositions. The CS turbidite (3.25 Ma) represents the thickest and most volumetric event in this time frame (2-4 m-thick and 110 km^3). This event has a basic composition of high Ti and Mg, and moderate Si, K, Cr and Zr, similar to those ascribed to El Hierro (Figure 6.15). The last events of this time frame (beds CR and CM) are similar to the DB turbidite. Although there is volcanic activity on La Gomera and Tenerife during this time, there is also volcanic activity and landslide activity on Gran Canaria (van den Bogaard and Schmincke, 1998; Acosta *et al.,* 2003).

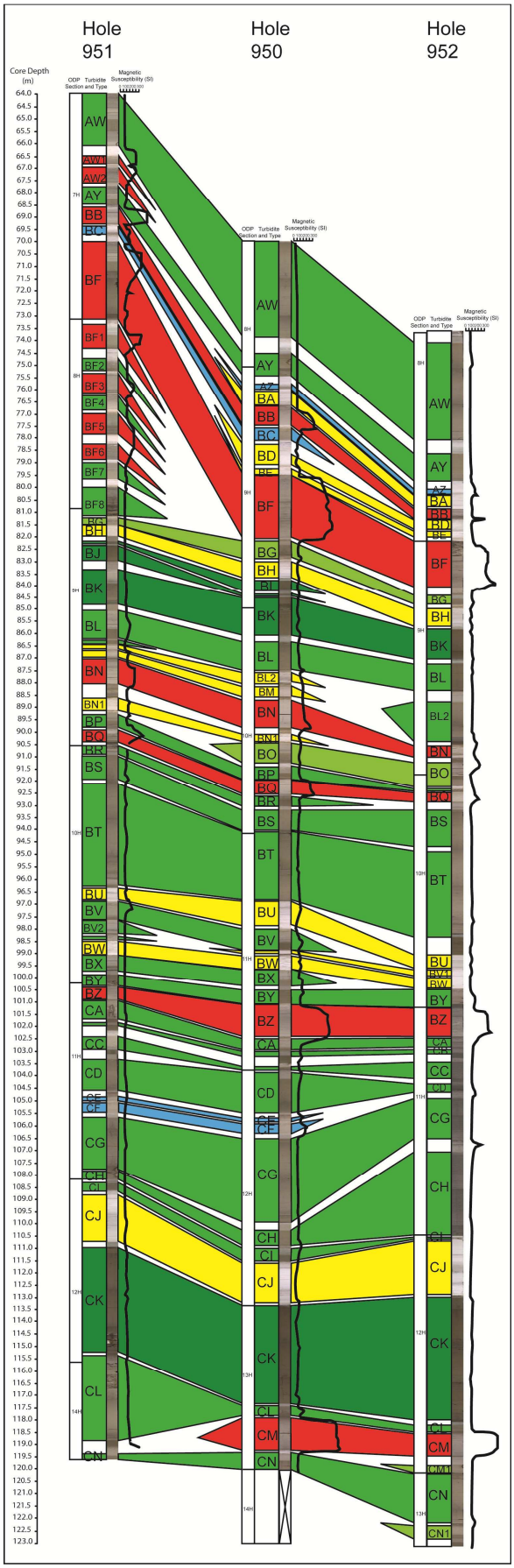

Figure 6.9 Correlation panel of ODP holes 950, 951 and 952 showing Late Pliocene-age turbidites in the Madeira Abyssal Plain. Turbidite legend from Figure 6.2.

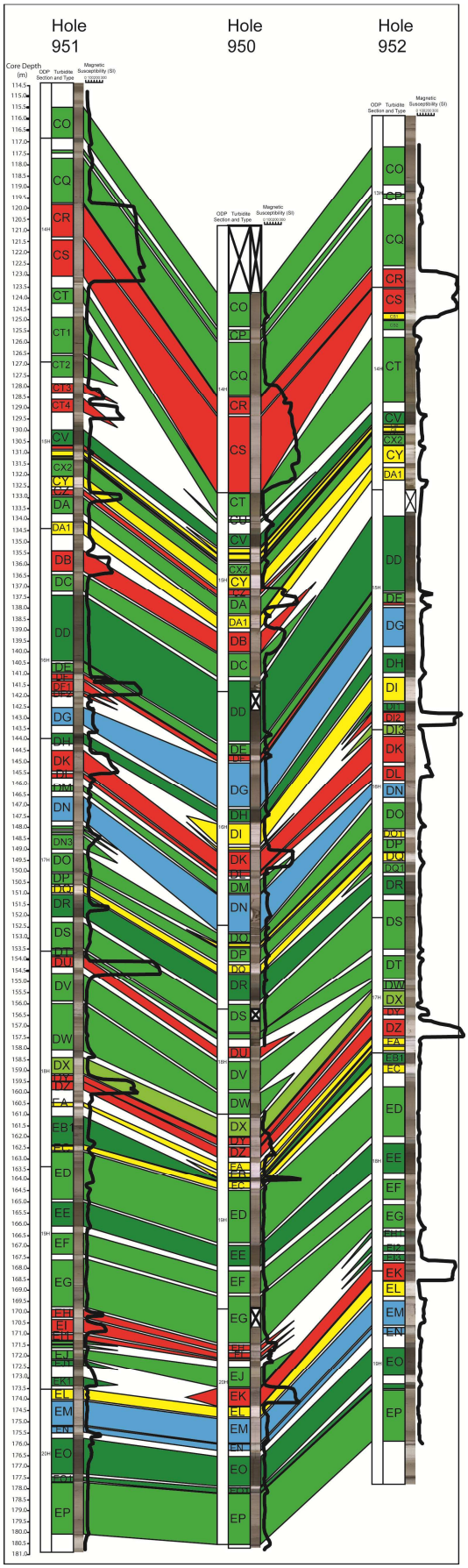

Figure 6.10 Correlation panel of ODP holes 950, 951 and 952 showing Early Pliocene-age turbidites in the Madeira Abyssal Plain. Turbidite legend from Figure 6.2.

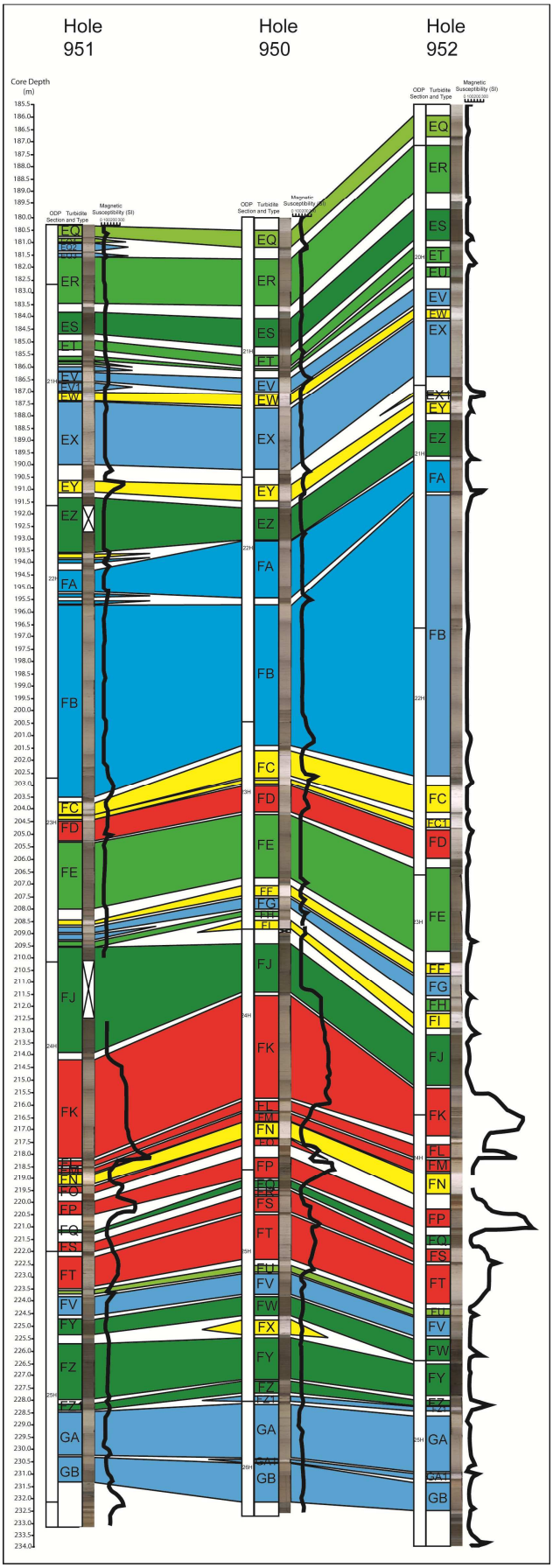

Figure 6.11 Correlation panel of ODP holes 950, 951 and 952 showing Late Miocene-age turbidites in the Madeira Abyssal Plain. Turbidite legend from Figure 6.2.

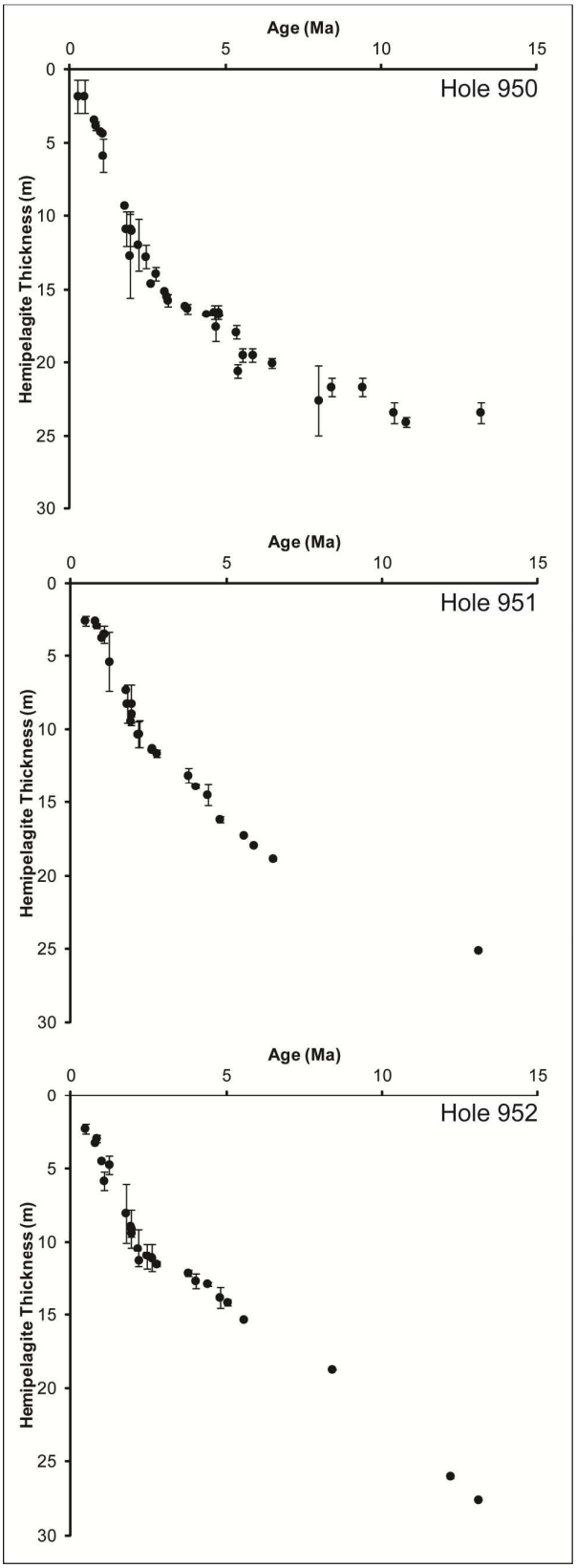

Figure 6.12 Hemipelagite sedimentation rates for the three ODP Holes in Madeira Abyssal Plain (Sites 950, 951 and 952, locations on Figure 1). These sedimentation rates were used to derive the dates of the turbidites that intervene the hemipelagite record.

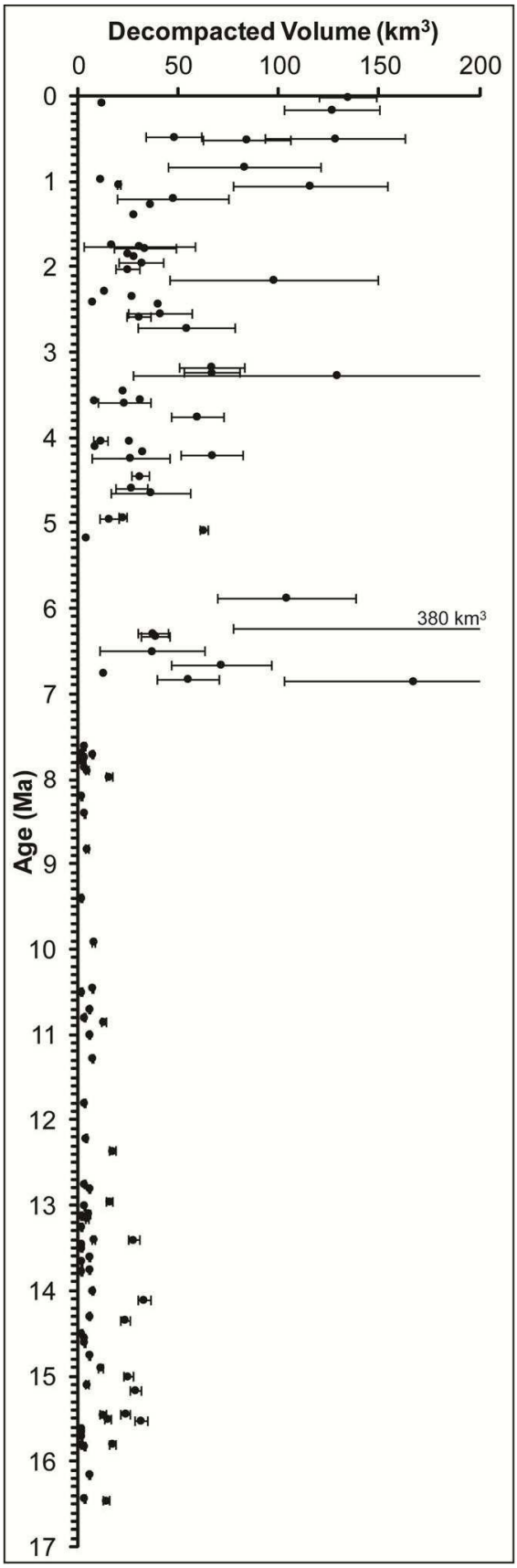

Figure 6.13 Graph showing decompacted volume of the volcaniclastic turbidites against the calculated age of the respective event. Error bars represent the range in volume calculated by applying Weaver (2003) method to each core site, rather than simply Site 951.

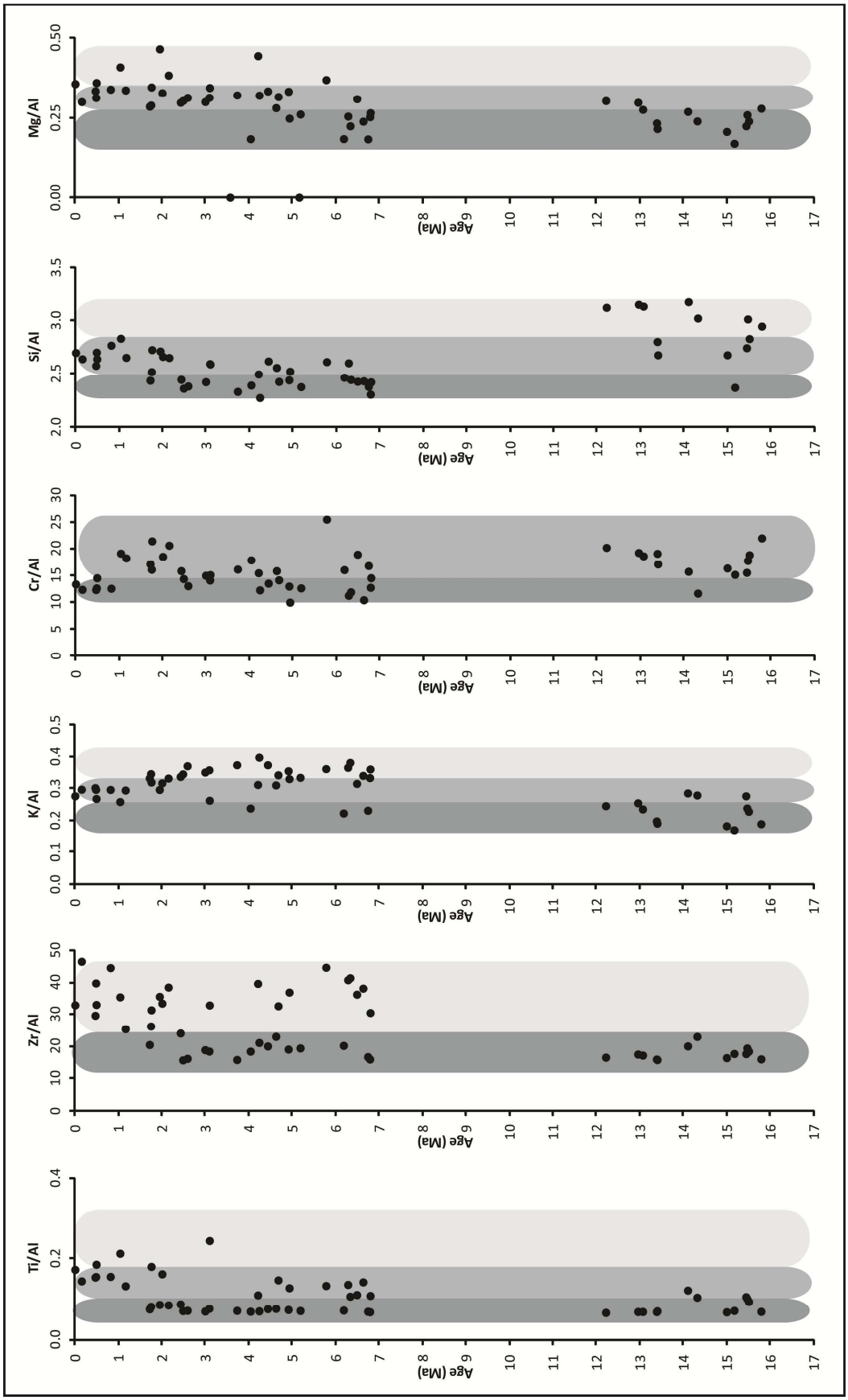

Figure 6.14 Carbonate-free major element composition of volcaniclastic turbidite mudcaps at hole 950 against depth, based on Jarvis *et al.* (1998) ODP published data.

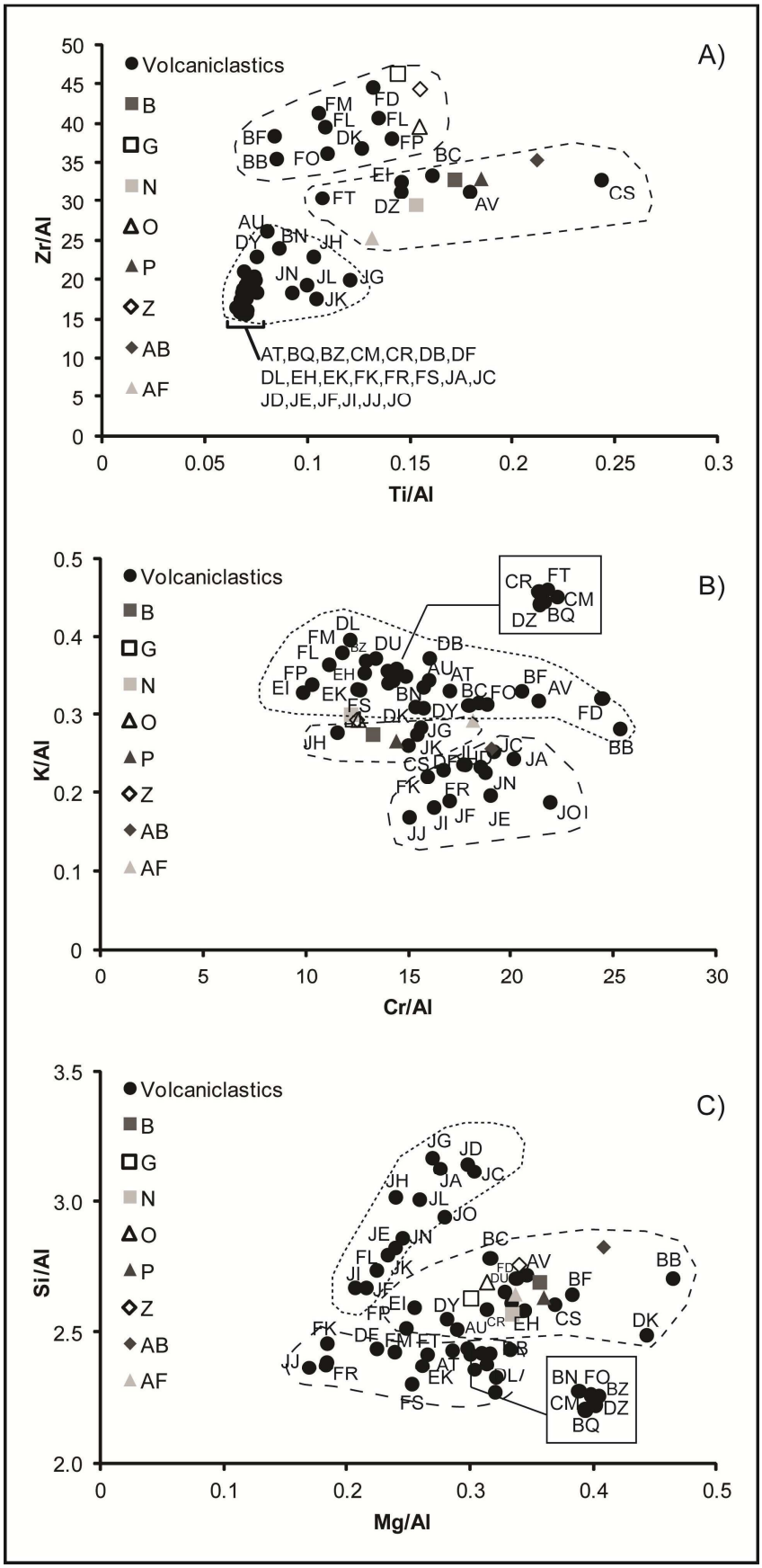

Figure 6.15 Cross-plots of mudcap geochemistry of the volcaniclastic turbidites sampled at hole 950 showing delineation of composition fields. A) Zr/Al against Ti/Al, B) K/Al against Cr/Al, and C) Si/Al against Mg/Al, based on Jarvis *et al.* (1998) ODP published data.

Late Pliocene 2.8-1.8 Ma Record

This turbidite sequence includes thin-bedded turbidites (<0.5 m-thick) and 1-4 m-thick voluminous turbidites (including turbidites BZ, BQ, BN, BF, BC, BB, AV, AU and AT). The BF turbidite, dated at ~2.2 Ma represents the thickest and most volumetric event in this time frame, and is has a composition of high Zr, K, Mg and Cr and low Ti (Figure 6.15), with a similar composition to those previously assigned to a Tenerife provenance. Turbidites BZ, BQ and AT have low Zr and Ti but moderate-to-high K and Mg. While turbidites BN, BC, AV, and AU have moderate (basic) Zr and Ti, and moderate-to-high K and Mg, similar to those ascribed to a La Palma or El Hierro provenance (Figure 6.15). During this period there is volcanic activity on Tenerife and Gran Canaria, with a cessation of activity on La Gomera (Paris *et al.,* 2005; Ancochea *et al.,* 2006). In addition volcanic activity commences on La Palma at the end of this time frame (Ancochea *et al.,* 1994; Carracedo *et al.,* 2001).

Pleistocene 1.6-0 Ma Record

This record has been documented previously and re-investigated in the current contribution (Weaver *et al.,* 1992; Pearce and Jarvis, 1992, 1995). The record represents a number of turbidites of evolved and basic compositions that can be correlated to Tenerife and western Canary Island provenances. The compositions have high Zr, K and Mg and high to moderate Ti and Si (Figure 6.15).

Discussions

Piston Core Records of 0-1.5 Ma Catastrophic Flank Collapses from the Canary Islands

The large-volume volcaniclastic turbidites in the Madeira Abyssal Plain record the catastrophic flank collapses of the western Canary Islands (Watts and Masson, 1995; Masson, 1996; Wynn and Masson, 2003; Hunt *et al.,* 2011). However, previously documented Madeira Abyssal Plain piston core stratigraphy only resolved these events to ~500 ka (Weaver *et al.,* 1992). The present study is able to extend this volcaniclastic turbidite history to ~1.5 Ma, supplemented with biostratigraphy, L* hemipelagite stratigraphy, new volcanic glass geochemistry and bulk major-element mudcap geochemistry from previous ODP studies (Figures 6.2-6.8).

Turbidites Mb (~15 ka), Mp (~540 ka) and Mab (~1.05 Ma) have a provenance from El Hierro, and can be assigned to the El Golfo, El Julán and Tiñor landslides

respectively (Figure 6.16 and Table 6.5). Turbidite Mn (~485 ka) has a speculated provenance from La Palma, and is potentially associated with the Cumbre Nueva landslide (Figure 6.16 and Table 6.5). Lastly, turbidites Mg (~165 ka), Mo (~535 ka), Mz (~850 ka) and Maf (~1175 ka) are attributed to a Tenerife provenance, and represent the Icod, Orotava, Güímar and Roques de García landslides respectively (Figure 6.16 and Table 6.5). Turbidite dates may have errors of ±10 ka and Canary Island geochemical compositions overlap considerably; thus it must be appreciated that there are varying degrees of certainty on the correlation between turbidite and onshore landslide.

Tenerife

The Icod landslide (bed Mg in Madeira Abyssal Plain and AB14 in Agadir Basin at ~165 ka) represents the last flank collapse from northern Tenerife. The consistent date of the turbidite ascertained by Hunt *et al.* (2011) coupled with onshore dating constraints of 150-170 ka (Ablay and Hürlimann, 2000), would indicate that the 165±5 ka date is accurate. The evolved composition of the turbidite mudcap and volcanic glasses support Tenerife as the provenance, and support the assignment of bed Mg to the Icod landslide (Figures 6.4 and 6.8, Table 6.5). The volume of this landslide has been previously calculated to 320±40 km^3 (Table 6.2) (Hunt *et al.,* 2011). The timing of the Icod landslide appears to be coincidental with the El Abrigo explosive eruption (dated at 170 ka by Huertas *et al.* 2002) at the end of the Diego Hernàndez eruptive cycle.

The Orotava landslide of northern Tenerife has been dated onshore from 540 to 710 ka (Marti *et* al., 1994; Watts and Masson, 1995; Ancochea *et al.,* 1999; Cantagrel *et al.,* 1999; Marti and Gudmundsson, 2000). The relatively poor onshore dating constraints mean that the associated turbidite presents the best dating control. Bed Mo has an evolved mudcap composition and volcanic glasses of basanite to predominantly phonolite composition, supporting Tenerife as the source (Figures 6.4 and 6.8). Bed Mo has a date of 535±10 ka, which is consistent with onshore dates of the Orotava landslide (Table 6.5). The offshore volume of the debris avalanche has been estimated at 80 km^3 (Ablay and Hürlimann, 2000). The volume of the turbidite within the Madeira Abyssal Plain is 130±30 km^3. However, the turbidite volume in the more proximal Agadir Basin is unknown, indicating that the total volume of ~210 km^3 is a minimum. The geometry of the La Orotava valley indicates an onshore failure component of 130 km^3 (Ablay and

Hürlimann, 2000), thus like the Icod landslide (Hunt *et al.,* 2011), a submarine component is required for mass balance. The La Orotava landslide could potentially be linked to the Granadilla explosive eruption (dated at 570 ka by Bryan *et al.* 2000) at the terminus of the Guajara eruptive cycle.

Bed Mz has a provenance of Tenerife (Figures 6.4 and 6.8), and an age of 850±10 ka. Although east-directed, the Güímar landslide (830-840 ka) from Tenerife could have generated a turbidite in the Madeira Abyssal Plain (Table 6.5). Bed Mz has a volume of 85±20 km^3, which is greater than the 37-47 km^3 subaerial volume quoted by Giachetti *et al*. (2011, and references therein) for the Güímar landslide. Indeed, the high volume of the turbidite coupled with the debris avalanche mapped by Krastel *et al.* (2001), would indicate a >120 km^3 volume, thus would also suggest a submarine component to accommodate mass balance (Krastel *et al.,* 2001; Masson *et al.,* 2002).

The Roques de García landslide from Tenerife has a speculative onshore age range of 0.6-1.7 Ma (Cantagrel *et al.,* 1999; Masson *et al.,* 2002). The turbidite Maf in the Madeira Abyssal Plain at 1.18±0.02 Ma has a composition signifying a Tenerife provenance (Figures 6.4 and 6.8, Table 6.5). From 0.9 to 1.7 Ma there is not another turbidite of defined Tenerife provenance with significant volume in the ODP or piston core record, thus bed Maf realistically represents the Roques de García landslide. The turbidite in the Madeira Abyssal Plain represents a volume of 50±25 km^3. Previous estimates of total volume are certainly in excess of this (Masson *et al.,* 2002, and references therein). The remaining volume may reside within a potential turbidite in Agadir Basin and/or a buried proximal debris avalanche, neither of which can be resolved. Although the present contribution implies that turbidite Mz correlates to the Güímar landslide, owing to the poor onshore dating controls, bed Mz could instead speculatively represent the Roques de García landslide and bed Maf represent an older buried event.

La Palma

The landslide history of La Palma is dominated by submarine debris avalanche evidence on the western island flank. This includes the Cumbre Neuva landslide and secondly the Playa de la Veta landslide complex buried beneath it (Table 6.2). There is a 50 ka discrepancy between a maximum 536 ka onshore date of the Cumbre Neuva landslide and that of the proposed turbidite (turbidite Mn at ~485 ka). This could be explained by the poor resolution of the onshore lower age range. There are no further turbidites

identified as having a La Palma provenance in the 0-1.5 Ma volcaniclastic turbidite history, thus bed Mn with a date of 485±10 ka most likely represents the Cumbre Neuva landslide (Tables 6.2 and 6.5).

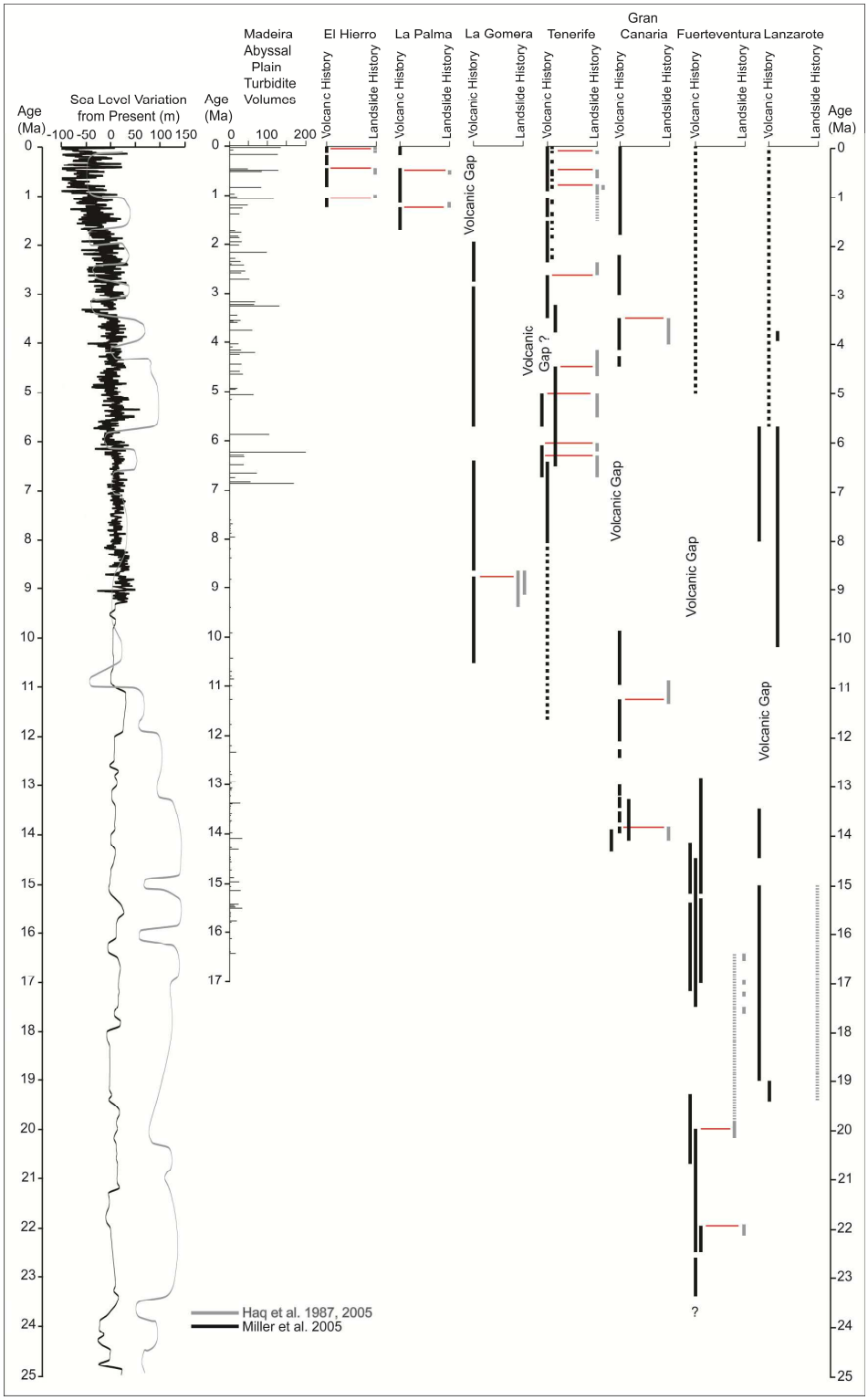

Figure 6.14 Summary of volcanic activity on the Canary Islands (black bars) and onshore landslide evidence (grey bars); compared to the volcaniclastic turbidite history and the Miller et al. (2005) sea level curve.

The Playa de la Veta complex has speculative onshore dates of 1.0 to 0.8 Ma age, cited by Masson *et al.* (2002). However, this age range is poorly constrained in the proximal region. There are two minor volcaniclastic events identified in ODP core at 1.3 to 1.0 Ma (Maa1 at 1.04 Ma and Mah1 at 1.27 Ma) (Table 6.5), but no provenance information is available. More voluminous and widespread volcaniclastic turbidites are present in the older 2.2 to 1.7 Ma ODP record, but these ages exceed onshore ages from the Playa de la Veta collapse(s).

El Hierro

The El Golfo landslide (bed Mb) represents the last catastrophic landslide in the Canary Islands at 15 ka. However, alternative age measures from pre-collapse lavas in the El Golfo embayment constrain landslide activity between 21 to 134 ka (Guillou *et al.,* 1996; Széréméta *et al.,* 1999; Carracedo *et al.,* 1999, 2001). Longpré *et al.* (2011) derive a younger maximum age constraint on this landslide at 87±8 ka and a minimum of 39±13 ka. Nonetheless bed Mb (at 15 ka) represents the only large-volume sediment gravity flow of basic provenance in a 0-480 ka time frame. There is a minor event (bed Md1) dated at 60-70 ka (Weaver *et al.,* 1992), which has been shown to have a basic composition akin to El Golfo (Table 6.5) (Pearce and Jarvis, 1995). The occurrence of smaller landslides overprinted by the later El Golfo event may cause the ambiguity seen in the onshore dates used to resolve the El Golfo age. Thus, the date of the large-volume sediment gravity flow best represents the age of the major landslide.

The southern aprons of El Hierro have also been the sites of landslide activity. The south-eastern flank features the Las Playas I and II failures. The activity on the San Andreas fault system on this flank identifies minor failures between 442-545 ka and 261-176 ka (Day *et al.,* 1997). The older Las Playas II event is perceived as being an aborted slump, thus may not have disaggregated and generated a turbidity current (Day *et al.,* 1997; Masson *et al.,* 2002). The El Julán landslide on the south-western flank has been speculatively dated at 15-190 ka (Krastel *et al.,* 2001) and 300-500 ka (Masson, 1996). Bed Mp (at ~540 ka) in the Madeira Abyssal Plain has been geochemically linked to El Hierro (Figures 6.4 and 6.8, and Table 6.5), and can be linked to the El Julán event due to the age and relatively large volume of the turbidite 100±20 ka.

The El Tiñor volcano represents initial growth of a subaerial edifice on El Hierro (Carracedo *et al.* 2001). Guillou *et al.* (1996) identify the oldest lavas of Tiñor at 1.04-1.12 Ma. The El Tiñor volcano suffered a major collapse prior to development of the El

Golfo edifice. Carracedo *et al.* (1999, 2001) provide a speculative 882 ka date for the El Tiñor collapse. However, there is an unconformity found in water galerías, whereby 543 ka aged lavas are located on 1.04 Ma basalts (Carracedo, 2001). The 1.04 Ma age of the unconformity coincides with the ~1.05 Ma date for bed Mab (Table 6.5), thus bed Mab with basic igneous composition may represent the El Tiñor collapse (Figures 6.4 and 6.8).

ODP Record of 1.5-7.5 Ma Catastrophic Flank Collapses of the Canary Islands

Mid-Late Miocene 7.5-6.0 Ma Record

Here are the first occurrence of metre-thick volcaniclastic turbidites and a distinctive change in the geochemistry. FT, FS and FR have basic compositions, while FP, FO, FM, FL and FD have compositions that implicate an evolved provenance such as Tenerife, similar to Neogene turbidites G, O and Z. These could represent failures of the earliest shield phases of the Anaga and Teno massifs of Tenerife. During this period there is volcanic activity on Lanzarote and La Gomera, but there is little evidence for prodigious landsliding. Thus the voluminous early basaltic phase shield-building on Tenerife is the most likely source of the voluminous ~6.2 Ma FK turbidite has a basic and trace-element depleted composition (Acosta *et al.,* 2003). Indeed, other than 6.65 to 6.0 Ma dated Masca, Carrizales and Teno landslides from Tenerife there are no alternative landslides documented.

Early Pliocene 5.3-4.0 Ma Record

The EK and DK events represent the thickest and most volumetric turbidites in the Madeira Abyssal Plain during this time. These have evolved compositions, with bed DK having a similar composition to those turbidites of Tenerife provenance. Indeed the ~4.2 Ma DK turbidite occurs at a similar time to the major collapse of the Anaga massif (Krastel *et al.,* 2001; Acosta *et al.*, 2003). The alternate turbidites (EI, EH, DZ, DY, DU, DL and DF) are basic to trace-element depleted in composition, but with increased K. During this period El Hierro and La Palma are yet to emerge, but there is volcanic activity persisting on Tenerife and La Gomera, with further activity recommencing on Gran Canaria (van den Bogaard and Schmincke, 1998). The composition would indicate greater weight to a La Gomera or Gran Canaria source, indeed Acosta *et al.* (2003) indicate numerous relatively small-scale landslides occur around La Gomera at ~4.0 Ma.

Late-Early Pliocene to Early-Late Pliocene 3.7-3.0 Ma Record

Bed DB with low Zr and Ti, but high K and Mg, is dated at ~3.75 Ma. The 3.27 Ma CS turbidite represents the thickest and volumetrically most significant landslide in this time frame, followed by turbidite CR (3.24 Ma) and CM (3.17 Ma). The remaining volcaniclastic turbidites in this time frame are minor thin-bedded events. Owing to the ages of these events Gran Canaria is suggested as a possible source, since there is renewed volcanism at this time and evidence of landslide activity (Acosta *et al.,* 2003), including the Roque Nublo and Galdar landslides.

Late Pliocene 2.8-1.8 Ma Record

This time frame commences with turbidites BZ, BQ and BN. The 2.7 to 2.5 Ma ages and moderate Zr, low Ti but high K composition of BZ and BQ would implicate Gran Canaria or La Gomera as the provenance. While BN, BC, AV, and AU have moderate (basic) Zr and Ti, and moderate-to-high K and Mg, similar to those ascribed to a La Palma or El Hierro provenance. Volcanic activity commences on La Palma towards the end of this time frame (Anacochea *et al.,* 1994), presenting a viable source for these later turbidites.

The BF turbidite, dated at ~2.2 Ma represents the thickest and most volumetric event in this time frame, and has an evolved composition similar to those previously ascribed to a Tenerife provenance. The date and potential Tenerife provenance of the BF turbidite would indicate a potential origin from the Tigaiga landslide, which has been dated at 2.3 Ma (Cantragrel *et al.,* 1999). As with similar Tenerife sourced events from the 1.5 Ma to recent turbidite record, this particular Tigaiga event is coincidental with terminal eruptions of a volcanic cycle (mafic Lower Group, dated at 3.5 to 2.1 Ma by Ablay and Marti (2000)). Lastly, the BB turbidite has a similar composition to BF, with an ascribed Tenerife provenance, and may represent a subsequent failure of the northern flank of Tenerife at ~1.95 Ma.

Controlling Factors on older Volcanic Island Landslide Occurrence from ODP Record

The chronology and provenance of the volcaniclastic turbidites in the Madeira Abyssal Plain, coupled with onshore dates of known Canary Island landslides can enable investigations into the controlling mechanisms on occurrence. The large-volume landslides can be correlated to periods of protracted and explosive volcanism on the

respective islands, rather than periods of volcanic quiescence (Figure 6.16). Therefore, loading of the volcanic edifice appears to be a major preconditioning factor for collapse of the island flanks.

Previously, warm and wet climates, associated with the transition from glacial lowstand conditions to interglacial highstand conditions, have been associated with flank collapses in the Hawaiian archipelago (McMurtry *et al.,* 2004). Numerous volcanic turbidites (70%) in the Madeira Abyssal Plain >10 km^3 occur at rising sea level or highstands of sea level in the 7.5 Ma to recent time frame (Miller *et al.* 2005 sea level curve), within the errors of dating. The sea level curves of both Miller *et al.* (2005) and Haq *et al.* (1987, 2005) are less constrained beyond 7.5 Ma, and the dating of the turbidites also becomes increasingly erroneous beyond 7.5 Ma. However, an estimated 90% of thin-bedded landslides within the 17 to 7.5 Ma volcaniclastic record occur at relative sea level highs. This could potentially support the findings of McMurtry *et al.* (2004). Keating and McGuire (2004) also advocate that climate change has a role in preconditioning volcanic island flank collapses (including the Canary Islands), and in particular, periods associated with rapid sea level rise.

Turner and Schuster (1996) implicate weak bedding and soil saturation with instability and onset of subaerial landslides, which are linked to climate. In a study of the Orotava landslide, it has been implied that the landslide failed on a weak horizon represented by a residual soil, the development of which is governed by climate (Hürlimann *et al.,* 2001). The preconditioning effects of climate change on volcanic island landslides can be tentatively suggested by the coincidence of major volcaniclastic turbidites with rising sea level and sea level highstands.

Furthermore, Marti *et al.* (1997) and Hürlimann *et al.* (1999b) suggest that caldera collapse eruptions are capable of preconditioning volcanic island slopes to failure. The present study can potentially implicate volcanic activity and loading of the island edifices in preconditioning failures. Although there can be debate whether landslides could potentially trigger explosive eruptions, or whether volcanic activity leads to flanks failures.

Conclusions

The Late Quaternary piston core record of turbidite deposition within the Madeira Abyssal Plain reveals a 0-1.5 Ma record of large-volume volcanic flank collapses in the Canary Islands. New volcanic glass geochemistry and bulk mudcap geochemistry

coupled with dating of the events has allowed assignment of the provenance of these beds. Furthermore, the knowledge of the documented landslides and debris avalanches in the Canary Islands has allowed designation of specific beds to their respective landslide.

ODP core in the Madeira Abyssal Plain has also allowed resolution of volcaniclastic turbidite activity in the last 17 Ma. Large-volume volcaniclastic landslides are recorded post-7.5 Ma, represented by metre-thick turbidites which are reliably correlated between the three ODP Holes. Mudcap geochemistry and dating of these turbidites has provided an important long-time record of volcanic island flank collapse in the Canary Islands. Indeed, this ODP record coupled with the Madeira Abyssal Plain piston core record has provided one of the most extensive archives of landslide activity from a volcanic archipelago.

The turbidite records show that landslide occurrence is potentially linked to loading of the respective edifice through both intrusive and extrusive volcanism. The largest-volume events also appear to occur during rising- and highstands of sea level, as suggested by McMurtry *et al.* (2003) for the Hawaiian archipelago. Thus wetter climates associated with interglacials could further precondition the flanks of the Canary Islands to fail. This study presents an excellent record of volcaniclastic turbidites with relatively accurate biostratigraphic dating. However, even with this record the exact preconditioning and eventual triggering mechanisms of submarine landslides are not accurately resolvable. However, there is tentative evidence to suggest that the occurrence of large-volume landslides on Tenerife may be related to explosive eruptions at the end of eruptive cycles.

Acknowledgements

The authors would like to thank the scientists and crew that worked on the original ODP Leg 157 core collection and the D108 cruise which collected the piston cores used in this study. JEH would like to acknowledge the PhD funding from Marine Geoscience Group at NOCS that aided completion of this work.

6.3 Summary

Biostratigraphic dating, new volcanic glass geochemistry, and bulk mudcap geochemistry from Jarvis *et al.* (1998) has allowed assignment of the provenance to 0-1.5 Ma volcaniclastic turbidites from the piston core record. These Late Quaternary Madeira Abyssal Plain volcaniclastic turbidites have been further correlated more precisely to the El Golfo, El Julán and Tiñor landslides from El Hierro, the Cumbre Neuva landslide from La Palma, and the Icod, La Orotava, Güímar and Roques de García landslides from Tenerife.

ODP core in the Madeira Abyssal Plain has also allowed resolution of volcaniclastic turbidite activity in the last 17 Ma. Mudcap geochemistry and dating of these turbidites has provided an important long-time record of volcanic island flank collapses in the Canary Islands. This ODP record coupled with the Madeira Abyssal Plain piston core record has provided an important archive of landslide activity from the Canary Islands.

Landslide occurrence is potentially linked to loading of the respective edifice through volcanism. Certainly large-volume failures occur after protracted periods of voluminous volcanism. The largest-volume events also appear to occur during rising- and highstands of sea level, as discovered by McMurtry *et al.* (2004) in the Hawaiian archipelago. Therefore there is a climate dimension to landslide occurrence, where warmer and wetter climates associated with interglacials may precondition the flanks to fail.

The 1.5 Ma to recent record of volcaniclastic turbidites in the Madeira Abyssal Plain is established in this Chapter. With this record in place, the subunits observed within them can be examined, and the subunit origin investigated. The next Chapter (Chapter 7) investigates whether the subunits within these 1.5 Ma to recent volcaniclastic turbidites represent multistage landslides.

Chapter 7

Further Evidence of Multistage Canary Island Landslides

7.1 Introduction and Aims

In Chapter 5, subunits within the Icod event bed in the Agadir Basin were identified as representing a multistage flank collapse. This Chapter revisits the Icod event bed in Agadir Basin, presenting additional correlation panels and volcanic glass geochemical data. This Chapter also presents correlation panels and volcanic glass data for the younger El Golfo event bed in Agadir Basin, which also contains subunits.

Chapter 6 established the 1.5 Ma to recent turbidite stratigraphy in the Madeira Abyssal Plain. Within this record are eight large-volume (>50 km^3) volcaniclastic turbidites that contain subunits. This Chapter investigates whether the subunits in these volcaniclastic turbidites also reflect multistage flank collapses. This would have profound implications for landslide-generated tsunami modelling and geohazard assessments. Previous studies present isolated case studies, including the Icod landslide from Chapter 5. This Chapter could highlight whether the last eight major landslides in the Canary Islands were multistage, thus demonstrating whether this failure and emplacement mechanism is more ubiquitous. The aims of this Chapter are listed below:

1. Correlate the subunits within the El Golfo and Icod event beds in Agadir Basin.
2. Determine the volcanic glass compositions of the subunits from these two event beds in Agadir Basin.
3. Identify and correlate the subunits within the volcaniclastic turbidites within the Madeira Abyssal Plain.
4. Determine the volcanic glass compositions of the subunits in the volcaniclastic turbidites within the Madeira Abyssal Plain.

This Chapter, after further editing, will be submitted to *Geochemistry Geophysics Geosystems* (July 2012) under the theme of interest: “Geodynamics of ocean islands in slow moving plates”, now that the theme of interest solicitation has been accepted. The data, analysis and interpretations are my own, with editorial help offered by my co-authors.

Late Quaternary Record of Volcanic Island Multistage Landslides: evidence from Madeira Abyssal Plain volcaniclastic turbidites from the Canary Islands

J.E. Hunt[1,2*], R.B. Wynn[1], D.G. Masson[1], P.J. Talling[1]

[1]National Oceanography Centre, University of Southampton Waterfront Campus, European Way, Southampton SO143ZH, UK

[2]School of Ocean and Earth Science, National Oceanography Centre Southampton, University of Southampton, European Way, Southampton SO143ZH, UK

* Corresponding author: jeh2g08@soton.ac.uk

Abstract

The record of volcaniclastic turbidites in the Madeira Abyssal Plain represents a history of the largest Late Quaternary volcanic island landslides from the Western Canary Islands. These 0-1.5 Ma volcaniclastic turbidites are composed of multiple fining-upwards turbidite sands, known as subunits. The subunits indicate that the landslides responsible for the sediment gravity flows were multistage. The compositions of volcanic glass assemblages from each individual subunit in an event bed are subtly different. This indicates that each subunit is discrete, implying that the subunit represents a separate failure as part of a multistage landslide. This has significant implications for geohazard assessment. Multistage failures distribute the total landslide volume amongst numerous smaller failures, therefore reducing the volume of rock entering the ocean at any one time. The multistage failure mechanism reduces individual landslide volumes from 200-300 km^3 to less than 100 km^3. Thus although multistage failures ultimately reduce the potential landslide and tsunami threat, the events will still have significant consequences.

Introduction

Lateral flank collapses are the most volumetrically significant mechanism that sculpt volcanic island geomorphology and redistribute volcaniclastic materials to the deep ocean. Large-volume landslides have been reported from the Canary Islands (Holcomb and Searle, 1991; Watts and Masson, 1995, 2001; Masson *et al.*, 2002, and references therein), Cape Verde archipelago (Le Bas *et al.*, 2007; Masson *et al.*, 2008), Réunion Island (Lénat *et al.*, 1989; Labazuy, 1996; Oehler *et al.*, 2004, 2008), Hawaiian archipelago (Moore *et al.*, 1989, 1994; McMurtry *et al.*, 2004), Lesser Antilles archipelago (Deplus *et al.*, 2001; Le Bas *et al.*, 2011; Watt *et al.*, 2012), and French Polynesian archipelago (Clouard *et al.*, 2001; Clouard and Bonneville, 2005; Hildenbrand *et al.*, 2006; Boulesteix *et al.*, 2008). In the last two million years alone there have been eleven landslides reported from the Western Canary Islands (Masson *et al.*, 2002, and references therein). The prevalence and potential volume of these landslides necessitates studies into the factors that instigated their occurrence and the mechanisms by which they failed. This will allow better assessment of the likely recurrence intervals and magnitudes of such large-scale flank collapses, and better inform tsunami modelling.

A future collapse has been theorised from the Cumbre Vieja volcano of La Palma, in the Canary Islands (Ward and Day, 2001). This Cumbre Vieja collapse has been modelled as a single 500 km^3 volume and 1,400 m-thick sliding-block (Ward and Day, 2001; Mader, 2001; Gisler *et al.*, 2006). The resulting tsunami from such an event could be capable of inundating the Atlantic coastline of the United States of America and Western Europe with a 10-20 m wave (Ward and Day, 2001). There have been numerous investigations of the initial input parameters from this proposed La Palma landslide, giving a variable spectrum of tsunami predictions (Mader, 2001; Pararas-Carayannis, 2002; Gisler *et al.*, 2006; Løvholt *et al.*, 2008). Although the far-field effects are debated, there is consensus that the near-field effects could be potentially catastrophic.

Landslide models, such as the hypothetical landslide-generated tsunami from the Cumbre Vieja collapse from La Palma (Ward and Day, 2001; Mader, 2001; Gisler *et al.*, 2006), 1888 Ritter Island landslide (Ward and Day, 2003), and 1988 landslide from Stromboli (Tinti *et al.*, 1999, 2000), have utilised single sliding-block models. However, there is growing evidence to suggest that such volcanic island flank collapses are not necessarily single-block failures, but may occur as multistage and potentially

retrogressive failures (Garcia and Hull, 1994; Garcia, 1996; Wynn and Masson, 2003; Di Roberto *et al.,* 2010; Giachetti *et al.,* 2011; Hunt *et al.,* 2011).

Tsunami models are extremely sensitive to initiation conditions, including whether the total volume is introduced to the surrounding water body by a single or multistage failure (Harbitz *et al.,* 1992, 1993, 2006; Fine *et al.,* 2003; Ward, 2001; Trifunac and Todorovska, 2002; Murty, 2003; Haugen *et al.*, 2005; Løvholt *et al*., 2005, 2008). This has a first order control on tsunamigenesis, since whether an event occurs as a single or multistage failure controls the volume introduced at any one time. Proven examples of multistage volcanic island landslides are limited. Thus far, only isolated case studies of multistage landslides have emerged from the Hawaiian, Aeolian, and Canary archipelagos (Garcia and Hull, 1994; Garcia, 1996; Wynn and Masson, 2003; Di Roberto *et al.,* 2010; Hunt *et al.,* 2011).

Details from the proximal debris avalanche deposits off northern Tenerife have been suggested to indicate multistage failures (Ablay and Hürlimann, 2000; Hunt *et al.,* 2011). However, proximal debris avalanche terrains are complex areas, which suffer from erosion and overprinting of events. As a consequence, studies have focused on the characteristics of the sediment gravity flow associated with the respective landslide (Garcia and Hull, 1994; Garcia, 1996; Wynn and Masson, 2003; Di Roberto *et al.,* 2010; Hunt *et al.,* 2011). The stacked sequence of interbedded turbidite sands and muds (subunits) within a single event bed has been interpreted to demonstrate an originally multistage landslide (Hunt *et al.,* 2011, and references therein). To demonstrate that the occurrence of multistage volcanic island landslides is ubiquitous and not isolated to these case studies, numerous further events need to be examined in detail.

Agadir Basin represents a depocentre proximal to the Canary Islands that is not fed by complex channel systems (Figure 7.1). Wynn and Masson (2003) inferred that the subunits present in the El Golfo and Icod event beds within this basin represent multistage failures. The first objective of the present study was to analyse volcanic glasses from subunit intervals in these two event beds, within the simple basin configuration of Agadir Basin. The initial aim was to determine whether analysis of the El Golfo and Icod deposits in Agadir Basin are consistent with the original results of Hunt *et al.* (2011), and support a theory that these subunits represent multistage failures, as posed by Wynn and Masson (2003).

In the last 1.5 Ma, eight >100 km^3 volume landslides from the Western Canary Islands have generated turbidity currents that reached the Madeira Abyssal Plain (Figure

7.1), including the El Golfo and Icod landslides (Chapters 3 and 6). The second aim of this paper is to investigate the failure mechanism of these Late Quaternary Canary Island landslides, based on the Madeira Abyssal Plain turbidite record. Sedimentological, geochemical and petrophysical studies of the deposits are used to characterise the subunit facies of these event beds. Volcanic glass geochemistry from the subunits within these beds can determine whether or not these are the product of multistage collapse. Identifying whether or not the majority of recent major landslides from the Canary Islands are multistage is of significant importance, since it will suggest that multistage collapse is a more ubiquitous process.

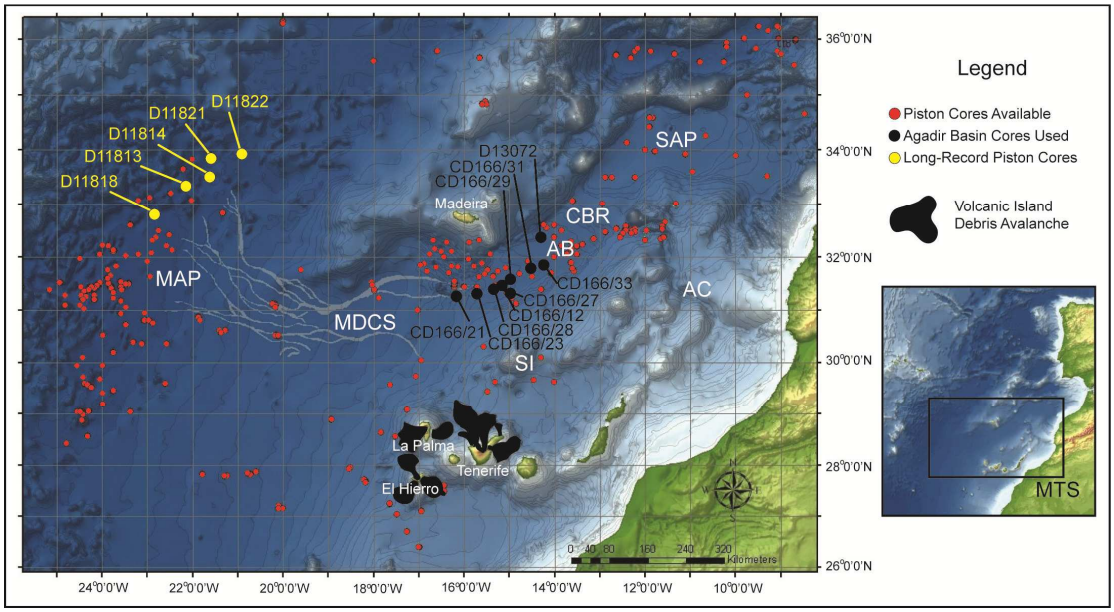

Figure 7.1 Map of the Moroccan Turbidite System offshore Northwest Africa, showing the distribution of Late Quaternary landslides in the Western Canary Islands and cores used in the present investigation to study the sediment gravity flows generated from them. MAP = Madeira Abyssal Plain, MDCS = Madeira Distributary Channel System, AB = Agadir Basin, SI = Selvage Islands, AC = Agadir Canyon, CBR = Casablanca Ridge and SAP = Seine Abyssal Plain.

Geologic and Geomorphic Setting

The Canary Islands form an archipelago associated with movement of Jurassic-age (156-176 Ma) Atlantic oceanic crust over a mantle plume (Klitgort and Schouten, 1986; Hoernle and Schmincke 1993; Hoernle *et al.,* 1995; Carracedo *et al.,* 1998; Schmincke *et al.,* 1998). The result is a general east-to-west age progression in the islands (Carracedo, 1994, 1999; Carracedo *et al.,* 1998). The western Canary islands of Tenerife, La Palma and El Hierro are the focus of this study, since geologically recent landslide activity has been recorded onshore and in the proximal submarine aprons (Masson *et al.,* 2002, and references therein; Acosta *et al.,* 2003, and references therein).

The study area comprises Agadir Basin and Madeira Abyssal Plain of the Moroccan Turbidite System, on the Northwest African passive margin (Wynn *et al.,* 2000, 2002). Agadir Basin represents a more proximal depocentre to both the Moroccan continental shelf and Canary Islands (Figure 7.1). Agadir Basin is located in ~4,400 m water depths and is bound to the north by the Madeira archipelago and to the south by the Selvagen Islands (Wynn *et al.,* 2000, 2002; Frenz *et al.*, 2009). The Madeira Abyssal Plain represents the most distal and deepest depocentre in the Moroccan Turbidite System, in 5,000-5,500 m water depths (Figure 7.1) (Weaver and Kuijpers, 1983; Weaver *et al.,* 1992). The Madeira Abyssal Plain is connected to the more proximal Agadir Basin via the Madeira Distributary Channel System (Masson, 1994; Frenz *et al.,* 2009; Stevenson *et al.,* 2012).

Late Quaternary Landslide and Turbidite Histories of the Canary Archipelagos

Submarine landslides have been extensively investigated in the Canary Islands with the application of low-frequency seismic reflection and side-scan sonar to the study of submarine debris fans (Holcomb and Searle, 1991; Watts and Masson, 1995, 2001; Masson, 1996; Urgeles *et al.,* 1997; 1999, 2001; Masson *et al.*, 1997; Gee *et al.,* 2001; Krastel *et al.,* 2001; Wynn *et al.,* 2000, 2002). In addition, piston coring in the distal Madeira Abyssal Plain and more proximal Agadir Basin has allowed correlation of dated volcaniclastic turbidites with onshore landslides (Masson, 1996; Masson *et al.,* 2002, 2006; Hunt *et al.,* 2011, Chapter 6). This section summarises previous work covering the 1.5 Ma to recent record of volcanic island landslides in the Western Canary and Madeira archipelagos (Table 7.1).

Tenerife

The Icod landslide represents the last major landslide to affect the northern flank of Tenerife. It has been dated at 165±5 ka by linking the turbidite (Agadir Basin bed A14 and Madeira Abyssal Plain bed Mg), submarine debris avalanche, and onshore landslide scar (Table 7.1) (Weaver and Rothwell, 1987; Watts and Masson, 1995; Masson *et al.,* 2002; Wynn *et al.,* 2002; Wynn and Masson 2003; Frenz *et al.,* 2009; Hunt *et al.,* 2011). The La Orotava landslide, also off the northern flank of Tenerife, has a suggested age in the range 560-710 ka based on onshore dating (Table 7.1) (Marti *et* al., 1994; Ancochea *et al.,* 1999; Marti and Gudmundsson, 2000). Bed Mo on the Madeira Abyssal Plain represents the Orotava event, and resolves the event to 530±20 ka (Chapter 6).

The east-ward directed Güímar landslide from the eastern flank of Tenerife has been dated at 780-840 ka (Ancochea *et al.,* 1990; Cantagrel *et al.,* 1999; Krastel *et al.,* 2001; Masson *et al.,* 2002; Giachetti *et al.,* 2011). This event has potentially produced the Madeira Abyssal Plain bed Mz, which has been dated at ~830 ka (Chapter 6). The Roques de García landslide represents the oldest flank collapse from the northern flank of Tenerife that could be recorded in the piston core turbidite record. Ages on basal avalanche fragments, headwall faults and dike cross-cutting relationships resolve a broad age range of 0.6-1.7 Ma (Table 7.1) (Cantagrel *et al.,* 1999). This event is potentially represented by bed Maf on the Madeira Abyssal Plain, and therefore has an age of ~1.2 Ma (Chapter 6).

La Palma

The Cumbre Nueva landslide represents a collapse from the Cumbre Nueva Ridge at 125-536 ka during volcanism associated with the Taburiente volcano (Table 7.1) (Urgeles *et al.,* 1999, 2001). Correlation to Madeira Abyssal Plain bed Mn confirms a 485±20 ka date. The Cumbre Neuva debris avalanche overlies the older Playa de la Veta complex deposit of unknown age (Masson *et al.,* 2002).

El Hierro

The El Golfo landslide represents the youngest volcanic flank collapse in the Canary archipelago at 15 ka (Table 7.1) (Weaver *et al.,* 1992; Masson, 1996). The landslide and proximal debris avalanche have been correlated with the turbidite bed b/b_1 (bed Mb of this study) in the Madeira Abyssal Plain (Weaver *et al.* 1992) and bed AB2 in Agadir Basin (Wynn *et al.,* 2002a; Wynn and Masson, 2003; Frenz *et al.,* 2009).

The El Julán landslide affected the southwest flank of El Hierro and contributed to the development of the resulting El Julán apron. Masson (1996) provides a potential date range of 320-500 ka for the El Julán landslide event, but there are no details on the constraint of this (Table 7.1). This landslide is dated at 540±20 ka based on correlation to bed Mp on the Madeira Abyssal Plain (Chapter 6).

The Tiñor volcano represented the first subaerial volcanism on El Hierro between 1.12 Ma and 882 ka (Table 7.1) (Guillou *et al.,* 1996; Carracedo *et al.,* 1999). In mining galleries within the El Golfo embayment, 543 ka El Golfo lavas overlie east-dipping Tiñor lavas dated at 1.04 Ma (Table 7.1) (Carracedo *et al.,* 1999). The inferred landslide

corresponding to the truncation of the Tinor lavas correlates to Madeira Abyssal Plain bed Mab, thus the event can be dated at ~1.05 Ma (Chapter 6).

Table 7.1 Summary of 0-1.5 Ma Volcanic Flank Collapses in the Western Canary Islands (where DA = debris avalanche and DF = debris flow)

Event	Type	Age	Volume (km^3)	Area (km^2)	Comments
Tenerife					
Roques de García	DA	0.6-1.3 Ma[7,14,16]	~500[14]	2,200-4,500[14,16]	Mapped using sidescan sonar, shallow 3.5 kHz seismic reflection, and swath bathymetry.[2,7,14,16]
Güímar	DA	830-850 ka[20]	44-120[14,20]	1,600[16]	Mapped using swath bathymetry.[16]
Orotava	Slide and DA	505-530 ka[24]	500[14]	2,100[14]	Debris avalanche deposit mapped using sidescan sonar and swath bathymetry.[2,7,11,16,17] Onshore dating range has been limited to 540-690 ka.[2,6,8,14]
Icod	Slide and DA/DF	165 ka[14]	320[14]	1,700[14]	Debris avalanche deposits mapped using sidescan sonar and swath bathymetry.[2,7,11,16,17] Onshore dating of the event is between 150-170 ka.[16,18]. Dating of the debris avalanche from the sediment drape is ~170 ka.[2] The turbidite in Agadir Basin has been dated at 160-165.[15,19,21]
La Palma					
Playa de la Veta	DA	0.8-1.0 Ma[14,16]	520-650 [12,14,16]	1,200-2,000[12,14,16]	Mapped using sidescan sonar, shallow seismic reflection and swath bathymetry.[10,13,14,16]
Santa Cruz	DA	0.9-1.2 Ma[4,14,16]	?	1,600[8]	Mapped using swath bathymetry.[8]
Cumbre Nueva	DA	~520 ka[18]	80-95[14,16]	700-780[14,16]	Mapped using sidescan sonar, shallow seismic reflection and swath bathymetry.[10,13,14,16]
El Hierro					
Tiñor	DA (buried)	0.54-1.12 Ma[4,9]	?	?	Theorised collapse from an unconformity in mining gallerias.[9]
San Andréas	Aborted Slump	176-545 ka[5]	?	?	Studied from onshore faults.[5] Could be related to early phases of failure during Las Playas I or II events, certainly the dates coincide with those for Las Playas events.[14]
Las Playas I	DA	176-545 ka[5,14]	?	1,700[14]	Broader debris avalanche with smoother sediment cover, mapped with sidescan sonar.[14]
El Julan	DA	320-500 ka[3,16]	60-130[12,14,16]	1,600-1,800[12,14,16]	Mapped using sidescan sonar, seismic reflection profiles and swath bathymetry, but little onshore record.[14,16]
Las Playas II	Failed slump with minor DA/DF	145-176[14]	~50[14]	950[14]	Confined elongate debris flow/avalanche.[14] Possible associated turbidite dated at ~152 ka.[18,21]
El Golfo	DA	15[3,13,14,15,16,19,21]	150-180[14,16]	1,500-1,700[14,16]	Mapped using sidescan sonar, swath bathymetry and shallow seismic reflection.[3,14,16] Correlation to a large-volume volcaniclastic turbidite in Agadir Basin and Madeira Abyssal Plain.[1,19,21]

Abbreviations are DA is debris avalanche and DF is debris flow. References include [1] Weaver *et al.* (1992), [2]Watts and Masson (1995), [3] Masson (1996), [4] Carracedo *et al.* (1997), [5] Day *et al.* (1997), [6] Marti *et al.,* (1998), [7] Watts and Masson (1998), [8] Cantagrel *et al.* (1999), [9] Carracedo *et al.* (1999), [10] Urgeles *et al.* (1999), [11] Ablay and Hürlimann (2000), [12] Krastel *et al.* (2001), [13] Urgeles *et al.* (2001), [14] Masson *et al.* (2002), [15] Wynn *et al.* (2002), [16] Acosta *et al.* (2003), [17] Hürlimann *et al.* (2004), [18] Georgiopoulou (2006), [19] Frenz *et al.* (2009), [20]Giachetti *et al.* (2011), and [21] Hunt *et al.* (2011).

Methodology and Data

This study is based on >100 piston cores from Agadir Basin and >150 piston cores from the Madeira Abyssal Plain (Figure 7.1). A core transect through the centre of Agadir Basin is used to characterise the turbidites from the most recent El Golfo and Icod landslides (Figure 7.1). A series of five piston cores from the northern Madeira Abyssal Plain (D11813, D11814, D11818, D11821 and D11822) show the most extensive temporal record of volcaniclastic turbidites entering the depocentre via the Madeira Channels (Figure 7.1). These also contain the highest coarse fraction (silt and sand), where the mud fraction has principally bypassed. Previous coccolithophore biostratigraphy and dates from corresponding ODP core have been used to constrain the turbidite dates (Weaver *et al.,* 1992; Chapter 6).

Visual and Geotechnical Logging

Visual sedimentological logging was initially used to assess the vertical sequence and depositional features of the cored turbidites. Magnetic susceptibility data was obtained at a 0.5 cm resolution using a *GeoTek* XYZ core scanner. Magnetic susceptibility importantly supports identification of volcaniclastic turbidites, where positive excursions represent magnetic volcanic sands. P-wave velocity data from the Madeira Abyssal Plain cores was previously collected using an acoustic profiler. P-wave velocities aid identification of turbidite sands, with increased P-wave velocities in sandstones. P-wave velocity and gamma-ray density profiles of Agadir Basin cores were collected using a *GeoTek* MSCL.

SEM Volcanic Glass Analysis

Bulk geochemical compositions have shown to be sufficient to discriminate between subunits (Hunt *et al.,* 2011). However, these bulk geochemical compositions can be affected by hydrodynamic sorting during passage of the turbidity current (Hunt *et al.,* 2011). Analysis of populations of unaltered volcanic glasses of similar size enable better comparison of compositional variations between subunit assemblages of the same turbidite (Appendix 5.8 and 6.1) (Di Roberto *et al.,* 2010; Hunt *et al.,* 2011).

Samples (~3 cm^3) were taken from the bases of each subunit within type-examples of the El Golfo and Icod deposits in Agadir Basin and then each of the volcaniclastic turbidites within the Madeira Abyssal Plain. These were sieved for the >63 μm fraction and subjected to acetic acid (0.1 M) leaching to remove carbonate and wash grain

surfaces. The volcanic grains were then mounted on a semi-conductor pad and placed within the vacuum chamber of a *Hitachi TM1000* SEM. Unaltered volcanic glasses (preferably 30 to 50 in each sample) of 90-125 μm size were analysed from each subunit, at 15 kV with a dwell time of 120 s. In some cases too few glasses met the aforementioned criteria, principally due to alteration, and as a result only 20-30 glasses were analysed. Calibrated results were verified for accuracy and precision using a series of glass standards produced from international standard reference materials (Appendix 5.8 and 7.1). Concentrations between 1-2 wt% have precisions of 4-6% of the value, 2-10 wt% values have precisions to within 2-5%, while those values >10 wt% have precisions of 0.5-4% (Appendix 5.8). Accuracies were generally within 1-5% of the certified value for the suite of standard reference materials.

Results

Visual Identification of Agadir Basin Subunits

Subunits can be identified visually as a series of multiple fining-upwards turbidites sands with interbedded turbidite muds. These are characterised by a marked planar, erosional, basal contact and a lithic- and carbonate-rich basal deposit. As with previous studies (Hunt *et al.,* 2011), a regular series of seven subunits were identified within the Icod event bed in Agadir Basin (SBU1-7) (Figure 7.2). The three lowermost subunits are amalgamated in the western Agadir Basin, more proximal to source. However, these become readily identified as separate units more distally in the eastern Agadir Basin (e.g. site D13072) (Figure 7.2).

The basal subunits (SBU1-3) of the Icod turbidite each comprise a sequence of parallel-, ripple cross-, and convolute-laminations. Mafic lithics and carbonate materials dominate the composition above an erosive base, followed by a vertical increase in volcanic glass content. The upper subunits (SBU4-7) represent separate coarse units interbedded with turbidite mud at each core site. Each subunit has a ripple- to parallel-laminated fine-sand to coarse-silt base with a laminated mud above (Figure 7.2).

The El Golfo event bed has five subunits (SBU1-5) in the most proximal sites (CD166/21 and CD166/23) in the western Agadir Basin (Figure 7.3). The uppermost subunits are progressively lost eastwards along the basin, with four regular subunits seen at core sites CD166/24 and CD166/28, and only three through the remainder of the western basin (CD166/12, CD166/29 and CD166/31) (Figure 7.3). Examples of the deposit both on the basin margins and further distally in the eastern Agadir Basin

demonstrate a progressive cut out of subunits to two and finally one. These subunits are characterised by a sequence of basaltic- and carbonate-rich laminations at the base, with a more carbonate-rich sequence of muddy silts above. These subunits rapidly fine towards the east and become fine silts and muds distally.

Visual identification of the subunits is supported by the magnetic susceptibility and p-wave velocity profiles. The coarse-to-medium sand subunit bases are distinguished by the peaks in p-wave velocity profiles, while the volcanic lithic-rich bases are distinguished by peaks in magnetic susceptibility (Figures 7.2 and 7.3).

Grain Specific Geochemistry within Agadir Basin Subunits

This investigation was carried out on volcanic glasses, where attention was made to select grains that had not been subjected to alteration. Samples from the subunit intervals of the Icod event bed were taken from CD166/27. CD166/27 site was chosen since it is found in the centre of Agadir Basin, and relatively proximal compared to other cores studied.

The total alkali-silica (TAS) diagram enables the delineation of compositional fields of the glasses relating to specific igneous rock types (Figure 7.4). The glasses fall into the TAS field for Tenerife phonolite and alkali trachyte compositions (Figure 7.4B). These onshore compositional fields represent data collated from the Max-Planck-Gesellschaft database for Geochemistry of Rocks of the Oceans and Continents (GEOROC). It was possible to delineate compositional fields for the different Icod subunit glasses populations (Figure 7.4B). For the Icod event bed, the SBU1-2 volcanic glasses were found to range from basalts to alkali trachyte-trachy andesite in composition. SBU3 had a mixed component composition with alkali trachyte-trachy andesite glasses, but a predominance of silica-rich alkali-trachyte composition (Figure 7.4B). SBU4 glasses have a more evolved phonolitic composition; with a proportion that is of phonolite-trachyte composition. SBU5 and SBU6 glasses lie at the phonolite-alkali trachyte boundary (Figure 7.4B). Lastly, SBU7 glasses show a different character, composed of strictly tephriphonolite-phonolite glasses (Figure 7.4B). These results are similar to previous volcanic glass analyses from the subunits of the Icod event bed (Hunt *et al.,* 2011), athough the new results show a lower abundance of basaltic glasses in SBU1 and SBU2.

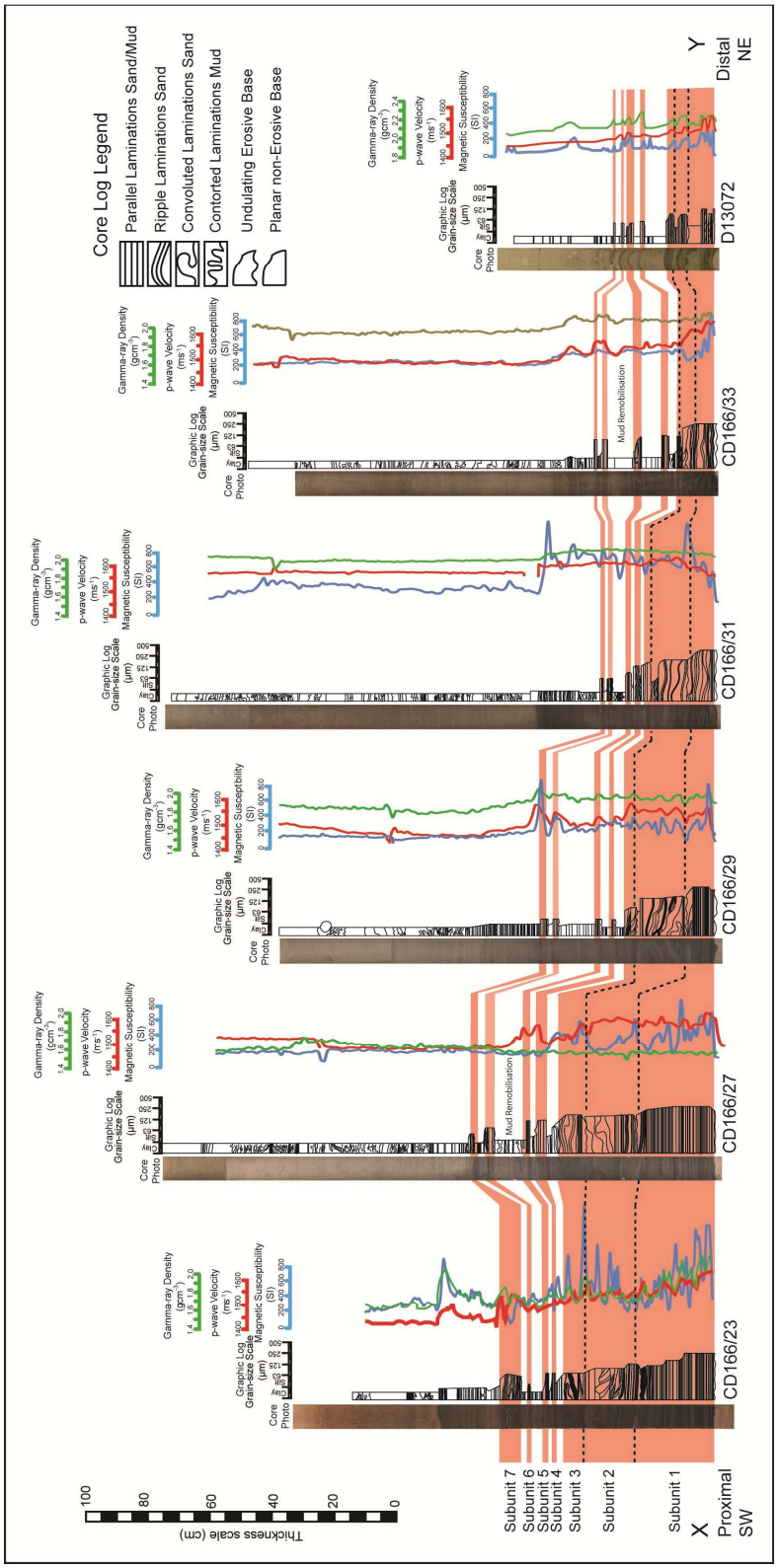

Figure 7.2 Up-basin correlation panel of the Icod bed in Agadir Basin (core locations on Figure 7.1). Shows the regular sequence of seven subunits and the ability for these to be highlighted in the petrophysical data (gamma-ray, p-wave velocity and magnetic susceptibility).

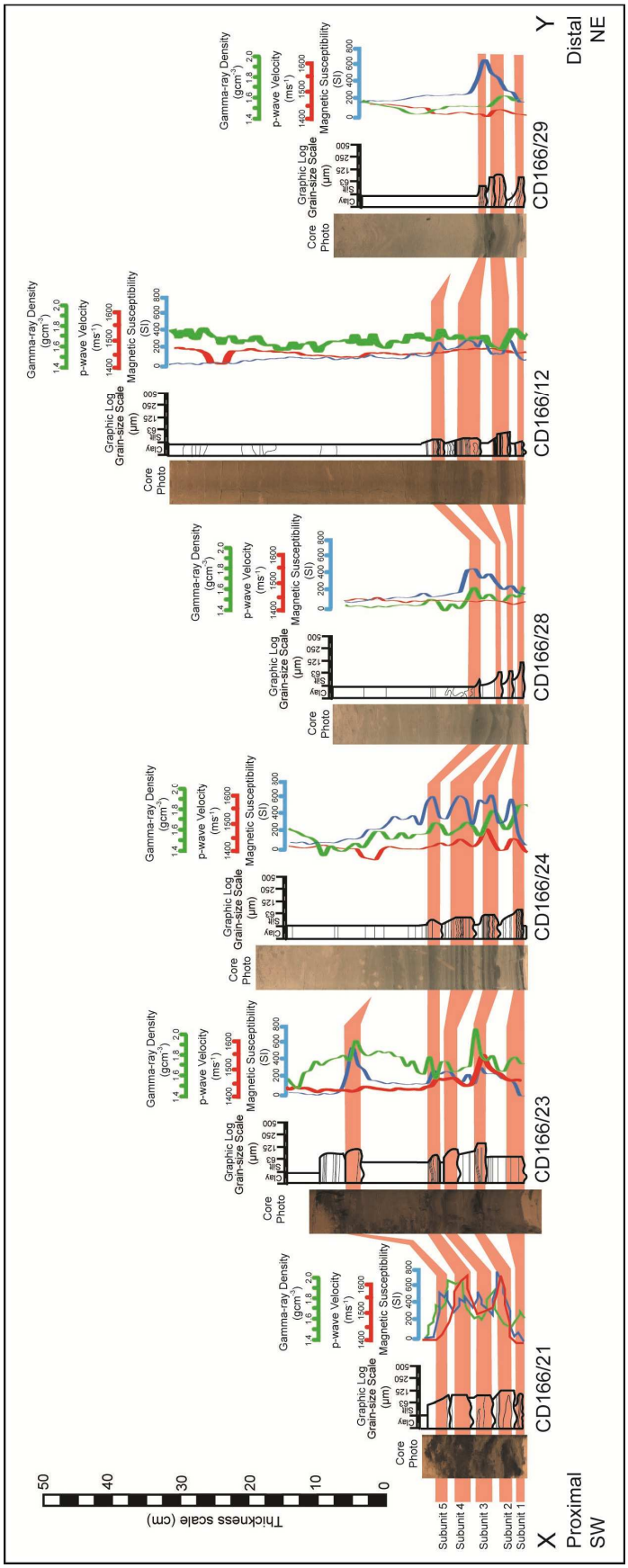

Figure 7.3 Up-basin correlation panel of the Icod bed in Agadir Basin (core locations on Figure 7.1). Shows the regular sequence of seven subunits and the ability for these to be highlighted in the petrophysical data (gamma-ray, p-wave and magnetic susceptibility).

In summary, Icod deposit volcanic glasses demonstrate that the compositions of each subunit form disparate compositional fields. Within the Icod event bed SBU1 and SBU2 are closely related, with less evolved basic compositions and lower silica and alkali concentrations. SBU3 has a range from the upper composition of SBU1 and SBU2 to those of SBU4-6, although SBU3 appears to also contain glasses with the most evolved composition. Finally, SBU7 contains glasses of compositions present in SBU3-6, but also has an assemblage with a different composition to those previous (Figure 4B).

The El Golfo volcanic glass compositions are more scattered than the onshore El Hierro whole rock compositional field (Figure 4A). SBU1 for the El Golfo event has a limited composition of volcanic glasses with alkalis <10 wt% and silica <50 wt%. The SBU1 volcanic glasses fall into two compositions of highly basic picro-basalts and basanite-phonotephrites. SBU2 volcanic glasses have a broad range over a more evolved composition, ranging from phonolites to basanites, but with no glasses of more basic basalt-picrobasalt composition (Figure 4A). The volcanic glasses from SBU3 have the broadest range of composition falling into picrobasalt, basalt, basanite, phonotephrite and phonolite classes (Figure 4A). The SBU4 volcanic glasses have compositions that fall into two groups. One group is evolved (>9 wt% alkalis and >52 wt% silica), the other basic (<7 wt% alkalis), although some glasses <41 wt% silica are questionable due to the low silica. Lastly, the SBU5 volcanic glasses of the El Golfo event are found to have highly restricted basic composition (40-45 wt% silica). They can be divided into two groups comprising 3-4 wt% alkali basanites and 0.5-2 wt% alkali picrobasalts (Figure 4A).

In summary the subunit glasses from the El Golfo event also form discrete compositional fields. Here SBU1 has a broad but relatively basic composition compared to SBU2-4, which have broad but relatively more evolved compositions. Within SBU2-4 distinctions can be made whereby SBU2 and SBU4 are generally more evolved than SBU3, and where SBU3 also contains glasses of ultrabasic composition. The last subunit of the El Golfo event (SBU5) has a restricted ultrabasic-basic composition, where the ultrabasic glasses are comparable to those SBU1 and SBU3, while the basanite glasses form a completely discrete compositional field (Figure 7.4A).

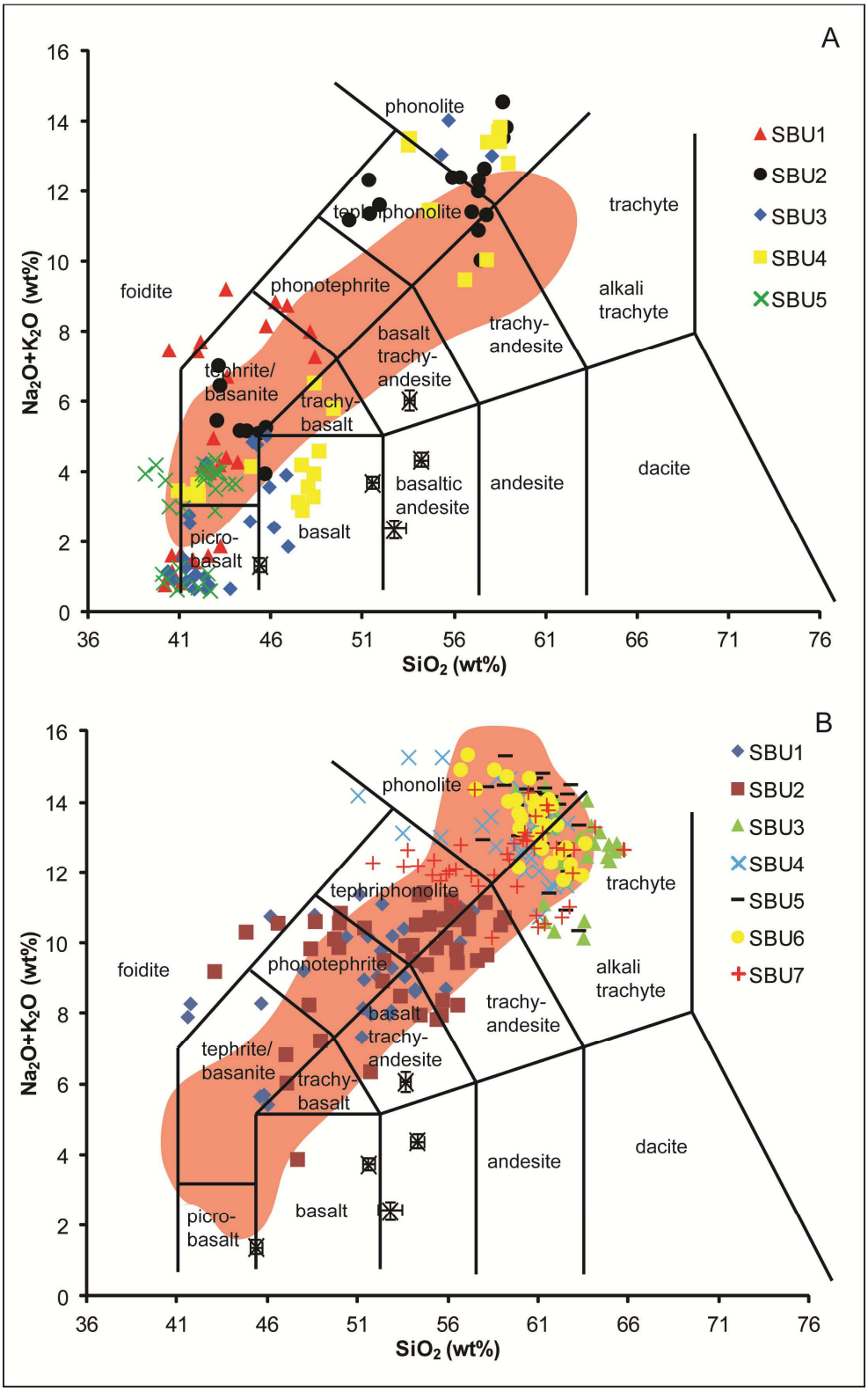

Figure 7.4 Total alkali-silica diagrams for the unaltered volcanic glasses taken from the Icod bed (site CD166/27) and El Golfo bed (site CD166/21) in Agadir Basin, whereby A) in El Golfo bed and B) is Icod bed. Geochemical comparison can be made with the basaltic El Hierro source of the El Golfo turbidite. Tenerife onshore data from GEOROCS database.

Identification of Subunits within Madeira Abyssal Plain Volcaniclastic Turbidites

The northern Madeira Abyssal Plain is fed by the Madeira Channels, which carry turbidity currents from Agadir Basin and offshore El Hierro and La Palma. As a result, turbidite subunits are generally amalgamated in proximal cores, with erosive removal and/or bypass of the turbidite mud, which is found elsewhere separating the subunit sands in Agadir and Madeira Basins. Both p-wave velocity and magnetic susceptibility profiles verify the visual log position of the subunits within the deposits (Figures 7.5-7). Bed Mb has had a regular series of five subunits (SBU1-5) identified in D11821, D11814 and D11813 (Figure 7.5). Bed Mg is more complex, with a series of seven potential subunits (SBU1-7) identified in D11814 and D11813, while these reduce to five at D11821 and D11818, and three at D11822 (Figure 7.5).

The majority of occurrences of bed Mn are as a thin <1 cm silt stringer with a 10-50 cm mudcap. However, two thick silts are indentified in D11818, suggesting two separate subunits (SBU1-2) (Figure 7.6). Bed Mo has a complex architecture. A calcareous-rich basal subunit in D11818 (SBU1), fines towards the NE through the core sites to D11822. Above this are a series of four well-defined volcanic-rich subunits (SBU2-5), which can be extensively correlated. SBU3 and SBU4 in bed Mo represent the coarsest subunits in D11822 (Figure 7.6). Like bed Mn, bed Mp predominantly comprises a thin silt stringer and mudcap. However there are two distinct subunits at sites D11818, D11813 and D11814 (Figure 7.6).

Of the older events, bed Mz has been found to have two subunits (SBU1-2) in both D11814 and D11821 (Figure 7.7). Bed Mab has five identified subunits in D11814 (SBU1-5), but only three subunits in D11822, where SBU2 and SBU3 are the coarsest (Figure 7.7). Lastly, bed Maf was only recovered at D11814, and was found to comprise four subunits (SBU1-4) (Figure 7.7).

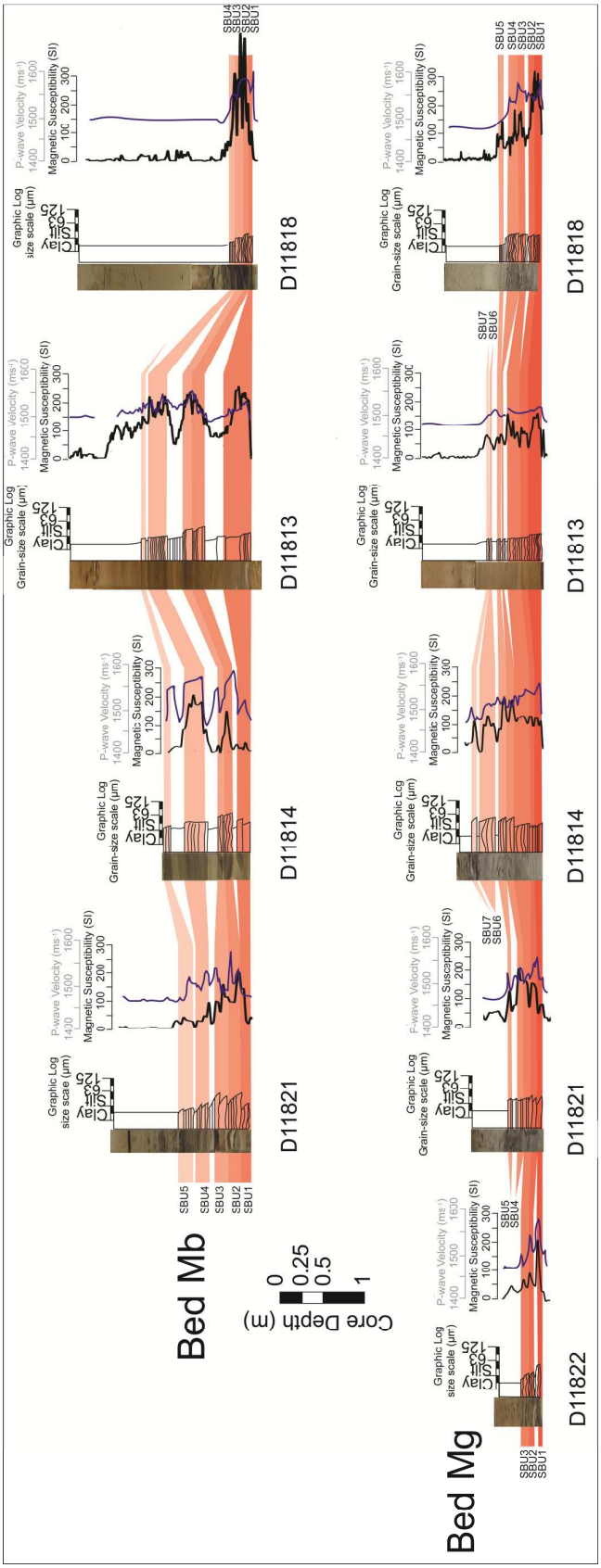

Figure 7.5 Identified and correlated subunits in the proximal Madeira Abyssal Plain core sites for beds Mb and Mg. Core photograph, visual sedimentary log, P-wave velocity and magnetic susceptibility data have been combined to highlight the presence of subunits.

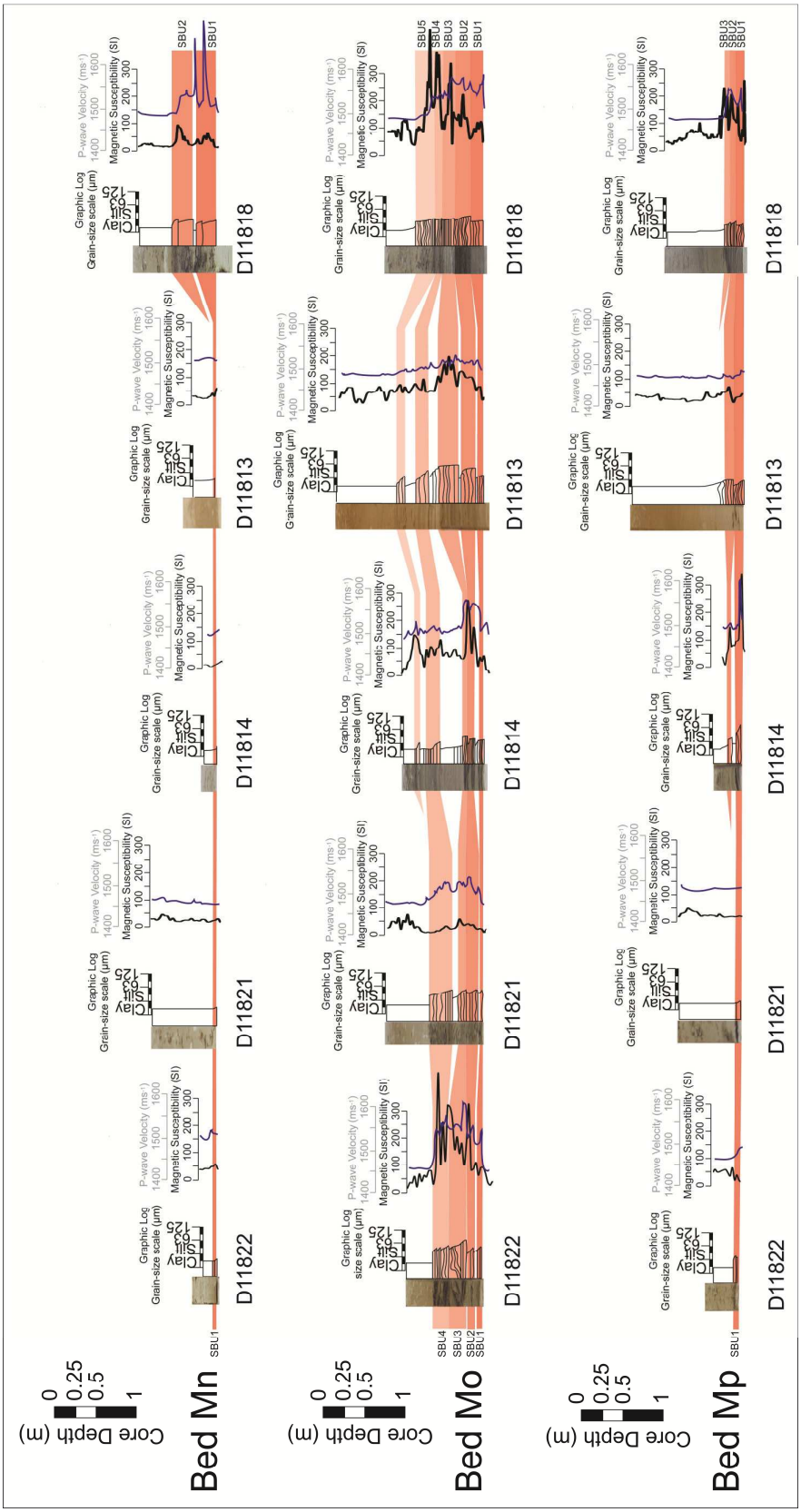

Figure 7.6 Identified and correlated subunits in the proximal Madeira Abyssal Plain core sites for beds Mn, Mo and Mp. Core photograph, visual sedimentary log, p-wave velocity and magnetic susceptibility data have been combined to highlight the presence of subunits.

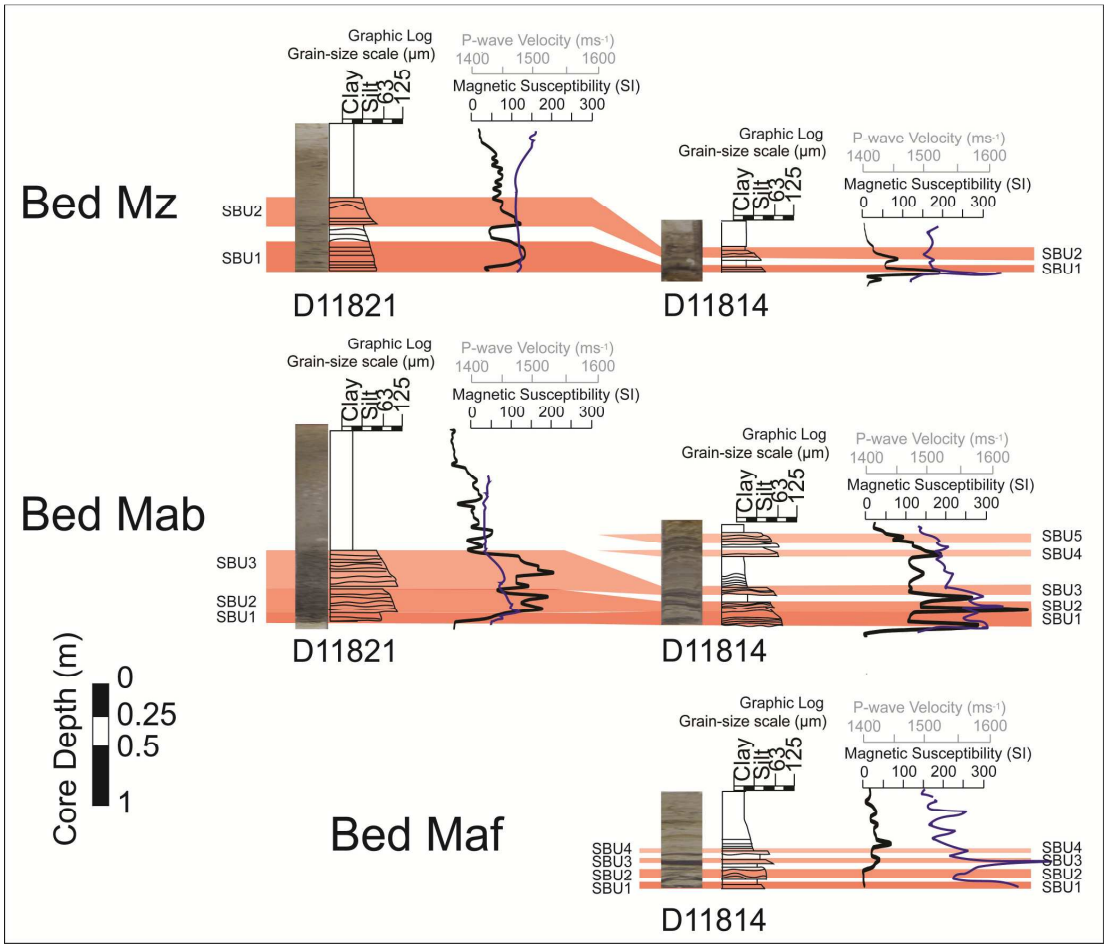

Figure 7.7 Identified and correlated subunits in the proximal Madeira Abyssal Plain core sites for the examples of beds Mz, Mab and Maf. Core photograph, visual sedimentary log, P-wave velocity and magnetic susceptibility data have been combined to highlight the presence of subunits.

Volcanic Glass Geochemistry of Madeira Abyssal Plain Volcaniclastic Turbidite Subunits

Volcanic glasses were analysed from each subunit from a type example of each volcaniclastic turbidite. These examples were chosen where the subunit record was most complete and the deposits were coarsest. Comparison of results from each subunit provides an opportunity to identify compositional hetero-/homogeneities between subunits.

Bed Mb comprises glasses of ultra-mafic picro-basalt to evolved trachyte-phonolite compositions. The glasses principally fall within the onshore compositional range for El Hierro, although the more evolved glasses have greater silica and alkali components on the total alkali-silica (TAS) diagram (Figure 7.8A) (Le Bas *et al.,* 1986). However, the presence of evolved glasses is supported by the original turbidite provenance work by Pearce and Jarvis (1992) that shows evolved trachyte glasses with similar compositions.

Furthermore, the onshore composition field is constrained using limited documented samples available.

The results of the present study show that the subunits in bed Mb have disparate compositions of volcanic glasses. SBU1 is shown to be principally basic in composition, with glasses of 38-51 wt% SiO_2 and alkalis (Na_2O and K_2O) <10 wt% restricted to basanites-to-phonotephrites (Figure 7.8A). SBU2 was found to be comprise evolved glasses of phonolite and trachyte composition, with SiO_2 >51 wt% and alkalis >8 wt% (Figure 7.8A). Both SBU3 and SBU4 have similar compositions, with a dominance of evolved phonolite-trachyte glasses. The SBU3 glasses show increased concentrations of both alkalis and silica, compared to the SBU4 glasses (figure 7.8A). Furthermore, both SBU3 and SBU4 have glasses of basic composition, with SBU3 restricted to a basalt composition, while the SBU4 basic glasses span basalt to basanite compositions. Lastly, the SBU5 glasses display compositions restricted to basanite-picrobasalt with alkalis <6 wt% and silica <46 wt% (Figure 7.8A).

The volcanic glasses from subunits of the El Golfo turbidite (bed Mb) in Madeira Abyssal Plain are broadly similar to those studied in Agadir Basin (bed A2 in Agadir Basin) (Figure 7.4A). However, SBU1 and SBU3 lack ultra-basic picrobasalt glasses in the Madeira Abyssal Plain example of the present study. Furthermore, the more basic basanite glasses of SBU2 and SBU4 in the Agadir Basin are lacking in the Madeira Abyssal Plain.

Bed Mg volcanic glasses are of alkali basalt to phonolite compositions (Figure 7.8B). These compositions fall within the onshore compositional field for Tenerife. Once more the volcanic glasses in the Mg subunits fall into disparate compositional groups. The initial subunits (SBU1 and SBU2) are the most basic with basalt-to-tephriphonolite compositions, with alkalis <11 wt%, but SiO_2 ranging from 45 to 62 wt% (Figure 7.8B). However, there are a greater number of more evolved tephriphonolite-to-trachy-andesite glasses in SBU2, compared to SBU1. SBU3 contains amongst the most evolved volcanic glasses, principally trachytes (Figure 7.8B). SBU4 is predominantly represented by 51-61 wt% SiO_2 phonolites with generally high alkali content (>12 wt%). SBU5 and SBU6 have broadly similar glass compositions, being composed of evolved phonolite-trachytes, although SBU5 has a greater proportion of lower silica phonolites than SBU6 (Figure 7.8B). Lastly, SBU7 is composed of glasses spanning all the compositions present in SBU4, SBU5 and SBU6, but also comprises glasses of ~56 wt% SiO_2 and 11.5-12.0 wt% alkalis that appear unique to this subunit (Figure 7.8B).

The Icod event bed is represented by bed Mg in the Madeira Abyssal Plain and AB14 in Agadir Basin. Previous studies have focussed on studying the volcanic glasses from the subunit divisions of the Icod event bed (Hunt *et al.,* 2011). The results of these previous studies are comparable to the present contribution, although the most basic basanitic and basaltic glasses appear to be absent, compared to the Hunt *et al.* (2011) proximal site.

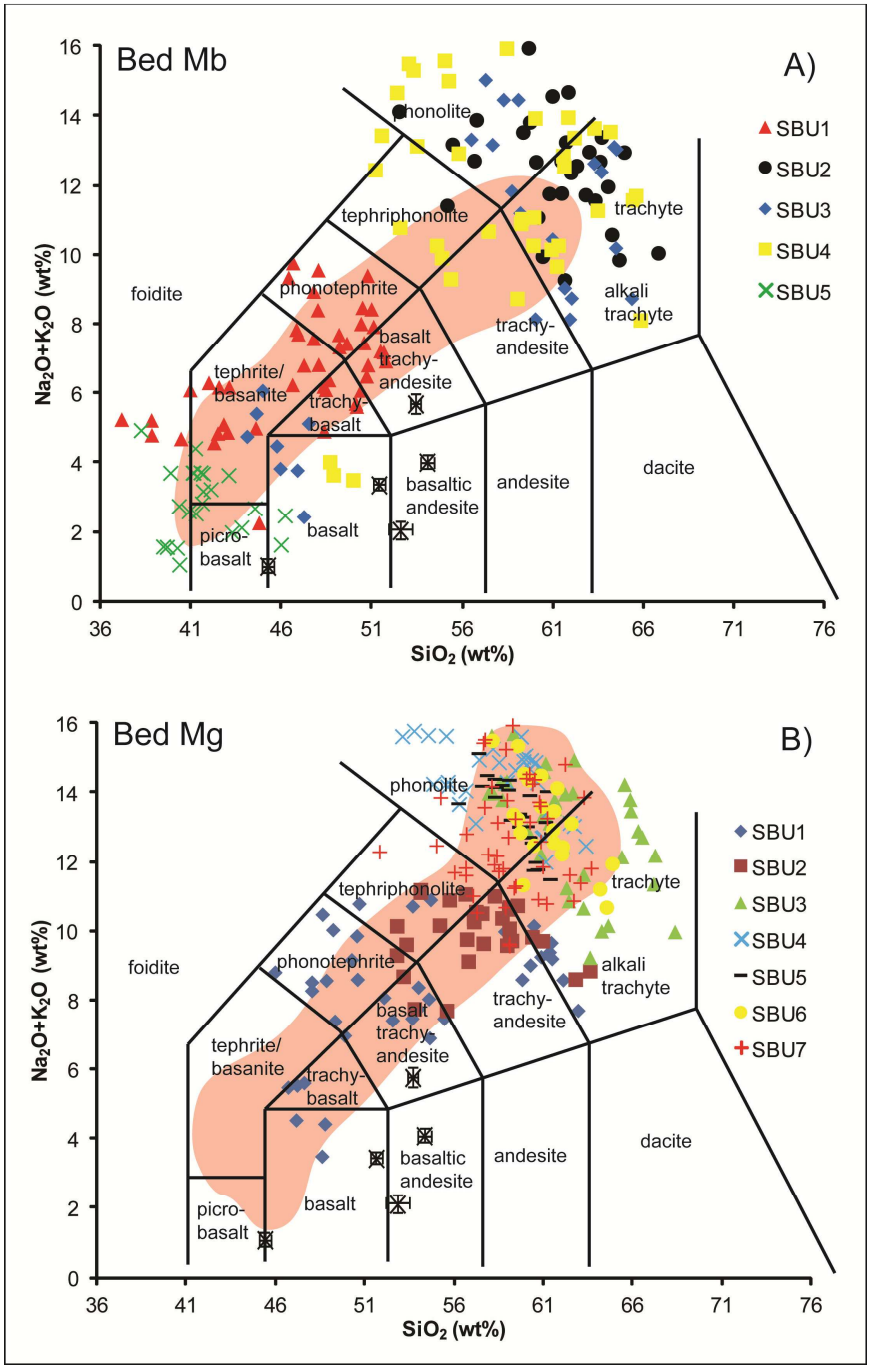

Figure 7.8 Composition of unaltered volcanic glasses recovered from the subunits of bed Mb (A) and bed Mg (B) in Madeira Abyssal Plain. Compositions are plotted on total alkali-silica (TAS) diagrams, showing the disparity between the compositions of the subunits. Geochemical comparison can be made with the basaltic El Hierro source of the El Golfo turbidite. Tenerife onshore data from GEOROCS database.

Bed Mn represents the next significant volcaniclastic turbidite in the Madeira Abyssal Plain stratigraphy. The volcanic glasses recovered from bed Mn lie within the onshore compositional field for La Palma (Figure 7.9A) (Chapter 6). The glasses are principally basic, ranging from picrobasalts to low-alkali tephriphonolites (Figure 7.9A). SBU1 is composed of principally picrobasaltic glasses (<46 wt% silica and <4 wt% alkalis) with some phonotephrite to basalt trachy-andesite glasses (51-53 wt% silica and <8.5 wt% alkalis). The SBU2 glasses have a composition different to those of SBU1, being mainly basanites, phonotephrites and tephriphonolites (Figure 7.9A).

Five subunits are identified in Bed Mo (Figure 7.9B). The overall glass compositional range is generally evolved, corresponding to the onshore compositional field for Tenerife (Figure 7.9B). The glasses from SBU1 have two compositions of basic basalt-basanites and tephriphonolite-phonolites (Figure 7.9B). SBU2 comprises a small number of phonotephrite-tephriphonolite glasses, but is predominantly composed of high-silica phonolites with >56 wt% SiO_2. SBU2 can be regarded as being composed of evolved glasses >8 wt% alkalis. SBU3 comprises phonolite and trachyte glasses >56 wt% SiO_2, but also has a minor group of basalt-basanite glasses (Figure 7.9B). SBU4 has a complex composition of volcanic glasses, with a low-silica phonolite group, a low-alkali tephriphonolite group, a high-alkali trachyte group and a confined group of basanite-to-trachy-basalt glasses (Figure 7.9B). Finally, the SBU5 glasses cover compositions of all the glasses recovered from the previous Mo subunits (Figure 7.9B).

Bed Mp contains three subunits, with an overall composition spanning picrobasalts to phonolites, akin to the compositional distribution of bed Mb from El Hierro (Figure 7.9C). The SBU1 glasses have two compositional groups of evolved >53 wt% SiO_2 tephriphonolites and phonolite-trachytes and basic <46 wt% SiO_2 basanites (Figure 7.9C). The SBU2 glasses comprise a group of ultra-mafic picrobasalts, basanites of variable alkali composition but restricted silica (44-45 wt%), and a group of 52-55 wt% SiO_2 tephroiphonolite-phonolites (Figure 7.9C). The SBU3 glasses form a restricted compositional field of 5-7 wt% alkali basanites, without any evidence of evolved glasses (Figure 7.9C).

Bed Mz lacks glasses of basic composition <46 wt% SiO_2 and <4 wt% alkalis, being instead composed predominantly of evolved volcanic glasses, supporting a Tenerife provenance. The SBU1 glasses have compositions spanning basanites to phonolites (Figure 7.10A). Due to reduced numbers of >90 μm grains and high numbers of altered

grains, only 20 measurements were taken of glasses from SBU2. Those glasses that could be measured were evolved, with SiO_2 >53 wt% and alkalis >8 wt% (Figure 10A).

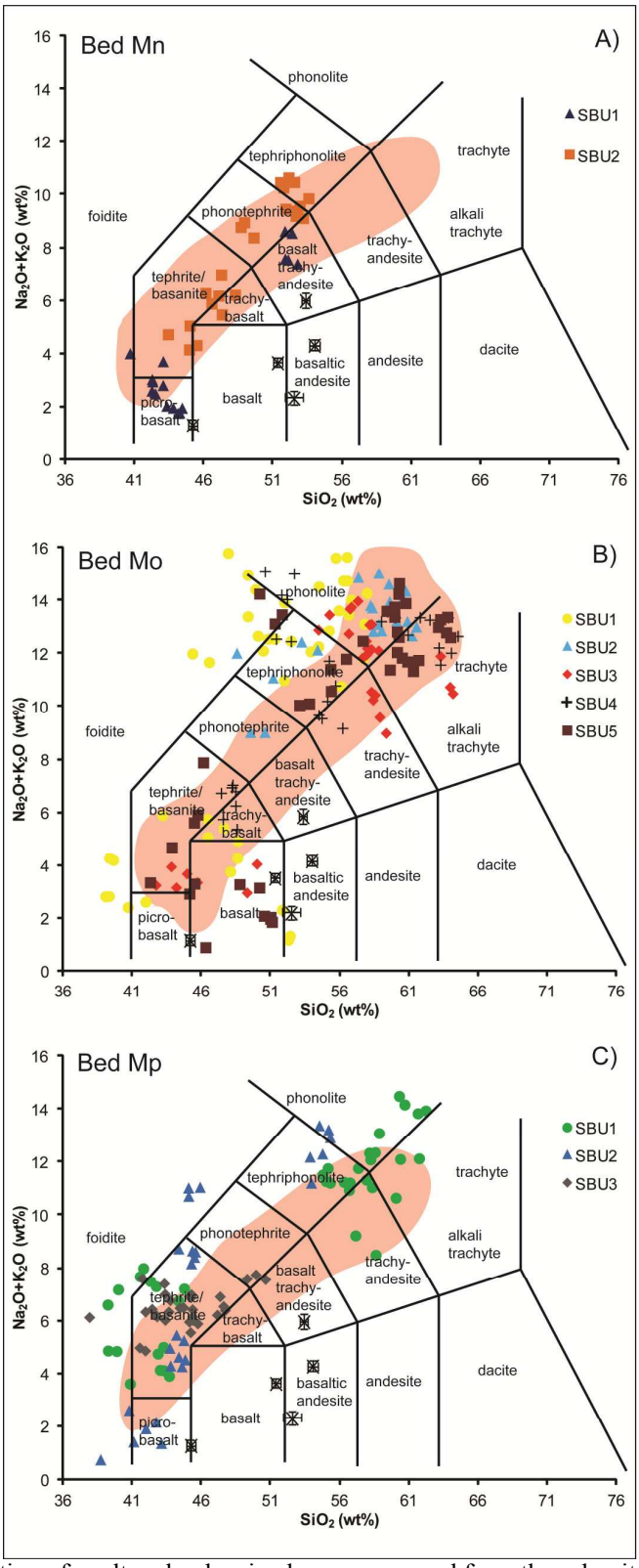

Figure 7.9 Composition of unaltered volcanic glasses recovered from the subunits of bed Mn (A), bed Mo (B), and bed Mp (C). Compositions are plotted on total alkali-silica (TAS) diagrams, showing the disparity between the compositions of the subunits. Geochemical comparison can be made with the basaltic El Hierro source of the El Golfo turbidite. Tenerife onshore data from GEOROCS database.

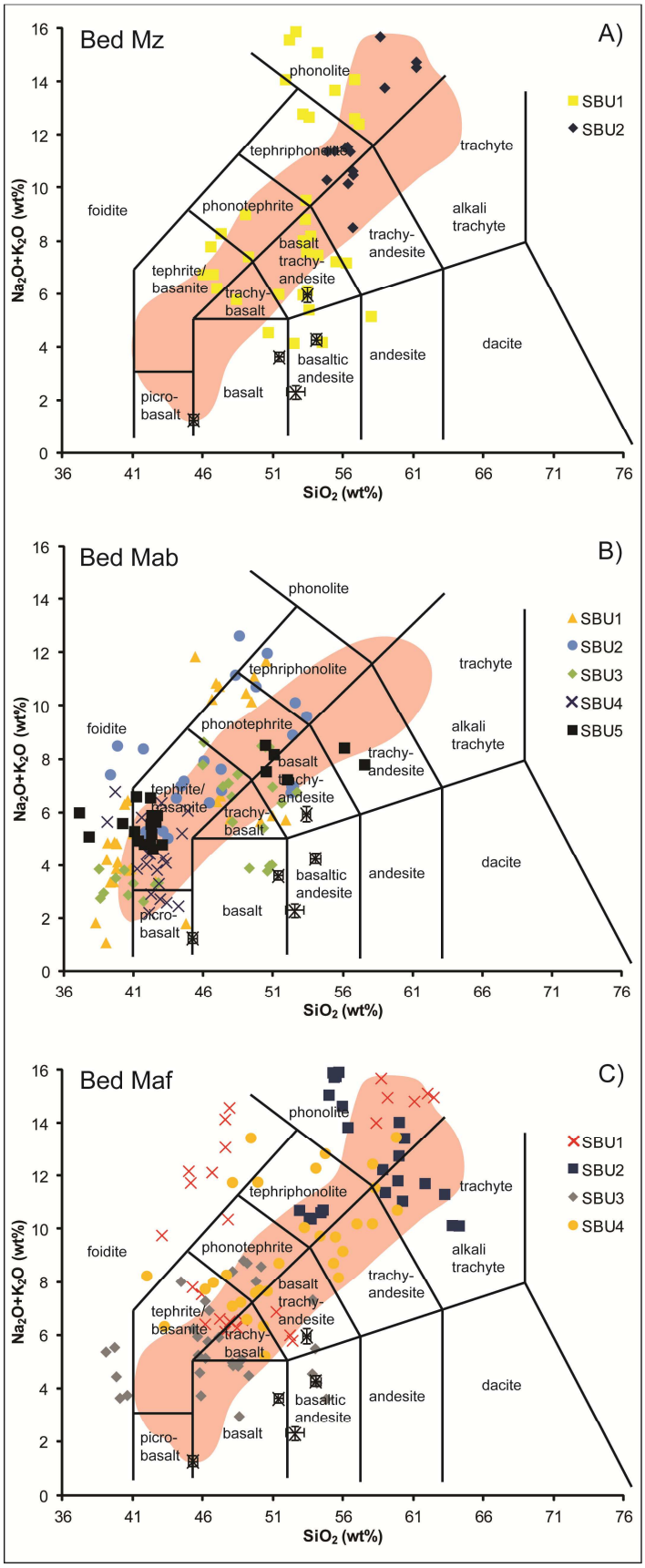

Figure 7.10 Composition of unaltered volcanic glasses recovered from the subunits of bed Mz (A), bed Mab (B), and bed Maf (C). Compositions are plotted on total alkali-silica (TAS) diagrams, showing the disparity between the compositions of the subunits. Geochemical comparison can be made with the basaltic El Hierro source of the El Golfo turbidite. Tenerife onshore data from GEOROCS database.

Bed Mab has five subunits, whereby the overall glass compositional range lies within that expected of El Hierro. SBU1 glasses cover a range from basic picrobasalts to tephriphonolites (Figure 7.10B). SBU2, glasses have compositions from alkalis basanites to phonolites and no glasses with compositions <5 wt% alkalis (Figure 7.10B). In comparison, SBU3 comprise glasses with two groups limited to less than 8-9 wt% alkalis, one being low alkalis and low silica basanites and then a group of 46-51 wt% SiO_2 and 4-8 wt% alkalis (Figure 7.10B). The SBU4 glasses have a restricted composition of low-alkali basanites and picrobasalts (Figure 10B). Lastly, the SBU5 components represent glasses of basanite compositions (4.5-6.5 wt% alkalis and <44 wt% SiO_2).

Bed Maf overall comprises predominantly evolved volcanic glasses >46 wt% SiO_2, and lies within the compositional range associated with Tenerife (Figure 7.10C). Here, SBU1 glasses are >6 wt% alkalis, ranging from alkali basanites to phonolites (Figure 7.10C). SBU2 glasses have restricted evolved compositions >10 wt% alkalis and >51 wt% SiO_2, with tephriphonolite, phonolite and trachyte compositions (Figure 7.10C). SBU3 glasses have a restricted basic composition, with <9 wt% alkalis and <54 wt% silica. Finally, the SBU4 glasses cover a range of compositions from high-silica basanites to phonolites (Figure 7.10C).

Mineral Alteration in Late Quaternary Madeira Abyssal Plain Volcaniclastic Turbidites

Geochemical analyses were conducted on unaltered volcanic glasses. SEM imagery has enabled identification of volcanic glasses that have undergone alteration. A common alteration fabric is the generation of clay minerals and iron-manganese oxides on the surface of the volcanic glasses and lithics (Figure 7.11). A second fabric is replacement by iron pyrite (Figure 7.11). These altered grains are present in all the volcaniclastic turbidites studied in the Madeira Abyssal Plain, with high concentrations in the lower subunits.

Discussion

Subunit Intervals in Volcaniclastic Turbidites

Subunits represent the deposits from a series of separate turbidity currents, closely related in time, that together form a single event bed composed of multiple fining-upward sequences of laminated turbidite sands and mud. The subunits are characterised by a sharp, sometimes erosive, base with an increase in grain-size above, and with

lithic- and carbonate-rich basal compositions. The coarser units can be separated by a turbidite mud or may be amalgamated. These subunits can be correlated over distances greater than 50 km. Indeed the subunits of both the Icod and El Golfo deposits can be regularly correlated over 300 km through Agadir Basin (Figures 7.2 and 7.3).

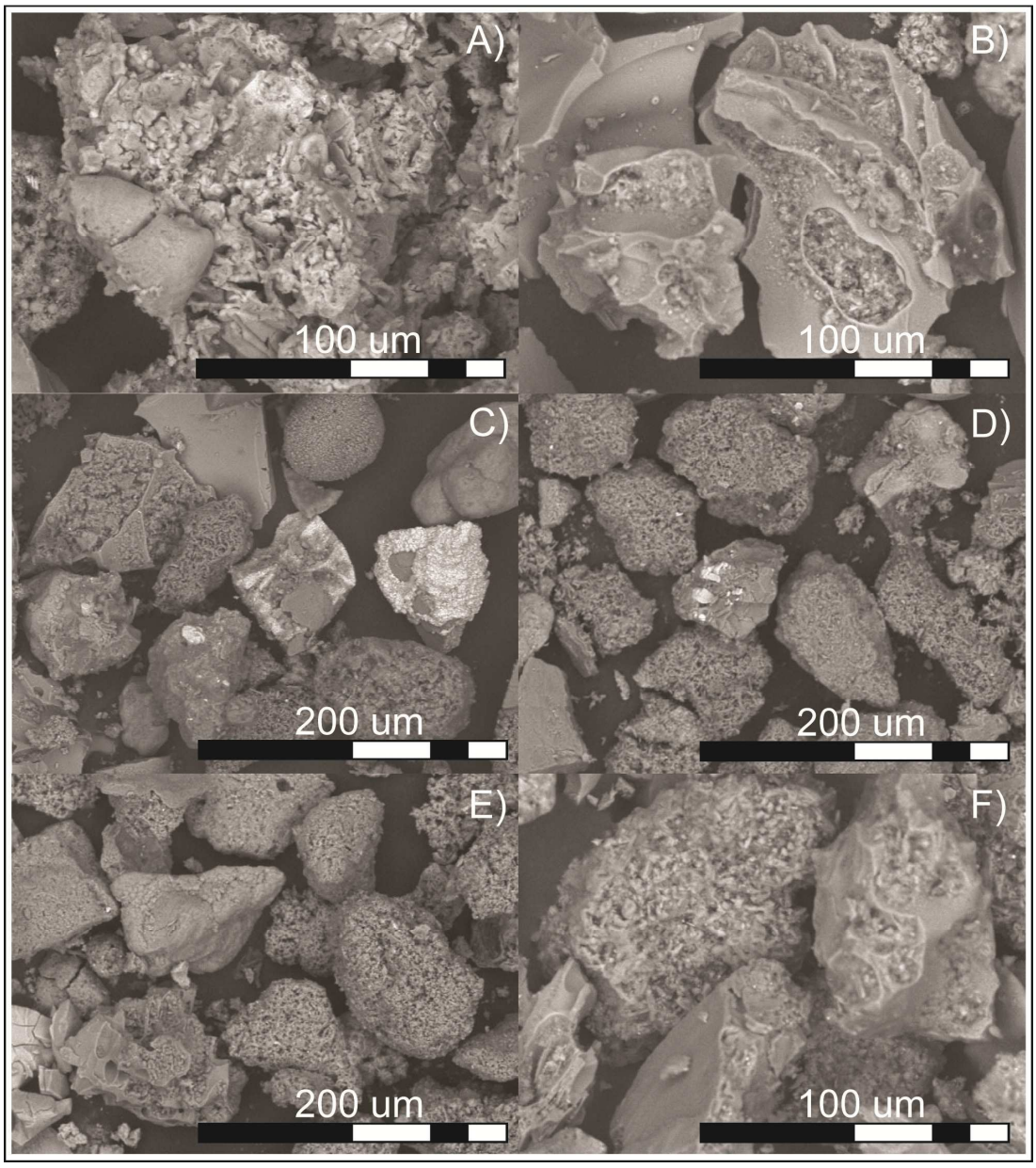

Figure 7.11 SEM images of altered volcanic glasses and lithics from volcaniclastic turbidites in the Madeira Abyssal Plain, A = bed Mn, B = bed Mo, C = bed Mp, D = bed Mz, E = bed Mab and F = bed Maf. Alteration is manifested by clay mineral growth on the grain surface and pyrite replacement of the grain.

Comparison of Results between Depocentres and the Origin of Subunits

Deriving the origin of the subunits has major implications for geohazards. The consistency of the volcanic glass compositions related to a specific island can aid ruling out multiple simultaneous sources (Figures 7.4 and 7.8-7.10). The lack of evidence from

Canary Island onshore and submarine debris apron studies of closely dated events also implies that multiple simultaneous sources are unlikely (Masson *et al.,* 2002). There is no complex channel system feeding Agadir Basin from the Western Canary Islands, thus production of subunits due to flows exiting channels at different times can be negated (Hunt *et al.,* 2011). Within Agadir Basin a combination of grain-size and geophysical data has previously ruled out flow reflection as the origin of the subunits in the Icod event bed (Hunt *et al.,* 2011).

A multistage landslide origin for the Icod landslide was confirmed from analysis of the subunit volcanic glasses from the Icod event bed from a proximal site (Hunt *et al.,* 2011). Geochemical analyses of glasses from subunits of the Icod deposit from Agadir Basin (bed A14) presented in this paper confirm a multistage failure origin (Figure 7.4B). Indeed, the analyses of glasses from each subunit from Agadir Basin (CD166/27) are consistent with those examined from the proximal site (JC27/02). This consistency shows that the seven subunits identified in the Icod deposit can be correlated over distances >300 km, further supporting a multistage failure.

Previously, Hunt *et al.* (2011) stated that analysis of the deposits in the more distal Madeira Abyssal Plain was complicated by the Madeira Channels that feed the Madeira Abyssal Plain from Agadir Basin. Theoretically, flows exiting the multiple channels at different times could generate the vertically stacked subunit texture. However, evidence suggests that flows travelling from Agadir Basin to Madeira Abyssal Plain may be accelerated within, but not confined by, the channels (Stevenson *et al*., 2012). Therefore the initial sediment gravity flow may not be separated by flowing through different channels.

The compositions of the volcanic glasses from Icod subunits within the Madeira Abyssal Plain (bed Mg) are entirely consistent with those from Agadir Basin (Figures 7.4B and 7.8B). This indicates that the subunits can be reliably correlated from Agadir Basin to the Madeira Abyssal Plain, ruling out possible effects due to channelised flows and flow reflection, and supporting a multistage failure.

The differing compositions between glasses from subunits within the El Golfo deposit in Agadir Basin (bed A2) further support a multistage failure mechanism. The subunit glass compositions of the El Golfo deposit in the Madeira Abyssal Plain (bed Mb) are also consistent with the glass compositions within Agadir Basin (Figures 7.4A and 7.8A). This shows that the subunits can also be correlated between the Agadir Basin and Madeira Abyssal Plain for the El Golfo event, again ruling out possible effects of

channelised flows and flow reflection upon entry to the basin, and supporting multistage failure.

The events responsible for the older Madeira Abyssal Plain volcaniclastic deposits (beds Mn, Mo, Mp, Mz, Mab and Maf) have not been sampled in Agadir Basin due to lack of core penetration to required depths. The aforementioned consistencies between the El Golfo and Icod subunits from both depocentres imply the presence of subunits within the older Madeira Abyssal Plain deposits likely represent multistage failures. The geochemistry of the volcanic glass assemblages from the subunits of beds Mn, Mo, Mp, Mz, Mab and Maf further supports the theory that subunits represent multistage failures. The volcanic glasses of the subunits from these beds have subtly different compositions from each other (Figures 7.9 and 7.10). This implies that each subunit represents an individual discrete failure.

Multistage Landslide Mechanisms and Implication for Tsunamigenesis

Sediment gravity flow deposit volumes in the Madeira Abyssal Plain provide a minimum estimate of the total volume involved in the failure. Total event bed volumes (i.e. summing all subunits in each event bed) range from 50-150 km^3 in the Madeira Abyssal Plain. An additional 10-150 km^3 could potentially be deposited in Agadir Basin, based on the two beds sampled to date. Adding proximal debris avalanche volumes of 50-200 km^3, the total landslide volumes, including sediment remobilised from the island flanks, appear not to exceed 500 km^3.

Previous studies of sediment gravity flow deposits associated with volcanic island landslides have shown that the failures were multistage (Garcia and Hull, 1994; Garcia, 1996; Wynn and Masson, 2003; Di Roberto *et al.,* 2010; Hunt *et al.,* 2011). This is further exemplified in the present study. Wynn and Masson (2003) and Hunt *et al.* (2011) identified the Icod and El Golfo landslides as being multistage and retrogressive. The present study supports this theory, and demonstrates supportive petrophysical and geochemical evidence that the last eight large-volume Canary Island landslides were all multistage.

The derivation of multistage failures for Canary Island landslides in the last 1.5 Ma is of first order importance. The volume of a landslide is a primary control on the magnitude of any resulting tsunami (Murty, 2003). Multistage collapses serve to divide the total landslide volume among several smaller events. Multistage collapse with sufficient lag time would significantly reduce tsunami magnitude (scale of minutes), as

shown by modelling of the Güímar landslide as a single and multistage failure (Giachetti *et al.,* 2011). Having shown that all the large-volume volcaniclastic failures in the last 1.5 Ma in the Canary Islands were multistage, it is likely that subsequent failures will also be multistage. However, even within a multistage landslide scenario, given the large volumes of the past events, associated tsunamis could still be catastrophic, at least locally (Paris *et al.,* 2011).

As shown by Hunt *et al.* (2011), the relative proportions of landslide material derived from the island flank also poses an important control on tsunamigenesis (Fine *et al.*, 2003). The results of the present study show altered volcanic glasses occur in all the volcaniclastic beds (Figure 11). Hunt *et al.* (2011) showed that altered volcanic glasses and elevated carbonate content in the basal subunits of the Icod event bed represent initial stages of failure with a significant submarine component. The presence of altered glasses and lithics, coupled with high carbonate content, would imply that other landslides also had a submarine component. Although the submarine portion of the failure would contribute to tsunamigenesis, this would be relatively lower compared to a purely subaerial failure.

Conclusions

The Madeira Abyssal Plain turbidite history has recorded the last eight large-volume (50-350 km^3) Canary Island landslides. This turbidite record not only represents an accurate record of landslide history, but preserves details concerning the failure mechanism of the landslide. Here each large-volume event bed comprises a series of multiple fining-upwards turbidite sands, known as subunits. Comparison of the geochemistry of volcanic glasses from the subunits indicates that these are discrete in composition from one another. Thus each subunit represents a separate failure, inferring that the subunit facies of the volcaniclastic deposits represent multistage failures. This has implications for the tsunamigenesis of volcanic island landslides, since multistage failures will act to reduce the volumes of volcanic flank being introduced to the marine realm at any one time, reducing the size of individual tsunamis. Furthermore, the sediment gravity flows contain altered volcanic glasses and high carbonate content indicative of materials failed from the submarine flanks of the islands. The incorporation of submarine flank sectors into the landslides is also important, since this also acts to further reduce tsunamigenesis. However, although reduced in volume due to

multistage failure mechanisms, the volume of these separate failures are still substantial (10-100 km^3) and capable of causing significant tsunamis.

Acknowledgements

The authors would like to thank the scientists and crew that worked on the D108 and CD166 cruises which collected the piston cores used in this study. JEH would like to acknowledge the PhD funding from Marine Geoscience Group at NOCS that aided completion of this work.

7.3 Summary

There are seven subunits that are regularly correlated within the Icod event bed (bed A14) within the Agadir Basin and five subunits within the El Golfo event bed (bed A2). The geochemical composition of glass populations from the subunits show that the Icod and El Golfo landslides were both multistage.

The volcaniclastic turbidites in the Madeira Abyssal Plain have been linked to the El Golfo (bed Mb), El Julán (bed Mp) and Tiñor (bed Mab) landslides from El Hierro, the Cumbre Neuva (bed Mn) landslide from La Palma, and the Icod (bed Mg), La Orotava (Bed Mo), Güímar (bed Mz) and Roques de García (bed Maf) landslides from Tenerife (Chapter 6). These volcaniclastic turbidites have been found to each comprise a series of subunits. The geochemical composition of the volcanic glasses in the subunits of each of these volcaniclastic turbidites indicates that the landslides responsible for these deposits were multistage.

This has implications for tsunamigenesis, since that the estimated large-volume (50-350 km^3) of these failures is divided amongst several smaller events. This Chapter supports the results from Chapter 5. This further indicates potential issues with the initial landslide parameters used in modelling landslide-generated tsunamis, such as the forecasted 500 km^3 Cumbre Vieja landslide from western La Palma (Ward and Day, 2001). This Chapter indicates that the last eight major volcanic island landslides were multistage, implying that multistage landslides are potentially ubiquitous amongst large-volume volcanic island landslides.

Chapter 8

Supplementary Results and Ongoing Research

8.1 Introduction

This Chapter presents results from ongoing research that supplements the results in the previous Chapters (Chapters 3 to 7). Given the time frame of this thesis, the results to-date are summarised in this Chapter, and do not contribute to the main body of the thesis. However, it is felt that the results of the studies, thus far, are both important to highlight and will enable for a more complete discussion on the recurrence, provenance, magnitude, preconditioning factors and failure mechanisms of submarine landslides on the Moroccan margin.

8.2 Quaternary landslide-induced volcaniclastic turbidites in the Canary Basin: a systematic investigation of distribution, provenance and event history

8.2.1 Introduction

Volumes of 50 to 500 km^3 have been reported for Canary and Hawaiian island submarine landslides (e.g. Chapter 7). The Hawaiian Wailau and Nuuanu events have even greater estimated volumes of 1,500 km^3 and 5,000 km^3 respectively (Moore *et al.,* 1989, 1994). Volcanic island flank collapses can affect proximal areas of 500-23,000 km^2 through the landslide deposits alone, and distal areas >350,000 km^2 due to associated debris flows and turbidity currents (Moore *et al.,* 1989, 1994; Masson *et al.,* 2002; Hunt *et al.,* 2011).

Lateral volcanic island flank collapses pose considerable environmental hazards, due to their capability to potentially generate tsunamis (Keating and McGuire, 2000; Ward and Day, 2001; Masson *et al.,* 2006, and references therein). The evolution of oceanic islands results in the formation of edifices and flanks that are over-steepened, gravitationally unstable, and prone to collapse (Carracedo, 1994, 1999; McGuire, 1996, and references therein). It is the potential hazard that these flank collapses pose that elicits the importance of characterising their occurrence, magnitude and preconditioning factors in a given area.

Pearce and Jarvis (1992, 1995) deduced a Western Canary Island or Madeira provenance for the volcaniclastic turbidites in the Madeira Abyssal Plain. Chapter 6 highlighted that the 1.5 Ma to recent record of large-volume (>100 km^3) flank collapses

in the Canary Islands are represented by associated sediment gravity flow deposits in the Madeira Abyssal Plain. Chapter 7 also demonstrated that these large-volume events were multistage. These landslides predominantly occurred during periods of protracted and voluminous volcanism and periods of warmer and wetter climates associated with rising and highstands of sea level (Chapter 6). This climate association is a premise originally discussed by McMurtry *et al.* (2004) concerning events in the Hawaiian archipelago.

As aforementioned, the events recorded in the Madeira Abyssal Plain represent large-volume landslides. This study focuses on the Mid-Pleistocene (1.5 Ma) to recent record of volcaniclastic turbidites within the proximal depocentres of the Moroccan Turbidite System and debris aprons of Madeira and the Western Canary Islands. These events range from large-scale flank collapses, documented by previous studies, to smaller failures of shallow marine volcaniclastic accumulations. This present study investigates the distribution, provenance and timing of volcanic island landslides recorded at these proximal sites.

A dataset of >150 shallow piston cores will be utilised in this study, including previously unpublished coverage of the turbidites on the proximal slope aprons of Madeira, Tenerife, La Palma and El Hierro. ODP core from the slopes of Gran Canaria will also be utilised to present a record of the landslides from that locale. This contribution therefore represents a complete volcanic island landslide history of the Western Canary Islands and Madeira in the last 0-1.5 Ma.

8.2.2 Results

Agadir Basin

Previous work has focused on resolving the Agadir Basin stratigraphy to oxygen isotope stage six (OIS 6), to the AB14 event at 165 ka (Wynn *et al.,* 2002a; Frenz *et al.,* 2009; Chapters 3 and 4). Figures 3.6, 3.8 and 8.1 show the presence of the A2, A8, A10.5 and A14 volcaniclastic turbidites, and that the A2 and A14 turbidites are the most extensive in thickness and distribution.

In addition to the events originally identified by Wynn *et al.* (2002a) and Frenz *et al.* (2009), an across-basin transect shows that there are volcaniclastic turbidites: A2.1, A2.5, A3.5, A4, A6, A6.1, A6.2, A8.5, A10.5 and A13.1 aged <165 ka (Figures 3.6 and 3.8). In the >200 ka Agadir Basin record there are also additional events: A16, A19, A20, A21 and A24 (Figures 3.6 and 3.8). Other than A2 (El Hierro) and A14 and A16

(Tenerife), the other volcaniclastic events recorded in the 0-600 ka history of Agadir Basin are derived from Madeira. This is based on their basic igneous composition and isolation to the lower sub-basin opposing the southern slope of Madeira.

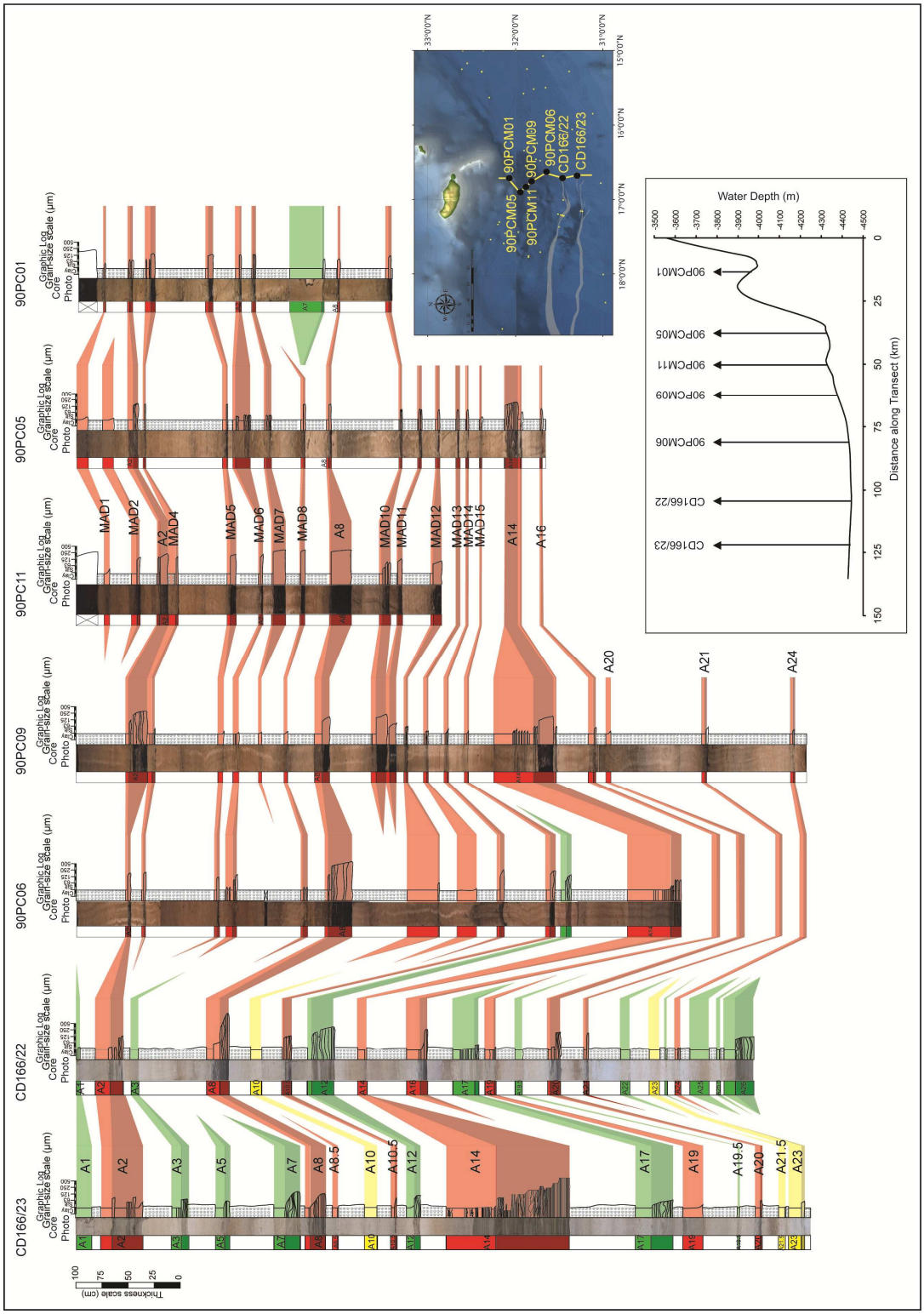

Figure 8.1 Correlation panel of volcaniclastic turbidites from the southern flank of Madeira into Agadir Basin. Core locations in shown in the inset map.

Southern and Western Madeira Slopes

An extensive and previously unpublished core dataset around the southern and western slopes of Madeira is presented here. It provides a much needed insight into the history of minor gravity flows from the submarine flanks of Madeira. Although without evidence of major flank failures, the correlation panels (Figures 8.1 and 8.2) show a summary of correlateable low-volume events that can be found across the entire western and southern Madeira slopes. Only turbidite AB8 (also named MAD9) of the Madeira slope turbidites is of large enough volume to develop substantial thicknesses in Agadir Basin (Figures 8.1 and 8.2). Most are too small to extend beyond the southern slope apron of Madeira.

These cores also show the presence of the Icod turbidite (~165 ka) from Tenerife, and show the sequence of vertical subunit intervals associated with it. The Icod turbidite, along with the El Golfo (~15 ka) event pose two marker beds for the lower slope successions. A stratigraphy and temporal record of these Madeira turbidites can be constructed using these marker beds, calculated sedimentation rates, magnetic susceptibility logs, and vertical variations in hemipelagic lithology (Figures 8.1 and 8.2). The stratigraphy of this apron shows a series of 30 events (Figures 8.1 and 8.2); assigned by MAD#, where 'MAD' denotes Madeira.

South Selvagen Islands

Three cores from the JC27 cruise in 2008 (JC27/01, /02 and /03) were supplemented with archived core from the Lamont Doherty Earth Science Observatory (Figure 8.3). This sequence of cores is located to the south of the Selvagen Islands and to the north of Tenerife, Gran Canaria and La Palma. JC27/01 records a number of thin fine-sand turbidites <165 ka, since the complete sediment record to the Icod turbidite was not penetrated. Whereas JC27/02 and /03 penetrate to and beyond the Icod turbidite (Figure 8.3). This is resolved through both bulk and volcanic glass geochemistry, demonstrating a phonolitic composition as reported in previous studies (Hunt *et al.,* 2011). In addition, the oxygen isotope stage six glacial clay is present both above and below this deposit, verifying the Icod turbidite identity and ~165 ka age (Figure 8.3).

This region on the southern flank of the Selvagen Islands potentially records flows from the northern flanks of the Western Canary Islands. However, there are very few turbidites recorded here, with the Icod turbidite being the most prominent. The western cores record a series of small thin volcaniclastic flows, presumably of La Palma origin.

JC27/02 records both the Icod turbidite (A14) and an equivalent bed A16 found in Agadir Basin of Tenerife provenance (Figure 8.3). Using a 0.85 cm/1000 year hemipelagic sedimentation rate (based on hemipelagic thickness to Icod turbidite at 165 ka) the A16 turbidite is dated at 215 ka in the Agadir Basin record, compared to the ~220 ka approximation from its location here (Figure 8.3).

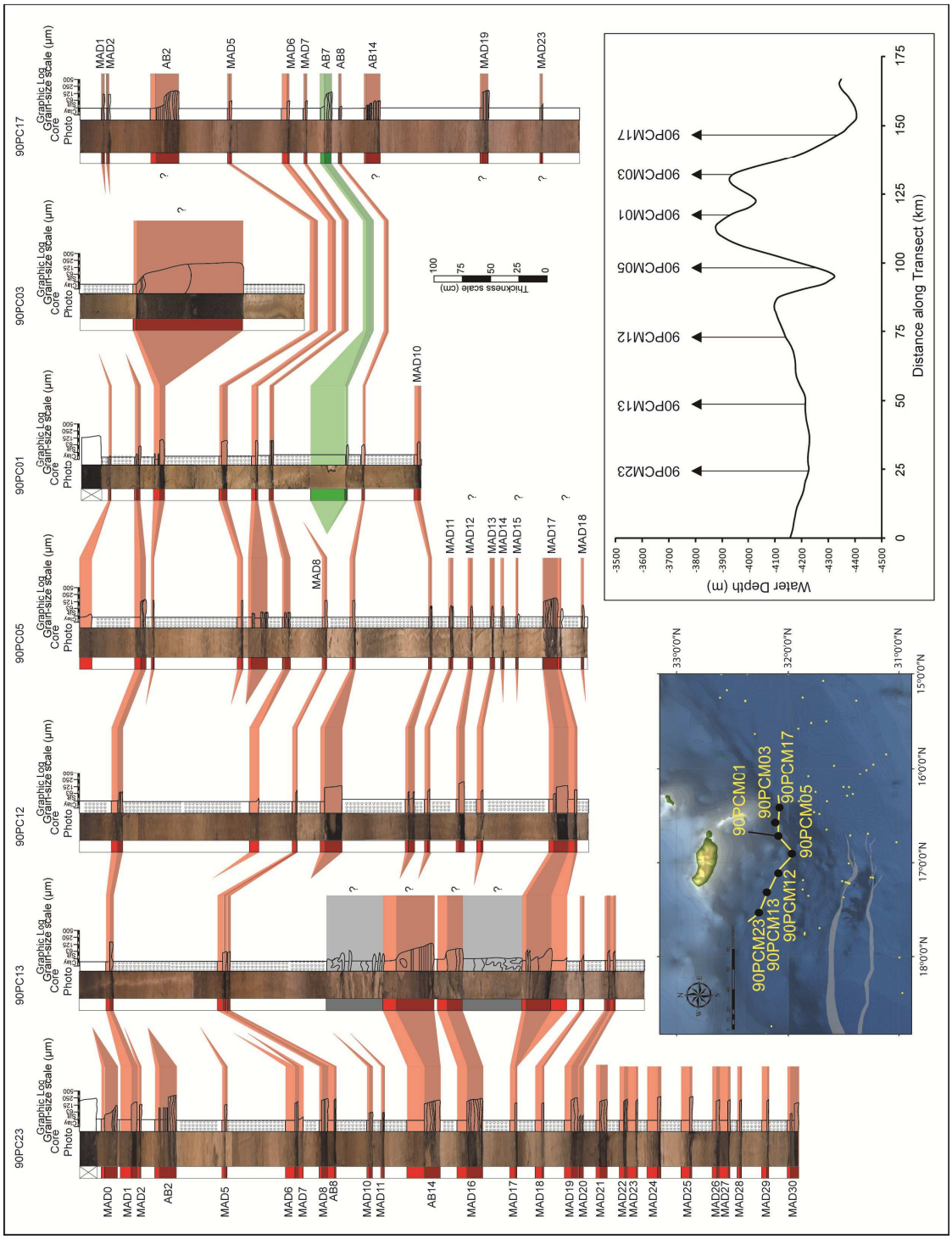

Figure 8.2 Correlation panel of volcaniclastic turbidites across the southern and south-west submarine flanks of Madeira. Highlighting the prevalence of thin-bedded basalt-rich turbidites. Core locations on inset map.

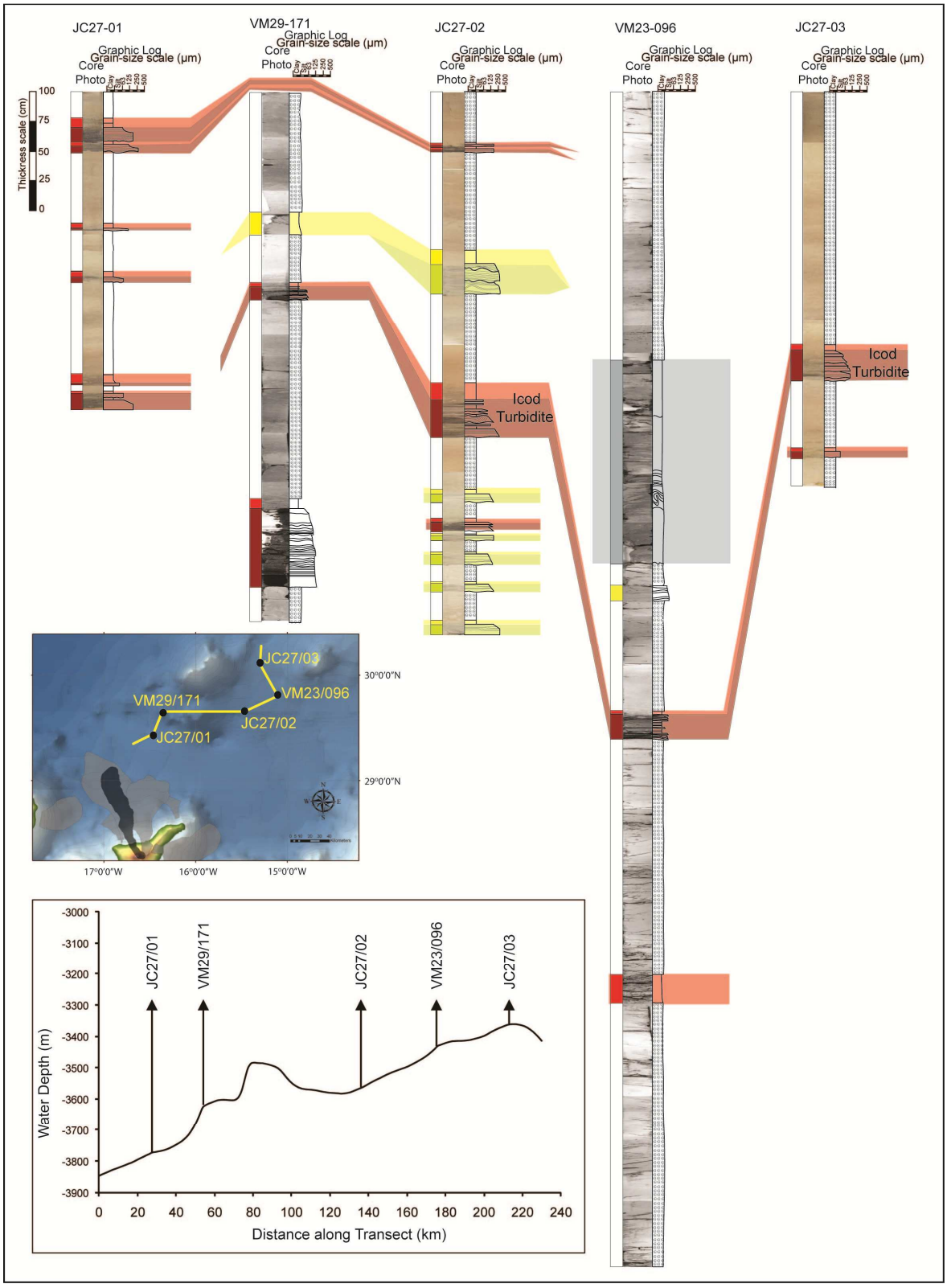

Figure 8.3 Core transect displaying turbidite correlations across the Southern Selvagen Islands. The Icod turbidite presents the only significant turbidite in the sediment record. Core locations on inset map.

Northern La Palma Apron and Sediment Wave Field

A relatively proximal suite of cores was taken across the northwest slope apron of La Palma, which incorporates the La Palma sediment wave field of Wynn *et al.* (2002b). An 80 cm-thick sequence of poorly sorted coarse-grained intervals of volcaniclastics and finer muds represents a debritic interval, and marks the only deposit in CD56/25. Core CD56/26 records nine thin-bedded turbidite sand-mud couplets, while core CD56/24 records six thin-bedded turbidites (Figure 8.4). Thus within this localised area of the La Palma sediment wave field there are heterogeneities present in the turbidite record.

In CD56/24, the thickest turbidite is composed of subunits of repeated interbedded turbidite sand and muds. This turbidite (NLAP3) has a darker hemipelagic sequence above and a paler hemipelagic sequence below, in addition to characteristic sequence of multiple sand layers (subunits) this could be correlated to the uppermost turbidite in cores CD126/04 and CD126/03 on the northern slope (Figure 8.4). Here the 'NLAP' prefix denotes North La Palma and 'WLAP' denotes West La Palma.

Cores CD126/03 and /04 record only 11 thin-bedded turbidites in an extensive hemipelagic record. However, VM32/025 contains 19 additional turbidites restricted to that core. The hemipelagic sediment potentially contains a record to 1.0 Ma, given the alternating history of interglacial-glacial hemipelagite sedimentation (Figure 8.4). This shows an increased number at VM32/025, but fewer immediately west at CD126/03 and CD126/04, thus showing heterogeneities over a small spatial scale.

Core CD56/028 taken relatively proximal to the western flank of La Palma (~70 km offshore) shows an extensive sequence of thin-bedded fine-sand turbidites (Figure 8.4), whereby 11 of the 15 turbidites present have subunits (Figure 8.4). Core CD56/027 only records two significant turbidites of La Palma or El Hierro provenance (Figure 8.4), both of which comprise coarse grains 1-3 cm in size. These western La Palma cores demonstrate further examples of local heterogeneities present in the proximal La Palma turbidite record.

Southern El Hierro El Julan and Las Playas Aprons

The westernmost cores in this region are CD126/05 and CD126/06, and record a long history of thin-bedded volcaniclastic turbidites. CD126/05 records sedimentation back to oxygen isotope stage (OIS) 13, indicating sparse occurrence of volcaniclastic turbidites directed from west El Hierro (Figure 8.5) (Georgiopoulou, 2006). Indeed, the

CD126/05 record has a turbidite recurrence of ~20 ka, although this may be affected by the Saharan Debris Flow.

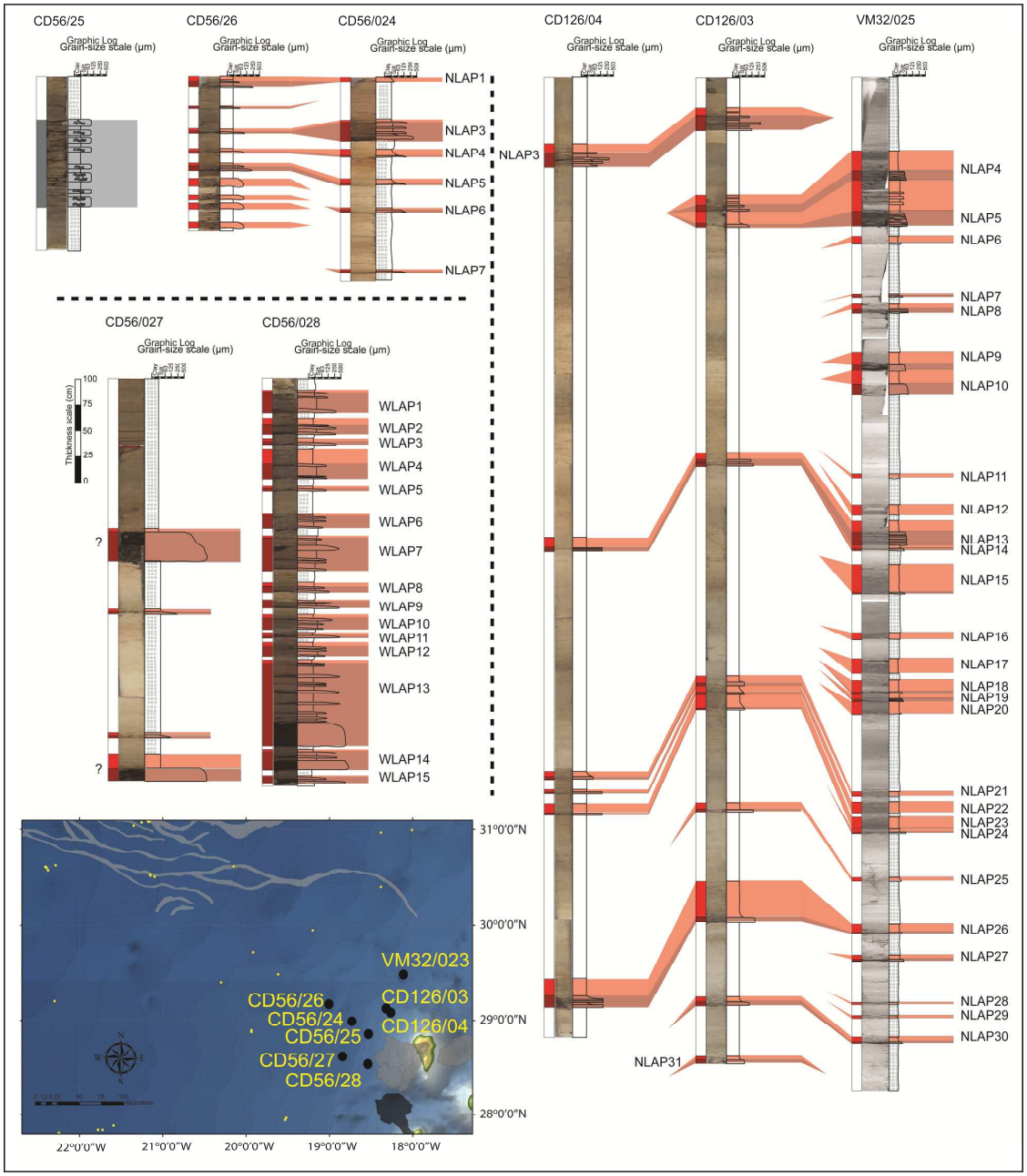

Figure 8.4 Cores from northwest and west La Palma apron and sediment wave field showing the variable record of turbidite activity. The northwest cores CD126/03, /04 and VM32/025 display a long record of punctuated turbidite activity. CD56/026 and /024 show the variable turbidite history in the sediment wave field to the northwest of La Palma. Finally, CD56/028 showing an abundance of thin-bedded basaltic turbidites with subunits located most proximal to western La Palma. Core locations on inset map.

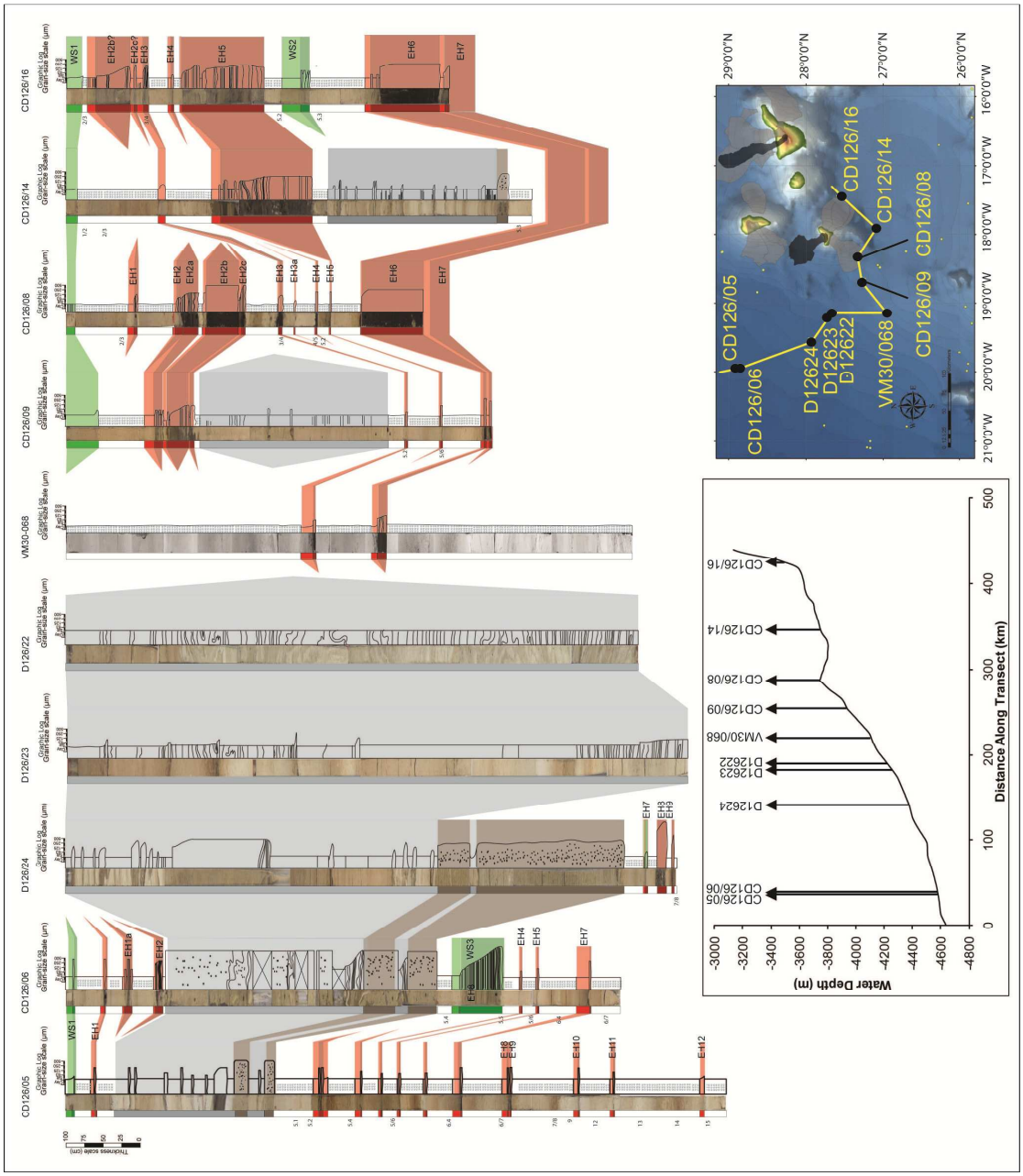

Figure 8.5 Core transect across the aprons of South El Hierro. Correlations of both metre-thick and thin-bedded turbidites are highlighted.Biostratigraphic markers to aid correlations and dating are provided next to respective cores. Biostratigraphy taken from Georgiopoulou (2006). Core locations on inset map and bathymetric transect.

The core transects across the southern El Julan and Las Playas aprons display different turbidite histories to those recorded west of El Hierro (Figure 8.5). These apron cores represent a 165 ka to recent history of hemipelagic sedimentation intersected by 13 volcaniclastic and 5 siliciclastic turbidites (Figure 8.5) (Georgiopoulou, 2006). Bed thickness, patterns in bedforms and basal grain-size indicate that many of the volcaniclastic turbidites owe their provenance to the Las

Playas (southeast) flank of El Hierro. A minor number of events deposited between 35-60 ka occur exclusively on the El Julan apron, represented in core CD126/08 (Figure 8.5).

These turbidites are given the 'EH' prefix to discriminate their provenance from El Hierro and the location of the deposits on the aprons of El Hierro. Of note, the cores of the Western Canary Island aprons do not record the El Golfo or Icod turbidites, which restricts the coverage of these deposits to the areas to the north of the Canary archipelago.

Volcaniclastic Sand Geochemistry and Provenance

The bulk geochemical analyses were undertaken from samples of known provenance to investigate the potential hetero- and homogeneities in volcanic sand composition. These samples were taken from turbidites from each volcanic apron.

Bulk ICP-OES results demonstrate that all the geochemical major and trace element variation plots discriminate Tenerife from the other sources. The Tenerife-sourced sands have higher sodic composition and a low MgO composition (Figure 8.6). These also have low TiO_2. Trace element compositions enabled definitive discrimination of the Tenerife source, with high La (>65 ppm), high Zr (>420 ppm), and low Cr (<100 ppm) (Figure 8.7). The Y-La trend is also disparate from the basalt-rich alternate sources (Figure 8.7).

The basaltic sources of Madeira, La Palma and El Hierro show similar compositions. Madeira can be partially distinguished from La Palma and El Hierro from having a higher range of MgO composition, lower Na_2O, lower TiO_2 and higher Al_2O_3 content (Figure 8.6). Trace element analysis shows that Madeira sourced sands have the highest Cr content. Furthermore, a Y-La trend provides Madeira with a discrete trend, but this does overlap with those of La Palma and El Hierro (Figure 8.7).

The bulk trace element analyses can distinguish the La Palma source from El Hierro and Madeira, since La Palma sands are found to have higher La (Figure 8.7). The southwest apron of El Hierro can also be distinguished as having the lowest values of La compared to the southeast and northern apron trends of that island. However, utilising the Y/Nb-Zr/Nb and Ba/Y-Zr/Nb comparative plots advocated by Abratis *et al.* (2002), the different sources are well discriminated (Figure 8.8). Firstly, the Tenerife source is identified by the very low Y/Nb ratio (Figure 8.8). However, there are two distinct groups of Tenerife samples, whereby one is denoted by a low Zr/Nb ratio and

the other by a Zr/Nb ratio similar to the younger basaltic sources of El Hierro and La Palma (Figure 8.8). The Tenerife samples are found to have a broad range in the Ba/Y ratio (Figure 8.8).

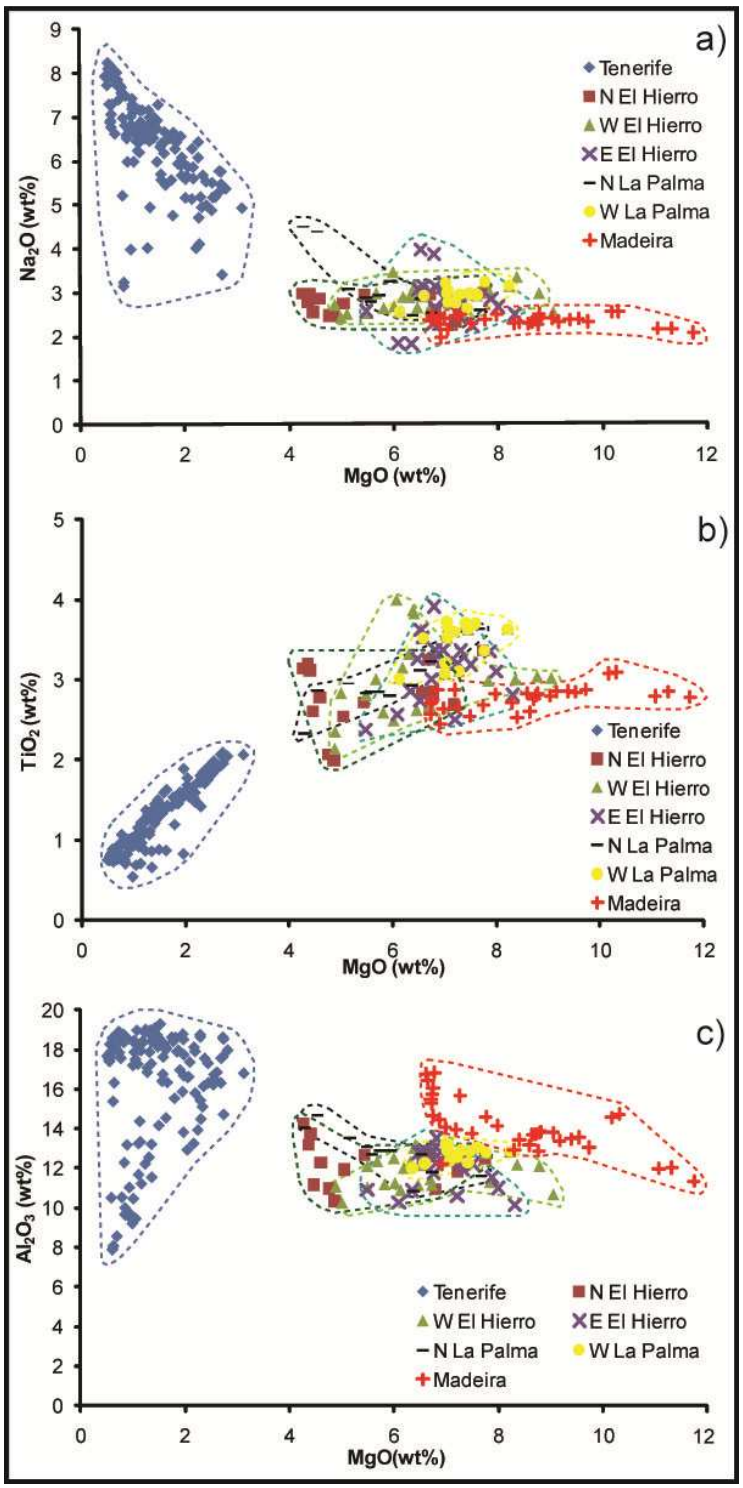

Figure 8.6 ICP-OES major element compositions for carbonate-free bulk volcaniclastic turbidite sand samples. Turbidites from give island aprons were used to investigate compositional variations between the provenances. A) Na_2O vs MgO, B) TiO_2 vs MgO, and C) Al_2O_3 vs MgO.

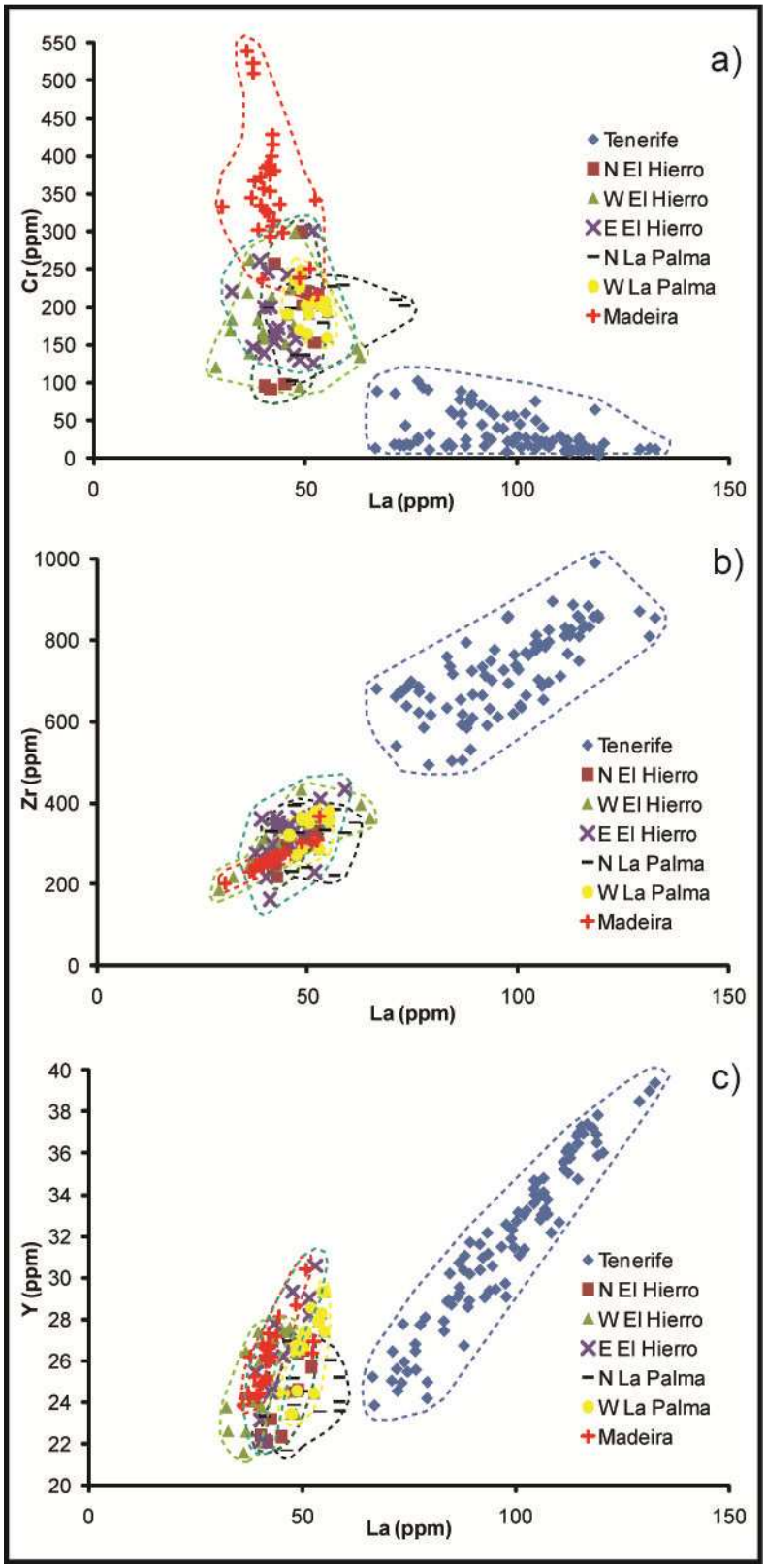

Figure 8.7 ICP-OES trace element compositions for carbonate-free bulk volcaniclastic turbidite sand samples. Turbidites from give island aprons were used to investigate compositional variations between the provenances. A) Cr vs La, B) Zr vs La, and C) Y vs La.

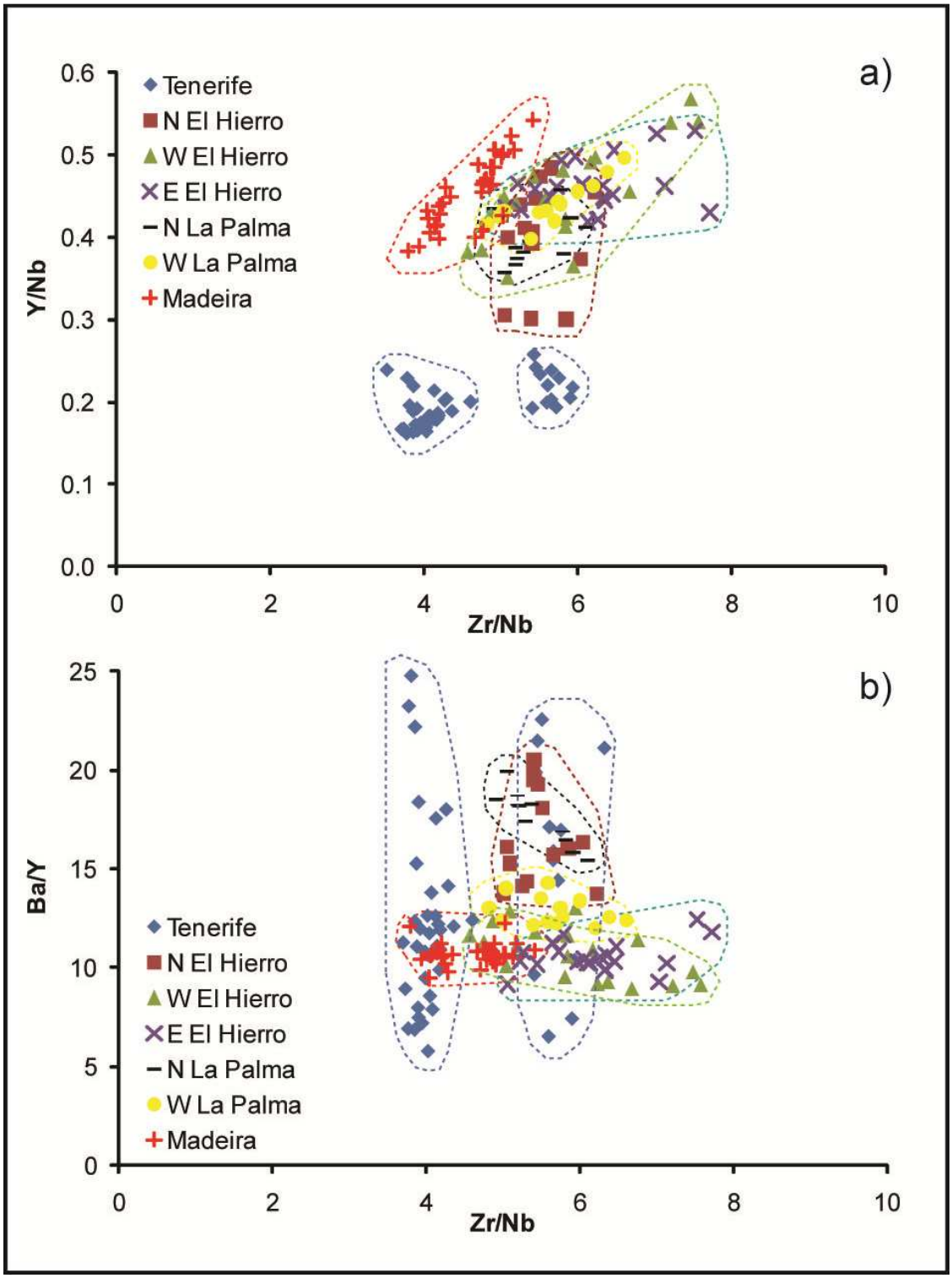

Figure 8.8 Trace element variations plots a) Y/Nb vs Zr/Nb and b) Ba/Y vs Zr/Nb, that provide insight into the relative enrichment/depletion of the sources of the turbidites in the Canary Basin. Enrichment trends include towards high Y/Nb and high Zr/Nb, and towards high Zr/Nb and low Ba/Y.

Madeira has a Y/Nb similar to the other basaltic sources, but higher than Tenerife (Figure 8.8). Although similar to the southwest and southeast El Hierro sources, the Madeira Ba/Y is lower than those of the northern La Palma, western La Palma and northern El Hierro aprons (Figure 8.8). The key discriminating factor for Madeira is the Zr/Nb ratio, where it is lower than all the other basaltic sources (Figure 8.8).

Both the northern and western La Palma sources have similar Y/Nb and Zr/Nb ratios, but can be differentiated from each other on the Ba/Y ratio, whereby the western La Palma source has a significantly lower Ba/Y ratio (Figure 8.8). The La Palma sources can also be distinguished from the El Hierro sources, whereby the Zr/Nb ratio is <6.2 and Ba/Y ratio >12, which is different from the southwest and southeast El Hierro sources (Figure 8.8). The La Palma sources can be partially distinguished from the broader Y/Nb range attributed to the northern El Hierro source (Figure 8.8).

The southwest and southeast El Hierro sources have broad ranges of Zr/Nb, which is in contrast to the more restricted range for northern El Hierro (Figure 8.8). However, the north El Hierro source is differentiated from southwest and southeast sources, since northern El Hierro turbidites are found with higher Ba/Y (Figure 8.8). Both southwest and southeast El Hierro-sourced turbidites have similar compositions that are indistinguishable using the variation plots of Abratis *et al.* (2004).

8.2.3 Remaining Work and Discussions

This study, thus far, has demonstrated the varying records of volcaniclastic turbidites on the aprons of Madeira and the Western Canary Islands. Furthermore, bulk major and trace element analyses have been completed to investigate the geochemical signatures of the different provenances. The current temporal record of the volcaniclastic turbidites from the island aprons is not robust. Coccolithophore biostratigraphy will be completed to add an accurate temporal framework to calculate both the age and recurrence of these volcanic island landslides. Bulk major-element and trace-element analyses have shown that the island provenances can be distinguished. However, SEM EDS will enable further grain-specific analysis of volcaniclastic turbidites.

These data will complete one of the most comprehensive studies of volcaniclastic turbidites from submarine island flanks. Although the Madeira Abyssal Plain records the most volumetric volcanic landslides from the Western Canary Islands, only analyses of the smaller-volume events from the island aprons that will enable a complete appraisal of the recurrence of volcanic island landslides.

8.3 Relationship between Caldera-forming Eruptions and Major Flank Collapses

8.3.1 Introduction

The May 1980 eruption of Mount St Helens drew much attention to the relationship between eruptions and flank collapses. This thesis has focused on submarine volcanic island landslides from the Western Canary Islands (Chapters 5, 6 and 7). Loading of volcanic flanks by intrusive and extrusive volcanism have been identified as a primary preconditioning factor for major landslides (Carracedo, 1994; Iverson, 1995; Elsworth and Voight, 1996; Voight and Elsworth, 1997). Chapter 6 has demonstrated that the Madeira Abyssal Plain volcaniclastic turbidite record demonstrates volcanic island landslides potentially occur in coincidence to periods of protracted island volcanism. However, there is a substantial lack of understanding of the relationship between volcanism and landslide activity. This lack of understanding is typified in the controversy over the origin of the Las Cañadas Caldera (Marti *et al.,* 1997; Hürlimann *et al.,* 2000; Masson *et al.,* 2002).

Numerous studies have invoked a vertical collapse origin from caldera-forming eruptions at the end of cycles of basaltic-phonolitic volcanism (Marti, 1994, 1996; Marti *et al.,* 1997; Hürlimann *et al.,* 1999, 2000). Lack of breccias from boreholes within the caldera has been cited as supporting evidence for a non-landslide origin (Marti *et al.*, 1997). While projection of a resistivity anomaly within the caldera, designated to be the failure plane of the Icod landslide, is judged to not reach the southern caldera wall (Coppo *et al.,* 2009). Alternatively, lateral collapses by large-volume landslides have also been argued as the origin for the southern Las Cañadas caldera wall (Navarro and Coello, 1989; Ancochea *et al.,* 1990, 1999; Carracedo, 1994; Watts and Masson, 1995, 1998; Huertas *et al.*, 2002). Evidence for both vertical and lateral collapses exist on the northern flank of Tenerife and within the Las Cañadas caldera, however the genetic link between these processes remains poorly understood.

Recent studies have highlighted that the Icod landslide and older Orotava, Güímar, and Roques de García landslides were multistage events (Hunt *et al.,* 2011; Chapter 7). These multistage landslides are represented by multiple fining-upwards sequences within deposited event beds, called subunits (Wynn and Masson, 2003; Hunt *et al.,* 2011). Volcanic glasses representing the explosive phonolitic El Abrigo at the end of Diego Hernendez Formation are only found in the uppermost subunit of the Icod deposit (Hunt *et al.,* 2011). Hunt *et al.* (2011) implied that the initial stages of the multistage

Icod landslide may have instigated the explosive El Abrigo eruption, resulting in El Abrigo glasses only being present in the lattermost stages.

However, the SEM EDS glass analysis study of Hunt *et al*. (2011) involved only one core and cited an average El Abrigo composition from literature. The present study aims to utilise analyses of glasses from subunits of the Icod sediment gravity flow deposit at multiple sites. This will produce more comprehensive compositional profiles for each subunit. These will be compared to measured compositions of onshore volcanic samples of the El Abrigo ignimbrite. A second aim will be to investigate the compositions of the sediment gravity flow deposit associated with the Orotava landslide, which has also been shown to be multistage (Chapter 7). The composition of the subunits from bed Mo in the Madeira Abyssal Plain will be compared to analyses of Granadilla ignimbrite samples.

8.3.2 Results

Work contributing to previous Chapters (Chapters 5 and 7) have analysed volcanic glasses from subunits from the Icod deposit from the southern Selvagen Islands, Agadir Basin and Madeira Abyssal Plain. Compilation of these data provides a more comprehensive overview of the glass populations present in each subunit. The SBU1-2 volcanic glasses range from basalts to alkali trachyte-trachy andesites. SBU3 has a mixed component composition with alkali trachyte-trachy andesite glasses but a predominance of silica-rich alkali-trachytes (Figure 8.9A). SBU4 glasses have a more evolved phonolitic composition, with a proportion that is of phonolite-trachyte composition (Figure 8.9A). SBU5 and SBU6 glasses lie at the phonolite-alkali trachyte boundary (Figure 8.9A). Lastly, SBU7 glasses show a different and discrete character, composed of strictly tephriphonolite-phonolite glasses (Figure 8.9A). The compilation of these data provides between 70 and 150 glass measurements per subunit.

Analysis of onshore pumice samples provides 30 SEM EDS measurements of volcanic glasses from the El Abrigo ignimbrite. These are found to be consistent with the previously published averaged bulk composition of the El Abrigo ignimbrite (Figure 8.9A). Furthermore, the broader composition of onshore El Abrigo glasses remain constrained to SBU7 (Figure 8.9A).

Previously obtained data from the Orotava deposit in the Madeira Abyssal Plain (bed Mo) has been utilised (Chapter 7). SBU1 have two compositions of basic basalt-basanites and tephriphonolite-phonolites (Figure 8.9B). SBU2 comprises a minor

number of phonotephrite-tephriphonolite glasses, but is predominantly composed of high-silica phonolites with 56 wt% SiO_2 and >8% alkalis (Figure 8.9B). SBU3 comprises phonolite and trachyte glasses of 56-61 wt% SiO_2, but also has a minor group of basalt-basanite glasses (Figure 8.9B). SBU4 has a complex composition of volcanic glasses, with a low-silica phonolite group, a low-alkali tephriphonolite group, a high-alkali trachyte group and a confined group of basanite-to-trachy-basalt glasses (Figure 8.9B). Finally, the SBU5 glasses cover compositions of all the glasses recovered from the previous bed Mo subunits (Figure 8.9B).

8.3.3 Remaining Work and Discussions

Firstly the compositions of volcanic glasses from each subunit within the Icod deposit confirm that each subunit represents a discrete landslide event, therefore supporting the Icod landslide being multistage. Measurements of El Abrigo volcanic glasses are consistent with literature values (e.g. Bryan *et al*., 2002) (Figure 8.9A). The glasses of El Abrigo composition are constrained to the uppermost subunit (SBU7) (Figure 8.9A), supporting the findings of Hunt *et al.* (2011).

Volcanic glass analyses from the subunits of the Orotava sediment gravity deposit confirm that each subunit represents a discrete landslide event. Therefore, like the Icod landslide, the Orotava landslide can be implied to be a multistage landslide. However, at present, only results from a single site in the Madeira Abyssal Plain have been utilised. For a more robust study additional sites should be used. The Orotava sediment gravity flow deposit is not penetrated in more proximal basins, thus an additional site(s) in the Madeira Abyssal Plain will be sought. Samples of the Granadilla ignimbrite have been collected, but as yet have not been analysed, these will be analysed shortly. However, using sample compositions from literature, volcanic glasses of Granadilla composition are restricted to SBU4 and SBU5, and the higher alkalis and lower silica samples also showing similar compositions to those glasses recovered from SBU2.

Both the Icod landslide and Orotava landslide have been speculatively linked to a major explosive eruption at the end of a terminal basalt-phonolite volcanic cycle (Chapter 6). The deposits associated with these landslides demonstrate that both were within ±20 ka of onshore dates of the El Abrigo and Granadilla eruptions respectively (Chapter 6). In both cases, volcanic glasses of the associated explosive eruptions are found in the upper subunits. This implies one of two models: 1) retrogressive failure mechanism that gradually excavates the island flank until the most recent effusive

deposits are failed, or 2) initial landslide stages act to unroof the magma chamber and instigate the eruption before further subsequent failures. This study potentially provides important information regarding the relationship between explosive volcanism and landslide activity.

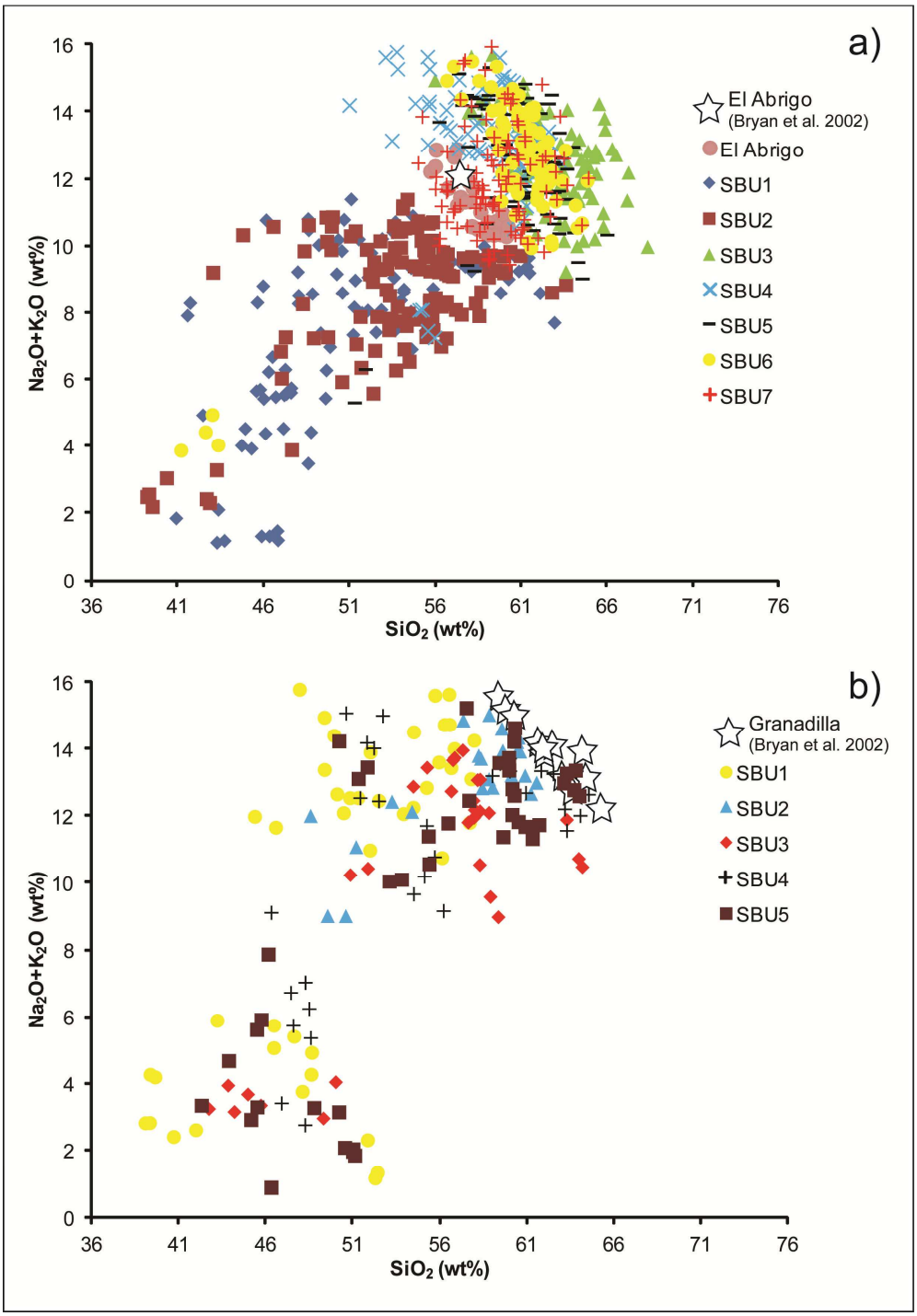

Figure 8.9 SEM EDS results for subunits from the Icod and Orotava deposits plotted on a total alkali-silica (TAS) diagram. Results show discrete compositions of glass populations in successive subunits in both deposits. Pink closed circles represent measurements of the El Abrigo ignimbrite, which are shown to have affinity with SBU7 of the Icod deposit. Open stars represent compositions of the relevant ignimbrite from literature.

8.4 Growth of the Canary Islands Recorded in the Distal Turbidite Record

8.4.1 Introduction

Volcanic island landslides have been ascribed to primarily occur during the developmental and mature stages of shield-building and edifice growth (Carracedo, 1999). The formation of tripartite rift systems associated with shield growth involves injection of dykes and effusion of lavas and pyroclastics that both load the flank and cause instability (Carracedo, 1994, 1999). These instabilities result in landslides that can be prodigious in volume, with many previous events in the Hawaiian and Canarian archipelagos exceeding 100 km^3 (Moore *et al.,* 1989, 1994; Masson *et al.,* 2002; Chapter 6). The excessive volumes and potential catastrophic nature of these failures necessitate the characterisation of such past events, in order to better understand the hazards and levels of risk associated with them. Much work has been conducted on the submarine landslides generated during the subaerial stages of island growth in the Canary Islands (Masson *et al.,* 2002, and references therein; Hunt *et al.,* 2011, Chapter 6). However, little is known about the island stability during the early initial stages of inception and emergence. The transition from submarine to subaerial stages of growth represents the largest emplacement of volcanic mass on the oceanic crust, thus this period could yield large-volume failures capable of tsunamigenesis. This study serves to highlight the occurrence of submarine landslides during this early stage of island growth that equal and exceed the magnitude of their subaerial counterparts.

The Canary archipelago represents an east-to-west chain of volcanic islands extending over ~500 km of the Northwest African passive margin. The origin of this archipelago has been much debated, and competing theories exist: propagating fracture model (Anguita and Hernán, 1975; Robertson and Stillman, 1979), uplift of tectonic blocks (Araña and Ortiz, 1986), Canary rift model (Fúster, 1975; Oyarzun *et al.,* 1997), classic plume model (Morgan, 1971; Burke and Wilson, 1972; Schmincke, 1973; Vogt, 1974; Khan, 1974; Morgan, 1983; Carracedo, *et al*., 1998), blob model (Hoernle and Schmincke, 1993) and upwelling sheet model (Anderson *et al.,* 1992). Anguita and Hernán (2000) generate a further unifying theory on the origin of the Canary Islands, combining the key notions of the aforementioned models. However, Carracedo *et al.* (1999, 2002) argued that the evidence, thus far, at least supports growth of the islands on a slow moving plate above a mantle plume.

The ages of initiation and emergence of the specific islands has been sought by numerous studies, in order to provide insight into the mechanisms responsible for the development of ocean island chains. Early studies have aimed to date (K-Ar methods) onshore basement complexes of the Canary Islands, and associate these to the seamount and emergent stages of island growth (Abdel-Monem *et al.,* 1971, 1972). Further improvements in geochronology have enabled more accurate dating of the onshore stratigraphy of the Canary Islands (Ancochea *et al.,* 1990, 1994; Guillou *et al.,* 1996, 1998; Carracedo, 1999; Carracedo *et al.,* 2001). Although a general east-to-west age progression is apparent in the Canary archipelago, there is greater divergence along this trend when compared to the Hawaiian archipelago (Carracedo, 1999). This could be attributed to the 'slow' movement (1.9 cm/year) of oceanic crust over a mantle plume and possible generation of a dual-line, compared to the singe-line Hawaiian chain operating on 'fast' moving (10 cm/year) oceanic crust (Sleep, 1992; Carracedo, 1999; Carracedo *et al.,* 1997, 1998, 1999).

The destabilisation of volcanic island flanks and subsequent landslides have been investigated in detail in numerous volcanic island archipelagos: Hawaii (Moore *et al*., 1989, 1994), Canary Islands (Holcomb and Searle, 1991; Watts and Masson, 1995, 2001; Masson *et al*., 2002, and references therein), Cape Verde (Le Bas *et al.,* 2007; Masson *et al.,* 2008), La Réunion (Lénat *et al.,* 1989; Labazuy, 1996; Oehler *et al*., 2004, 2008), Lesser Antilles (Deplus *et al.,* 2001; Watt *et al.,* 2012) and French Polynesia (Clouard *et al.,* 2001). These landslides represent failures of the over-steepened island edifices, commonly associated with gravitational stresses induced by volcanic overgrowth and tensional stresses induced by dyke intrusion and rift arm activity (Elsworth and Voight, 1996; Carracedo *et al.,* 1999; Elsworth and Day, 1999). Indeed, these failures are evident in the Canary archipelago, and are recorded in a multitude of proximal debris avalanche deposits on the submarine flanks (Masson *et al.,* 2002, and references therein; Acosta *et al.,* 2003, and references therein) and associated large-volume turbidity currents recorded in distal depocentres (Pearce and Jarvis, 1992, 1995; Weaver *et al.,* 1992; Rothwell *et al.,* 1992; Wynn *et al.,* 2002; Wynn and Masson, 2003; Frenz *et al.,* 2009; Hunt *et al.,* 2011, Chapter 6).

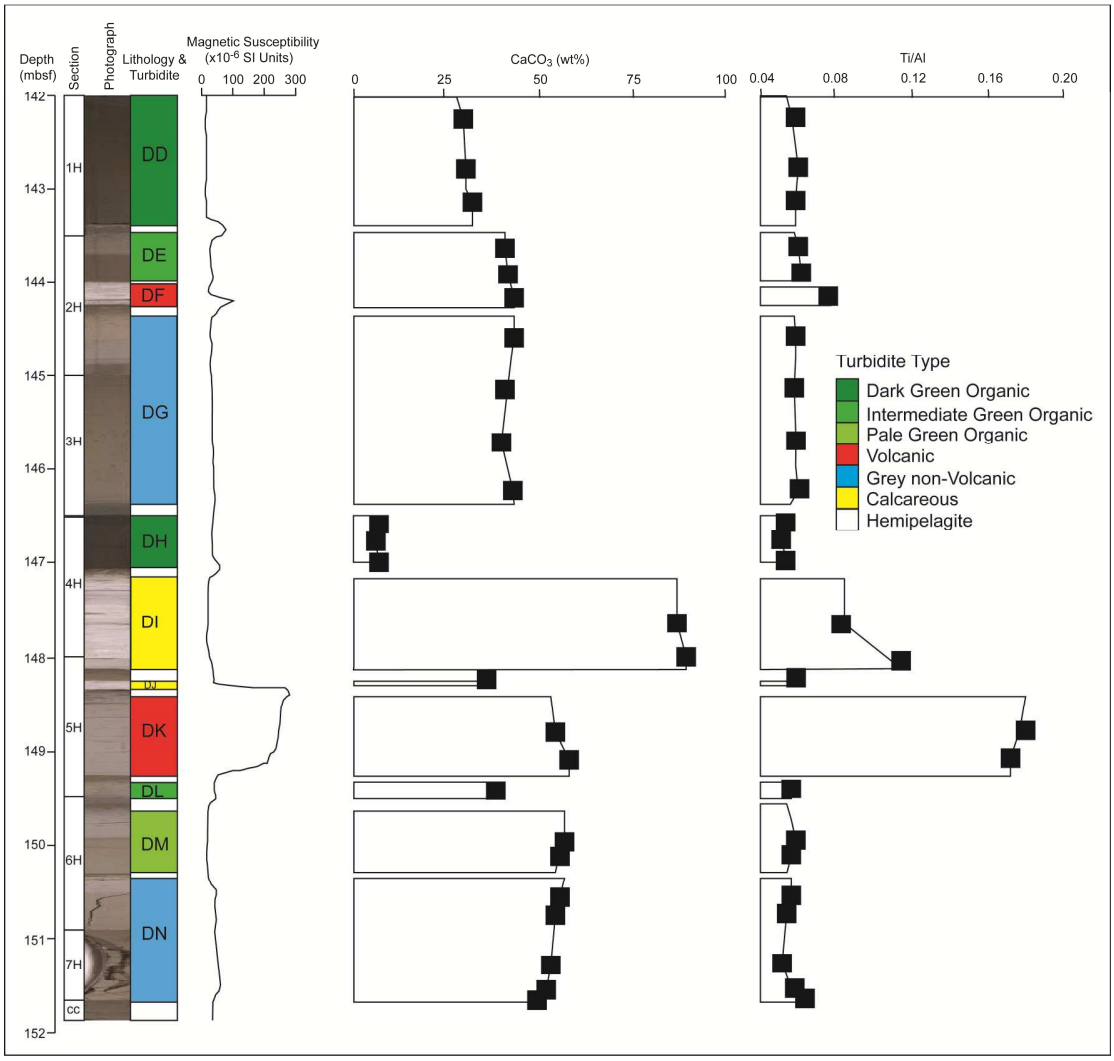

Figure 8.10 Example featuring sections from core section 16H from ODP hole 950 (142-152 mbsf). This demonstrates all the turbidite types with the grey non-volcanic turbidites of interest highlighted in blue. Note the grey colour, but lack of magnetic susceptibility response, and low Ti/Al seen in DG and DN, compared to the volcanic turbidite DK.

However, little is known about the emergent stages of the islands and the inherent internal stresses exerted on the growing island flanks during this stage. Carracedo (1999) stated that the initial stage of island growth involves the development of tensional stresses. These tensional stresses are associated with doming and fracturing caused by triple-rift development and magma ascension. The present study theorises that doming of the emerging subaerial edifice would act to inflate and over-steepen the submarine flanks. This would result in gravitationally induced collapse of the surficial sediment and flank materials. Failure of the early developing submarine flanks is proposed to be responsible for the metre-thick pale grey 'non-volcanic' turbidites deposited in the Madeira Abyssal Plain (Figure 8.10) (Weaver *et al.,* 1998; Jarvis *et al.,*

1998). This present contribution explores this concept, using the turbidite records from ODP sites 950, 951 and 952 in the Madeira Abyssal Plain. This study will provide dated records of these pale grey 'non-volcanic' turbidites, which will allow comparison of the occurrence of these turbidites with the temporal record of volcaniclastic turbidites from Chapter 6 and detailed volcanic histories of the Canary Islands.

8.4.2 Results

The large-volume volcaniclastic turbidites of the Madeira Abyssal Plain are attributed to the large scale submarine-subaerial flank collapses associated with protracted periods of subaerial volcanic growth (Weaver *et al.,* 1998; Jarvis *et al.,* 1998; Hunt *et al.,* 2011, Chapter 6). Thus the composition of these turbidites better reflect the subaerial and submarine flank volcanics that are incorporated into the failure, enabling provenance to be determined. However, the pale grey 'non-volcanic' turbidites comprise a higher component of calcareous nanofossil-rich sediment and a reduced component of volcanic materials. Thus these turbidites pose an exclusively submarine origin with small proportions of volcanic material included. While a general provenance is the submarine flanks of the growing and emerging volcanic islands of the Canary archipelago, the exact island provenance remains unobtainable from the geochemistry.

Dating of these turbidites is resolved using nanofossil biostratigraphy of the hemipelagite between the turbidites. Ages derived from the biostratigraphy of Howe and Sblendorio-Levy (1998) has been applied to generate hemipelagic sedimentation rates. Weaver (1994) demonstrated that the turbidity currents in abyssal plain settings are principally non-erosive. Thus turbidites are either dated from samples taken immediately above and below the event, or from where the turbidite intersects the dated hemipelagic record. The events were dated at each hole (950, 951 and 952) to obtain viable age distributions, from which an average was taken. Decompacted volumes of these events are calculated using the methodology outlined by Weaver (2003), but calculated at each hole to gain a more representative figure. This provided volumes at the point of deposition, which can be better compared.

The pre-7 Ma record is predominantly composed of thin-bedded (10-50 cm-thick) turbidites only recorded at either hole 951 or 952. Whereas the record of pale grey non-volcanic turbidites demonstrates a prevalence of broadly distributed and correlateable events post-7 Ma. These turbidites range from 0.20-12.0 m-thick, but are principally metre-thick (average 220 cm decompacted thickness) and comprise uniform ungraded

muds (Figure 8.10). Indeed, the pale grey non-volcanic turbidite FB (dated at 5.8 Ma) represents the thickest and most volumetric turbidite in the Madeira Abyssal Plain turbidite history (12 m-thick and 400 km^3-volume once compaction is accounted for).

The occurrence of the pale grey non-volcanic turbidites can be separated into a number of periods that correlate to: 1) oldest dates of subaerial volcanism on the individual Canary Islands marking emergence from the submarine realm, and 2) initiation of periods of major volcanic activity and subsequent flank collapse (Figure 8.11). The most voluminous events appear to occur immediately prior to: subaerial emergence of Tenerife (7.0-7.3 Ma), growth of the Teno and Anaga massifs on Tenerife (6.0-5.5 Ma), initiation of growth of Roque Nuble edifice on Gran Canaria (~4.0 Ma), and subaerial emergence of La Palma and El Hierro (2.0-1.2 Ma) (Figure 8.11). Other periods of deposition of pale grey non-volcanic turbidites appear to occur: prior to commencement of the volcanic island flank collapse record of Fuerteventura (~16.5 Ma), subaerial emergence of Gran Canaria (~14.5 Ma), subaerial emergence of La Gomera and second eruptive phase of Gran Canaria (~13-11.5 Ma), commencement of post-erosional volcanism on Lanzarote and/or commencement of growth on La Gomera associated with the Upper Old Series basalts (~9.0 Ma), growth of the Cañadas edifice on Tenerife (~3.0 Ma), and finally commencement of Cumbre Vieja rift volcanism on La Palma and/or development of Hijas seamounts (0.8-0.4 Ma) (Figure 8.11).

8.4.3 Remaining Work and Discussions

Potential provenance work can be conducted on these beds, utilising the mudcap geochemistry reported by Jarvis *et al.* (1998). The present study has profound implications for the development of ocean island archipelagos. The submarine growth, early subaerial emergence, and initiation of periods of active edifice growth appear synonymous with inflation of the submarine flanks by intrusive igneous activity and magma ascension (Carracedo *et al.,* 1999). The implication is that early growth stages of both islands and individual edifices are capable of instigating prodigious failures, which are potentially tsunamigenic. Previous studies have identified volcanic flank collapse in the Canary Islands as being prevalent after sustained periods of volcanic activity (Chapter 6). This study supports a notion that failure of the submarine flanks of the Canary Islands also occur as the result of tectonic inflation prior to island emergence and magma ascension associated with volcanic activity, as postulated by Jarvis *et al.* (1998) and Weaver *et al.* (1998).

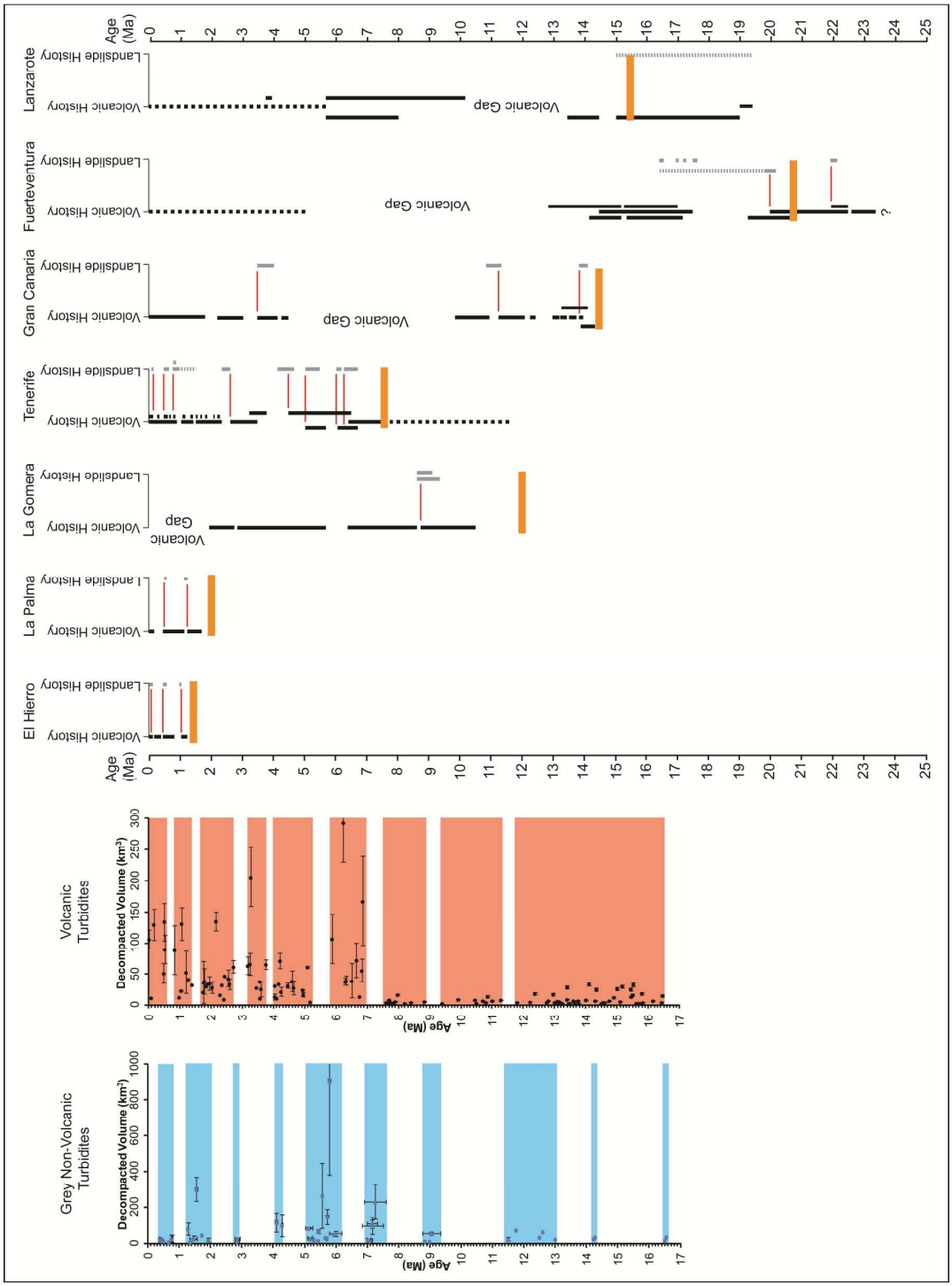

Figure 8.11 Summary diagram showing the timing and decompacted volume of grey non-volcanic turbidites (blue shade) and volcanic turbidites (red shade). These are plotted against the onshore records of landslide and volcanic activity of the Canary Islands. Orange bars indicate subaerial emergence of the island. Red lines connect volcanism and potentially associated landslides.

Therefore, not only are volcanic island edifices prone to failure of large-volumes of materials capable of tsunamigenesis, but submarine regions of the island flanks are also capable of failing significant volumes of material. With development of Las Hijas seamounts and current volcanic activity on El Hierro, there is an increased hazard of

submarine landslides occurring in the Western Canary Islands. Although no evidence exists of major landslides or debris flows around Las Hijas, similar structures such as the Loihi seamount in Hawaii have undergone extensive geomorphic alteration by landsliding (Rihm *et al.,* 1998). The ages of generation of the two largest seamounts that comprise the Las Hijas group are ~500 ka and ~200 ka (Rihm *et al.,* 1998). There are minor grey non-volcanic turbidites, recorded as beds L2 and L3 at 350-400 ka and beds S2, V1, X and X1 at 680-820 ka (Chapter 6). These two groups of pale-grey non-volcanic turbidites could represent failure of surficial sediment from Las Hijas due to inflation of the seafloor as these two aforementioned seamounts began to grow.

In conclusion, the present study highlights an ability to identify the points of emergence of the Canary Islands and inflation due to magmatic ascension prior to volcanic activity. These points in island evolution in the Canary Islands are recorded as pale-grey non-volcanic turbidites in the Madeira Abyssal Plain. There failures are amongst the largest volume events in the Moroccan Turbidite System, and yield turbidites of 50-400 km^3, which are equal or greater than volumes of subaerial island landslides. Thus they not only pose an important record of island evolution, but pose potentially significant and as yet unrecognised geohazards.

8.5 Turbidite record of Northwest African Continental Slope Landslides

8.5.1 Introduction

Submarine landslides pose significant geohazards on both local and far-field scales, owing to the destruction they cause and their potential to generate catastrophic tsunamis (Ward and Day, 2001; Locat *et al.*, 2009; Geist *et al.*, 2009). Submarine landslides occur most commonly in areas with thick sedimentary deposits, sloping sea floors, and with external triggers such as earthquakes (Hampton *et al.*, 1996). Submarine landslides are commonly associated with a series of 'territories', including: fjords, active river deltas, submarine canyon-fan systems, open continental slopes, and volcanic islands (Lee, 2009). The open continental slope and canyon-fan systems are the most commonly occurring 'territories' in the modern North Atlantic. Characterising the location, recurrence and preconditioning factors of submarine landslides in such environments is thus a necessity for quantifying the geohazard potential for a particular seaboard. This is important due to the high population densities of coastal regions,

exploitation of submarine regions by the hydrocarbon industry, and the increasing number of telecommunication cables laid in areas of increased sediment instability.

Modern examples of continental slope failures from the Gulf of Mexico are generally between 0.5 to 10 km^3, with some being 20-150 km^3 (McAdoo *et al.,* 2000). On the U.S. Atlantic margin, submarine landslides range from 0.002 to 180 km^3 (Chaytor *et al.,* 2009). However, larger events have been recorded in the broader North Atlantic area, with the largest events in the last 45 ka ranging from 20-3,200 km^3 (Maslin *et al.*, 2004, and references therein).

Much work has been completed on characterising continental slope derived landslides in the North Atlantic (Embley and Jacobi, 1986; Booth *et al.,* 1993; Weaver *et al.*, 2000; Hühnerbach *et al.*, 2004; Lee, 2009; Claytor *et al.*, 2007, 2009; Twitchell *et al.,* 2009). However, difficulties with surveying large areas of the continental slope and studies focussing on submarine canyons has resulted in biased records of submarine landslide occurrence (Lee, 2009). Furthermore, continental slope areas with submarine landslide activity can have a complex geomorphology, with overprinting of failure events, and seafloor erosion obscuring the hemipelagite records often used to date the landslides.

Therefore, it is prudent to instead study the records of distal sediment gravity flows associated with these submarine landslides (Weaver, 2003). Indeed, the Late Quaternary turbidite record of the Madeira Abyssal Plain has previously been used to represent continental slope landslides from the Northwest African margin (Weaver and Kuijpers, 1983; Weaver and Rothwell, 1989; Weaver *et al.*, 1992; Wynn *et al.*, 2002). The Middle Miocene to recent turbidite history of the Madeira Abyssal Plain was drilled by ODP Leg 157 (sites 950, 951 and 952) in 1994 (Schmincke *et al.*, 1995; Weaver *et al.,* 1998). Average recovery exceeded 95% (Schmincke *et al.*, 1995), which therefore provides one of the most complete turbidite records of a passive margin. Weaver (2003) previously documented the 17 Ma to recent siliciclastic turbidite record in the Madeira Abyssal Plain, and inferred the patterns in landslide activity to be associated with variations in upwelling on the continental slope.

The present study aims to re-analyse the record of siliciclastic turbidite deposition in the Madeira Abyssal Plain. Furthermore, by utilising the mudcap geochemistry of Jarvis *et al.* (1998), variations in the continental slope provenance may be inferred, which will better enable a statistical assessment of turbidite recurrence and magnitude. The present study will also incorporate details of temporal variability in continental sediment flux

and upwelling recorded on the slope (ODP Hole 398 from Leg 108 and Hole 658 from Leg 159T). This will enable an evaluation of the hypothesis of Weaver (2003), that the Middle Miocene to recent turbidite history reflects the effects of climate on sediment accumulation and slope stability. The present study also investigates whether the events responsible for the turbidites in the Madeira Abyssal Plain and more proximal Agadir Basin, originate from single or multi-stage landslides.

8.5.2 Results

General Synopsis of ODP 17 Ma to recent Siliciclastic Record

Deposition of siliciclastic turbidites primarily commences at ~15.8 Ma after the deposition of the major Cruiser Turbidite. Although some minor events are found in the 22 to 16 Ma turbidite record. After the Cruiser Turbidite there is a rapid influx of thin (10-90 cm-thick) dark and intermediate green siliciclastic turbidites. Indeed, during this time site 952 comprises a sequence of 112 events dominated by thin-bedded dark and intermediate (olive) green siliciclastic turbidites. The frequency of events at the southerly 952 site far exceed those at 951 (northern) and 950 (central) (Figure 8.12). From 15 to 10 Ma the frequency of events at site 952 declines to 35-40 events per million years, and broadly equals those at 951 (Figure 8.12). Site 950 has a much reduced record of turbidite deposition between 17 and 10 Ma compared to sites 951 and 952.

At 10 Ma there is a dramatic reduction in the frequency of siliciclastic turbidites, with a reduction of 20 to 3 events per million years from 10 to 6.5 Ma (Figure 8.12). The frequency of siliciclastic turbidites at 950 remains low (10 per million years) from 14 to 6 Ma, with reductions between 10-9 Ma and 7-6 Ma (Figure 8.12). The thickness of these siliciclastic events also remains low at 10-90 cm (Figure 8.13).

At ~7.3 Ma there is a 1.8-2.1 m-thick dark green siliciclastic turbidite (Figure 8.13). However, the commencement of regular metre-thick siliciclastic turbidites commences at ~6.2 Ma, with a 4 m-thick dark green turbidite. After 6.2 Ma the frequency of siliciclastic turbidites increases to 15-20 events per million years and thicknesses increase to 0.5-5.0 m-thick (Figures 8.12 and 8.13). The thickest siliciclastic turbidites are the intermediate green type, which are found to commonly 2.0-5.0 m-thick (Figure 8.13). Although both frequencies and volumes of siliciclastic turbidites remains relatively high during the 6.2 Ma to recent record, there is a decrease in the frequency after ~2.0 Ma (Figures 8.12 and 8.13).

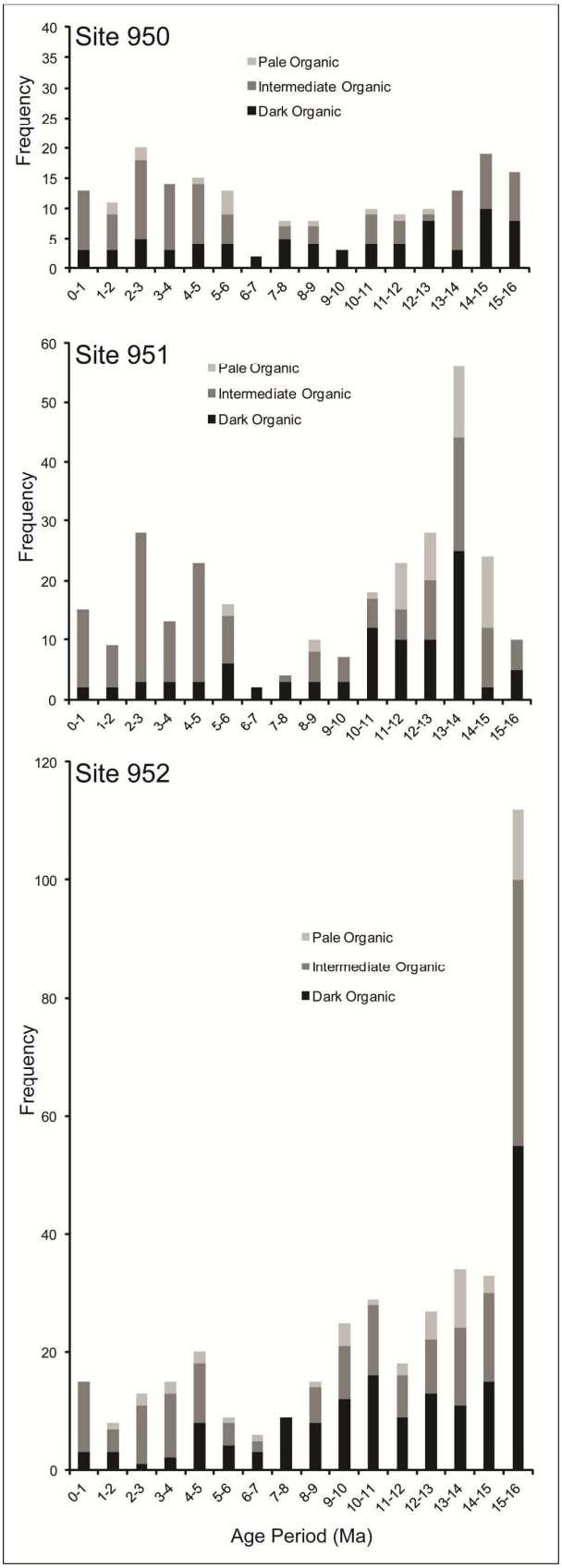

Figure 8.12 Number of pale, intermediate (olive), and dark green organic-rich siliciclastic turbidites deposited per million years at site 950, 951 and 952.

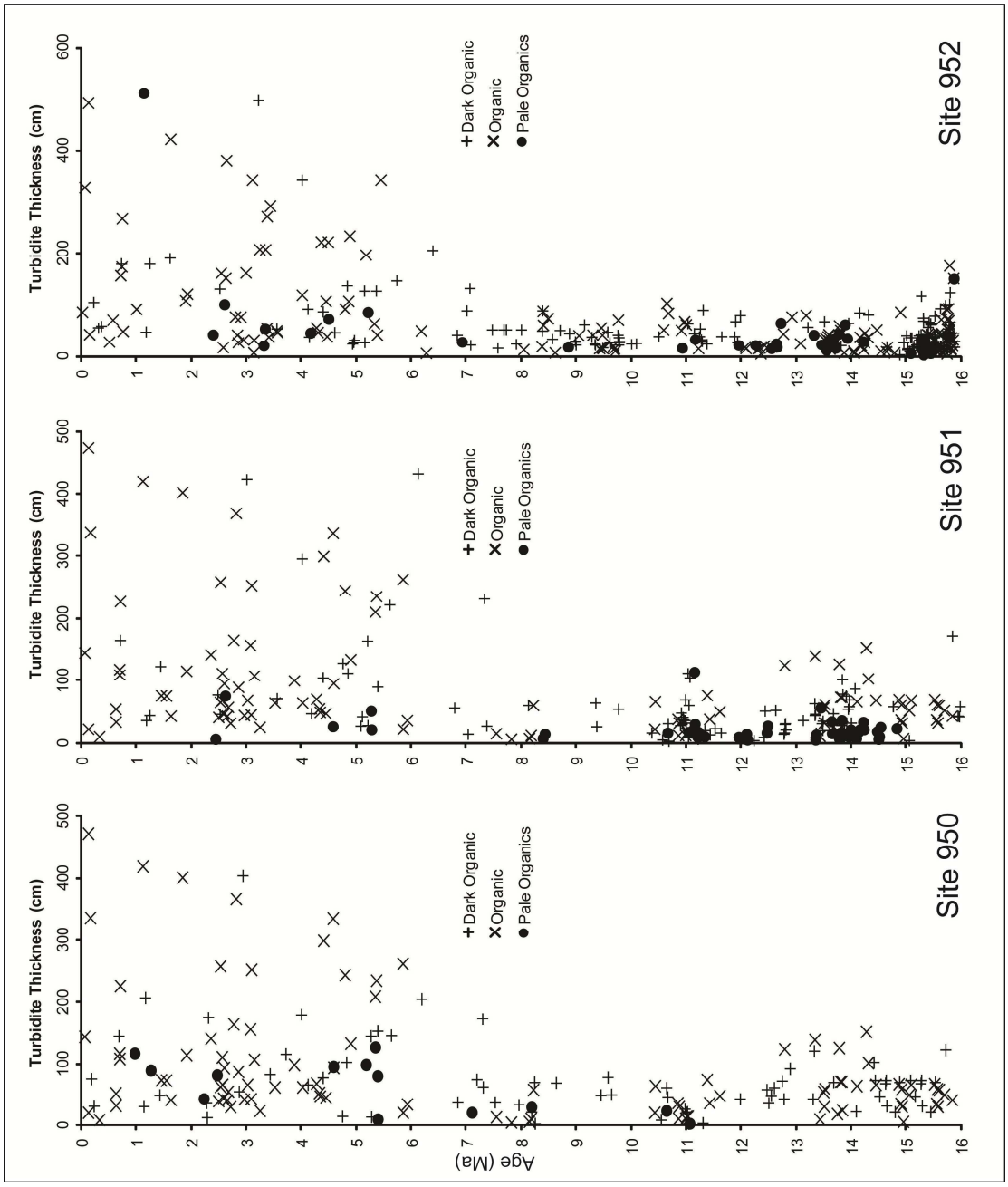

Figure 8.13 Temporal records of siliciclastic turbidite thickness at sites 950, 951 and 95.

Mudcap Geochemistry

Pearce and Jarvis (1995) stated that Late Quaternary siliciclastic turbidites, within the Madeira Abyssal Plain, from a northern (olive green) and southern (dark green) provenance can be distinguished geochemically. The initial discrimination of dark, intermediate (olive), and pale green turbidites is investigated geochemically within the ODP record. Previously, Jarvis *et al.* (1998) had analysed multiple (2 to 5) samples for

the turbidite mudcaps recovered from Site 950. In the present study, samples pertaining to a single turbidite were averaged to give a bulk composition. The carbonate-free compositions were plotted on a series of variation cross plots to investigate whether the colour of the turbidite could be indicative of a variation in provenance.

The variation plots indicate that indeed the carbonate-free major element compositions delineate a number of compositional fields highlighted in the turbidite colour (pale, intermediate and dark green) (Figure 8.14). Firstly there is a difference in regard to the carbonate content. The dark green siliciclastic turbidites have compositions of 2 to 55 wt%, with a dominance of turbidites with less than 40 wt% $CaCO_3$ (Figure 8.14A). The predominance of the dark green siliciclastic turbidites have >80-100 ppm Zr, between 2.0-3.0 wt% K_2O, and <3.8 wt% MgO (Figures 8.14A and 8.14C). This is in contrast to the intermediate green siliciclastic turbidites, which have $CaCO_3$ compositions within 38-78 wt%, which a small cluster with carbonate compositions of 20-30 wt% (Figure 8.14A). The intermediate green siliciclastic turbidites differ further from dark green siliciclastic turbidites with predominantly <90-110 ppm Zr, >3.2 wt% MgO, and >3.0 wt% K_2O (Figures 8.14A and 8.14C). The Al_2O_3-TiO_2 cross plot shows that the dark green siliciclastic turbidites define a tightly constrained mixing line, while the intermediate green siliciclastic turbidites define a small cluster of roughly 15-20 wt% Al_2O_3 and 0.8-1.2 wt% TiO_2. The pale green siliciclastic turbidites demonstrate an affinity with the intermediate green siliciclastic turbidites. Certainly major element geochemistry supports two provenance regions diagnosed by turbidite mudcap compositions of K_2O, MgO, Zr and $CaCO_3$ (Figure 8.14), these two potential provenances are manifested in the colour of the siliciclastic mudcaps.

There are also temporal changes in the geochemistry of the siliciclastic turbidites, as discussed by Jarvis *et al.* (1998), where the major elements are normalised to Al. The siliciclastic turbidites initially have low $CaCO_3$, high Si/Al, low-to-medium K/Al, low Zr/Al, and low-to-medium Mg/Al (Jarvis *et al.,* 1998). During the Late Miocene there is a transition in the composition, with turbidites deposited of increasing $CaCO_3$, medium-to-high K/Al, Mg/Al and Zr/Al, and lower Si/Al (Jarvis *et al.,* 1998). Indeed, from ~7.4 Ma onwards the turbidites are characterised by higher $CaCO_3$ and medium-to-high K/Al and Zr/Al (Jarvis *et al.,* 1998).

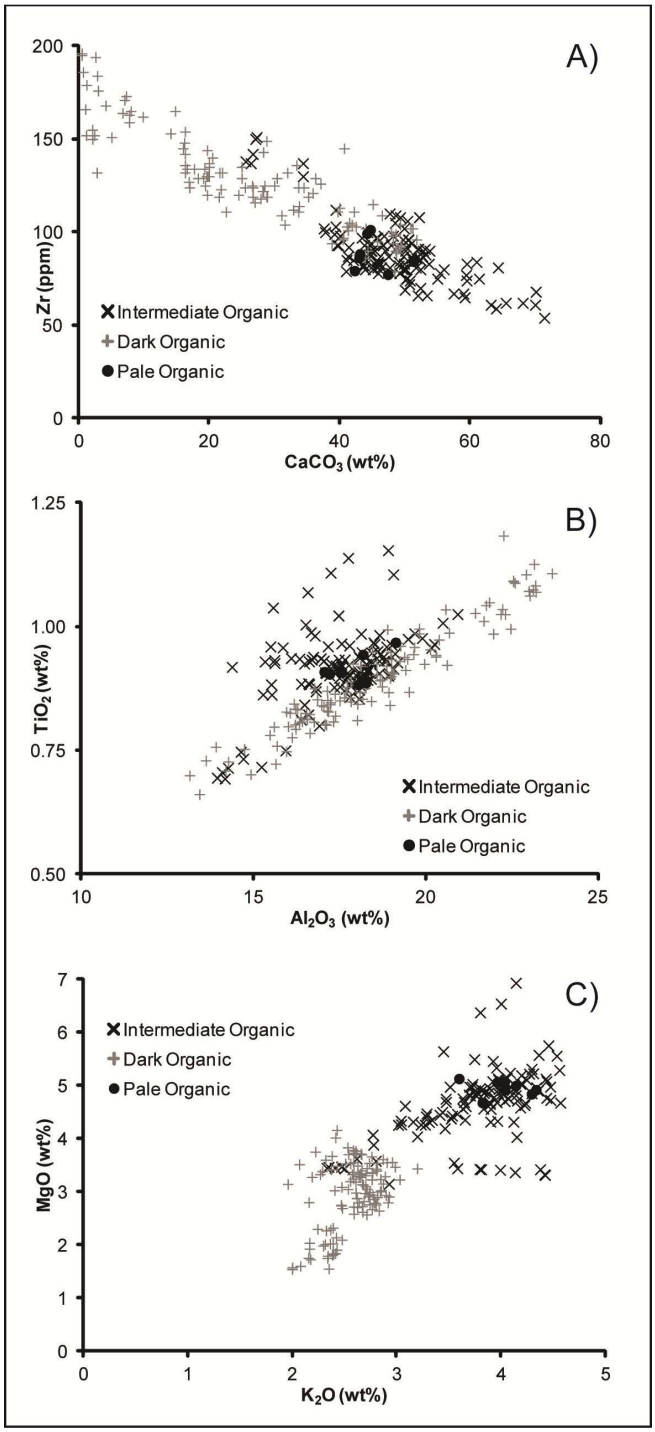

Figure 8.14 Variation plots of the mudcap geochemical composition for the dark green, intermediate green and pale green siliciclastics. A) Zr vs $CaCO_3$, B) TiO2 vs Al2O3, and C) MgO vs Al2O3. Element concentrations re recalculated on a carbonate-free basis, utilising geochemical results of Jarvis *et al*. (1998).

Turbidite Statistics

Statistical analysis of the siliciclastic turbidite thickness and the time interval prior to the turbidite can give an indication of the controlling factors on both turbidite occurrence and magnitude. Given invariant sedimentation rates on the continental shelf

and a potential control of earthquake magnitude on turbidite magnitude, a possible relationship exists between the time interval prior to turbidite occurrence and the turbidite magnitude (thickness and/or volume). Turbidite thickness-frequency plots have been used to investigate the influences on turbidite occurrence and magnitude (Beattie and Dade, 1996; Drummond, 1999). Log-log plots of cumulative exceedence probability of turbidite thickness against thickness of the respective bed demonstrate an exponential trend (Figure 8.15). This trend is also present when considering the separate dark green, intermediate (olive) green and pale green siliciclastic types (Figure 8.15).

Furthermore, log-log plots of the cumulative exceedence probability of the time interval against time interval prior to the respective turbidite demonstrate an exponential distribution (Figure 8.16). Again, this trend is consistent when factoring in the complete sequence of organic-rich siliciclastic turbidites, and when also investigating the separate sequences of the different types. This exponential trend is again supported by the traditionally binned data (Figure 8.16). In similar fashion to the thickness-frequency relationship of the turbidites, the time intervals prior to the occurrence of respective turbidites also follow a poissonian trend.

Subunits within Siliciclastic Turbidites in the Madeira Abyssal Plain

The three largest organic-rich siliciclastic turbidites (Md, Me and Mf) in this Late Quaternary record demonstrate basal coarse-fractions comprising two broadly upwards-fining sequences, known as subunits (Figure 8.17). These are confirmed in the p-wave profiles (Figure 8.17). These basal upwards-fining fractions consist of alternating sets of ripple-laminated sands and parallel-laminated silts (Figure 8.17). Subunits have been previously defined as repeated upwards-fining sequences with repeated sequences of parallel-laminated sands, ripple-laminated sands and laminated silts, which are commonly capped by a mud (Hunt *et al*., 2011). However, the proximal Icod event bed, in the Agadir Basin, and alternate volcaniclastic turbidites in the Madeira Abyssal Plain show that these subunits can be amalgamated (Hunt *et al.,* 2011, Chapter 7). The subunits reported in the siliciclastic turbidites of the Madeira Abyssal Plain in the present study are both discrete and amalgamated (Figure 8.17), depending on proximity to the site of entry to the basin.

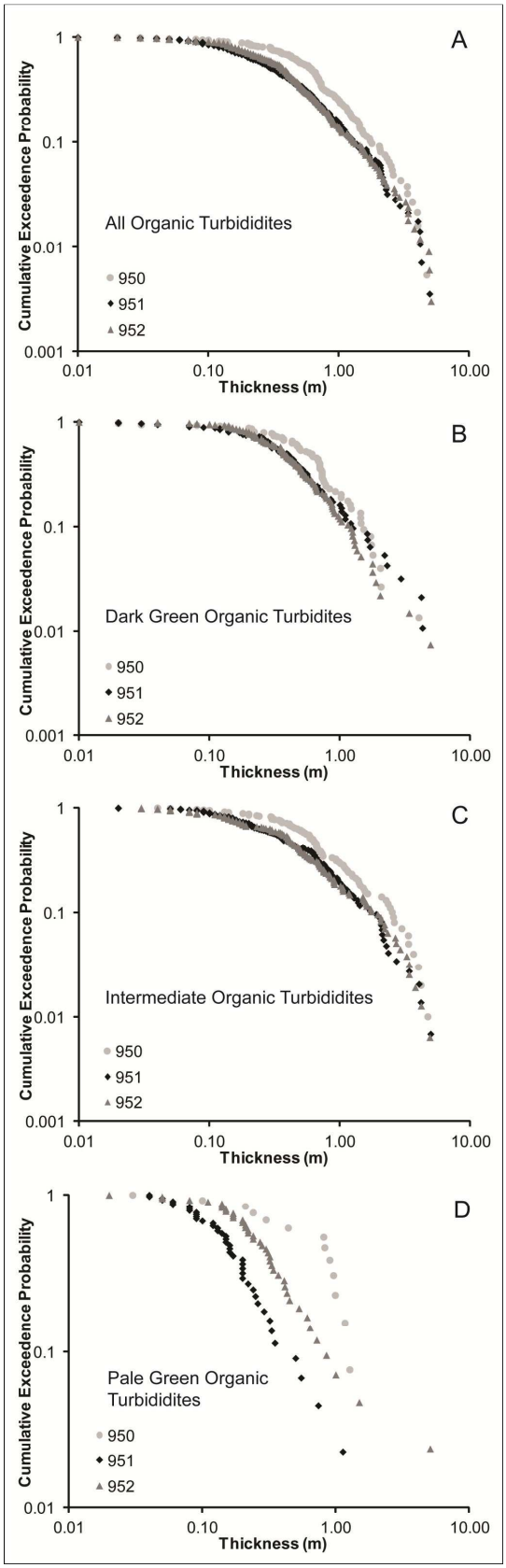

Figure 8.15 Log-Log plots of Thickness-frequency, with thickness plotted against the exceedence probability of that thickness. A) complete siliciclastic record, B) dark green siliciclastics, C) intermediate green siliciclastics, and D) pale green siliciclastics.

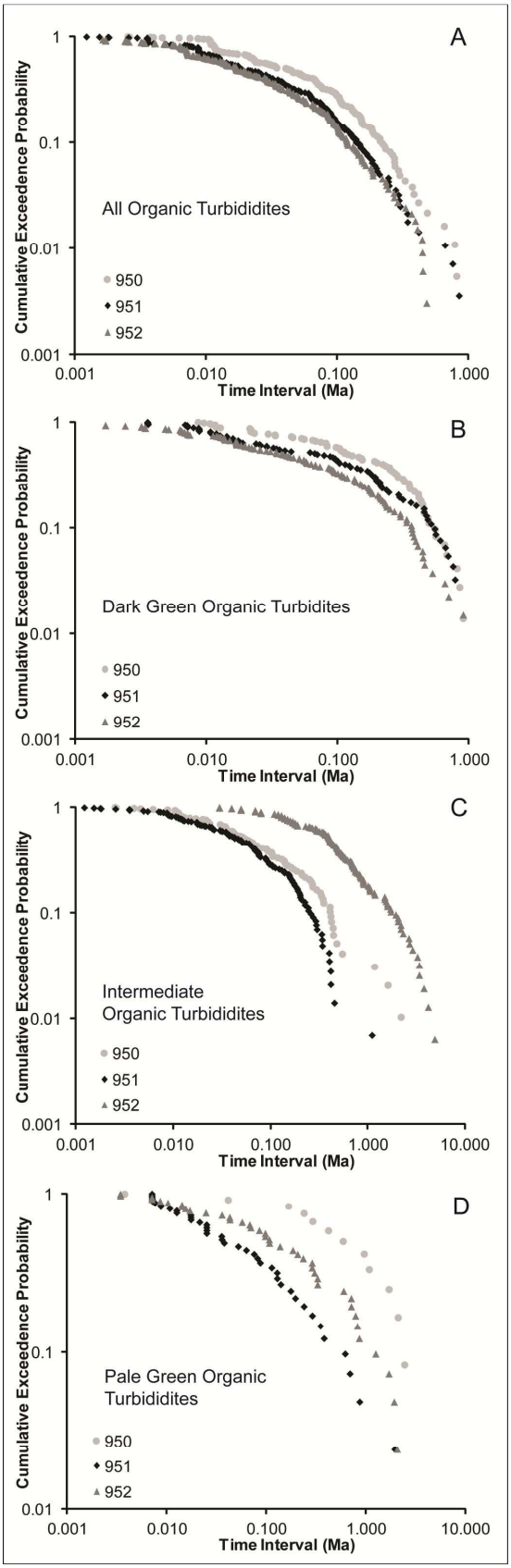

Figure 8.16 Log-Log plots of Recurrence Intrval-frequency, with recurrence interval plotted against the exceedence probability of that recurrence interval. A) complete siliciclastic record, B) dark green siliciclastics, C) intermediate green siliciclastics, and D) pale green siliciclastics.

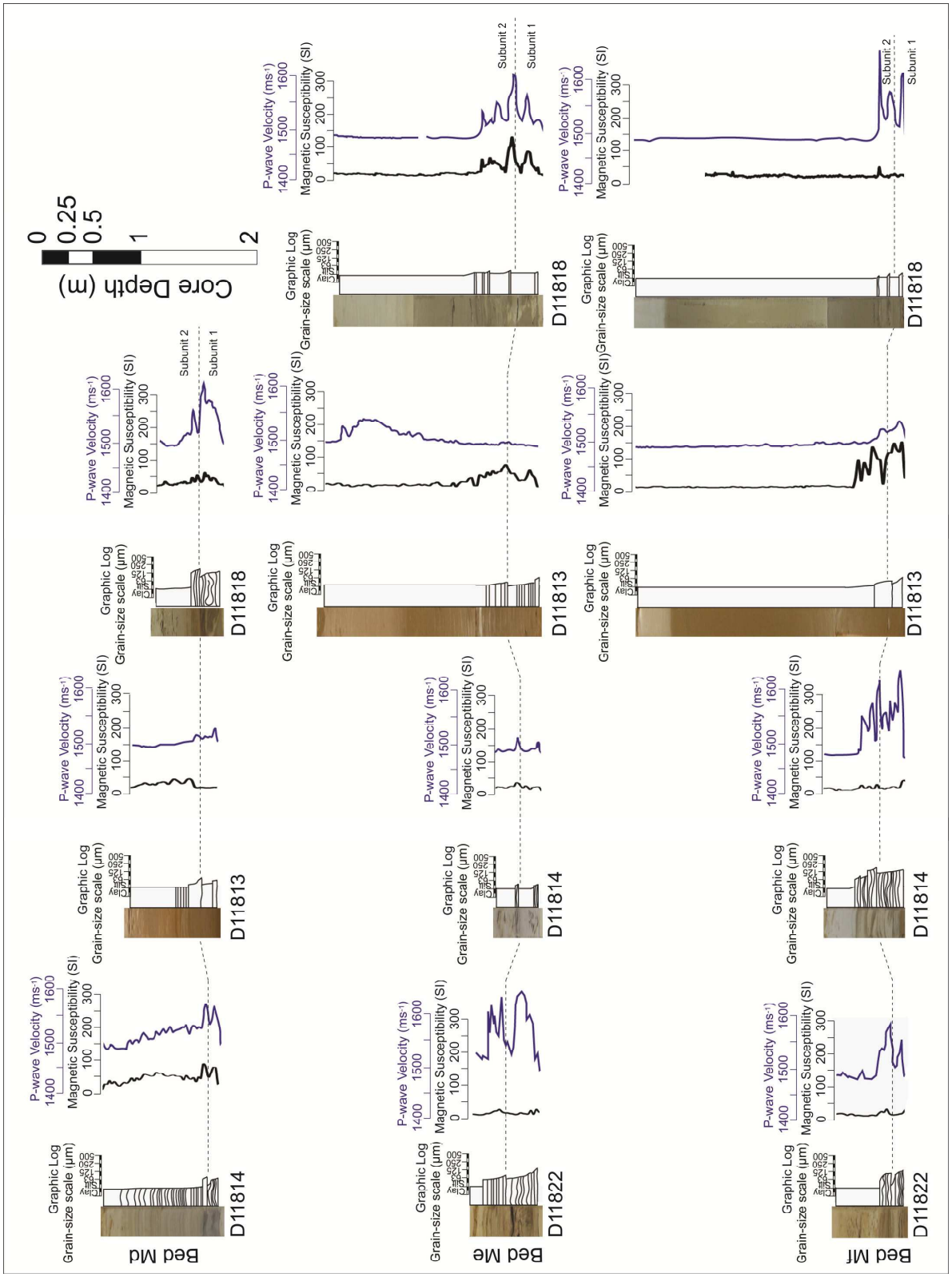

Figure 8.17 Examples of siliciclastic turbidites Md, Me and Mf, showing the presence of two subunits in each, and the response of these in the p-wave velocity and magnetic susceptibility logs.

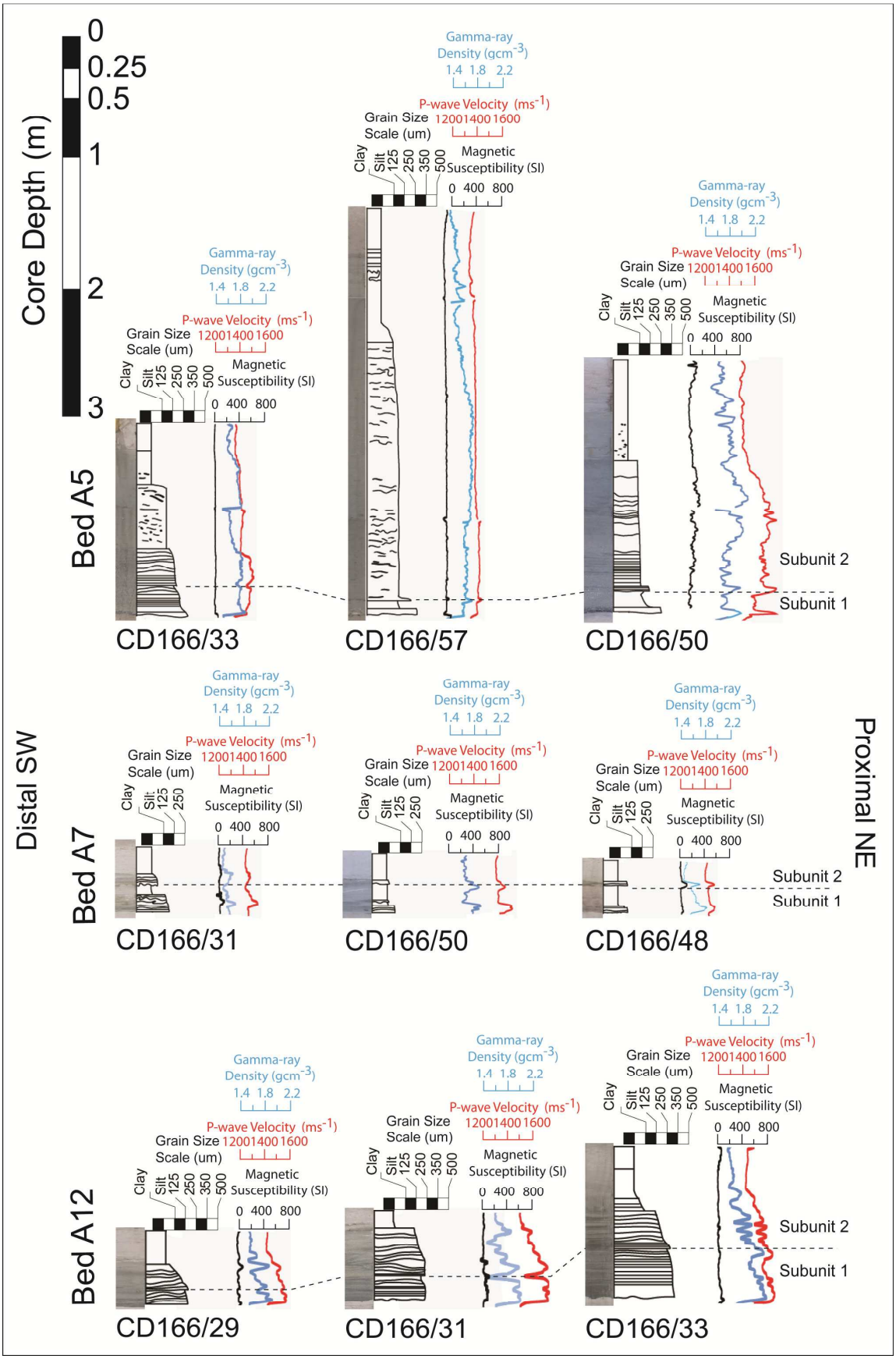

Figure 8.18 Exmaples of the main siliciclastic turbidites A5 (Md equivalent), A7 (Me equivalent) and A12 (Mf equivalent), showing the presence of two subunits in each and verification of this in the down-core petrophysical data.

Subunits within the Siliciclastic Turbidites in the Agadir Basin

An issue with identifying the origin of subunits in the Madeira Abyssal Plain is the implied influence of the Madeira Distributary Channels (Hunt *et al.*, 2011). Previously, Wynn and Masson (2003) and Hunt *et al*. (2011) state that prior to entering the Madeira Abyssal Plain from the Agadir Basin, the siliciclastic turbidites comprise only one fining-upward sequence. This premise is interrogated in the present study, with an investigation into the presence of subunits within siliciclastic turbidites in the more proximal Agadir Basin.

The Agadir Basin stratigraphy has been well established (Wynn *et al.,* 2002a; Frenz *et al.,* 2009; Chapter 3). On detailed inspection the large-volume turbidites A5 (MAP bed Md), A7 (MAP bed Me), and A12 (MAP bed Mf) have basal turbidite sands that commonly comprise a double upwards-fining sequence (Figure 8.18). These upwards-fining sands are commonly amalgamated in beds A5 and A12, although separated by a laminated silt and turbidite mud in bed A7 (Figure 8.18). Within bed A5 there is initially two coarse-grained gravels at the base separated by a finer muddy-silt (Figure 8.18). Beyond the examples in CD166/50 and CD166/57 the subunits are distinguished by the presence of two fining-upwards sequences within the sand fraction, with a repeated succession of basal parallel-laminated sands (Figure 8.18). This is confirmed in the repeated fining-upwards trends in the p-wave velocity and gamma-ray density profiles in the base of the bed A5.

Bed A7 has a more obvious repeated upwards-fining pattern, with two thin-bedded turbidite sands separated by a turbidite mud (Figure 8.18). Bed A12 shows two repeated sequences of parallel-laminated and ripple-laminated sands, in addition to the two general upwards-fining trends (Figure 8.18). Again this is confirmed in the p-wave velocity and gamma-ray density profiles within the sands (Figure 8.18).

8.5.3 Remaining Work and Discussions

This study demonstrates the importance of turbidite records in providing insight into the recurrence, magnitude, preconditioning/trigger factors, and failure mechanisms. Thus far this work has shown that the turbidite colour of the siliciclastic turbidites is representative of provenance, and shown in bulk geochemistry. Pearce and Jarvis (1995) identified that northern and southern provenances to turbidites within the Madeira Abyssal Plain are reflected in the mudcap geochemistry. Data presented in this study support this notion.

Thus far, statistical investigations into siliciclastic turbidite recurrence and magnitude (bed thickness) have shown Poisson frequency distributions. These distributions have been linked to earthquake-triggers (Beattie and Dade, 1996; Drummond, 1999). However, Talling *et al*. (2002) and Sylvester (2004) present issues in reporting log-log and log-normal frequency distributions of turbidite bed thickness. Thus further statistical tests will be required to verify these initial results and interpretations.

Furthermore, the role of sediment flux to the slope as a potential preconditioning factor will be further investigated using data from DSDP holes on the continental slope. Thus far these data have not been evaluated in regards to the coincidence of large-volume siliciclastic turbidites with periods of increased sediment flux to the shelf. Previously, periods of sea level change associated with climatic changes between glacial and interglacial conditions have been proposed for the occurrence of continental margin and volcanic island landslides (Weaver and Kuijpers, 1983; Weaver, 2003; McMurtry *et al.,* 2004; Chapters 3 and 6). Utilising high resolution sea level records (e.g. Miller *et al.*, 2005), the role of climate change as a preconditioning factor for submarine landslide occurrence can be evaluated.

Chapter 9

Discussions

9.1 Turbidite Correlations and Basin Stratigraphy

The Moroccan Turbidite System comprises multiple depocentres, including Agadir Basin, Madeira Abyssal Plain and Seine Abyssal Plain (Wynn *et al.,* 2000a, 2002a). Turbidites have been correlated across all three of these depocentres (Wynn *et al.,* 2002a). Earlier studies showed the capability to correlate turbidites across the Madeira Abyssal Plain using coccolithophore biostratigraphy and turbidite chemostratigraphy (Weaver and Kuijpers, 1983; de Lange *et al.,* 1987; Pearce and Jarvis, 1995). The present study utilises a number of different methodologies for supporting turbidite correlations through both Agadir Basin and the Madeira Abyssal Plain. Chapter 3 demonstrates a use of hemipelagite CaO content to correlate turbidites, whereby lows in CaO (<25 wt%) correspond to glacial clays and highs in CaO (>35 wt%) correspond to interglacial clays. The down-core Fe_2O_3 composition of the hemipelagite was used in addition to CaO in Chapter 4, where it is found to anti-correlate with CaO. Correlation of down-core hemipelagite CaO composition (anti-correlation of Fe_2O_3) with the Lisiecki and Raymo (2005) global benthic foraminifera $\delta^{18}O$ curve has enabled dating of turbidites that intersect the record (Chapters 3 and 4).

The ITRAX CaO record correlates to carbonate variability within the hemipelagite (Figure 3.2), supporting notions that the Ca content of the hemipelagite is predominantly within $CaCO_3$. Indeed, Moreno *et al.* (2002) demonstrate strong correlations between carbonate content (wt%) and Ca (counts), and that these records resemble traditional $\delta^{18}O$ profiles. Hemipelagite carbonate content varies according to interglacial-glacial conditions, and the position of the CCD according to the relative mixing of the NABW and ABBW water bodies (Berger, 1970; Crowley, 1983; Jarvis and Higgs, 1987; Weaver and Rothwell, 1987). The ITRAX methodology, with a measurement resolution of 200-500 μm, enables acquisition of high resolution down-core profiles of glacial-interglacial cyclicity, even given the slow hemipelagite accumulation rates (0.5-1.8 cm/1000 years). However, these profiles still require datum horizons to produce robust temporal records, since even with high resolution $\delta^{18}O$ profiles it can be difficult to differentiate specific glacial and interglacials. Traditionally in the Moroccan Turbidite System coccolithophore biostratigraphy has provided these datum levels (Figure 3.2).

Another method for analysing compositional variation in the hemipelagite was spectrophotometry. This primarily utilised L* as a measure of reflectance, whereby white interglacial pelagic oozes would yield higher L* values (towards 100) than red glacial clays which yield lower values (towards 0). However, although reflectance values, such as L*, show affinities for carbonate content of the sediment, there are numerous other factors that influence the sediment reflectance, such as water content and clay mineral content (Balsam *et al.,* 1999, and references therein). The L* values for Madeira Abyssal Plain hemipelagite sediments demonstrated a usefulness in supporting turbidite correlations and provide an additional means of dating the events in Chapter 6. However, not all peaks and troughs within the L* profile could be correlated, and ultimately the profiles required previous biostratigraphy to provide datum horizons.

Dating of the turbidites from the Madeira Abyssal Plain ODP record, presented in Chapters 3, 6 and 8, is based on hemipelagite sedimentation rates derived from hemipelagite coccolithophore biostratigraphy and magnetostratigraphy presented by Howe and Sblendorio-Levy (1998). Coccolithophore biostratigraphy has been shown to produce robust turbidite correlations based on relative ratios of species, including *Emiliania huxleyi*, *Gephyrocapsa muellerae*, *Gephyrocapsa aperta*, *Gephyrocapsa caribbeanica* and *Pseudoemiliania lacunosa* (Weaver and Kuijpers, 1983; Hine and Weaver, 1998). Acme zones based on the relative abundance of these aforementioned species enable datum horizons to be identified. Furthermore, first observation (FO) and last observation (LO) of the aforementioned and alternative species also provide specific datum levels. These include *Discoaster brouweri* (LO at 1.99 Ma), *Gephyrocapsa caribbeanica* (FO at ~1.763 Ma), *Gephyrocapsa oceanica* (FO at ~1.706 Ma), *Calcidicus macintyrei* (LO at 1.54 Ma), *Helicosphaera selli* (LO at 1.219-1.4 Ma), *Pseudo lacunosa* (LO at 0.506 Ma), *Reticulofenestra asanoi* (FO at 1.06 Ma and LO at 0.83-0.853 Ma), *Gephyrocapsa parallela* (FO at 0.987 Ma and LO at 0.48 Ma), *Helicosphaera inversa* (FO at 0.48 Ma and LO at 0.14-0.15 Ma), *Gephyrocapsa ericsonii* (FO at and LO at), and finally *Emiliania huxleyi* (FO at 0.265-0.294 Ma) (Hine and Weaver, 1998, and references therein; Sato *et al.,* 2009). This biozonation provides relatively robust dates, however the methodologies require subjective counting, which is dependent on the resolution of the microscope, expertise of the biostratigrapher and quality of the smear slide or SEM mount produced.

Chapter 3 also uses down-core p-wave velocity, gamma-ray density and magnetic susceptibility profiles to support the correlation of turbidites. Elevated values of p-wave

velocity and gamma-ray density correspond to coarse-grained turbidite bases, while highs in magnetic susceptibility correspond to the bases of volcaniclastic turbidites. Magnetic susceptibility is used in the ODP record to verify the presence of volcaniclastic turbidites, such as in Chapter 6. Indeed, magnetic susceptibility has been previously used to support the correlation of turbidites across the Moroccan Turbidite System (Wynn *et al.,* 2002a).

Multidisciplinary methodologies have enabled robust correlation of these turbidites over distances of >1,000 km through the Moroccan turbidite System (Chapters 2 and 6). The correlations have enabled studies of the depositional processes of these turbidity currents. One such example is that of the bed A5 in Agadir Basin, which has allowed study of linked debrite development (Talling *et al.,* 2007). Another example would be bed A14 (Icod landslide) in Agadir Basin, which is discussed in Chapters 5 and 7. Identifiying this bed at numerous sites in Agadir Basin has allowed investigations into the subunits that are contained within it. From these investigations, bed A14 (Icod landslide) has been shown to originate from a multistage landslide (Hunt *et al.,* 2011, Chapter 5). Single bed correlations have also enabled study of the bed A2 (El Golfo landslide) multistage turbidite in Agadir Basin (Chapter 7). Furthermore, single bed correlations have enabled investigations into the presence of subunits within additional volcaniclastic and siliciclastic turbidites in the Madeira Abyssal Plain and Agadir Basin (Chapters 7 and 9).

Robust correlations of single beds throughout the Moroccan Turbidite System have also enabled accurate calculations of deposit volumes. This has been achieved by producing high resolution isopach maps of the relevant beds within Agadir Basin and Madeira Abyssal Plain. Although the debris avalanche deposits from volcanic island flank collapses are voluminous (50-500 km^3 in Canary Islands), the turbidite deposits contain equal or more volume (10-380 km^3). An example would be the Icod landslide from northern Tenerife, which produced a debris avalanche of 110±40 km^3 and a turbidite of 210±20 km^3 (Hunt *et al.,* 2011, Chapter 5). Without an appreciation of the turbidite volume, the true magnitude of the landslide is grossly underestimated.

9.2 Occurrence and Magnitude of Siliciclastic Turbidites sourced from the Northwest African Continental Slope

There are misconceptions that turbidite and landslide activity is restricted to periods of lowstands and falling sea level conditions (Vail *et al.,* 1977; Mitchum *et al.,* 1977a, b; Vail and Todd, 1981; Mitchum, 1985; Vail, 1987; Shanmugam and Moiola, 1982; Kolla and Macurda, 1988; Posamentier and Vail, 1988; Posamentier *et al.,* 1988; Kolla, 1993; Kolla and Perlmutter, 1993). The turbidite record recovered from Agadir Basin demonstrates that this is not the case (Chapter 3). There is a prevalence of siliciclastic turbidites during sea level highstands and the transition from lowstand conditions. Furthermore, there is greater frequency and volume of turbidites associated with higher frequency sea level changes (Chapter 3). Climate influenced productivity and sediment flux to the continental shelf are found to have an influence on occurrence and volume of shelf-derived siliciclastic turbidites. While volcanic activity presents a major influence on the occurrence and magnitude of large-volume volcaniclastic turbidites (Chapter 3 and 6).

Preliminary results from Chapter 8.5 indicate that 50-300 km^3 landslides occurred from 6.2 Ma to recent, having been of lower magnitude prior to this (17 to 7 Ma). These continental slope landslides are commonly in excess of 100 km^3, thus potentially pose a significant risk in regards to landslide-generated tsunamis. Chapter 8.5 also indicates that these large-volume events are primarily triggered by earthquakes, due to the Poisson-distribution in regards to recurrence intervals and magnitudes. In regards to preconditioning factors, both biogenic and terrigenous fluxes to the shelf appear to be amongst the main influences on turbidite occurrence and magnitude, supporting findings from the Late Quaternary record in Chapter 3. However, given the resolution of the sediment dynamics on the shelf and dating error of the turbidites from the ODP record, preconditioning factors cannot be accurately resolved (Chapter 8.5).

9.3 Occurrence and Magnitude of Volcaniclastic Turbidites Sourced from the Canary Islands

There are considerable difficulties in gaining accurate landslide characteristics from past landslides. Proximal areas often suffer from overprinting of events and erosion, which precludes accurate dating of the landslides. Volcanism around the headwall scarp and subsequent fill are often not synchronous with the landslide, preventing accurate dating of the event. Turbidity currents are generated from submarine landslides and are

deposited in adjacent deepwater basins. Since these distal turbidites are often non-erosive and intermittent, the hemipelagite sediment between the turbidites can be used to date the landslides accurately (Weaver and Thomson, 1993; Weaver, 1994; Weaver, 2003). Previously, biostratigraphy has been used to date the events in the turbidite stratigraphy (Weaver and Kuijpers, 1983; Wynn *et al.,* 2002a). Chapters 3 and 6 have alluded to additional methodologies that can be used, including hemipelagite CaO and spectrophotometric profiles.

The Late Quaternary volcaniclastic turbidite record in the Madeira Abyssal Plain and Agadir Basin have identified the El Golfo, El Julán and Tiñor landslides from El Hierro, the Cumbre Nueva landslide from La Palma, and Icod, La Orotava, Güímar and Roques de García landslides from Tenerife (Chapter 6). The ODP volcaniclastic turbidite record represents a near-complete history of volcanic island flank collapses from the Canary Islands in the last 17 Ma (Chapter 6). These events can be correlated to periods of major protracted and voluminous volcanism on the respective islands (Chapter 6). This may imply that loading of the volcanic edifices represents a key preconditioning factor for volcanic island landslides.

Warm and wet climate conditions associated with deglaciations have been associated with prodigious landslides in the Hawaiian archipelago (McMurtry *et al.,* 2004). However, deriving K-Ar dates for these events is problematic, due to the low-K lavas from these islands. The ages of the volcaniclastic turbidites derived from the Canary Islands are calculated from hemipelagite sedimentation rates derived from biostratigraphy (Howe and Sblendorio-Levy, 1998). These are certainly less erroneous than the K-Ar dates from the Hawaiian archipelago. Chapter 6 determines that there is a preferential occurrence of Canary Island landslides during deglaciations and subsequent interglacial periods, which supports the interpretations of McMurtry *et al.* (2004) for Hawaiian Island landslides.

The volumes of the Madeira Abyssal Plain volcaniclastic turbidites alone are 50-350 km^3. Debris avalanche deposits from the Western Canary Islands have been found to be 50-200 km^3, with speculatively larger, older deposits of up to 500 km^3. Therefore these combined turbidite and debris avalanche volumes represent landslides comparable in size to those reported from the Hawaiian archipelago (Moore *et al.,* 1989, 1994). The debris avalanche deposits from the Western Canary Islands are certainly comparable to those from the Cape Verde Islands of Fogo, Santo Antao and Sao Vincente (50-160 km^3) (Masson *et al.,* 2008).

An important finding of this thesis is the recognition of turbidites sourced from submarine failures of the volcanic flanks during island emergence and later magmatic ascension (Chapter 8.4). These 'pale grey non-volcanic' turbidites are voluminous and represent potentially significant hazards. However, these beds provide a novel insight into the geodynamics of emerging volcanic islands. They occur prior to dates associated with emergence of the individual Western Canary Islands and prior to periods of protracted volcanism and mass wasting. Magmatic ascension would cause doming of the seafloor, which may destabilise and fail, resulting in these pale grey non-volcanic turbidites.

9.4 Derivation of Landslide Mechanisms from the Turbidite Record and Effects on Tsunamigenesis

Turbidites have been highlighted in the previous sections as posing excellent records of Canary Island landslides in the Madeira Abyssal Plain and Agadir Basin. Previous chapters (Chapters 3, 4 and 6) have presented records of volcaniclastics within the turbidite stratigraphy of both these aforementioned depocentres. In addition to age, further important landslide characteristics can be derived from these turbidite records.

Volcanic island landslides have been shown to produce potentially catastrophic tsunamis (Latter, 1981; Keating and McGuire, 2000; Ward and Day, 2001, 2003; Tappin *et al.,* 2001; Synolakis *et al*., 2002; Whelan and Kelletat, 2003; McGuire, 2006; Gisler *et al.,* 2010). Landslide volume has been highlighted as being the main contributing factor in landslide-generated tsunamigenesis (Murty, 2003). The excellent core coverage afforded to the Late Quaternary record has allowed accurate volumes to be calculated (Wynn *et al.,* 2002a; Frenz *et al*., 2009; Hunt *et al*., 2011 (Chapter 5)). Utilising volumes of seismic units have enabled volumes of the older events to be calculated from decompacted thicknesses from ODP core in the Madeira Abyssal Plain (Alibes *et al.,* 1999; Weaver, 2003; Chapter 6). The volumes of these volcanic island flank collapses are on an order of 10 to 350 km^3 (Chapter 6). Previous studies have highlighted the potentially devastating tsunamis that could be generated from such landslides, assuming single slab failure; for example the hypothetical Cumbre Vieja landslide-generated tsunamis from La Palma (Ward and Day, 2001; Mader, 2001; Gisler *et al.,* 2006), the 1888 Ritter Island lateral collapse (Ward and Day, 2003), the 1988 landslide-induced tsunami on Vulcano Island (Tinti *et al.,* 1999), and the theorised collapse from Stromboli (Tinti *et al.,* 2000).

Wynn and Masson (2003) theorised that turbidite textures could provide information regarding the failure mechanism of volcanic island landslides. Indeed, the presence of repeated fining-upwards sequences of turbidite sands and muds (known as subunits) have been previously linked to multistage collapses (Garcia, 1996; Wynn and Masson, 2003; Di Roberto *et al*. 2010). Hunt *et al.* (2011 (Chapter 5)) tested the theory of Wynn and Masson (2003) on the Icod event bed. The Icod event bed was found to comprise seven regular subunits. Using a combination of basal grain-size data, mineralogy and volcanic glass geochemistry, the subunits have been shown to originate from a multistage and retrogressive landslide from the northern flank of Tenerife (Hunt *et al.,* 2011 (Chapter 5)), identified as the Icod landslide.

The Icod landslide only represents a single case study of a multistage landslide. The last eight landslides from the Western Canary Islands have been identified from the turbidite records in the Madeira Abyssal Plain and Agadir Basin (Chapter 6). These have been identified as representing the El Golfo, El Julán and Tiñor landslides from El Hierro, the Cumbre Nueva landslide from La Palma, and Icod, La Orotava, Güímar and Roques de García landslides from Tenerife (Chapter 6). These turbidites have also been found to comprise a series of subunits, which have been also been found to represent multistage landslides (Hunt, Chapter 7). This implies that the last eight catastrophic landslides in the Canary Islands have been multistage, and certainly shows that multistage landslides are more ubiquitous.

Multistage landslides will reduce the volumes involved in tsunamigenesis. This has been shown in modelling of the Güímar landslide (Giachetti *et al.,* 2011). However, considering the total volumes involved in these landslides, the subunit events will still involve a minimum of 10-30 km^3. Thus these individual subunit failures still pose significant geohazards and will potentially produce tsunamis capable of much destruction to the Canary Islands and adjacent continental margin.

Siliciclastic turbidites recovered from the Madeira Abyssal Plain demonstrate volumes of 20 to 300 km^3, which occur with recurrences of 20 to 100 ka. Results show that there are two regular subunits found within the large-volume Late Quaternary siliciclastic turbidites (Chapter 8.5). This would imply that these submarine landslides from the continental slope on the Moroccan margin may also be multistage, reducing the tsunamigenic potential.

In summary, studies of turbidity currents generated by submarine landslides can provide key information on landslide characteristics. These include accurate event ages

and better estimations of volume (Chapters 3, 6, 8.4 and 8.5). However, with additional data from onshore records of volcanism or offshore records of sediment flux, preconditioning factors for submarine landslides can be investigated (Chapters 3, 6, 8.4 and 8.5). The most important finding of this study has been that submarine landslides commonly occur as multistage and retrogressive failures, and that there is often a significant submarine component (Chapters 5, 7 and 8.5). This has major implications for tsunami modelling and resultant hazard mitigation for the Canary Islands and the entire North Atlantic seaboard.

Chapter 10
Conclusions and Future Work

10.1 Conclusions

This thesis concludes that turbidite records from deepwater depocentres adjacent to continental margins and volcanic islands can represent excellent records of submarine landslides. The turbidite records can present important information regarding landslide characteristics, such as age, recurrence interval, provenance, volume, failure mechanism and even depth of failure. Resolving accurate boundary conditions such as volume, depth of failure and runout are important for landslide and tsunami modelling. Inventories of this data can better inform geohazard mitigation for submarine landslides and tsunamis for a given ocean seaboard.

The key findings of this thesis are summarised as follows:

1. Turbidite records pose excellent and near-complete records of submarine landslides from neighbouring continental margins and volcanic islands. However, piston core records throughout the turbidity current pathway are vital in determining the complete turbidite record of events varying from 1 to 100 km^3. Targeting the distal depocentres will provide biased records of only the largest-volume turbidity currents capable of long-runouts. In contrast, targeting only the proximal regions elicits problems of erosion and flow bypass that may obscure dating or present incomplete records. However, these turbidite records must be perceived as being minimum records of occurrence, since not all landslides will potentially generate a turbidity current.
2. Although turbidite sand mineralogy can aid identification of provenance, there are problems with grain-size control and hydrodynamic sorting. Mudcap geochemistry enables identification of turbidite provenance, and better enables comparison between turbidites.
3. Analysis of turbidite mudcap geochemistry from multiple sites along the flow pathway can indicate whether flows have been erosive.
4. Late Quaternary records of siliciclastic turbidites of continental slope provenance in the Moroccan Turbidite System are generated from landslides. These landslides predominantly occur at deglaciations, at the transitions between glacial and interglacials. Often large-volume continental slope landslides occur during rapid, high-frequency shifts in sea level and climate. The trigger

mechanism for these events is probably earthquakes, owing to the random Poisson-distribution of recurrence intervals and magnitude through the turbidite record.

5. Large-volume volcaniclastic turbidites in the Moroccan Turbidite System present a near-complete record of volcanic island landslides from the Western Canary Islands. Indeed, the last eight >50 km^3 landslides from Tenerife, La Palma and El Hierro in the last 1.5 Ma are represented as turbidites in the Madeira Abyssal Plain and Agadir Basin. Furthermore, the 17 Ma ODP record in the Madeira Abyssal Plain shows that volcaniclastic turbidites have recorded the major landslides from the Western Canary Islands, including La Gomera and Gran Canaria. The timing and magnitude of these events appear to be coincidental with periods of protracted onshore volcanism. Thus loading of the edifices by volcanism is a key preconditioning factor for volcanic island landslides. Furthermore, there is evidence to suggest that warmer and wetter climate conditions associated with deglaciations and interglacial periods may act to precondition volcanic island failures.
6. Large-volume pale-grey non-volcanic beds have been identified in the Madeira Abyssal Plain ODP record. These beds have relatively high carbonate contents and low magnetic susceptibility. However, their grey colour and geochemical composition does associate them with a volcanic origin, albeit not directly from subaerial island flanks. This thesis supports earlier notions that these deposits represent failures of predominantly calcareous surficial sediment from the submarine flanks. These failures are proposed to occur as the result of doming and over-steepening of the sea floor in response to island emergence or magma ascent.
7. Multiple-fining upwards sequences, known as subunits, within turbidites are postulated as representing multistage landslides. An exhaustive dataset has shown that the subunits within the Icod event bed in Agadir Basin indicate that the landslide was indeed multistage. This included core logs, down-core petrophysics, grain-size data, mineralogy, carbonate content, bulk sand geochemistry, and volcanic glass geochemistry. These data were able to also rule out flow reflection and multiple synchronous sources, and channels are absent between Tenerife and Agadir Basin. Thus subunits, in this case study, represent a multistage collapse.

8. The compositions of subunits in the El Golfo event bed in Agadir Basin indicate that it too represents a multistage landslide. Furthermore, the composition of subunits from the El Golfo and Icod events beds in Agadir Basin and distal Madeira Abyssal Plain have similar compositions. Therefore, the subunits identified in Madeira Abyssal Plain deposits are not influenced by the channels feeding from Agadir Basin, as previously thought.
9. The volcanic island landslides during the last 1.5 Ma have been shown to be multistage and potentially retrogressive. Analysis of volcanic glasses from subunits from the volcaniclastic turbidites within the Madeira Abyssal Plain show that each event comprises a sequence of multiple and discrete failures. This demonstrates that multistage volcanic island landslides are more ubiquitous than previously recognised.
10. Double-coarse bases and the presence of two regular fining-upwards sequences are present in the large-volume siliciclastic beds in both Agadir Basin and Madeira Abyssal Plain. These potentially indicate that these Late Quaternary continental landslides were also multistage.

10.2 Suggestions for Future Work

The following represents proposals for future work regarding four key areas: volcanic island submarine landslides, landslide and turbidite occurrence in deepwater basins of the Northeast Atlantic, deepwater depositional processes, and the transport and burial of organic carbon in deepwater sediment gravity flows.

10.2.1 Volcanic Island Submarine Landslides

1. ODP Expedition 340 involved drilling of the submarine flanks of the Lesser Antilles, to study the prevalence of volcanism and submarine landslides. ODP core from the Madeira Abyssal Plain and the submarine flanks of Gran Canaria represent excellent records of volcanic island landslides from the Canary Islands. This thesis conducted work on the Madeira Abyssal Plain volcaniclastic turbidite record. However, there is little detail on the turbidite records from sites 953, 954, 955 and 956 from the flanks of Gran Canaria. These sites potentially record landslides from the Gran Canaria and Tenerife. Completing a study on volcanic island landslides from a passive margin setting (slow plate movement),

such as Gran Canaria, will provide an excellent comparison to the convergent margin setting of the Lesser Antilles.

10.2.2 Turbidites in deepwater basins of the Northeast Atlantic

1. The Seine Abyssal Plain represents a component of the Moroccan Turbidite System situated to the north of Agadir Basin. New core coverage to the east and north of the basin will provide insight into the flow pathways within the Moroccan Turbidite System and records of events sourced from the northern Moroccan margin.
2. Stratigraphy of the Horseshoe and Tagus Abyssal Plains will provide insight into the temporal and spatial distributions of turbidites from a seismically active section of the Iberian margin. Previous studies have correlated synchronous turbidites in both depocentres in the last 15 ka, and found these to be triggered by margin-wide earthquakes. A study of the full available stratigraphy will enable a longer time-frame study of turbidite initiation on the margin. Incorporation of cores from canyon levees and from additional basin entry points will also enable a more complete appraisal of controls on turbidite distribution.
3. The Iberian Abyssal Plain has not been studied previously. An investigation into the stratigraphy of the basin will provide insight into the controls on turbidite occurrence on this glacially-influenced margin. Furthermore, a study of sediments in the basin will enable an appraisal of the sediments exiting Nazare canyon, which represents one of the longest canyons on earth.
4. Another proposal is a review of turbidite occurrence, volume and composition of turbidites from the deepwater basins from the Porcupine Abyssal Plain to the regions south of the Canary Islands. This will provide a review of turbidites from climate conditions ranging from glacial-influenced to arid, from a variety of sediment accumulation rates, different hinterland terrains and sediment delivery systems.

10.2.3 Deepwater Depositional Processes

1. The turbidity currents associated with the El Golfo and Icod landslides have been found to travel 350 km and 880 km up-gradient towards the northwest respectively. Indeed, there is a deposit from Icod landslide recovered from the

easternmost Seine Abyssal Plain. Furthermore, a turbidite representing a 1 ka collapse from the Western Sahara margin is located in Agadir Basin. These long-runout flows have travelled up-gradient for hundreds of kilometres. Investigating the mechanisms by-which these flows have done this will improve our understanding of the transport mechanisms of fine-grained suspension clouds.

2. The core control present in the Moroccan Turbidite system will enable a fine-detailed investigation in turbidity current deposition. Indeed, grain-size and geochemical composition (and coccolithophore composition) of these deposits in axial and transverse sections will enlighten the processes and conditions responsible for deposition of turbidite facies such as: structureless sands, parallel-laminated sands, ripple-laminated sands and convolute-laminated sands, in addition to complex bedforms present in the mudcaps. The study of siliciclastic, volcaniclastic and calcareous turbidites from the Moroccan Turbidite System, in addition to those from mica-rich sediments from the northern basins, will enable an evaluation of deposition from different sediment assemblages.
3. A focussed study of the bed A5 linked debrite (and A12 structureless sand) will provide insight into the mechanisms by which hybrid beds develop in mud-rich conditions. This has potential importance to the hydrocarbon industry.
4. Core coverage, grain-size data and geochemistry will enable an investigation into the remobilised mudcaps in Agadir Basin. These are signified by contorted mudcap facies and ponding at base of slopes and into the basin centres. Resolving the mechanism responsible for these deposits may provide insight into the mechanisms responsible for the ponded mudcaps in the Madeira Abyssal Plain and basins of the Mediterranean.

10.2.4 Burial of Organic Carbon in Deepwater Turbidites

1. Recent studies from the Bengal Fan have demonstrated that large quantities of labile and refractory organic carbon can be buried in sediment gravity flows. Study of a single deposit (bed A5) will highlight how organic carbon is partitioned within the different flow regimes, partitioned within different depositional processes and affected by post depositional geochemical processes (diagenetic oxidation).

2. Following from the above, a comprehensive study of the quantities and compositions of organic carbon buried within the turbidites of the Late Quaternary successions of the Moroccan Turbidite System will improve our understanding of carbon burial. This can be extended to the ODP core from the Madeira Abyssal Plain.
3. The Moroccan Turbidite System represents siliciclastic turbidites sourced from continental slope landslides, where sediments accumulate primarily by oceanic productivity and minor terrigenous fluxes. Investigating organic burial within turbidites from the basins of the Iberian margin will provide insight into the affects of variable climate, different sediment accumulation rates, different sediment compositions, and gravity flows sourced from littoral drift and river-fed systems.

References

A

Abdel-Monem, A., N. D. Watkins, and P. M. Gast (1971). Potassium-Argon ages, volcanic stratigraphy, and geomagnetic polarity history of the Canary Islands: Lanzarote, Fuerteventura, Gran Canaria, and La Gomera. *American Journal of Science*, *271*, 490-521.

Abdel-Monem, A., N. D. Watkins, and P. M. Gast (1972), Potassium-Argon ages, volcanic stratigraphy, and geomagnetic polarity history of the Canary Islands: Tenerife, La Palma, and Hierro, *American Journal of Science*, *272*(9), 805-825.

Ablay, G., and M. Hurlimann (2000), Evolution of the north flank of Tenerife by recurrent giant landslides, *Journal of Volcanology and Geothermal Research*, *103*(1-4), 135-159.

Ablay, G., and P. Kearey (2000), Gravity constraints on the structure and volcanic evolution of Tenerife, Canary Islands, *J. Geophys. Res.*, 105(B3), doi:10.1029/1999JB900404.

Ablay, G. J., and J. Marti (2000), Stratigraphy, structure, and volcanic evolution of the Pico Teide Pico Viejo formation, Tenerife, Canary Islands, *Journal of Volcanology and Geothermal Research*, *103*(1-4), 175-208.

Abratis, M., H. U. Schmincke, and T. H. Hansteen (2002), Composition and evolution of submarine volcanic rocks from the central and western Canary Islands, *International Journal of Earth Sciences*, *91*(4), 562-582.

Acosta, J., E. Uchupi, A. Munoz, P. Herranz, C. Palomo, M. Ballesteros, and Z. E. E. W. Grp (2003), Geologic evolution of the Canarian Islands of Lanzarote, Fuerteventura, Gran Canaria and La Gomera and comparison of landslides at these islands with those at Tenerife, La Palma and El Hierro, *Marine Geophysical Researches*, *24*(1-2), 1-40, doi:10.1007/s11001-004-1513-3.

Adams, J. (1990), Paleoseismicity of the Cascadia subduction zone: evidence from turbidites off the Oregon-Washington margin, *Tectonics*, *9*(4), 569-583.

Alibés, B., M. Canals, B. Alonso, S.M. Lebreiro, P.P.E Weaver (1996), Quantification of neogene and quaternary sediment input to the Madeira Abyssal Plain. *Geogaceta, 20*(2), 394-397.

Alibés, B., R. G. Rothwell, M. Canals, P. P. E. Weaver, and B. Alonso (1999), Determination of sediment volumes, accumulation rates and turbidite emplacement frequencies on the Madeira Abyssal Plain (NE Atlantic): a correlation between seismic and borehole data, *Marine Geology*, *160*(3-4), 225-250.

Allan, P.G. (1998), Geotechnical Aspects of Submarine Cables, *IBC Conference on Subsea Geotechnics,* November 1998, Aberdeen, Scotland.

Allen, J.R.L. (1977), The possible mechanics of convolute lamination in graded beds, *J. Geol. Soc. London*, 134, 19-31.

Anastasakis, G. C., and D. J. W. Piper (1991), The character of seismo-turbidites in the S-1 sapropel, Zakinthos and Strofadhes basins, Greece, *Sedimentology*, *38*(4), 717-733.

Ancochea, E., J. M. Fuster, E. Ibarrola, A. Cendrero, J. Coello, F. Hernan, J. M. Cantagrel, and C. Jamond (1990), Volcanic evolution of the island of Tenerife (Canary Islands) in light of new K-Ar data, *Journal of Volcanology and Geothermal Research*, *44*(3-4), 231-249, doi:10.1016/0377-0273(90)90019-C.

Ancochea, E., F. Hernan, A. Cendrero, J. M. Cantagrel, J. M. Fuster, E. Ibarrola, and J. Coello (1994), Constructive and destructive episodes in the building of a young Ocean Island, La Palma, Canary Islands, and the genesis of the Caldera de Taburiente, *Journal of Volcanology and Geothermal Research*, *60*(3-4), 243-262.

Ancochea, E., J. M. Cantagrel, J. M. Fuster, M. J. Huertas, and N. O. Arnaud (1998), Vertical and lateral collapses on Tenerife (Canary Islands) and other volcanic ocean islands: Comment, *Geology*, *26*(9), 861-862.

Ancochea, E., M. J. Huertas, J. M. Cantagrel, J. Coello, J. M. Fuster, N. Arnaud, and E. Ibarrola (1999), Evolution of the Canadas edifice and its implications for the origin of the Canadas Caldera (Tenerife, Canary Islands), *Journal of Volcanology and Geothermal Research*, *88*(3), 177-199.

Ancochea, E., F. Hernan, M. J. Huertas, J. L. Brandle, and R. Herrera (2006), A new chronostratigraphical and evolutionary model for La Gomera: Implications for the overall evolution of the Canarian Archipelago, *Journal of Volcanology and Geothermal Research*, *157*(4), 271-293.

Anderson, D. L., T. Tanimoto, and Y. S. Zhang (1992), Plates-Tectonics and Hotsopts – the 3rd-Dimension, *Science*, *256*(5064), 1645-1651.

Andrade, S. D., and B. V. de Vries (2010), Structural analysis of the early stages of catastrophic stratovolcano flank-collapse using analogue models, *Bulletin of Volcanology*, *72*(7), 771-789.

Anguita, F., and F. Hernan (1975), A propagating fracture model versus a hot-spot origin for the Canary Islands, *Earth and Planetary Science Letters*, *27*(1), 11-19.

Anguita, F., and F. Hernan (2000), The Canary Islands origin: a unifying model, *Journal of Volcanology and Geothermal Research*, *103*(1-4), 1-26.

Anguita, F., L. G. Cacho, F. Colombo, A. G. Camacho, and R. Vieira (1991), Roque Nublo caldera: a new stratocone caldera in Gran Canaria, Canary Islands, *Journal of Volcanology and Geothermal Research*, *47*(1-2), 45-63.

Araña, V., and R. Ortiz (1986), Marco godinámico del volcanismo carnario, *An. Física, 82*, 202-231.

Arnaud, N., M.J. Huertas, J.M. Cantagrel, E. Ancochea, J.M. Fúster (2001), ^{40}Ar-^{39}Ar ages of the Roques de García deposits (Las Cañadas, Tenerife), *Geogaceta, 29*, 19-22.

Assier-Rzadkiewicz, S., P. Heinrich, P. C. Sabatier, B. Savoye, and J. F. Bourillet (2000), Numerical modelling of a landslide-generated Tsunami: The 1979 Nice event, *Pure and Applied Geophysics*, *157*(10), 1707-1727.

Athy, L.F. (1930), Density, Porosity, and Compaction of Sedimentary Rocks, *AAPG Bull., 14*, doi: 10.1306/3D93289E-16B1-11D7-8645000102C1856D.

B

Backman, J., and N. J. Shackleton (1983), Quantitative biochronology of Pliocene and early Pleistocene calcareous nannofossils from the Atlantic, Indian and Pacific oceans, *Marine Micropaleontology*, 8, 141-170.

Bagnold, R.A. (1954), Experiments on gravity free dispersion of large solid spheres in a Newtonian fluid under shear, *Proceedings of the Royal Society of London (A)*, *225*, 49-63.

Bagnold, R.A. (1956), The flow of cohesionless grains in fluids, *Philisophical Transaction of the Royal Society of London*, Series A, Mathematical and Physical Sciences, *249*, 235-297.

Bagnold, R.A. (1962), Auto-suspension of transported sediment: turbidity currents, *Royal Society of London Proceedings*, *Series A*, *265*, 315-319.

Baldwin, B., Butler, C.O. (1985). Compaction Curves, *AAPG Bull.*, *69*, doi:10.1306/AD462547-16F7-11D7-8645000102C1865D.

Balsam, W. L., B. C. Deaton, and J. E. Damuth (1999), Evaluating optical lightness as a proxy for carbonate content in marine sediment cores, *Marine Geology*, *161*(2-4), 141-153.

Beattie, P. D., and W. B. Dade (1996), Is scaling in turbidite deposition consistent with forcing by earthquakes?, *Journal of Sedimentary Research*, *66*(5), 909-915.

Beauchamp, W., R. W. Allmendinger, M. Barazangi, A. Demnati, M. El Alji, and M. Dahmani (1999), Inversion tectonics and the evolution of the High Atlas Mountains, Morocco, based on a geological-geophysical transect, *Tectonics*, *18*(2), 163-184.

Beget, J. E., and J. Kienle (1992), Cyclic formation of debris avalanches at Mount-St-Augustine Volcano, *Nature*, *356*(6371), 701-704.

Bender, M. L., and D. T. Heggie (1984), Fate of organic carbon reaching the deep sea floor: a status report, *Geochimica et Cosmochimica Acta*, *48*(5), 977-986.

Berger, W. H. (1970), Biogenous deep-sea sediments: fractionation by deep-sea circulation, *Geological Society of America Bulletin*, *81*(5), 1385-&.

Berndt, C., J. Mienert, M. Vanneste, and S. Bunz (2005), Gas hydrate dissociation and sea-floor collapse in the wake of the Storegga Slide, Norway, *Onshore-Offshore Relationships on the North Atlantic Margin*, *12*, 285-292.

Berner, R. A. (1981), A new geochemical classification of sedimentary environments, *Journal of Sedimentary Petrology*, *51*(2), 359-365.

Blais-Stevens, A., and J. J. Clague (2001), Paleoseismic signature in late holocene sediment cores from Saanich Inlet, British Columbia, *Marine Geology*, *175*(1-4), 131-148.

Blumberg, S., F. Lamy, H. W. Arz, H. P. Echtler, M. Wiedicke, G. H. Haug, and O. Oncken (2008), Turbiditic trench deposits at the South-Chilean active margin: A Pleistocene-Holocene record of climate and tectonics, *Earth and Planetary Science Letters*, *268*(3-4), 526-539.

Booth, J.S., O'Leary, D.W., Popenoe, P., Danforth, W.W. (1993), U.S. Atlantic continental slope landslides: their distribution, general attributes, and implications, in

Submarine Landslides: Selected Studies in the U.S. Exclusive Economic Zone, edited by W.C. Schwab, H.J. Lee, D.C. Twichell, U.S. Geol. Surv. Bull., 2002, pp. 14-22.

Borgia, A. (1994), Dynamic basis of volcanic spreading, *Journal of Geophysical Research-Solid Earth*, *99*(B9), 17791-17804.

Boudreaux, J. E., and W. W. Hay (1967), in Calcareous Nannoplanktonic Zonation of the Gulf Coast and Caribbean-Antillean Area, and Transoceanic Correlation, *Transactions of the Gulf Coast Assocaition of Geological Societies*, 17, 428-480.

Boulesteix, T., A. Hildenbrand, K. Kelfoun, V. Soler, and P.Y. Gillot (2009), Influence of landslide geometry on the dynamics of large debris-avalanches: a comparative study on Tenerife and Tahiti volcanic island, *Geophys. Res. Abs.*, *10*, EGU2008-A-0907, doi:1607-7962/gra/EGU2008-A-0907.

Boulesteix, T., A. Hildenbrand, P. Y. Gillot, and V. Soler (2012), Eruptive response of oceanic islands to giant landslides: New insights from the geomorphologic evolution of the Teide-Pico Viejo volcanic complex (Tenerife, Canary), *Geomorphology*, *138*(1), 61-73.

Bouma, A.H. (1962), *Sedimentology of some Flysch Deposits*, Elsevier Pub. Co., 168p.

Broecker, W. S., and T. Takahashi (1978), The relationship between lysocline depth and in situ carbonate ion concentration, *Deep-Sea Research*, *25*(1), 65-95.

Brown, R. J., T. L. Barry, M. J. Branney, M. S. Pringle, and S. E. Bryan (2003), The Quaternary pyroclastic succession of southeast Tenerife, Canary Islands: explosive eruptions, related caldera subsidence, and sector collapse, *Geological Magazine*, *140*(3), 265-288.

Bryan, S. E., R. A. F. Cas, and J. Marti (1998a), Lithic breccias in intermediate volume phonolitic ignimbrites, Tenerife (Canary Islands): constraints on pyroclastic flow depositional processes, *Journal of Volcanology and Geothermal Research*, *81*(3-4), 269-296.

Bryan, S. E., J. Marti, and R. A. F. Cas (1998b), Stratigraphy of the Bandas del Sur Formation: an extracaldera record of Quaternary phonolitic explosive eruptions from the Las Canadas edifice, Tenerife (Canary Islands), *Geological Magazine*, *135*(5), 605-636.

Bryan, S. E., R. A. F. Cas, and J. Marti (2000), The 0.57 Ma plinian eruption of the Granadilla Member, Tenerife (Canary Islands): an example of complexity in eruption dynamics and evolution, *Journal of Volcanology and Geothermal Research*, *103*(1-4), 209-238.

Bryan, S. E., J. Marti, and M. Leosson (2002), Petrology and geochemistry of the Bandas del Sur Formation, Las Canadas Edifice, Tenerife (Canary Islands), *Journal of Petrology*, *43*(10), 1815-1856.

Bryan, S. E. (2006), Petrology and geochemistry of the quaternary caldera-forming, phonolitic Granadilla eruption, Tenerife (Canary Islands), *Journal of Petrology*, *47*(8), 1557-1589.

Bryn, P., K. Berg, C. F. Forsberg, A. Solheim, and T. J. Kvalstad (2005), Explaining the Storegga Slide, *Marine and Petroleum Geology*, *22*(1-2), 11-19.

Bukry, D. (1973), Low-latitude coccolith Biostratigraphic zonation, in *Initial Reports*, edited by N. T. Edgard and J. B. Saunders, *Init. Repts. DSDP*, 15, 685-703, U.S. Govt. Printing, Washington.

Burke, K., and J. T. Wilson (1972), Is the African Plate Stationary, *Nature*, *239*(5372), 387-390.

Burnett, A. P., M. J. Soreghan, C. A. Scholz, and E. T. Brown (2011a), Tropical East African climate change and its relation to global climate: A record from Lake Tanganyika, Tropical East Africa, over the past 90+ kyr, *Palaeogeography Palaeoclimatology Palaeoecology*, *303*(1-4), 155-167.

C

Cacho, L. G., J. L. Diezgil, and V. Arana (1994), A large volcanic debris avalanche in the Pliocene Roque-Nublo stratovolcano, Gran Canaria, Canary Islands, *Journal of Volcanology and Geothermal Research*, *63*(3-4), 217-229.

Cantagrel, J. M., N. O. Arnaud, E. Ancochea, J. M. Fuster, and M. J. Huertas (1999), Repeated debris avalanches on Tenerife and genesis of Las Canadas caldera wall (Canary Islands), *Geology*, *27*(8), 739-742.

Carey, S., Maria, T., and Cornell, W. (1998), Processes of volcaniclastic sedimentation during the early growth stages of Gran Canaria based on sediments from site 953, in *Proceedings of the Ocean Drilling Program, Scientific Results*, 157, edited by P.P.E. Weaver, H.-U. Schmincke, J.V. Firth and W. Duffield, 183-200.

Carracedo, J. C. (1994), The Canary Islands: an example of structural control on the growth of large oceanic-island volcanoes, *Journal of Volcanology and Geothermal Research*, *60*(3-4), 225-241.

Carracedo, J. C. (1999), Growth, structure, instability and collapse of Canarian volcanoes and comparisons with Hawaiian volcanoes, *Journal of Volcanology and Geothermal Research*, *94*(1-4), 1-19.

Carracedo, J. C., S. Day, H. Guillou, E. R. Badiola, J. A. Canas, and F. J. P. Torrado (1998), Hotspot volcanism close to a passive continental margin: The Canary Islands, *Geological Magazine*, *135*(5), 591-604.

Carracedo, J. C., S. J. Day, H. Guillou, and F. J. P. Torrado (1999a), Giant Quaternary landslides in the evolution of La Palma and El Hierro, Canary Islands, *Journal of Volcanology and Geothermal Research*, *94*(1-4), 169-190.

Carracedo, J. C., S. J. Day, H. Guillou, and P. Gravestock (1999b), Later stages of volcanic evolution of La Palma, Canary Islands: Rift evolution, giant landslides, and the genesis of the Caldera de Taburiente, *Geological Society of America Bulletin*, *111*(5), 755-768.

Carracedo, J.C., E. Rodríguez Badiola, H. Guillou,, J. de la Nuez, and F.J. Pérez Torrado (2001), Geology and Volcanology of La Palma and El Hierro (Canary Islands), *Estudios Geológicos*, *57*, 175-273.

Carvajal, C. R., and R. J. Steel (2006), Thick turbidite successions from supply-dominated shelves during sea-level highstand, *Geology*, *34*(8), 665-668.

Chappell, J., and N. J. Shackleton (1986), Oxygen Isotopes and Sea-Level, *Nature*, *324*(6093), 137-140.

Chappellaz, J. A., I. Y. Fung, and A. M. Thompson (1993), The Atmospheric CH_4 Increase since the Last Glacial Maximum, *Tellus Series B-Chemical and Physical Meteorology*, *45*(3), 228-241.

Chaytor, J. D., D. C. Twichell, U. S. Ten Brink, B. J. Buczkowski, and B. D. Andrews (2007), Revisiting submarine mass movements along the US Atlantic continental margin: Implications for tsunami hazards, *Submarine Mass Movements and Their Consequences*, *27*, 395-403.

Chaytor, J. D., U. S. ten Brink, A. R. Solow, and B. D. Andrews (2009), Size distribution of submarine landslides along the US Atlantic margin, *Marine Geology*, *264*(1-2), 16-27.

Chaytor, J. D., D. C. Twichell, P. Lynett, and E. L. Geist (2010), Distribution and Tsunamigenic Potential of Submarine Landslides in the Gulf of Mexico, *Submarine Mass Movements and Their Consequences*, *28*, 745-754.

Chiocci, F. L., and G. de Alteriis (2006), The Ischia debris avalanche: first clear submarine evidence in the Mediterranean of a volcanic island prehistorical collapse, *Terra Nova*, *18*(3), 202-209.

Chiocci, F. L., C. Romagnoli, P. Tommasi, and A. Bosman (2008), The Stromboli 2002 tsunamigenic submarine slide: Characteristics and possible failure mechanisms, *Journal of Geophysical Research-Solid Earth*, *113*(B10), 11.

Clouard, V., A. Bonneville, and P. Y. Gillot (2001), A giant landslide on the southern flank of Tahiti Island, French Polynesia, *Geophysical Research Letters*, *28*(11), 2253-2256.

Clouard, V., and A. Bonneville (2005), Ages of seamounts, islands, and plateaus on the Pacific plate, *Geololgical Society of. America*, 388, 71-90.

Coleman, J. M., and D. B. Prior (1988), Mass-wasting on Continental Margins, *Annual Review of Earth and Planetary Sciences*, *16*, 101-119.

Colley, S., and J. Thomson (1985), Recurrent uranium relocations in distal turbidites emplaced in pelagic conditions, *Geochimica Et Cosmochimica Acta*, *49*(11), 2339-2348.

Colley, S., J. Thomson, T. R. S. Wilson, and N. C. Higgs (1984), Post-depositional migration of elements during diagenesis in brown clay and turbidite sequences in the North East Atlantic, *Geochimica Et Cosmochimica Acta*, *48*(6), 1223-1235.

Coppo, N., P. A. Schnegg, W. Heise, P. Falco, and R. Costa (2008), Multiple caldera collapses inferred from the shallow electrical resistivity signature of the Las Canadas caldera, Tenerife, Canary Islands, *Journal of Volcanology and Geothermal Research*, *170*(3-4), 153-166.

Coppo, N. P., P. A. Schnegg, P. Falco, and R. Costa (2009), A deep scar in the flank of Tenerife (Canary Islands): Geophysical contribution to tsunami hazard assessment, *Earth and Planetary Science Letters*, *282*(1-4), 65-68.

Corella, J.P., Amrani, A.E., Sigró, J., Morellón, M., Rico, E., & Valero-Garcés, B.L. In press, Recent evolution of Lake Arreo, northern Spain: influences of land use change and climate, *Journal of Paleolimnology*, doi: 10.1007/s10933-010-9492-7.

Covault, J. A., and S. A. Graham (2010), Submarine fans at all sea-level stands: Tectono-morphologic and climatic controls on terrigenous sediment delivery to the deep sea, *Geology*, *38*(10), 939-942.

Covault, J. A., W. R. Normark, B. W. Romans, and S. A. Graham (2007), Highstand fans in the California borderland: The overlooked deep-water depositional systems, *Geology*, *35*(9), 783-786.

Crans, W., G. Mandl, and J. Harembourne (1980), On the theory of growth faulting: a geomechanical delta model based on gravity sliding, *J. Petrol. Geol.*, 2, 265-307.

Cronan, D. S., G. Rothwell, and I. Croudace (2010), An ITRAX Geochemical Study of Ferromanganiferous Sediments from the Penrhyn Basin, South Pacific Ocean, *Marine Georesources & Geotechnology*, *28*(3), 207-221.

Croudace, I. W., and O. Williams-Thorpe (1988), A low dilution, wavelength-dispersive X-ray fluorescence procedure for the analysis of archaeological rock artifacts, *Archaeometry*, *30*, 227-236.

Croudace, I. W., and J. M. Gilligan (1990), Versatile and accurate trace-element determinations in iron-rich and other geological samples using X-ray fluorescence, *X-Ray Spectrometry*, *19*(3), 117-123.

Croudace, I.W., A. Rindby, and G. Rothwell (2006), ITRAX: description and evaluation of a multi-function X-ray core scanner, in *New Techniques in Sediment Core Analysis*, 267, edited by R.G. Rothwell, Geological Society of London, Special Publication, pp. 51-63, London, UK.

Crowley, T. J. (1983), Calcium-carbonate preservation patterns in the Central North Atlantic during the last 150,000 years, *Marine Geology*, *51*(1-2), 1-14.

D

Dadson, S., N. Hovius, S. Pegg, W. B. Dade, M. J. Horng, and H. Chen (2005), Hyperpycnal river flows from an active mountain belt, *Journal of Geophysical Research-Earth Surface*, *110*(F4), 14.

Dallmeier-Tiessen, S. (2005), A megaturbidite across the Moroccan Turbidite System – detailed sedimentological characterisation of AB5 with special reference to the cogenetic occurrence of a debris flow and turbidity current, *MSc Thesis*, Faculty of Geosciences of Bremen University.

Dasgupta, P. (2003), Sediment gravity flow - the conceptual problems, *Earth-Science Reviews*, *62*(3-4), 265-281.

Davies, T. L., B. VanNiel, R. B. Kidd, and P. P. E. Weaver (1997), High-resolution stratigraphy and turbidite processes in the Seine Abyssal Plain, northwest Africa, *Geo-Marine Letters*, *17*(2), 147-153.

Davison, I. (2005), Central Atlantic margin basins of North West Africa: Geology and hydrocarbon potential (Morocco to Guinea), *Journal of African Earth Sciences*, *43*(1-3), 254-274.

Day, S.J. (1996), Hydrothermal pore-fluid pressure and the stability of porous, permeable volcanoes, in *Volcano Instability on the Earth and Other Planets,Geol. Soc. Spec. Publ.,* 110, edited by W.J. McGuire, A.P. Jones and J. Neuberg, Geological Society London, Special Publication, pp. 77-94, London, UK.

Day, S. J., J. C. Carracedo, and H. Guillou (1997), Age and geometry of an aborted rift flank collapse: The San Andres fault system, El Hierro, Canary Islands, *Geological Magazine*, *134*(4), 523-537.

De Alteriis, G., D. D. Insinga, S. Morabito, V. Morra, F. L. Chiocci, F. Terrasi, C. Lubritto, C. Di Benedetto, and M. Pazzanese (2010), Age of submarine debris avalanches and tephrostratigraphy offshore Ischia Island, Tyrrhenian Sea, Italy, *Marine Geology*, *278*(1-4), 1-18.

De Lange, G.J., I. Jarvis, and A. Kuijpers, (1987), Geochemical characteristics and provenance of late Quaternary sediment from the Madeira Abyssal Plain, N Atlantic, in *Geology and Geochemistry of Abyssal Plains*, 31, edited by P.P.E. Weaver and J. Thomson, Geological Society of London, Special Publication, pp.147-165,

De Paolo, D.J., Stolper, E., and Thomas, D.M. (2001), Deep drilling in a Hawaii volcano, *EOS*, *82*, 149, 154-155.

Deeming, K. R., B. McGuire, and P. Harrop (2010), Climate forcing of volcano lateral collapse: evidence from Mount Etna, Sicily, *Philosophical Transactions of the Royal Society a-Mathematical Physical and Engineering Sciences*, *368*(1919), 2559-2577.

Deplus, C., A. Le Friant, G. Boudon, J. C. Komorowski, B. Villemant, C. Harford, J. Segoufin, and J. L. Cheminee (2001), Submarine evidence for large-scale debris avalanches in the Lesser Antilles Arc, *Earth and Planetary Science Letters*, *192*(2), 145-157.

Di Roberto, A., M. Rosi, A. Bertagnini, M. P. Marani, and F. Gamberi (2010), Distal Turbidites and Tsunamigenic Landslides of Stromboli Volcano (Aeolian Islands, Italy), *Submarine Mass Movements and Their Consequences*, *28*, 719-731.

Dickinson, R. R., and J. Brown (1994), The production of North Altantic Deep Water: Sources, rates, and pathways, *J. Geophys. Res*., 99(6), 12,319-12,341, doi:10.1029/94JC00530.

Dillon, W.P., W.W. Danforth, D.R. Hutchinson, R.M. Drury, M.H. Taylor, and J.S. Booth (1998), Evidence of faulting related to dissociation of gas hydrate and release of methane off the southeastern United States, in *Gas Hydrates: Relevance to World Margin Stability and Climate Change*, 137, edited by J.-P. Henriet, Geological Society of London, Special Publication, pp. 293-302, doi:10.1144/GSL.SP.1998.137.01.23.

Driscoll, N. W., J. K. Weissel, and J. A. Goff (2000), Potential for large-scale submarine slope failure and tsunami generation along the US mid-Atlantic coast, *Geology*, *28*(5), 407-410.

Drummond, C. N. (1999), Bed-thickness structure of multi-sourced ramp turbidites: Devonian Brallier Formation, Central Appalachian Basin, *Journal of Sedimentary Research*, *69*(1), 115-121.

Ducassou, E., S. Migeon, T. Mulder, A. Murat, L. Capotondi, S. M. Bernasconi, and J. Mascle (2009), Evolution of the Nile deep-sea turbidite system during the Late Quaternary: influence of climate change on fan sedimentation, *Sedimentology*, *56*(7), 2061-2090.

Duffield, W. A., L. Stieltjes, and J. Varet (1982), Huge landslide blocks in the growth of Piton de la Fournaise, La Réunion, and Kilauea volcano, Hawaii, *Journal of Volcanology and Geothermal Research*, *12*(1-2), 147-160.

Dymond, J., E. Suess, and M. Lyle (1992), Barium in deep-sea sediment: a geochemical proxy for paleoproductivity, *Paleoceanography*, *7*(2), 163-181181.

E

Eckel, E.B. (1958), Introduction to Landslides and Engineering Practice, *Highway Research Board Special Report*, Transportation Research Board Business Office, Washington.

Edgar, C. J., J. A. Wolff, P. H. Olin, H. J. Nichols, A. Pittari, R. A. F. Cas, P. W. Reiners, T. L. Spell, and J. Marti (2007), The late quaternary Diego Hernandez Formation, Tenerife: Volcanology of a complex cycle of voluminous explosive phonolitic eruptions, *Journal of Volcanology and Geothermal Research*, *160*(1-2), 59-85.

Einsele, G., and Kelts, K. (1982), Pliocene and Quaternary mud turbidites in the Gulf of California; sedimentology, mass physical properties and significance, *Init. Rep. Deep Sea drill. Proj.*, *64*, 511-528.

Elsworth, D., and B. Voight (1995), Dike intrusion as a trigger for large earthquakes and the failure of volcano flanks, *Journal of Geophysical Research-Solid Earth*, *100*(B4), 6005-6024.

Elsworth, D., and B. Voight (1996), Evaluation of volcano flank instability triggered by dyke intrusion, *Volcano Instability on the Earth and Other Planets*(110), 45-53.

Elsworth, D., and S. J. Day (1999), Flank collapse triggered by intrusion: the Canarian and Cape Verde Archipelagoes, *Journal of Volcanology and Geothermal Research*, *94*(1-4), 323-340.

Elsworth, D., B. Voight, and J. Taron (2007), Contemporary views of slope instability on active volcanoes, paper presented at International Workshop on Volcanic Rocks, Taylor & Francis Ltd, Ponta Delgada, PORTUGAL, Jul 14-15.

Embley, R. W., and R. D. Jacobi (1977), Distribution and morphology of large submarine sediment slides and slumps on Atlantic continental margins, *Marine Geotechnology*, *2*, 205-228.

Embley, B.D., and R.D. Jacobi (1986), Mass wasting in the western North Atlantic, in *The Geology of North America, The Western North Atlantic*, Geol. Soc. Am., Boulder, Colorado, 479-490.

Ercilla, G., B. Alonso, F. Perez-Belzuz, F. Estrada, J. Baraza, M. Farran, M. Canals, and D. Masson (1998), Origin, sedimentary processes and depositional evolution of the Agadir turbidite system, central eastern Atlantic, *Journal of the Geological Society*, *155*, 929-939.

Evans, D., M.S. Stoker, and A. Cramp (1998), Geological processes on continental margins: sedimentation, mass-wasting and stability: an introduction, in *Geological Processes on Continental Margins: Sedimentation, Mass-Wasting and Stability*, 129, edited by M.S. Stoker and D. Evans, Geological Society of London, Special Publications, 1-4.

F

Faugeres, J.C., E. Gonthier, and D.A.V. Stow (1984), Contourite drift molded by deep Mediterranean outflow, *Geology*, 12(5), 296-300.

Faugeres, J. C., and D. A. V. Stow (1993), Bottom-current controlled sedimentation – a synthesis of the contourite problem, *Sedimentary Geology*, *82*(1-4), 287-297.

Faugeres, J. C., M. L. Mezerais, and D. A. V. Stow (1993), Contourite drift types and their distribution in the North and South Atlantic Ocean Basins, *Sedimentary Geology*, *82*(1-4), 189-203.

Field, M. E., J. V. Gardner, A. E. Jennings, and B. D. Edwards (1982), Earthquake-induced sediment failures on a 0.25-degree slope, Klamath River Delta, California, *Geology*, *10*(10), 542-546.

Filipsson, H. L., O. E. Romero, J.-B. W. Stuut, and B. Donner (2011), Relationships between primary productivity and bottom-water oxygenation off northwest Africa during the last deglaciation, *J. Quatern. Sci.*, 26(4), 448-456.

Fine, I.V., E.V. Kulikov, R.E. Thomson, and A.B. Rabinovich (2001), Modeling of tsunami generation by submarine and subaerial landslides, *Proceedings International Tsunami Symposium*, Seattle, Washington, 7-10 August, 663.

Fine, I.V., A.B. Rabinovich, R.E. Thomson, and E.A. Kulikov (2003), Numerical modelling of tsunami generation by submarine and subaerial landslides, in *Submarine Landslides and Tsunamis*, edited by A.C. Yalçiner, E. Pelinovsky and C.E. Synolakis, Kluwer Academic Publishers, Netherlands.

Fine, I. V., A. B. Rabinovich, B. D. Bornhold, R. E. Thomson, and E. A. Kulikov (2005), The Grand Banks landslide-generated tsunami of November 18, 1929: preliminary analysis and numerical modeling, *Marine Geology*, *215*(1-2), 45-57.

Firth, C., I. Stewart, W. J. McGuire, S. Kershaw, and C. VitaFinzi (1996), Coastal elevation changes in eastern Sicily: Implications for volcano instability at Mount Etna, *Volcano Instability on the Earth and Other Planets*(110), 153-167.

Flood, R.D., Manley, P.L., Kowsmann, R.O., Appi, C.J. & Pirmez, C. 1991, Seismic facies and late Quaternary growth of Amazon submarine fan, in *Seismic facies and sedimentary processes of modern and ancient submarine fans and turbidite systems*, edited by P. Weimer and M.H. Link, pp. 415-433, Springer-Verlag, New York, USA.

Frenz, M., R. B. Wynn, A. Georgiopoulou, V. B. Bender, G. Hough, D. G. Masson, P. J. Talling, and B. T. Cronin (2009), Provenance and pathways of late Quaternary turbidites in the deep-water Agadir Basin, northwest African margin, *International Journal of Earth Sciences*, *98*(4), 721-733.

Freudenthal, T., H. Meggers, J. Henderiks, H. Kuhlmann, A. Moreno, and G. Wefer (2002), Upwelling intensity and filament activity off Morocco during the last 250,000 years, *Deep-Sea Research Part Ii-Topical Studies in Oceanography*, *49*(17), 3655-3674.

Fritz, H. M., F. Mohammed, and J. Yoo (2009), Lituya Bay Landslide Impact Generated Mega-Tsunami 50(th) Anniversary, *Pure and Applied Geophysics*, *166*(1-2), 153-175.

Froelich, P. N., G. P. Klinkhammer, M. L. Bender, N. A. Luedtke, G. R. Heath, D. Cullen, P. Dauphin, D. Hammond, B. Hartman, and V. Maynard (1979), Early

oxidation of organic matter in pelagic sediments of the eastern equatorial Atlantic: suboxic diagenesis, *Geochimica Et Cosmochimica Acta*, *43*(7), 1075-1090.

Fryer, G. J., P. Watts, and L. F. Pratson (2004), Source of the great tsunami of 1 April 1946: a landslide in the upper Aleutian forearc, *Marine Geology*, *203*(3-4), 201-218.

Fúster, J.M. (1975), Las Islas Canarias: un ejemplo de evolución temporal y especial del vulcanismo oceanic, *Est. Geol.*, *31*, 439-463.

G

Galipp, K., A. Klugel, and T. H. Hansteen (2006), Changing depths of magma fractionation and stagnation during the evolution of an oceanic island volcano: La Palma (Canary Islands), *Journal of Volcanology and Geothermal Research*, *155*(3-4), 285-306.

Garcia, M. O. (1996), Turbidites from slope failure on Hawaiian volcanoes, *Volcano Instability on the Earth and Other Planets*(110), 281-294.

Garcia, M. O., and D. M. Hull (1994), Turbidites from giant Hawaiian landslides: Results from Ocean Drilling Program Site 842, *Geology*, *22*(2), 159-162.

García Cacho, L., J.L. Díez-Gil, and V. Araña (1994), A large volcanic debris avalanche in the Pliocene Roque Nublo Stratovolcano, Gran Canaria, Canary Islands, *Journal of Volcanology and Geothermal Research*, *63*, 3-4.

Garfield, N., T. A. Rago, K. J. Schnebele, and C. A. Collins (1994), Evidence of a turbidity current in Monterey Submarine Canyon associated with the 1989 Loma Prieta earthquake, *Continental Shelf Research*, *14*(6), 673-686.

Gartner, S. (1969), Correlation of Neogene planktonic foraminifera and calcareous nannofossil zones, *Transactions of the Gulf Coast Association of the Geological Societies*, 19, 585-599.

Gartner, S. (1977), Calcareous nannofossil biostratigraphy and revised zonation of the Pleistocene, *Marine Micropaleontology*, 2, 1-25.

Gee, M. J. R., D. G. Masson, A. B. Watts, and P. A. Allen (1999), The Saharan debris flow: an insight into the mechanics of long runout submarine debris flows, *Sedimentology*, *46*(2), 317-335.

Gee, M. J. R., A. B. Watts, D. G. Masson, and N. C. Mitchell (2001), Landslides and the evolution of El Hierro in the Canary Islands, *Marine Geology*, *177*(3-4), 271-293.

Geist, E. L., and T. Parsons (2009), Assessment of source probabilities for potential tsunamis affecting the US Atlantic coast, *Marine Geology*, *264*(1-2), 98-108.

Geist, E. L., and T. Parsons (2010), Estimating the Empirical Probability of Submarine Landslide Occurrence, *Submarine Mass Movements and Their Consequences*, *28*, 377-386.

Geldmacher, J., and K. Hoernle (2000), The 72 Ma geochemical evolution of the Madeira hotspot (eastern North Atlantic): recycling of Paleozoic (<500 Ma) oceanic lithosphere, *Earth and Planetary Science Letters*, *183*(1-2), 73-92.

Geldmacher, J., P. van den Bogaard, K. Hoernle, and H. U. Schmincke (2000), The Ar-40/Ar-39 age dating of the Madeira Archipelago and hotspot track (eastern North Atlantic), *Geochemistry Geophysics Geosystems*, *1*, 26.

Geldmacher, J., K. Hoernle, P. van der Bogaard, S. Duggen, and R. Werner (2005), New Ar-40/Ar-39 age and geochemical data from seamounts in the Canary and Madeira volcanic provinces: Support for the mantle plume hypothesis, *Earth and Planetary Science Letters*, *237*(1-2), 85-101.

Geldmacher, J., K. Hoernle, A. Klugel, P. van den Bogaard, and S. Duggen (2006), A geochemical transect across a heterogeneous mantle upwelling: Implications for the evolution of the Madeira hotspot in space and time, *Lithos*, *90*(1-2), 131-144.

Gelfenbaum, G., and B. Jaffe (2003), Erosion and sedimentation from the 17 July, 1998 Papua New Guinea tsunami, *Pure and Applied Geophysics*, *160*(10-11), 1969-1999.

GEOREM Database for Geological and Environmenta Reference Materials, Max-Planck-Gesellschaft, georem.mpch-mainz.gwdg.de.

Georgiopoulou, A. (2006), Turbidity currents and the giant Sahara Slide, northwest African margin: triggers, flow processes and deposits, *PhD Thesis*, University of Southampton, Southampton.

Georgiopoulou, A., D. G. Masson, R. B. Wynn, and S. Krastel (2010), Sahara Slide: Age, initiation, and processes of a giant submarine slide, *Geochemistry Geophysics Geosystems*, *11*, 22.

GEOROC Database for Geochemistry of Rocks of the Oceans and Continents, Max-Planck-Gesellschaft, georoc.mpch-mainz.gwdg.de/georoc.

Giachetti, T., R. Paris, K. Kelfoun, and F. J. Perez-Torrado (2011), Numerical modelling of the tsunami triggered by the Guimar debris avalanche, Tenerife (Canary Islands): Comparison with field-based data, *Marine Geology*, *284*(1-4), 189-202.

Giese, P., and V. Jacobshagen (1992), Inversion Tectonics of Intracontinental Ranges – High and Middle Atlas, Morocco, *Geologische Rundschau*, *81*(1), 249-259.

Giresse, P., H. Pauc, J. Deverchere, and P. Maradja Shipboard Sci (2009), Sedimentary processes and origin of sediment gravity-flow deposits on the western Algerian margin during late Pleistocene and Holocene, *Marine and Petroleum Geology*, *26*(5), 695-710.

Gisler, G., R. P. Weaver, amd M. L. Gittlings (2006), SAGE calculations of the tsunami threat from La Palma, *Sci. Tsunami Hazards*, 24, 288-301.

Gisler, G., R. P. Weaver, and M. Gittings (2010), Calculations of Tsunamis from Submarine Landslides, *Submarine Mass Movements and Their Consequences*, *28*, 695-704.

Goldfinger, C. (2009), Subaqueous paleoseismology, in *Paleoseismology*, 95, edited by J.P. McAlpin, pp. 119–70, Elsevier, Amsterdam.

Goldfinger, C. (2011), Submarine Paleoseismology Based on Turbidite Records, in *Annual Review of Marine Science, Vol 3*, edited by C. A. Carlson and S. J. Giovannoni, pp. 35-66, Annual Reviews, Palo Alto.

Goldfinger, C., C. H. Nelson, J. E. Johnson, and P. Shipboard Sci (2003a), Deep-water turbidites as Holocene earthquake proxies: the Cascadia subduction zone and Northern San Andreas Fault systems, *Annals of Geophysics*, *46*(5), 1169-1194.

Goldfinger, C., C. H. Nelson, J. E. Johnson, and P. Shipboard Sci (2003b), Holocene earthquake records from the Cascadia subduction zone and northern San Andreas

Fault based on precise dating of offshore turbidites, *Annual Review of Earth and Planetary Sciences*, *31*, 555-577.

Goldfinger, C., A. E. Morey, C. H. Nelson, J. Gutierrez-Pastor, J. E. Johnson, E. Karabanov, J. Chaytor, A. Eriksson, and Shipboard Scientific Party (2007), Rupture lengths and temporal history of significant earthquakes on the offshore and north coast segments of the Northern San Andreas Fault based on turbidite stratigraphy, *Earth and Planetary Science Letters*, *254*(1-2), 9-27.

Goldfinger, C., K. Grijalva, R. Burgmann, A.E. Morey, J.E. Johnson, C.H. Nelson, J. Gutiérrez-Pastor, A. Erisson, E. Karabanov, J.D Chaytor, and J. Patton (2008), Late Holocene rupture of the northern San Andreas fault and possible stress linkage to the Cascadia subduction zone, *Bulletin of the Seismological Society of America*, *98*(2), 861-889.

Goldfinger, C., C.H. Nelson, A. Morey, J.E. Johnson, and J. Gutiérrez-Pastor (2010), Turbidite event history: Methods and implications for Holocene paleoseismicity of the Cascadia Subduction Zone, *USGS Professional Paper*, U.S. Geological Survey, Reston, 178.

Goldstrand, P.M. (1998), Provenance and sedimentologic variations of turbidite and slump deposits at Sites 955 and 956, in *Proceedings of the Ocean Drilling Program, Scientific Results*, 157, edited by P.P.E. Weaver, H.-U. Schmincke, J.V. Firth and W. Duffield, pp. 343-360.

Gonthier, E.G., J.-C. Faugères and D.A.V. Stow (1984), Contourite facies of the Faro Drift, Gulf of Cadiz, in *Fine-grained Sediments: Deep-water Processes and Facies*, 15, edited by D.A.V. Stow and D.J.W. Piper, Geological Society of London, Special Publications, pp. 275-292.

Gorsline, D. S., T. De Diego, and E. H. Nava-Sanchez (2000), Seismically triggered turbidites in small margin basins: Alfonso Basin, Western Gulf of California and Santa Monica Basin, California Borderland, *Sedimentary Geology*, *135*(1-4), 21-35.

Gracia, E., A. Vizcaino, C. Escutia, A. Asioli, A. Rodes, R. Pallas, J. Garcia-Orellana, S. Lebreiro, and C. Goldfinger (2010), Holocene earthquake record offshore Portugal (SW Iberia): testing turbidite paleoseismology in a slow-convergence margin, *Quaternary Science Reviews*, *29*(9-10), 1156-1172.

Grilli, S. T., and P. Watts (2005), Tsunami generation by submarine mass failure. I: Modeling experimental validation, and sensitivity analyses, *Journal of Waterway Port Coastal and Ocean Engineering-Asce*, *131*(6), 283-297.

Guillou, H., J. C. Carracedo, F. P. Torrado, and E. R. Badiola (1996), K-Ar ages and magnetic stratigraphy of a hotspot-induced, fast grown oceanic island: El Hierro, Canary Islands, *Journal of Volcanology and Geothermal Research*, *73*(1-2), 141-155.

Guillou, H., J. C. Carracedo, and S. J. Day (1998), Dating of the Upper Pleistocene Holocene volcanic activity of La Palma using the unspiked K-Ar technique, *Journal of Volcanology and Geothermal Research*, *86*(1-4), 137-149.

Guillou, H., J. C. Carracedo, and R. A. Duncan (2001), K-Ar, Ar-40-Ar-39 ages and magnetostratigraphy of Brunhes and Matuyama lava sequences from La Palma Island, *Journal of Volcanology and Geothermal Research*, *106*(3-4), 175-194.

Guillou, H., J. C. Carracedo, R. Paris, and F. J. P. Torrado (2004), Implications for the early shield-stage evolution of Tenerife from K/Ar ages and magnetic stratigraphy, *Earth and Planetary Science Letters*, *222*(2), 599-614.

H

Haflidason, H., H. P. Sejrup, A. Nygard, J. Mienert, P. Bryn, R. Lien, C. F. Forsberg, K. Berg, and D. Masson (2004), The Storegga Slide: architecture, geometry and slide development, *Marine Geology*, *213*(1-4), 201-234.

Haflidason, H., R. Lien, H. P. Sejrup, C. F. Forsberg, and P. Bryn (2005), The dating and morphometry of the Storegga Slide, *Marine and Petroleum Geology*, *22*(1-2), 123-136.

Hampton, M. A. (1975), Competence of Fine-grained Debris Flows, *Journal of Sedimentary Petrology*, *45*(4), 834-844.

Hampton, M. A. (1979), Buoyancy in Debris Flows, *Journal of Sedimentary Petrology*, *49*(3), 753-758.

Hampton, M. A., H. J. Lee, and J. Locat (1996), Submarine landslides, *Reviews of Geophysics*, *34*(1), 33-59.

Haq, B. U., and A. M. Al-Qahtani (2005), Phanerozoic cycles of sea-level change on the Arabian Platform, *Geoarabia*, *10*(2), 127-160.

Haq, B. U., J. Hardenbol, and P. R. Vail (1987), Chronology of Fluctuating Sea Levels since the Triassic, *Science*, *235*(4793), 1156-1167.

Harbitz, C. B. (1992), Model Simulations of Tsunamics Generated by the Storegga Slide, *Marine Geology*, *105*(1-4), 1-21.

Harbitz, C. B., G. Pedersen, and B. Gjevik (1993), Numerical Simulations of Large Water-waves due to Landslides, *Journal of Hydraulic Engineering-Asce*, *119*(12), 1325-1342.

Harbitz, C. B., F. Lovholt, G. Pedersen, and D. G. Masson (2006), Mechanisms of tsunami generation by submarine landslides: a short review, *Norwegian Journal of Geology*, *86*(3), 255-264.

Haug, G. H., K. A. Hughen, D. M. Sigman, L. C. Peterson, and U. Rohl (2001), Southward migration of the intertropical convergence zone through the Holocene, *Science*, *293*(5533), 1304-1308.

Haug, G. H., D. Gunther, L. C. Peterson, D. M. Sigman, K. A. Hughen, and B. Aeschlimann (2003), Climate and the collapse of Maya civilization, *Science*, *299*(5613), 1731-1735.

Haugen, K. B., F. Lovholt, and C. B. Harbitz (2005), Fundamental mechanisms for tsunami generation by submarine mass flows in idealised geometries, *Marine and Petroleum Geology*, *22*(1-2), 209-217.

Heezen, B. C., C. D. Hollister, and W. F. Ruddiman (1966), Shaping of the continental rise by deep geostrophic contour currents, *Science (New York, N.Y.)*, *152*(3721), 502-508.

Heinrich, P., S. Guibourg, A. Mangeney, and R. Roche (1999), Numerical Modeling of a Landslide-Generating Tsunami following a Potential Explosion of the Montserrat Volcano, *Phys. Chem. Earth(A)*, 24, 2, 163-168.

Helmke, J. P., and H. A. Bauch (2001), Glacial-interglacial relationship between carbonate components and sediment reflectance in the North Atlantic, *Geo-Marine Letters*, *21*(1), 16-22.

Helmke, J. P., M. Schulz, and H. A. Bauch (2002), Sediment-color record from the Northeast Atlantic reveals patterns of millennial-scale climate variability during the past 500,000 years, *Quaternary Research*, *57*(1), 49-57.

Henderiks, J., T. Freudenthal, H. Meggers, S. Nave, F. Abrantes, J. Bollmann, and H. R. Thierstein (2002), Glacial-interglacial variability of particle accumulation in the Canary Basin: a time-slice approach, *Deep-Sea Research Part Ii-Topical Studies in Oceanography*, *49*(17), 3675-3705.

Heyman, M.A.W. (1989), Tectonic and depositional history of the Moroccan continental margin, in *Extensional Tectonics and Statigraphy of the Northern Atlantic Margins*, 46, edited by A.J. Tankard and H.R. Balkwill, Am. Assoc. Pet. Geol. and Can. Geol. Found. AAPG Mem., pp. 323-340.

Hildenbrand, A., P. Y. Gillot, and A. Bonneville (2006), Offshore evidence for a huge landslide of the northern flank of Tahiti-Nui (French Polynesia), *Geochemistry Geophysics Geosystems*, *7*, 12.

Hine, N. (1990), *Late Cenozoic Calcareous Nannoplankton from North Atlantic*, PhD Thesis, Unversity of East Anglia.

Hine, N., and P. P. E. Weaver (1998), Quaternary, in *Calcareous nannofossil biostratigraphy*, edited by P. R. Brown, British Micropaleontological Society Series, 266-282, Kluwer Academic.

Hiscott, R. N., and K. T. Pickering (1984), Reflected turbidity currents on an Ordovician basin floor, Canadian Appalachians, *Nature*, *311*(5982), 143-145.

Hodell, D. A., J. E. T. Channell, J. H. Curtis, O. E. Romero, and U. Rohl (2008), Onset of "Hudson Strait" Heinrich events in the eastern North Atlantic at the end of the middle Pleistocene transition (similar to 640 ka)?, *Paleoceanography*, *23*(4), 16.

Hoernle, K., and H. U. Schmincke (1993), The Role of Partial Melting in the 15 Ma Geochemical Evolution of Gran Canaria: A Blob Model for the Canary Hotspot, *Journal of Petrology*, *34*(3), 599-626.

Hoernle, K., Y. S. Zhang, and D. Graham (1995), Seismic and geochemical evidence for large-scale mantle upwelling beneath the eastern and western and central Europe, *Nature*, *374*(6517), 34-39.

Holcomb, R.T., and R.C. Searle (1991), Large landslides from oceanic volcanoes, *Marine Geotechnology*, 10, 1-2, 19-32.

Hollister, C. D. (1993), The Concept of Deep-Sea Contourites, *Sedimentary Geology*, *82*(1-4), 5-11.

Howe, R.W., amd J. Sblendorio-Levy (1998), Calcareous nannofossil biostratigraphy and sediment accumulation of turbidite sequences on the Madeira Abyssal Plain, Sites 950-952, in *Proceedings of the Ocean Drilling Programme Scientific Results*, 157, edited by P.P.E. Weaver, H.-U. Schmincke, J.V. Firth, and W. Duffield, pp.

501-520, College Station, TX (Ocean Drilling Program), doi:10.2973/odp.proc.sr.157.147.1998.

Hsu, S. K., J. Kuo, C. L. Lo, C. H. Tsai, W. B. Doo, C. Y. Ku, and J. C. Sibuet (2008), Turbidity Currents, Submarine Landslides and the 2006 Pingtung Earthquake off SW Taiwan, *Terrestrial Atmospheric and Oceanic Sciences*, *19*(6), 767-772.

Huertas, M. J., N. O. Arnaud, E. Ancochea, J. M. Cantagrel, and J. M. Fuster (2002), Ar-40/Ar-39 stratigraphy of pyroclastic units from the Canadas Volcanic Edifice (Tenerife, Canary Islands) and their bearing on the structural evolution, *Journal of Volcanology and Geothermal Research*, *115*(3-4), 351-365.

Huhnerbach, V., and D. G. Masson (2004), Landslides in the North Atlantic and its adjacent seas: an analysis of their morphology, setting and behaviour, *Marine Geology*, *213*(1-4), 343-362.

Hunt, J. E., R. B. Wynn, D. G. Masson, P. J. Talling, and D. A. H. Teagle (2011), Sedimentological and geochemical evidence for multistage failure of volcanic island landslides: A case study from Icod landslide on north Tenerife, Canary Islands, *Geochemistry Geophysics Geosystems*, *12*, 36.

Hurlimann, M., E. Turon, and J. Marti (1999a), Large landslides triggered by caldera collapse events in Tenerife, Canary Islands, *Physics and Chemistry of the Earth Part a-Solid Earth and Geodesy*, *24*(10), 921-924.

Hurlimann, M., A. Ledesma, and J. Marti (1999b), Conditions favouring catastrophic landslides on Tenerife (Canary Islands), *Terra Nova*, *11*(2-3), 106-111.

Hurlimann, M., J. Marti, and A. Ledesma (2000a), Mechanical relationship between catastrophic volcanic landslides and caldera collapses, *Geophysical Research Letters*, *27*(16), 2393-2396.

Hurlimann, M., J. O. Garcia-Piera, and A. Ledesma (2000b), Causes and mobility of large volcanic landslides: application to Tenerife, Canary Islands, *Journal of Volcanology and Geothermal Research*, *103*(1-4), 121-134.

Hurlimann, M., A. Ledesma, and J. Marti (2001), Characterisation of a volcanic residual soil and its implications for large landslide phenomena: application to Tenerife, Canary Islands, *Engineering Geology*, *59*(1-2), 115-132.

Hurlimann, A., J. Marti, and A. Ledesma (2004), Morphological and geological aspects related to large slope failures on oceanic islands - The huge La Orotava landslides on Tenerife, Canary Islands, *Geomorphology*, *62*(3-4), 143-158.

Hutton, E. W. H., and J. P. M. Syvitski (2004), Advances in the numerical modeling of sediment failure during the development of a continental margin, *Marine Geology*, *203*(3-4), 367-380.

I

Inouchi, Y., Y. Kinugasa, F. Kumon, S. Nakano, S. Yasumatsu, and T. Shiki (1996), Turbidites as records of intense palaeoearthquakes in Lake Biwa, Japan, *Sedimentary Geology,* 104, 117–125.

Iverson, R. M. (1995), Can magma-injection and groundwater forces cause massive landslides on Hawaiian volcanoes, *Journal of Volcanology and Geothermal Research*, *66*(1-4), 295-308.

Iverson, R. M., M. E. Reid, and R. G. LaHusen (1997), Debris-flow mobilization from landslides, *Annual Review of Earth and Planetary Sciences*, *25*, 85-138.

J

Jacobs, C.L. (1995), Mass wasting along the Hawaiian Ridge: giant debris avalanches, in *Atlas of Deep Water Environments. Architectural Style in Turbidite Systems* edited by K.T. Pickering, R.N. Hiscott, N.H. Kenyon, R. Ricci Lucchi and R.D.A. Smith, pp. 26-28, Chapman & Hall, New York.

Jarvis, I., and N. Higgs (1987), Trace-element mobility during early diagenesis in distal turbidites: late Quaternary of the Madeira Abyssal Plain, N Atlantic, in *Geology and geochemistry of Abyssal Plains,* 31, edited by P.P.E. Weaver and J. Thomson, Geological Society of London ,Special Publication, pp. 179-214, London.

Jarvis, I., J. Moreton, and M. Gérard, M. (1998), Chemostratigraphy of Madeira Abyssal Plain Miocene-Pleistocene turbidites, Site 950, in *Proceedings of the Ocean Drilling Programme Scientific Results*, 157, edited by P.P.E. Weaver, H.-U. Schmincke, J.V. Firth, and W. Duffield, pp. 535-558, College Station, TX (Ocean Drilling Program), doi:10.2973/odp.proc.sr.157.129.1998.

Jenkins, R. (1999), *X-ray Fluorescence Spectrometry*, 2nd edn, Wiley, Chichester.

Jones, K.P.N., I.N. McCave, and P.P.E. Weaver (1992), Textural and Dispersal Patterns of Thick Mud Turbidites from the Madeira Abyssal Plain, *Mar. Geol*., 107, 3, 149-173, doi:10.1016/0025-3227(92)90165-E.

Johnson, A.M. (1970), *Physical Processes in Geology*, Freeman, Cooper and Co., San Francisco.

K

Kastens, K. A. (1984), Earthquakes as a triggering mechanism for debris flows and turbidites on the Calabrian Ridge, *Marine Geology*, *55*(1-2), 13-33.

Kayen, R.E., and H.J. Lee (1991), Pleistocene slope instability of gas hydrate-laden sediment on the Beaufort Sea margin, *Marine Geotechnology*, *10*, 1-2, 125-141.

Keating, B. H., and W. J. McGuire (2000), Island edifice failures and associated tsunami hazards, *Pure and Applied Geophysics*, *157*(6-8), 899-955.

Keating, B. H., and W. J. McGuire (2004), Instability and structural failure at volcanic ocean islands and the climate change dimension, *Advances in Geophysics, Vol 47*, *47*, 175-271.

Kelfoun, K., T. Giachetti, and P. Labazuy (2010), Landslide-generated tsunamis at Reunion Island, *Journal of Geophysical Research-Earth Surface*, *115*, 17.

Kennett, J. P., and B. N. Fackler-Adams (2000), Relationship of clathrate instability to sediment deformation in the upper Neogene of California, *Geology*, *28*(3), 215-218.

Kennett, J., K.G. Cannariato, I.L. Hendy, and R.J. Behl (2003), *Methane hydrates in Quaternary climate change: The clathrate gun hypothesis*, American Geophysical Union, Washington.

Khan, M. A. (1974), Dynamic Implications of Mantle Hotspots, *Nature*, *251*(5476), 596-597.

Klitgort, K.D., and H. Schouten (1986), Plate kinematics of the central Atlantic, in *The Geology of North America, vol. M, The Western North Atlantic Region*, edited by P.R. Vogt and B.E. Tucholke, pp. 351-377, Geological Society of America, Boulder, Colorado.

Klump, J., D. Hebbeln, and G. Wefer, G. (2002), The impact of sediment provenance on barium-based productivity estimates, *Marine Geology*, 169, 3-4, 259-271.

Kneller, B. C., and M. J. Branney (1995), Sustained High-Density Turbidity Currents and the Deposition of Thick Massive Sands, *Sedimentology*, *42*(4), 607-616.

Kneller, B., and W. McCaffrey (1999), Depositional effects of flow nonuniformity and stratification within turbidity currents approaching a bounding slope: Deflection, reflection, and facies variation, *Journal of Sedimentary Research*, *69*(5), 980-991.

Kneller, B., and C. Buckee (2000), The structure and fluid mechanics of turbidity currents: a review of some recent studies and their geological implications, *Sedimentology*, *47*, 62-94.

Kneller, B., D. Edwards, W. McCaffrey, and R. Moore (1991), Oblique Reflection of Turbidity Currents, *Geology*, *19*(3), 250-252.

Kolla, V. (1993), Lowstand deep-water siliciclastic depositional systems: characteristics and terminologies in sequence stratigraphy and sedimentology, *Bull. Centres Rech. Explor.-Prod. Elf-Aquitain*, *17*, 1, 67-78.

Kolla, V., and D.B. Macurda (1988), Sea-level changes and timing of turbidity-current events in deep-sea fan systems, in *Sea-Level Changes – an Integrated Approach*, 42, edited by C.K. Wilgus, B.S. Hastings, C.G. Kendall, H.W. Posamentier, C.A. Ross, J.C. Van Wagoner, SEPM Special Publication, pp. 381-392.

Kolla, V., and M.A. Perlmutter (1993), Timing of turbidite sedimentation on the Mississippi Fan, *Bulletin of the American Association of Petroleum Geologists, 77*, 1129-1141.

Knoll, M., A. Hernandez-Guerra, B. Lenz, F. L. Laatzen, F. Machin, T. J. Muller, and G. Siedler (2002), The Eastern Boundary Current system between the Canary Islands and the African Coast, *Deep-Sea Research Part Ii-Topical Studies in Oceanography*, *49*(17), 3427-3440.

Krastel, S., H. U. Schmincke, C. L. Jacobs, R. Rihm, T. P. Le Bas, and B. Alibes (2001), Submarine landslides around the Canary Islands, *Journal of Geophysical Research-Solid Earth*, *106*(B3), 3977-3997.

Kuenen, P.H. (1951), Properties of turbidity currents of high density, in J.L. Hugh (ed), *Turbidity currents and the transportation of coarse sediments to deepwater*, A Symposium, SEPM Special Publication, 2, 14-33.

Kuenen, P.H. (1953), Significant features of graded bedding, *AAPG Bulletin*, 37, 1044-1066.

Kuenen, P.H. (1957), Sole markings of graded greywacke beds, *Journal of Geology*, 65, 231-258.

Kuenen, P.H., and C.L. Migliorini (1950), Turbidity Currents as a Cause of Graded Bedding, *Journal of Geology*, 58, 2, 91-127.

Kuijpers, A., Rispens, F.B., and Burger, A.W. (1984), Late Quaternary sedimentation and sedimentary processes on the Madeira Abyssal Plain, Eastern North Atlantic, in *Geological Studies in the Eastern North Atlantic*, 38(2), edited by A. Kuijpers, R.T.E. Schüttenhelm and J.W. Verbeek, Mededelingen Rijks Geologische Dienst. Nieuwe Serie, pp. 91-118, Rijks Geologische Dienst, Haarlem.

Kulikov, E. A., A. B. Rabinovich, R. E. Thomson, and B. D. Bornhold (1996), The landslide tsunami of November 3, 1994, Skagway Harbor, Alaska, *Journal of Geophysical Research-Oceans*, *101*(C3), 6609-6615.

Kvalstad, T. J., L. Andresen, C. F. Forsberg, K. Berg, P. Bryn, and M. Wangen (2005), The Storegga slide: evaluation of triggering sources and slide mechanics, *Marine and Petroleum Geology*, *22*(1-2), 245-256.

L

Labazuy, P. (1996), Recurrent landslides events on the submarine flank of Piton de la Fournaise volcano (Reunion island), in *Volcano Instability on the Earth and Other Planets*, 110, edited by W.J. McGuire, A.P. Jones and J. Neuberg, Geological Society of London, Special Publication, pp. 295-306, London.

Lamb, M. P., and D. Mohrig (2009), Do hyperpycnal-flow deposits record river-flood dynamics?, *Geology*, *37*(12), 1067-1070.

Large, R. R., J. B. Gemmell, H. Paulick, and D. L. Huston (2001), The alteration box plot: A simple approach to understanding the relationship between alteration mineralogy and lithogeochemistry associated with volcanic-hosted massive sulfide deposits, *Economic Geology and the Bulletin of the Society of Economic Geologists*, *96*(5), 957-971.

Lastras, G., M. Canals, R. Urgeles, M. De Batist, A. M. Calafat, and J. L. Casamor (2004), Characterisation of the recent BIG'95 debris flow deposit on the Ebro margin, Western Mediterranean Sea, after a variety of seismic reflection data, *Marine Geology*, *213*(1-4), 235-255.

Latter, J.H. (1981), Tsunami of Volcanic Origin: Summary of Causes, with Particular Reference to Krakatoa, 1883, *Bulletin of Volcanology*, *3*, 467-490.

Le Bas, M.J., R.W. Le Maitre, A. Streckeisen, B. Zannettin, and IUGS Subcommission on the Systematics of Igneous Rocks (1986), A Chemical Classification of Volcanic Rocks based on the Total Alkali-Silica Diagram, *J. Petrology*, *27*, 3, 745-750, doi:10.1093/petrology/27.3.745.

Le Bas, T. P., D. G. Masson, R. T. Holtom, and I. Grevemeyer (2007), Slope failures of the flanks of the southern Cape Verde Islands, *Submarine Mass Movements and Their Consequences*, *27*, 337-345.

Le Bas, T. P. A. Le Friant, G. Boudon, S. F. L. Watt, P. J. Talling, N. Feuillet, C. Deplus, C. Berndt, and M. E. Vardy (2011), Mutliple widespread landslides during the long-term evolution of a volcanic island: Insights from high-resolution seismic data, Monserrat, Lesser Antilles, *Geochem. Geophys. Geosys.*, 12(5), Q05006, doi:10.1029/2010GC003451.

Le Roy, P., F. Guillocheau, A. Pique, and A. M. Morabet (1998), Subsidence of the Atlantic Moroccan margin during the Mesozoic, *Canadian Journal of Earth Sciences*, *35*(4), 476-493.

LeBlond, A.B., and A.T. Jones (1995), Underwater landslides ineffective at tsunami generation, *Science of Tsunami Hazards*, 13 (1), 25-26.

Lebreiro, S. M., I. N. McCave, and P. P. E. Weaver (1997), Late Quaternary turbidite emplacement on the Horseshoe abyssal plain (Iberian margin), *Journal of Sedimentary Research*, *67*(5), 856-870.

Lebreiro, S.M., P.P.E. Weaver, and R.W. Howe (1998), Sedimentation on the Madeira Abyssal Plain: the history of turbidite infill, in *Proceedings of the Ocean Drilling Programme Scientific Results*, 157, edited by P.P.E. Weaver, H.-U. Schmincke, J.V. Firth, and W. Duffield, College Station, TX (Ocean Drilling Program), pp. 523-531, doi:10.2973/odp.proc.sr.157.129.1998.

Lee, H. J. (2009), Timing of occurrence of large submarine landslides on the Atlantic Ocean margin, *Marine Geology*, *264*(1-2), 53-64.

Lee, H.J., R.E. Kayen, J.V. Gardner, and J. Locat (2003), Characteristics of several tsunamigenic submarine landslides, *Submarine Mass Movements and Their Consequences*, *19*, 357-366.

Leeder, M. (1999), Sedimentology and Sedimentary Basins: From Turbulence to Tectonics, *Blackwell Science Ltd.*, Oxford.

Lenat, J. F., P. Vincent, and P. Bachelery (1989), The off-shore continuation of an active basaltic volcano: Piton de la Fournaise (Réunion Island, Indian Ocean); structural and geomorphological interpretation from sea beam mapping, *Journal of Volcanology and Geothermal Research*, *36*(1-3), 1-36.

Leonhardt, R., and H. C. Soffel (2006), The growth, collapse and quiescence of Teno volcano, Tenerife: new constraints from paleomagnetic data, *International Journal of Earth Sciences*, *95*(6), 1053-1064.

Lepland, Aivo., Andersen, T.J., Lepland, Aave., Arp, H.P.H., Alve, E., Breedveld, G.D., & Rindby, A. Sedimentation and chronology of heavy metal pollution in Oslo harbour, Norway, *Marine Pollution Bulletin*, *60*, 1512-1522.

Lick, W. (1982), Entrainment, Deposition and Transport of Fine-grained Sediments in Lakes, *Hydrobiologia*, *91-2*(JUL), 31-40.

Lipman, P. W., W. R. Normark, J. G. Moore, J. B. Wilson, and C. E. Gutmacher (1988), Giant Submarine Alika Debris Slide, Mauna Loa, Hawaii, *Journal of Geophysical Research-Solid Earth and Planets*, *93*(B5), 4279-4299.

Lisiecki, L. E., and M. E. Raymo (2005), A Pliocene-Pleistocene stack of 57 globally distributed benthic delta O-18 records, *Paleoceanography*, *20*(1), 17.

Llanes, P., A. Munoz, A. Munoz-Martin, J. Acosta, P. Herranz, A. Carbo, C. Palomo, and Z. E. E. W. Grp (2003), Morphological and structural analysis in the Anaga offshore massif, Canary Islands: fractures and debris avalanches relationships, *Marine Geophysical Researches*, *24*(1-2), 91-112.

Llanes, P., R. Herrera, M. Gomez, A. Munoz, J. Acosta, E. Uchupi, and D. Smith (2009), Geological evolution of the volcanic island La Gomera, Canary Islands, from analysis of its geomorphology, *Marine Geology*, *264*(3-4), 123-139.

Locat, J., and H. J. Lee (2002), Submarine landslides: advances and challenges, *Canadian Geotechnical Journal*, *39*(1), 193-212.

Lo Giudice, E., and E. Rasa (1992), Very shallow earthquakes and brittle deformation in active volcanic areas: The Eatean region as an example, *Tectnophysics*, *202*, 2-4, 257-268, doi: dx.doi.org/10.1016/0040-1951(92)90111-I.

Longpre, M. A., V. R. Troll, T. R. Walter, and T. H. Hansteen (2009), Volcanic and geochemical evolution of the Teno massif, Tenerife, Canary Islands: Some repercussions of giant landslides on ocean island magmatism, *Geochemistry Geophysics Geosystems*, *10*, 31.

Longpre, M. A., J. P. Chadwick, J. Wijbrans, and R. Iping (2011), Age of the El Golfo debris avalanche, El Hierro (Canary Islands): New constraints from laser and furnace (40)Ar/(39)Ar dating, *Journal of Volcanology and Geothermal Research*, *203*(1-2), 76-80.

Lonsdale, P. (1982), Sediment drifts of the Northeast Atlantic and their relationship to the observed abyssal currents, *Bull. Inst. Geol. Bassin d'Aquitaine, Bordeaux*, 31, 141-150.

Lovholt, F., C. B. Harbitz, and K. B. Haugen (2005), A parametric study of tsunamis generated by submarine slides in the Ormen Lange/Storegga area off western Norway, *Marine and Petroleum Geology*, *22*(1-2), 219-231.

Lovholt, F., G. Pedersen, and G. Gisler (2008), Oceanic propagation of a potential tsunami from the La Palma Island, *Journal of Geophysical Research-Oceans*, *113*(C9), 21.

Lowe, D. R. (1976), Subaqueous Liquified and Fluidised Sediment Flows and their Deposits, *Sedimentology*, *23*(3), 285-308.

Lowe, D.R. (1979), Sediment gravity flows: their classification and some probems of application to natural flows and deposits, in *Geology of Continental Slopes*, edited by L.J. Doyle and O.H. Pilkey, *Soc. Econ. Paleontol. Mineral. Spec. Publ.*, 27.

Lowe, D. R. (1982), Sediment Gravity Flows: II Depositional Models with Special Reference to the Deposits of High-Density Turbidity Currents, *Journal of Sedimentary Petrology*, *52*(1), 279-298.

Lowemark, L., M. Jakobsson, M. Morth, and J. Backman (2008), Arctic Ocean manganese contents and sediment colour cycles, *Polar Research*, *27*(2), 105-113.

Lowemark, L., H. F. Chen, T. N. Yang, M. Kylander, E. F. Yu, Y. W. Hsu, T. Q. Lee, S. R. Song, and S. Jarvis (2011), Normalizing XRF-scanner data: A cautionary note on the interpretation of high-resolution records from organic-rich lakes, *Journal of Asian Earth Sciences*, *40*(6), 1250-1256.

M

MacDonald, H. A., R. B. Wynn, V. A. I. Huvenne, J. Peakall, D. G. Masson, P. P. E. Weaver, and S. D. McPhail (2011), New insights into the morphology, fill, and remarkable longevity (>0.2 m.y.) of modern deep-water erosional scours along the northeast Atlantic margin, *Geosphere*, 7(4), 845-867, doi:10.1130/GES00611.1.

Mader, C.L. (2001), Modelling the La Palma landslide tsunami, *Science of Tsunami Hazards*, *19*, 150-170.

Maramai, A., L. Graziani, G. Alessio, P. Burrato, L. Colini, L. Cucci, R. Nappi, A. Nardi, and G. Vilardo (2005), Near- and far-field survey report of the 30 December 2002 Stromboli (Southern Italy) tsunami, *Marine Geology*, *215*(1-2), 93-106.

Marinoni, L. B., and G. Pasquare (1994), TECTONIC EVOLUTION OF THE EMERGENT PART OF A VOLCANIC OCEAN ISLAND - LANZAROTE, CANARY-ISLANDS, *Tectonophysics*, *239*(1-4), 111-137.

Marsh, R., R. A. Mills, D. R. H. Green, I. Salter, and S. Taylor (2007), Controls on sediment geochemistry in the Crozet region, *Deep-Sea Research Part Ii-Topical Studies in Oceanography*, *54*(18-20), 2260-2274.

Marshall, M.H., Lamb, H., Huws, D., Davies, S.J., Bates, R., Bloemendal, J., Boyle, J., Leng, M.J., Umer, M., & Bryant, C. In press, Late Pleistocene and Holocene drought events in Lake Tana, the source of the Blue Nile, *Global and Planetary Change*, DOI: 10.1016/j.gloplacha.2011.06.004.

Marti, J., and A. Gudmundsson (2000), The Las Canadas caldera (Tenerife, Canary Islands): an overlapping collapse caldera generated by magma-chamber migration, *Journal of Volcanology and Geothermal Research*, *103*(1-4), 161-173.

Marti, J., J. Mitjavila, and V. Arana (1994), Stratigraphy, structure and geochronology of the La Canadas caldera, Tenerife (Canary Islands), *Geological Magazine*, *131*(6), 715-727.

Marti, J., G. J. Ablay, and S. Bryan (1996), The Canary Islands: An example of structural control on the growth of large oceanic-island volcanoes - Comment, *Journal of Volcanology and Geothermal Research*, *72*(1-2), 143-149.

Marti, J., M. Hurlimann, G. J. Abley, and A. Gudmundsson (1997), Vertical and lateral collapses on Tenerife (Canary Islands) and other volcanic ocean islands, *Geology*, *25*(10), 879-882.

Marti, J., C. Soriano, I. Galindo, and R. A. F. Cas (2010), Resolving problems with the origin of the Las Cañadas caldera (Tenerife, Canary Islands): Los Roques de García Formation – Part of a major debris avalanche or an in situ, stratified, edifice-building succession? in Stratigraphy and Geology of Volcanic Areas, edited by G. Gropelli and L. Viereck-Goette, *Geol. Soc. Am. Spec. Pap.*, 464, 113-132, doi:10.1130/2010.2464(06).

Martin, G., Finn, W., Seed, H. (1975), Fundamentals displacements due to cyclic wave loading, *J. Geotechn. Engineer. Div.*, ASCE 107, 1129-1149.

Martinsen, O.J. (1989), Styles of soft-sediment deformation on a Namurian (Carboniferous) delta slope, western Irish Namurian Basin, Ireland, in *Deltas: Sites and Traps for Fossil Fuels*, edited by M.K.G. Whateley and K.T. Pickering, Spec. Publ. Geol. Soc. Lond., 41.

Martinson, D. G., N. G. Pisias, J. D. Hays, J. Imbrie, T. C. Moore, and N. J. Shackleton (1987), Age dating and the orbital theory of the ice ages: Development of a high-resolution 0 to 300,000-year chronostratigraphy, *Quaternary Research*, *27*(1), 1-29.

Maslin, M., N. Mikkelsen, C. Vilela, and B. Haq (1998), Sea-level- and gas-hydrate-controlled catastrophic sediment failures of the Amazon Fan, *Geology*, *26*(12), 1107-1110.

Maslin, M., M. Owen, S. Day, and D. Long (2004), Linking continental-slope failures and climate change: Testing the clathrate gun hypothesis, *Geology*, *32*(1), 53-56.

Masson, D. G. (1994), Late Quaternary turbidity current pathways to the Madeira Abyssal Plain and some constraints on turbidity current mechanisms, *Basin Research*, *6*(1), 17-33.

Masson, D. G. (1996), Catastrophic collapse of the volcanic island of Hierro 15 ka ago and the history of landslides in the Canary Islands, *Geology*, *24*(3), 231-234.

Masson, D. G., and T. P. Le Bas (2008), Flank collapse and large-scale landsliding in the Cape Verde Islands, off West Africa, *Geochem. Geophys. Geosys.*, 9, Q07015, doi:10.1029/2008GC001983.

Masson, D. G., R. B. Kidd, J. V. Gardner, Q. J. Hugget, and P. P. E. Weaver (1992), Saharan Continental Rise: facies distribution and sediment slides, in *Geologic Evolution of Atlantic Continental Rises*, edited by C. W. Poag and P. C. de Graciansky, 327-343, Van Nostrand Reinhold, New York.

Masson, D. G., A. B. Watts, M. J. R. Gee, R. Urgeles, N. C. Mitchell, T. P. Le Bas, and M. Canals (2002), Slope failures on the flanks of the western Canary Islands, *Earth-Science Reviews*, *57*(1-2), 1-35.

Masson, D. G., C. B. Harbitz, R. B. Wynn, G. Pedersen, and F. Lovholt (2006), Submarine landslides: processes, triggers and hazard prediction, *Philosophical Transactions of the Royal Society a-Mathematical Physical and Engineering Sciences*, *364*(1845), 2009-2039.

Masson, D. G., R. G. Arzola, R. B. Wynn, J. E. Hunt, and P. P. E. Weaver (2011), Seismic triggering of landslides and turbidity currents offshore Portugal, *Geochemistry Geophysics Geosystems*, *12*, 19.

Matthewson, A. P., G. B. Shimmield, D. Kroon, and A. E. Fallick (1995), A 300 kyr high-resolution aridity record of the North African Continent, *Paleoceanography*, *10*(3), 677-692.

McAnally, W. H., C. Friedrichs, D. Hamilton, E. Hayter, P. Shrestha, H. Rodriguez, A. Sheremet, A. Teeter, and A. T. C. M. Flu (2007), Management of fluid mud in estuaries, bays, and lakes. I: Present state of understanding on character and behavior, *Journal of Hydraulic Engineering-Asce*, *133*(1), 9-22.

McCave, I. N., and S. A. Swift (1976), Physical model for the rate of deposition of fine-grained sediments in the deep sea, *Geological Society of America Bulletin*, *87*(4), 541-546.

McCave, I. N., and K. P. N. Jones (1988), Deposition of ungraded muds from non-turbulent turbidity currents, *Nature*, *333*(6170), 250-252.

McGuire, W. J. (1996), Volcano instability: A review of contemporary themes, in *Volcano Instability on the Earth and Other Planets*, 110, edited by W.J. McGuire, A.P. Jones, Geological Society of London, Special Publication, pp. 1-23, London.

McGuire, W.J. (2006), Lateral collapse and tsunamigenic potential of marine volcanoes, in *Mechanisms of Activity and Unrest at Large Calderas,* 269, edited by C. Troise and D. De Natale, pp. 121–140, Blackwell, Oxford.

McGuire, W. J., A. D. Pullen, and S. J. Saunders (1990), Recent dyke-induced large-scale block movement at Mount Etna and potential slope failure, *Nature*, *343*(6256), 357-359.

McGuire, W. J., J. B. Murray, A. D. Pullen, and S. J. Saunders (1991), Ground deformation monitoring at Mt Etna – evidence for dyke emplacement and slope instability, *Journal of the Geological Society*, *148*, 577-583.

McHugh, C. M., L. Seeder, N. Braudy, M.-H. Cormier, M.B. Davis, J.B. Diebold, N. Dieudonne, R. Douilly. S.P.S. Gulick, M.J. Hornbach, H.E. Johnson, K.R. Mishkin, C.C. Sorlien, M.S. Steckler, S.J. Symithe, and J. Templeton (2011), Offshore sedimentary effects of the 12 January 2010 Haiti earthquake, *Geology*, *39*(8), 723-726.

McMurtry, G. M., P. Watts, G. J. Fryer, J. R. Smith, and F. Imamura (2004a), Giant landslides, mega-tsunamis, and paleo-sea level in the Hawaiian Islands, *Marine Geology*, *203*(3-4), 219-233.

McMurtry, G. M., G. J. Fryer, D. R. Tappin, I. P. Wilkinson, M. Williams, J. Fietzke, D. Garbe-Schoenberg, and P. Watts (2004b), Megatsunami deposits on Kohala volcano, Hawaii, from flank, collapse of Mauna Loa, *Geology*, *32*(9), 741-744.

Mehl, K. W., and H. U. Schmincke (1999), Structure and emplacement of the Pliocene Roque Nublo debris avalanche deposit, Gran Canaria, Spain, *Journal of Volcanology and Geothermal Research*, *94*(1-4), 105-134.

Mehta, A. J. (1991), Understanding Fluid Mud in a Dynamic Environment, *Geo-Marine Letters*, *11*(3-4), 113-118.

Micallef, A., D. G. Masson, C. Berndt, and D. A. V. Stow (2007), Morphology and mechanics of submarine spreading: A case study from the Storegga Slide, *Journal of Geophysical Research-Earth Surface*, *112*(F3), 21.

Middleton, G. V. (1993), Sediment deposition from turbidity currents, *Annual Review of Earth and Planetary Sciences*, *21*, 89-114.

Middleton, G.V., and M.A. Hampton (1973), Sediment Gravity Flows: mechanics of flow and deposition, in *Turbidites and Deep-water Sedimentation*, edited by G.V Middleton and A.H. Bouma, SEPM Pacific Section Short Course, Anaheim, California.

Middleton, G.V., and M.A. Hampton (1976), Subaqueous sediment transport and deposition by sediment gravity flows, in *Marine Sediment Transport and Environmental Management*, edited by D.J. Stanley and D.J.P. Swift, John Wiley and Sons, New York.

Mienert, J., J. Posewang, and M. Baumann (1998), Gas hydrates along the northeastern Atlantic margin: instabilities and possible release of methane, in *Gas Hydrates: Relevence of World Margin Stability and Climate Change*, 137, edited by J.-P. Henriet, Geological Society of London, Special Publications, pp. 275-291, doi:10.1144/GSL.SP.1998.137.01.22.

Mienert, J., M. Vanneste, S. Bunz, K. Andreassen, H. Haflidason, and H. P. Sejrup (2005), Ocean warming and gas hydrate stability on the mid-Norwegian margin at the Storegga Slide, *Marine and Petroleum Geology*, *22*(1-2), 233-244.

Milia, A., M. M. Torrente, and A. Zuppetta (2003), Offshore debris avalanches at Somma-Vesuvius volcano (Italy): implications for hazard evaluation, *Journal of the Geological Society*, *160*, 309-317.

Miller, K. G., M. A. Kominz, J. V. Browning, J. D. Wright, G. S. Mountain, M. E. Katz, P. J. Sugarman, B. S. Cramer, N. Christie-Blick, and S. F. Pekar (2005), The phanerozoic record of global sea-level change, *Science*, *310*(5752), 1293-1298.

Mitchell, N. C., D. G. Masson, A. B. Watts, M. J. R. Gee, and R. Urgeles (2002), The morphology of the submarine flanks of volcanic ocean islands - A comparative study of the Canary and Hawaiian hotspot islands, *Journal of Volcanology and Geothermal Research*, *115*(1-2), 83-107.

Mitchum, R.M. 1985, Seismic Stratigraphic Expression of Submarine Fans: Chapter 7, In: Orvillle, R.B. & Woolverton, D.G. (ed) *Seismic Stratigraphy II: An Integrated Approach to Hydrocarbon Exploration*, AAPG Special Volumes, M39, 117-136.

Mitchum, R.M., Vail, P.R. & Sangree, J.B. 1977a, Seismic stratigraphy and global changes of sea level, Part 6: stratigraphic interpretation of seismic reflection patterns in depositional sequences, In: Payton, C.E. (eds) *Seismic Stratigraphy – Application to Hydrocarbon Exploration*, Mem. Am. Ass. petrol. Geol., 26, Tulsa, USA.

Mitchum, R.M., Vail, P.R. & Thompson III, S. 1977b, Seismic stratigraphy and global changes of sea level, Part 2: The depositional sequence as a basic unit for stratigraphic analysis, In: Payton, C.E. (eds) *Seismic Stratigraphy – Application to Hydrocarbon Exploration*, Mem. Am. Ass. petrol. Geol., 26, Tulsa, USA.

Mitjavila, J. (1990), Aplicación de técnicas de geoquímica isotopic y de geocronología al estudio vulcanológico del edifice de Diego Hernández y su relacíon con la Caldera de Las Cañadas (Tenerife), PhD Thesis, Universidad de Barcelona, Barcelona.

Mitjavila, J., and Villa, I. (1993), Temporal evolution of Diego Hernández formation (Las Cañadas, Tenerife) and confirmation of the age of the caldera using the ^{40}Ar-^{39}Ar method, *Rev. Soc. Geol. Esp.,* 6, 61-65.

Montalto, A., S. Vinciguerra, S. Menza, and G. Patane (1996), Recent seismicity of Mount Etna: Implications for flank instability, in *Volcano Instability on the Earth and Other Planets*, 110, edited by W.J. McGuire, A.P. Jones and J. Neuberg, Geological Society of London, Special Publication, pp. 169-177, London.

Moore, J. G., D. A. Clague, R. T. Holcomb, P. W. Lipman, W. R. Normark, and M. E. Torresan (1989), Prodigious submarine landslides on the Hawaiian Ridge, *Journal of Geophysical Research-Solid Earth and Planets*, *94*(B12), 17465-17484.

Moore, J. G., W. R. Normark, and R. T. Holcomb (1994a), Giant Hawaiian landslides, *Science*, *264*(5155), 46-47, doi:10.1146/annurev.ea.22.050194.001003.

Morabet, A.M., R. Bouchta, and H. Jabour (1998), An Overview of the Petroleum Systems of Morocco, in *Petroleum Geology of North Africa*, 132, edited by D.S. MacGregor, R.T.J. Moody, and D.D. Clark-Lowes, Geological Society of London, Special Publications, pp. 283-281, doi:10.1144/GSL.SP.1998.132.01.16.

Moreno, A., S. Nave, H. Kuhlmann, M. Canals, J. Taragarona, T. Freudenthal, and F. Abrantes (2002), Productivity response in the North Canary Basin to climate changes during the last 250 000 yr: a multi-proxy approach, *Earth and Planetary Science Letters*, *196*, 147-159.

Morgan, W. J. (1971), Convection plumes in the lower mantle, *Nature*, *230*(5288), 42-43.

Morgan, W. J. (1983), Hotspot tracks and early rifting of the Altantic, *Tectonophysics*, *94*(1-4), 123-139.

Moy, C. M., R. B. Dunbar, T. P. Guilderson, N. Waldmann, D. A. Mucciarone, C. Recasens, D. Ariztegui, J. A. Austin, and F. S. Anselmetti (2011), A geochemical and sedimentary record of high southern latitude Holocene climate evolution from Lago Fagnano, Tierra del Fuego, *Earth and Planetary Science Letters*, *302*(1-2), 1-13.

Mulder, T., and P. Cochonat (1996), Classification of offshore mass movements, *Journal of Sedimentary Research*, *66*(1), 43-57.

Mulder, T., and J. Alexander (2001), The physical character of subaqueous sedimentary density flows and their deposits, *Sedimentology*, *48*(2), 269-299.

Mulder, T., B. Savoye, and J. P. M. Syvitski (1997), Numerical modelling of a mid-sized gravity flow: The 1979 Nice turbidity current (dynamics, processes, sediment budget and seafloor impact), *Sedimentology*, *44*(2), 305-326.

Mulder, T., O. Weber, P. Anschutz, F. J. Jorissen, and J. M. Jouanneau (2001), A few months-old storm-generated turbidite deposited in the Capbreton Canyon (Bay of Biscay, SW France), *Geo-Marine Letters*, *21*(3), 149-156.

Murray, J. B., and B. Voight (1996), Slope stability and eruption prediction on the eastern flank of Mount Etna, in *Volcano Instability on the Earth and Other Planets*, 110, edited by W.J. McGuire, A.P. Jones and J. Neuberg, Geological Society of London, Special Publication, pp. 111-114, London.

Murty, T. S. (2003), Tsunami wave height dependence on landslide volume, *Pure and Applied Geophysics*, *160*(10-11), 2147-2153.

N

Nagao, S., and S. Nakashima (1992), The factors affecting vertical colour variations of North Atlantic Madeira Abyssal Plain sediments, *Marine Geology*, *109*(1-2), 83-94.

Nakajima, T. (2000), Initiation processes of turbidity currents; implications for assessments of recurrence intervals of offshore earthquakes using turbidites, *Bulletin of the Geological Survey of Japan*, *51*, 79–87.

Nakajima, T., and Y. Kanai (2000), Sedimentary features of seismoturbidites triggered by the 1983 and older historical earthquakes in the eastern margin of the Japan Sea, *Sedimentary Geology*, *135*, 1–19.

Nederbragt, A.J., R.B. Dunbar, A.T. Osborn, A. Palmer, J.W. Thurow, and T. Wagner (2006), Sediment colour analysis from digital images and correlation with sediment composition, in *New Techniques in Sediment Core Analysis*, 267, edited by R.G. Rothwell, Geological Society of London, Special Publication, pp. 113-128, London.

Nemec, W., and R.J. Steel (1984), Alluvial and coastal conglomerates: their significant features and some comments on gravelly mass-flow deposits, in *Sedimentology of Gravels and Conglomerates*, 10, edited E.H. Koster and R.J. Steel, Memoires of the Canadaian Society of Petroleum Geologists, pp. 1-31.

Normark, W.R., and D.J.W. Piper (1991), Initiation processes and flow evolution of turbidity currents implications for the depositional record, in *From Shoreline to Abyss*, 46, edited by R.H. Osborne, SEPM Special Publication, pp. 207-230.

Nisbet, E. G., and D. J. W. Piper (1998), Giant submarine landslides, *Nature*, *392*(6674), 329-330.

O

O'Leary, D. (1991), Structure and morphology of submarine slab slides: clues to origin and behaviour, *Marine Geotechnology*, *10*, 53-69.

Oehler, J. F., P. Labazuy, and J. F. Lenat (2004), Recurrence of major flank landslides during the last 2-Ma-history of Reunion Island, *Bulletin of Volcanology*, *66*(7), 585-598.

Oehler, J. F., B. V. de Vries, and P. Labazuy (2005), Landslides and spreading of oceanic hot-spot and arc shield volcanoes on Low Strength Layers (LSLs): an analogue modeling approach, *Journal of Volcanology and Geothermal Research*, *144*(1-4), 169-189.

Oehler, J. F., J. F. Lenat, and P. Labazuy (2008), Growth and collapse of the Reunion Island volcanoes, *Bulletin of Volcanology*, *70*(6), 717-742.

Orsi, A. H., G. C. Johnson, and J. L. Bullister (1999), Circulation, mixing, and production of Antarctic Bottom Water, *Prog. Oceanogr.*, 43, 55-109.

Oyarzun, R., M. Doblas, J. LopezRuiz, and J. M. Cebria (1997), Opening of the central Atlantic and asymmetric mantle upwelling phenomena: Implications for long-lived magmatism in western North Africa and Europe, *Geology*, *25*(8), 727-730.

P

Pantin, H. M. (1979), Interaction between velocity and effective density in turbidity flow – phase-plane analysis, with criteria for autosuspension, *Marine Geology*, *31*(1-2), 59-99.

Pararas-Carayannis, G. (2002), Evaluation of the threat of mega tsunami generation from postulated massive slope failures of island stratovolcanoes on La Palma, Canary Islands, and on the island of Hawaii, *Science of Tsunami Hazards*, *20*(5), 251-277.

Paris, R., H. Guillou, J. C. Carracedo, and F. J. P. Torrado (2005), Volcanic and morphological evolution of La Gomera (Canary Islands), based on new K-Ar ages and magnetic stratigraphy: implications for oceanic island evolution, *Journal of the Geological Society*, *162*, 501-512.

Paris, R., T. Giachetti, J. Chevalier, H. Guillou, and N. Frank (2011), Tsunami deposits in Santiago Island (Cape Verde archipelago) as possible evidence of a massive flank failure of Fogos volcano, *Sedimentary Geology*, *239*(3-4), 129-145.

Parker, E.J., C. Traverso, R. Moore, T. Evans, and N. Usher (2008), Evaluation of Landslide Impact on Deepwater Submarine Pipelines, *Offshore Technology Conference*, 5-8 May 2008, Houston Texas.

Parker, G., M. Garcia, Y. Fukushima, and W. Yu (1987), Experiments on Turbidity Currents over an Erodible Bed, *Journal of Hydraulic Research*, *25*(1), 123-147.

Pearce, T. J., and I. Jarvis (1992a), Composition and provenance of turbidite sands: Late Quaternary: Late Quaternary, Madeira Abyssal Plain, *Marine Geology*, *109*(1-2), 21-51.

Pearce, T. J., and I. Jarvis (1992b), Applications of geochemical data to modelling sediment dispersal patterns in distal turbidites; late Quaternary of the Madeira Abyssal Plain, *Journal of Sedimentary Research*, *Journal of Sedimentary Petrology*, *62*(6), 1112-1129.

Pearce, T.J., and I. Jarvis (1995), High-resolution chemostratigraphy of Quaternary distal turbidites: a case study of new methods for the analysis and correlation of barren sequences, in *Non-biostratigraphical methods of dating and correlation*, 89, edited by R.E. Dunay and E.A. Hailwood, E.A., Geological Society of London, Special Publication, pp. 107–143, London.

Perez-Torrado, F. J., J. C. Carracedo, and J. Mangas (1995), Geochronology and Stratigraphy of teh Roque Nublo Cycle, Gran Canaria, Canary Islands, *Journal of the Geological Society*, *152*, 807-818.

Perez-Torrado, F. J., R. Paris, M. C. Cabrera, J. L. Schneider, P. Wassmer, J. C. Carracedo, A. Rodriguez-Santana, and F. Santana (2006), Tsunami deposits related to flank collapse in oceanic volcanoes: The Agaete Valley evidence, Gran Canaria, Canary Islands, *Marine Geology*, *227*(1-2), 135-149.

Pickering, K. T. (1979), Possible retrogressive flow slide deposits from the Kongsfjord Formation: a Precambrian submarine fan, Finnmark, N. Norway, *Sedimentology*, *26*(2), 295-305.

Pickering, K., D. Stow, M. Watson, and R. Hiscott (1986), Deep-water Facies, Processes and Models – A Review and Classical Scheme for Modern and Ancient Sediments, *Earth-Science Reviews*, *23*(2), 75-174.

Pierau, R., T. J. J. Hanebuth, S. Krastel, and R. Henrich (2010), Late Quaternary climatic events and sea-level changes recorded by turbidite activity, Dakar Canyon, NW Africa, *Quaternary Research*, *73*(2), 385-392.

Pierau, R., R. Henrich, I. Preiss-Daimler, S. Krastel, and J. Geersen (2011), Sediment transport and turbidite architecture in the submarine Dakar Canyon off Senegal, NW-Africa, *Journal of African Earth Sciences*, *60*(3), 196-208.

Piper, D.J.W., and W.R. Normark (1982), Effects of the 1929 Grand Banks earthquake on the continental slope off eastern Canada, in *Geol. Surv. Can. Paper*, 82-1B, 147-151.

Piper, D. J. W., and W. R. Normark (2009), Processes that initiate Turbidity Currents and their influence on Turbidites: a marine geology perspective, *Journal of Sedimentary Research*, *79*(5-6), 347-362.

Piper, D. J. W., A. N. Shor, J. A. Farre, S. Oconnell, and R. Jacobi (1985), Sediment Slides and Turbidity Currents on the Laurentian Fan – sidescan sonar investigations near the epicentre of the 1929 Grand Banks Earthquake, *Geology*, *13*(8), 538-541.

Piper, D. J. W., P. Cochonat, and M. L. Morrison (1999), The sequence of events around the epicentre of the 1929 Grand Banks earthquake: initiation of debris flows and turbidity current inferred from sidescan sonar, *Sedimentology*, *46*(1), 79-97.

Piper, D.J.W., D.C. Mosher, B.-J. Gauley, K. Jenner, and D.C. Campbell (2003), The chronology and recurrence of submarine mass movements on the continental slope off southeastern Canada, in *Submarine Mass Movements and their Consequences*, *19*, edited by J. Locat and J. Mienert, pp. 299–306, Kluwer Academic Publishers, Netherlands.

Pique, A., and A. Michard (1989), Moroccan Hercynides – A Synopsis – The Paleozoic Sedimentary and Tectonic Evolution at the Northern Margin of West-Africa, *American Journal of Science*, *289*(3), 286-330.

Pirmez, C., and J. Imran (2003), Reconstruction of turbidity currents in Amazon Channel, *Marine and Petroleum Geology*, *20*(6-8), 823-849.

Plink-Bjorklund, P., and R. J. Steel (2004), Initiation of turbidity currents: outcrop evidence for Eocene hyperpycnal flow turbidites, *Sedimentary Geology*, *165*(1-2), 29-52.

Porter, M., C. Logue, K.W. Savigny, F. Esford, and I. Bruce (2004), Estimating the Influence of Natural Hazards on Pipeline Risk and System Reliability, *Proceedings of the International Pipeline Conference*, October 2004, Calgary, Canada.

Posamentier, H.W., and P.R. Vail (1988), Eustatic controls on clastic deposition II – sequence and system tract models, in *Sea-Level Changes – an Integrated Approach* Wilgus, 42, edited by C.K., Hastings, B.S., Kendall, C.G., Posamentier, H.W., Ross, C.A., and J.C. Van Wagoner, Spec. Publ. Soc. Econ. Paleont. Miner., pp. 125-154.

Posamentier, H.W., M.T. Jervey and P.R. Vail (1988), Eustatic controls on clastic deposition I – conceptual framework, in *Sea-Level Changes – an Integrated Approach*, 42, edited by C.K. Wilgus, B.S. Hastings, C.G. Kendall, H.W. Posamentier, C.A. Ross, and J.C. Van Wagoner, Spec. Publ. Soc. Econ. Paleont. Miner., pp. 110-124.

Prins, M. A., and G. Postma (2000), Effects of climate, sea level, and tectonics unraveled for last deglaciation turbidite records of the Arabian Sea, *Geology*, *28*(4), 375-378.

Prior, D.B., and J.M. Coleman (1982), Active slides and flows in underconsolidated marine sediments on the slopes of the Mississippi delta, in *Marine Slides and Other Mass Movements*, 6, edited by S. Saxon and J.K. Nieuwenhuis, pp. 21-49, Plenum, New York.

Prior, D.B., B.D. J.M. Coleman, and B.D. Bornhold (1982), Results of a known sea floor instability event, *Geomarine Letters*, *2*, 117-122.

Prospero, J.M. (2006), Saharan Dust Impacts and Climate Change, *Oceanography*, *19*, 2, 60-61.

Prospero, J. M., and T. N. Carlson (1972), Vertical and Areal Distribution of Saharan Dust over Western Equatorial North-Atlantic, *Journal of Geophysical Research*, *77*(27), 5255-5265.

Postma, G. (1986), Classification of sediment gravity-flow deposits based on flow conditions during sedimentation, *Geology*, 14, 291-294.

Q

Quidelleur, X., A. Hildenbrand, and A. Samper (2008), Causal link between Quaternary paleoclimatic changes and volcanic islands evolution, *Geophysical Research Letters*, *35*(2), 5.

R

Rabinovich, A. B., R. E. Thomson, E. A. Kulikov, B. D. Bornhold, and I. V. Fine (1999), The landslide-generated tsunami of November 3, 1994 in Skagway Harbor, Alaska: A case study, *Geophysical Research Letters*, *26*(19), 3009-3012.

Reynolds, O, (1885), On the dilatancy of media composed of rigid particles in contact, with experimental illustrations, *Philosophical Magazine*, Series 5, 20, 469-481.

Ridley, W. I. (1971), Origin of some collapse structures in the Canary Islands, *Geological Magazine*, *108*(6), 477-&.

Ries, A. C. (1978), Opening of the Bay of Biscay, *Earth-Science Reviews*, *14*(1), 35-63.

Rihm, R., C. L. Jacobs, S. Krastel, H. U. Schmincke, and B. Alibes (1998), Las Hijas seamounts - the next Canary Island?, *Terra Nova*, *10*(3), 121-125.

Roa, K. (2003), Nature and origin of toreva remnants and volcaniclastics from La Palma, Canary Islands, *Journal of Volcanology and Geothermal Research*, *125*(3-4), 191-214.

Roberts, J. A., and A. Cramp (1996), Sediment stability on the western flanks of the Canary Islands, *Marine Geology*, *134*(1-2), 13-30.

Robertson, A. H. F., and C. J. Stillman (1979), Submarine volcanic and associated sedimentary rocks of the Fuerteventura Basal Complex, Canary Islands, *Geological Magazine*, *116*(3), 203-214.

Rodehorst, U., Schmincke, H.-U., and Sumita, M. (1998), Geochemistry and petrology of Pleistocene ash layers erupted at the Las Cañadas Edifice, in *Proceedings of the Ocean Drilling Program, Scientific Results*, 157, edited by P.P.E. Weaver, H.-U. Schmincke, J.V. Firth and W. Duffield, College Station, TX (Ocean Drilling Program), pp. 315-328.

Rodine, J. D., and A. M. Johnson (1976), Ability of Debris, Heavily Freighted with Coarse Clastic Materials, to flow on Gentle Slopes, *Sedimentology*, *23*(2), 213-234.

Rogerson, M., P.P.E. Weaver, E.J. Rohling, L.J. Lourens, J.W. Murray, and A. Hayes, (2006), Colour logging as a tool in high-resolution palaeoceanography, in *New Techniques in Sediment Core Analysis*, 267, edited by R.G. Rothwell, Geological Society of London, Special Publication, pp. 99-112, London.

Rothe, P. (1974), Canary Islands – Origin and Evolution, *Naturwissenschaften*, *61*(12), 526-533.

Rothwell, R. G., Pearce, T. J. and Weaver, P. P. E. (1992), Late quaternary evolution of the Madeira Abyssal plain, NE Atlantic, *Basin Res.*, 4, 103–131.

Rothwell, R.G., and F.R. Rack (2006), New techniques in sediment core analysis: an introduction, in *New Techniques in Sediment Core Analysis*, 267, edited by R.G. Rothwell, Geological Society of London, Special Publications, pp. 1-29, London.

Ruddimann, W.F., M. Sarnthein, J. Backman, J.G. Baldauf, W. Curry, L.M. Dupont, T. Janecek, E.M. Pokras, M.E. Raymo, B. Stabell, R. Stein, and R. Tiedemann (1989), Late Miocene to Pleistocene evolution of climate in Africa and the low-latitude Atlantic: overview of Leg 108 Results, *Preceeding of the Ocean Drilling Programme Science Results,* 108, 463-484.

S

Sarnthein, M., J. Thiede, U. Pflaumann, H. Erlenkeuser, D. Fuetterer, B. Koopmann, H. Large, and E. Seibold (1982), Atmospheric and oceanic circulation patterns off Northwest Africa during the past 25 million years, in: *Geology of the Northwest African continental margin*, edited by K.H.U von Rad, M. Sarnthein, and E. Seibold, pp. 584-604, Springer-Verlag, Berlin.

Satake, K., J.R. Smith, and K. Shinozaki (2001), Three-dimensional reconstruction and tsunami model of the Nuuanu and Wailau giant landslides, Hawaii, *Geophysical Monograph*, *128*, 333-346.

Sato, T., S. Chiyonobu, and D. Hodell (2009), Data Report: Quaternary calcareous nannofossil datums and biochronology in the North Atlantic Ocean, IODP Site U1308, in *Preceedings of the Integrated Ocean Drilling Program*, edited by J. E. T. Channell, T. Kanamatsu, T. Sato, R. Stein, C.A. Alvarez Zarikian, and M. J. Malone, Proc. IODP, 303/306, College Station, TX, doi:10.2204/iodp.proc.303306.210.2009.

Sblendorio-Levy, J., and R.W. Howe (1998), Calcareous nannofossil biostratigraphy of Site 953, Canary Basin, northeastern Noth Atlantic, in *Proceedings of the Ocean Drilling Program, Scientific Results*, 157, edited by P.P.E. Weaver, H.-U. Schmincke, J.V. Firth and W. Duffield, pp. 83-96, College Station, TX (Ocean Drilling Program).

Schiffman, P., and R. J. Southard (1996), Cation exchange capacity of layer silicates and palagonitized glass in mafic volcanic rocks: A comparative study of bulk extraction and in situ techniques, *Clays and Clay Minerals*, *44*(5), 624-634.

Schiffman, P., H. J. Spero, R. J. Southard, and D. A. Swanson (2000), Controls on palagonitization versus pedogenic weathering of basaltic tephra: Evidence from the consolidation and geochemistry of the Keanakako'i Ash Member, Kilauea Volcano, *Geochemistry Geophysics Geosystems*, *1*, 16.

Schmincke, H.-U. (1973), Magmatic evolution and tectonic regime in the Canary, Madeira and Azones island groups, *Geological Society of America Bulletin*, *84*(2), 633-648.

Schmincke, H.-U. (1982), Volcanic and chemical evolution of the Canary Islands, in *Geology of the Northwest African Continental Margin*, edited by U. Rad, K. Hinz, M. Santhein, and E. Seibold, Springer, New York.

Schmincke, H.-U., and B. Segschneider (1998), Shallow submarine to emergent basaltic shield volcanism of Gran Canaria: evidence from drilling into the volcanic apron, in *Proceedings of the Ocean Drilling Program, Scientific Results*, 157, edited by P.P.E. Weaver, H.-U. Schmincke, J.V. Firth and W. Duffield, pp. 141-181, College Station, TX (Ocean Drilling Program).

Schmincke, H.-U., P.P.E. Weaver, J.V. Firth, W.A. Duffield (1995), In: P.P.E. Weaver, H.-U. Schmincke, J.V. Firth, and W. Duffield (eds), *Proceeding of the Ocean*

Drilling Programme Initial Reports, 157, College Station, TX (Ocean Drilling Program).

Schmincke, H. U., A. Klugel, T. H. Hansteen, K. Hoernle, and P. van den Bogaard (1998), Samples from the Jurassic ocean crust beneath Gran Canaria, La Palma and Lanzarote (Canary Islands), *Earth and Planetary Science Letters*, *163*(1-4), 343-360.

Schneider, J.-L., Brunner, C.A., and Kuttner, S. (1998a), Epiclastic sedimentation during the upper Miocene-lower Pliocene volcanic hiatus of Gran Canaria: evidence from Sites 953 and 954, in *Proceedings of the Ocean Drilling Program, Scientific Results*, 157, edited by P.P.E. Weaver, H.-U. Schmincke, J.V. Firth and W. Duffield, pp. 293-314, College Station, TX (Ocean Drilling Program).

Scholz, C. A., M. R. Talbot, E. T. Brown, and R. P. Lyons (2011), Lithostratigraphy, physical properties and organic matter variability in Lake Malawi Drillcore sediments over the past 145,000 years, *Palaeogeography Palaeoclimatology Palaeoecology*, *303*(1-4), 38-50.

Schuster, R.L., and R.J. Krizek (1978), Landslides: analysis and control, *Transportation Research Board Special Report*, *176*, National Research Council, Washington.

Sclater, J.G., and P.A.F. Christie (1980), Continental Stretching: an explanation of the post-Cretaceous subsidence of the Central North Sea Basin, *Journal of Geophysical Research*, *85*, B7, 3711-3739.

Seville, J. P. K., C. D. Willett, and P. C. Knight (2000), Interparticle forces in fluidisation: a review, *Powder Technology*, *113*(3), 261-268.

Shackleton, N. J. (1987), Oxygen isotopes, ice volume and sea level, *Quaternary Science Reviews*, *6*(3-4), 183-190.

Shackleton, N. J. (2006), Formal Quaternary stratigraphy - What do we expect and need?, *Quaternary Science Reviews*, *25*(23-24), 3458-3461.

Shanmugam, G. (1997), The Bouma Sequence and the turbidite mind set, *Earth-Science Reviews*, *42*(4), 201-229.

Shanmugam, G. (2000), 50 years of the turbidite paradigm (1950s-1990s): deep-water processes and facies models – a critical perspective, *Mar. Petrol. Geol.*, 17, 2, 285-342.

Shanmugam, G. (2006), Deep-water Processes and Facies Models: Implications for Sandstone Petroleum Reservoirs, *Handbook of Petroleum Exploration and Production*, 5, Elsevier, Amsterdam.

Shanmugam, G., and R. J. Moiola (1983), Eustatic Control of Turbidites and Winnowed Turbidites – reply, *Geology*, *11*(1), 58-59.

Shiki, T., F. Kumon, Y. Inouchi, Y. Kontani, T. Sakamoto, M. Tateishi, H. Matsubara, and K. Fukuyama (2000a), Sedimentary features of the seismo-turbidites, Lake Biwa, Japan, *Sedimentary Geology*, *135*(1-4), 37-50.

Shiki, T., F. Kumon, Y. Inouchi, Y. Kontani, T. Sakamoto, M. Tateishi, H. Matsubara, and K. Fukuyama (2000b), Sedimentary features of the seismo-turbidites, Lake Biwa, Japan, *Sedimentary Geology*, *135*(1-4), 37-50.

Shipboard Scientific Party (1995), Site 950, in *Proceeding of the Ocean Drilling Programme Initial Reports*,H.-U. Schmincke, edited by H.-U. Schmincke, P.P.E

Weaver, J.V. Firth et al., pp. 51-104, College Station TX (Ocean Drilling Program), doi:10.2973/odp.proc.ir.157.104.1995.

Shipboard Scientific Party (1995), Site 951, in *Proceeding of the Ocean Drilling Programme Initial Reports*,H.-U. Schmincke, edited by H.-U. Schmincke, P.P.E Weaver, J.V. Firth et al., pp. 105-134, College Station TX (Ocean Drilling Program), doi:10.2973/odp.proc.ir.157.105.1995.

Shipboard Scientific Party (1995), Site 952, in *Proceeding of the Ocean Drilling Programme Initial Reports*,H.-U. Schmincke, edited by H.-U. Schmincke, P.P.E Weaver, J.V. Firth et al., pp. 135-1178, College Station TX (Ocean Drilling Program), doi:10.2973/odp.proc.ir.157.106.1995.

Siebert, L. (1984), Large volcanic debris avalanches: Characteristics of source areas, deposits, and associated eruptions, *Journal of Volcanology and Geothermal Research*, *22*(3-4), 163-197.

Siebert, L., H. Glicken, and U. Tadahide (1987), Volcanic hazards from Bezymianny- and Bandai-type eruptions, *Bulletin of Volcanolog*, *49*(1), 435-459.

Skene, K. I., and D. J. W. Piper (2003), Late Quaternary stratigraphy of Laurentian Fan: a record of events off the eastern Canadian continental margin during the last deglacial period, *Quaternary International*, 99-100, 135-152.

Skene, K. I., and D. J. W. Piper (2006), Quaternary seismic stratigraphy of Laurentian Fan, *Mar. Geol.*, 227, 67-82.

Sleep, N. H. (1992), Hotspot Volcanism and Mantle Plumes, *Annual Review of Earth and Planetary Sciences*, *20*, 19-43.

Stein, R. (1985), Late Neogene changes in paleoclimate and paleoproductivity off Northwest Africa (D.S.D.P Site 397), *Palaeogeography Palaeoclimatology Palaeoecology*, *49*(1-2), 47-59.

Steiner, C., A. Hobson, P. Favre, G. M. Stampfli, and J. Hernandez (1998), Mesozoic sequence of Fuerteventura (Canary Islands): Witness of Early Jurassic sea-floor spreading in the central Atlantic, *Geological Society of America Bulletin*, *110*(10), 1304-1317.

Stets, J., and Wurster, P. (1982), Atlas and Altantic-structural relationships, in *Geology of the Northwest African Continental Margin*, edited by U. von Rad, K. Hinz, M. Sarnthein and E. Seiboid, Springer-Verlag, Berlin.

Stevenson, C.J., P.J. Talling, R.B. Wynn, D.G. Masson, J.E. Hunt, M. Frenz, A. Akhmetzhanhov, and B.T. Cronin (in press), The flows that left no trace: Very large-volume turbidity currents that bypassed sediment through submarine channels without eroding the sea floor, *Marine Petroleum Geology,* doi:10.1016/j.marpetgeo.2012.008.

Stillman, C. J. (1999), Giant Miocene landslides and the evolution of Fuerteventura, Canary Islands, *Journal of Volcanology and Geothermal Research*, *94*(1-4), 89-104.

Stow, D. A. V., and A. J. Bowen (1980), Physical model for the transport and sorting of fine-grained sediment by turbidity currents, *Sedimentology*, *27*(1), 31-46.

Stow, D. A. V., and G. Shanmugam (1980), Sequence of Structures in Fine-Grained Turbidite – Comparison of Recent Deep-sea and Ancient Flysch Sediments, *Sedimentary Geology*, *25*(1-2), 23-42.

Stow, D.A.V., and D.J.W. Piper (1984), Deep-water fine-grained sediments; history, methodology and terminology, in *Fine-grained Sediments: Deep-water Processes and Facies*, 15, edited by D.A.V. Stow and D.J.W. Piper, Geological Society of London, Special Publications, pp. 3-14, London, doi:10.1144/GSL.SP.1984.015.01.01.

Stow, D.A.V., and A.R. Tabrez (1998), Hemipelagites: processes, facies and model, in *Geological Processes on Continental Margins: Sedimentation, Mass-Wasting and Stability*, 129, edited by M.S. Stoker and D. Evans, Geological Society of London, Special Publications, pp. 317-337, London.

Stow, D.A.V., H.G. Reading, and J.D. Collinson (1996), Deep Seas, in H.G. Reading (ed), *Sedimentary Environments: Processes, Facies and Stratigraphy*, 3rd edn., Blackwell Science Ltd., Oxford

Stow, D. A. V., J.-C. Faugeres, A. Viana, and E. Gonthier (1998), Fossil contourites: a critical review, *Sedimentary Geology*, *115*(1-4), 3-31.

Stow, D.A.V., J.-C. Faugeres, J.A. Howe, C.J. Pudsey, and A.R. Viana (2002), Bottom currents, contourites and deep-sea sediment drifts: current state-of-the-art, in Deep-Water Contourite Systems: Modern Drifts and Ancient Series, Seismic and Sedimentary Characteristics, edited by D.A.V. Stow, C.J. Pudsey, J.A. Howe, J.-C. Faugeres, and A.R. Viana (2002), Spec. Publ. Geol. Soc. London, 22, 7-20.

Stroncik, N. A., and H. U. Schmincke (2001), Evolution of palagonite: Crystallization, chemical changes, and element budget, *Geochemistry Geophysics Geosystems*, *2*, 43.

Stroncik, N. A., and H. U. Schmincke (2002), Palagonite - a review, *International Journal of Earth Sciences*, *91*(4), 680-697.

Strout, J. M., and T. I. Tjelta (2005), In situ pore pressures: What is their significance and how can they be reliably measured?, *Marine and Petroleum Geology*, *22*(1-2), 275-285.

Sultan, N., P. Cochonat, J. P. Foucher, and J. Mienert (2004), Effect of gas hydrates melting on seafloor slope instability, *Marine Geology*, *213*(1-4), 379-401.

Sumita, M., and H.-U. Schmincke (1998), Tephra event stratigraphy and emplacement of volcaniclastic sediments, Morgan and Fataga stratigraphic intervals, Part 1: mineral and chemical stratigraphy of volcaniclastic units and correlation to the subaerial record, in *Proceedings of the Ocean Drilling Programme Scientific Results,* 157, edited by P.P.E. Weaver, H.-U. Schmincke, J.V. Firth, and W. Duffield (eds), pp. 219-266, College Station, TX (Ocean Drilling Program).

Summerhayes, C.P., A.H. Nutter, and J.S. Tooms (1971), Geological Structure and Development of Continental Margin of Northwest Africa, *Marine Geology*, *11*(1), 1-25.

Summerhayes, C. P., J. D. Milliman, S. R. Briggs, A. G. Bee, and C. Hogan (1976), Northwest African Shelf Sediments – Influence of Climate and Sedimentary Processes, *Journal of Geology*, *84*(3), 277-300.

Swanson, D.A., W.A. Duffield, and R.S. Fiske (1976), *Displacement of the south flank of Kilauea Volcano: The result of forceful intrusion of magma into the rift zones: interpretation of geodetic and geologic information leads to a new model for the structure of Kilauea Volcano*, U.S. Government, Washington, QE523.K5.S9.

Synolakis, C. E., J. P. Bardet, J. C. Borrero, H. L. Davies, E. A. Okal, E. A. Silver, S. Sweet, and D. R. Tappin (2002), The slump origin of the 1998 Papua New Guinea Tsunami, *Proceedings of the Royal Society of London Series a-Mathematical Physical and Engineering Sciences*, *458*(2020), 763-789.

Szeremeta, N., C. Laj, H. Guillou, C. Kissel, A. Mazaud, and J. C. Carracedo (1999), Geomagnetic paleosecular variation in the Brunhes period, from the island of El Hierro (Canary Islands), *Earth and Planetary Science Letters*, *165*(3-4), 241-253.

T

Talling, P. J., R.B. Wynn, D.G. Masson, M. Frenz, B.T. Cronin, R. Schiebel, A.M. Akhmetzhanov, S. Dallmeier-Tiessen, S. Benetti, P.P.E. Weaver, A. Georgiopoulou, C. Zühlsdorff, and L.A. Amy (2007), Onset of submarine debris flow deposition far from original giant landslide, *Nature*, *450*(7169), 541-544.

Tappin, D.R., P. Watts, G.M. McMurtry, Y. Lafoy, and T. Matsumoto (2001), The Sissano, Papua New Guinea tsunami of July, 1998: offshore evidence on the source mechanism, *Marine Geology*, *175*, 1-24.

Tappin, D. R. (2010), Submarine mass failures as tsunami sources: their climate control, *Philosophical Transactions of the Royal Society a-Mathematical Physical and Engineering Sciences*, *368*(1919), 2417-2434.

Taron, J., D. Elsworth, G. Thompson, and B. Voight (2007), Mechanisms for rainfall-concurrent lava dome collapses at Soufriere Hills Volcano, 2000-2002, *Journal of Volcanology and Geothermal Research*, *160*(1-2), 195-209.

Ten Brink, U. S., R. Barkan, B. D. Andrews, and J. D. Chaytor (2009), Size distributions and failure initiation of submarine and subaerial landslides, *Earth and Planetary Science Letters*, *287*(1-2), 31-42.

Ternois, Y., M. A. Sicre, and M. Paterne (2000), Climatic changes along the northwestern African continental margin over the last 30 kyrs, *Geophysical Research Letters*, *27*(1), 133-136.

Thirlwall, M. F., B. S. Singer, and G. F. Marriner (2000), Ar-39-Ar-40 ages and geochemistry of the basaltic shield stage of Tenerife, Canary Islands, Spain, *Journal of Volcanology and Geothermal Research*, *103*(1-4), 247-297.

Thomson, J., S. Colley, N.C. Niggs, D.J. Hydes, T.R.S Wilson, and J. Sørensen (1987), Geochemical oxidation fronts in NE Atlantic distal turbidites and their effects in the sedimentary record, in *Geology and Geochemistry of Abyssal Plains*, 31, edited by P.P.E. Weaver and J. Thomson, Geological Society of London, Special Publication, pp. 167-177, London.

Thomson, J., I. Jarvis, D.R.H. Green, and D. Green (1998), Oxidation fronts in Madeira Abyssal Plain turbidites: persistence of early diagenetic trace-element enrichments during burial, Site 950, in, *Proceeding of the Ocean Drilling Programme Scientific Result*, 157, edited by P.P.E. Weaver, H.-U. Schmincke, J.V. Firth, and W. Duffield, pp. 559-571, College Station, TX (Ocean Drilling Program).

Thomson, J., I.W. Croudace, and R.G. Rothwell (2006), A geochemical application of the ITRAX scanner to a sediment core containing eastern Mediterranean sapropel

units, in *New Techniques in Sediment Core Analysis*, 267, edited by R.G. Rothwell, Geological Society of London, Special Publications, pp. 1-29, London.

Thunell, R. C. (1982), Carbonate dissolution and abyssal hydrography in the Atlantic Ocean, *Marine Geology*, *47*(3-4), 165-180.

Tinti, S., E. Bortolucci, and A. Armigliato (1999), Numerical simulation of the landslide-induced tsunami of 1988 on Vulcano Island, Italy, *Bulletin of Volcanology*, *61*(1-2), 121-137.

Tinti, S., E. Bortolucci, and C. Romagnoli (2000), Computer simulations of tsunamis due to sector collapse at Stromboli, Italy, *Journal of Volcanology and Geothermal Research*, *96*(1-2), 103-128.

Tjallingii, R., U. Rohl, M. Kolling, and T. Bickert (2007), Influence of the water content on X-ray fluorescence core-scanning measurements in soft marine sediments, *Geochemistry Geophysics Geosystems*, *8*, 12.

Trifunac, M. D., A. Hayir, and M. I. Todorovska (2003), A note on tsunami caused by submarine slides and slumps spreading in one dimension with nonuniform displacement amplitudes, *Soil Dynamics and Earthquake Engineering*, *23*(3), 223-234.

Trofimovs, J., et al. (2010), Evidence for carbonate platform failure during rapid sea-level rise; ca 14 000 year old bioclastic flow deposits in the Lesser Antilles, *Sedimentology*, *57*(3), 735-759.

Turner, A.K., and R.L. Schuster, R.L. (1996), Landslides: Investigation and Mitigation, *Trans. Res. Board Spec. Rep.,* 247, National Academy Press, Washington, DC.

Twichell, D. C., J. D. Chaytor, U. S. ten Brink, and B. Buczkowski (2009), Morphology of late Quaternary submarine landslides along the US Atlantic continental margin, *Marine Geology*, *264*(1-2), 4-15.

U

Urgeles, R., M. Canals, J. Baraza, B. Alonso, and D. Masson (1997), The most recent megalandslides of the Canary Islands: El Golfo debris avalanche and Canary debris flow, west El Hierro island, *Journal of Geophysical Research-Solid Earth*, *102*(B9), 20305-20323.

Urgeles, R., D. G. Masson, M. Canals, A. B. Watts, and T. Le Bas (1999), Recurrent large-scale landsliding on the west flank of La Palma, Canary Islands, *Journal of Geophysical Research-Solid Earth*, *104*(B11), 25331-25348.

Urgeles, R., M. Canals, and D. G. Masson (2001), Flank stability and processes off the western Canary Islands: a review from El Hierro and La Palma, *Scientia Marina*, *65*, 21-31.

V

Vail, P.R. (1987), Seismic stratigraphy interpretation procedure, in *Seismic Stratigraphic Atlas*, *American Association of Petroleum Geologists*, *Studies in Geology*, 27, edited by B. Bailey, pp. 1-10, Tulsa, USA.

Vail, P.R., and R.G. Todd (1981), Northern and North Sea Jurassic unconformities, chronostratigraphy and sea-level changes from seismic stratigraphy, in *Petroleum Geology of the Continental Shelf of North-West Europe*, *Proceedings of Second Conference*, edited by L.V. Illing and G.D. Hobson, pp. 216-235, Heyden, London, UK.

Vail, P.R., R.M. Mitchum, and S. Thompson III (1977), Seismic stratigraphy and global changes of sea level, Part 4: Global cycles of relative changes of sea level, in Payton, C.E. (eds) *Seismic Stratigraphy – Application to Hydrocarbon Exploration*, *American Association of Petroleum Geologists*, 26, Tulsa, USA.

Van den Bogaard, P., and H.-U. Schmincke (1998), $^{40}Ar/^{39}Ar$ of Pliocene-Pleistocene fallout tephra layers and volcaniclastic deposits in the sedimentary aprons of Gran Canaria and Tenerife (Sites 953, 954, and 956), in *Proceedings of the Ocean Drilling Programm*, 157, edited P.P.E. Weaver, H.-U. Schmincke, J.V. Firth, and W. Duffield, pp. 329-341, College Station, TX (Ocean Drilling Program).

Van Nieuwkoop, J.C.C. (2007), Experimental and numerical modelling of tsunami waves generated by landslides, Unpublished *MSc thesis*, 164pp, Delft University of Technology, Nov. 2007.

Velde, B. (1995), Clay Minerals: a physcio-chemical explanation of their occurrence, *Developments in Sedimentology*, 40, Elsevier Science Publishers, Amsterdam, Netherlands.

Venturi, M., and S. Bughi (2001), Geo-hazard Assessment for Pipelines Crossing the Continental Slope, *Proceedings of the Eleventh (2001) International Offshore and Polar Engineering Conference*, June 17-22, 2001, Staveanger, Norway.

Vogt, P. R. (1974), Volcano spacing and thickness of the lithosphere, *Earth and Planetary Science Letters*, *21*(3), 235-252.

Voight, B., and D. Elsworth (1997), Failure of volcano slopes, *Geotechnique*, *47*(1), 1-31.

Voight, B., R. J. Janda, H. Glicken, and P. M. Douglass (1983), Nature and mechanics of the Mount St Helens rockslide-avalanche of 18 May 1980, *Geotechnique*, *33*(3), 243-273.

Volker, D., T. Reichel, M. Wiedicke, and C. Heubeck (2008), Turbidites deposited on Southern Central Chilean seamounts: Evidence for energetic turbidity currents, *Marine Geology*, *251*(1-2), 15-31.

W

Walter, T. R., and H. U. Schmincke (2002), Rifting, recurrent landsliding and Miocene structural reorganization on NW-Tenerife (Canary Islands), *International Journal of Earth Sciences*, *91*(4), 615-628.

Walter, T. R., V. R. Troll, B. Cailleau, A. Belousov, H. U. Schmincke, F. Amelung, and P. Von der Bogaard (2005), Rift zone reorganization through flank instability in ocean island volcanoes: an example from Tenerife, Canary Islands, *Bulletin of Volcanology*, *67*(4), 281-291.

Ward, S. N. (2001), Landslide tsunami, *Journal of Geophysical Research-Solid Earth*, *106*(B6), 11201-11215, doi:10.1029/2000JB900450.

Ward, S. N., and S. Day (2001), Cumbre Vieja Volcano - Potential collapse and tsunami at La Palma, Canary Islands, *Geophysical Research Letters*, *28*(17), 3397-3400, doi:10.1029/2001GL013110.

Ward, S. N., and S. Day (2003), Ritter Island Volcano - lateral collapse and the tsunami of 1888, *Geophysical Journal International*, *154*(3), 891-902.

Watt, S. F. L., P. J. Talling, M. E. Vardy, V. Heller, V. Huhnerbach, M. Urlaub, S. Sarkar, D. G. Masson, T. J. Henstock, T. A. Minshull, M. Paulattu, A. Le Friant, E. Lebas, C. Berndt, G. J. Crutchley, J. Karstens, A. J. Stinton, and F. Maeno (2012), Combinations of volcanic-flank and seafloor-sediment failure offshore Monserrat, and their implications for tsunami generation, *Earth Planet. Sci. Lett.*, 319-320, 228-240.

Watts, A. B., and D. G. Masson (1995), A giant landslide on the north flank of Tenerife, Canary Islands, *Journal of Geophysical Research-Solid Earth*, *100*(B12), 24487-24498, doi:10.1029/95JB02630.

Watts, A. B., and D. G. Masson (1998), Comment on "A giant landslide on the north flank of Tenerife, Canary Islands" by A.B. Watts and D.G. Masson - Reply, *Journal of Geophysical Research-Solid Earth*, *103*(B5), 9949-9952.

Watts, A. B., and D. G. Masson (2001), New sonar evidence for recent catastrophic collapses of the north flank of Tenerife, Canary Islands, *Bulletin of Volcanology*, *63*(1), 8-19, doi:10.1007/s004450000119.

Watts, P. 2003, Probabilistic analyses of landslide tsunami hazards, *Submarine Mass Movements and Their Consequences*, 19, 163-170.

Waythomas, C. F., P. Watts, F. Y. Shi, and J. T. Kirby (2009), Pacific Basin tsunami hazards associated with mass flows in the Aleutian arc of Alaska, *Quaternary Science Reviews*, *28*(11-12), 1006-1019.

Weaver, P. P. E. (1994), Determining the erosional characteristics from reworked coccolith assemblages, Canary Basin, N.E. Atlantic, *Sedimentology*, *41*(5), 1025-1038.

Weaver, P. P. E. (2003), Northwest African Continental Margin: History of sediment accumulation, landslide deposits, and hiatuses as revealed by drilling the Madeira Abyssal Plain, *Paleoceanography*, *18*(1), 13.

Weaver, P. P. E., and A. Kuijpers (1983), Climatic control of turbidite deposition on the Madeira Abyssal Plain, *Nature*, *306*(5941), 360-363.

Weaver, P.P.E., and R.G. Rothwell (1987), Sedimentation on the Madeira Abyssal Plain over the last 300,000 years, in *Geology and Geochemistry of Abyssal Plains*, 31, edited by P.P.E. Weaver and J. Thomson, Geological Society of London, Special Publication, pp. 71-86, London.

Weaver, P. P. E., and J. Thomson (1993), Calculating erosion by deep-sea turbidity currents during initiation and flow, *Nature*, *364*(6433), 136-138.

Weaver, P. P. E., R. G. Rothwell, J. Ebbing, D. Gunn, and P. M. Hunter (1992), Correlation, frequency of emplacement and source directions of megaturbidites on the Madeira Abyssal Plain, *Marine Geology*, *109*(1-2), 1-20.

Weaver, P.P.E., I. Jarvis, S.M. Lebreiro, B. Alibes, J. Baraza, R. Howe, and R.G. Rothwell (1998), The Neogene turbidite sequence on the Madeira Abyssal Plain – a

history of basin filling and early diagenesis, in *Proceedings of the Ocean Drilling Scientific Results*, 157, edited by P.P.E. Weaver, H.-U. Schmincke, J.V. Firth, and W. Duffield, pp. 619-634, College Station, TX (Ocean Drilling Program).

Weaver, P. P. E., R. B. Wynn, N. H. Kenyon, and J. Evan (2000), Continental margin sedimentation, with special reference to the north-east Atlantic margin, *Sedimentology*, *47*, 239-256.

Weber, M. E., M. H. Wiedicke, H. R. Kudrass, C. Hubscher, and H. Erlenkeuser (1997), Active growth of the Bengal Fan during sea-level rise and highstand, *Geology*, *25*(4), 315-318.

Weber, M. E., M. Wiedicke-Hombach, H. R. Kudrass, and H. Erlenkeuser (2003), Bengal Fan sediment transport activity and response to climate forcing inferred from sediment physical properties, *Sedimentary Geology*, *155*(3-4), 361-381.

Wei, W., and A. Peleo-Alampay (1993), Updated Cenozoic Nannofossil Magnetobiochronology, *INA Newsletter*, 15, 15-17.

Weltje, G. J., and R. Tjallingii (2008), Calibration of XRF core scanners for quantitative geochemical logging of sediment cores: Theory and application, *Earth and Planetary Science Letters*, *274*(3-4), 423-438.

Whelan, F., and D. Kelletat (2003), Submarine slides on volcanic islands - a source for mega-tsunamis in the Quaternary, *Progress in Physical Geography*, *27*(2), 198-216.

Whelan, T., J. M. Coleman, J. N. Suhayda, and H. H. Roberts (1977), Accoustical penetration and shear-strength in gas-charged sediment, *Marine Geotechnology*, *2*, 147-160.

Wilson, J. T. (1963), A possible origin of the Hawaiian Islands, *Can. J. Phys.*, 41, 863-870.

Wilson, C.K., D. Long, and J. Bulat (2003), The Afen Slide – a Multistage Slope Failure in the Faroeshetland Channel, *Submarine Mass Movements and Their Consequences*, *19(2)*, 317-324, doi:10.1007/978-94-010-0093-2_35.

Wilson, T. R. S., J. Thomson, D. J. Hydes, S. Colley, F. Culkin, and J. Sorensen (1986), Oxidation fronts in pelagic sediments – diagenetic formation of metal-rich layers, *Science*, *232*(4753), 972-975.

Wynn, R. B., and D.G. Masson (2003), Canary island landslides and tsunami generation: can we use turbidite depositis to interpret landslide processes, *Submarine mass movements and their consequences*, *19*, 325–332.

Wynn, R. B., D. G. Masson, D. A. V. Stow, and P. P. E. Weaver (2000a), The Northwest African slope apron: a modern analogue for deep-water systems with complex seafloor topography, *Marine and Petroleum Geology*, *17*(2), 253-265.

Wynn, R. B., P. P. E. Weaver, G. Ercilla, D. A. V. Stow, and D. G. Masson (2000b), Sedimentary processes in the Selvage sediment-wave field, NE Atlantic: new insights into the formation of sediment waves by turbidity currents, *Sedimentology*, *47*(6), 1181-1197.

Wynn, R. B., N. H. Kenyon, D. G. Masson, D. A. V. Stow, and P. P. E. Weaver (2002c), Characterization and recognition of deep-water channel-lobe transition zones, *AAPG Bulletin*, *86*(8), 1441-1462.

Wynn, R. B., P. P. E. Weaver, D. G. Masson, and D. A. V. Stow (2002a), Turbidite depositional architecture across three interconnected deep-water basins on the north-west African margin, *Sedimentology*, *49*(4), 669-695.

Wynn, R. B., D. J. W. Piper, and M. J. R. Gee (2002b), Generation and migration of coarse-grained sediment waves in turbidity current channels and channel-lobe transition zones, *Marine Geology*, *192*(1-3), 59-78.

Wynn, R. B., P. J. Talling, D. G. Masson, C. J. Stevenson, B. T. Cronin, and T. P. Le Bas (2010), Investigating the Timing, Processes and Deposits of One of the World's Largest Submarine Gravity Flows: The 'Bed 5 Event' Off Northwest Africa, *Submarine Mass Movements and Their Consequences*, *28*, 463-474.

Wynn, R. B., P. J. Talling, D. G. Masson, T. P. Le Bas, B. T. Cronin, and C. J. Stevenson (2012), The influence of subtle gradient changes on deep-water gravity flows: a case study from the Moroccan Turbidite System, *SEPM Spec. Publ.*, 99, 371-383.

Y

Yuan, F., L. Z. Wang, Z. Guo, and R. W. Shi (2012), A refined analytical model for landslide or debris flow impact on pipelines. Part I: Surface pipelines, *Applied Ocean Research*, *35*, 95-104.

Z

Zakeri, A., K. Hoeg, and F. Nadim (2008), Submarine debris flow impact on pipelines - Part I: Experimental investigation, *Coastal Engineering*, *55*(12), 1209-1218.

Zhou, Z., and W. S. Fyfe (1989), Palagonitisation of basaltic glass from DSDP Site 335, Leg 37: textures, chemical composition, and mechanism of formation, *American Mineralogist*, *74*(9-10), 1045-1053.